

# Geodätisch-geophysikalische Arbeiten in der Schweiz

(Fortsetzung der Publikationsreihe  
«Astronomisch-geodätische Arbeiten in der Schweiz»)

herausgegeben von der

Schweizerischen Geodätischen Kommission  
(Organ der Akademie der Naturwissenschaften Schweiz)

**Siebenundneunzigster Band**  
**Volume 97**

**Co-Location of  
Geodetic Observation Techniques  
in Space**

Benjamin Männel

2016

Adresse der Schweizerischen Geodätischen Kommission:

Institut für Geodäsie und Photogrammetrie  
Eidg. Technische Hochschule Zürich  
ETH Zürich  
8093 Zürich  
Switzerland

Internet: <http://www.sgc.ethz.ch>

ISBN 978-3-908440-43-7

Redaktion des 97. Bandes:  
Dr. B. Männel, J. Müller-Gantenbein, Prof. M. Rothacher  
Druck: Print-Atelier ADAG, Zürich

## VORWORT

Sehr genaue und äusserst stabile terrestrische Referenzsysteme sind heute von grosser Bedeutung für die Positionierung auf der Erde und im Weltraum und für das Erfassen des Systems Erde. Dabei stellt das Messen von Meeresspiegeländerungen sicherlich die grösste Herausforderung dar. Daher fordert das Globale Geodätische Beobachtungs-System (GGOS) der International Assoziation für Geodäsie (IAG), dass der terrestrische Bezugsrahmen eine Genauigkeit von 1 mm für Stationspositionen und eine Stabilität von 0.1 mm/Jahr für Stationsgeschwindigkeiten aufweisen soll. Zurzeit sind wir noch weit vom Erreichen dieser Anforderungen entfernt.

Das genaueste terrestrische Referenzsystem ist heute das International Terrestrial Reference Frame (ITRF2014). Es ist das Resultat einer Kombination der vier wichtigsten geodätischen Weltraumverfahren, nämlich Global Navigation Satellite Systems (GNSS), Very Long Baseline Interferometry (VLBI), Satellite Laser Ranging (SLR) und Doppler Orbitography and Radiopositioning Integrated by Satellite (DORIS). Um ein einheitliches und konsistentes ITRF zu erhalten, müssen die vier Beobachtungstechniken auf Fundamentalstationen verknüpft werden, wo Instrumente von mehr als einer Technik am selben Ort aufgestellt sind. Die lokalen Verknüpfungen zwischen den Referenzpunkten (die Exzentrizitätsvektoren) der Instrumente müssen dabei sehr genau bekannt sein ( $\leq 1$  mm), heute einer der kritischsten Aspekte für die Genauigkeit und die Stabilität des ITRF. Neben den Defiziten in diesen lokalen Exzentrizitätsmessungen ist es zudem schwierig, die Ursachen für technik-spezifische systematische Fehler der individuellen Techniken zu ergründen und diese Fehler zu reduzieren. Als eine Alternative und eine echte Ergänzung zur Verknüpfung der vier geodätischen Beobachtungstechniken am Boden kann die Verknüpfung im Prinzip auch auf Satelliten mit entsprechenden Empfängern und Sendern erfolgen. Dies ist genau das Thema der Dissertation von Dipl.-Ing. Benjamin Männel. Die Doktorarbeit befasst sich sehr grundsätzlich mit den Vor- und Nachteilen einer Ko-lokation im Weltraum, sei es auf GNSS- oder auf tieffliegenden Satelliten (LEO). Die Bedeutung dieses Themas ist offensichtlich, da bereits zwei Anträge für Satellitenmissionen – die GRASP-Mission bei der NASA und die E-GRASP/Erathostenes-Mission bei ESA – eingereicht wurden, um diese Ko-lokation auf einem LEO zu realisieren. Sogar in der Schweiz wurde eine erste Studie für eine kombinierte Mission mit Tests der Allgemeinen Relativitätstheorie und mit der Ko-lokation von geodätischen Instrumenten im Weltraum, die sogenannte E-GRIP (Einstein General Relativity Invariance Principle) Mission, für das Swiss Space Office (SSO) durchgeführt. Vor Kurzem wurden zudem erstmals erfolgreiche Messungen des L-Band Signals von GPS- und GLONASS-Satelliten mit VLBI-Teleskopen vorgenommen, was einen neuen Weg für die Verknüpfung verschiedener Beobachtungstechniken eröffnet. Ein bedeutender Teil der Dissertation widmet sich schliesslich der kombinierten Verarbeitung von GNSS-Beobachtungen, die von GNSS-Empfängern am Boden (IGS-Netz) und von GNSS-Empfängern auf tieffliegenden Satelliten stammen. Benjamin Männel konnte dabei zeigen, dass die Bestimmung der Koordinaten des Massenschwerpunkts der Erde durch das Hinzufügen von Beobachtungen auf tieffliegenden Satelliten stark verbessert werden kann. Insgesamt leistet Benjamin Männel mit den umfassenden, im Rahmen seiner Dissertation durchgeführten Studien einen international bedeutenden Beitrag zum Thema der Ko-lokation der geodätischen Beobachtungstechniken im Weltraum. Die SGK dankt sowohl dem Autor Benjamin Männel für den wertvollen Beitrag als auch der Schweizerischen Akademie für Naturwissenschaften (SCNAT) für die Übernahme der Druckkosten.

**Prof. Dr. M. Rothacher**  
Institut für Geodäsie und Photogrammetrie  
ETH Zürich

**Prof. Dr. A. Geiger**  
ETH Zürich  
Präsident der SGK

## PREFACE

De nos jours, il est extrêmement important de pouvoir disposer de cadres de références précis et stable. Ceci, afin de pouvoir garantir le positionnement sur Terre, dans l'espace et pour permettre le monitoring du système physique de notre Terre. A ce propos, la détermination globale de la variation du niveau des mers en est certainement la plus dépendante. Par conséquent, le système global d'observation géodésique (GGOS) de l'association internationale de géodésie (IAG) stipule que le cadre de référence terrestre doit être connu avec une précision de 1mm et de 0.1mm/année pour les positions et les vitesses des stations, respectivement. Actuellement, nous sommes encore loin de remplir ces exigences.

Aujourd'hui, le International Terrestrial Reference Frame (ITRF2014) représente le cadre de référence global le plus précis. Il résulte de la combinaison de quatre techniques de géodésie spatiale qui sont : les systèmes globaux de positionnement par satellites (GNSS), l'interférométrie à longue base (VLBI), la télémétrie laser sur satellites (SLR) ainsi que le système de détermination d'orbite et radiopositionnement intégré par satellite (DORIS). Afin d'obtenir un cadre ITRF consistant et unique, les quatre techniques doivent être reliées aux stations fondamentales qui disposent de l'instrumentation de plusieurs de ces techniques. Ces liaisons locales (vecteurs excentriques) entre les points de références des différents instruments doivent être connus très précisément ( $\leq 1$  mm) et sont actuellement une des problématique les plus critique pour garantir la précision et la stabilité de l'ITRF. Outre les déficiences de ces liaisons locales terrestres, les biais spécifiques aux différentes techniques géodésiques spatiales s'avèrent très difficiles à identifier et à réduire. Comme alternative et comme complément réel pour relier les techniques spatiales géodésiques au sol, les liaisons pourraient être réalisées à bord des satellites en embarquant des récepteurs ou des émetteurs des quatre techniques sur des satellites préalablement parfaitement bien calibrés. C'est exactement là où la thèse du Dipl.-Ing. Benjamin Männel s'inscrit. Sa thèse est consacrée aux recherches sur les avantages d'une co-localisation des techniques géodésiques spatiales à bord des satellites, qu'il s'agisse de satellites GNSS ou satellite en orbite basse (LEO). L'importance de ce sujet devient évidente étant donné que deux missions satellites (proposition GRASP soumise à la NASA et proposition E-GRASP / Erathostenes soumise à l'ESA) ont été proposées pour réaliser la co-localisation des quatre techniques à bord d'un satellite en orbite basse (LEO). Même en Suisse, une première étude pour une mission combinée de relativité et de co-localisation appelée E-GRIP (principe d'invariance de la relativité générale d'Einstein) a été réalisée pour le programme spatial suisse (SSO). De plus, les premières observations des signaux GPS et GLONASS (bande L) avec les télescopes VLBI ont été couronnées de succès, ouvrant une nouvelle voie pour relier les différentes techniques de géodésie spatiale. Enfin, une partie importante du travail a été consacrée au traitement combiné des LEO avec récepteurs GNSS embarqués et du réseau GNSS au sol, montrant que la détermination des coordonnées du centre de masse de la Terre peut être considérablement améliorée par l'ajout de données GNSS provenant des LEO.

En résumé, les recherches approfondies menées par Benjamin Männel au cours de sa thèse représentent une contribution internationale importante au thème général de la co-localisation dans l'espace. La Commission Géodésique Suisse (CGS) est reconnaissante envers l'Académie Suisse des Sciences Naturelles (SCNAT) pour avoir pris à sa charge les coûts d'impression du présent manuscrit.

**Prof. Dr. M. Rothacher**  
Institut de Géodésie et Photogrammétrie  
ETH Zürich

**Prof. Dr. A. Geiger**  
ETH Zürich  
Président de la CGS

## FOREWORD

Nowadays highly accurate and stable terrestrial and celestial reference frames are extremely important for the positioning on the Earth and in space and the monitoring of the Earth system. The most stringent requirements are certainly arising from measurements of sea-level change. Therefore, the Global Geodetic Observing System (GGOS) of the International Association of Geodesy (IAG) states that the terrestrial reference frame has to be accurate at the 1 mm level for station positions and stable at the 0.1 mm/year level for station velocities. At present, we are still far away from fulfilling these requirements.

The most accurate terrestrial reference frame is the International Terrestrial Reference Frame (ITRF2014). It is the result of a combination of four space geodetic techniques, namely Global Navigation Satellite Systems (GNSS), Very Long Baseline Interferometry (VLBI), Satellite Laser Ranging (SLR) and Doppler Orbitography and Radiopositioning Integrated by Satellite (DORIS). In order to obtain a unique and consistent ITRF, the four techniques have to be linked at fundamental stations, where instruments from more than one observation technique are co-located. The local ties (eccentricity vectors) between the reference points of the instruments have to be very accurately known ( $\leq 1$  mm) and represent one of the most critical issues today for the accuracy and stability of the ITRF. Besides deficiencies in these local ties, the technique-specific biases of the individual space geodetic techniques prove to be very difficult to identify and reduce.

As an alternative and as a real complement to linking the space-geodetic techniques on ground, the links could be realized onboard satellites by putting receivers or emitters for the four techniques onboard well-calibrated satellites. This is exactly, where the PhD thesis of Dipl.-Ing. Benjamin Männel sets in. The thesis is devoted to investigations of the benefits from a co-location of the space geodetic techniques onboard satellites, be it GNSS or Low Earth Orbiting (LEO) satellites. The importance of this topic becomes obvious in view of the fact, that two satellite missions (GRASP proposal submitted to NASA and E-GRASP/Erathostenes proposal submitted to ESA) have been proposed to realize the co-location of the four techniques onboard a Low Earth Orbiting (LEO) satellite. Even in Switzerland, a first study for a combined relativity and co-location mission called E-GRIP (Einstein General Relativity Invariance Principle) has been performed for the Swiss Space Office (SSO). In addition, first measurements of the GPS and GLONASS L-band signals with VLBI telescopes have been successful, opening a new way to connect the different space geodetic techniques. Finally, a significant part of the work was dedicated to the combined processing of LEOs with GNSS receivers onboard and the GNSS ground network, showing that the determination of the coordinates of Earth's geocenter can be significantly improved by adding GNSS data from LEOs.

In summary, the comprehensive studies conducted by Benjamin Männel in the course of his dissertation represent an important international contribution to the overall theme of co-location in space.

The SGC thanks the author for his valuable contribution as well as the Swiss Academy of Sciences (SCNAT) for covering the printing costs of this volume.

**Prof. Dr. M. Rothacher**  
Institute for Geodesy and Photogrammetry  
ETH Zürich

**Prof. Dr. A. Geiger**  
ETH Zürich  
President of SGC



# Contents

<b>List of Contents</b>	<b>I</b>
<b>List of Tables</b>	<b>III</b>
<b>List of Figures</b>	<b>V</b>
<b>1 Motivation and Introduction</b>	<b>1</b>
<b>2 Geodetic Observation Techniques in a Nutshell</b>	<b>7</b>
2.1 An Overview of the Geodetic Observation Techniques . . . . .	8
2.1.1 Global Navigation Satellite Systems . . . . .	8
2.1.2 Satellite Laser Ranging . . . . .	10
2.1.3 Very Long Baseline Interferometry . . . . .	11
2.1.4 Other Techniques . . . . .	12
2.2 The Propagation of Space Geodetic Signals Through the Atmosphere . . . . .	12
2.2.1 Space Geodetic Signals in the Ionosphere . . . . .	13
2.2.2 Space Geodetic Signals in the Troposphere . . . . .	14
2.3 Processing Space Geodetic Techniques using the Bernese GNSS Software . . . . .	15
2.3.1 Introduction to the Bernese GNSS Software . . . . .	15
2.3.2 Implementation and Discussion of new Capabilities for the Bernese GNSS Software . . . . .	16
2.3.3 Assessment of Bernese VLBI Capabilities: Results for the Continuous VLBI Campaign 2014 . . . . .	20
<b>3 Reference Systems and the Combination and Co-location of Space Geodetic Techniques</b>	<b>25</b>
3.1 Definition and Realization of the Celestial Reference System . . . . .	25
3.2 Definition and Realization of the Terrestrial Reference System . . . . .	26
3.2.1 The ITRF Datum Definition and the Role of Space Geodetic Techniques . . . . .	27
3.2.2 The Historical Evolution of the IERS Station Network and the ITRF . . . . .	29
3.2.3 Site Displacements and their Consideration . . . . .	30
3.2.4 Discussions on the Current Concept of the Terrestrial Reference Frame . . . . .	33
3.3 Transformation Between Celestial and Terrestrial Reference Frame . . . . .	35
3.4 Combination Levels in Space Geodesy . . . . .	36
3.4.1 Combination at the Observation Level . . . . .	36
3.4.2 Combination at the Normal Equation Level . . . . .	39
3.4.3 Combination at the Parameter Level . . . . .	40
3.5 Co-location of Space Geodetic Techniques . . . . .	41
3.5.1 Co-location in Space . . . . .	42
3.5.2 Other Co-location Approaches . . . . .	51
3.5.3 Comparison of Co-location Approaches . . . . .	54
3.5.4 Studying Receiver Clock Differences between the Wettzell Radio Telescopes . . . . .	54
<b>4 Investigations on GPS-based Precise Orbit Determination for Low Earth Orbiters</b>	<b>59</b>
4.1 Introduction of Low Earth Orbiting Spacecraft using GPS . . . . .	59
4.2 Representing Satellite Motion in Space . . . . .	61
4.2.1 Keplerian Orbit and Gravitational Perturbations . . . . .	62
4.2.2 Treatment of Non-Gravitational Perturbations . . . . .	63
4.2.3 Precise Orbit Determination in the Bernese GNSS Software . . . . .	71
4.2.4 Validation of LEO Orbit Determination . . . . .	71

4.3	LEO-specific Orbit Validation Results . . . . .	72
4.3.1	Orbit Determination Strategy . . . . .	72
4.3.2	Analysis of Carrier Phase Residuals . . . . .	72
4.3.3	Comparison Against External Orbit Solutions . . . . .	74
4.3.4	SLR Validation Results . . . . .	77
4.3.5	Long-term GRACE-A Solution . . . . .	79
4.4	Impact of Non-Gravitational Forces and Pseudo-Stochastic Parameters on the Orbit Determination . . . . .	84
4.5	Orbit Determination from Single-frequency GPS Observations . . . . .	87
4.5.1	The Nano-satellite Mission CubETH . . . . .	87
4.5.2	The Impact of the Ionosphere on LEO Orbit Determination . . . . .	89
<b>5</b>	<b>Investigations on the Combined Processing of Ground- and Space-based GPS Observations</b>	<b>93</b>
5.1	Combined Processing Strategy . . . . .	93
5.1.1	Combination Approaches . . . . .	93
5.1.2	Database and Processing Scheme . . . . .	95
5.2	The Geocenter . . . . .	97
5.2.1	Geocenter Estimation Approaches . . . . .	98
5.2.2	Geocenter Results from the Combined GPS Processing . . . . .	101
5.3	GPS Satellite Antenna Phase Centers . . . . .	110
5.3.1	Impact of LEO GPS Observations on the Determination of GPS Satellite Antenna Patterns . . . . .	111
5.3.2	Determination of LEO Receiver Antenna Phase Centers . . . . .	112
5.3.3	Determination of GPS Satellite Antenna Phase Center Offsets . . . . .	114
5.4	Station Coordinates and Transformation Parameters with Respect to ITRF2008 . . . . .	118
5.5	Earth Rotation Parameter and GPS Satellite Orbits . . . . .	120
5.6	Transition to a Long-term Solution . . . . .	121
<b>6</b>	<b>Investigations on VLBI Satellite Tracking</b>	<b>127</b>
6.1	Tracking Satellites by Radio Telescopes . . . . .	127
6.1.1	General Remarks on VLBI Spacecraft Tracking . . . . .	127
6.1.2	Recent Achievements in VLBI tracking of GNSS satellites . . . . .	128
6.1.3	Considerations for VLBI tracking of Earth-orbiting satellites . . . . .	130
6.2	Ionospheric Delay Corrections for Single-frequency VLBI Satellite Tracking . . . . .	131
6.2.1	Idea and Formalism . . . . .	132
6.2.2	Database for the Validation of the L4R Method . . . . .	136
6.2.3	Analysis of Phase Residuals . . . . .	136
6.2.4	Validation using GNSS Signals . . . . .	141
6.2.5	Validation using VLBI signals . . . . .	143
6.2.6	Applications of L4R apart from G-VLBI . . . . .	146
6.3	Simulation Studies for VLBI Satellite Tracking . . . . .	146
6.3.1	Simulation Approach . . . . .	147
6.3.2	Simulation Study for GNSS Satellites . . . . .	153
6.3.3	Simulation Study for LEO Satellite . . . . .	156
6.3.4	Simulation Study for Elliptical Orbiters . . . . .	160
6.3.5	Conclusions and Recommendations for Future Co-location Satellite . . . . .	165
<b>7</b>	<b>Conclusions and Outlook</b>	<b>167</b>
	<b>Bibliography</b>	<b>170</b>
	<b>Appendix</b>	<b>185</b>
A	List of Co-location Satellites . . . . .	187
B	Satellite Macro-models . . . . .	197
C	Station list . . . . .	198

# List of Tables

1.1	Space geodetic techniques . . . . .	4
2.1	Sensitivity of space geodetic techniques to geodetic parameters . . . . .	7
2.2	Characterization of space geodetic transmitters and receivers . . . . .	18
2.3	Characterization of space geodetic platforms . . . . .	19
2.4	Differences in tropospheric zenith delays between VLBI and GNSS during CONT14 . . . . .	23
3.1	Overview of the ITRF realizations compiled by the IERS . . . . .	30
3.2	Comparison of inter-technique combination approaches . . . . .	41
3.3	Observation types for co-location in space . . . . .	43
3.4	Proposed satellites for co-location in space . . . . .	46
3.5	Orbit characteristics for the LEO used in the GPS difference study . . . . .	48
3.6	Local ties in ITRF2008 and DTRF2008 . . . . .	52
3.7	Alternative co-location strategies . . . . .	53
3.8	Co-location approaches . . . . .	55
3.9	Clock comparison TWOTT-VLBI for Wettzell . . . . .	56
4.1	Overview of LEO GPS receivers and antennas . . . . .	61
4.2	LEO orbit determination strategy . . . . .	73
4.3	Daily RMS of residuals in POD for GRACE, GOCE, and OSTM/Jason-2 . . . . .	74
4.4	Mean and RMS of SLR residuals . . . . .	79
4.5	Statistics of the GRACE-A long-term solution . . . . .	80
4.6	Setup of pseudo-stochastic orbit parameters . . . . .	85
4.7	Impact of modeling non-gravitational forces on the orbit comparison RMS . . . . .	86
4.8	Impact of modeling non-gravitational forces on GRACE and OSTM/Jason-2 orbits as seen by SLR . . . . .	88
5.1	Summary of estimation and processing strategy . . . . .	96
5.2	Annual signals of geocenter motion I . . . . .	109
5.3	GPS satellite block types . . . . .	116
5.4	Annual signals in the weekly transformation parameters to ITRF2008 . . . . .	119
5.5	Discontinuities for the selected stations . . . . .	123
5.6	Annual signals of geocenter motion II . . . . .	126
6.1	Overview of performed GNSS satellite tracking sessions . . . . .	129
6.2	Comparison of diverse approaches to derive ionospheric corrections for VLBI processing . . . . .	135
6.3	Selected radio telescopes and GNSS receivers for each fundamental site in the L4R study . . . . .	137
6.4	Selected GNSS baselines for the L4R study . . . . .	138
6.5	RMS statistics for baseline Matera-Wettzell . . . . .	141
6.6	RMS statistics for baseline Greenbelt-Wettzell . . . . .	141
6.7	Coordinate repeatabilities for Matera-Wettzell . . . . .	142
6.8	Stations for the VLBI simulation . . . . .	150
6.9	Orbital elements of satellites considered in the VLBI simulation . . . . .	151
6.10	Options in VLBI satellite tracking simulation . . . . .	153
6.11	Simulated vs. estimated wet delays and receiver clocks . . . . .	155
6.12	Summary VLBI satellite tracking simulation . . . . .	166
A.1	List of satellite missions suitable for co-location in space . . . . .	188
A.2	List of available space ties . . . . .	190

B.1	Satellite-specific macro-model for GPS satellites, OSTM/Jason-2, and GRACE . . . . .	197
C.1	List of stations used within the project . . . . .	198

# List of Figures

1.1	Space geodetic observations and co-location approaches . . . . .	3
2.1	Schematic sketches of space geodetic techniques . . . . .	8
2.2	Characterization of the ionosphere by $K_P$ index, $D_{ST}$ index, and mean TEC (2000.0 to 2016.0) . . . . .	14
2.3	CONT14 station map . . . . .	21
2.4	CONT14 station coordinate repeatabilities . . . . .	21
2.5	CONT14 VLBI residuals for baselines with station WETTZELL . . . . .	22
2.6	CONT14 tropospheric zenith delays for Wettzell . . . . .	22
2.7	CONT14 ERP estimates and comparison against CODE ERP products and C04 ERP series . . . . .	24
3.1	IERS tracking network as used in the ITRF2014 realization . . . . .	31
3.2	Available satellites for co-location in space . . . . .	45
3.3	Number of GPS single-differences simulated for the selected LEO baselines . . . . .	48
3.4	Histogram of the number of GPS single-differences per epoch for LEO baselines . . . . .	48
3.5	Satellite tracking scenarios for different LEO baselines . . . . .	49
3.6	Concept of SLR differentiation . . . . .	50
3.7	Monthly number of SLR differences for LAGEOS and GLONASS (archive data) . . . . .	51
3.8	Number of SLR differences depending on allowed time difference and baseline length for LAGEOS and GLONASS (archive data) . . . . .	51
3.9	Clock difference RTW-TWIN1 derived by VLBI . . . . .	56
3.10	Clock difference RTW-TWIN1 derived by TWOTT and by VLBI global solutions . . . . .	56
3.11	Clock difference RTW-TWIN1 derived by TWOTT and by VLBI baseline solutions . . . . .	57
3.12	Difference between TWOTT and VLBI clock results . . . . .	58
4.1	Artists interpretation of the GOCE, GRACE, and OSTM/Jason-2 spacecraft . . . . .	59
4.2	Geographical distribution of GPS observations for GRACE, GOCE, and OSTM/Jason-2 . . . . .	60
4.3	Number of daily LEO GPS observations . . . . .	61
4.4	Gravitational attractions and tidal forces acting on GRACE-A (January 3rd, 2010) . . . . .	64
4.5	Gravitational attractions and tidal forces acting on GRACE-A (2003-2013) . . . . .	65
4.6	Relative geometry between Earth, satellite and Sun (GPS case) . . . . .	65
4.7	Non-gravitational accelerations acting on GOCE, GRACE-A, and OSTM/Jason-2 (January 3rd, 2010) . . . . .	67
4.8	Comparison of air density values derived from MSIS86 and JB2008 . . . . .	69
4.9	Comparison of non-gravitational forces for January 3, 2010 and October, 26, 2011 . . . . .	69
4.10	Daily RMS of residuals in POD for GRACE, GOCE, and OSTM/Jason-2 . . . . .	74
4.11	Impact of a priori applied receiver PCV on GOCE phase residuals . . . . .	75
4.12	Orbit comparison for GRACE-A red.-dyn. solution against JPL GPS-based red.-dyn. orbits . . . . .	75
4.13	Orbit comparison for GRACE-B red.-dyn. solution against JPL GPS-based red.-dyn. orbits . . . . .	76
4.14	Orbit comparison for GOCE red.-dyn. solution against ESA GPS-based red.-dyn. orbits . . . . .	76
4.15	Orbit comparison for OSTM/Jason-2 red.-dyn. solution against ESO combined dynamic orbits . . . . .	76
4.16	Geographical distribution of SLR observations to GRACE, GOCE, and OSTM/Jason-2 . . . . .	78
4.17	Number of SLR observations per station for GRACE, GOCE, and OSTM/Jason-2 . . . . .	78
4.18	GRACE and OSTM/Jason-2 SLR residuals in an azimuth vs. nadir plot . . . . .	79
4.19	OSTM/Jason-2 SLR residuals in an argument of latitude vs $\beta_0$ angle plot . . . . .	80
4.20	Phase residuals of the GRACE-A long-term orbit solution . . . . .	80
4.21	Time series of GRACE-A orbital elements . . . . .	82
4.22	Orbit comparison for GRACE-A red.-dyn. solution against kinematic orbit solution . . . . .	83
4.23	Orbit comparison for GRACE-A red.-dyn. solution against JPL GPS-based red.-dyn. orbit solution . . . . .	83

4.24	Helmert transformation parameters for GRACE-A red.-dyn. solution against with respect to the JPL GPS-based red.-dyn. orbit solution . . . . .	84
4.25	Impact of orbit modeling on the RMS of orbit comparison with the reference orbits for GRACE and OSTM/Jason-2 . . . . .	86
4.26	Impact of orbit modeling on the SLR validation for GRACE and OSTM/Jason-2 . . . . .	87
4.27	Artists interpretation of CubETH . . . . .	88
4.28	Ionospheric zenith delays for GRACE-A and GRACE-B . . . . .	89
4.29	Geographical distribution of estimated ionospheric zenith delays for GRACE-A . . . . .	89
4.30	Orbit differences for GRACE-A $L_1$ kinematic and reduced-dynamic orbit solutions with respect to the reference $L_3$ reduced-dynamic orbit . . . . .	91
5.1	Ground station network and number of stations for the combined processing . . . . .	95
5.2	Processing strategy for the ground- and space-based GNSS combination . . . . .	96
5.3	Number of daily observations and RMS of carrier phase residuals for all LEOs and stations . . . . .	97
5.4	Schematic sketch of geocenter motion . . . . .	98
5.5	Geocenter results from a ground-only and a ground + four LEO combination . . . . .	102
5.6	Amplitude spectra of geocenter coordinates with constrained and freely estimated OPR parameters . . . . .	103
5.7	Mean vertical Earth crust deformation computed from GRACE AOD products . . . . .	103
5.8	Mean vertical Earth crust deformation computed from TU Vienna non-tidal atmospheric loading corrections . . . . .	104
5.9	Impact of non-tidal loading on the geocenter z-component . . . . .	104
5.10	Mean formal errors of geocenter estimates for several ground+LEO combinations . . . . .	106
5.11	Formal error of geocenter z-component compared against LEO node differences . . . . .	107
5.12	Impact of individual LEOs on the geocenter z-component . . . . .	108
5.13	Geographical distribution of LAGEOS SLR observations . . . . .	108
5.14	Geocenter z-component time series from GPS and SLR solutions . . . . .	109
5.15	Concept of GNSS phase center calibration based on ground receivers and LEOs . . . . .	112
5.16	Weekly solutions of receiver antenna phase centers variation for GRACE, GOCE, and OSTM/Jason-2 . . . . .	113
5.17	Azimuth-elevation dependent receiver antenna phase centers for GOCE and OSTM/Jason-2 (a priori, estimated, differences) . . . . .	114
5.18	Mean corrections for satellite PCO z-component (ground-only and ground+LEO solutions) . . . . .	115
5.19	Differences of mean corrections for satellite PCO z-component . . . . .	116
5.20	Mean satellite antenna PCO corrections . . . . .	117
5.21	Weekly results of GPS satellite antenna phase center offsets in x- and y-direction . . . . .	118
5.22	Formal errors of GPS satellite antenna phase center offsets in x- and y-direction . . . . .	119
5.23	Time series of translation and scale with respect to ITRF2008 . . . . .	120
5.24	ERP results (improvements) . . . . .	121
5.25	GPS orbit comparison (transformation parameters) . . . . .	122
5.26	Horizontal and vertical station velocities (2010-2013) . . . . .	124
5.27	Differences between estimated (>2 years) and ITRF2008 velocities . . . . .	124
5.28	Geocenter results based on the unified approach . . . . .	125
5.29	Geocenter results based on a different parameterization in the unified approach . . . . .	125
5.30	Comparison of geocenter results: unified and translational approach . . . . .	126
6.1	Considerations for VLBI tracking of Earth-orbiting satellites . . . . .	131
6.2	Estimation of the E-GRIP microwave link signal budget for VLBI observation . . . . .	132
6.3	Schematic sketch of ionospheric delay corrections from co-located GNSS observations . . . . .	132
6.4	Processing procedure for L4R-based ionospheric delay corrections . . . . .	134
6.5	Station map and VLBI sessions for the L4R study . . . . .	137
6.6	Analysis of double-differences in the L4R study . . . . .	138
6.7	Epoch-wise standard deviations and number of observed GNSS satellites . . . . .	139
6.8	Difference between delay corrections of consecutive epochs for baseline ONSA-WTZR . . . . .	139
6.9	Ionospheric delay corrections computed for the Hobart-Ceduna experiment (August 24, 2015) . . . . .	140
6.10	Daily mean vertical delays and their monthly median value for NOT1, WTZR, and NYAL . . . . .	140
6.11	Daily RMS of residuals for baseline Matera-Wetzell . . . . .	142

---

6.12	Daily height coordinate repeatability for Matera-Wetzell . . . . .	142
6.13	Coordinate repeatabilities for $V_{L3}$ , $V_{L4R}$ , and $V_M$ solutions . . . . .	143
6.14	Differences of ionospheric delay correction from NGS Card files and L4R . . . . .	144
6.15	Statistics for the validation using VLBI observations . . . . .	145
6.16	Effect of the chosen threshold values for time and separation angle in the VLBI-based validation . . . . .	146
6.17	Probability of finding a GNSS satellite around a fictitious source . . . . .	147
6.18	Effect of chosen parameters for simulating troposphere and receiver clock . . . . .	150
6.19	Ground tracks of satellites considered in the VLBI simulation . . . . .	152
6.20	Station coordinate repeatabilities derived from tracking a GPS satellite constellation . . . . .	154
6.21	VLBI observations of GPS satellites as skyplot . . . . .	154
6.22	Differences between estimated zenith wet delays and receiver clocks with respect to simulation . . . . .	156
6.23	Number of simulated VLBI observations to circular LEO orbits per baseline (EUROPE network) . . . . .	157
6.24	Number of simulated VLBI observations to circular LEO orbits per baseline (global network) . . . . .	157
6.25	Observed baselines and distribution of their lengths for GPS constellation and LEO <sub>89</sub> tracking . . . . .	158
6.26	Station coordinate repeatabilities LEO <sub>63</sub> . . . . .	158
6.27	VLBI observations of the LEO <sub>63</sub> satellite as skyplot . . . . .	159
6.28	Station coordinate repeatabilities for different core station definitions (LEO <sub>63</sub> ) . . . . .	159
6.29	Station coordinate repeatabilities LEO <sub>89</sub> . . . . .	160
6.30	Direction to the observed LEO satellites as skyplot . . . . .	160
6.31	Station coordinate repeatabilities LEO <sub>107</sub> . . . . .	161
6.32	Number of simulated VLBI observations to elliptically-orbiting satellites per baseline (EUROPE network) . . . . .	161
6.33	Number of simulated VLBI observations to elliptically-orbiting satellites per baseline (global network) . . . . .	162
6.34	Observed baselines and distribution of their lengths for EGRIP-A and E-GRASP tracking . . . . .	162
6.35	Station coordinate repeatabilities EGRIP-A . . . . .	163
6.36	Direction to the observed satellites in elliptical orbits as skyplot . . . . .	163
6.37	Station coordinate repeatabilities EGRIP-B . . . . .	164
6.38	Station coordinate repeatabilities E-GRASP . . . . .	164
6.39	E-GRASP orbit determination: differences between simulated and estimated orbit . . . . .	165
6.40	Mean station coordinate repeatability derived from processing $n$ days up to a weekly solution . . . . .	166



# 1 Motivation and Introduction

Aristotle's famous statement "*the totality is not, as it were, a mere heap, but the whole is something besides the parts*" or in the common more simplified version "*the whole is greater than the parts*" gives a perfect characterization for the combination of geodetic observation techniques, also called space geodetic techniques. The four different space geodetic techniques can be seen as the parts. They are (a) Global Navigation Satellite Systems (GNSS), (b) Satellite Laser Ranging (SLR), (c) Very Long Baseline Interferometry (VLBI), and (d) Doppler Orbitography and Radiopositioning Integrated by Satellite (DORIS). These techniques and their observations are unique in their way to observe our changing Earth and its behavior in inertia space. They are also unique in their sensitivity to different aspects of the environment, like the Earth's interior, the Earth's lithosphere, or the Earth atmosphere. However, it is well known that none of the individual technique is able to observe and monitor all processes in and around the Earth's system. Especially, it is not possible to derive the whole set of parameters necessary to realize a highly accurate and long-time stable reference system by just one technique. Indeed, having such a reference frame, which allows a consistent monitoring of the Earth, is not a wishful thinking of some geodesists, it is a major requirement for treating all Earth observations in a consistent and homogeneous way.

As an individual space geodetic technique cannot provide sensitivity to all essential parameters, a combination of techniques is required. This combination should be more than a simple addition of several sub-results or parameter groups. The combined result should surpass each single-technique solution by taking advantage of the individual strengths that each techniques has. However, the most crucial question arises: How can this combination be done in an appropriate way, in a way that avoids limitations due to artificial constraints, over-parameterization, or unmodelled biases? This work aims to take place in the current discussions on the perfect combination of space geodetic techniques by describing a combination approach on the satellite level, or, in other word, by characterizing the idea of assembling all space geodetic techniques on a platform in orbit and connecting them there. This idea was introduced more than fifteen years ago and reached now an experimental stage. Even if the idea seems to be very simple, several practical issues have to be discussed and to be solved. Such issues are: How can we connect VLBI observations to the satellite level? How can we perform orbit determination on an accuracy level, which is worth to combine space techniques on-board satellites? What is an appropriate platform and what is the optimal orbit type to assemble the techniques in space? As the list of questions is long, and several hardware developments are required, this work represents the current status on the way to a co-location in space. Therefore, several topics will be discussed, like precise orbit determination for several low Earth orbiters (LEO), the combination of ground and space-based data sets, preparations for new observation scenarios and simulations for future missions. Perhaps, these topics are detached from each other, but together they are more than an assembly of separated parts, they are relevant key topics for a successful combination of geodetic observation techniques in space.

One of the primary tasks of geodesy is to provide the means to represent points by coordinates as a function of time. Both, position and velocity of points in space cannot be called absolute quantities as they are referred to a specific coordinate system. In geodesy such a coordinate system is called a reference system and its special realization, defined by the coordinates of distinct points, a reference frame. Obviously, the accuracy of estimated station coordinates depends on the quality and stability of the underlying reference frame. Or in other words, the quality of derived station coordinates is limited by the (1) accuracy of the observation technique and by (2) the quality of the applied reference frame. Using today's space geodetic techniques one is able to derive station coordinates at the mm level. This accuracy was unimaginable two

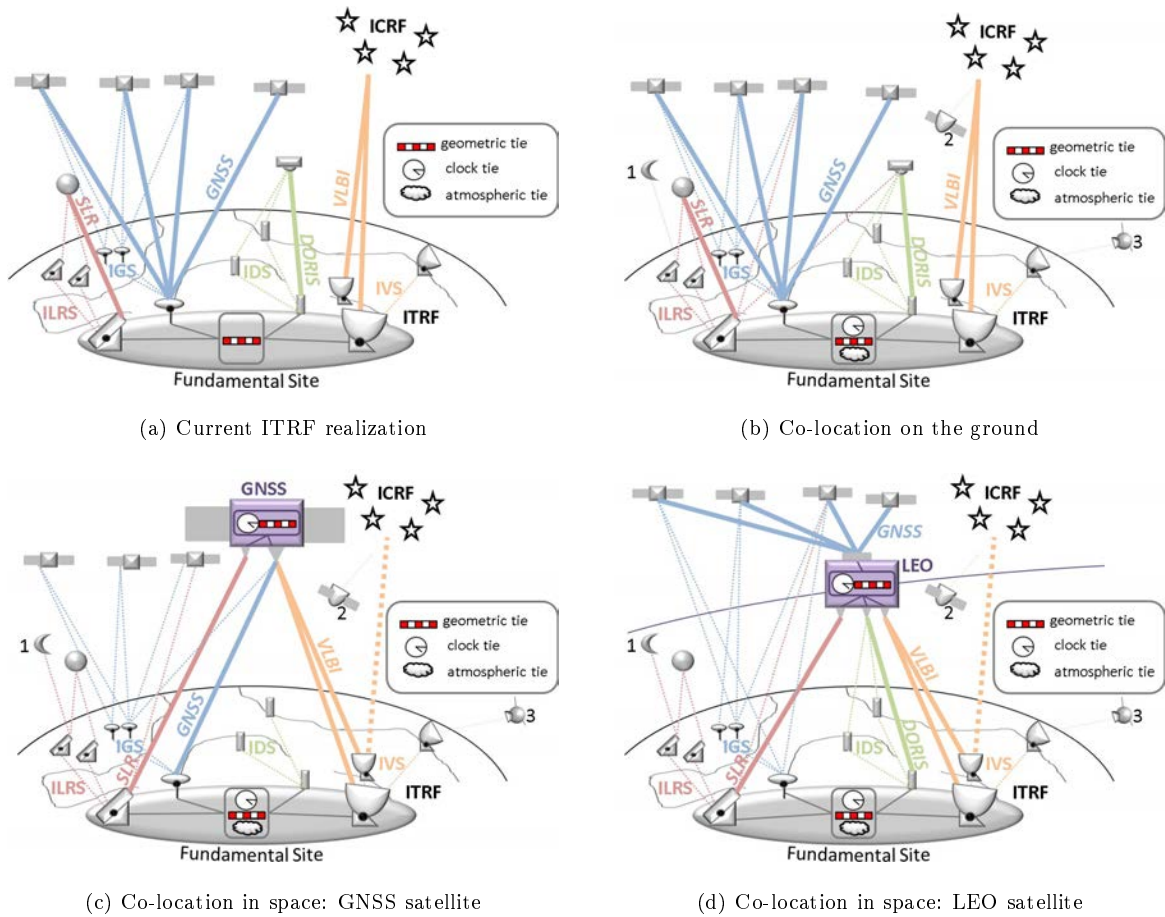
decades ago, but is needed for monitoring our dynamic and changing planet. One of the most important and discussed phenomena in this context is global sea level change. Apart from seasonal and regional effects a global trend of 2-3 mm/yr was observed during the past decades (Blewitt et al., 2010). As the sea level is observed relative to tide gauges, their vertical displacements have to be monitored at the mm level. The derived tide gauge positions and velocities have to be given in a global reference frame for two reasons. Firstly, the positions of all available tide gauges have to be realized in a consistent global reference frame to derive global and regional sea level information. Secondly, the tide gauge positions have to be monitored in a long-term reference frame stable over decades to derive sea level trends. Otherwise, a possible sea level rise cannot be separated from displacements affecting the tide gauge positions like post-glacial uplift and reference frame inconsistencies (cf. Beckley et al., 2007 and Morel & Willis, 2005). However, a highly accurate and stable reference frame is necessary also to monitor other geophysical phenomena affecting our society. For example, plate tectonics with horizontal velocities of several mm/yr have to be observed with an accuracy of 1 mm/yr (Plag & Pearlman, 2009). The same is true for post-glacial uplift and loading displacements due to the changing climate and secular variations in hydrosphere, cyrosphere, and atmosphere. According to Plag & Pearlman (2009) the required measurement accuracies are 1 mm for positions and 0.1 mm/yr for velocities. Obviously, the monitoring of these (but many more) small and long-term variations needs a stable reference frame as otherwise reference frame errors will propagate into the estimates. Concerning our society the monitoring of the mentioned processes are essential as they are the associated with earthquakes, volcanic activities, flooding, tsunamis, and other kinds of natural hazards. To provide a corresponding reference frame the Global Geodetic Observing System (GGOS) was established in the last years as the observing system of the International Association of Geodesy (IAG). Within GGOS the requirements for a terrestrial reference frame, suitable for a global society on a changing planet, were defined as 1 mm accuracy and 0.1 mm/yr stability of corresponding station positions (Plag & Pearlman, 2009). Following Altamimi et al. (2013) these requirements exceed today's accuracy by one order of magnitude. The limitations the reference frames currently suffer from can be summarized in three major aspects. Firstly, the four space geodetic techniques are limited by several so-called technique-specific error sources. These are for example biases in the electronics, the atmosphere, or offsets and systematic effects regarding the instrumental reference points. Secondly, the observation networks are not optimal distributed for realizing a reference frame (except for the DORIS network). Grown historically, the majority of GNSS, SLR, and VLBI stations are located in North America and Europe, whereas larger areas in the southern hemisphere are not adequately covered. Thirdly, the techniques are combined at fundamental sites, where the terrestrially measured offset vectors between the reference points of the assembled instruments are sometimes not consistent, inaccurate, or even outdated. The analysis, evaluation, and realization of potential improvements in all three areas is the aim of the research unit "Space-Time Reference Systems for Monitoring Global Change and for Precise Navigation" funded by the German Research Foundation and the Swiss National Science Foundation<sup>1</sup>. This thesis and the corresponding work was done within the research unit sub-project "Co-location on Ground and in Space" (PN7). It must be noted that, within the project and, therefore, in this work, DORIS was not considered as the Bernese GNSS Software version used is currently not capable to process DORIS data.

Fig. 1.1(a-d) shows the world from a space geodetic perspective. The four space geodetic techniques are represented also by their scientific communities, which are:

- the International GNSS Service (IGS),
- the International Laser Ranging Service (ILRS),
- the International VLBI Service for Geodesy and Astrometry (IVS), and
- the International DORIS Service (IDS).

Additionally, the International Earth Rotation and Reference Systems Service (IERS) should be mentioned at this stage, as this service realizes the International Terrestrial Reference Frame (ITRF). This frame is

<sup>1</sup> <http://www.referenzsysteme.de>, accessed June 2016



**Fig. 1.1:** Space geodetic observations and co-location approaches; 1 Moon, 2 VLBI telescope in space, 3 deep space missions

derived as shown in Fig. 1.1(a). The four space geodetic techniques with their observations to different types of satellites and, in the case of VLBI, to quasars are combined solely via local ties. These are the above mentioned terrestrially measured vectors between the technique-specific instruments at fundamental sites. This approach is called co-location on the ground and the fundamental sites are sometimes referred to as co-location sites. However, as indicated by Fig. 1.1(b) the techniques can be combined locally also by non-geometrical ties, for example by a common estimation of the wet zenith delays, tropospheric gradients, or the receiver clock. The combination of techniques is, however, also possible by estimating global parameters together, like the Earth rotation parameters (ERP). In this context the term “global ties” is sometimes used. Additionally, other observation types of the space geodetic techniques than those shown in Fig. 1.1(a) are available. For example, LEO satellites were observed by GPS and SLR for many years. Also laser distance measurements to reflectors placed on the lunar surface (Lunar Laser Ranging, LLR) and experimental VLBI observations to satellites orbiting the Earth are available. The operational or potential observation types in space geodesy are described in Tab. 1.1. This table provides for each observation type the signals, the corresponding equipment locations and the current status. Using the additional observations mentioned above a new type, of co-location can be established, called co-location in space, where the techniques are combined on-board satellites. Fig. 1.1(c) shows this type of combination on-board a GNSS satellite, which is additionally observed by SLR and VLBI. The combination itself is based on the measured offset vectors between the on-board instruments. These offset vectors are usually called space ties. However, also an on-board clock tie is feasible. Obviously, DORIS is excluded from this combination type, as GNSS satellites are not equipped with DORIS receivers. Also VLBI is limited to challenging L-band observations in the foreseeable future as a dedicated VLBI transmitter on-board a GNSS satellite is currently not planned. A dedicated co-location satellite is not limited in this direction and might carry

**Tab. 1.1:** Space geodetic techniques: signals, equipment, and observation availability; status of observations: operational (*ops.*), experimental (*exp.*) or currently not available (*n/a*)

technique	signals		equipment location			observations			
	type	freq. [GHz]	transmitter	reflector	receiver	ops.	exp.	n/a	
GNSS	microwave	1.2 & 1.6	GNSS satellite	-	station	✓			
			GNSS satellite	-	LEO	✓			
SLR	optical	$\approx 10^5$	station	geod. satellite	station	✓			
			station	GNSS satellite	station	✓			
			station	LEO	station	✓			
LLR			station	Moon	station	✓			
VLBI	microwave	2.4 & 8.4	quasar	-	station	✓			
			1.2 & 1.6	GNSS satellite	-	station		✓	
			2.4 & 8.4	LEO	-	station			✓
			2.4 & 8.4	space probe	-	station	✓		
			2.4 & 8.4	quasar	-	LEO		✓	
			2.4 & 8.4	Moon	-	station		✓	
DORIS	microwave	0.4 & 2.0	station	-	LEO	✓			

a DORIS receiver and a VLBI transmitter as shown in Fig. 1.1(d). Currently, a set of Earth observation satellites is equipped with a subset of space geodetic techniques but a dedicated co-location satellite is still missing. The main difference between Fig. 1.1(c) and Fig. 1.1(d) is the access to the GNSS observations, as the co-location satellite acts either as a transmitter or as a receiver. It has to be mentioned here that low Earth orbiting satellites are addressed as LEO within Fig. 1.1(d) and within this thesis. However, a corresponding co-location satellite is not limited to a low Earth orbit (usually defined by altitudes below 2000 km above Earth surface). For example, elliptical orbits with apogee heights above the GNSS constellations are discussed within this thesis. The term “LEO” is, therefore, not correct in a strict sense but is used to distinguish between the two types of co-location in space. Co-location in space is, in short, a promising way to access and even to overcome the limitations of the current reference frame. Apart from that, co-location in space provides a connection between the terrestrial ITRF and the inertial International Celestial Reference Frame (ICRF). This connection, expressed by the Earth orientation parameters (EOP), is provided by determining the satellite positions with respect to the quasars. Estimating positions with respect to both, satellites and quasars, will allow to establish so-called frame ties.

Co-location in space requires actions in three main areas as outlined above. These are (1) LEO orbit determination as a prerequisite for a successful co-location, (2) the combination of ground- and space GPS observations, and (3) satellite tracking with radio telescopes. Therefore, the main questions discussed within this thesis are

- How can we achieve a LEO orbit accuracy which allows co-location in space on-board satellites? This topic includes:
  - How should we take non-gravitational forces into account?
  - What is the impact of taking these non-gravitational forces a priori into account?
  - Which accuracy levels can be reached for different LEOs?
- How can the LEO co-location in space and the geodetic ground observation network be linked? This question arises as the GNSS receivers on ground are not directly part of this type of co-location. To answer this question LEO and ground GNSS observations have to be combined. Therefore, the following questions need to be answered:
  - How can this combination be done properly?

- What is the impact and potential improvement due to additional LEOs on the geocenter coordinates, the station coordinates, the terrestrial scale, antenna phase centers, and ERPs?
- Is the degree of improvement related to the added LEO and its orbit characteristic?
- Is there a benefit from adding more than one LEO?
- How can VLBI be part of a co-location in space? In recent years L-band GNSS signals were observed by radio telescopes within several experiments and also VLBI transmitters were designed to be carried by dedicated co-location satellites. However, the follow questions have to be considered:
  - What is the current status of VLBI satellite tracking?
  - How can the ionospheric refraction be corrected for the recently performed single-frequency GNSS satellite tracking experiments?
  - Which orbit type is, from the VLBI perspective, best suited for co-location in space: nearly circular low Earth orbits, highly elliptical orbits, or the GNSS MEO orbits?

This thesis is structured in the following way. Following this introduction, an overview of the space geodetic techniques and relevant topics will be provided as a comprehensive summary in Chap. 2. Also the Bernese GNSS Software and the newly implemented capabilities are described. The chapter is completed by a VLBI processing example for the CONT14 sessions to proof the implemented functionality. Reference systems and their current realizations are discussed in Chap. 3. However, the main focus in this chapter is on the combination and co-location of space geodetic techniques. Also recently proposed satellite missions dedicated to co-location in space, like GRASP or E-GRASP/Eratosthenes, are discussed there. In Chap. 4 the main focus lies on precise orbit determination for low Earth orbiters. Beyond an introduction about perturbing forces focusing on the so-called non-gravitational perturbations, ways to account for them in the orbit determination process are studied. Based on that the derived orbits for GRACE, GOCE, and OSTM/Jason-2 are analyzed and validated using several internal and external approaches. These satellite missions were selected as high-quality GPS observations and attitude information are available, as their orbit characteristics are different, and not only GPS but also SLR observations are performed to them. In addition to these Earth exploring missions the small satellite mission CubETH is introduced in the last part of Chap. 4. The impact of the ionosphere above the satellite on the orbit determination is studied in the framework of this mission. The combined processing of ground- and space-based GPS data is addressed in Chap. 5. The impact of the additional LEO GPS observations on the geocenter coordinates is assessed after describing the processing effort firstly. As the satellite phase centers benefit from the LEO orbit dynamics, this parameter group is analyzed in a second step. Thirdly, station coordinates and transformation parameters with respect to the ITRF2008 are discussed. The fourth part of this chapter provides a short discussion on determined ERPs and GPS orbits while the last part shows a long-term solution including station velocities and geocenter results based on surface load densities. Tracking satellites by radio telescopes is the main topic of Chap. 6. Current possibilities, especially the recent achievements in the tracking of GNSS satellites in the L-band, are addressed in the first section of this chapter. The important question of how to correct the ionospheric delay for the single-frequency observations performed so far is answered by introducing an approach based on co-located GNSS observations. In the third part of this chapter VLBI satellite tracking simulations for several orbit types are presented, including a detailed description of the simulation approach. Chap. 7 is dedicated to the conclusions and further prospects of the co-location issues in space.



## 2 Geodetic Observation Techniques in a Nutshell

It is well known that the sensitivity to the geodetic parameters varies significantly between the geodetic observation techniques, also called space geodetic techniques (e.g., Montag, 1996). The sensitivity of Global Navigation Satellite Systems (GNSS), Satellite Laser Ranging (SLR), Very Long Baseline Interferometry (VLBI), and Doppler Orbitography and Radiopositioning Integrated by Satellite (DORIS) to a selection of such geodetic parameters is provided in Tab. 2.1. In general, geodetic parameters can be divided into two categories. The first group contains parameters directly connected to an individual technique. These parameters are usually called technique-specific parameters. Obviously, they are necessary to account for effects which are not calibrated or modeled, for any conceptual or practical reasons (e.g., range biases in SLR or receiver clock offsets in VLBI). The second group contains parameters common to two or more techniques, consequently called common parameters. Unlike the first group, these parameters are mostly

**Tab. 2.1:** Sensitivity of the different space geodetic techniques to geodetic parameters; Lunar Laser Ranging (LLR), which is similar to SLR, was added here; the upper box contains co-location in space, the lower box co-location on ground; (✓) indicates a low sensitivity, an unusual estimation, or estimation based on experimental observations (please see the corresponding notes)

classification	type	parameter	VLBI	GNSS	SLR	DORIS	LLR
common, global	satellite orbits	GNSS orbits	(✓) <sup>a</sup>	✓	✓ <sup>b</sup>		
		LEO orbit		✓	✓	✓	
		LEO clock		✓	(✓) <sup>c</sup>		
		ded. co-loc sat orbit	✓	✓	✓	✓	
		ded. co-loc sat clock	✓	✓	✓	✓	
	EOP	pole coordinates	✓	✓	✓	✓	✓
		UT1	✓				(✓) <sup>g</sup>
		LOD (length of day)	(✓)	✓	✓	✓	✓
		nutation	✓				✓
		nutation rates	✓	✓	✓	✓	✓
	gravity field	Earth's center of mass			(✓) <sup>d</sup>	✓	(✓) <sup>d</sup>
		low-degree coefficients			✓	✓	(✓)
		scale	✓	(✓) <sup>e</sup>	✓	(✓)	✓
	common, local	atmosphere	ionospheric parameters	✓	✓	(✓) <sup>f</sup>	✓
tropospheric parameters			✓	✓		✓	
TRF		station positions	✓	✓	✓	✓	✓
		station velocities	✓	✓	✓	✓	✓
time & frequency		station clocks	✓	✓	✓		✓
technique-specific	CRF	quasar positions	✓				
	Moon	lunar orbit					✓
	instrumental biases	GNSS satellite clocks		✓			
		range biases			✓		✓

<sup>a</sup> requires further advance in G-VLBI observations (tracking GNSS L-band signals with radio telescopes)

<sup>b</sup> small number and poor coverage of SLR tracking observations compared to GNSS observations

<sup>c</sup> requires photon counter on-board LEO

<sup>d</sup> correlations with orbit determination (see Sect. 5.2)

<sup>e</sup> correlations with phase center patterns (see Sect. 5.3)

<sup>f</sup> negligible ionospheric delay in optical domain (see Sect. 2.2)

<sup>g</sup> UT0 is observed instead of UT1

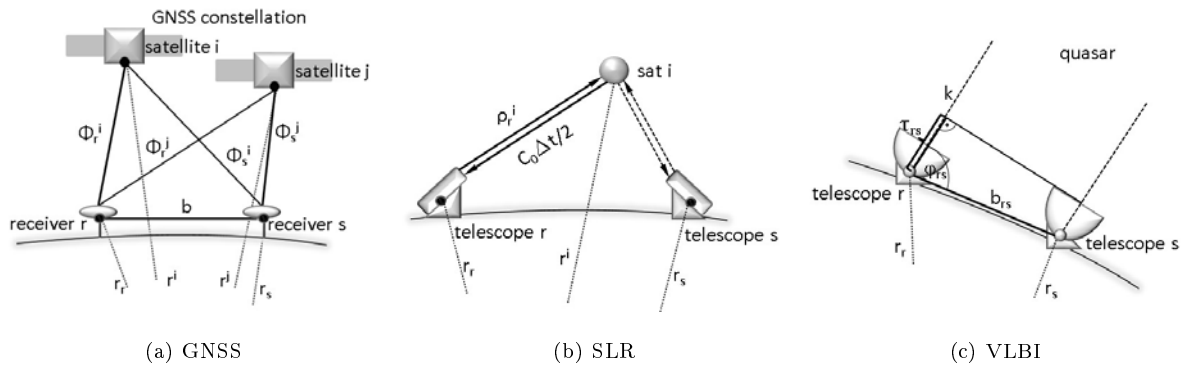


**Fig. 2.1:** Schematic sketches of the space geodetic techniques GNSS, SLR, and VLBI

linked directly to the three pillars of geodesy (i.e., Earth’s geometry, Earth rotation, and Earth’s gravity field) and their estimation is an essential task of geodesy. In order to characterize their scope common parameters can be divided into global and local parameters where the latter are related to individual stations. Obviously, common parameters are only set up once in a multi-technique processing. By doing this the techniques are combined with benefits from technique-specific strengths. The Earth orientation parameter UT1-UTC, accounting for variations in the Earth’s rotation phase, serves as an example here. The parameter is solely observed by VLBI, as the absolute Earth rotation can only be observed with respect to fixed points outside the solar system (Schuh & Behrend, 2012). The daily variation  $\Delta UT1$  or Length of Day (LOD) is also observable with VLBI, but a determination using GNSS, which is a satellite technique, allows a higher temporal resolution. Therefore, Earth rotation can be estimated, with the highest possible accuracy on short and on long time scales, by combining both techniques.

Within the first part of this chapter the different space geodetic techniques are described concerning their underlying concepts as well as their advantages and limitations. The atmosphere, affecting all space geodetic techniques, and their impact on signals crossing this sphere is discussed in the second part of this chapter. The third part describes the Bernese GNSS Software (BSW) as a software tool to process and analyze space geodetic techniques.

## 2.1 An Overview of the Geodetic Observation Techniques

The different space geodetic techniques are introduced in a summarized way by discussing the principle observation equations, relevant processing strategies, and their most important error sources. Some further details are discussed in the further course of this thesis. Fig. 2.1 shows the basic observation concept for the space geodetic techniques GNSS, SLR, and VLBI.

### 2.1.1 Global Navigation Satellite Systems

The space geodetic technique Global Navigation Satellite Systems (GNSS) contains the space segments of the fully operational U.S. American Global Position System (GPS), the Russian Global’naya Nawigatsionnaya Sputnikowaya Sistema (GLONASS), and the uprising Chinese BeiDou and the European Galileo systems. GNSS, especially GPS, has been used intensively in geodesy for more than 30 years. Correspondingly, system details, signal structure, observation concepts, error sources and applications are widely discussed in the literature (e.g., Xu, 2003; Hofmann-Wellenhof et al., 2008; Leick et al., 2015). Therefore, this section will only provide a brief overview on key facts and aspects relevant to this work. As the major concepts are similar to all GNSS, GPS is described here as a representative example. In Chap. 4 the usage of GNSS receivers on-board LEOs in order to determine their orbits is discussed in more detail. Several challenges in the GNSS processing are addressed in more detail in Chap. 5.

The GPS space segment contains currently a constellation of 32 satellites, which orbit the Earth in a

medium Earth orbit (MEO) at an altitude of around 20'200 km and an inclination of  $55^\circ$ <sup>1</sup>. Each satellite  $i$  transmits code signals on at least two L-band carrier frequencies. These code signals contain the signal transmitting time, the satellite position, and satellite clock corrections with respect to the GPS time scale and other information, like the almanac. However, as satellite position and clock information are predicted they have not the highest possible quality. As an alternative the IGS and its analysis centers provide post-processed GNSS orbits and satellite clock corrections with an accuracy level of 2-3 cm and 5 ns, respectively (IGS, 2015). A geodetic receiver  $r$  tracks the code signals  $c_r^i$  and the corresponding phases  $\Phi_r^i$  of the carrier signal (cf. Fig. 2.1). The observation equation for the phase measurements, in units of length, reads as

$$\begin{aligned} \Phi_r^i(t) = & \rho(t, t - \tau_r^i) - \delta\rho_{ion_r^i} + \delta\rho_{trop_r^i} + \delta\rho_{mul_r} + c_0(\delta t_r(t) - \delta t^i(t - \tau_r^i)) + \\ & \delta\rho_{pcv_r}(t) + \delta\rho_{pcv^i}(t) + \delta\rho_{rel_r^i} + \lambda N_r^i + \epsilon_r^i. \end{aligned} \quad (2.1)$$

In Eqn. 2.1  $\rho(t, t - \tau_r^i)$  is the geometrical distance between satellite (at transmitting time  $\tau_r^i$ ) and receiver (at reception time  $t$ ), the clock errors are  $\delta t_r$  and  $\delta t^i$ .  $\delta\rho_{ion_r^i}$  is the ionospheric delay,  $\delta\rho_{trop_r^i}$  is the tropospheric delay;  $\delta\rho_{mul_r}$  contains multipath effects and  $\delta\rho_{rel_r^i}$  relativistic effects. The antenna characteristics are contained in  $\delta\rho_{pcv_r}(t)$  and  $\delta\rho_{pcv^i}(t)$ .  $N_r^i$  are the phase ambiguities and  $\lambda$  the signal wavelengths.  $\epsilon_r^i$  contains the measurement error. The geometrical distance  $\rho(t, t - \tau_r^i)$  contains station coordinates in an Earth-fixed and orbital positions in an inertial frame, thus, providing the access to orbits, station coordinates, and Earth rotation parameters. The geometrical distance has to be corrected for the atmospheric delays (see Sect. 2.2) and several technique-specific delays. Usually a geodetic GNSS receiver tracks both GNSS-specific signals,  $L_1$  and  $L_2$ , with frequencies  $f$  of 1.575 and 1.227 GHz, corresponding to wavelengths  $\lambda$  of 19 and 24.4 cm, respectively<sup>2</sup>. Linear combinations like the ionosphere-free linear combination  $L_3 = \frac{1}{f_1^2 - f_2^2}(f_1^2 L_1 - f_2^2 L_2)$  or the geometry-free linear combination  $L_4 = L_1 - L_2$  are used to minimize or even eliminate some error sources. Moreover, the GNSS processing can be characterized by the level of differentiation. Consequently, the processing can be done in the so-called zero-differenced mode shown in Eqn. 2.1 or by forming differences. Differences can be defined as baselines  $\Phi_{rs}^i = \Phi_r^i - \Phi_s^i$ , as station-specific single-differences  $\Phi_r^{ij} = \Phi_r^i - \Phi_r^j$ , or as double-differences  $\Phi_{rs}^{ij} = (\Phi_r^i - \Phi_s^i) + (\Phi_r^j - \Phi_s^j)$ . Based on double-differences of consecutive epochs triple-differences can be formed. In this thesis zero-difference observations are used for the LEO orbit determination and the combined solutions in Chap. 4 and Chap. 5, respectively. The estimation of ionospheric delays in Chap. 6 is based on double-differences.

The ambiguities  $N_r^i$  containing the full signal cycles between satellite and receiver, can be fixed to their integer value in both approaches. Important algorithms for the ambiguity fixing based on double-differences are the SIGMA-dependent (e.g., Dach et al., 2007) and the quasi ionosphere-free (QIF, Mervant, 1993) approaches. In the zero-difference mode hardware delays inside satellite and receiver have to be known a priori (Ge et al., 2008). Corresponding strategies were presented within the last years, e.g., based on hardware delay calibrations (Laurichesse et al., 2009) or based on wide-lane and phase bias information (Bertiger et al., 2010a). The satellite and receiver clocks are deviating slightly from the GPS time scale. Therefore, the clock errors  $\delta t^i$  and  $\delta t_r$  have to be estimated in a zero-difference processing. Obviously, both clock errors cancel out when forming double-differences. Due to constructional characteristics the electrical phase center of transmitting and receiving antennas do not coincide with the geometric antenna reference points. Therefore, constant phase center offsets (PCO) and elevation- and azimuth-dependent phase center variations (PCV)  $\delta\rho_{pcv_i}(t)$  and  $\delta\rho_{pcv^k}(t)$  are estimated during antenna calibrations or by using special processing strategies. More details on that topic can be found in Sect. 5.3, and in the literature (e.g., Schmid & Rothacher, 2003; Schmid et al., 2005, 2007; Jäggi et al., 2009; Montenbruck et al., 2009; Bock et al., 2011a). The correction term  $\delta\rho_{rel_r^i}$  contains several relativistic effects acting on the satellite clocks, the signal propagation and the satellite orbits (Hofmann-Wellenhof et al., 2008). A detailed description

<sup>1</sup> For the other GNSS the space segment is characterized by: GLONASS 19'100 km and  $64.8^\circ$ ; Galileo 23'200 km and  $56^\circ$ ; BeiDou 22'000 km and  $55^\circ$  plus geostationary satellites and inclined geostationary satellites.

<sup>2</sup> For the other GNSS these signals are: for GLONASS  $L_1=1.598$  to  $1.605$  and  $L_2=1.243$  to  $1.249$  GHz, for Galileo  $E_1=1.575$  and  $E_5=1.191$  GHz, and for BeiDou:  $B_1=1.561$  and  $B_2=1.207$  GHz.

and correction formulas can be found in the IERS conventions (Petit & Luzum, 2010). Multipath effects  $\delta\rho_{mul_r^i}$ , caused by signals reaching the antenna after being reflected in the antenna near-field, are difficult to model and are usually minimized by averaging, by a suitable antenna design, and by having a multipath-reduced surrounding at the fundamental sites. The measurement error  $\epsilon_r^i$  for phase observations is around 2 mm. For the code observations an equation similar to Eqn. 2.1 can be formed. Compared to Eqn. 2.1 the ambiguity term can be dropped, whereas instrumental biases, so-called differential code biases (DCB), have to be considered. Due to the higher noise level the measurement accuracy is only at the meter level for code observations. Therefore, they are mostly ignored during the final processing step in space geodesy. However, for applications in navigation, natural hazard monitoring, and time synchronization much cheaper single-frequency receivers providing code-based solutions are widely used. The usage of such receivers on-board the CubETH satellite is described in Sect. 4.5.1.

### 2.1.2 Satellite Laser Ranging

Satellite Laser Ranging (SLR) is an optical technique using laser pulses transmitted by a ground telescope  $r$  to determine the distance to a corner-cube retro-reflector on-board a satellite  $i$  by measuring the round-trip light travel time (cf. Fig. 2.1). In order to ensure that enough energy returns, reflectors of 2 to 4 cm diameter are assembled usually in arrays or pyramids. Using today's ruby and Neodymium-YAG laser systems, ranging accuracies of 1-3 mm are achieved (Seeber, 2003). The main disadvantages of SLR are the strong dependence on appropriate weather conditions, i.e., a cloud-less sky, and the very inhomogeneous station distribution between northern and southern hemisphere<sup>3</sup>. The observation equation for the observed time difference  $\Delta\tau_r^i$  between pulse emission and pulse reception reads as

$$c_0\Delta\tau = 2(\rho_r^i + \delta\rho_{trp_r^i} + \delta\rho_{rel_r^i}) + \delta\rho_{ex_r} + \delta\rho_{ex^i} + c_0\delta t_r + \epsilon_r^i. \quad (2.2)$$

In Eqn. 2.2  $\rho_r^i$  contains the geometrical distance between satellite and ground station.  $\delta\rho_{trp_r^i}$  are tropospheric delays and  $\delta\rho_{rel_r^i}$  contains relativistic corrections. Eccentricities at station and satellites are described by  $\delta\rho_{ex_r}$  and  $\delta\rho_{ex^i}$ , respectively.  $\delta t_r$  is the time biases and the measurement noise is  $\epsilon_r^i$ . The geometrical distance  $\rho_r^i$ , computed in a similar way as in Eqn. 2.1, allows the determination of orbits, station coordinates and ERPs. An important difference is the time epoch for the position computation which is the signal reflection time at the satellite in SLR. The correction term  $\delta\rho_{trp_r^i}$  for the tropospheric delay is discussed in Sect. 2.2.2 and the relativistic corrections  $\delta\rho_{rel_r^i}$  are similar to those in Sect. 2.1.1. As SLR is a passive technology from the satellite point of view, relativistic effects on the satellite clock are not relevant. Eccentricities at the SLR station  $\delta\rho_{ex_r}$  and the satellite  $\delta\rho_{ex^i}$  are estimated and published by the ILRS as range biases and center-of-mass corrections. As SLR is based purely on an accurate timing system, the observations have to be corrected for signal delays  $\delta t_r$  in the electronics (called time biases). Remaining effects like unknown or insufficiently known eccentricity vectors, reflector offsets, and systematic environmental effects are often absorbed by additional range bias parameters which can be setup in the SLR processing. Unfortunately, range biases are highly correlated with the station height estimation, which causes problems, if the SLR observations are not uniformly distributed over the hemisphere. Also the separation of the effects absorbed by the range biases is not possible in the undifferenced SLR processing. However, in recent years, initial efforts were undertaken to organize simultaneous SLR tracking sessions to allow SLR processing on the single- or double-difference level (Svehla et al., 2016). These efforts are discussed in more detail in Sect. 3.5.1.

The space segment of SLR can be divided into three groups. Geodetic satellites like LAGEOS 1/2, ETALON 1/2, STARLETTE and other spherical satellites are optimized to reduce to effects of non-gravitational perturbations allowing SLR to exploit its full potential to derive station coordinates, geocenter coordinates, and other parameters. Seeber (2003) provides a comprehensive overview of these satellites,

<sup>3</sup> According to Sošnica (2015) the number of observations is, however, nearly equally distributed between both hemispheres as the southern stations benefit from better local weather conditions.

their properties, and orbits. The second group are GNSS satellites, where SLR allows an independent orbit validation (Urschl et al., 2005, 2007). Today this opportunity is given for GLONASS, Galileo, and BeiDou satellites<sup>4</sup>. The third group contains non-spherical Earth observation satellites at mainly low altitudes, where SLR is used for orbit determination and orbit validation. Recently SLR is also considered for time transfer by equipping satellites with photon counter units (see the ACES mission or the E-GRIP and E-GRASP/Eratosthenes proposals). More details about SLR can be found in Degnan (1993), Seeber (2003), Combrinck (2010), and (Xu, 2010).

### 2.1.3 Very Long Baseline Interferometry

In the purely geometrical technique Very Long Baseline Interferometry (VLBI) the time delay  $\tau_{rs}$  between the reception of the signal transmitted by extragalactic radio sources at two (or more) telescopes  $r$  and  $s$  (cf. Fig. 2.1) is observed with a precision of 10 to 30 ps (Schuh & Behrend, 2012). Usually, the observed frequencies are in the X-band ( $\approx 8.2$  to  $8.9$  GHz) and in the S-band (2.2 to 2.4 GHz), but also in the K- and Ka-band (20 to 40 and 26.5 to 40 GHz, respectively). With the new VGOS system VLBI will observe in four frequency bands between 3 and 14 GHz. The arriving wave fronts are plane as the observed radio sources are far away ( $> 1.5$  billion light years). Therefore, the observation equation for the observed time delay  $\tau_{rs}$  reads as

$$c_0\tau_{rs} = b_{rs}\cos\varphi_{rs} - \delta\rho_{ion_r} + \delta\rho_{trp_r} + c_0\rho_{t_r}(t) + \delta\rho_{tel_r}(t) + \delta\rho_{rel_r} + \delta\rho_{ion_s} + \delta\rho_{trp_s} + c_0\rho_{t_s}(t - \tau_{rs}) + \delta\rho_{tel_s}(t) + \delta\rho_{rel_s} + \epsilon_{rs} . \quad (2.3)$$

In Eqn. 2.3 the length and the orientation of the baseline between the two telescopes is given by  $b_{rs}$  and  $\varphi_{rs}$ , respectively. The station-specific clock offsets are  $\rho_{t_r}$  and  $\rho_{t_s}$ . Ionospheric and tropospheric delays are contained in  $\delta\rho_{ion_r}$ ,  $\delta\rho_{ion_s}$ ,  $\delta\rho_{trp_r}$  and  $\delta\rho_{trp_s}$ , respectively. The telescope characteristic and relativistic effects are given by  $\delta\rho_{tel_r}$ ,  $\delta\rho_{tel_s}$ ,  $\delta\rho_{rel_r}$  and  $\delta\rho_{rel_s}$ , respectively. The measurement noise is  $\epsilon_{rs}$ . The vector  $\mathbf{b}_{rs}$  is the geometrical baseline between the two telescopes, transformed into the inertial system. Together with the angle  $\varphi_{rs}$  between the baseline and the unit vector  $\mathbf{k}$  pointing towards the observed quasar, the access to station coordinates, source positions and ERPs is provided. As the signal reception times are not identical, individual transformation matrices have to be applied for the exact observation epochs at both stations. Relative clock errors  $\rho_t(t)$  are accounting for the imperfect synchronization between the individual receiver clocks, which is, and has to be, at the  $1\ \mu\text{s}$  level (Sovers et al., 1998). In the processing, clock corrections are setup as piece-wise linear functions relative to a fixed reference clock, which ensures the connection to UTC. Additionally, linear and quadratic clock functions are estimated session-wise in common VLBI processing software packages. Usually the estimated clock offsets also absorb some instrumental biases. This topic is discussed in more detail in Sect. 6.2. Tropospheric and ionospheric delays,  $\delta\rho_{trp}$  and  $\delta\rho_{ion}$ , at both stations  $r, s$  are comparable to the corresponding corrections in a single-differenced GNSS observation equation. Based thereon, several authors published atmospheric comparisons (Hobiger, 2006) or showed combined solutions (Krügel et al., 2007; Steigenberger et al., 2007) between GPS and VLBI. In most cases the ionosphere-like effects of intergalactic, interstellar and interplanetary plasma can be ignored as the electron density within these structures does not vary significantly within an Earth's diameter and the ray paths are, thus, affected in the same way (Hobiger, 2006). As part of the relativistic corrections  $\delta\rho_{rel}$  also the general relativistic, i.e., gravitational influence of bodies in our Solar System, especially of the Sun, on the signal has to be taken into account (Schuh, 1987; Sovers et al., 1998). The offset  $\delta\rho_{tel}(t)$  between the geometrical antenna reference point, defined by the intersection of the telescope axes, and the electrical phase center depends on the telescope mounting type and can reach several meters. Also thermal expansion (Wresnik et al., 2007; Nothnagel, 2009) and gravitational deformation (Sarti et al., 2010) of the telescopes are included in the term  $\delta\rho_{tel}(t)$ . The offset  $\delta\rho_{tel}(t)$  can vary by up to 15 mm with seasonal and up to 5 mm with daily periods (Haas, 1996). Corrections are provided by the IVS.

<sup>4</sup> The deactivated GPS-35 and GPS-36 spacecraft were also equipped with retro-reflectors.

In contrast to the other space geodetic techniques the VLBI telescopes are used not exclusively for geodetic purposes but mainly for astrometry<sup>5</sup>. Therefore, VLBI observations are performed with different station networks in three to five 24 h sessions per week (called rapid turn-around or shortly R1 and R4 sessions), plus daily intensive sessions, where two stations observe UT1 over one hour. Additional continuous VLBI sessions over two weeks, so-called CONT sessions, are performed every few years. With the modernization program VLBI2010 (Petrauchenko et al., 2012) and the VLBI Global Observing System (VGOS) the IVS aims at achieving continuous geodetic VLBI observations starting in 2020 (Hase et al., 2015). As opposed to the other space geodetic techniques, classical VLBI also benefits from the absence of satellite orbits and errors in the corresponding orbit force models. However, since many years, VLBI is also used to track space probes, like the VEGA balloons during their descent in the Venus atmosphere, or the descent of Huygens to Saturn's moon Titan, and lunar missions, like the Apollo Lunar Surface Experiment Packages or the Chinese Chang'E-3 mission. Earth-orbiting satellites, like GNSS satellites, were tracked in recent years (see Sect. 6.1.2). With RadioAstron (Kardashev et al., 2013) also the old idea of a VLBI telescopes orbiting the Earth was recently realized (Burke, 1991). From these developments it is obvious that fundamental steps towards a VLBI participation in the co-location task in space were achieved. More details about VLBI can be found in the literature (e.g., Sovers et al., 1998; Schuh & Behrend, 2012; Schuh & Böhm, 2013).

#### 2.1.4 Other Techniques

Doppler Orbitography and Radiopositioning Integrated by Satellite (DORIS) is the fourth space geodetic technique and is related to LEO orbit determination. Microwave signals of 0.401 and 2.036 GHz transmitted by a very well distributed station network with around 50 stations are tracked by several satellites, like the Jason, SPOT, and Sentinel satellite families. The Doppler shifts observations performed by the satellites are used to compute orbits, station coordinates, ERPs. More details on this technique can be found in Willis et al. (2010). As the Bernese GNSS Software version used is not capable to process DORIS this technique was disregarded in this work.

In the strict sense Lunar Laser Ranging (LLR) is not an individual space geodetic technique, as it is very similar to Satellite Laser Ranging while observing reflectors located at the lunar surface instead of reflectors on satellites. Corresponding reflector arrays were installed by the U.S. Apollo and the Soviet Lunochod missions between 1969 and 1973. Due to the much larger distance the signal loss is much higher (approximately  $10^{-21}$  as stated by Dickey et al., 1994), therefore, strong laser systems and large telescopes are required for LLR observations. Consequently, only a small set of laser stations is currently capable of performing LLR observations. As the relative measurement accuracy is  $1:10^{10}$  ( $\approx 2$  cm in the absolute sense) the observation equation and corresponding models have to be expressed in the post-Newtonian approximation (Seeber, 2003).

During the 1970s and 1980s the idea of using an SLR telescope orbiting the Earth to determine station coordinates of Earth-based reflectors was discussed. As GPS arose, it was never realized and the principle was adopted by the Geoscience Laser Altimeter System (GLAS) in the ICESAT and CryoSat missions, measuring Earth surface elevation from the orbit. Usually, altimetry is not counted as a space geodetic technique, as ground station positions cannot be estimated in a strict sense.

## 2.2 The Propagation of Space Geodetic Signals Through the Atmosphere

Signals from the microwave (0.3 to 300 GHz) and optical part (430 to 788 THz) of the electromagnetic spectrum are observed in space geodesy. As all space geodetic observations are based on run-time measurements, the knowledge of the speed of light in the propagation medium is crucial. The ratio between the

<sup>5</sup> A couple of telescopes, especially the new VGOS antennas, are only used for geodetic purposes.

speed of light in the vacuum  $c_0$  and the speed of light in the atmosphere  $c_a$  is referred to as the refractive index  $n$ . This index varies according to the atmospheric conditions and the observed signals. Therefore, the index for wave groups  $n_{gr}$  (relevant for, e.g., GNSS code observations) is different to the index for an individual wave  $n_{ph}$  (relevant for, e.g., GNSS phase observations). Due to refraction an electromagnetic signal passing through the atmosphere will be delayed or accelerated and will not follow the straight-line path length  $G$ , but the electrical (or optical) path length  $L_E$ . This difference, called excess of path length  $\delta\rho_{atm}$ , reads as

$$\delta\rho_{atm} = L_E - G = \int_L n(s)ds - G = \int_L (n(s) - 1)ds + (S - G). \quad (2.4)$$

Here  $S$  refers to the length of the real signal path, the difference  $S - G$  is negligible in most cases. Depending on the sign of  $\delta\rho_{atm}$  the observed signal is either delayed or accelerated. As  $\delta\rho_{atm}$  also depends on the atmospheric composition, the atmosphere is often divided (considering physical properties) into the neutral troposphere and the electrically charged ionosphere. Both atmospheric layers are addressed in the next two sections, whereas a more detailed description is given e.g., in Seeber (2003) and in Böhm & Schuh (2013).

### 2.2.1 Space Geodetic Signals in the Ionosphere

In the upper part of the Earth's atmosphere (40 to 1000 km altitude) gas molecules are heavily ionized by the absorption of solar radiation (Hobiger, 2006). The ionospheric refraction index for microwave-band frequencies reads as

$$n_{gr/ph} = 1 \pm a \frac{N_e}{f^2} \quad \text{with} \quad a = 40.3 \cdot 10^{16} \left[ \frac{\text{m}^3}{\text{s}^2 \cdot \text{TECU}} \right]. \quad (2.5)$$

The electron density  $N_e$  varies heavily in time and space. Latitudinally the ionosphere is segmented into the equatorial (below 30°), mid latitude and high latitude (above 60°) belts<sup>6</sup>. In the vertical direction the D-, E-, and F-layers are differentiated. Short time spans with a highly perturbed electron density are called ionospheric storms (Prölss, 2008). Fig. 2.2 shows the ionospheric behavior based on three different quantities during the time considered within this work. The characterization is similar to that given in Männel & Rothacher (2015). The first quantity, the 3 h  $K_p$  index, characterizes the effect of solar particles on the Earth's magnetic field in 27 steps from 0 to 9. Ionospheric storms are typically indicated by values larger than 5. Fig. 2.2 shows the daily maximum  $K_p$  indices<sup>7</sup> for the considered time span. The second quantity, the disturbed storm time index  $D_{ST}$ , represents the strength of the ring current around the Earth caused by solar particles. As the ring current is directed opposite to the Earth's magnetic field, negative values indicate a weakening of the Earth's magnetic field. Therefore, the daily minimum value is plotted in Fig. 2.2<sup>8</sup>. Values below -100 nT, indicating a moderate/strong ionospheric storm, occur only rarely. The third quantity, the daily global mean total electron content (TEC) derived from GNSS observations, represents the seasonal variability of the electron density. For each day the coefficient of degree and order zero between 12 UT and 14 UT is plotted as given in the global ionospheric maps (GIM, Schaer, 1999) provided by the Center of Orbit Determination in Europe (CODE). Concerning solar activity, the 11-year cycle is visible with two periods of higher solar activity in 2000 to 2002 and in 2012 to 2014, respectively (Klobuchar, 1996; Lee et al., 2006). Integrating the electron density along the signal path  $s$  leads to the total electron content (TEC)  $E$

$$E = \int N_e(s)ds, \quad (2.6)$$

<sup>6</sup> These zones are defined with respect to a magnetic reference frame (the geomagnetic north pole has a geographical latitude of 87.2° N).

<sup>7</sup> data source: [http://umbra.nascom.nasa.gov/sdb/yohkoh/ys\\_dbase/indices\\_raw/](http://umbra.nascom.nasa.gov/sdb/yohkoh/ys_dbase/indices_raw/), Oct. 2015

<sup>8</sup> data source: <http://wdc.kugi.kyoto-u.ac.jp/dstae/index.html>, Oct. 2015

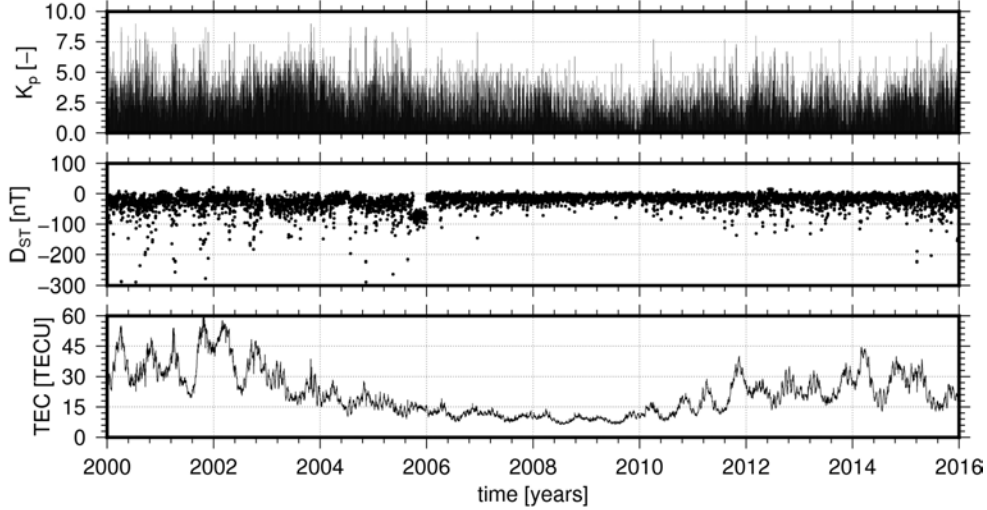


**Fig. 2.2:** Characterization of the ionosphere from 2000 to 2015. *top*: daily maximum  $K_P$  index, *middle*: daily minimum  $D_{ST}$  index, and *bottom*: daily mean TEC (derived from CODE GIMs)

which is expressed in total electron content units per square meter (TECU). The ionospheric effect on wave groups  $\delta\rho_{ion_{gr}}$  and on phase measurements  $\delta\rho_{ion_{ph}}$  can be expressed as

$$\delta\rho_{ion_{gr/ph}} = \pm \frac{aE}{f^2}. \quad (2.7)$$

Obviously, wave groups, e.g., GNSS code observations, are delayed in the ionosphere, whereas carrier phases are accelerated. From the relationship between delay and frequency in Eqn. 2.7 it is also obvious that the ionospheric delay is dispersive and can be eliminated (to first-order) by forming the ionosphere-free linear combination  $L_3$ . For X- and S-band signals in VLBI the remaining ionospheric delay is negligible (Hawarey et al., 2005). For GNSS so-called second- and third-order terms contain 0.1 % of the ionospheric delay (Hernández-Pajares et al., 2011) and should be taken into account as shown by Kedar et al. (2003) and Fritsche et al. (2005). If only single-frequency observations are available, the ionospheric delay in both techniques has to be corrected using suitable models, a topic which is discussed concerning orbit determination in Sect. 4.5.2 and concerning VLBI satellite tracking in Sect. 6.2. Eqn. 2.7 also shows that the ionospheric effect is negligible in the case of optical frequencies.

### 2.2.2 Space Geodetic Signals in the Troposphere

In the lowest atmospheric layer, called the troposphere (0 to 10 km), space geodetic signals are affected by air pressure and water vapor, usually referred to as the dry and the wet part of the troposphere. The refractivity of the dry  $N_d$  and wet part  $N_w$  for radio waves - depending on the pressure of dry air  $P$ , the water vapor  $e$ , the compressibilities  $Z_d$ ,  $Z_w$ , and the temperature  $T$  - reads as

$$N = N_d + N_w = k_1 \frac{P}{T} Z_d^{-1} + k_2 \frac{e}{T} Z_w^{-1} + k_3 \frac{e}{T^2} Z_w^{-1}. \quad (2.8)$$

The coefficients  $k_1, k_2, k_3$  in Eqn 2.8 are determined empirically and are part of the corresponding model. Obviously, as no frequency-dependent term can be found in Eqn. 2.8, the troposphere is non-dispersive for radio signals. The corresponding delay in GNSS and VLBI amounts to  $\approx 2.3$  m (or  $\approx 8$  ns) in zenith direction. The tropospheric delay  $\delta\rho_{trp}$  for the zenith distance  $z$  can be written as follows

$$\delta\rho_{trp}(z) = m_{trp,d}(z)\delta\rho_{trp,d}(z_0) + m_{trp,w}(z)\delta\rho_{trp,w}(z_0) \quad (2.9)$$

where  $m_{trp,d/w}$  are mapping functions, transforming the tropospheric delay from zenith direction  $z_0 = 0$  to the zenith distance  $z$ . The Vienna Mapping Function VMF1 (Böhm et al., 2006b), the Niell Mapping

Function (Niell, 1996, 2000), or the Global Mapping Function GMF (Böhm et al., 2006a) are examples of commonly used mapping functions for microwaves. During the processing, the rather stable tropospheric dry part is accounted for by corresponding models, whereas the highly variable zenith wet delay is estimated as a piece-wise linear function. Additionally, tropospheric gradients accounting for spatial variations are estimated when processing GNSS and VLBI. In the optical domain the troposphere behaves as a dispersive medium with a very small contribution of water vapor to the total delay, which amounts to around 2.2 m in zenith direction. The dispersive behavior of the troposphere is currently not exploited in SLR/LLR, as only a few stations observe in a dual-frequency mode and forming laser ranging linear combinations was only shown on an experimental level (Abshire & Gardner, 1985; Wijaya & Brunner, 2011). Therefore, in SLR and LLR, the tropospheric delay is usually corrected by the models of Marini & Murray (1973) and Mendes & Pavlis (2004).

## 2.3 Processing Space Geodetic Techniques using the Bernese GNSS Software

Thinking about the ideal processing software for co-location in space, one would search for an unique software package capable to

- process (and simulate) all space geodetic techniques with highest accuracy standards,
- perform accurate orbit determination for all relevant types of satellites, and
- combine the techniques on the observation level or at least on the normal equation level.

Within the project “Co-location on Ground and in Space” the Bernese GNSS Software (BSW, Dach et al., 2007, 2015) was selected for processing the wide range of space geodetic observations. The BSW provides high-quality processing capabilities for GNSS observations and reasonable functionalities for LEO orbit determination and SLR processing. A selection of other software packages available will be discussed in Sect. 3.4. Within this section, after a short introduction, to the BSW the implementations required for the thesis work and a further concept for a refinement of the BSW co-location capabilities are described. As a major part of the implementation work, VLBI capabilities were added to the BSW functionality. Therefore, exemplary VLBI results are shown in the last part of this section.

### 2.3.1 Introduction to the Bernese GNSS Software

The development of the Bernese GPS Software<sup>9</sup> as a software tool to process double-differenced GPS observations started at the Astronomical Institute of the University of Bern (AUIB) in 1983/84. With the currently available software version 5.2, released in December 2012, GPS, GLONASS, and Galileo observations can be processed in zero- and double-differencing mode. Also SLR data processing and LEO orbit determination is possible (Dach et al., 2015). Designed as a scientific tool, the BSW provides high-performance post-processing capabilities on the highest quality level. The BSW structure and its program components are described in Dach et al. (2007), Meindl (2011) and Dach et al. (2015). In general, the BSW consists of more than 100 programs, 1500 subroutines, and more than 450'000 lines of FORTRAN code (Dach et al., 2015). Usually, a BSW GNSS processing consists of the following steps (corresponding program names are provided in brackets):

- data import and conversion (RXOBV3, QLRINEXO, CRD2RNXO),
- auxiliary data preparation like ERPs and orbits (POLUPD, ORBGEN),
- pre-processing and outlier detection (CODSPP, MAUPRP, GPSEST, RESRMS, QLRSUM, SATMRK),
- final least-squares adjustment and generation of daily normal equations (GPSEST)

<sup>9</sup> With the release of version 5.2 in December 2012 the name was switched to Bernese GNSS Software.

- combination, manipulation and solving of normal equations (ADDNEQ2).

As CODE derive its final GNSS products using the BSW, processing GNSS observations with the BSW and using these CODE products leads to a consistency benefit (Dach et al., 2007). However, as the BSW was not intended to be a co-location software initially, several limitations have to be mentioned. Firstly, some techniques like VLBI or DORIS cannot be processed within the official version and a combination of techniques is, in some cases, restricted to the normal equation level. Secondly, the data structure was initially designed for classical ground-based receiver observations of GNSS satellites. Several amendments subsequently added for LEO and SLR processing complicated the house-keeping structures significantly. And thirdly, some aspects of the source code for LEO and SLR processing, do not work perfectly in all possible combinations. Within the next section new implemented capabilities and further concepts for a BSW co-location version are discussed.

### 2.3.2 Implementation and Discussion of new Capabilities for the Bernese GNSS Software

During the project “Co-location on Ground and in Space” major efforts were made in implementing new BSW capabilities. All implementations were done in the BSW project structure based on the official version 5.2. In the following these implementations are described.

#### VLBI capabilities

Major efforts were undertaken to add capabilities for VLBI into the BSW. Ralf Schmid implemented already a processing chain for classical VLBI in the former BSW version 4.3 (Schmid, 2009). Therefore, the main work was the adaption of his subroutines into the version 5.2 and to ensure that all GNSS and SLR functionalities are still available. The VLBI processing line starts with the program FMTOVLBI, where VLBI observations provided in NGS card files are extracted into baseline-wise Bernese single-difference code observation files. Contrary to GNSS, ionosphere-corrected X-band observations are processed in VLBI instead of the ionosphere-free linear combination in GNSS. Correspondingly, the X-band observations are corrected by the following term (Hobiger, 2006)

$$\Delta\tau_{ion,X} = \frac{f_S^2}{f_X^2 - f_S^2}(\tau_X - \tau_S) + \tau_{1,inst} - \tau_{2,inst} . \quad (2.10)$$

The instrumental biases  $\tau_{1,inst}$ ,  $\tau_{2,inst}$  comparable to the DCBs in GNSS, will be absorbed by the receiver clock estimates during the processing. The resulting single-differences are subsequently processed in GPSEST. According to Schmid (2009) the main differences compared to a GNSS processing are the quasar coordinates, the partial derivatives regarding the EOPs, and the handling of the receiver clocks. The partial derivatives concerning EOPs containing quasar instead of satellite positions are provided in Schmid (2009). As mentioned previously, receiver clock variations are considered in VLBI software packages also by estimating linear and quadratic clock polynomials in addition to a piece-wise linear function. However, in the BSW implementation, only the piece-wise linear representation similar to the tropospheric delays was implemented. In the new implementation receiver clock offsets can now also be handled in ADDNEQ2. When combining VLBI sessions on the normal equation level in ADDNEQ2, it is ensured that the piece-wise linear clock parameters are not estimated across session boundaries. Consequently, a new set of parameters is set up after telescope resets. Major BSW house-keeping changes result from the new observation type (4=VLBI) and the usage of 4-digit quasar numbers instead of 3-digit satellite numbers. However, further work is needed to ensure a complete VLBI functionality, e.g., a special internal VLBI observation file type, the estimation of source positions, quality checks like residual screening and other utilities have to be implemented. Additionally, simulation and processing paths for VLBI observations to Earth orbiting satellites have been implemented. The processing of satellite VLBI tracking data has been implemented similar to the processing of differential code observations, i.e., it is based on

the light-time equation. Dedicated VLBI near-field models (e.g., Sekido & Fukushima, 2006; Duev et al., 2012; Plank, 2013) have not been considered within this thesis. In order to simulate the VLBI tracking of Earth orbiting satellites the program GPSSIM was extended. The simulation principle of GPSSIM can be summarized as computing geometric delays, applying corrections, and adding user-specified white noise. As recommended by Wresnik (2009) and Plank (2013), a receiver clock and a turbulence model for the troposphere were implemented for the VLBI simulations. The simulation procedure follows Böhm et al. (2006c) and is described in more detail in Chap. 6. So far it is not possible to simulate classical VLBI observations of quasars in the modified Bernese GNSS Software. Within this project additional subroutines were implemented to compute ionospheric delay corrections from co-located GNSS observations. Therefore, the program IONEST was modified to perform the transformation of double-difference residuals into baseline-wise residuals (based on the work of Wang et al., 2014). Also the splitting into zero-difference residuals and the possibility to apply ionospheric corrections to GNSS and G-VLBI observations were implemented (for more details see Sect. 6.2.1).

### **SLR capabilities**

The most important features for SLR simulations were added within the existing program GPSSIM. However, special SLR-biases, like range biases, are currently not considered. Similarly, station-specific accuracy levels and cloud coverage probabilities are currently not available. The satellite, for which SLR observations are to be simulated, is selected either by the introduced orbit file or by providing a schedule file containing the time epochs and satellite number for each simulated observation. Obviously, the latter is crucial for GNSS satellite tracking. Therefore, the implemented capabilities for SLR simulations are helpful to test concepts for co-location in space concepts and to assess improvements due to simultaneous SLR observations, but not for generating realistic scenarios.

### **Orbit determination capabilities**

The official BSW orbit determination scheme was initially developed for GPS satellites, where non-gravitational forces (namely solar radiation pressure) were considered by setting up empirical parameters according to the CODE radiation pressure model (Springer et al., 1999). For LEO orbit determination, that was implemented later, pseudo-stochastic orbit parameters were set up to account for the unmodelled non-gravitational forces (Bock, 2003). In Sect. 4.2.2 and 4.4 these parameters and their impact on the orbit determination quality are discussed in more detail. Additionally, a priori models for the non-gravitational forces (solar radiation pressure, Earth albedo, and air drag) were implemented based on common force models and satellite-specific box-wing specifications. The necessary subroutines were provided by C. Rodriguez and P. Stephanek. However, several adjustments were necessary to adopt their source code for the BSW project version used for this thesis.

### **Combination capabilities**

On the level of inter- and intra-technique combinations less implementation work was required. So far the most important issue is the current limitation to only one orbit type in the program ADDNEQ2. To be able to process ground- and LEO-based GNSS data together a separate handling of the orbit pre-elimination options for GNSS and LEO satellites was implemented in GPSEST. The implemented pre-elimination is done before writing the normal equations in order to circumvent the mentioned restrictions in ADDNEQ2. In the future also the handling of terrestrially measured offset vectors (local ties) and other (tropospheric and clock) ties has to be improved.

### **An Extended Concept for a BSW Co-location Refinement**

To refine the BSW into an optimized co-location software several more general issues should be considered. Primarily, the structure of transmitting satellite and receiving station should be modified into a pure sensor-

Tab. 2.2: Characterization of space geodetic transmitters and receivers

feature	GT	RR	VT	DT	VQ	GR	SR	VR	DR	implementation remarks
description	GNSS trans-mitter	retro-reflector	VLBI trans-mitter	DORIS trans-mitter	quasar	GNSS receiver	laser station	VLBI tele-scope	DORIS receiver	
name	PRN	SVN <sup>f</sup>	SVN	IDS	ICRS	IGS	ILRS	IVS	SVN	short and extended name (4 and 20 characters, respectively)
platform										
ground	(✓) <sup>d</sup>	(✓) <sup>d</sup>	(✓) <sup>d</sup>		✓	✓	✓	✓	✓	6-dim 0/1 array
kinematic						✓				
LEO	✓	✓	✓			✓		✓		
GNSS		✓	✓							
Moon		✓								
Quasar					✓					
frequency bands	L	optical	S,X,K	S	optical	L	optical	(L),S,X,K	S	4-dim array [GHz] <sup>e</sup>
observation type	✓		(✓)			✓		(✓)		2-dim array (group, phase)
system-specific						✓		(✓)		4-dim 0/1 array
offset vector	✓	✓	✓	✓		✓	✓	✓	✓	3-dim array [m]
azimuth vector	✓	✓	✓			✓		✓	✓	3-dim array [unity]
bore-sight vector	✓	✓	✓			✓		✓	✓	3-dim array [unity]
PCO & PCV mounting type	✓	(✓)	(✓)			✓		✓		link to separate file
hard-coded delays		✓ <sup>a</sup>					✓ <sup>b</sup>	✓ <sup>c</sup>		correction value [m]
time	✓	✓	✓	✓		✓	✓	✓	✓	start/end time

<sup>a</sup> CoM correction<sup>b</sup> range bias<sup>c</sup> cable delay<sup>d</sup> ground-based common target concept<sup>e</sup> assuming that pre-processed observations will be available for not more than four frequencies<sup>f</sup> special ID for the Moon

**Tab. 2.3:** Characterization of space geodetic platforms; type GNSS is separately defined due to their importance in space geodesy

feature	ground	kinematic	LEO	GNSS	Moon	quasar	implementation
name	IERS	individual	SVN	SVN/PRN	ILRS	ICRS	short and extended name (4 or 20 char., resp.)
observation type							
GNSS	✓	✓	✓				4-dim 0/1 array
SLR			✓	✓	✓		
VLBI			✓	✓	✓ <sup>a</sup>	✓	
DORIS			✓				
static platform							
position	✓	TRF $(x, y, z)$	orbit $(x, y, z, \dot{x}, \dot{y}, \dot{z}, \ddot{x}, \ddot{y}, \ddot{z})$	orbit $(x, y, z, \dot{x}, \dot{y}, \dot{z}, \ddot{x}, \ddot{y}, \ddot{z})$	lunar system $(x, y, z)$	✓ $\delta, \alpha$	9-dim array, epoch-specific coordinates
tectonic plate							
macro-model	✓		✓	✓		✓	4-character name, pre-defined list 0/1 and link to separate file
source structure						✓	0/1 and link to separate file
orbit model			✓	✓	✓	✓	12 structured lines of each 80 characters containing all relevant information (as currently in BSW) e.g., DE405
ephemeris					✓		
reference point	sensor reference point	sensor reference point or vehicle reference point	center of mass	center of mass	center of mass (Moon)	center of mass	
time	✓	✓	✓	✓	✓	✓	start/end time

<sup>a</sup> e.g., Apollo Lunar Surface Experiment Package observations and ChangE-3

specific structure, where all information (a priori position, sensor type, offsets) are linked to the sensor class. A potential draft of such a concept is shown in Tab. 2.2. In total nine space geodetic sensor types can be defined: GNSS transmitter, retro-reflector, artificial VLBI transmitter, DORIS transmitter, quasar, GNSS receiver, laser station, VLBI telescope, DORIS receiver. A large set of features can be assigned to each of them, like a name, frequencies, orientation, and active periods. Consequently, each space geodetic observation will be assigned to two sensor types. By establishing a definition matrix a subset of sensors will be unlocked for each space geodetic observation type mentioned in Tab. 1.1. A main feature of the defined sensors is the related platform. The six defined platform types are listed in Tab. 2.3 as ground (static), kinematic, satellite, GNSS, Moon, and quasar. In the same way several features are assigned to each platform type, like platform coordinates, orbit, and reference point. Again each platform will be unlocked for a set of observation types by implementing an appropriate matrix. Please note that the platform type “GNSS” is defined separately from the “Satellite” class due to its importance in space geodesy. In the present BSW implementation, a comparable but more basic and less general concept is realized. For example, stations can be assigned to be space-borne, in order to prevent the application of tidal corrections. In the current satellite file, available on-board sensors including their orientation can be defined. However, looking at the processing, a large set of uncoordinated features from multiple sources (satellite file, observation files, user interface) is tested in order to apply appropriate corrections for each observation type. Having all necessary features in a well-defined data structure, as it is realized, e.g., for the normal equation elements in ADDNEQ2, filled during the program initialization, will be necessary for a consolidated processing of different space geodetic techniques. However, implementing such a concept will most likely result in a nearly complete re-writing of the source code of the main BSW programs. A comparable process was initiated for the transition from a single GPS to a multi-GNSS software package in recent years. Meindl (2011) presented a dedicated new software concept and architecture for the BSW allowing to handle all GNSS and to form all possible linear combinations. However, the huge implementation process (Bernese Version 6) is presently stuck.

However, smaller changes are more easily realized than the described concept. For example, local ties should be included in ADDNEQ2 as pseudo-observations or an appropriate concept to handle station coordinate discontinuities should be applied.

### 2.3.3 Assessment of Bernese VLBI Capabilities: Results for the Continuous VLBI Campaign 2014

In order to test the implemented VLBI capabilities the VLBI observations derived during the CONT14 campaign were processed. This continuous VLBI campaign took place in 2014 from May 6 to 20 and involved 17 VLBI stations, which are shown in Fig. 2.3 and listed in Tab. C.1. To assess the achieved processing quality station coordinate repeatabilities, VLBI residuals, tropospheric zenith delays, and ERP results were studied within this section. The comparisons were performed against (1) CONT14 results published so far, (2) results from other space geodetic techniques for common parameters, and (3) results from previous CONT sessions. The processing was done in a daily session mode (0-24 h UT), generating daily normal equation files. The estimated parameters include station coordinates (constant for one day), tropospheric zenith wet delays (piece-wise linear, 2h), tropospheric gradients (piece-wise linear, 24h), receiver clock offsets (piece-wise linear, 2 h), and ERPs (piece-wise linear, 24h). As CONT14 sessions were defined in the same daily mode (0-24 h UT), clock jumps were only required in the case of clock breaks (e.g., due to telescope resets). The individual daily normal equations were then stacked to obtain the final solution. As the simultaneous estimation of coordinates for all stations produces a rank defect, the net-translation and net-rotation with respect to ITRF2008 coordinates were constrained to zero for eleven core stations during the ADDNEQ2 program run (see Tab. C.1).

Firstly, the station coordinates  $dr_i$  of the daily processing were compared against the station coordinates of the combined solution  $dr_m$  in order to assess the quality of the derived station coordinates. These so-called



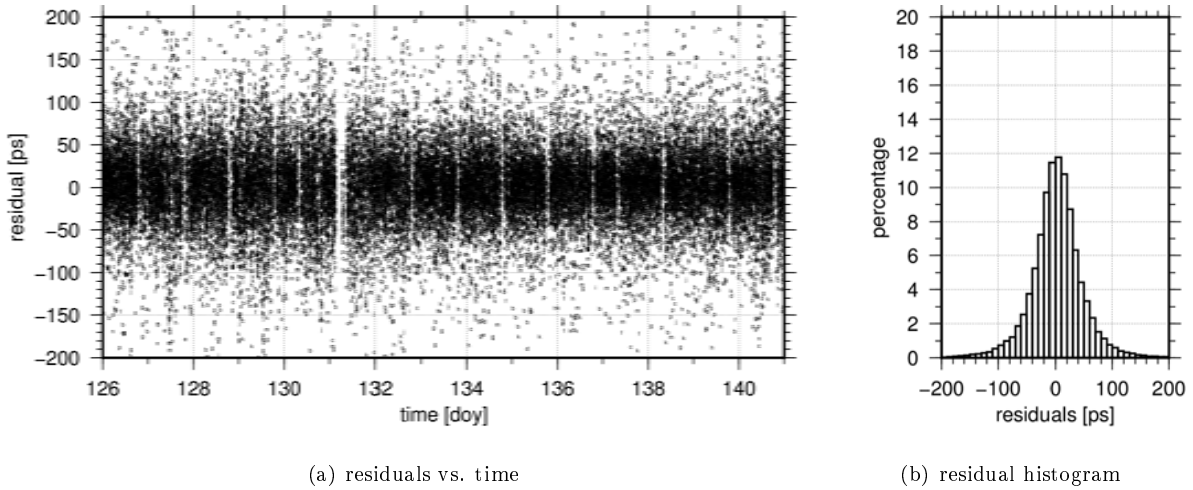


**Fig. 2.5:** VLBI residuals for baselines with station WETTZELL during CONT14, same letters indicate same baselines

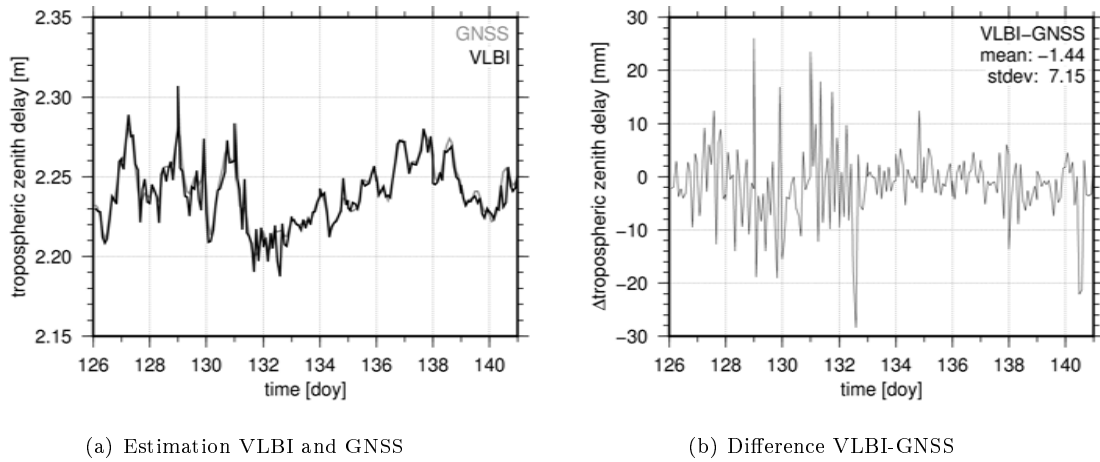


**Fig. 2.6:** Tropospheric zenith delays for Wetzell during CONT14 estimated from VLBI (RTW) and GNSS (WTZZ) observations

gaps are visible: Wetzell joined each day the hourly INT session (intensive baseline observation to derive UT1) and a 3.5 h gap due to a servo failure occurred on day 131 (May 11). The derived residuals are mainly below 50 ps (79.1 %) and the overall  $RMS = \sqrt{\frac{\sum r^2}{n}}$  amounts to 46.67 ps ( $\approx 1.39$  cm). Comparing the RMS for each WETTZELL baseline shows that the best determined baseline is formed with NYALES20 (RMS = 30.48 ps, 4838 X-band observations) and the weakest baseline with HOBART12 (108.99 ps, 174 X-band observations). The overall RMS of 46.67 ps is comparable to the results derived by Schmid (2009). Compared to the 30 ps weighted root mean square, which is derived by standard VLBI software packages for usual VLBI sessions, 46.67 ps seems to be large. However, in the presented solution observations are equally weighted and no outlier detection was performed except for the exclusion of observations marked already in the NGS card files. By manually eliminating all observations with residuals above 3 cm, Schmid (2009) decreased the RMS in a second processing step for one arbitrary chosen daily solution from 42.3 to 36.0 ps.

Thirdly, a comparison against externally estimated tropospheric delays was performed to assess the quality of the derived troposphere values. As the troposphere is non-dispersive for microwave observations, GNSS and VLBI observations are affected in the same way (see Sect. 2.2.2). Consequently, tropospheric zenith delays computed homogeneously from GNSS and VLBI observations should be similar. Several authors compared troposphere parameters derived by GNSS, VLBI and other techniques, like DORIS or water

**Tab. 2.4:** Differences VLBI-GNSS in tropospheric zenith delays between VLBI and GNSS during CONT14 (mean and standard deviation); GNSS-based tropospheric estimates from CODE, where YEBE is not included; CONT02 and CONT08 solutions from Teke et al. (2011) and the IVS results from Schuh et al. (2005)

IVS station	IGS station	$\Delta D = h_{VLBI} - h_{GNSS}$ [m]	# ZWD par.	CONT14 [mm]	CONT02 [mm]	CONT08 [mm]	IVS <sup>c</sup> [mm]
BADARY	BADG	10.19	191	$-3.98 \pm 6.77$			
FORTLEZA	BRFT	1.40	194	$-1.24 \pm 15.69$			$13.5 \pm 9.6$
HART15M	HRAO	1.96	194	$1.54 \pm 5.91$	$-3.4 \pm 5.8$	$0.1 \pm 5.2$	$5.2 \pm 8.1$
HOBART12	HOB2	-0.16	191	$5.06 \pm 9.93$			
HOBART26	HOB2	24.03	188	$-5.84 \pm 10.68$			$3.2 \pm 7.4$
KATH12M	KAT1	4.96	175	$-2.29 \pm 8.27$			
KOKEE	KOKB	9.24	194	$-2.72 \pm 9.16$	$-5.7 \pm 6.6$	$1.9 \pm 9.5$	
MATERA	MATE	7.72	183	$-4.50 \pm 9.59$			$3.9 \pm 6.8$
NYALES20	NYA1	3.10	162	$-2.20 \pm 4.62$	$0.1 \pm 3.3^a$	$0.0 \pm 3.9^a$	$4.1 \pm 3.8^a$
ONSALA60	ONSA	13.71	193	$-2.44 \pm 6.31$	$0.7 \pm 4.1$	$3.1 \pm 5.0$	$4.8 \pm 4.5$
TSUKUB32	TSKB	17.37	194	$-5.26 \pm 9.28$		$1.4 \pm 11.6$	
WESTFORD	WES2	1.75	194	$-6.30 \pm 9.90$	$-6.5 \pm 3.5$	$-3.7 \pm 6.4$	$6.7 \pm 3.7$
WETTZELL	WTZZ	3.10	194	$-1.44 \pm 7.15$	$-2.1 \pm 4.5^b$	$-2.1 \pm 4.6^b$	$2.4 \pm 4.3^b$
YARRA12M	YARR	6.86	194	$-4.94 \pm 9.21$			
YEBES40M	YEBE	7.11		n/a			
ZELENCHK	ZECK	8.16	168	$9.32 \pm 15.45$			

<sup>a</sup> compared against NYAL

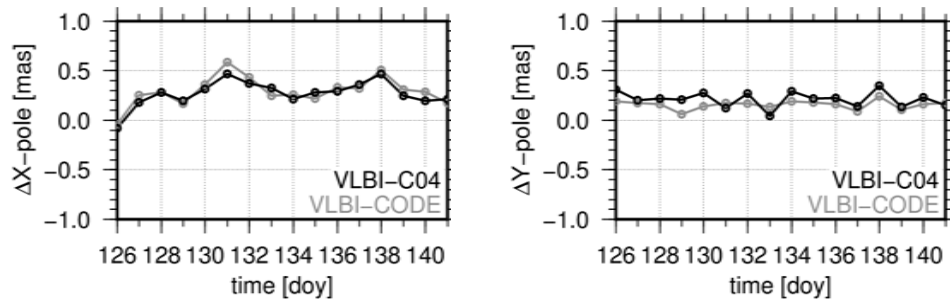
<sup>b</sup> compared against WTZR

<sup>c</sup> provided as GNSS-VLBI, as given in Schuh et al. (2005)

vapor radiometers (e.g., Krügel et al., 2007; Steigenberger et al., 2007; Teke et al., 2011; Rothacher, 2011). As shown in Fig. 2.3, all CONT14 radio telescopes are co-located with GNSS receivers. The delay comparison shown here was done based on the tropospheric zenith delays provided by CODE (temporal resolution 2h). A very simple interpolation for the GNSS values was performed, as these values are provided at the odd hours and the VLBI-derived tropospheric delays are given at even hours. Fig. 2.6 shows the derived results for Wettzell. The good agreement between both time series is obvious. Small differences are related to (1) the applied interpolation and (2) the uncorrected height differences  $\Delta D$  between VLBI and GNSS reference points. However, the differences for Wettzell are mostly below 20 mm. In their studies, Krügel et al. (2007) and Steigenberger et al. (2007) showed similar differences for Onsala (CONT02) and Alongquin Park (long-term processing), respectively. Tab 2.4 shows the derived biases and standard deviations for all CONT14 stations except YEBES40M, as the co-located IGS station YEBE was not included in the CODE solution. Both, biases and standard deviations are comparable to the results shown by Teke et al. (2011) for CONT02 and CONT08 and by Schuh et al. (2005) for IVS R1 and R4 sessions during 2002. As the biases are partly caused by the neglected height difference between VLBI and GNSS, Tab. 2.4 also provides the corresponding station height differences  $\Delta D = h_{VLBI} - h_{GNSS}$ . The effect of the hydrostatic part of the troposphere, i.e., related to air pressure, amounts to roughly 0.3 mm per meter<sup>10</sup>. Consequently, the derived biases for some of the stations can be explained by the neglect of this effect. For example for Wettzell, 1 mm of the 1.4 mm bias can be attributed to the height difference of 3.1 m. The ways of how to take the height differences into account are discussed in more detail in Sect. 3.5 concerning tropospheric ties. The formal errors are in the range of 1 to 3 mm for the VLBI solution, whereas the CODE tropospheric estimates have formal errors of 4 to 6 mm.

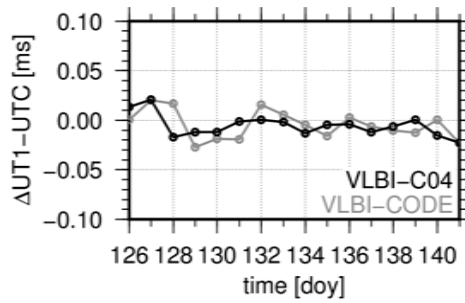
Fourthly, in a last step, also the derived results for the pole coordinates and the difference UT1-UTC were compared. A similar analysis is provided by Thaller et al. (2006) and Rothacher (2011). For the pole coordinates, clear offsets of  $0.27 \pm 0.13$  mas and  $0.21 \pm 0.08$  mas were found between the VLBI and the IERS 08 C04 series for x and y, respectively. However, there are only minimal differences between the comparison against CODE ERP and against C04, which were introduced a priori in the CODE ERP estimation. For

<sup>10</sup> According to the Saastamoinen model the corresponding relationship is  $\delta\rho_{trp,d}(z_0) = 2.277 \cdot 10^{-3}p$ .



(a) Differences X pole coordinate

(b) Differences Y pole coordinate



(c) Differences in UT1-UTC

**Fig. 2.7:** Comparison of CONT14 ERP estimates against CODE ERP products and C04 ERP series

UT1-UTC no offset was found between VLBI and C04 and the differences are below 0.2 ms.

Summarizing, the BSW CONT14 processing shows a good performance and the derived results are comparable to other solutions. The results achieved in the BSW VLBI processing show similar accuracy as the results that Ralf Schmid derived for CONT02 and the results derived from the CONT14 campaign derived by dedicated VLBI software packages. In general, it was shown that the remaining residuals are slightly larger than in other software packages ( $\approx 45$  ps instead of  $\approx 30$  ps) as no sophisticated outlier detection was performed. Therefore, the processing of VLBI sessions with the BSW project version is reasonable.

# 3 Reference Systems and the Combination and Co-location of Space Geodetic Techniques

A geodetic reference system allows the representation of geodetic observations as a function of unknown parameters (Torge & Müller, 2012). Therefore, a well-defined and unambiguous reference system provides the metrological basis for all geodetic measurements on the Earth and in space (Kovalevsky et al., 1989; Nothnagel et al., 2010). Any reference system shall ensure precision, stability and accessibility on the base of a clear mathematical and physical basis. In the framework of space geodesy, a global reference system can be defined as inertial, i.e., fixed to distinct directions in space, or as Earth-fixed, i.e., co-rotating with the Earth. The first one is called celestial reference system, whereas the latter is usually called terrestrial reference system. In geodesy the term reference system consists of: (1) the purely theoretical ideal reference system, and (2) the conventional reference system. The latter gives the connection between the reference system and definite points by a set of physical models, e.g., tidal models, loading coefficients and others. The users, e.g., geodesists, geoscientists, or GNSS users, have access to a reference system via a set of coordinates for distinct markers. The whole set of these markers is called reference frame. Therefore, a reference frame is defined to be one realization of a certain reference system. This realization is achieved physically by a solid materialization of points, and mathematically, by the determination of geometric coordinates, which provides the relation between the reference system and the reference frame (Nothnagel et al., 2010). The concept of terrestrial reference systems has been broadly discussed in the astronomical and geodetic communities, for example by Kovalevsky et al. (1989); Boucher (2000); Drewes (2009a); Nothnagel et al. (2010); Angermann et al. (2013). Within this chapter the main aspects of both, the celestial and the terrestrial reference system and their realizations are discussed with the main focus on the issue of combination and co-location of the space geodetic techniques.

## 3.1 Definition and Realization of the Celestial Reference System

In an inertial reference system, which is either in a state of rest or, with respect to another inertial system, in a constant, rectilinear motion, the Newtonian laws and the dynamic equations of motion are valid. Consequently, no fictitious forces, like the Coriolis, the centrifugal or the Euler force, have to be taken into account. Therefore, an inertial reference system is the natural system to describe the motion of the Earth, planetary orbits, or the trajectories of artificial spacecraft. At present inertial systems are approximated by a space-fixed system realized by a set of extra-galactic sources. Several inertial systems can be designed depending on the definition of the reference system origin. By neglecting external galactic and extra-galactic matter the barycenter, the center of mass of the solar system, can be used as the origin resulting in the barycentric celestial reference system (BCRS). This reference system is applied for the development of solar system ephemerides, interplanetary spacecraft navigation and modeling light propagation from distant celestial objects (Sovers et al., 1998; Nothnagel et al., 2010; Plank et al., 2014). Since January 1st, 1998 the International Celestial Reference System (ICRS) is the conventional version of the BCRS (Feissel & Mignard, 1998). The axes of the ICRS are defined by the directions to extra-galactic radio sources and are kinematically non-rotating with respect to these axes. The radio sources are quasi-stellar radio sources (quasars), BL Lac sources and active galactic nuclei (Sovers et al., 1998; Nothnagel et al., 2010). According to the IAU Recommendation VII from 1991 the principal plane of the ICRS is stipulated close to the mean equator at epoch J2000.0 and the origin of this principle plane and the origin of the

right ascension of the ICRS are close to the dynamical equinox at epoch J2000.0 (Feissel & Mignard, 1998). The origin of the right ascension is defined by the mean right ascension of 23 radio sources, with consistent positions achieved by fixing the position of the source 3C273B to the fundamental star catalogue FK5 (Fricke, 1982). Furthermore the direction of the conventional reference pole is also stipulated to be consistent with that of the FK5. More details are given in the IERS Conventions 2010 (Petit & Luzum, 2010). Based on VLBI observations a first realizations of the ICRS was constructed in 1995, called ICRF (Ma et al., 1998). In total, observations to 608 sources were considered, 212 of them were so-called defining sources, which were used to realize the axes of the reference system at the  $\pm 0.02$  mas level<sup>1</sup>. The median uncertainties of these defining sources were  $\pm 0.35$  mas and  $\pm 0.40$  mas in right ascension and declination, respectively. Later on two extensions of the ICRF were published, named ICRF-Ext. 1 (59 new sources) and ICRF-Ext. 2 (109 new sources). However, significant systematic biases were identified by Sokolova & Malkin (2007) and other authors. The successor, the currently used ITRF2 (Ma et al., 2009) has been realized by analyzing 30 years of VLBI observations and contains 3414 radio sources (295 defining sources) in total. The stability of the ICRF2 axes is specified to be approximately 0.01 mas. The noise level, caused by structural instabilities of the sources, is at a level of 0.04 mas (Ma et al., 2009). Currently a third version, ICRF3, is under development (Malkin et al., 2014). In the optical domain the ICRS is realized by the HIPPARCOS Celestial Reference Frame (HCRF, IAU Resolution B1.1). The position accuracy of the 118'322 stars contained in this catalogue is at the 1 mas level. With ESA's GAIA mission, launched in 2013, a new catalogue and a new optical reference frame will be realized including 1 billion stars and reaching position accuracies of about  $24 \mu\text{as}$ .

The Geocentric Celestial Reference System (GCRS), where the origin is shifted from the Barycenter to Earth's geocenter and the spatial coordinates are kinematically non-rotating with respect to the barycentric ones, is more appropriate to describe the trajectory of Earth orbiting satellites (Nothnagel et al., 2010). There, the geocenter is defined to be the center of mass of the Earth including the mass of the solid Earth, the cryosphere, the oceans, the continental hydrosphere and the Earth's atmosphere (for more details see Sect. 5.2). However, as VLBI is a purely geometrical observation technique, no information concerning the Earth's center of mass can be derived from quasar observations (Sovers et al., 1998)<sup>2</sup>. To establish the GCRS a combination of VLBI and geodetic satellite techniques or the representation of VLBI stations in a geocentric system (based on satellite techniques) is necessary. Due to the gravitational attractions of the Sun, the Moon, and the planets the GCRS is accelerated and not inertial anymore. Therefore, caused by Earth's revolution around the Sun and the (much smaller) geodetic precession-nutation, the Coriolis force appears in a dynamic equation of motion set up in the GCRS. Even though the effect is small it is recommended by the IERS Conventions to take this additional force into account.

### 3.2 Definition and Realization of the Terrestrial Reference System

A terrestrial reference system is defined to co-rotate with the Earth. Hence, station coordinates are expected to show not the daily rotation of the Earth, but only small temporal variations, due to non-modeled geophysical processes. Obviously, this reference system is accelerated and fictitious forces have to be considered, when solving for the dynamic equation of motion. It can be concluded, that the terrestrial system is convenient to describe positions and slow movements of objects connected to Earth's surface. The ideal terrestrial reference system has its origin in the geocenter. The directions of three orthogonal base vectors give the orientation, where the z-axis is close to the rotation axis of the Earth. The scale, defined by the length of the base vectors, is close to the SI definition of the meter. By a set of models and conventions the conventional terrestrial reference system, called International Terrestrial Reference System (ITRS), is defined and adjusted to the moving and deformable Earth surface. Following Resolution No. 2

<sup>1</sup> The other sources are either candidate (294, less observations) or other (102, less appropriate for astrometry) sources.

<sup>2</sup> From the theoretical point of view, the geocenter could be estimated from VLBI observations by calculating the loading displacement and using an inverse strategy (Lavallée & Blewitt, 2002).

of the IUGG adopted in 1991 and the most recent version of the IERS conventions, the ITRS is defined as:

- a geocentric reference system with the origin in the center of mass of the Earth,
- with the meter as unit of length and a scale consistent with the time coordinate of a geocentric celestial reference frame, i.e., consistent with the geocentric coordinate time TCG (*temps-coordonnée géocentrique*),
- an initial orientation consistent with the orientation of the BIH Terrestrial System at epoch 1984.0 (BIH *Bureau International de l'Heure*), and
- a time evolution of the orientation constrained by applying a no-net-rotation condition with respect to the horizontal Earth surface.

The International Terrestrial Reference Frame (ITRF) is the most important realization of the ITRS and station coordinates and velocities for a selected set of stations (markers). The computation of the ITRF is based on the combination of station coordinates and velocities derived from the four space geodetic techniques. The different reference points of each technique are connected into account by using local tie vectors at fundamental sites (cf. Fig. 1.1).

In the following the ITRF datum realization (Sect. 3.2.1), the historical evolution of the ITRF realizations, and the IERS station network (Sect. 3.2.2), and the site displacements (Sect. 3.2.3) are discussed. A compendium on the current discussion concerning the ITRF definition and realization is provided in Sect. 3.2.4. Important topics, discussed in the following sections, are the transformation between terrestrial and inertial systems (Sect. 3.3), the combination of space geodetic techniques (Sect. 3.4), and the co-location concepts (Sect.3.5).

### 3.2.1 The ITRF Datum Definition and the Role of Space Geodetic Techniques

In the following the role of space geodetic techniques in the ITRS datum definition is discussed. From the definition given above it is obvious that conventions and/or observations independent from measurements defining the reference frame are required for the datum definition (cf. Drewes, 2009a).

Based on the ITRS definition above, the origin should coincide with the geocenter. Therefore, coordinates of the geocenter must be zero by definition (i.e.,  $x_0 = y_0 = z_0 = 0$ ). However, as the geocenter is the center of the Earth gravity field, the geocentric origin can also be realized by gravimetric parameters (Nothnagel et al., 2010)

$$x_0 = \iiint x \, dm / M_E \quad (3.1)$$

$$y_0 = \iiint y \, dm / M_E \quad (3.2)$$

$$z_0 = \iiint z \, dm / M_E \quad (3.3)$$

where  $M_E$  is the total mass of the Earth. The formulas 3.1-3.3 are nearly identical to the spherical harmonic coefficients of the Earth's gravity field (with the Earth's semi-major axis  $a_E$ )

$$C_{11} = \iiint x \, dm / a_E M_E \quad (3.4)$$

$$S_{11} = \iiint y \, dm / a_E M_E \quad (3.5)$$

$$C_{10} = \iiint z \, dm / a_E M_E . \quad (3.6)$$

Therefore, if a gravity field model with  $C_{11} = S_{11} = C_{10} = 0$  is used in satellite orbit determination, automatically a geocentric reference system with  $x_0 = y_0 = z_0 = 0$  is introduced (Nothnagel et al., 2010). In very basic terms, the relationship between the geocentric position  $\mathbf{r}^i$  of a satellite  $i$  and the position  $\mathbf{r}_r$

of a receiver  $r$  reads as (Meindl et al., 2013)

$$D_r^i = |\mathbf{r}^i(t_e) - (\mathbf{r}_r(t_r) + \mathbf{G}(t_r))| + \epsilon. \quad (3.7)$$

In Eqn. 3.7  $D_r^i$  describes the satellite geodetic measurement (with measurement noise  $\epsilon$ ), whereas  $\mathbf{r}^i(t_e)$  is the geocentric satellite position and  $\mathbf{r}_r(t_r)$  the station coordinates. The position of the geocenter is referred to as  $\mathbf{G}(t_r)$ .  $D_r^i$  with its characteristic signal delays, sensor offsets, technique-specific biases;  $\epsilon$  contains the measurement noise. The derived station coordinates  $\mathbf{r}_r$  will be geocentric, if no additional constraints are introduced and the observations are unbiased. Consequently, the reference system's origin realized by the corresponding station network will coincide with the center of mass and the position vector  $\mathbf{G}(t_r)$  of the origin relative to the center of mass will be zero. In summary, the origin is defined dynamically. Currently only SLR observations are used to derive the origin. Other satellite techniques are not considered for several reasons (for more details see Sect. 5.2). However, due to mass re-distributions, station coordinates vary in time with respect to the origin. An overview of the most important processes is provided in Sect. 3.2.3. A detailed discussion of the interaction between geophysical processes, station coordinates and the origin is given in Sect. 5.2 and in the literature (e.g., Dong et al., 1997; Wu et al., 2012). In a reference frame, coordinates of points anchored on the Earth solid crust, so-called terrestrial points, are expressed by (Nothnagel et al., 2010)

$$\mathbf{r}_r(t) = \bar{\mathbf{r}}_r(t) + \sum_i \Delta \mathbf{x}_i(t). \quad (3.8)$$

The regularized or conventional position  $\bar{\mathbf{r}}_r(t)$  is introduced to remove the effect of short-term variations (mainly geophysical effects) using conventional corrections  $\Delta \mathbf{x}_i(t)$ . The result is a position with a regular time evolution. Currently a linear station model is widely used, i.e., for each station a position at a reference epoch  $t_0$  and constant velocity  $v_i$  is estimated. The regularized position is then computed by:

$$\bar{\mathbf{r}}_r(t) = \bar{\mathbf{r}}_{r_0} + \mathbf{v}_{r_0}(t - t_0). \quad (3.9)$$

The numerical values  $\bar{\mathbf{r}}_{r_0}$  and  $\mathbf{v}_{r_0}$  of all network stations constitute a specific reference frame solution. In Eqn. 3.9 the term  $\mathbf{v}_{r_0}(t - t_0)$  accounts for linear changes of the coordinates relative to the center of mass. Obviously, the linear model cannot account for abrupt discontinuities which occurs during earthquakes or as a result of hardware changes. Therefore, for many stations, the positions and velocities have to be estimated in a piece-wise linear mode with pre-defined station-specific intervals (Altamimi et al., 2007; Steigenberger, 2009; Rülke, 2009; Altamimi et al., 2011). Obviously, if  $\mathbf{r}_r(t)$  does not account for all periodic coordinate variations the term  $\mathbf{r}_r(t_r) + \mathbf{G}(t_r)$  in Eqn. 3.7 is not constant over time. Or in other words, the origin and the center of mass do not coincide for every epoch. Consequently, the ITRF origin is a mean coordinate origin concerning the used observation period. The derived coordinate origin and the mean center of mass are nearly identical for the selected reference epoch. In recent years some groups estimated annual and seasonal deformation and tried to improve the linear model by estimating also annual and semi-annual signals (e.g., Tesmer et al., 2009; Bloßfeld et al., 2014). In the recently released ITRF2014 annual and semi-annual terms were estimated during the stacking process of sufficient long coordinate time series (ITRF, 2016; Altamimi et al., 2016). However, until now there is no commonly agreed strategy to consider these signals. Consequently, estimating satellite orbits and station coordinates together allows the determination of  $\mathbf{G}(t_r)$ . This possibility will be discussed in detail in Sect. 5.2.

The orientation of the reference axes could also be defined by the gravity field as the spherical harmonic coefficients  $C_{21}$ ,  $S_{21}$ , and  $S_{22}$  are functions of the Earth's principal axes of inertia. If  $C_{21} = S_{21} = S_{22} = 0$ , the reference frame axis coincide with the Earth's principal axes of inertia. However, this approach seems rather theoretical due to the weak sensitivity of satellite orbits regarding  $C_{21}$ ,  $S_{21}$ , and  $S_{22}$ . Instead, the z-axis is conventionally defined to be consistent with the orientation of the BIH Terrestrial System at epoch 1984.0 and, therefore, defined to coincide with the Earth's rotation axis at the epoch 1984.0. To

prevent a common rotation of the whole network, the realization ITRF92 was adjusted to be consistent with the NNR-NUVEL-1A plate tectonic model (Boucher et al., 1993). Since ITRF94, realizations are derived in a way that no rotations occur with respect to the previous solution<sup>3</sup>. In a frame defined in this way, deformations of the Earth's surface have no impact on the Earth's angular momentum (Seitz, 2009). As the effect of the introduced constraints depends on the number and the distribution of core sites, two realizations of the same reference system might slightly differ in their orientation (Rülke, 2009).

The metric scale is defined by the geocentric gravitational constant  $GM$ , the speed of light in vacuum  $c$ , and relativistic models applied in the processing. Consequently, refraction effects in the atmosphere, variations of the electrical and optical centers, and delays in electronic components have to be considered when deriving the reference frame. For all ITRF solutions, except ITRF2005, the scale was defined by a combination of the SLR and VLBI solutions. In the ITRF2005 combination the scale was solely derived from VLBI (Altamimi et al., 2007). As mentioned previously, the scale is defined by the IERS conventions to be consistent with TCG. However, satellite geodetic observations are usually referred to the terrestrial time scale (TT, *temps terrestre*). Therefore, a correction of 0.7 ppb was introduced in some older ITRF solutions (e.g., ITRF94, ITRF96, ITRF97). Since the realization of ITRF2000 the scale is given directly in TT (Rülke, 2009). GNSS and DORIS are not used so far for the scale estimation as the poorly known antenna phase center variations are highly correlated with the scale (see Sects. 5.3 and 5.4).

An alternative terrestrial reference system definition is given by the crust-fixed approach, where station coordinates are constrained with respect to their tectonic plate (Drewes et al., 2013). Correspondingly, if one station motion changes, not the station coordinates itself, but the coordinates system, i.e., the datum parameters are affected. In other words, in this approach the datum definition depends on the distribution of the station network on the plate. One example for this definition is the European Terrestrial Reference System ETRS89, where station coordinates are constrained to the Eurasian Plate at epoch 1989.0.

### 3.2.2 The Historical Evolution of the IERS Station Network and the ITRF

Due to the beginning of the space age the concept of global terrestrial reference frames became highly relevant and popular within the geodetic and surveying community in the late 1960. Within the Monitoring Earth Rotation and Intercomparison of Techniques (MERIT) project established in 1978 the terrestrial reference frame was, for the first time, realized based on geometrical positions of space geodetic networks, primarily SLR, VLBI and TRANSIT, instead of astronomic observations (Boucher & Altamimi, 1985). Since 1988 the IERS is responsible for the establishment and maintenance of the ITRF. The ITRF has been and will be updated repeatedly, as the IERS tracking network is constantly growing, station coordinates are affected by earthquakes and other geological events, and models are constantly improved. Since the first version, the ITRF88, twelve realizations have been released (cf. Tab. 3.1). In 2013, the call for participation for a new ITRF solution, the ITRF2014, was published (Altamimi et al., 2014); this new ITRF realization was released on January 21, 2016 (ITRF, 2016). As documented in Tab. 3.1, the ITRF solutions up to ITRF2005 were based on several multi-year solutions per technique. These solutions contained time-dependent station positions and velocities for each observation technique. From the ITRF2005 onwards daily and weekly solutions were used allowing for a more consistent analysis and modeling. In addition, beginning with ITRF2005 pole coordinates (including their temporal derivatives) and length of day derived from each technique were combined (Altamimi et al., 2007). Concerning the techniques considered a historical evolution is presented in Tab. 3.1. GPS was considered for the first time for ITRF91, whereas DORIS was included beginning with the ITRF94 realization. GLONASS was considered as second GNSS for the first time in the ITRF2014 realization. The other GNSS will probably be included in the next or the next but one realization, when the corresponding time series will cover a sufficient interval length. Other observations like LEO-based GNSS data or SLR tracking to LEOs and GNSS satellites are still not considered for the ITRF solutions. However, such observations have the potential to further improve the

<sup>3</sup> As ITRF93 was aligned to the IERS EOP series, the ITRF94 was realized in the way that no rotations occur with respect to ITRF92.

**Tab. 3.1:** Overview of the ITRF realizations compiled by the IERS; <sup>1</sup>coordinate time series solutions provided by IVS, ILRS, IGS, IDS; <sup>2</sup>6 global and 8 regional solutions; <sup>3</sup>according to the coordinate files available on ITRF (2016)

name	# stations	# solutions				reference
		VLBI	SLR/LLR	GNSS	DORIS	
ITRF88	120	5	6	-	-	Boucher & Altamimi (1991a)
ITRF89	113	6	8	-	-	Boucher & Altamimi (1989)
ITRF90	120	4	7	-	-	Boucher & Altamimi (1991b)
ITRF91	131	5	7	1	-	Boucher et al. (1992)
ITRF92	155	5	6	6	-	Boucher et al. (1993)
ITRF93	260	6	4	5	-	Boucher et al. (1994)
ITRF94	209	6	1	5	3	Boucher et al. (1996)
ITRF96	290	4	2	7	3	Sillard et al. (1998)
ITRF97	309	4	5	6	3	Boucher et al. (1999)
ITRF2000	477	3	9	6+8 <sup>2</sup>	3	Altamimi et al. (2002b)
ITRF2005	608	1 <sup>1</sup>	1 <sup>1</sup>	1 <sup>1</sup>	1 <sup>1</sup>	Altamimi et al. (2007)
ITRF2008	934	1 <sup>1</sup>	1 <sup>1</sup>	1 <sup>1</sup>	1 <sup>1</sup>	Altamimi et al. (2011)
ITRF2014	1478 <sup>3</sup>	1 <sup>1</sup>	1 <sup>1</sup>	1 <sup>1</sup>	1 <sup>1</sup>	ITRF (2016)

terrestrial reference frame solutions. For example, it might be interesting to note that some SLR stations observe LEOs more frequently than LAGEOS<sup>4</sup>. Consequently, the corresponding station coordinates will certainly benefit from considering LEO SLR tracking data in the ITRF realization. Evaluating the potential of existing and future observation constellations for improving the ITRF is one goal of the GGOS Standing Committee PLATO (Performance Simulation and Architectural Trade-Offs) established in 2013<sup>5</sup>.

Today's IERS tracking network consists of the tracking networks of the IVS, the ILRS, the IGS, and the IDS. As an order of magnitude the global geodetic network consists nowadays of 40 VLBI telescopes, 30 SLR telescopes, 60 DORIS stations, and more than 300 GNSS receivers (Angermann et al., 2013). Apart from these stations also historical observation sites and markers for mobile platforms are part of the station network. Fig. 3.1 shows the globally distributed station network and the number of techniques co-located at each fundamental site. Since the start of MERIT each tracking site is assigned an unambiguous number, the DOMES number (historically "Directory of MERIT Sites"). Each individual sensor, which is co-located at a station, is associated to one observation site by having the same DOMES number. This includes not only space geodetic sensors but also other instruments, tide gauges and meteorological sensors.

### 3.2.3 Site Displacements and their Consideration

Various geophysical processes resulting in mass re-distribution and loading effects cause deformations of the Earth surface and lead to time-dependent variations in terrestrial station coordinates. Obviously, they are affecting all space geodetic techniques. The treatment of these effects is standardized by the definition of a conventional reference system and is published in the IERS Conventions. The most important effects and their impact on station coordinates are discussed within this subsection. In principle, geophysical effects should be taken into account by applying conventional models as shown in Eqn. 3.8. According to Ray et al. (2007) and Petit & Luzum (2013) these models can be divided into three classes. Class 1 are essential models, their use is recommended to correct the raw observations before estimating parameters. Commonly they are applied a priori and corresponding parameters are usually not estimated during the processing. The model accuracy, therefore, has to be equal to or (better than) the observation accuracy i.e., in terms of displacements at least at the mm level. Class 1 models are derived from geophysical

<sup>4</sup> For example, according to the ILRS the following amount of normal points were obtained for LAGEOS-1, LAGEOS-2, and OSTM/Jason-2 between Dec. 2014 and Nov. 2015: at Svetloe (ILRS 1880) 2603, 1660, 4268 and at Badary (ILRS 1890) 813, 1561, 7708.

<sup>5</sup> <http://192.106.234.28/Components/WorkingGroups/WG%20PLATO/GGOS%20WG%20PLATO.html>, accessed June 2016

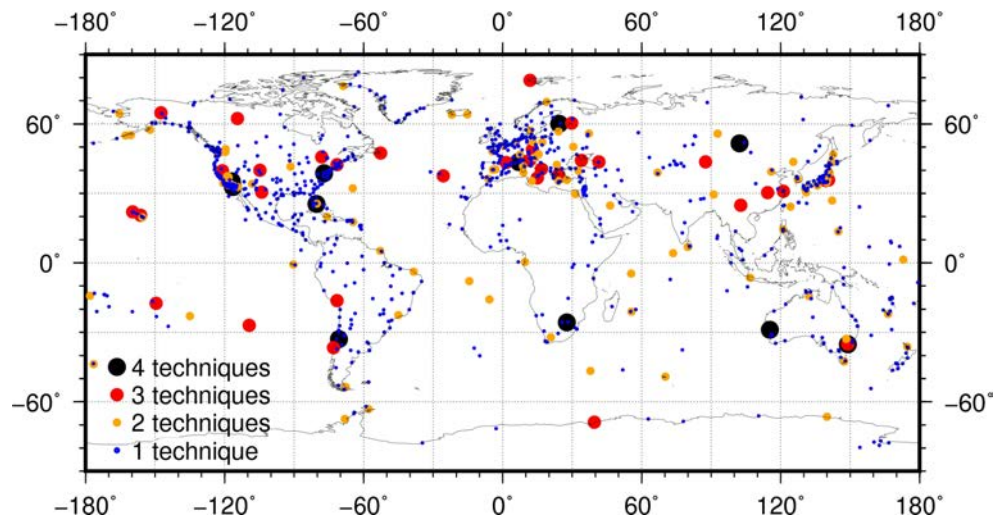


**Fig. 3.1:** IERS tracking network as used in the ITRF2014 realization; according to the coordinate files available on ITRF (2016)

knowledge, whereas class 2, the conventional models, are purely theoretical. However, they are necessary to avoid singularities in the observations and include physical constants and minimum constrain conditions (e.g., the no-net-rotation condition). The “useful” models of class 3 are beneficial in some cases, but fulfill currently not the requirements of class 1 or 2.

### Tectonic Displacements

As part of the Earth mantle convection, the lithospheric plates, forming the upper part of the Earth crust, are moving with velocities of some centimeters per year (Wegener, 1912, 1929; Lambeck, 1988). Apart from deformation zones these motions can be described as horizontal and linear motions of rigid plates with respect to each other. With this formulation, the motion of an individual plate can be described as a rotation on a sphere around an Euler pole. Consequently, the velocity of a terrestrial station can be estimated by the cross product of the station vector and the corresponding plate rotation vector. Tectonic models are based either (1) on geophysical observations, like spreading rates, azimuths of transform faults, and earthquake characteristics, or (2) on station velocities derived from space geodetic techniques. Examples for the first type are NUVEL-1A (DeMets et al., 1990) or PB2003 (Bird, 2003), models of the second type are APKRIM2005 (Drewes, 2009b), the ITRF2005 Plate Motion Model (Altamimi et al., 2007) or the work presented by Argus & Heflin (1995). Strong earthquakes, which occur primarily at plate boundaries, result in an instantaneous displacement of up to some meters. More detailed information, also concerning the impact on reference frames, can be found in the literature (e.g., Kreemer et al., 2006).

### Tidal Displacements of the Solid Earth

The gravitational attraction of external bodies, mainly Sun, Moon, Jupiter, Mars and Venus, causes a deformation of the Earth (Lambeck, 1988; Torge & Müller, 2012). This deformation is conventionally divided into direct (geometrical) and indirect (loading displacements due to mass re-distribution) deformations. Only the direct displacements are discussed in this paragraph. The tidal deformation of the solid Earth consists of a time-independent and several time-dependent signals with periods from hours to 18.6 years. The time-independent, permanent displacement, amounts to -12 cm and +6 cm at the poles and at the equator, respectively. The computation algorithms for the position displacements are based on the tidal potential of the attracting bodies and the Earth’s elasticity expressed by the dimensionless Love numbers  $h$  and  $k$  and the Shida number  $l$ . The numerical values of these numbers depend on the station latitude and the frequency of the corresponding tidal wave (Wahr, 1981). Applying the reduction for the time-dependent displacements leads to a mean-tide system, which was recommended by the Resolution 16

of the 18th IAG General Assembly in 1983. Usually in space geodesy an additional reduction is applied for the permanent displacement. Consequently, a tide-free system is realized, i.e., a system totally unaffected by Sun, Moon and planets. A reference frame based on this conventional reductions is called to be conventional tide-free. Because of the offset between true and mean Earth rotation axis (visible in polar motion) and the variations of the rotational speed the Earth centrifugal potential is changed. The resulting Earth's crust deformation is referred to as pole tide (Munk & MacDonald, 1960). Based on the maximal amplitude of polar motion, which is 400 mas the corresponding displacement is 25 mm in the vertical and 7 mm in the horizontal direction. The effect due to the variation of the rotation rate is below 1 mm and is, therefore, negligible.

### Tidal Loading Displacements

Each tidal displacement causes a mass re-distributions, best visible in the oceans, but also in the atmosphere. As stated by the loading theory, a time-dependent mass  $A$  at the Earth's surface will cause a horizontal and vertical displacement of a terrestrial station  $P$  (Lambeck, 1988). These displacements are mainly vertical, the horizontal deformation is usually five times smaller (James & Ivins, 1998). The reaction of the crust depends on its rheological properties and is expressed by the dimensionless Love numbers  $h'$ ,  $k'$  and the Shida number  $l'^6$ . The reaction of the Earth is firstly elastic, i.e., an instantaneous compression or decompression of the Earth crust. If the loading is larger, also a time-consuming mass re-distribution is initiated in the Earth's mantle<sup>7</sup>. This reaction is called viscous and the combination of both reactions is referred to as visco-elastic. In principle, loading effects are represented in two ways. Firstly, a global representation using spherical harmonics might be used, if globally distributed measurements with a low spatial resolution are available (Blewitt, 2003)<sup>8</sup>. Secondly, for a regional, high-resolution data set a representation based on the Green's functions is suitable (Lambeck, 1988). Here the displacement at the point  $P$  caused by the mass at the point  $A$  is considered with the Green's functions as weighting functions depending on the spherical distance between  $P$  and  $A$ . Detailed information about loading effects and their modeling were presented by Peltier (1974); Mitrovica et al. (1994); James & Ivins (1998) and others. The oceanic tidal loading causes displacements of some centimeters in the vertical and a few millimeters in the horizontal component (Haas & Scherneck, 1999) and is usually computed by using frequency, amplitude, phase and the astronomical arguments of eleven major partial tides (Petit & Luzum, 2010). Phases and amplitudes of the partial tides can be estimated using the ocean loading provider<sup>9</sup> based on a specified tide model, e.g., FES2004 (Letellier et al., 2004) or EOT11a (Savcenko & Bosch, 2012). Additionally, polar motion causes a water mass re-distribution in the oceans, the so-called oceanic pole tide. According to Desai (2002) the displacement is below 1.8 mm in the vertical and 0.5 mm in the horizontal component. Atmospheric tides are visible in the variation of air pressure, temperature, and wind. The dominating frequencies are the daily  $S_1$  and the semi-diurnal  $S_2$  tide. The effect can be corrected by using the geophysical model from Ray & Ponte (2003), which is part of the IERS conventions (Petit & Luzum, 2010). However, the effect of atmospheric tides is around ten times smaller than non-tidal atmospheric effects. For example, the tidal air pressure variations are below 200 Pa<sup>10</sup>, which is ten times less than the non-tidal variations (Volland, 1997).

### Non-tidal Loading Displacements

Periodic and secular non-tidal loading displacements are in general difficult to model. Consequently, they are mostly not corrected when realizing a terrestrial reference frame (Collilieux et al., 2010; Altamimi et al., 2011). Available corrections are provided mainly in gridded files, like the non-tidal atmospheric loading

<sup>6</sup> As indicated by the primes, the Love and Shida numbers are different for forces acting on a volume, e.g., tidal forces, and forces acting on a surface, e.g., loading forces (Lambeck et al., 1998).

<sup>7</sup> As an order of magnitude: up to a spherical extension of 100 km a mass is compensated by the crust only.

<sup>8</sup> A high spatial resolution requires a development of higher-order spherical harmonics, e.g., up to order 1'000, c.f. Farrell (1972).

<sup>9</sup> <http://froste.oso.chalmers.se/loading>, accessed August 2015

<sup>10</sup> This is around 0.2 % of the nominal air pressure at the Earth surface.

corrections provided by TU Vienna (Wijaya et al., 2013). Especially, for SLR observations correcting the atmospheric loading (tidal and non-tidal) is essential, as SLR stations observe mainly during high pressure periods, correlated with a cloudless sky. This effect, called the blue sky effect, causes a systematically negative vertical station displacement of several mm (Sośnica, 2015). The ocean water masses are re-distributed by the global ocean circulation, driven by temperature, wind, air pressure, and salinity. The corresponding displacements reach a few centimeters in the vertical and a few millimeters in the horizontal direction. The most prominent example of such re-distribution cycles is the El Niño Southern Oscillation (ENSO) with periods of 5-7 years. Atmospheric non-tidal loading, driven by the global weather conditions, has annual and semi-annual frequencies for equatorial stations and periods of some days or weeks at middle latitudes. In the oceans, atmospheric tidal and non-tidal loading is compensated to a large extent by a re-distribution of water masses, known as inverse barometer effect. A compensation of 50% can be assumed for coastal regions and islands. The non-tidal atmospheric loading displacement can be computed by using numerical weather models from the National Centers for Environmental Prediction (NCEP) or the European Centre of Medium-Range Weather Forecast (ECMWF). Continental hydrology, with the variations of snow coverage, ground water, and seasonal surface water storage, causes vertical deformations with dominant annual signals of up to 30 mm (van Dam et al., 2001). These displacements exceed those by the atmosphere for seasonal periods (Blewitt et al., 2001). Especially local effects have a huge impact. For example, Bevis et al. (2005) found vertical deformations up to 75 mm related to the water level of the Amazon for the IGS station in Manaus, Brazil. However, modeling deformations caused by the hydrology with an accuracy at the mm level is difficult due to missing high resolution datasets. For example, the often used Global Land Data Assimilation System (GLDAS, Rodell et al., 2004) has a temporal resolution of only one month (spatial resolution of  $0.25^\circ \times 0.25^\circ$ ). Whereas hydrological processes are mainly periodic, large-scale ice mass changes and glacial-isostatic adjustments are secular effects. Today mainly two effects are observable: (1) slow deformations occur due to the Earth's viscous reaction to the ice mass losses related to the last glacial maximum (e.g., Peltier, 1994; Scherneck et al., 2003), and (2) rapid vertical displacements occur due to the elastic reaction to recent accumulation and ablation processes (e.g., Dietrich et al., 2005; Sauber et al., 2000). For example, Dietrich et al. (2010) found uplift rates of 60 mm/yr in Patagonia. They explained these extreme velocities by a combination of ablation, tectonic movement and volcanism. In general, both types of displacement are not corrected, however, for the viscous reaction, models are available (e.g., Lambeck et al., 1998; Larsen et al., 2004; Peltier, 2004).

In summary, many processes in the Earth's system affect station positions in a mostly non-linear mode. Therefore, the assumption of a linear station behavior in time is very simplified and requires excellent models for the various displacements. This is crucial, especially, concerning the GGOS requirements for a consistent and long-time stable reference frame. Even the recently proposed estimation of annual and semi-annual terms cannot completely absorb the existing model deficiencies.

### 3.2.4 Discussions on the Current Concept of the Terrestrial Reference Frame

This section shall provide an overview of the aspects currently discussed within the scientific community concerning the terrestrial reference frame. Recapitulating the GGOS requirements for the terrestrial reference frame of 1 mm accuracy and 0.1 mm/yr stability, today's reference frame realization concepts need to be further improved concerning station networks, corrections, models, and parameterization, as well as combination approaches.

The inhomogeneous network distributions for VLBI, SLR, and GNSS might be addressed first. In the ITRF2008 solution 35% of the ground stations are located in North America and 22% in Europe. As these clusters dominate the transformation parameters, geophysical effects in both regions are over-represented compared to the global network (Drewes et al., 2013). Additionally, DORIS with its very well distributed network only shared few local ties with VLBI and SLR. Therefore, one goal for GGOS is the establishment of around 40 globally distributed core stations, assembling all four techniques (Plag & Pearlman, 2009).

Within the GGOS Standing Committee PLATO simulation studies are performed to derive an optimized future geodetic station network. The required accuracy of the terrestrially measured local ties is analyzed as well within PLATO. Two different concepts are currently used for introducing local ties. In the ITRF solutions all available local ties were introduced with different weights (Altamimi et al., 2007), whereas the DTRF2008 solution is based on the set of local ties showing the best agreement (with respect to the space geodetic results), but with an identical weighting of 1 mm (Krügel & Angermann, 2007).

As mentioned above a consistent modeling is a prerequisite for an inter-technique combination. Especially, correcting site displacements plays an important role for an appropriate co-location on the ground. Even if the most recent IERS conventions are widely adopted, several inconsistencies exist between the technique solutions as described by Angermann et al. (2013) and Glaser (2014). However, for the new ITRF2014 solution a consistent set of models was defined to ensure highest possible consistency. An additional topic is the handling of periodic and instantaneous station movements. As uncorrected periodic and non-periodic station motions currently disturb the linear station model, station velocities are usually computed based on long time series (at least 2.5 years)<sup>11</sup>. Comparing the concepts of velocity determination at IGN and DGFI, a totally different approach is used. Whereas at IGN positions and velocities are derived from 14-parameter Helmert transformations of technique-specific time series, DGFI expands the normal equations by introducing velocity parameters. According to Angermann et al. (2013) differences of up to 2 cm are present between actual station positions and the corresponding ITRF2008 coordinates. Consequently, the geometry of the reference frame at epoch  $t_1$  differs from the true geometry of the tracking network at epoch  $t_i$ . Also the EOP at epoch  $t_i$  are mean orientation parameters and differ from their instantaneous values. One alternative mentioned by Bloßfeld et al. (2014) are short-time reference frames computed over a relative short time period like one week or one month. Consequently, such frames represent the true network geometry more correctly. The drawback is the lower accuracy due to the shorter time series used. Short-time reference frames are discussed in detail in Bloßfeld et al. (2014). As discussed in Nothnagel et al. (2010) and Angermann et al. (2013), large earthquakes destroy the access to the current reference frame for whole regions<sup>12</sup>. They concluded that short-time reference frames released frequently are required to cure this issue. It has to be mentioned that in the recent ITRF2014 release a post-seismic deformation model for the GNSS time series is included which should be applied to the three other techniques (ITRF, 2016).

Regarding the combination of geodetic observation techniques, the transition to a rigorous combination on the normal equation or even on the observation level is widely discussed. Both strategies will certainly improve the consistency of the derived reference frame. However, an official TRF solution based on a combination on the observation level is not feasible within the next decade, as dedicated software packages are not yet available (see Sect. 3.4). Therefore, the main effort should be put into by combining consistent and constraint-free, i.e., datum-free, normal equations. Today technique-specific normal equations are mostly prepared with loose or minimum constraints, that have to be removed before a combination<sup>13</sup>. In general, the concept of minimum constraints was reported by Schuh et al. (2015) to rather not just cure the rank deficiency of the normal equations. According to them more appropriate “non-distorting constraints”, described by Angermann et al. (2004), should be used. Also the handling of discontinuities has to be homogenized between the techniques. The handling of environmental influences, affecting all instruments co-located at fundamental sites equally also needs to be homogenized (e.g., tropospheric delays, tidal effects). In the optimal case these effects should be estimated jointly from all affected techniques. Based on the ITRS definition, Drewes (2009a) claimed that the current ITRF concept (1) is not strictly geocentric, as the origin is shifted with respect to the geocenter, (2) is not strictly rotating with the real Earth, due to the introduced geological plate tectonic model, and (3) is not strictly metric because the scale is replaced by the network expansion (if the scale is derived by Helmert transformations). However, to derive a long-

<sup>11</sup> As already mentioned, in ITRF2014 annual and semi-annual terms were estimated during the stacking of sufficient long coordinate time series. However, the estimated values are not yet published.

<sup>12</sup> Also stations located much more than 1000 km away from the epicenter might be affected (Angermann et al., 2013).

<sup>13</sup> Only the IVS delivers datum-free normal equations.

term stable, highly accurate and consistent reference frame further investigations are necessary. In the following sections the combination strategies and co-location approaches will be discussed in more detail.

### 3.3 Transformation Between Celestial and Terrestrial Reference Frame

Whenever terrestrial coordinates  $\mathbf{r}_e(t)$  linked to the Earth's surface and coordinates  $\mathbf{r}_g(t)$  in an inertial frame shall be used together, a transformation from the terrestrial to the celestial systems or vice-versa is necessary. In space geodesy, where observations connect inertial satellite orbits and terrestrial station coordinates, this transformation is essential and is described in detail in the literature (Lambeck, 1988; Torge & Müller, 2012). Because the origins of both reference systems coincide usually with the Earth's center of mass and the scale is the same, the transformation can be represented by three Eulerian angles (Richter, 1995). As the Eulerian angles vary rapidly in time, their usage requires much more computational power than a transformation based on a sequence of rotation matrices, accounting for precession, nutation, Earth rotation angle and polar motion. Precession and nutation are induced by gravitational forces exerted by space bodies like Sun, Moon and planets, on the Earth's equatorial bulges resulting in torques forcing the Earth's equatorial plane into the ecliptic. As the Earth rotates the resulting effect is a precession of the rotation axis around a cone of  $23.5^\circ$  during 25'500 years with nutation periodic effects from days up to 18.6 years. As the precession can be modeled very precisely, only small corrections for the nutation have to be derived by observations. The motion of the Celestial Ephemeris Pole (CEP) with respect to the IERS Reference Pole called polar motion, cannot be modeled and is observed by the IERS<sup>14</sup>. The Earth rotation angle  $\Theta$  contains, apart from one rotation in one sidereal day, small difference  $\Delta\text{UT}=\text{UT1}-\text{UTC}$ , where UT1 has to be observed. Today polar motion and UT1-UTC are observed as time-dependent Earth Orientation Parameters and published by the IERS with an accuracy of about 0.1 mas for polar motion and 0.01 ms for UT1 (Torge & Müller, 2012).

Two transformation strategies can be applied between the inertial and terrestrial reference frame, namely the classical equinox-based approach and the IAU recommended CIO-based transformation strategy. The Celestial Intermediate Origin (CIO) and Celestial Intermediate Pole (CIP) refer to the Celestial Intermediate Reference System (CIRS), which is derived from the GCRS by a time-dependent rotation. Using the rotation matrices  $\mathbf{R}_i(\alpha)$ , representing a rotation by an angle  $\alpha$  around the axis  $i$ , the equinox-based transformation reads as:

$$\mathbf{r}_g(t) = \mathbf{P}(t)\mathbf{N}(t)\mathbf{R}_3(-\Theta(t))\mathbf{R}_2(x_p(t))\mathbf{R}_1(y_p(t))\mathbf{r}_e(t) . \quad (3.10)$$

The product  $\mathbf{R}_1(y_p(t))\mathbf{R}_2(x_p(t))$ , accounting for polar motion, transforms  $\mathbf{r}_e(t)$  from the ITRS into the Terrestrial Intermediate Reference System. By turning by the Earth rotation angle  $\Theta(t)$ , also called Greenwich Apparent Sidereal Time (GAST), around the Earth's rotation axis, the true equatorial system of date is realized. The nutation matrix  $\mathbf{N}$  transforms this system into the mean equatorial system of date. Following the IAU 1980 nutation theory,  $\mathbf{N}$  contains the obliquity of the ecliptic and the nutation angles in obliquity and in ecliptic longitude and is modeled by a series expansion in time. The precession matrix  $\mathbf{P}$  transforms the mean equatorial system of date into the equatorial system at the reference epoch J2000.0. Analogous to the nutation matrix,  $\mathbf{P}$  is given by a series expansion depending on the lunisolar and the planetary precession constants (Lieske et al., 1977). Within the Bernese GNSS Software this older transformation strategy is implemented (Dach et al., 2007). According to the IAU Resolution the CIO-based transformation reads as:

$$\mathbf{r}_g(t) = \mathbf{Q}(X_p(t), Y_p(t))\mathbf{R}_3(s(t))\mathbf{R}_3(-ERA)\mathbf{R}_3(s'(t))\mathbf{R}_2(x_p(t))\mathbf{R}_1(y_p(t))\mathbf{r}_e(t) . \quad (3.11)$$

<sup>14</sup> Before 1988 polar motion was observed by the International Latitude Service.

Here the rotation due to polar motion is supplemented by the small correction angle  $s'$ , which represents the Terrestrial Intermediate Origin (TIO) and is zero for epoch J2000.0 with a changing rate of  $-50$  mas/century. The Earth rotation angle  $ERA$  is defined as the angle between CIO and TIO measured along the CIP equator. The matrix  $Q$  combines precession and nutation making use of the CIP coordinates  $X_p, Y_p$  in the geocentric celestial reference frame. The small correction angle  $s$  accounts for the movement of the CIO position on the CIP equator.

### 3.4 Combination Levels in Space Geodesy

As mentioned already in Chap. 1 space geodetic techniques are combined to exploit their individual strengths for the benefit of the derived geodetic products. Therefore, the overall goal of an inter-technique combination is to improve the accuracy of the estimated results. Examples for such combinations are (1) the realizations of the ITRS (Altamimi et al., 2011; Seitz et al., 2012), (2) the computation of gravity field products by combining GNSS and SLR (Meyer et al., 2015b), (3) multi-technique estimations of atmospheric delays (Dettmering et al., 2011; Krügel et al., 2007), and (4) multi-technique satellite orbit determination (Thaller et al., 2011; Flohrer et al., 2011). Usually, the processing of space geodetic techniques is based either on (1) a Kalman filter or (2) a least-squares adjustment based on the Gauss-Markoff model (Brockmann, 1997; Koch, 2004; Niemeier, 2008). As the processing work within this thesis is based on the least-squares adjustment, the Kalman filter approach will not be discussed here. Combining different techniques can be done at three different levels of the Gauss-Markoff model: (1) at the observation level, (2) at the level of normal equations, or (3) at the solution level. However, a reasonable combination of different techniques requires a connection between the different observation types by common parameters that are (1) identical, e.g., the ERPs or the geocenter for GNSS, SLR and DORIS, (2) connected by mathematical or physical models, e.g., a delay model connecting the different tropospheric delays, or (3) connected by external measurements, e.g., local ties.

#### 3.4.1 Combination at the Observation Level

The combination at the observation level can be described by the Gauss-Markoff model itself. In a least-squares adjustment  $n$  independent observations  $\mathbf{l}$  are used to determine a set of  $u$  unknowns  $\mathbf{x}$ . The functional relationship between one observation  $l_i$  and the parameter vector  $\mathbf{x}$  are expressed mathematically by an observation equation  $\mathbf{f}(\mathbf{x})$  (called functional model)

$$\mathbf{l} + \mathbf{v} = \mathbf{f}(\mathbf{x}) \quad \text{with} \quad \mathbf{E}(\mathbf{v}) = 0 \quad \text{and} \quad \mathbf{C}_{\mathbf{ll}} = \sigma_0^2 \mathbf{P}^{-1}. \quad (3.12)$$

In Eqn. 3.12  $\mathbf{v}$  is the vector of residuals (expected to be zero),  $\mathbf{C}_{\mathbf{ll}}$  is the variance-covariance matrix with the variance factor  $\sigma_0^2$ , and the matrix  $\mathbf{P}$  contains the stochastic model. As space geodetic observations are influenced by various error sources and as the number of observations is usually much larger than the number of unknowns, the vector of residuals  $\mathbf{v}$  has to be introduced to ensure consistency in Eqn. 3.12. It is assumed that the observation stochastic errors are normally distributed and described by the known variance-covariance matrix  $\mathbf{C}_{\mathbf{ll}}$  and the variance factor  $\sigma_0^2$ . However, as Eqn. 3.12 can only be solved, if it is linear, the space geodetic observation equations  $\mathbf{f}(\mathbf{x})$  must be linearized. This is usually done by a first-order Taylor series expansion around the a priori values  $\mathbf{x}^0$ . The design matrix  $\mathbf{A}$  (Jacobian matrix) is composed of all first-order derivatives of the function  $\mathbf{f}(\mathbf{x})$  with respect to the estimated parameters  $\mathbf{x}$  evaluated at  $\mathbf{x}^0$ . Therefore, Eqn. 3.12 can be written as

$$\mathbf{l}' + \mathbf{v} = \mathbf{f}(\mathbf{x}^0) + \mathbf{A} \cdot \Delta\mathbf{x} \quad \text{with} \quad \mathbf{A} = \left. \frac{\partial \mathbf{f}(\mathbf{x})}{\partial \mathbf{x}} \right|_{\mathbf{x}=\mathbf{x}^0} \quad \text{and} \quad \Delta\mathbf{x} = \mathbf{x} - \mathbf{x}^0. \quad (3.13)$$

Based on to the linearization only small corrections  $\Delta\mathbf{x}$  are estimated with respect to the a priori values  $\mathbf{x}^0$ . The vector  $\mathbf{l}'$  is often called observed-computed (O-C) and is derived by reducing  $\mathbf{l}$  by the a priori

values  $\mathbf{f}(\mathbf{x}^0)$ . To solve Eqn. 3.13 the weighted square sum of the residuals is minimized in the least-squares adjustment by the condition  $\mathbf{v}^T \mathbf{P} \mathbf{v} \Rightarrow \min$ . The matrix  $\mathbf{P}$  (called stochastic model) is composed of the weights of the observations and residuals. In the case of uncorrelated observations the non-diagonal elements are zero and the diagonal elements are computed by using the standard deviation  $\sigma_i$  of the observations  $i$  and the a priori standard deviation  $\sigma_0$  of the unit weight

$$P(i, i) = \left( \frac{\sigma_0}{\sigma_i} \right)^2. \quad (3.14)$$

The a posteriori standard deviation  $\hat{\sigma}_0$  of the unit weight is estimated by

$$\hat{\sigma}_0 = \frac{\mathbf{v}^T \mathbf{P} \mathbf{v}}{n - u}. \quad (3.15)$$

The system of normal equations, based on Eqn. 3.12, is then written as

$$\mathbf{A}^T \mathbf{P} \mathbf{A} \Delta \mathbf{x} = \mathbf{A}^T \mathbf{P} \mathbf{l}' \quad \text{or} \quad \mathbf{N} \Delta \mathbf{x} = \mathbf{b} \quad \text{with} \quad \mathbf{N} = \mathbf{A}^T \mathbf{P} \mathbf{A} \quad \text{and} \quad \mathbf{b} = \mathbf{A}^T \mathbf{P} \mathbf{l}'. \quad (3.16)$$

When combining  $m$  different space geodetic techniques ( $k = 1..m$ ) Eqn. 3.13 can be re-written as

$$\mathbf{l}_m + \mathbf{v}_m = \mathbf{A}_m \cdot \Delta \mathbf{x} \quad \text{or} \quad \begin{bmatrix} \mathbf{l}_1 \\ \dots \\ \mathbf{l}_m \end{bmatrix} + \begin{bmatrix} \mathbf{v}_1 \\ \dots \\ \mathbf{v}_m \end{bmatrix} = \begin{bmatrix} \mathbf{A}_1 \\ \dots \\ \mathbf{A}_m \end{bmatrix} \Delta \mathbf{x} \quad \text{with} \quad \mathbf{C}_{11} = \sigma_0^2 \begin{bmatrix} \mathbf{P}_1^{-1} & \dots & 0 \\ \vdots & \ddots & \vdots \\ 0 & \dots & \mathbf{P}_m^{-1} \end{bmatrix}. \quad (3.17)$$

This combined observation equation (Eqn. 3.17) is then solved according to Eqn. 3.16. The main advantage of a combination at the observation level is the direct access to individual observations. Consequently, an inter-technique outlier detection is possible based on all observations. Also weighting individual observations (e.g., elevation-dependent weighting) could be applied consistently. Parameters, which are estimated epoch-wise, can be combined in this approach prior to their pre-elimination. Therefore, highest consistency can be achieved without the need to save enormous normal equations. The last, but very important issue is the consistent definition of fundamental constants and a priori models which is easy, if all techniques are processed in the same software package. However, this advantage is also given, when processing techniques in different runs of the same software package and combining them on the normal equation level. Even if this is not a rigorous combination at the observation level, the results are identical, if all parameters are handled in the same way as in the combination at the observation level (Brockmann, 1997).

Several authors expect the most robust results and the highest consistency from a combination on the observation level (e.g., Schmid, 2009; Hobiger & Otsubo, 2014; Seitz, 2015). However, the main drawback is the initial requirement of having a software package capable of processing all techniques on a very high quality level. Based on this requirement Coulot et al. (2007) declared a combination on the observation level as an utopic goal. Nevertheless, remarkable progress was achieved in this field in recent years. In 2009 the IERS Working Group “IERS Working Group on Combination at the Observation Level” was founded. Its main goal is to review the interest in combining techniques at the observation level for EOP and reference frames (Richard et al., 2012). However, the main results presented so far by this working group are based on combinations of technique-specific normal equations derived within technique-specific runs of the same software package. For clarification, this combination approach is called “combination of stacked observations” in the following. Obviously, this procedure does not allow for common observation weighting and outlier detection. Also parameters estimated epoch-wise cannot be combined due to the required pre-elimination scheme. The derived weekly normal equations are stacked by the combination centers of the working group using scaling factors derived via Helmert’s variance component analysis (Gambis et al., 2013). One primary software package used in the working group is GINS/DYNAMO (*Géodésie par Intégrations Numériques Simultanées*) developed by the *Groupe de Recherches de Géodésie*

*Spatiale* (GRGS). The combination of techniques is realized in the part DYNAMO based on normal equations derived with GINS. Based on three months of VLBI, GPS, SLR, DORIS, and LLR data, Yaya (2002) showed commonly estimated EOPs with increased temporal resolution without losing accuracy. The largest contribution for the pole coordinates was coming from GPS. Coulot et al. (2007) confirmed this finding by extending the processing time to one year. In both cases only EOPs were combined, local ties to combine station coordinates were not introduced. Gambis et al. (2009, 2013) extended the processing up to 121 GPS stations, DORIS observations to Spot-2/4/5 and ENVISAT, SLR measurement to LAGEOS, and VLBI R1, R4, and CONT08 data. They showed an increased quality of pole coordinate and UT1 results for the combined solution compared to C04. The standard deviation decreased from 270/230/1930/1030  $\mu\text{as}$  (GPS/VLBI/DORIS/SLR) to 150  $\mu\text{as}$  (combined) and from 160/210/1700/990  $\mu\text{as}$  to 120  $\mu\text{as}$  for the x- and y-component, respectively. For the UT1-TAI correction the mean difference to C04 decreased from 0.40  $\mu\text{s}$  (VLBI) to 0.03  $\mu\text{s}$  (combined solution). Several other software packages like EPOS, Bernese GNSS Software, and DOGS, are also capable of performing the described combination on the pseudo-observation level, at least for a subset of space geodetic techniques.

However, the number of software packages capable of processing different space geodetic techniques at the observation level is rather limited. Anderson (2000) claimed GEOSAT as the first software package capable to combine techniques directly on the observation level. GEOSAT is based on a Kalman filter and developed and maintained by the Norwegian Mapping Authority. However, the combination at the observation level was never explicitly demonstrated<sup>15</sup>. ESOC's NAPEOS (NAVigation Package for Earth Observation Satellites) software allows the combination at the observation level by processing GNSS, SLR, and DORIS in one processing run. Otten et al. (2012) presented a combined solution of GPS (184 stations), SLR tracking data to LAGEOS, and DORIS observations of Spot-2/4/5, OSTM/Jason-2, and ENVISAT during August 2008. Their focus was also on the combination in space, as Jason-2 (GPS, SLR, DORIS) and ENVISAT (SLR, DORIS) allowed this. They reported a considerable improvement in station coordinate repeatabilities and in the geocenter z-component by combining the techniques. In a second step they concentrated on station-specific errors (Otten et al., 2014). A software package dedicated to the combination at the observation level is the c5++ software (Hobiger et al., 2010). Hobiger & Otsubo (2014) showed a decrease in the station coordinate repeatabilities from 10 to 5 mm for the CONT11 campaign, when combining GPS and VLBI. They used local ties, tropospheric delays and the common station clocks as connecting parameters. So far, GEOSAT as well as c5++, are not capable to process DORIS as it is under development in GEOSAT and not included in c5++. Therefore, the perfect software package capable to process ground- and space-based VLBI, SLR, DORIS and GPS data on highest standards is still missing.

When processing space geodetic observations, the system of normal equations mostly becomes singular ( $\text{rg}(\mathbf{N}) < u$ ), as the observations do not contain all information needed to derive the aspired solution (Brockmann, 1997). To solve this issue the rank deficiency of the normal matrix must be remedied by introducing additional constraints. These constraints can be inserted as fictitious or pseudo-observations with an individual standard deviation  $\sigma_i$ . Based on the observation equation of the pseudo-observations  $\mathbf{v}_h = \mathbf{H}\mathbf{x} - \mathbf{h}$ , the normal equation contribution can be written as

$$\mathbf{H}^T \mathbf{P}_h \mathbf{H} \mathbf{x} = \mathbf{H}^T \mathbf{P}_h \mathbf{h} \quad (3.18)$$

where  $\mathbf{H}$  is the normal equation of the constraints. Consequently, by adding Eqn. 3.18 to Eqn. 3.16 the following normal equation system is obtained

$$(\mathbf{N} + \mathbf{H}^T \mathbf{P}_h \mathbf{H}) \mathbf{x} = \mathbf{b} + \mathbf{H}^T \mathbf{P}_h \mathbf{h}. \quad (3.19)$$

Three types of constraints are applied in the course of this work. Firstly, if a parameter value is known,

<sup>15</sup> Currently GEOSAT is re-written and will allow high-quality processing for all space geodetic techniques in the future, E. Mysen pers. communication in April 2016.

the parameter can be forced to this value by introducing an absolute constraint. A special case of absolute constraints is fixing parameters to their a priori value. Secondly, if the relation between two parameters is known, both parameters can be forced to fulfill this relation by introducing a relative constraint. For example, a local tie introduces a relative constraint between station coordinates. And thirdly, a free or datum network constraint allows it, to align the estimated network to the a priori reference frame. To avoid deformed solution minimum constraints have to be introduced, where the rank of the normal matrix of the constraints is equal to the rank deficiency  $d$  of the normal matrix, i.e.,  $\text{rg}(\mathbf{N}) = u - d$  (Altamimi et al., 2002a). In the following these minimum constraints are discussed shortly, more details can be found in Brockmann (1997).

### No-net-translation constraint (NNT)

A no-net-translation condition ensures that no network translation regarding the a priori positions and no translation concerning the origin occur. As a network translation can be expressed by a displacement of the coordinate origin the estimated origin  $\Delta\mathbf{r}_\mathbf{N}$  should be identical to the origin of the a priori network. With the weights  $\mu_r$  ( $\sum_{r=1}^n \mu_r = 1$ ) for all stations  $r = 1..n$  the no-net-translation condition can be written as (Seitz, 2009)

$$\Delta\mathbf{r}_\mathbf{N} = \sum_{r=1}^n \mu_r \Delta\mathbf{r}_r = 0 \quad (3.20)$$

where the sum of all station coordinate improvements  $\Delta\mathbf{r}_r$  must be zero. The velocity of the origin  $\Delta\mathbf{v}_\mathbf{N}$  of the network stations must be fixed in an analogous way.

### No-net-rotation constraint (NNR)

In a rotation-free network no rotations and no changes occur in the orientation regarding the a priori positions. Therefore, the station coordinate improvements  $\Delta\mathbf{r}_r$  cannot introduce a network torsion and the sum of all rotations  $\mathbf{r}_r^0 \times \Delta\mathbf{r}_r$  at the stations  $r = 1..n$  must be zero (Seitz, 2009)

$$\sum_{r=1}^n \mu_r \mathbf{r}_r^0 \times \Delta\mathbf{r}_r = 0. \quad (3.21)$$

If station velocities are considered, their rotations must also be constrained to zero.

### No-net-scale constraint (NNS)

A no-net-scale-condition is usually not applied. However, this constraint is necessary to estimate parameters, which are highly correlated with the network scale, e.g., GNSS antenna phase centers (Steigenberger, 2009).

## 3.4.2 Combination at the Normal Equation Level

The combination on the normal equation level is applicable in three cases:

- normal equations derived by the same software package for the same technique are combined,
- normal equations derived by the same software package but for different techniques are combined, and
- normal equations derived by different software packages are combined.

For the first case, called here stacked-observation level, the combination on the normal equation level is equivalent to the combination at the observation level, if parameters are handled in the same way (Brockmann, 1997). The main benefit is the reduced processing load for the individual least-squares

adjustments. However, measurement outlier detection and observation weighting cannot be performed at this level as the normal equation systems do not provide access to them. The second and moreover the third case require identical parameterization and a fully consistent modeling to generate correct results. This can be ensured by a rigorous implementation of the IERS conventions. After a technique-specific pre-processing the observation equations for each technique  $k$  are transformed into a normal equation system (cf. Eqn. 3.16)

$$\mathbf{N}_k \mathbf{x}_k = \mathbf{b}_k \quad (3.22)$$

by minimizing the squared sum of the residuals. For the combination all normal equation systems must have the same size  $u \times u$ , otherwise the normal equations must be expanded to the full amount of all parameters  $\mathbf{x}_c$ . This can be done by adding zero lines and columns to the normal equation matrix  $\mathbf{N}_k$  and zero elements to the vector  $\mathbf{b}_k$ . The normal equations of all techniques ( $k \in 1..m$ ) are then combined by adding the elements that are related to the same parameter. By considering the estimated variance factors  $\sigma_k^2$  the combined normal equation system  $\mathbf{N}_c$  reads as (Seitz, 2015)

$$\mathbf{N}_c = \mathbf{N}_1 + \dots + \mathbf{N}_m = \mathbf{A}_1^T \mathbf{P}_1 \mathbf{A}_1 + \dots + \mathbf{A}_m^T \mathbf{P}_m \mathbf{A}_m \quad \text{and} \quad (3.23)$$

$$\mathbf{b}_c = \mathbf{b}_1 + \dots + \mathbf{b}_m = \mathbf{A}_1^T \mathbf{P}_1 \mathbf{l}_1 + \dots + \mathbf{A}_m^T \mathbf{P}_m \mathbf{l}_m . \quad (3.24)$$

Examples for recent inter-technique combinations at the normal equation level are the reprocessing effort by Fritsche et al. (2014), the combination efforts within the GGOS-D project (Rothacher, 2011), or the DGF1 reference frame realization DTRF2008 (Seitz et al., 2012).

In order to keep the normal equations small, parameters that are not relevant in the combined solution or parameters that would blow up the dimensions of the normal equations can be pre-eliminated without changing the remaining parameters. For a pre-elimination the normal equation system is divided into (1) a normal equation system containing parameters that will be retained, and (2) a normal equation system containing those parameters that will be pre-eliminated

$$\begin{bmatrix} \mathbf{N}_{11} & \mathbf{N}_{12} \\ \mathbf{N}_{21} & \mathbf{N}_{22} \end{bmatrix} \cdot \begin{bmatrix} \mathbf{x}_1 \\ \mathbf{x}_2 \end{bmatrix} = \begin{bmatrix} \mathbf{b}_1 \\ \mathbf{b}_2 \end{bmatrix} . \quad (3.25)$$

Introducing the result from solving the equation  $\mathbf{N}_{21}\mathbf{x}_1 + \mathbf{N}_{22}\mathbf{x}_2 = \mathbf{b}_2$  for  $\mathbf{x}_2$  into the equation  $\mathbf{N}_{11}\mathbf{x}_1 + \mathbf{N}_{12}\mathbf{x}_2 = \mathbf{b}_1$  leads to a normal equation system, where  $\mathbf{x}_2$  has been pre-eliminated

$$(\mathbf{N}_{11} - \mathbf{N}_{12}\mathbf{N}_{22}^{-1}\mathbf{N}_{21})\mathbf{x}_1 = \mathbf{b}_1 - \mathbf{N}_{12}\mathbf{N}_{22}^{-1}\mathbf{b}_2 . \quad (3.26)$$

In this approach the influence of a pre-eliminated parameter on other parameters are still the same. Therefore, especially epoch-wise parameters, that are not relevant for a combined solution, are commonly pre-eliminated. Obviously, only parameters that do not have to be combined can be pre-eliminated. It is also possible to back-substitute these parameters by introducing the estimated parameters epoch-wise in the basic observation equations. More information on this topic can be found in Brockmann (1997).

### 3.4.3 Combination at the Parameter Level

The combination at the parameter level also called the combination of solutions is done in an additional least-squares adjustment based on the full variance-covariance matrices from technique-specific solutions. This new observation equation (at the parameter level) is written as (Seitz, 2015)

$$\mathbf{I}\mathbf{x}_k = \hat{\mathbf{x}} + \bar{\mathbf{v}}_k . \quad (3.27)$$

**Tab. 3.2:** Comparison of inter-technique combination approaches

	observation level	stacked-observation level	normal-equation level	parameter level
common outlier determination	✓			
common observation weighting	✓			
no pseudo-observations needed for combination	✓	✓	✓	
no additional transformation parameters needed	✓	✓	✓	
rigorous method	✓	(✓)	(✓)	
software package available	(✓)	✓	✓	✓

The individual observation equations are then composed to a combined system (Seitz, 2015)

$$\mathbf{I} \begin{bmatrix} \mathbf{x}_1 \\ \dots \\ \mathbf{x}_m \end{bmatrix} = \begin{bmatrix} \hat{\mathbf{x}}_1 \\ \dots \\ \hat{\mathbf{x}}_m \end{bmatrix} + \begin{bmatrix} \bar{\mathbf{v}}_1 \\ \dots \\ \bar{\mathbf{v}}_m \end{bmatrix} \quad \text{with} \quad \mathbf{C}_{\hat{\mathbf{x}}\hat{\mathbf{x}}} = \begin{bmatrix} \mathbf{P}_1^{-1} & \dots & 0 \\ \vdots & \ddots & \vdots \\ 0 & \dots & \mathbf{P}_m^{-1} \end{bmatrix} \quad (3.28)$$

which is solved according to Eqn. 3.16. This procedure is used to derive the ITRF realizations or the EOP series IERS C04. According to Seitz (2015) a combination of parameters is not straightforward as the technique-specific datum definition is very critical and information gets lost by setting up solution-specific transformation parameters. The latter is caused by the setup of parameters of similarity transformations for each solution in order to realize the datum independently.

Tab. 3.2 shows as a summary the most important aspects of the combination approaches discussed above (based on Seitz, 2015). Please note that the term “stacked-observation level” was introduced to distinguish between the pure observation level and the stacking of normal equations derived by the same software. Within this work the stacked-observation approach is used, since technique-specific normal equations derived by the BSW are combined.

### 3.5 Co-location of Space Geodetic Techniques

For intra- and inter-technique combinations in space geodesy the term “co-location” has been defined in the report “Precise Geodetic Infrastructure: National Requirements for a Shared Resource” of the National Research Council<sup>16</sup>

“[...] as two or more geodetic techniques or systems occupying simultaneously or subsequently very close locations[...].”

This rough definition states the required close location of techniques but does not characterize the location itself nor does it define, how to consider the finite distance between the individual sensors. Therefore, co-location can be done wherever corresponding sensors are located close together. Usually, this is the case at ground station and on-board satellites. Regarding Sect. 3.4 common parameters are required for inter-technique combinations. Therefore, co-location could be stated as locating space geodetic sensors within a distance wherein the relationship between common parameters can be modeled or measured with an accuracy better than the uncertainties of the estimated parameters.

Co-location in space is addressed in the first part of this section. The general concept of this type of combination was shown already in Fig. 1.1. The corresponding offset vectors on-board the satellite are called space ties. Usually co-location in space is mentioned as an alternative to co-location on the ground,

<sup>16</sup> <http://www.nap.edu/catalog/12954/precise-geodetic-infrastructure-national-requirements-for-a-shared-resource>, accessed August 2016

however, this order is reversed here to highlight co-location in space. Co-location on the ground is, therefore, discussed within the second part (Sect. 3.5.2) covering alternative co-location strategies. Both approaches base, however, on sensor coordinates and externally measured offset vectors. Co-location on the ground takes place at fundamental sites tied to the Earth crust; the terrestrially measured offset vectors are called local ties as mentioned already in Chap. 1. It has to be mentioned that this approach is state-of-the-art and the intention of this thesis is rather to strike out in a new direction than to abolish local ties. Sect. 3.5.2 discusses also other ways to consider the distance between the sensors for co-location sites on the Earth crust. The third part (Sect. 3.5.3) compares the approaches discussed before, whereas the last section (Sect. 3.5.4) provides a closer look at the clock ties and short VLBI baselines.

### 3.5.1 Co-location in Space

Co-location in space describes the combination of space geodetic techniques on-board of satellites. Three prerequisites must be satisfied in order to combine geodetic observation techniques rewardingly in space. Firstly, a spacecraft is required carrying sensors of different space geodetic techniques. Even if this seems to be obvious, it is a challenging requirement considering existing spacecraft. Secondly, the offset vectors between these sensors and the spacecraft center of mass (CoM), the so-called space ties, have to be known at the mm-level in the space-fixed frame. Concerning these offset vectors, it is required to know: (1) the CoM position in the body-fixed frame, (2) the offset vectors between the CoM and the physical reference points of the sensors, (3) the optical and electrical offsets and patterns of the sensors, and (4) the precise spacecraft attitude to transform body-fix values into the inertial frame. The knowledge of the CoM requires not only a pre-launch calibration but, for many satellites, also an in-orbit monitoring as the fuel consumption due to orbit maneuvers and attitude maintenance will change the spacecraft's state of equilibrium and, therefore, the CoM. For example, during GOCE's mission duration 4.5 years a CoM shift of 3.2 cm was observed. To ensure sensor offset calibrations at the mm level, anechoic chamber calibrations are required. The precise attitude information is usually provided by star cameras and described in more detail in Sect. 4.2.2. As a third requirement, a cm level orbit determination has to be achieved. Therefore, non-gravitational forces have to be taken into account as described in Sect. 4.2.2. In the next sections general applications of co-location in space are described followed by a description of currently available spacecraft for co-location and dedicated future missions. The last two paragraphs are dedicated to the ideas of LEO GNSS constellations and SLR single- and double-difference forming.

#### Recent Applications and Future Possibilities

Basically, a co-location in space is applied, whenever a multi-technique orbit determination is performed. Corresponding results were published for GPS, SLR, and DORIS orbit solutions of TOPEX-Poseidon, Jason-1, and OSTM/Jason-2 (Luthcke et al., 2003; Lemoine et al., 2010; Flohrer et al., 2011). The combination of GPS and SLR for GPS satellite orbit determination has been done but has not been shown so far to improve the results due to the huge different in the data amount from GPS and SLR (Zhu et al., 1997; Eanes et al., 2000; Flohrer, 2008).

Three major benefits can be expected from co-location in space. Firstly, station- and technique-specific problems can be assessed regarding the same spacecraft. In this case a co-location satellite will act as a target common to different techniques at one station (inter-technique), and as common target to one technique at several stations (intra-technique). However, this requires a highly accurate satellite orbit and a direct observation link between ground stations and satellite. Secondly, applying space ties in a multi-technique processing will allow to validate a TRF realization based on local ties independently. Tab. 3.6 (given in Sect. 3.5.2) shows discrepancies between space geodetic results and local ties, analogous values can be obtained, in principle, if space ties are introduced. According to Seitz et al. (2012) co-location in space can be seen as a consistency test. Thirdly, co-location in space provides an alternative to local ties. This is by far the most interesting application. For example, 115 stations with two or more techniques

**Tab. 3.3:** Observation types for co-location in space; brackets indicate experimental observations only

technique	GNSS satellite				LEO satellite				remarks
	GNSS	SLR	VLBI	DORIS	GNSS	SLR	VLBI	DORIS	
GNSS		✓	(✓)			✓	(✓)	✓	only for a subset of GNSS sat. experimental
SLR	✓		(✓)		✓		(✓)	✓	
VLBI	(✓)	(✓)			(✓)	(✓)		(✓)	
DORIS					✓	(✓)	✓		

were considered in the ITRF2008 combination. Collecting the local tie information and keeping them up to date is a huge task. Terrestrial surveys are also required in a timely manner for new instruments or if reference point have been affected by reconstruction work. Furthermore, it was recommended to repeat terrestrial surveys on an annual basis and, especially, after earthquakes (Altamimi, 2005). As mentioned in Sect. 3.5.2, today’s ground-based co-location faces inaccurate, incomplete, or even missing local tie information. In general, every missing or inaccurate local tie is a missed chance for linking and combining the space geodetic techniques. Co-location in space, however, requires basically not more than one dedicated satellite and one space tie for each technique. As the satellite orbits the Earth, all sensors and techniques can be tied to the satellite (nearly) independent from their geographical locations. Co-location in space is, therefore, a promising way to improve the terrestrial reference frame. A very comprehensive study about the improvement achieved, when combining the available GNSS and SLR observations on-board GNSS satellites, was published by Thaller et al. (2011). They show coordinate accuracies for SLR stations of 1-2 cm, when combining GNSS and SLR on-board the GNSS satellites. In addition, satellite antenna offsets and SLR range biases are discussed and they show that both parameter types can be estimated simultaneously. Including VLBI observations to a co-location in space would also provide an additional link between the terrestrial and the inertial reference system, a connection sometimes called “frame tie” (Plank, 2013). A connection between the frames can be achieved either by determining the GNSS orbits in the celestial frame or by determining the VLBI telescope coordinates directly in the GNSS frame. However, today the potential of co-location in space is not really used to estimate station coordinates, geocenter coordinates, or ERPs.

When thinking about co-location in space, it is necessary to distinguish between today’s possibilities and future plans. Tab 3.3 shows the different observation types, which can be included in a co-location in space. Two very basic statements can be derived: (1) VLBI observations are not available or only at a very rough experimental status (see Chap. 6 for more details), and (2) there is a clear distinction between co-location on-board a LEO and on-board GNSS satellites. This distinction was already shown in Fig. 1.1. Using a LEO as co-location satellite, GNSS ground instruments are not necessarily included in the combination. Rigorously, they can be included via ground-LEO baselines or via commonly estimates GNSS orbits and clocks. This topic is discussed in more detail in Chap. 5. In the case of co-location on-board GNSS satellites, the GNSS ground instrumentation is directly connected to the other techniques. However, in this case DORIS cannot be included. In principle, also a simultaneous combination of co-location on-board a LEO and on-board GNSS satellites would be possible.

### Available Co-location Satellites

Fig. 3.2 shows a selection of past, current, and future satellite missions allowing co-location in space. The figure provides also the orbital altitudes, the inclinations, and the available space geodetic techniques for each satellite. As indicated in Fig. 3.2 the satellites can be divided into four groups. Their individual contribution will be discussed in the following. The first group contains scientific Earth-observing LEOs like the gravity field missions CHAMP, GRACE, and GOCE, remote-sensing missions like PROBA-2, TerraSAR-X, and TanDEM-X, or Earth explorer missions like SWARM. The orbit heights are between

200 and 800 km and some missions consist of more than one spacecraft, like GRACE (2 spacecraft) and SWARM (3 spacecraft). The space geodetic techniques on-board the satellites are primarily used for precise orbit determination. GPS tracking data with a data rate of 0.1 or 1 Hz are available, however, the data quality and the number of GPS satellites tracked vary significantly between the missions (see Sect. 4.1). Extensive SLR observation records are available for nearly all missions mentioned in Fig. 3.2. Due to DORIS improvements, some of the more recent missions are equipped with high-quality multi-channel receivers allowing an accuracy level of a few centimeters for orbit determination (Auriol & Tourain, 2010). Due to the strong non-gravitational forces in the corresponding altitudes, spacecraft macro-models or additional observations (e.g., accelerometer data) are needed to achieve an appropriate orbit accuracy. The Chinese Atmospheric density detection and Precise Orbit Determination mission (APOD<sup>17</sup>) launched in autumn 2015 is the first LEO mission equipped with a dedicated VLBI transmitter<sup>18</sup>. Furthermore the payload comprises a density detector, a dual-frequency GNSS receiver (GPS/BeiDou), and an SLR reflector. The satellite orbits the Earth in 450 km altitude (the inclination is 97.4°). However, until now no VLBI observations have been performed and no co-location results have been published. It seems that the primarily mission objective of APOD, also named Xiwang-2A or XW-2A, is in the area of communication. The second group, actually a subset of the first, consists of the altimetry satellites of the TOPEX/Poseidon and Jason (Jason-1, OSTM/Jason-2, Jason-3) family. These satellites are in a nearly circular orbit with an altitude of 1360 km and, therefore, nearly unaffected by air drag (see Sect. 4.2.2). However, due to their size and their large solar panels (cf. Tab. B.1), they are significantly perturbed by solar radiation pressure. To achieve the tight orbit accuracy requirements for altimetry, i.e., a radial orbit accuracy better than 1 cm, all of these satellites are equipped with GPS, SLR, and DORIS instruments. Concerning DORIS and SLR, the situation is similar to that of the first LEO group. However, in general, more SLR observations are available and the DORIS receivers are of the newest generation. For GPS, three issues have to be mentioned: (1) the GPS antennas are not zenith facing<sup>19</sup>, (2) the receivers suffer from several hardware problems (see Sect. 4.1), and (3) GPS signals from nadir angles up to 17° can be tracked. The last aspect is critical, since the official satellite antenna PCV information provided by the IGS are just extrapolated beyond 14° (Schmid, 2014). Additionally the Chinese altimeter mission HY-2A has to be mentioned. Equipped with GPS, SLR, and DORIS instruments, this mission is comparable to the Jason satellites but flies in a lower orbit (altitude 970 km). In summary, satellites of both groups are highly useful for co-location in space. The third group consists of the GNSS satellites at altitudes of around 20'000 km. SLR observations to GNSS satellites are used for orbit validation since many years and are available for several spacecraft (GPS-35, GPS-36, all GLONASS and Galileo satellites, several BeiDou satellites). It has to be mentioned that the future GPS III satellites will be equipped with retro-reflector arrays<sup>20</sup>. VLBI observations of GNSS satellites are possible, as some radio telescopes are able to track GNSS L-band signals (see Sect. 6.1). The fourth group consists of geostationary GNSS satellites and, therefore, the remarks made for group three apply as well. However, due to the geostationary position, the GNSS-based orbit determination is more challenging (Steigenberger et al., 2015). In addition to the mentioned satellites, RadioAstron allows co-location in space as this satellite carries a VLBI telescope and an SLR retro-reflector. A detailed overview of the satellites allowing co-location in space is provided in Appendix A (Tab. A.1). Tab. A.2 provides the space ties for these satellites.

### Dedicated Future Co-location Satellites

In recent years several dedicated co-location satellites were considered. The most important missions are described briefly in this section. Tab. 3.4 provides an overview of their main characteristics. There might exist other missions, ideas, and concepts allowing co-location in space but with the objectives primary

<sup>17</sup> [http://ilrs.gsfc.nasa.gov/missions/satellite\\_missions/current\\_missions/pn1a\\_general.html](http://ilrs.gsfc.nasa.gov/missions/satellite_missions/current_missions/pn1a_general.html), accessed August 2016

<sup>18</sup> In addition to the nano-satellite (PN-1A) considered here APOD consists also of three pico-satellites (PN-1B, PN-1C, PN-1D).

<sup>19</sup> For Jason-1 the antenna is tilted by 30° and for OSTM/Jason-2 by 15°.

<sup>20</sup> <http://www.gps.gov/multimedia/presentations/2015/12/APRSAF/miller.pdf>, accessed July 2016.

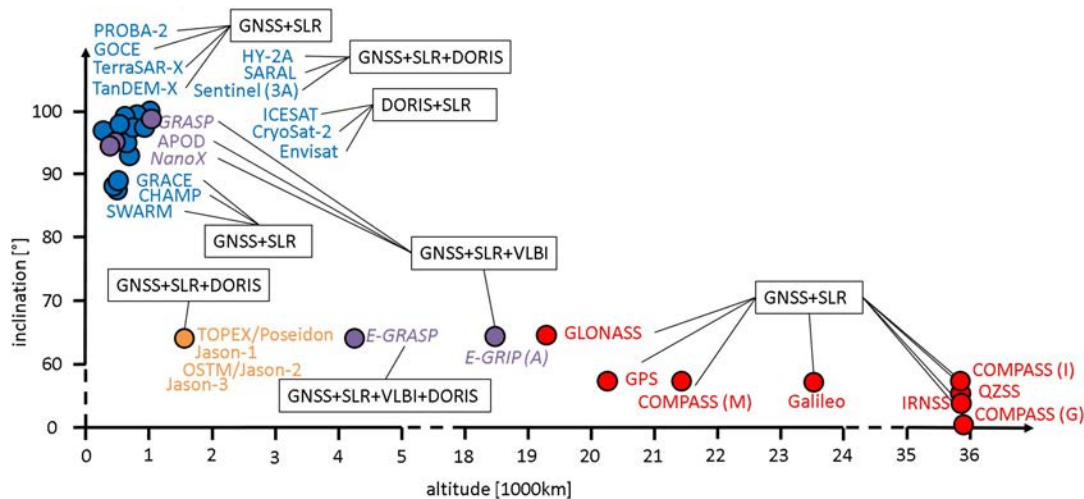


**Fig. 3.2:** Available satellites for co-location in space ordered by their altitude and inclination (approximations); planned missions are set in italics; for the elliptically-orbiting missions GRASP, E-GRASP, and E-GRIP (orbit scenario A) the altitude is given by semi-major axis minus Earth radius

in other research fields. However, the selection presented here contains the major international activities concerning a dedicated co-location satellite.

Probably the most advanced mission is the JPL/CNES Geodetic Reference Antenna in Space (GRASP, Bar-Sever et al., 2009). This micro-satellite mission will carry a tri-band GNSS receiver, SLR retro-reflectors, and a VLBI transmitter. The envisaged orbit accuracy is 1 mm in the mean radial component with a stability of 0.1 mm per year (Plank, 2013). To achieve this ambitious aim, a pre-launch anechoic chamber calibration of the sensor offsets is planned, the spacecraft is optimized by a simple shape, without moving parts and a stable center of mass, and a sun-synchronous orbit (925 km perigee height and 1400 km apogee height) was selected. With its ambitious concept and proposed accuracy, GRASP claims to be a key to achieve the GGOS requirements. With the exception of the VLBI transmitter the geodetic instruments were already flown on several missions mentioned above. According to Plank (2013) the VLBI transmitter will be based on the X/S-Band transmitter of the lunar gravity field mission GRAIL. Consequently, each geodetically used radio telescope will be able to track the transmitted signals assuming an appropriate slew rate. As mentioned by Plank (2013), the GRASP VLBI observations will be done either as classical multi-telescope observations, or in a single-telescope mode comparable to one-way integrated Doppler measurements<sup>21</sup>. GRASP was proposed but not selected in NASA's Earth Venture Mission Program in 2011, a second proposal was submitted in December 2015<sup>22</sup>.

Around 2008 the mission Microsatellite for GNSS-Earth-Monitoring (MicroGEM, Brieß et al., 2009) was initiated at GeoForschungsZentrum Potsdam (GFZ) as a small satellite constellation for GNSS applications and co-location in space. A geodetic GNSS receiver connected to one antenna for orbit determination and two antennas for occultation, an SLR retro-reflector, and a VLBI transmitter were intended as payload for each spacecraft. In order to reduce the presumed costs, the mission was re-designed as a joint effort of GFZ and ETH Zürich now called NanoGEM (Wickert et al., 2011). With nearly the same instrumentation the mission was classified as technology demonstration without full-time operations. A second re-design was carried out in 2012 ending up with NanoX (Buhl et al., 2012). Similarly structured as a technology demonstration on an existing platform, the project seemed to be feasible. However, due to missing financial support, none of the three concepts was realized so far.

Common to all projects mentioned above is a LEO orbit with an apogee height below 1400 km. A different orbit type is intended for the Einstein Gravitational Red-shift Probe (E-GRIP, Jetzer et al., 2015, Männel

<sup>21</sup> A PRN type signal will be modulated on the transmitted VLBI signals, pers. communication Y. Bar-Sever.

<sup>22</sup> A NASA decision is expected for August 2016, pers. communication S. Nerem.

**Tab. 3.4:** Proposed satellites for co-location in space (as of June 2016); please note that for NanoX and E-GRIP the definitive orbit was not selected yet

	NanoX	GRASP	E-GRASP/ Eratosthenes	E-GRIP
primary mission goal	co-location in space	co-location in space	co-location in space	fundamental physics
mission lead	GFZ Potsdam, ETH Zürich	JPL, GRASP science team	CNES, E-GRASP/ Eratosthenes science team	University Zürich, ETH Zürich, CSEM, Spectratime
space techniques				
VLBI	✓	✓	✓	✓
SLR	✓	✓	✓	✓
GNSS	✓	✓	✓	✓
DORIS		(✓)	✓	
intended orbit				
semi-major axis [km]	6871 / 6939	7453	10481	24450 / 35000
eccentricity [-]	0.0 / 0.0	0.03	0.32	0.636 / 0.8
inclination [°]	90.0 / 97.64	99.02	63.4	63.4 / 63.4
mission status				
intended launch	-	2020	2024	2024
current status	postponed due to financing issues	proposal submitted to NASA, decision expected for August 2016	proposal submitted to ESA, decision expected for December 2016	extended phase 0/A; further decision by Swiss Space Office

et al., 2016) which will fly in a highly elliptical orbit. The scientific objectives of this joint project of University of Zürich, ETH Zürich, Centre Suisse d'Électronique et de Microtechnique, and Spectratime are the measurement of the space-time curvature around the Earth and the performance of multiple tests of general relativity. Therefore, E-GRIP will fly in a highly eccentric orbit ( $e > 0.6$ , apogee height above Earth's surface  $> 35'000$ km) and will carry a narrow-angle and a wide-angle microwave link (both at X and K-band), two GNSS antennas, an SLR retro-reflector array, and, as core instrument, an active space hydrogen maser provided by Spectratime. Consequently, E-GRIP could act as a co-location satellite with suitable observation conditions for VLBI. Currently this mission study is within an extended phase A/0. Considering the orbit, it is obvious that the apogee height is far beyond the GNSS altitude range. Therefore, a theoretical observation concept with high gain GNSS antennas mounted on the nadir- and zenith-facing side of E-GRIP was developed. Using this strategy a reasonable number of GNSS satellites is observable. A more detailed assessment on GNSS tracking for highly eccentric orbits is given by Winternitz et al. (2016) in the framework of NASA's Magnetospheric Multi-Scale Mission. The long distance between Earth and E-GRIP during apogee is also challenging for SLR. However, observations to a small reflector array are feasible assuming a reasonable SLR station performance<sup>23</sup>.

Recently, a group of scientists from several institutions in Europe proposed an European co-location satellite mission to ESA<sup>24</sup>. The mission E-GRASP/Eratosthenes can be seen as an European alternative to GRASP, in the case GRASP is not funded by NASA, or as a follow-on mission. The spacecraft will be equipped with a dual-frequency multi-GNSS receiver, a DORIS receiver, a VLBI transmitter, and an SLR retro-reflector array. An ultra-stable oscillator, most probably an active hydrogen maser from Spectratime, will serve as a unique frequency standard. In addition, a photon counter will be used for clock comparisons, known as time transfer by laser link, T2L2). Although, the concept is similar to E-GRASP/Eratosthenes orbit is intended to be more eccentric than the GRASP orbit. To fit within the ESA cost frame, an orbit is currently considered that is characterized by an altitude of 755 km and 7465 km for perigee and apogee, respectively, a prograde inclination of 63.4°, and a frozen perigee. The payload will consist of GNSS, DORIS, SLR and VLBI instruments connected to the common ultra-stable oscillator and

<sup>23</sup> The station capability was assumed to allow LAGEOS observations regularly.

<sup>24</sup> In February 2016 R. Biancale et al. sent a letter of intent to ESA, the information provided here are based on this letter. The corresponding proposal was submitted to ESA by June 24, 2016.

an electrostatic micro-accelerometer will help to consider non-gravitational forces. A mission duration of five years starting before 2024 is envisaged.

To summarize, four mission ideas are currently discussed in the geodetic community: the technology demonstrator NanoX, the most advanced GRASP mission, and the two mission ideas E-GRIP and E-GRASP/Eratosthenes. However, a dedicated co-location mission will be available at the earliest around 2020.

### Simulation Study: Forming GPS Differences on LEO Level

Associated with the studies for dedicated co-location satellites also ideas for co-location constellations were discussed. For example, the NanoGEM and NanoX studies contained the possibility of building more than one spacecraft. This constellation idea is driven mainly by GNSS and the idea of forming baselines in space. Assuming a stable baseline between two satellites, this baseline can be well determined by fixing the GNSS ambiguities with space-based observations. Several studies were carried out concerning double-difference orbit determination for formation flying satellites like GRACE or TerraSAR-X/TanDEM-X (e.g., Svehla & Rothacher, 2003; Jäggi, 2007; Jäggi et al., 2007). As several LEO missions were analyzed within this thesis a small study was carried out concerning the possibility to form a constellation out of the available LEO missions. Therefore, the number of available single-differences between the various LEO missions usable for co-location in space was analyzed.

This study comprises the 15 satellites listed in Tab. 3.5. Looking at the Keplerian elements of these LEOs, three close formations can be found: (1) the two GRACE spacecraft are separated by  $\approx 200$  km on the same trajectory, (2) Jason-3 follows OSTM/Jason-2 within one minute on the same trajectory for calibration purposes, and (3) Swarm-A and Swarm-C are flying side-by-side<sup>25</sup>. Obviously, TanDEM-X and TerraSAR-X would provide an additional formation. However, additional insights into co-location to be gained by TanDEM-X are negligible, as both spacecraft are separated by only 200 m. For the simulation, a 10-channel GPS receiver and a 0.1 Hz tracking rate was assumed for each satellite. The 10-channel assumption is very generalized as, for example, Swarm has receivers with eight channels only. Fig. 3.3(a) shows the number of single-differences that can be formed per day for all LEO combinations. Obviously, the observation number is highest for the GRACE, Swarm and Jason formations. For all other baselines the corresponding numbers are below 35'000, where 50 % of them have values between 10'000 and 20'000. These numbers indicate already that forming baselines between different LEO missions is most promising for missions with similar orbits. However, more important than the absolute numbers are the number of epochs with at least five single-differences. The corresponding numbers are presented in Fig. 3.3(b). Here, a number of 8640 epochs per day indicates, that the two LEO orbits are entirely covered by a suitable number of single-differences. Again this is reached for the formations only. For all other baselines, not more than 50 % of the orbits are covered, for 74 % of the baselines the coverage rate is below 20 %. Interestingly, the baselines formed with the Sentinel satellites are characterized by a lower number of single-differences. This was expected, as their orbital elements differ significantly from those of the other missions. The number of single-differences formed per epoch is given as histograms for several baselines in Fig. 3.4. For the closely flying GRACE and Swarm satellites no epochs with less than 8 single-differences occur. The baseline between Swarm-B and Swarm-C shows that almost no single-differences are available due to the different orbit planes ( $\Delta\Omega = 60^\circ$ )<sup>26</sup>. Epochs with only 5 and 6 single-differences occur for the Jason baseline because of the higher altitude of the Jason orbits. For the other four arbitrarily selected baselines in the bottom row of Fig. 3.4, the low number of epochs with more than four single-differences per epoch mentioned above is visible.

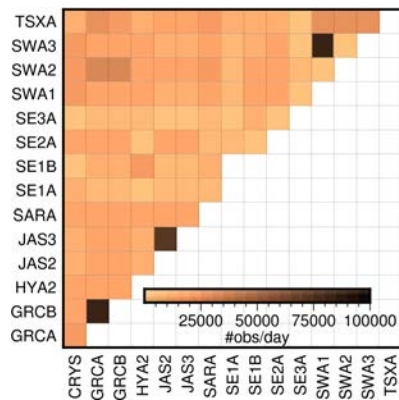
Fig. 3.5 shows the observed GPS satellites for selected space baselines in bins of 6 minutes. Obviously, for satellite pairs flying in formation these plots are very dense, showing relatively long observation periods of

<sup>25</sup> The node difference between both orbits comprises  $1-1.4^\circ$  corresponding to  $\approx 120$  to  $170$  km longitudinal separation at the equator, with  $\approx 10$  s along-track difference.

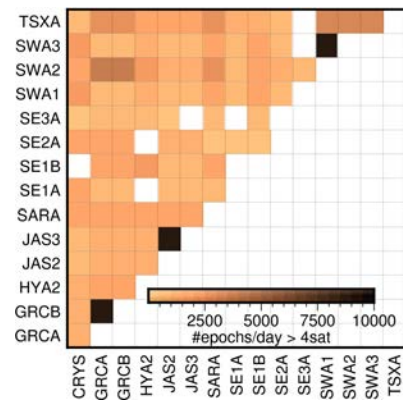
<sup>26</sup> The corresponding distance between both satellites vary between  $11'500$  and  $13'500$  km.

**Tab. 3.5:** Orbit characteristics for the LEO used in the GPS difference study; Keplerian elements were extracted from two-line elements; data source: <https://www.celestrak.com/NORAD/elements/>, accessed June 2016

LEO	name	reference epoch [mjd]	$a$ [km]	$e$ [°]	$i$ [°]	$\Omega$ [°]	$\omega$ [°]	$u$ [°]
CRYS	CryoSat-2	57547.85	7096687.16	0.00	92.03	111.90	158.33	0.16
GRCA	GRACE-A	57547.87	6737831.95	0.00	88.99	15.18	116.16	108.84
GRCB	GRACE-B	57547.87	6737814.69	0.00	88.99	15.18	116.16	107.14
HYA2	Haiyang 2A (HY-2A)	57548.06	7346584.65	0.00	99.34	171.01	73.96	0.12
JAS2	OSTM/Jason-2	57547.51	7715872.32	0.00	66.04	180.01	270.77	154.55
JAS3	Jason-3	57547.51	7715868.80	0.00	66.04	180.01	270.77	151.37
SARA	SARAL	57547.17	7162312.21	0.00	98.54	346.62	61.02	0.13
SE1A	Sentinel-1A	57548.75	7073904.36	0.00	98.18	167.72	80.72	0.13
SE1B	Sentinel-1B	57548.30	7074460.31	0.00	98.19	167.10	72.68	0.50
SE2A	Sentinel-2A	57547.84	7167129.25	0.00	98.57	234.19	98.19	0.13
SE3A	Sentinel-3A	57548.72	7180801.73	0.00	98.63	227.49	87.47	0.13
SWA1	Swarm-A	57547.54	6821893.14	0.00	87.35	306.82	74.31	0.16
SWA3	Swarm-C	57547.54	6821888.46	0.00	87.35	308.23	73.63	0.16
SWA2	Swarm-B	57547.16	6882211.01	0.00	87.75	0.02	75.60	0.16
TSXA	TerraSAR-X	57547.98	6886531.94	0.00	97.44	166.99	82.56	83.69



(a) Number of single-difference observations per day



(b) Number of epochs with >4 single differences per day

**Fig. 3.3:** Number of GPS single-differences simulated for the selected LEO baselines

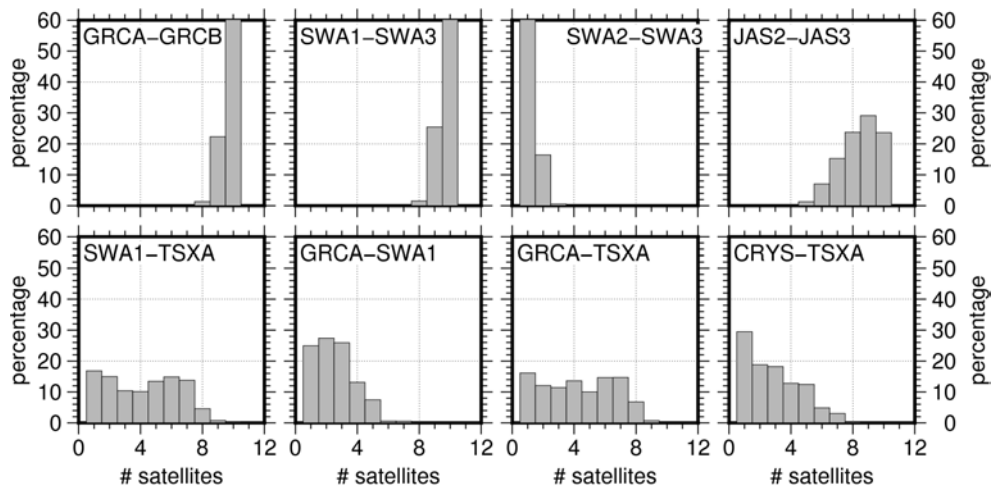


**Fig. 3.4:** Histogram of the number of GPS single-differences per epoch for LEO baselines

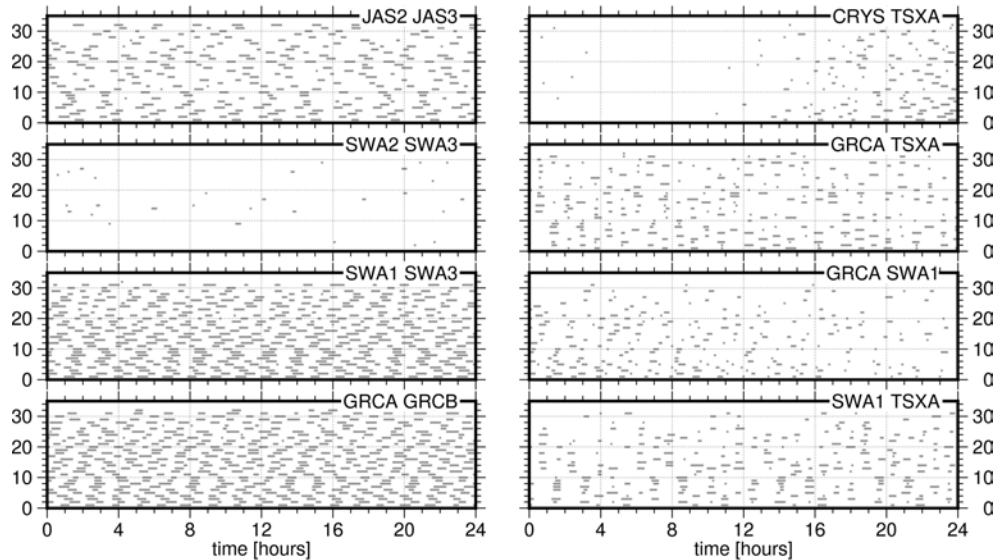


**Fig. 3.5:** Satellite tracking scenarios for different LEO baselines; six minute intervals (corresponds to 60 epochs) were considered; satellite PRN along y-axis

up to 40 min, which is roughly half an orbit. But also the number of satellites and the overlapping between individual GPS satellite observations is promising. For the other baselines the situation is different. For the baseline between Swarm-B and Swarm-C as well as for the baseline between CryoSat and TerraSar-X, no observations are available over longer periods. For Swarm-1 and TerraSar-X, more than a few GPS satellites are observed at individual epochs but without a good overlap. Consequently it will be difficult to connect epochs for a reliable ambiguity resolution. However, a LEO orbit might be covered completely, if considering all LEO baselines.

In summary, forming baselines between several LEOs is rather challenging. In general, a high number of single-differences is only present for formation flying LEOs. It has to be mentioned that this study was performed for one arbitrary day only. Therefore, different numbers will be obtained when extending the simulation time span taking into account the mission-specific motion of the nodal lines. Further studies are required, as this very preliminary simulation only aimed at baseline formation. The real challenge will be the orbit determination process based on these baselines. So far it is obvious that the major prerequisite is a highly accurate force model to bridge the orbit parts that are weakly observed, otherwise, the observed orbit parts are not connected appropriately.

### SLR Differentiation and Database Inventory

Contrary to other space geodetic techniques, SLR observations are performed station-wise, independently from other stations and without coordinated observation epochs. However, “simultaneous range differencing” was studied already 30 years ago (Pavlis, 1985). As mentioned in Sect. 2.1.2 range biases are estimated to account for several uncalibrated effects, like unknown reflector offsets, or time delays in the electronics. Analog to benefits in GNSS, these station- and satellite-specific effects could be mitigated or eliminated when forming SLR differences. In the other direction, processing SLR differences would allow to determine the biases for the common un-differenced SLR processing. The general concept of SLR differentiation is shown in Fig. 3.6(*left*). A single-difference can be formed, if two stations  $r, s$  observe the same satellite  $i$  within a time interval  $\Delta t_1$ . By considering the spacecraft velocities a time difference  $\Delta t_1$  of only 100 ns will result in a orbital position difference of 0.4 and 0.8 mm for GNSS and LEO satellites, respectively. Therefore, a synchronization accuracy of better than 10 ns between the two stations is required. Otherwise, the SLR normal points have to be interpolated to one common epoch which requires highly accurate orbits (Svehla et al., 2016). If both stations switch to another common satellite  $j$  within a suitable time interval  $\Delta T$  (observations within  $\Delta t_2$ ) a double-difference, can be formed. The satellite orbit accuracy

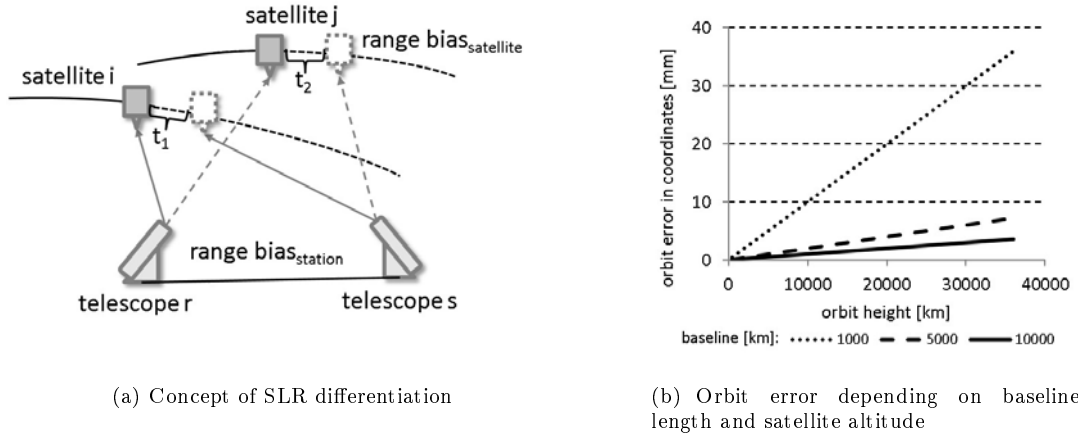


**Fig. 3.6:** Concept of SLR differentiation and orbit errors depending on baseline length and satellite altitude

is the limiting factor defining the acceptable length of  $\Delta t_1$  and  $\Delta t_2$ . Fig. 3.6(right) shows an estimation on the required orbit accuracy. Assuming that the effect on the baseline  $\delta_b$  should not exceed 1 mm the maximal orbit error  $\delta_r$  within  $\Delta t$  is scaled by the ratio of the satellite altitude  $h$  and the baseline length  $b$ . This consideration is based on the following rule of thumb  $\delta_b[\text{mm}] = \frac{b[\text{km}]}{h[\text{km}]} \delta_r[\text{mm}]$  (Bauersima, 1983). Obviously, the acceptable orbit error is more critical for longer baselines and for lower satellite altitudes. Fig. 3.6(right) shows, that for a 1000 km long baseline, the required orbit accuracies is 6 mm and 25 mm for LAGEOS and GLONASS, respectively. For a very long baseline of 10'000 km, a LAGEOS orbit accuracy in the sub-millimeter range would be required. It has to be mentioned that the required orbit accuracy refers to  $\Delta t$  and not to the whole orbit arc, therefore, shorting this time difference with coordinated SLR observations will allow SLR differentiation also for very long baselines.

Today, only a few data sets for coordinated SLR experiments are available. Recent experiments were performed between Herstmonceux and Graz observing Galileo satellites in late 2011 and between the two SLR stations in Wettzell in 2016. Therefore, as initial investigation, a small part of the SLR data archives was screened for observations allowing the forming of difference by chance. In the following, observations which allow differentiation, i.e., observations to the same satellite within a specified time span, will be called single- or double-difference possibilities, respectively. Fig. 3.7(a,b) shows the monthly number of SLR normal points for LAGEOS 1/2 and all GLONASS satellites found in the ILRS database (very roughly 12'000 and 6'000 normal points, respectively). Searching for potential baseline observations, while allowing  $\Delta t=1$  min, results in around 200 and 100 single-difference possibilities per month for LAGEOS and GLONASS, respectively. Searching also for double-differences ( $\Delta T < 10$  min) reveals only a few dozen possibilities per month for both satellite systems. Consequently, forming differences from the existing "uncoordinated" SLR observations only allows for a proof-of-concept for SLR differentiation. The number of available double-difference possibilities for increased time intervals  $\Delta t$  is shown in Fig. 3.8(a,b). Here all possibilities within 2010.00-2015.75 have been added up. In order to find an acceptable number of possibilities at least a 10 min time difference  $\Delta T$  has to be considered. Each additional 10 min increases the number of possibilities by around 500 a nearly similar contribution to the various baseline ranges. Due to the higher number of LAGEOS observations, a few possibilities for the very long baselines ( $>10'000$ ) can be found.

In summary, SLR differentiation is an interesting study area promising considerable insights into SLR biases. Dedicated studies planned for the second phase of the project "Co-location on Ground and in Space" will be based on coordinated observation efforts between the two SLR telescopes in Wettzell (WLRS and SOS-W) and the presented inventory search. Due to the required software modifications these datasets were not processed yet.

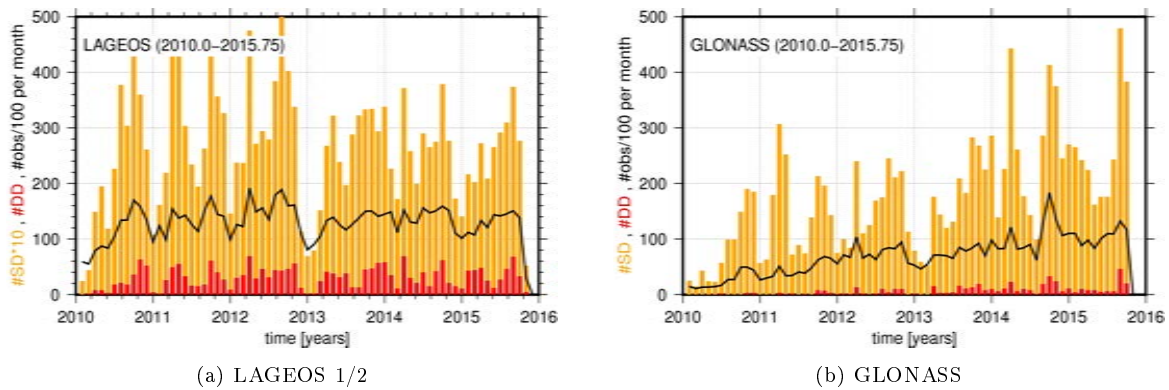


**Fig. 3.7:** Monthly number of SLR differences formed for LAGEOS and GLONASS (archive data); SD single-difference (1 min spacing), DD double-difference (10 min spacing)

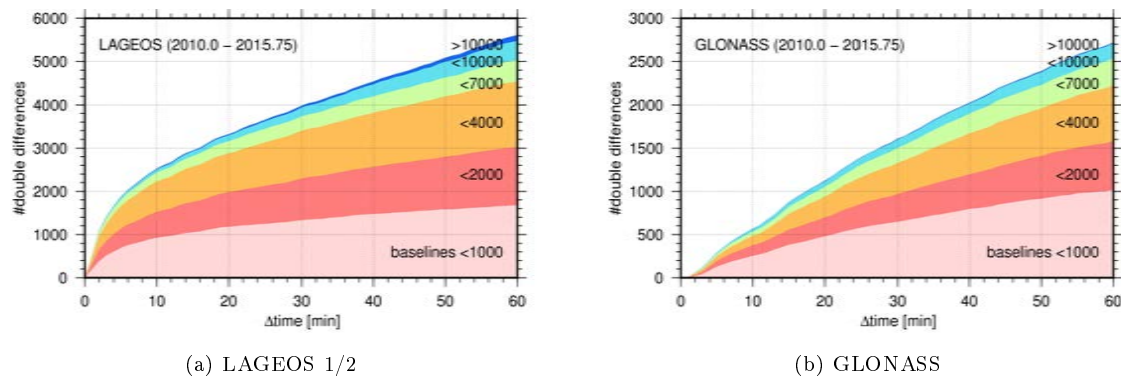


**Fig. 3.8:** Number of SLR differences depending on allowed time difference and baseline length for LAGEOS and GLONASS (archive data); please note the different scales

### 3.5.2 Other Co-location Approaches

This section comprises alternative ways to co-locate space geodetic techniques. The strategies described within this section range from the current state-of-the-art to very theoretical tie concepts.

#### Co-location on the Ground

Co-location on the ground describes the connection of space geodetic techniques using local ties. In Sect. 3.2.2 local ties were introduced as external measurements, as they are terrestrially surveyed three-dimensional offset vectors between the instruments at a fundamental site. At these co-location sites two or more space geodetic techniques are located simultaneously or sequentially close together. Normally the instruments are located not more than a few hundred meters apart. The geographical distribution of these sites is shown in Fig. 3.1. Sarti et al. (2013) described the process of local tie estimation in detail and potential error sources thereby. In general, it should be mentioned that a highly accurate local survey is the basis for a local tie estimation. By using terrestrial surveying instruments the positions of the different instruments, i.e., their geometrical reference points, are determined within a local reference system. The geometrical reference points are by convention the antenna reference point (ARP) for GNSS and DORIS and the intersection of the telescope axes for SLR and VLBI. Surveying instruments and the adapted surveying concept have to be carefully optimized to minimize uncertainties in the measured local ties. For well-performing stations the achieved uncertainties are at the mm level, as showed by repeated surveys. However, for some stations too optimistic standard deviations in the sub-mm range are published (Seitz, 2009). Two critical issues remain for co-location on ground: (1) in addition to the local ties also the variations of electrical and optical centers have to be considered, and (2) the adjusted local ties have to be transformed into the global terrestrial reference frame. For example, Ray & Altamimi (2005) showed a

**Tab. 3.6:** ITRF2008 and DTRF2008 co-locations: types, numbers, and level of agreement to space geodetic results; based on Altamimi et al. (2011) and Angermann et al. (2013), respectively; please note the different accuracy levels; *np* = value not provided

local tie type	number	ITRF2008			number	DTRF2008		
		discrepancy [%]				discrepancy [%]		
		< 6 mm	6-10 mm	> 10 mm		< 5 mm	5-10 mm	> 10 mm
GPS-VLBI	44	47	24	29	32	22	33	45
GPS-SLR	48	43	29	28	29	14	45	41
GPS-DORIS	45	34	12	54	40	5	30	65
SLR-VLBI	8	<i>np</i>	<i>np</i>	<i>np</i>	9	11	22	67
SLR-DORIS	10	<i>np</i>	<i>np</i>	<i>np</i>				
VLBI-DORIS	10	<i>np</i>	<i>np</i>	<i>np</i>				

reduction of the discrepancy to space geodetic results for the GPS-VLBI local tie in Medicina from 7.3 to 2.7 mm by changing the alignment of the local tie vector.

Globally more than 80 co-location sites have been established, where instruments of the four major observing techniques are operational or have been operational in the past (see Fig. 3.1). Tab. 3.6 shows the number of local ties between the individual techniques applied in the ITRF2008 (Altamimi et al., 2011) and DTRF2008 (Seitz et al., 2012) solutions including their corresponding discrepancy level with respect to space geodetic results. From this table, three general aspects are noticeable about the current situation of local ties. Firstly, GNSS as a rather cheap and easy-to-handle technique plays a major role in connecting the techniques. According to Altamimi et al. (2011) the large impact of GNSS is problematic as any GNSS intrinsic error will be transferred to the estimated ITRF parameters. However, from today's point of view there is no alternative to GNSS in terms of co-location on the ground. Secondly, as the quality of local ties between GNSS and VLBI is rather good, the high-quality determination of geometrical reference points of radio telescope seems to be feasible. And thirdly, the local ties between GNSS and DORIS are significantly worse than between GNSS and the other space techniques. This degradation is related to the rather large separation between DORIS and the other techniques, which is necessary as DORIS transmits and VLBI observes in the S-band domain. For the new ITRF2014, Altamimi et al. (2016) stated that an agreement between terrestrial tie vectors and space geodesy estimates of better than 5 mm is achieved for 24 out of 57 GPS-VLBI (42%), 12 out of 41 GPS-SLR (29%), and 18 out of 78 GPS-DORIS (23%) co-locations. A very interesting analysis of local ties was published recently by Glaser et al. (2015). Based on homogeneously reprocessed GNSS and SLR normal equations (Fritsche et al., 2014), they computed local ties from the adjusted station coordinates. The combination between GNSS and SLR was done by estimating common ERPs. In summary, 95 % of north components of the local ties and 50 % of the height components were smaller than 10 mm (10 % of each component have been smaller than 1 mm). They found differences of up to some cm for comparing local ties against coordinate differences derived by space geodetic results. The differences reported by Thaller et al. (2011) are in the same range.

Apart from the geometrical co-location approaches also several non-geometrical ties are available for ground co-location sites. Tab. 3.7 provides an overview of alternative ties and the associated observations.

### Co-location based on the Troposphere

According to Sect. 2.2.2 the troposphere is a non-dispersive medium for microwave observations. Consequently, the tropospheric zenith delay above a station should be identical for all co-located microwave techniques except for a small offset due to a height difference  $\Delta D$  between the geometric reference points. This was already shown for the inter-technique comparison of tropospheric delays derived by VLBI and GNSS for the CONT14 campaign (Sect. 2.3.3). The offset  $\Delta D$  is called tropospheric tie and can be derived from the height difference measured by a terrestrial survey. According to the literature several

approaches can be applied to compute the corresponding difference in the zenith delay  $\Delta\rho_{trp}(z_0)$  between both instruments. The easiest way is to consider a “rule of thumb” where 1 m height difference amounts to 0.3 mm of tropospheric zenith delay. A more advanced way is the computation of the dry part based on the Saastamoinen model using standard atmosphere values or real meteorological measurements. Applying the tropospheric tie, the station-specific zenith wet delay for a VLBI observation can be parameterized with respect to a co-located GNSS observations as (Hobiger & Otsubo, 2014)

$$\delta\rho_{trp,VLBI}(z) = m_{trp,d}(z)(\delta\rho_{trp,d,GNSS}(z_0) + \Delta\rho_{trp}(z_0)) + m_{trp,w}(z)\delta\rho_{trp,w}(z_0). \quad (3.29)$$

Consequently, a common troposphere parameter is estimated for VLBI and GNSS. Tropospheric ties were investigated by several authors. Krügel et al. (2007) and Thaller (2008) presented tropospheric ties estimated by a “rule of thumb”, using the Saastamoinen formula with standard atmosphere values, and based on meteorological data for the CONT02 VLBI campaign. They showed a good agreement between the different tropospheric ties for height differences that are not too large. Teke et al. (2011) and Teke et al. (2013) presented a set of ties between VLBI, GNSS, DORIS, and water vapor radiometers for the stations involved in CONT08 and CONT11, respectively. In both publications the estimated biases in the difference between the tropospheric delays were significantly reduced, when correcting for the offset  $\Delta D$ . Hobiger & Otsubo (2014) used tropospheric ties in their combination studies in addition to local ties. The derived station coordinate repeatabilities for the CONT11 time were slightly improved due to the additional tropospheric ties (from 4.95 mm to 4.82 mm). A combination of tropospheric delays is much simpler at the normal equation level ( $\delta\rho_{VLBI} - \delta\rho_{GNSS} = \delta\rho_{trp}(z_0)$ ). Krügel et al. (2007) stated that, contrary to the delays, tropospheric gradients can be compared and combined directly as both techniques observe the same tilt of the tropospheric layer.

### Co-location based on the Ionosphere

An ionospheric tie could be established by estimating common ionospheric zenith delays. Contrary to tropospheric ties no geometrical offset is required to count for the height difference of antenna reference points. Instead, a frequency offset has to be applied, as the ionospheric delay is dispersive and depends on the observed frequency. However, as normally ionospheric-free observations or linear-combinations are processed, ionospheric ties were never used for combinations. The approach can be considered as theoretical, but could be reasonable for estimating common ionosphere models.

### Co-location based on a common clock

Common clock corrections can be set up, if a common time and frequency standard is distributed to co-located instruments. However, an inter-system bias remains as, for example, GNSS receivers usually do not use the 1 pulse-per-second signal as VLBI does (Hobiger & Otsubo, 2014). Due to uncalibrated instrumental delays, an offset  $\Delta L(t)$  is required in the common clock estimation. According to Hobiger & Otsubo (2014) the relation between the VLBI and the GNSS clock can be written as

$$\text{clock}_{VLBI} = \text{clock}_{GNSS} + \Delta L(t). \quad (3.30)$$

**Tab. 3.7:** Alternative co-location strategies at ground co-location sites

Technique	Tropospheric Ties				Ionospheric Ties				Receiver Clock Ties			
	GNSS	SLR	VLBI	DORIS	GNSS	SLR	VLBI	DORIS	GNSS	SLR	VLBI	DORIS
GNSS	■	(✓)	✓	✓	■	■	✓	✓	■	(✓)	✓	✓
SLR	(✓)	■	(✓)	(✓)	■	■	■	■	(✓)	■	(✓)	(✓)
VLBI	✓	(✓)	■	✓	✓	■	■	✓	✓	(✓)	■	✓
DORIS	✓	(✓)	✓	■	✓	■	✓	■	✓	(✓)	✓	■

For the ideal station, where all biases are monitored, it can be assumed that  $\Delta L(t) = \text{const}$ . However, in reality some small variations occur. Within the project “Co-location on Ground and in Space” clock differences between two radio telescopes in Wettzell were analyzed (see Sect. 3.5.4).

### 3.5.3 Comparison of Co-location Approaches

When comparing the discussed co-location concepts it is obvious that only co-location on ground and on-board LEOs are capable to tie all four space geodetic techniques. In principle, co-location on ground is the most convenient approach, as the local terrestrial network is extendable to other sensor systems and the local ties are totally independent measurements. All other concepts rely either on additional estimations like LEO orbit determination or directly on highly correlated parameters, like the troposphere and the receiver clocks. However, it requires a huge effort of station providers to derive the local ties very accurately and to keep them up to date. Considerable initial efforts are also required for clock ties as a time and frequency distribution system has to be installed at the co-location site as a prerequisite. Today there are not more than a few pilot projects for frequency distribution, but in the future, such systems might be naturally installed at fundamental sites. No action is needed from the station providers for co-location based on the troposphere and co-location in space. Consequently, both concepts can be applied homogeneously for all ground stations, whereas the inhomogeneous accuracy level of local ties might introduce systematic effects in the derived reference frame realization. Concerning the required infrastructure, the spacecraft costs for co-location in space are rather daunting. However, the benefits are obvious: one set of ties allows a nearly instantaneous combination of all sensors distributed at the co-location sites. Especially for new stations and after earthquakes, co-location in space offers the possibility to derive technique connections rather fast. Concerning the information reliability, the tropospheric co-location has the unique benefit of relying basically on information provided by the observation itself. This is in principle also true for the clock approach, but, instrumental biases might degrade the common clock estimates depending on the system architecture. Local and space ties including their accuracies are provided by the station or satellite provider without possibility for the user to adjust them. Concerning the tie accuracy it can be said that: local as well as space ties are, in the optimal case, accurate at the 1 mm level and tropospheric ties show accuracies of a few millimeters. Space ties on-board of GNSS satellites are reported by the system providers. Based on GNSS and SLR results an accuracy at the level of several millimeters can be assumed for these official offset vectors. The accuracy of clock ties is difficult to judge, however, time distribution accuracies of around 20 ps have been reported (Pánek et al., 2013). Tab. 3.8 summarizes the individual co-location approaches and highlights their advantages with respect to each other.

### 3.5.4 Studying Receiver Clock Differences between the Wettzell Radio Telescopes

Clock parameters estimated in the processing can absorb several technique-specific biases (see Sect. 6.2.5 for more details). One goal of the project “Co-location on Ground and in Space” is the comparison and analysis of receiver clock results and terrestrial clock measurements to assess the uncalibrated internal delays. Some preliminary results and comparisons from this ongoing work are discussed in the following. In order to calibrate and monitor instrumental delays in the space geodetic techniques, an actively stabilized two-way compensated optical time & frequency distribution system was built up at the geodetic observatory Wettzell in the last years. This system, called Two-Way Optical Time Transfer (TWOTT) system, allows the exchange of timing signals with an accuracy below 1 ps over tens of kilometers via standard optical telecommunications small form-factor pluggable transceivers (Kodet et al., 2016). Conceptually, this system relies on an event timing module, which uses surface acoustic wave filters for the registration of the time-of-arrival of electrical pulses with sub-picosecond timing resolution, linearity and stability. In September 2015 the TWOTT system was installed between the hydrogen maser clocks connected to the VLBI telescopes RTW and TWIN1. Starting on June 22, 2015 also the TWIN1 telescope joined the IVS

**Tab. 3.8:** Co-location approaches; please note that concerning the atmosphere only the troposphere is considered; <sup>(1)</sup> aspired accuracy; <sup>(2)</sup> comprises only the time distribution accuracy

	co-location on ground	co-location in space		alternative approaches	
		GNSS	LEO	atmosphere	receiver clock
tie name	local tie	space tie	space tie	tropospheric tie	clock tie
accuracy level	1 mm <sup>(1)</sup>	several mm <sup>(1)</sup>	1 mm <sup>(1)</sup>	several mm	20 ps <sup>(2)</sup>
connected techniques					
VLBI	✓	(✓)	✓	✓	✓
SLR	✓	✓	✓	(✓)	(✓)
GNSS	✓	✓	✓	✓	✓
DORIS	✓		✓	✓	
other instruments	✓	✓		(✓)	
infrastructure / station efforts					
co-location satellite			✓		
time & frequency distribution					✓
local surveying network	✓				
required measurements					
terrestrial survey	✓			(✓)	
chamber calibration	✓		✓		
combination of estimates	✓	✓	✓	✓	✓
required models					
antenna pattern		✓	✓		
SLR range biases		✓	✓		
tropospheric model				✓	
clock model					✓
availability					
per station (materialized)	✓				✓
per station (parameterized)				✓	
globally		✓	✓		

VLBI sessions regularly (one “R” session per week, alternating between R1 and R4). Consequently, both, the RTW and the TWIN1 participate regularly in the same IVS sessions, which makes it possible to estimate VLBI-based clock differences and to compare them against the TWOTT values. In order to do this, several VLBI R1 and R4 sessions in which the RTW and TWIN1 participated between July 13, 2015 and February 29, 2016 were processed. The VLBI processing was done in two modes:

- **global:** similar to the processing described in Sect. 2.3.3
- **local:** for the baseline RTW-TWIN1 by constraining the station coordinates to 1 cm and without estimating tropospheric wet delays.

In both cases the processing time was defined from 18h UT to 16h UT of the following day. The clock parameter resolution was increased to 30 min. It has to be mentioned that the local baseline cannot be correlated anymore for sessions after January 26, 2016 due to interferences with the phase calibration system (pCal), which has been activated for both telescopes<sup>27</sup>. Fig. 3.9 shows the VLBI-derived clock differences between the RTW and the TWIN1 estimated based on the global solution (*red dots*). The differences between the two clocks is of the order of  $-30 \mu\text{s}$  over the considered time with a linear trend of  $a_{VLBI} = -17.71 \text{ ns/day}$ . This trend is related to the free running hydrogen masers at both telescopes. As the VLBI clock parameterization in the BSW does not contain session-wise linear or quadratic terms a session-wise linear trend was subtracted a posteriori. The remaining residuals are plotted in Fig. 3.9 (*blue dots*). They are mainly below 50 ps. According to the histogram in Fig. 3.9, 73.3 % of the derived residuals

<sup>27</sup> Pers. communication J. Kodet

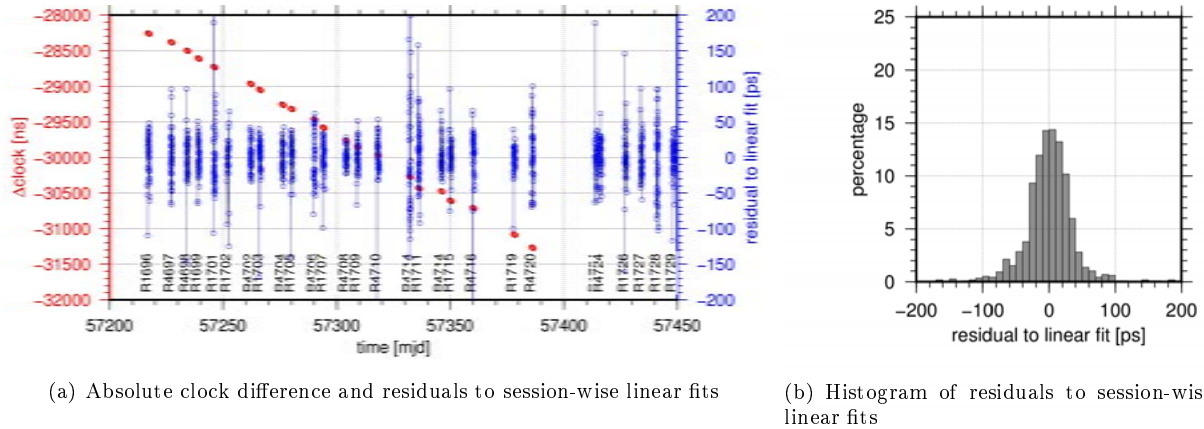


Fig. 3.9: Clock difference RTW-TWIN1 derived by VLBI

Tab. 3.9: Clock comparison TWOTT-VLBI for Wettzell; the bias was estimated and subtracted session-wise from the VLBI solution; session-wise RMS of the differences TWOTT-VLBI after removing a common linear trend; three sessions (two in the global, one in the local solution) are excluded as their clock estimates shows large formal errors; the station abbreviations are given in Tab. C.1; DoY referred to the session begin

name	year	DoY	global solution			local solution	
			participating stations	bias [ns]	RMS [ps]	bias [ns]	RMS [ps]
R1707	2015	271	FtHtKeKkNyTsWnWwWzYg	13.84±0.01	13.99	16.55±0.02	16.81
R4708	2015	281	FtHoHtKeKkMcNySvWnWzYgZc	17.85±0.01	14.60	20.55±0.01	13.56
R1709	2015	286	FtHoHtKeKvMaNyOnTsWnWwWzYg	14.09±0.02	22.58	16.79±0.02	23.72
R4710	2015	295	FtHoHtKeKkMaWnWwWzYg	-36.56±0.04	43.93	-33.83±0.03	29.68
R1711	2015	299				-3.05±0.03	30.06
R4712	2015	309	FtHoHtKeKkMaNyWnWwWzYg	15.18±0.06	57.44	17.84±0.07	66.29
R1713	2015	313	FtHhHoHtKeNyOnTsWnWwWzYg	107.42±0.05	45.78		
R4714	2015	323	HbHtKeKkMaNySvWnWwWzYgZc	-15.73±0.03	28.99	-13.00±0.03	26.85
R1715	2015	327	FtHbHtKeKvNyOnWnWwWzYg	50.62±0.03	27.11	53.34±0.02	24.12
R4716	2015	337	FtHbHtKeKkNySvWnWwWzYgZc	-15.62±0.06	62.55	-12.97±0.17	170.73
R1717	2015	341				28.30±0.02	15.56
R1719	2015	355	HbHtKeKvNyOnTsWnWzYg	46.57±0.02	22.46	49.26±0.02	14.94
R4720	2015	363	BdFtKkNySvWnWzYsZc	87.84±0.04	41.77	90.62±0.03	27.96
R1721	2016	4	FtHtKkKvMaNyTsWnWz	58.56±0.03	26.99	61.21±0.04	42.66

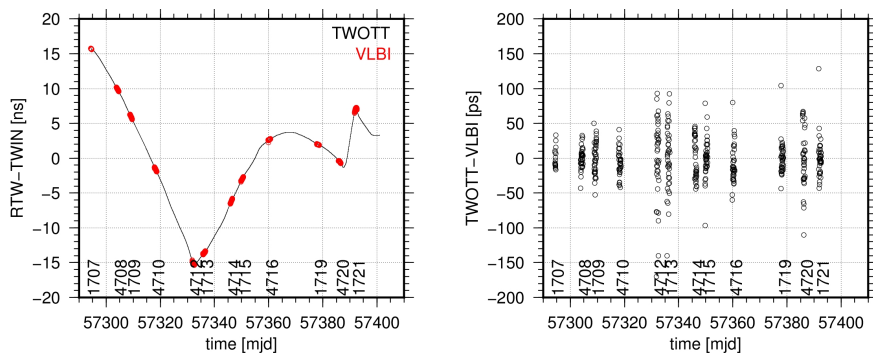
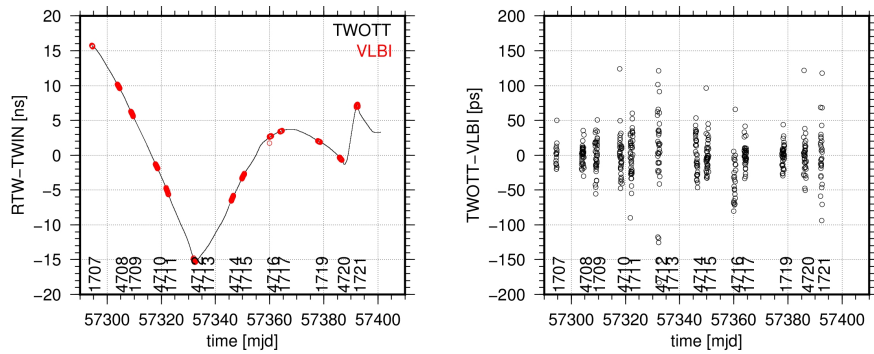


Fig. 3.10: Clock comparison for Wettzell (global); left clock difference RTW-TWIN1 as seen by TWOTT and by VLBI global solutions; right difference of TWOTT and VLBI results; a common linear trend was removed



**Fig. 3.11:** Clock comparison for Wettzell (local); *left* clock difference RTW-TWIN1 as seen by TWOTT and by VLBI baseline solutions; *right* difference of TWOTT and VLBI results; a common linear trend was removed

are below 30 ps and 88.6% are below 50 ps. Similar to the trend in the VLBI difference series a clock model also has to be applied to the TWOTT measurements. A linear trend of  $a_{TWOTT} = -17.34 \text{ ns/day}$  was estimated. In order to compare TWOTT and VLBI, the VLBI clock residuals were computed by using  $a_{TWOTT}$ . The resulting differences TWOTT-VLBI are biased due to un-calibrated instrumental delays absorbed in the VLBI estimates. These station- and session-specific delays are absorbed by the estimated receiver clock and, therefore, distort the estimated clock differences by tens of nanoseconds. As instrumental delays are usually constant during one session (Hobiger, 2006), a session-wise mean bias between TWOTT and VLBI was subtracted from the VLBI results. Tab. 3.9 provides an overview of the analyzed VLBI sessions including the subtracted bias for each session. Two global and one local solution were excluded as their clock estimates show large formal errors. The derived clock differences RTW-TWOTT are plotted in Fig. 3.10. The figure on the left shows the difference of the clocks estimated by TWOTT and VLBI after subtracting the above mentioned linear trend. Obviously, the TWOTT time series is continuous, whereas the VLBI series consists of around 45 distinct data points per analyzed session. The differences between the two hydrogen masers are up to  $\pm 15 \text{ ns}$  with a characteristic temporal behavior. The TWOTT-VLBI differences estimated for each VLBI data point (Fig. 3.10, right) differs in general by not more than 50 ps (89% are below 50 ps). The corresponding RMS for each session is also provided in Tab. 3.9. Reaching values up to 60 ps an average RMS of 34.0 ps was found. A similar plot is shown for the local processing (Fig. 3.11). A remaining outlier of around 0.8 ns is visible for session R4716. Comparing the TWOTT-VLBI values between the global and the local processing a good agreement is visible with slightly smaller differences in the local case. Comparing the derived RMS for global and local mode, in general, smaller values are obtained in the local mode. When excluding the outlier in session R4716, the correspond RMS for the local solution decreases to 28 ps. The slightly better agreement in the local case is related to the advantage of eliminating the tropospheric delays<sup>28</sup>. Additionally, station- or baseline-related problems that influence in a global network have no impact on the local processing. However, a better agreement between local solution and TWOTT might be achievable, if estimating a common troposphere and refining the station coordinate constraints. Kodet et al. (2016) presented a comparable TWOTT-VLBI analysis based on a local VLBI solution derived by the Levika software. By fixing the coordinates to their a priori values and constraining the tropospheric delays they were able to estimate one clock parameter from each VLBI observation. The derived differences between their VLBI solution and TWOTT reaches also  $\pm 50 \text{ ps}$  with a RMS of 20 ps. Fig. 3.12 shows the time series of the TWOTT-VLBI differences for a subset of the analyzed sessions. First of all, a good agreement is visible between the differences derived from the global and local BSW solutions. However, for a few sessions (R1709, R4716, and R4720), differences of up to 100 ps can be found. This is reasonable as the troposphere might absorb some systematic effects in the global solutions. There seems to be no systematic effect regarding the local time. In the next project step the derived clock differences will be analyzed and compared against instrumental delays, environmental

<sup>28</sup> The difference in the zenith wet delay due to height difference of 3.41 m was not considered.

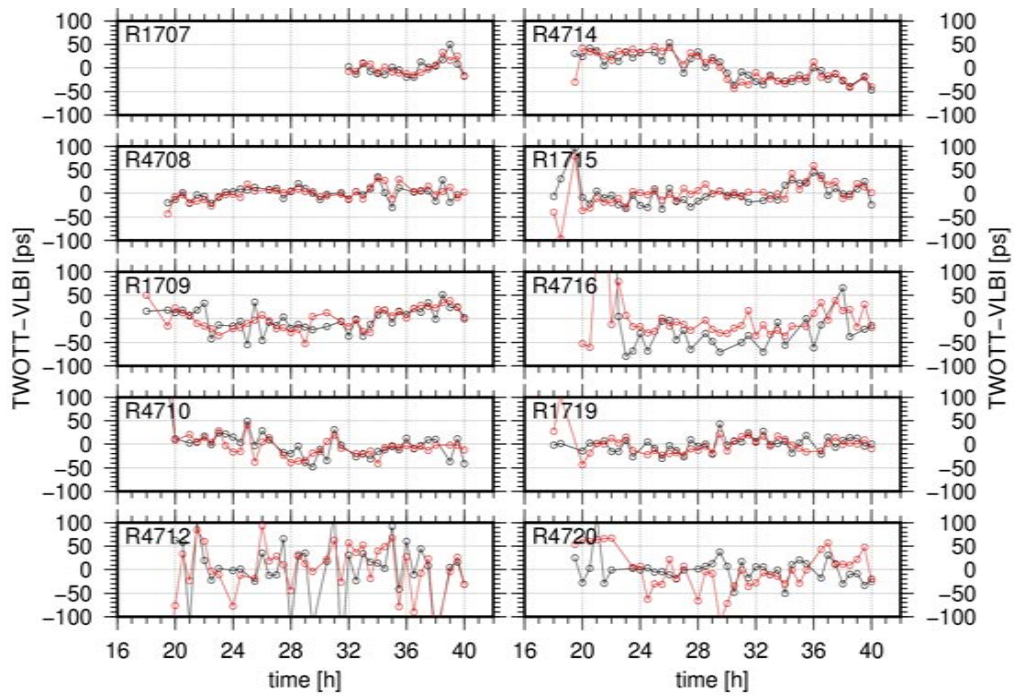


**Fig. 3.12:** Difference between TWOTT and VLBI clock results for the analyzed sessions; *black* global solution; *red* local solution

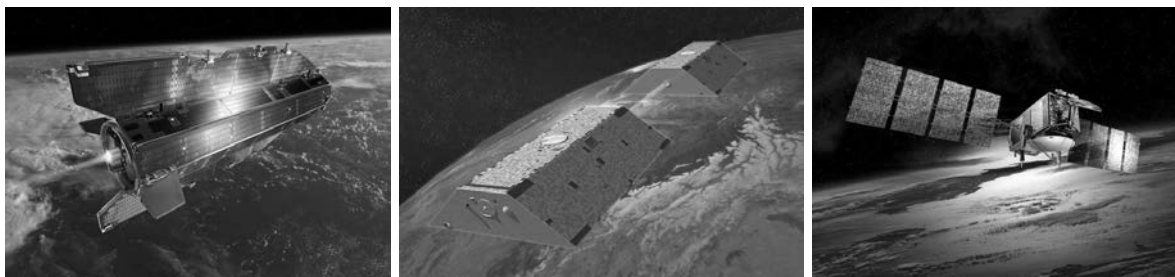
effects and observation characteristics. Comparable investigations are envisaged for the GNSS receivers.

# 4 Investigations on GPS-based Precise Orbit Determination for Low Earth Orbiters

As shown in Sect. 3.5.1 co-location in space requires highly accurate satellite orbits and, therefore, appropriate models to describe the satellite motion in space. Within this work LEO orbits are determined based on GPS observations. The LEO missions considered in this work are GOCE, GRACE, and OSTM/Jason-2. They are introduced in the first section of this chapter (Sect 4.1). The basic principles of representing spacecraft motion are discussed in the subsequent Sect. 4.2. The third section (Sect. 4.3) is dedicated to the results for the three LEO missions including several validations. The impact of modeling non-gravitational forces is addressed in Sect. 4.4. Section 4.5 is dedicated to the small satellite mission CubETH. In the framework of CubETH, the ionospheric delays in LEO altitudes and their impact on a single-frequency orbit determination is discussed. Although this whole chapter focuses on LEOs, some information relevant to orbit determination for GNSS and geodetic satellites, like LAGEOS, are provided additionally.

## 4.1 Introduction of Low Earth Orbiting Spacecraft using GPS

According to Jäggi (2007) the first ideas of using GPS to determine LEO positions dates back to the seventies. The first GPS receivers were flown on LANDSAT-4 and LANDSAT-5, launched in 1982 and 1984, respectively. The feasibility of clock synchronization and position solutions with 50 m accuracies were shown for the second mission (Heuberger, 1984). GPS-based precise orbit determination with accuracies down to a few centimeters started in 1992, when TOPEX/Poseidon brought the first dual-frequency GPS receiver into space (Bertiger et al., 1994). Since those days a large number of satellites were launched equipped with single- and dual-frequency GPS receivers developed by various manufactures. Comprehensive overviews of those missions and the receivers used are provided, for example, in Montenbruck et al. (2008) or in Kahr et al. (2013). A subset of these missions that is useful for co-location in space, was listed already in Fig. 3.2 (cf. Tab. A.1). As mentioned before, three of them have been selected for studying precise orbit determination and co-location in space within this work. The satellite OSTM/Jason-2 (Ocean Surface Topography Mission, see Fig. 4.1(c)) is a follow-on of the altimeter missions TOPEX/Poseidon and Jason-1 (Lambin et al., 2010) and was launched on June 28, 2008. The OSTM/Jason-2 orbit follows that of TOPEX/Poseidon with a high altitude of 1336 km and an inclination of  $66^\circ$ . Apart from the Poseidon-3 radio altimeter the satellite is equipped with a JPL BlackJack GPS receiver, a DORIS receiver and a laser



(a) GOCE (courtesy of ESA)

(b) GRACE (courtesy of NASA)

(c) OSTM/Jason-2 (courtesy of NASA)

**Fig. 4.1:** Artists interpretation of the GOCE, GRACE, and OSTM/Jason-2 spacecraft

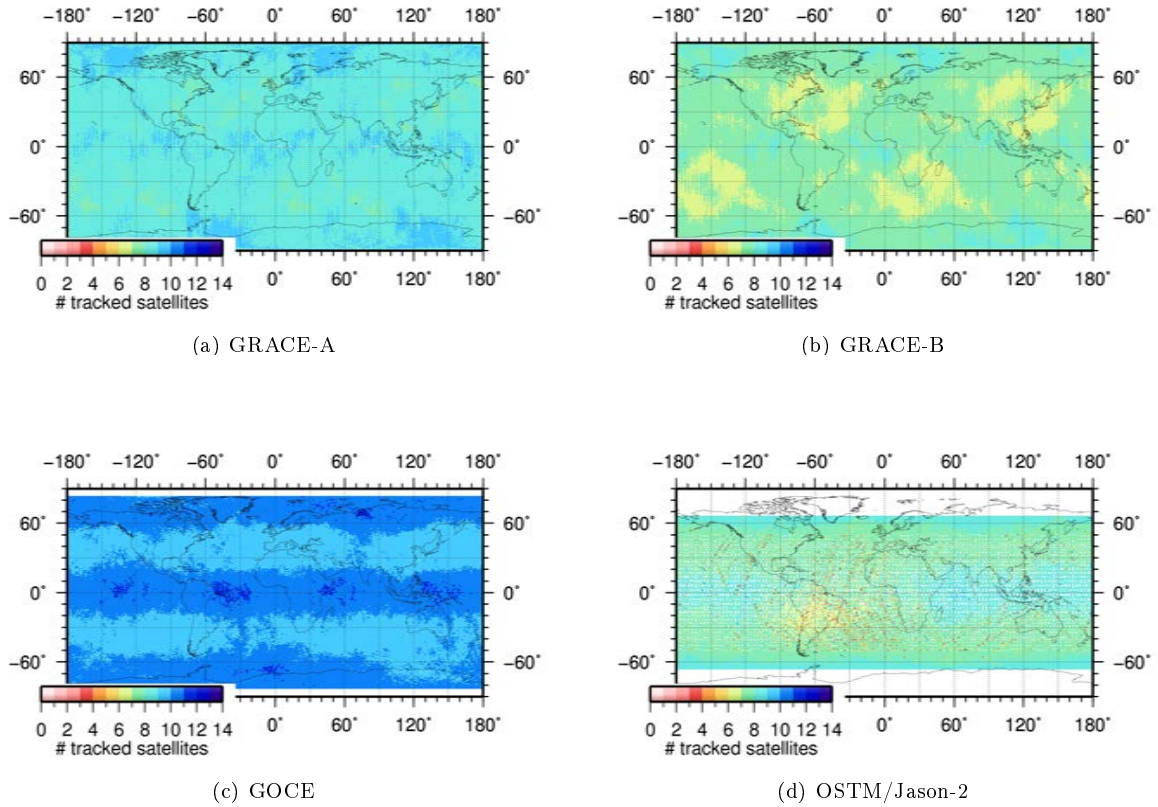


**Fig. 4.2:** Geographical distribution of the number of tracked GPS satellites per epoch for GRACE, GOCE, and OSTM/Jason-2, averaged in  $1^\circ \times 1^\circ$  bins; time span 2010.0 to 2011.0

retro-reflector array. The two GPS antennas (one for redundancy) are tilted around the satellite-fixed Y-axis by about  $15^\circ$  (Cerri & Ferrage, 2015). Amplified by the high altitude the Jason-2 electronics are affected by high energetic radiation events. The effected electronic components are reset by default after such events. Unfortunately, due to a software issue, the GPS receiver is also reset, if GPS acquisition is not achieved within a certain time limit. Consequently, a significant loss of tracking data occurs (Cerri et al., 2010). Fig. 4.2(d) shows the geographical distribution of the number of tracked GPS satellites. A significantly lower number can be found for OSTM/Jason-2 over South America and the South Atlantic Ocean. In this region the Earth magnetic field is comparably weak due to the South Atlantic Anomaly. Because of the higher radiation more receiver resets occur. OSTM/Jason-2 is the largest spacecraft of the missions considered within this work. Different to the other satellites, OSTM/Jason-2 is equipped with adjustable solar panels (cf. Tab. B.1). The Jason family grew recently by the launch of Jason-3 in January 2016.

The Gravity field and steady-state Ocean Circulation Explorer (GOCE, see Fig. 4.1(a)) was the first ESA Earth explorer core mission, launched on March 17, 2009 (Floberghagen et al., 2011). The main objective was to determine the stationary parts of Earth's gravity field with highest spatial resolution. The mission was benefitting from a very low orbit with an altitude of 259.6 km during the first operation phase<sup>1</sup>. The orbit was sun-synchronous dusk-dawn with an inclination of  $96.7^\circ$ . To compensate the atmospheric drag (and other non-gravitational forces) GOCE used an ion propulsion assembly. In addition to the 3-axis accelerometer, a 12-channel GPS Lagrange receiver and a laser retro-reflector assembly were carried by the spacecraft. Shortly after running out of fuel, GOCE re-entered the Earth atmosphere on November 11, 2013, after a very successful mission. Due to the 12-channel GPS receiver and the low altitude a larger number of GPS satellites could be tracked (Fig. 4.2(c)). The characteristic stripe structure is caused by a resonance between the GPS constellation and GOCE's orbit characteristics. During the mission, GOCE

<sup>1</sup> Altitude is considered as mean geocentric distance minus Earth equatorial radius.

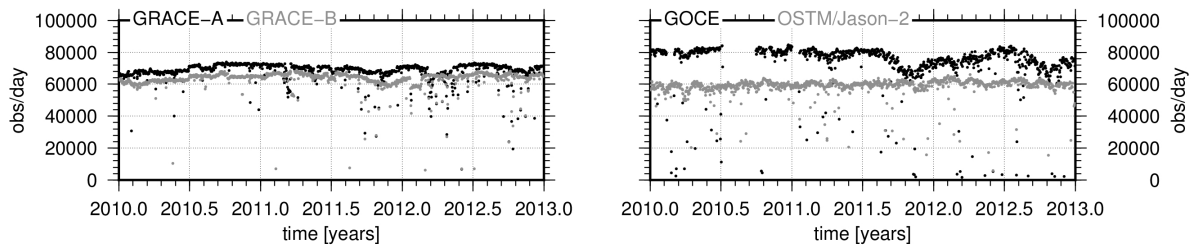


**Fig. 4.3:** Number of daily LEO GPS observations

**Tab. 4.1:** LEO GPS receivers, antennas, and tracking remarks

mission	receiver	channels	antenna	remarks
GRACE	BlackJack	10(12)	Choke-ring S67-1575-14+CRG	two channels are permanently switched off
GOCE	LAGRANGE	12	Quadrifilar Helix (RYMSA)	
OSTM/Jason-2	BlackJack	10	Choke-ring S67-1575-14+CRG	antenna tilted by 15°, systematical tracking problems due to the South Atlantic Anomaly

faced two months of data loss due to telemetry problems in summer 2010 (Floborghagen et al., 2011).

The Gravity Recovery and Climate Experiment (GRACE) mission (Tapley et al., 2004) is an US-German partnership in NASA’s Earth System Science Pathfinder program. The main mission objective is the mapping of the time-varying gravity field. The mission consists of two identical satellites orbiting the Earth in the same orbital trajectory separated by  $220 \pm 50$  km (see Fig. 4.1(b)). Both satellites were launched on March 17, 2002 into a polar orbit with an inclination of  $89^\circ$  and an altitude of around 460 km. Both satellites are equipped with JPL BlackJack GPS receivers, laser retro-reflector arrays, and a K/Ka-band ranging system. In order to limit surface erosion of the K-band horns, a switching maneuver was performed on December 10, 2005 (03:40 UTC). Since that time GRACE-B is flying ahead of GRACE-A. Comparing the number of tracked GPS satellites in Fig. 4.2(a,b), very similar patterns are visible for GRACE-A and GRACE-B. It has to be mentioned that only ten of the twelve available receiver channels are used in order to keep the number of receiver resets low (Dunn et al., 2003). On average GRACE-A was tracking for each epoch one GPS satellite more than GRACE-B. The regular pattern with regions, where systematically one observation less is available, is again caused by an resonance between GPS and GRACE orbits.

All four satellites are equipped with star cameras and thruster systems to determine and control their attitude. The number of daily observations for all four LEOs is shown in Fig. 4.10. In general, the number of observations is between 60’000-80’000 per day corresponding to seven to nine GPS satellites tracked per epoch. The before mentioned systematic difference between GRACE-A and GRACE-B is observable. Days with considerably less observations occur for GRACE more frequently in 2012 than in the two years before. Most probably, this effect is caused by aging and repeated activation of power safe modes. The higher number of observations due to the 12-channel receiver and the lower altitude is typical for GOCE. The two-months data gap in 2010 is also observable. For OSTM/Jason-2 the very stable but lower number of observations is related to the higher altitude and the maintained orbit height. Some of the visible satellite-specific events indicated by a lower number of daily observations are discussed in Sect. 4.2.4. Tab. 4.1 provides an overview of the GPS receivers and antennas on-board these LEO spacecraft.

## 4.2 Representing Satellite Motion in Space

Within this thesis the term “satellite” describes an artificial and extended object orbiting the Earth. By definition orbit determination and the terms “satellite motion”, “satellite position”, and “satellite velocity”

refer to the satellites center of mass (CoM)<sup>2</sup>. As mentioned already in Sect. 3.5.1, the offset vectors between the CoM and all relevant sensors like GPS antennas, SLR retro-reflectors, and DORIS antennas have to be known in a body-fixed frame. The positions of the various sensors are transformed into the inertial frame by applying the actual spacecraft orientation. The simplest representation of a satellite's motion in space is a kinematic representation, i.e., a series of epoch-wise determined positions. This representation is done in an Earth-fixed frame and is independent from any physical orbit model. However, the practical value is limited due to its distinct sensitivity to bad measurements and data outages. Within this section, the dynamic and reduced-dynamic orbit representations are discussed.

#### 4.2.1 Keplerian Orbit and Gravitational Perturbations

To represent the motion of a satellite in a dynamic way the geocentric position and velocity  $\mathbf{r}$ ,  $\dot{\mathbf{r}}$  of the satellite are propagated in time by applying dynamic force models. In the inertial reference frame the corresponding equation of motion can be written as

$$\ddot{\mathbf{r}} = -GM \frac{\mathbf{r}}{r^3} + \mathbf{f}_1(t, \mathbf{r}, \dot{\mathbf{r}}, q_1, \dots, q_d) = \mathbf{f}_0 + \mathbf{f}_1 = \mathbf{f} \quad (4.1)$$

where the first term on the right-hand side ( $\mathbf{f}_0$ ) represents the acceleration of a Keplerian orbit taking into account Earth and satellite as point masses and an unperturbed two-body problem. The coefficient  $\mathbf{f}_1$  denotes the perturbing accelerations and depends on the state ( $\mathbf{r}$ ,  $\dot{\mathbf{r}}$  or Keplerian elements<sup>3</sup>) and on scaling factors  $q_1, \dots, q_d$  for analytically known perturbing accelerations. Consequently,  $\mathbf{f}$  is usually called total acceleration. Eqn. 4.1 is called to be deterministic, if all accelerations are computed from analytical models. In general, orbit perturbations can be divided into perturbations depending only on the satellite position (gravitational perturbations) and perturbations depending on the area-to-mass ratio (non-gravitational perturbations, see Sect. 4.2.2). Gravitational perturbations acting on a spacecraft are caused by the Earth gravity field including the oblateness of the Earth, direct attraction of Sun, Moon and planets, solid Earth, ocean, and pole tides, as well as tidal and non-tidal loading effects. The gravitational attraction caused by the Earth gravity field coefficient  $C_{20}$  is by far the largest perturbation acting on an Earth-orbiting satellite. The equatorial bulges of the oblate Earth exert a force that tries to align the orbital plane with the equator. Due to its angular momentum the orbit reacts with a precessional motion and a shift of the line of nodes. The precession  $\dot{\Omega}_i$  of the ascending node of a satellite  $i$  (with orbital period  $T$ ) is given by (Montenbruck & Gill, 2000)

$$\dot{\Omega}_i = -3\pi \frac{C_{20}}{T} \left( \frac{R_E}{a} \right)^2 \cdot \cos(i) \quad (4.2)$$

where  $T$  is the orbital period,  $R_E$  denotes the Earth radius. The satellite orbit characteristics are represented by the semi-major axis  $a$  and the inclination  $i$ . The precession of the ascending node influences the period between the same orientation of the orbit plane with respect to the Sun in such a way that it is not necessarily equal to one year. The corresponding satellite-specific period  $T_R$  (period of nodal precession) is computed as

$$T_R = \frac{2\pi}{2\pi - \dot{\Omega}_i \cdot T_a} \cdot T_a \quad (4.3)$$

where  $T_a$  denotes the annual period. Usually the period  $T_R$  is called draconitic year. For example, the draconitic period for GPS satellites is 351.4 days, for GRACE 322 days, and for OSTM/Jason-2 120 days. Higher-order gravity field coefficients have to be considered depending on the satellite orbit height. For GPS satellites usually the Earth gravity field has to be considered up to degree and order=8 (Bock, 2003),

<sup>2</sup> In Chap. 5 the center of mass of the system Earth is addressed. To distinguish between both, CoM is the satellite center of mass, whereas CM refers to Earth center of mass.

<sup>3</sup> The Keplerian elements are semi-major axis  $a$ , numerical eccentricity  $e$ , inclination  $i$ , right ascension of the ascending node  $\Omega$ , argument of perigee  $\omega$ , and perigee passing time  $T_0$  or alternatively the argument of latitude  $u$  as sixth element.

for LAGEOS an expansion to degree and order=30 seems to be sufficient (Sośnica, 2015), and for LEOs a further expansion up to degree and order=120 is necessary (Bock, 2003). Gravitational perturbations caused by celestial bodies different from Earth (so-called third bodies) can be divided into direct (attraction) and indirect (tidal) effects. Fig. 4.4 shows perturbations caused by direct attraction acting on GRACE-A based on JPL's Development Ephemeris DE405 over one day. The direct attractions are periodic, with a dominant impact of the Sun (on average  $3.7 \cdot 10^{-7} \frac{m}{s^2}$ ) and the Moon ( $1.1 \cdot 10^{-6} \frac{m}{s^2}$ ). The acceleration due to Venus ( $1.7 \cdot 10^{-13} \frac{m}{s^2}$ ), Mars ( $3.5 \cdot 10^{-13} \frac{m}{s^2}$ ), and Jupiter ( $2.2 \cdot 10^{-12} \frac{m}{s^2}$ ) are too small to have a significant impact. Considering the corresponding amplitude spectra, the dominant period is 48 min for the direct attractions. As expected this corresponds to half the orbit period. The behavior of these perturbations over longer timescales is shown in Fig. 4.5 (2003.0-2013.0). The accelerations due to Sun and Moon show only small variations of less than half a magnitude, whereas the impact of the planets vary by more than two orders of magnitude. The corresponding amplitude spectra shows a dominant period of 27.49 days for the Moon, which is very close to the lunar orbital period. For the acceleration related to the Sun, the main period of 163.8 days is very close to half a draconitic year of GRACE. The main period of the direct attraction caused by a planet corresponds to the commensurability period  $P_c$ , which reads as (Beutler, 2005a)

$$P_c = \left| \frac{P_E P_i}{P_i - P_E} \right|. \quad (4.4)$$

Inserting the corresponding revolution periods for the Earth  $P_E$  and for the planets  $P_i$  ( $i=1,2,3$ ),  $P_c$  amounts to 1.09, 1.63, and 2.13 years for Jupiter, Venus, and Mars, respectively. The periods with the maximal amplitudes in Fig. 4.5 are in good agreement as they are approximately 1.13, 1.60, and 2.24 years. The indirect effects of third bodies are tidal effects acting either directly on the satellite or indirectly due to the gravitational deformation of the Earth. The corresponding accelerations due to Sun, Moon, and solid Earth, oceanic, and pole tides are shown in Fig. 4.4. The magnitude of related accelerations is between  $10^{-6}$  and  $10^{-10} \frac{m}{s^2}$ . Large variations of up to one order of magnitude are present in the perturbing accelerations caused by ocean and pole tides. In the pole tides, also a semidiurnal period is present. In the frequency spectra, dominant amplitudes exist at two and four times per revolution. The ocean tides show a less strong correlation with the harmonics of the orbit frequency. In the long-term plot (Fig. 4.5) rather constant accelerations can be found except for the pole tides. The pole tides show a long-term period of around 6 years due to polar motion. In general, strong peaks exist related to the lunar orbital period.

Gravitational perturbations can be computed accurately based on standard products like ephemeris, gravity field models, and tidal models. In general, no information about the spacecraft except for the a priori position is needed. Today's orbit determination processes are usually not limited by gravitational perturbations. More details can be found in the literature (e.g., Montenbruck & Gill, 2000; Seeber, 2003; Beutler, 2005a,b).

## 4.2.2 Treatment of Non-Gravitational Perturbations

All perturbing forces depending on the satellite area-to-mass ratio are called non-gravitational forces. In general, these effects are much smaller than the major gravitational forces, however, they can significantly impede precise orbit determination. Within this section the major non-gravitational forces are introduced and two ways to account for these forces are discussed, either by correcting them a priori or by estimating additional parameters. The a priori correction of non-gravitational forces is done in three steps. Firstly, the direction and value of a perturbing force is derived from dedicated models. Secondly, the satellite macro-model is rotated into the inertial frame by considering the spacecraft's attitude. Thirdly, the corresponding acceleration is computed based on the force vector, the surface area, and the surface characteristics.

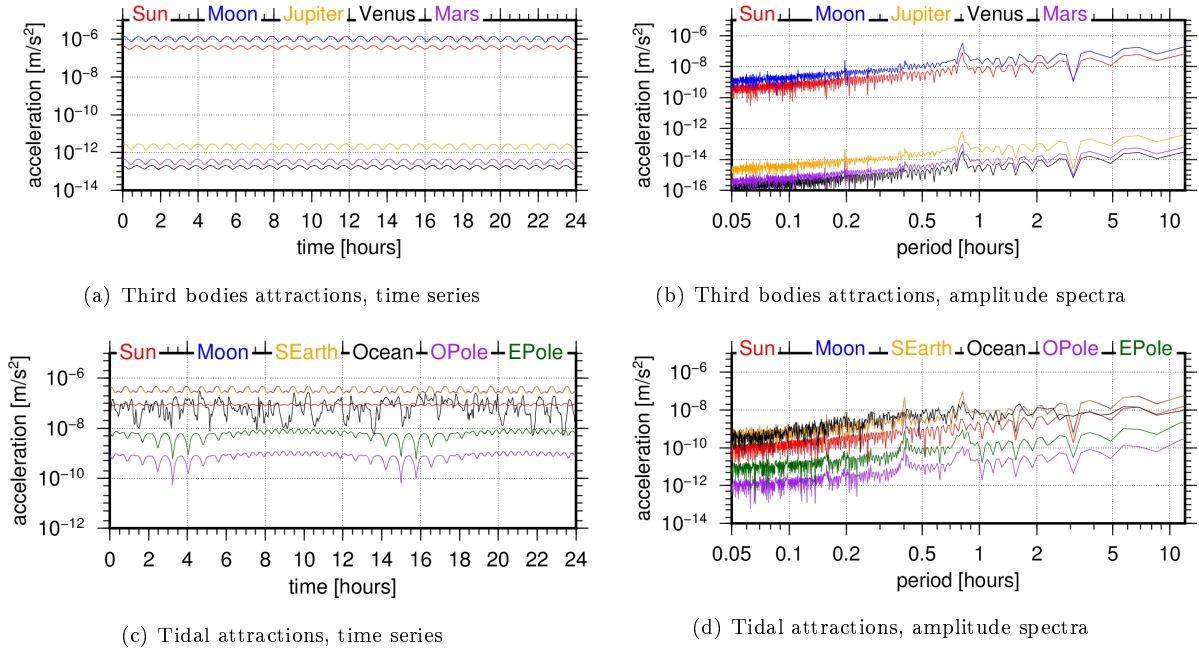


**Fig. 4.4:** Gravitational attraction and tidal forces acting on GRACE-A (January 3rd, 2010); *SEarth* = solid Earth tides, *OPole* = oceanic pole tides, *EPole*=solid Earth pole tides

### Satellite Attitude

The accurate knowledge of the satellite orientation in the inertial frame, called spacecraft attitude, is crucial for correcting non-gravitational forces. Fig. 4.6 shows the relative geometry between Earth, satellite and Sun for a GPS satellite. The different reference frames are illustrated too, as they are

- the body-fixed frame XYZ (satellite-specific, here: normal to the surface illuminated by the Sun, parallel to solar panel rotation axis, and towards the Earth, respectively),
- the orbit-fixed RSW frame, moving along the orbit trajectory (radial, along-track, and cross-track, respectively), and
- the sun-fixed DYB frame (towards Sun, parallel to solar panel rotation axis, and  $\mathbf{B} = \mathbf{D} \times \mathbf{Y}$ , respectively).

The angles shown in Fig. 4.6 describe the Sun's elevation above the orbit plane ( $\beta_0$ ), the argument of latitude of the satellite with respect to the argument of latitude of the Sun ( $\Delta u$ ), the angle between Earth, satellite, and Sun ( $\epsilon$ ), and the satellite's yaw angle ( $\Psi$ ). For all LEOs considered here, attitude is determined and controlled precisely. For GOCE, the attitude was maintained by the drag-free and attitude control system (Sechi et al., 2011). Herman et al. (2004) described the different attitude control regimes for GRACE. However, the main objective of GRACE attitude control is the orientation towards the other spacecraft to enable the K-band link. The attitude regime on OSTM/Jason-2 ensures that the z-axis points always towards the Earth (Cerri & Ferrage, 2015). Depending on the angle  $\beta_0$ , a yaw-steering or a fixed-yaw regime is defined. The transition from the fixed to the steered yaw regime is called ramp-up and reverse ramp down maneuver (Cerri & Ferrage, 2015). For these LEOs the actual attitude information is observed by star cameras. The corresponding attitude information is provided as quaternions, which are a convenient mathematical notation for describing the orientation of objects in three dimensions. Within this work the actual attitude information was applied for transforming the body-fixed frame into the inertial space and vice-versa.

However, observation-based attitude information is not provided for GNSS satellites. Therefore, the attitude has to be derived from nominal attitude models (e.g., Bar-Sever, 1996; Dilkner, 2010; Montenbruck et al., 2015). For GPS satellites the attitude regime ensures that, firstly, the z-axis points towards the Earth

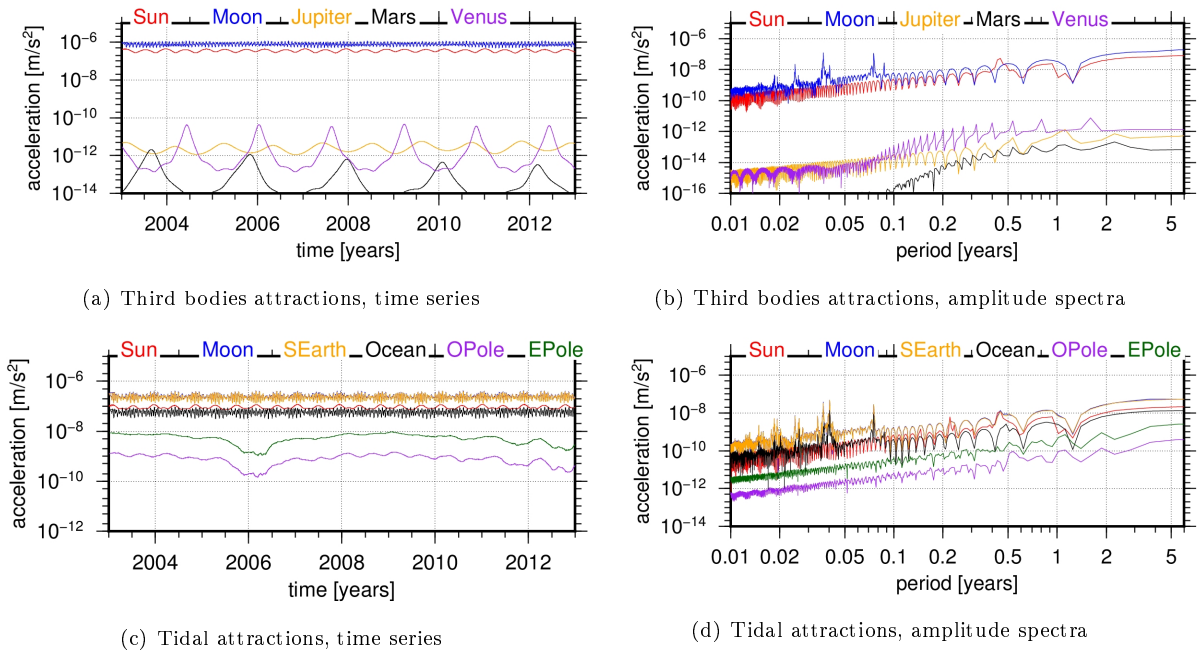


**Fig. 4.5:** Gravitational attraction and tidal forces acting on GRACE-A (2003-2013); *SEarth* = solid Earth tides, *OPole* = oceanic pole tides, *EPole*=solid Earth pole tides

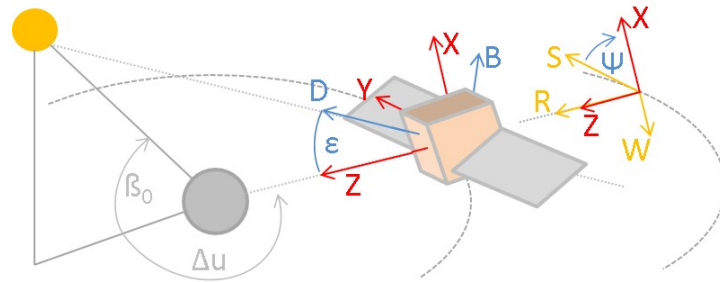


**Fig. 4.6:** Relative geometry between Earth, satellite and Sun; reference frames: XYZ satellite-specific body-fixed (red), RSW orbit fixed (orange), DYB sun-fixed (blue)

and, secondly, the solar panel normals are always pointing towards the Sun<sup>4</sup>. Therefore, the GPS satellites rotate continuously around their Z-axis. This nominal attitude model is similar to that of OSTM/Jason-2. The actual yaw angle  $\Psi$  is defined as (Bar-Sever, 1996)

$$\Psi = \tan\left(\frac{-\tan(\beta_0)}{\sin(\Delta u + \pi)}\right). \quad (4.5)$$

Deviations from the nominal yaw-steering are caused by yaw maneuvers during and after eclipses and by the non-alignment of the solar panels. The GPS satellites cross the Earth shadow for small  $\beta_0$  angles, resulting in (1) a loss of the Sun sensor's orientation, and (2) a required yaw rate which exceeds the maximal yaw rate. The consequences depend on the satellite block type; in general, yaw maneuvers occur at noon and midnight for small  $\beta_0$  angles. The characterization of the non-nominal GPS attitude is a widely discussed topic for many years. Therefore, this section provides only a very short summary. For GPS II/IIA satellites noon maneuvers occur for  $|\beta_0| < 4.8^\circ$  and eclipse periods for  $|\beta_0| < 13.9^\circ$ , where the satellite rotates with the maximum yaw rate. The direction of the rotation depends on the yaw bias; the rate is defined by the satellite-specific yaw rate. After leaving the shadow, a post-shadow maneuver is performed to re-align the satellite to the nominal yaw-steering. Several publications provide models to

<sup>4</sup> For GPS block I, II, and IIA satellites a third condition forced the angle between the satellite Z-axis and the direction to the Sun to be between  $0^\circ$  and  $180^\circ$  (Rodríguez-Solano, 2014).

account for these maneuvers, e.g., Bar-Sever (1996); Kouba (2009); Rodriguez-Solano et al. (2013). For GPS-IIR satellites noon maneuvers occur for  $|\beta_0| < 2.4^\circ$ , and as the satellites follow nominal attitude during eclipses, the post-shadow maneuvers are comparable to noon maneuvers (Rodriguez-Solano et al., 2013). Dilksner (2010) discovered yaw maneuvers also for GPS-IIF satellites.

### Satellite Macro-models

To estimate the perturbations caused by non-gravitational forces, the spacecraft surface exposed to each of these forces has to be known. Since the very rough assumption of a cannonball model<sup>5</sup> is not adequate, satellite macro-models are required. These models are an approximation of the satellite and contain the size, the shape, the movability, and the optical properties for all relevant surfaces. The surface location is represented by the corresponding surface normal vector given in the body-fixed reference frame. Usually, a satellite can be approximated by a six-surface box, accounting for the satellite bus, and, if necessary, by a two-surface wing for solar panels. Additional surfaces can be defined to account for beams, antennas, and other structures. According to Milani et al. (1987) the interaction between photons and a surface can be described by absorption  $\alpha$ , reflection  $\delta$ , and diffusion  $\rho$ . The sum of all three coefficients is defined to be equal to one. Sometimes also reflectivity  $\nu$  and specularity  $\mu$  are provided. They can be converted into the three coefficient by

$$\alpha = 1 - \nu \quad \delta = \nu(1 - \mu) \quad \rho = \mu\nu . \quad (4.6)$$

Tab. B.1 provides the macro-models for the different GPS block types, for OSTM-Jason-2, and the GRACE spacecraft. Depending on the mission-specific attitude regime, some of the optical properties are not relevant. For example, the infrared properties of the GPS satellites are only necessary for the +Z side and the solar panels, as all other surfaces are not oriented towards the Earth and are, therefore, not exposed to Earth radiation pressure during operation.

### Non-Gravitational Perturbations in Low Earth Orbits

Regarding their origin non-gravitational perturbations can be divided into external and internal (i.e., satellite-induced) forces. The main external perturbations are direct solar radiation pressure, thermal satellite re-radiation forces (e.g., the Yarkovsky and the Yarkovsky-Schach effect), Earth radiation pressure (albedo), de-spinning due to interactions with the Earth's magnetic field, and air drag. Satellite-induced perturbations are anisotropic thermal emission, outgasing, orbit maneuvers, the antenna recoils, and electrostatic effects. Within this section, direct solar radiation pressure, Earth radiation pressure, and air drag are considered. Non-gravitational forces are referred to as surface forces as their impact depend on the relationship between the satellite's cross-section  $A$  and its mass  $m$  ("surface-to-mass-ratio").

Solar radiation pressure is caused by transferring the linear momentum carried by photons to directly illuminated surfaces. The interaction between photons and surfaces can be described as absorption or reflection. According to Montenbruck & Gill (2000) the resulting acceleration  $\ddot{\mathbf{r}}_{\mathbf{S}}$  can be written as

$$\ddot{\mathbf{r}}_{\mathbf{S}} = -\nu P_S \frac{1 \text{ AU}^2}{r_{\odot}^2} \frac{A}{m} \cos(\alpha) [(1 - \delta) \mathbf{e}_{\mathbf{S}} + 2\delta \cos(\alpha) \mathbf{n}] . \quad (4.7)$$

In Eqn. 4.7  $P_S$  describes the solar radiation pressure, which amounts to  $4.56 \cdot 10^{-6} \frac{\text{N}}{\text{m}^2}$  in the vicinity of the Earth. To account for shadow crossing the shadow function  $\nu$  is applied.  $\alpha$  is the angle between the normal vector  $\mathbf{n}$  of the illuminated surface and the direction to the Sun  $\mathbf{e}_{\odot}$  (geocentric Sun distance  $r_{\odot}$ ). The reflectivity  $\delta$  provides the optical properties. The nominal distance between Earth and Sun is given by the astronomical unit AU. As visible in Eqn. 4.7 the acceleration due to solar radiation pressure

<sup>5</sup> The cannonball assumption also requires a very rough knowledge of the spacecraft surface area and optical properties.

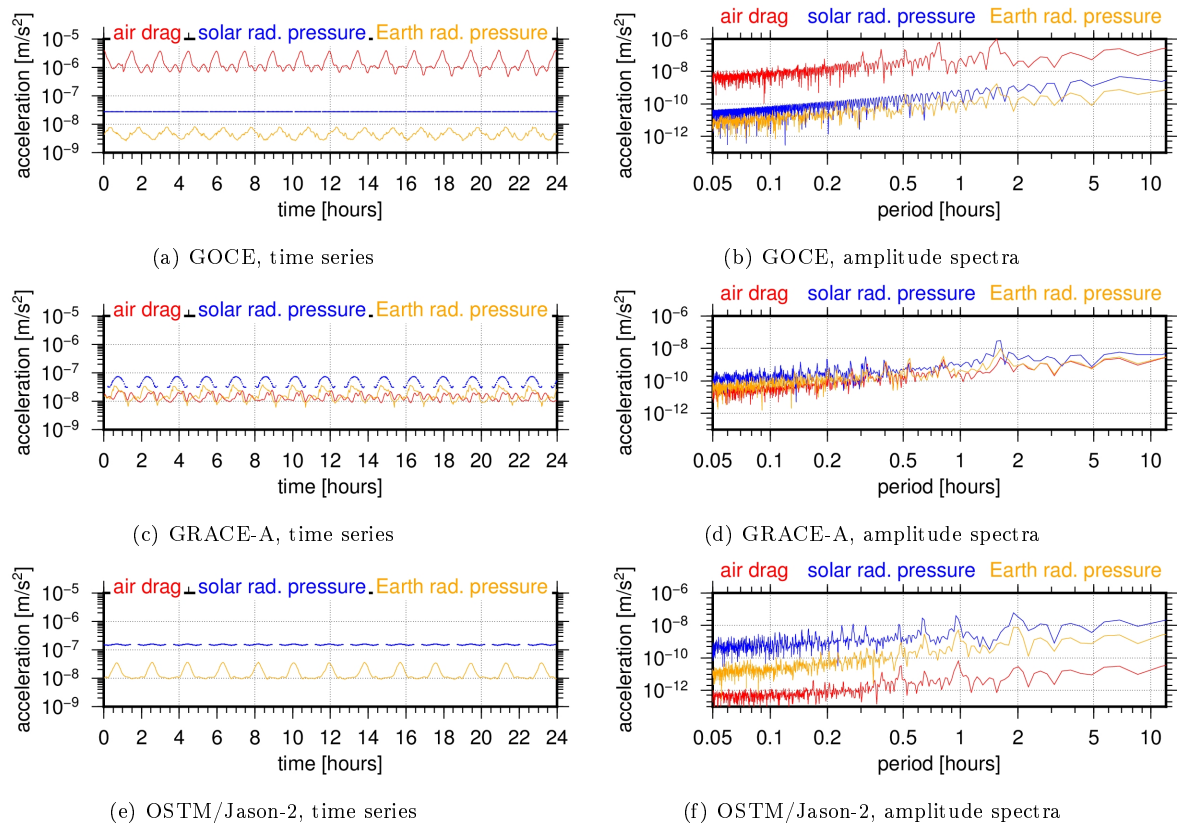


**Fig. 4.7:** Non-gravitational accelerations acting on GOCE, GRACE-A, and OSTM/Jason-2 over one day (January 3rd, 2010)

depends on the satellite properties, but not on the satellite altitude. In general, the solar radiation varies slightly within a year's period due to the eccentricity of the Earth orbit ( $e_E = 0.0167$ ). This is accounted by the scale factor computed by the ratio  $AU/r_{\odot}$ . The annual variation of the solar radiation pressure is  $\pm 3.3\%$  (Montenbruck & Gill, 2000). Obviously, satellites are not affected by solar radiation pressure during Earth and Moon shadow crossings. This is considered by the shadow function  $\nu$ , which is defined by  $\nu=0$ , if the satellite is in the umbra,  $\nu=1$ , if the satellite is in the sunlight, and  $0 < \nu < 1$ , if the satellite is in the penumbra (Steigenberger, 2009). Fig. 4.7 shows the acceleration due to solar radiation pressure for GOCE, GRACE-A, and OSTM/Jason-2. A constant acceleration of  $2.7 \cdot 10^{-8} \frac{m}{s^2}$  was estimated, for GOCE as instead of a complex satellite model only a cannonball approximation was used and the satellite is in a sun-synchronous orbit without Earth shadow crossings. Comparing the averaged accelerations for GRACE-A ( $5.1 \cdot 10^{-8} \frac{m}{s^2}$ ) and OSTM/Jason-2 ( $1.5 \cdot 10^{-7} \frac{m}{s^2}$ ) a significantly larger acceleration is observed for the much larger spacecraft OSTM/Jason-2. Additionally, the solar radiation pressure for OSTM/Jason-2 shows only small variations, whereas for GRACE-A the acceleration changes by up to half a magnitude. This change is caused by the different attitude regimes. The large solar panels of OSTM/Jason-2 are always orientated perpendicular to the Sun direction, whereas GRACE is orientated along the trajectory exposing either a small or a large cross-section to the Sun. Both satellites, GRACE-A and OSTM/Jason-2, cross the Earth shadow during each revolution for the discussed day. These shadow crossings take 30 minutes for GRACE and 24 minutes for OSTM/Jason-2. The main period in the acceleration can be found between 93 and 97.5 minutes, nearly matching the orbit period (approximate 94.5 minutes). For OSTM/Jason-2 main periods in the acceleration can be found at 113.4 minutes (matching the orbit period of 112.4 minutes) and higher harmonics thereof.

Earth radiation pressure refers to radiation re-emitted by the Earth. Simplistically, Earth re-radiation can be divided into an optical (short wavelength) and an infrared (long wavelength) part. While the first part contains solar radiation reflected by the Earth surface and clouds, the second part contains absorbed solar radiation which is re-emitted by the Earth (Frommknecht, 2008). According to Knocke et al. (1988) the

magnitude of the resulting acceleration amounts to 10-35 % of the acceleration resulting from the direct solar radiation pressure. Obviously, the optical radiation depends on the characteristics of the reflecting surface area. The albedo value  $a$  describes the fraction of reflected solar radiation. Globally averaged, a value of 0.34 can be found, with large variations due to local time, surface characteristics, and cloud coverage (Montenbruck & Gill, 2000). The infrared part does not depend on local time and is nearly isotropic. According to Montenbruck & Gill (2000) the resulting acceleration  $\ddot{\mathbf{r}}_{\mathbf{E}}$  is estimated as the sum over  $n$  Earth area elements  $j$  with area  $A_j$

$$\ddot{\mathbf{r}}_{\mathbf{E}} = \sum_{j=1}^n C_R \left( \nu_j a_j \cos(\alpha_j^E) + \frac{1}{4} \epsilon_j \right) P_S \frac{A}{m} \cos(\alpha_j^i) \frac{A_j}{\pi r_j^2} \mathbf{e}_j. \quad (4.8)$$

In Eqn. 4.8 each area element  $j$  is characterized by its shadow function  $\nu_j$ , its albedo value  $a_j$ , its averaged emissivity  $\epsilon_j$ , its unit vector to the satellite  $\mathbf{e}_j$ , and its distance to the satellite  $r_j$ .  $\alpha_j^E$  and  $\alpha_j^i$  are the angles of the surface normals of Earth and satellite with respect to the incident radiation. The radiation pressure coefficient  $C_R$  is estimated by  $C_R = 1 + \frac{4}{9} \rho$  (Sošnica, 2015). The accelerations in Fig. 4.7 are computed based on data of the Clouds and the Earth's Radiant System (CERES). The largest accelerations are  $1.8 \cdot 10^{-8} \frac{m}{s^2}$  and  $1.6 \cdot 10^{-8} \frac{m}{s^2}$  for OSTM/Jason-2 and GRACE, respectively. These values reach 12 % and 31 % of the accelerations due to the direct solar pressure for OSTM/Jason-2 and GRACE-A, respectively. In contrast to the direct solar radiation pressure, Earth radiation pressure depends on the satellite's altitude  $h$  by  $1/h^2$ . However, the main differences are related to the spacecraft size and attitude, when comparing the acceleration caused by Earth radiation on two bulky satellites. For example, the corresponding perturbations are larger for the higher altitude mission OSTM/Jason-2 than for the smaller GRACE spacecraft. Smallest values are obtained for the low-altitude GOCE satellite approximated as a cannonball. The relevant periods are close to the orbit period and higher harmonics thereof, similar to those observed for direct radiation pressure. No periodic behavior is present for the acceleration due to solar radiation pressure for GOCE, whereas the acceleration due to Earth radiation pressure it is. The reason is that, even if the spacecraft is permanently in the sunlight, the Earth albedo varies significantly during one revolution.

Drag due to neutral and charged atmospheric particles is the dominating non-gravitational force for satellites in low orbits. The effect of air drag (also called atmospheric drag) can be describes as a loss of energy due to interactions with the atmospheric molecules resulting in a reduction of the satellite's semi-major axis. The perturbing acceleration  $\ddot{\mathbf{r}}_{\mathbf{A}}$  reads as (Montenbruck & Gill, 2000)

$$\ddot{\mathbf{r}}_{\mathbf{A}} = -\frac{C}{2} \frac{A}{m} \rho \dot{\mathbf{r}}'^2 \frac{\dot{\mathbf{r}}'}{|\dot{\mathbf{r}}'|} \quad \text{with} \quad \dot{\mathbf{r}}' = \dot{\mathbf{r}} - \omega_E \times \mathbf{r} \quad (4.9)$$

where  $\dot{\mathbf{r}}'$  is the relative velocity with respect to the atmosphere.  $C$  denotes the ballistic coefficient, and  $\omega_E$  is the Earth's angular velocity. The direction of this acceleration is anti-parallel to the satellite's relative velocity  $\dot{\mathbf{r}}'$  with respect to the atmosphere. As the atmosphere is co-rotating with the Earth,  $\omega_E$  represents the momentary angular velocity vector of the Earth. The satellite-specific ballistic coefficient  $C$  amounts to  $\approx 2$  for spherical satellites and up to  $\approx 3$  for bulky satellites. The impact of air drag, however, depends significantly on the air density  $\rho$  in the upper atmosphere, i.e., in the thermosphere and the exosphere. The main constituents in these layers of the upper atmosphere are hydrogen, helium, oxygen, nitrogen, and argon. Their densities vary significantly with the altitude as known from the barometric formula. As additional air density variations depend mainly on the solar activity. Temporal variations can be found on daily, seasonal, annual, and solar cycle periods. Beutler (2005b) provides a comprehensive overview of air density variations. Obviously, very accurate density information is required to model air drag. Fig. 4.8 shows air density values for GRACE-A's altitude over one day and over several years. The Mass Spectrometer and Inherent Scatter Model MSIS-86 (Hedin, 1987) is based on data records from satellite, sounding rockets, and inherent scatter measurements. The actual density is computed by complex formulas including around 850 coefficients as a function of height, time, latitude, longitude, and

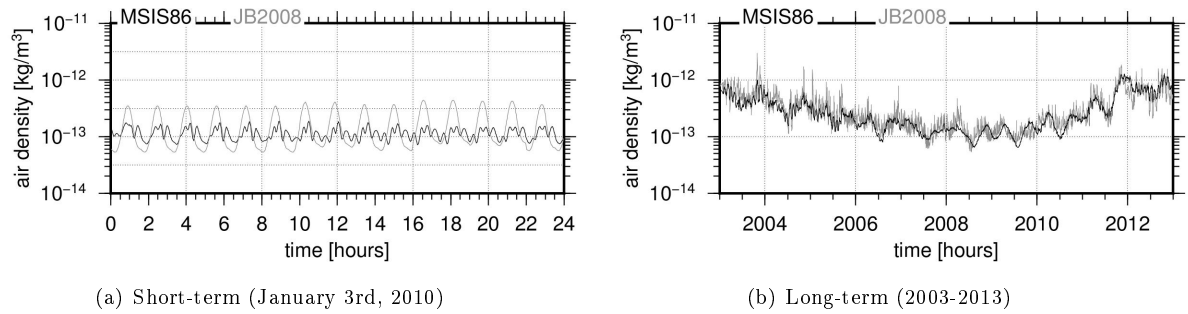


**Fig. 4.8:** Comparison of air density values derived from MSIS86 and JB2008 for GRACE-A on the short and on the long period

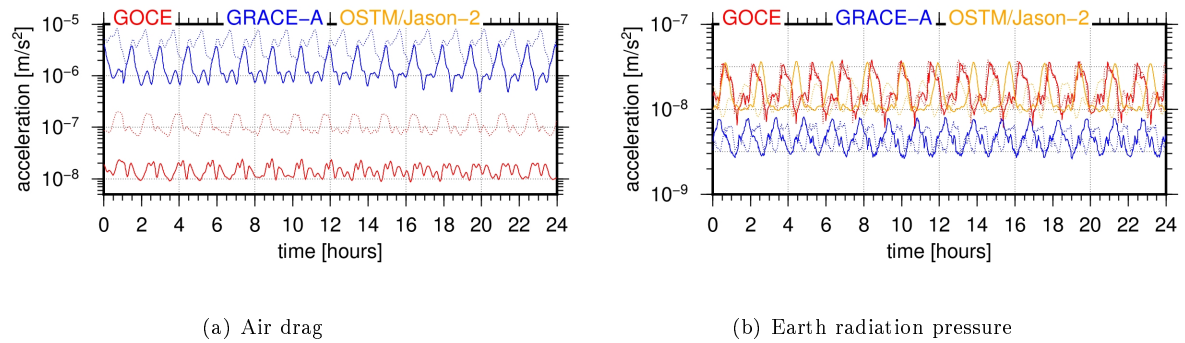


**Fig. 4.9:** Comparison of non-gravitational forces for January 3, 2010 (*solid*) and October 26, 2011 (*dotted*); solar radiation pressure is not shown as no significant differences are present

true solar time. The Jacchia-Bowman model JB2008 is based on the Jacchia diffusion equations (Bowman et al., 2008). The data sources are accelerometer measurements from CHAMP and GRACE, and density values provided by the US Air Force. Due to the equilibrium assumption in the diffusion equation, short-periodic dynamical variations are not covered accurately in this model. The higher degree of detail in the MSIS model and large differences of up to half a magnitude are visible, when comparing both models in Fig. 4.8. However, as air density is subject to fast and substantial variations, the statistical accuracy of the customary models is around 20% (Montenbruck & Gill, 2000). The corresponding accelerations are plotted in Fig. 4.7. Variations due to altitude changes are clearly visible, the averaged accelerations are  $1.55 \cdot 10^{-6} \frac{m}{s^2}$ ,  $1.46 \cdot 10^{-8} \frac{m}{s^2}$ , and  $2.2 \cdot 10^{-10} \frac{m}{s^2}$  for GOCE, GRACE-A, and OSTM/Jason-2, respectively. The main frequencies are related to the orbit period and higher harmonics thereof.

Comparing the accelerations due to air drag and Earth radiation pressure, large variations are visible between the two days, January 3, 2010, and October 26, 2011 (Fig. 4.9). Concerning air drag the lower orbital height of GOCE in 2011 causes the increase in acceleration by around one order of magnitude. However, also the higher solar activity during October 2011 compared to January 2010 increases the derived accelerations (cf. Fig. 2.2). The acceleration caused by Earth radiation does not vary much between both days. The observed phase shift is caused by the geometry change between Earth, satellite, and Sun.

### Mitigation of Orbit Modeling Deficiencies with Additional Parameters

Additional parameters can be introduced into an orbit determination process to account for orbit maintaining maneuvers, attitude control affecting the spacecraft trajectory, and deficiencies of the applied force model (Beutler, 2005a). The latter contains mismodeling effects (e.g., an inaccurate air density) but also unmodeled forces (e.g., self-shadowing or thermal re-radiation). According to the literature four non-deterministic approaches can be found to mitigate the above mentioned effects.

- **method 1** The first method is called short-arc method, as the orbit is cut into short pieces. Cor-

responding deficiencies are absorbed by the initial state vector of each arc. The main disadvantages are the loss of dynamic information and boundary errors at the large number of break points. Alternatively, an initial state vector and instantaneous velocity changes can be set up (Beutler, 2005a; Jäggi, 2007).

- **method 2** Due to the periodic nature of many types of perturbations once-per-revolution accelerations can often absorb specific orbit errors. However, this procedure requires some knowledge on the considered effects. An example are empirical radiation pressure coefficients estimated in a GPS orbit determination process (Springer, 2002; Arnold et al., 2015).
- **method 3** In an orbit determination based on a Kalman filter stochastic accelerations can be introduced on top of all deterministic forces. Accordingly, a stochastic differential equation system has to be solved.
- **method 4** Similarly to method 3, pseudo-stochastic orbit parameters can be introduced as velocity (first derivative) or acceleration (second derivative) changes in predefined directions at predefined epochs. Within the Bernese GNSS Software and within this work this method has been applied. To distinguish between this method and the stochastic accelerations described in method (3) the term pseudo-stochastic orbit parameters was introduced by Yunck et al. (1990) and Wu et al. (1991).

Beutler (2005a) summarizes the advantages of this pseudo-stochastic orbit parameters. Compared to method (1) the orbit is still continuous, compared to method (2) no information or knowledge about the mismodeling effects is required, and compared to method (3) the orbit determination based on a least-squares adjustment is still applicable as each parameter has an expectation value and a variance. Consequently, the arc is represented piece-wise by the deterministic equation of motion. The pseudo-stochastic parameters can be set up very flexibly regarding their directions, their spacing, and their weights. Estimating pseudo-stochastic orbit parameters for each epoch is equal to the above mentioned kinematic orbit representation, whereas the renunciation of any parameter leads to a purely dynamic modeling. Setting up these parameters results in a reduced-dynamic orbit representation as described by e.g., Wu et al. (1991); Svehla & Rothacher (2003); Montenbruck (2003); Jäggi et al. (2006); Jäggi (2007). The weight of the estimated pseudo-stochastic orbit parameters has to be defined by introducing the additional pseudo-observation equation

$$\delta v = 0 \quad \text{with the weight} \quad w = \frac{\sigma_0^2}{\sigma^2(\delta v)}. \quad (4.10)$$

Adding the empirical parameters  $p_1, \dots, p_s$  to Eqn. 4.1, the adapted equation of motion reads as

$$\ddot{\mathbf{r}} = -GM \frac{\mathbf{r}}{r^3} + \mathbf{f}_1(t, \mathbf{r}, \dot{\mathbf{r}}, q_1, \dots, q_d, p_1, \dots, p_s). \quad (4.11)$$

According to Jäggi (2007) pseudo-stochastic orbit parameters can be introduced as (1) piece-wise constant accelerations, (2) as instantaneous velocity changes, and (3) as piece-wise linear accelerations. The position, velocity, and acceleration vectors of the improved orbit will be continuous only in the last case (Jäggi, 2007). The second option is used for GPS orbit determination and can be seen as a special case of the short-arc method (Beutler et al., 1994). In summary, estimating pseudo-stochastic orbit parameters is a very efficient way to mitigate unmodelled perturbations, especially non-gravitational forces. However, every introduced parameter weakens the estimated dynamic parameters and information about the orbit dynamics gets lost. This effect was assessed by Jäggi et al. (2006), who studied the behavior of carrier phase residuals, when varying the constraints applied to the parameters. From his results one can conclude that a  $\sigma_0$  of around  $1 \cdot 10^{-9} \frac{m}{s^2}$  is a reasonable compromise between a kinematic-like ( $\sigma_0 > 1 \cdot 10^{-4} \frac{m}{s^2}$ ) and a dynamic-like ( $\sigma_0 < 1 \cdot 10^{-10} \frac{m}{s^2}$ ) orbit.

### 4.2.3 Precise Orbit Determination in the Bernese GNSS Software

Within the Bernese GNSS Software LEO precise orbit determination can be described as a three step orbit improvement process. In the first step an a priori orbit is estimated based on kinematic coordinates derived from zero-differenced code observation. These positions are approximated by a numerical integration of the equation of motion using a high-order collocation method and the adjustment of Keplerian elements and dynamic parameters (Beutler, 2005a). The accuracy of this purely dynamic orbit is at the level of tens of meters. The second step is a pre-processing step to clean the GPS observations. At this stage the LEO clock is also synchronized with respect to the GPS time scale. The second step ends with a renewed initial orbit based on the screened code observations. The third step is the orbit improvement itself. The improved orbit  $\mathbf{r}(t)$  is developed into a truncated Taylor series with respect to the  $n = 6 + d$  unknown orbit parameters  $p_i$  ( $i=1, \dots, n$ ) about the a priori orbit  $\mathbf{r}_0(t)$  and its parameters  $p_{i_0}$ . The truncated Taylor series for the parameter  $p_i$  read as (Jäggi, 2007)

$$\mathbf{r}(t) = \mathbf{r}_0(t) + \sum_{i=1}^n \frac{\partial \mathbf{r}_0(t)}{\partial p_i} (p_i - p_{i_0}). \quad (4.12)$$

The partial derivative of the a priori orbit  $\mathbf{r}_0(t)$  with respect to the parameter  $p_i$  is abbreviated by the substitution (Jäggi, 2007)

$$\mathbf{z}_{p_i}(t) := \frac{\partial \mathbf{r}_0(t)}{\partial p_i} \quad (4.13)$$

and is computed from the variational equation of parameter  $p_i$ . These variational equations are derived by taking the partial derivative of the equation of motion (Eqn. 4.1) and read as (Jäggi, 2007)

$$\ddot{\mathbf{z}} = \mathbf{A}_0 \mathbf{z}_{p_i} + \mathbf{A}_1 \dot{\mathbf{z}}_{p_i} + \frac{\partial \mathbf{f}_1}{\partial p_i} \quad \text{with} \quad \mathbf{A}_{0,i,k} = \frac{\partial f_i}{\partial r_{0,k}} \quad \text{and} \quad \mathbf{A}_{1,i,k} = \frac{\partial f_i}{\partial \dot{r}_{0,k}}. \quad (4.14)$$

In Eqn. 4.14  $f_i$  describes the component  $i$  of Eqn. 4.1 and  $r_{0,k}$  and  $\dot{r}_{0,k}$  denotes the component  $k$  of the geocentric satellite position and velocity, respectively. More details on variational equations and efficient algorithms for orbit improvements can be found in the literature (e.g., Montenbruck & Gill, 2000; Beutler, 2005a,b; Jäggi, 2007). With the partial derivatives in Eqn. 4.13, corrections to the a priori orbit parameters can be estimated in a least-squares adjustment based solely on GPS phase observations. The improved orbit is then derived from Eqn. 4.12 or by propagating the improved state vector using numerical integration while taking into account the improved dynamic parameters (Jäggi et al., 2009). Two features in the BSW orbit determination process are worth to be mentioned. Firstly, only “velocity-change” pseudo-stochastic orbit parameters can be set up for GNSS satellites, whereas “velocity-change” parameters or piece-wise constant accelerations can be estimated for LEOs orbits. Secondly, a combined estimation of LEO and GNSS orbits on the normal equation level is currently not possible as the data structure for the combination of normal equations (program ADDNEQ2) can only handle one type of force model. Additionally, only “velocity-change” pseudo-stochastic parameters are allowed when combining normal equations.

### 4.2.4 Validation of LEO Orbit Determination

Several methods can be used to validate LEO orbits based on internal or external data. Residuals and overlap errors can be analyzed based on the estimated orbit itself. For the latter one orbital arcs are extended to be overlapping (e.g., 30 h instead of 24 h orbital arc) with the next orbit arc and the differences between corresponding orbital positions are analyzed (e.g., Luthecke et al., 2003; Bertiger et al., 2010b). Additionally, dynamic orbital positions can be compared against a purely kinematic orbit estimation. The derived differences may show, apart from the scatter of the kinematic position estimates, deficiencies in the force models chosen (e.g., Bock, 2003; Svehla & Rothacher, 2003; Bock et al., 2014). In a similar way orbits can be validated against other orbit solutions (e.g., Jäggi, 2007; Flohrer et al., 2011). Within this

comparison also transformation parameters in the sense of a similarity transformation can be set up to account for effects like a different datum realization, or differences in the applied Earth rotation parameters. However, the estimated transformation parameters can absorb also some other systematic orbit differences. Moreover, the orbit comparison methods mentioned so far allow only a relative validation, as no distinction concerning the better solution is allowed for orbits with similar accuracy levels. A validation based on totally independent measurements is offered by SLR observations which are very precise in the radial direction (e.g., Urschl et al., 2005, 2007; Arnold et al., 2015). Fixing SLR station coordinates and the satellite orbit, the derived SLR residuals are an ideal orbit accuracy indicator. The amount of available SLR measurements is, in general, satellite-specific and depends on the mission support provided by the ILRS. Fig. 4.16 shows the significant differences in the geographical distribution of SLR data available for the selected LEO missions in 2010. For GRACE an additional relative validation of the orbit positions is offered by the K-band link (e.g., Jäggi, 2007). Orbits determined for altimetry satellites can be validated also by a crossover analysis (e.g., Lemoine et al., 2010). Satellite tracking by optical telescopes is a further orbit validation tool, but rarely used in space geodesy (Flohner, 2008).

### 4.3 LEO-specific Orbit Validation Results

Within this section the derived orbits are discussed and validated by using a selection of the methods described above. The time period considered for the orbit determination within this work is 2010 till end of 2012. However, for GRACE-A also a longer time span is considered and analyzed in the last paragraph.

#### 4.3.1 Orbit Determination Strategy

Within this paragraph the adopted processing strategy is highlighted. An overview of the introduced a priori information and products, the orbit parameterization, and the reference data sets required for the validation steps is given in Tab. 4.2. As mentioned above, kinematic orbits were estimated for validation purposes in an extension of the orbit determination process. The determination of the kinematic orbits was done as a precise point positioning, i.e., the LEO positions and clock corrections were estimated with fixed GPS satellite orbits and clocks. To ensure the quality of the derived kinematic orbits, positions were not estimated for epochs with less than six GPS observations. The number of unknowns can be estimated roughly based on the processing options given in Tab. 4.2. This number amounts to  $\approx 9400$  parameters in the reduced-dynamic orbit determination over 24 h. Around 90 % of them are epoch-wise receiver clock corrections (nominally 8640 clock parameters were set up). In the case of kinematic orbit determination the number of unknowns increases to  $\approx 35'000$  parameters. The receiver clock corrections are estimated in the same way in both approaches; in order to decrease the processing load, they are usually pre-eliminated. The number of observations per day is, according to Fig. 4.3, around 60'000 to 80'000 depending on the receiver, the orbit geometry, and mission-specific events.

#### 4.3.2 Analysis of Carrier Phase Residuals

Carrier phase residuals, also called post-fit observation residuals, are considered in a first orbit validation step. As mentioned already in Sect. 2.3.3 and defined in Eqn. 3.13, residuals are an indicator for the level of agreement between the applied models and the observations. In terms of orbit validation carrier phase residuals allow the analysis of the agreement between the derived orbit and the original observation. Fig. 4.10 shows the daily RMS of post-fit  $L_3$  (ionosphere-free) carrier phase residuals obtained in a reduced-dynamic orbit determination for all four LEOs. The daily RMS of phase residuals is below 1 cm for all satellites with a few exceptional days for GOCE. Concerning the two GRACE satellites a similar behavior in time is visible with an offset of  $\approx 1$  mm between the two curves, which are around 0.6 and 0.7 cm for GRACE-B and GRACE-A, respectively. The higher values for GRACE-A are related to a slightly worse

**Tab. 4.2:** LEO orbit determination strategy (reduced-dynamic approach)

<b>modeling and a priori information</b>	
base observations	zero-difference code and phase observations provided by GFZ <sup>a</sup> , ESA <sup>b</sup> , and CNES <sup>d</sup> , data rate: 10 s
GPS-related products	final products from CODE: orbits, 5 s clock corrections, Earth rotation parameters
attitude information	star camera quaternions provided by GFZ <sup>a</sup> , ESA <sup>b</sup> , and CNES <sup>d</sup>
antenna phase center	absolute phase center offsets and variations for GPS satellites, GOCE (Bock et al., 2011a), and OSTM/Jason-2 (Garcia & Montenbruck, 2007); GPS satellite antenna patterns beyond 14° from Schmid (2014)
gravitational forces	EIGEN5C gravity field up to degree and order 120 (Förste et al., 2008) solid Earth, pole, and ocean tides (IERS2010, FES2004) luni-solar-planetary gravity (DE405)
non-gravitational forces	box-wing models for GRACE (Bettadpur, 2012) and OSTM/Jason-2 <sup>e</sup> CERES data set for Earth albedo MSIS-86 air density model (Hedin, 1987)
<b>parameterization</b>	
LEO orbit modeling	six Keplerian elements per 24 h arc nine empirical radiation pressure parameters per 24 h arc piece-wise constant accelerations every six minutes (constraint 5 nm/s <sup>2</sup> )
receiver clocks	pre-eliminated every epoch
phase ambiguities	pre-eliminated as soon as possible
<b>Reference data</b>	
LEO orbits	sp3 files (data rate 10 s, if not available 60 s) GRACE orbit: reduced-dynamic GPS-based provided via GFZ <sup>a</sup> GOCE orbit: reduced-dynamic GPS-based provided via ESA <sup>b</sup> (Bock et al., 2014) OSTM/Jason-2: dynamic GPS+DORIS+SLR-based provided via ESOC <sup>c</sup> (Flohrer et al., 2011)
SLR observations	normal point data provided via the EUROLAS Data Center ( <a href="http://edc.dgfi.tum.de/en/">http://edc.dgfi.tum.de/en/</a> , accessed May 2016)

<sup>a</sup> <http://isdc.gfz-potsdam.de/>, accessed May 2016<sup>b</sup> <http://eo-virtual-archive1.esa.int/Index.html> [restricted], accessed May 2016<sup>c</sup> <ftp://dgn6.esoc.esa.int/jason2/sol3/>, accessed May 2016<sup>d</sup> <ftp://avisoftp.cnes.fr/AVISO/pub/doris/jason-2/>, accessed May 2016<sup>e</sup> [http://www.avisooceanobs.com/en/calval/orbit/precise-orbit-determination-verification/index.html#\\_c6061](http://www.avisooceanobs.com/en/calval/orbit/precise-orbit-determination-verification/index.html#_c6061), accessed May 2016

data quality compared to GRACE-B (Bock et al., 2009). Haines et al. (2015) mentioned an interference from the side-looking occultation antenna as reason for the lower data quality. While the RMS values are stable until mid-2011, an increase of 2 mm and 1 mm is found during autumn 2011 and autumn 2012, respectively. In general, both periods of increased RMS values are caused by the higher solar activity in 2011 and 2012, resulting in a more dynamic atmospheric behavior which causes difficulties in air drag modeling. A very stable behavior is present for the OSTM/Jason-2; the RMS values are at the level of 0.7 cm. The corresponding peak-to-peak variations are below 2 mm. A very small long-term trend of around 0.3 mm per year is visible, probably caused by a neglected trend in OSTM/Jason-2's center of mass driven by fuel consumption<sup>6</sup>. In the case of GOCE several mission-specific events are present. The large gap in summer 2010 was described already in Sect. 4.1. A second smaller gap and some increased RMS values in January 2011 are caused by receiver problems as mentioned in the monthly quality reports<sup>7</sup>. In August 2012 the final mission stage was entered by a step-wise lowered altitude. During August and November, the GOCE altitude was lowered by 8.6 and 6.7 km to 244.3 km (Ghisi et al., 2014). The increased ionospheric delays due to the increased solar activity and the lower altitude seems to cause the higher RMS values in the second half of 2012. Bock et al. (2014) estimated correlation coefficients of 0.70 and 0.86 between the mean TEC and the 3D RMS values and between the mean TEC and missing  $L_2$  observations, respectively. According to them the increased TEC values had a negative influence on the

<sup>6</sup> According to <ftp://ftp.ids-doris.org/pub/ids/satellites/ja2mass.txt> (accessed August 2016) the satellite's center of gravity was shifted by 2 mm between 2009.9 and 2016.3.<sup>7</sup> Available at <https://earth.esa.int/sppa-reports/goce/egg/monthly/>, accessed May 2016

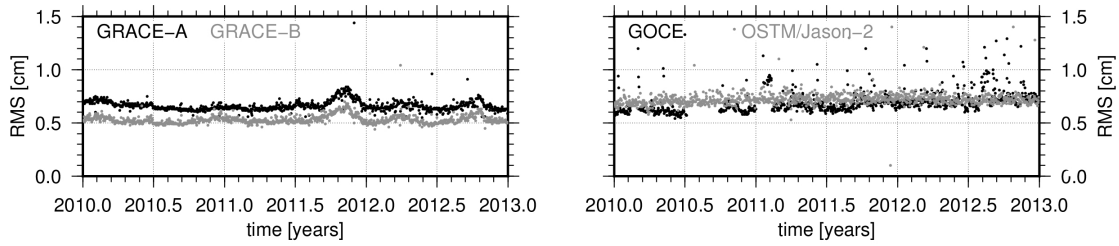


**Fig. 4.10:** Daily RMS of carrier phase residuals in orbit determination for GRACE, GOCE, and OSTM/Jason-2

**Tab. 4.3:** Mean value and standard deviation of daily RMS of carrier phase residuals in orbit determination for GRACE, GOCE, and OSTM/Jason-2; unit: cm

solution	GRACE-A	GRACE-B	GOCE	OSTM/Jason-2	remark
this study	$0.75 \pm 0.14$	$0.64 \pm 0.15$	$0.74 \pm 0.33$	$0.74 \pm 0.22$	
Jäggi et al. (2009)	0.45	0.37			w/o PCV
	0.65	0.50			with ground-calibrated PCV
Flohrer et al. (2011)				$0.70 \pm 0.2$	GPS+DORIS+SLR (GDS3)
				$0.68 \pm 0.3$	GPS (G3)

GOCE GPS receiver tracking performance. Additionally, the ascending tracks of GOCE crossed areas of large ionospheric activities shortly after dusk due to the orbital geometry.

Tab. 4.3 provides statistical information for the derived residuals and their RMS values including some literature-based values for comparison. The smaller values found in the literature are mainly related to orbit determination with estimated LEO antenna phase center variations and the estimation of scale factors for non-gravitational forces, respectively. The larger RMS values Jäggi et al. (2009) found, when applying ground calibrated phase patterns, are related to the fact that the GRACE GPS antennas are lowered with respect to the satellite surface and, therefore, the antenna near-field heavily affects the actual PCV. The impact of LEO receiver antenna PCVs on the RMS of the residuals is shown, exemplary, for GOCE in Fig. 4.11. Without taking the a priori GOCE antenna PCV into account the derived RMS is  $\approx 0.95$  cm. Applying the antenna pattern provided by Bock et al. (2011a) as a priori, the daily RMS values are reduced by around 3 mm which is a reduction by one third. Bock et al. (2011a) found a reduction from 0.79 cm to 0.46 cm when estimating the antenna pattern in addition to the orbit determination. However, contrary to SLR residuals, the GPS phase residuals do not directly reflect the orbit quality. In order to really assess the orbit quality validation methods based on external data are required.

### 4.3.3 Comparison Against External Orbit Solutions

Within this section the derived LEO orbits are compared against the external reference solutions mentioned in Tab. 4.2. The orbit comparison is performed in two ways:

- **method 1** by directly computing the position differences, and
- **method 2** by estimating simultaneously seven Helmert transformation parameters per day.

As mentioned above, the transformation in method 2 can absorb systematic differences due to an inconsistent datum definition or different ERP values between both orbit determination processes. However, also their systematic orbit differences might be absorbed by the estimated transformation parameters. For example, a radial orbit error for OSTM/Jason-2 caused by an inaccurate receiver antenna z-offset will be absorbed completely by the estimated scale parameter, but will bias the derived altimeter results directly. Orbit differences beyond 3 m were detected as outliers and not considered within this comparison<sup>8</sup>.

<sup>8</sup> Orbit differences were estimated as differences of orbital positions.

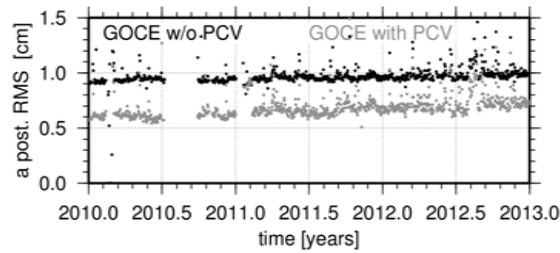


Fig. 4.11: Impact of a priori applied receiver PCV on GOCE phase residuals (PCV provided by Bock et al., 2014)

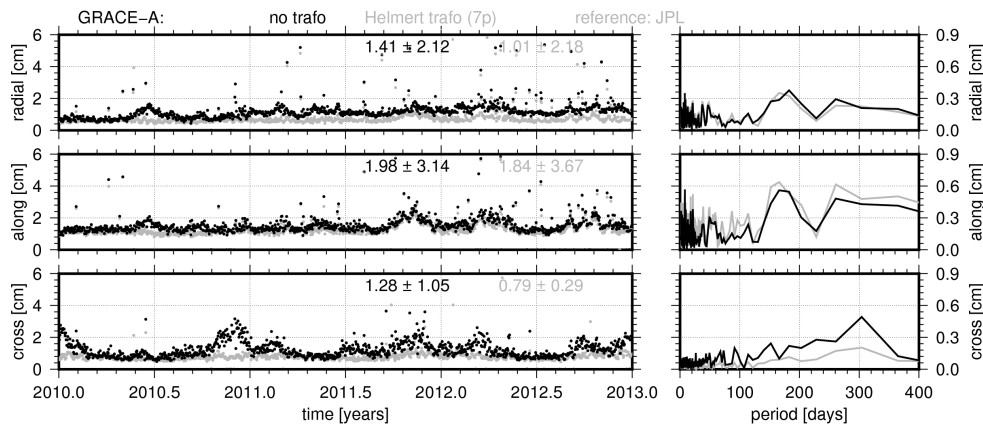


Fig. 4.12: Orbit comparison for GRACE-A reduced-dynamic solution against JPL reduced-dynamic orbits based on GPS

For GRACE, GPS-based orbits were used as reference solutions as they are provided as GRACE level 2 product. They are indicated by “JPL”. The daily RMS of the derived differences estimated for both comparison methods is shown for GRACE-A and GRACE-B in Fig. 4.12 and 4.13, respectively. The RMS values for radial, along-track, and cross-track are mostly below 2 cm. Annual and semi-annual signals of some millimeters are observable in the radial and along-track differences. In both orbit components the derived amplitude spectra show nearly identical signals for both comparison methods. Therefore, the observed differences are most probably related to differences in the modeling of non-gravitational forces, which are not absorbed by the transformation parameters. A significant reduction of the 300-day signal of 3 mm in the cross-track component is achieved, when estimating transformation parameters for GRACE-A. The GRACE-B time series shows, however, a significantly smaller signal at 300 days in cross-track. Therefore, the observed signal in the cross-track of GRACE-A must be related to spacecraft issues. The overall average RMS values are around 1.4 cm in radial, 2.0 cm in along-track, and 1.2 cm in cross-track for both spacecraft. These values decrease to 1.0 cm, 1.8 cm, and 0.8 cm, respectively, when estimating transformation parameters simultaneously. Concerning the radial component, it is probable that the transformation parameters absorb orbit differences caused by a GRACE antenna pattern introduced in the “JPL” orbits.

The derived GOCE orbits are compared to final orbits provided by the GOCE high-level processing facility (Bock et al., 2011a). These GPS-based orbits are derived as level 2 products; they are referred to as “ESA”. Fig. 4.14 shows the corresponding orbit differences. The RMS in radial and along-track is mainly below or close to 2 cm. Average RMS values of 2.0, 2.5, and 2.7 cm can be derived. They decrease slightly to 1.8, 2.5, and 2.4 cm, when estimating transformation parameters in the orbit comparison. Similarly to the residual plot (Fig. 4.10), larger RMS values are obtained for the second half of 2012. As described above, the main reasons for this are the problem of missing  $L_2$  observations and the increased ionospheric activity. Interestingly, there is nearly no reduction of the RMS values, when estimating additional transformation parameters except in the radial component before April 2011. Further periods of higher RMS values visible in Fig. 4.14 can be assigned to GOCE-related events, which are described in the corresponding monthly

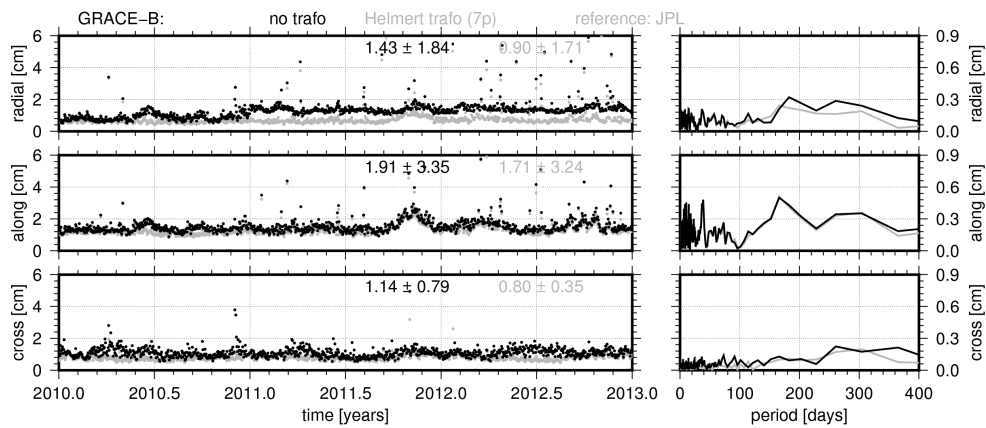


Fig. 4.13: Orbit comparison for GRACE-B reduced-dynamic solution against JPL reduced-dynamic orbits based on GPS

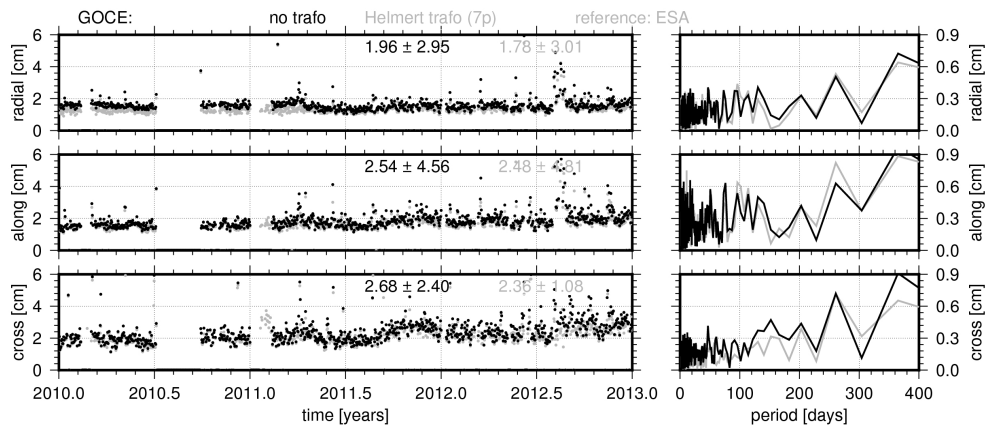


Fig. 4.14: Orbit comparison for GOCE reduced-dynamic solution against ESA reduced-dynamic orbits based on GPS

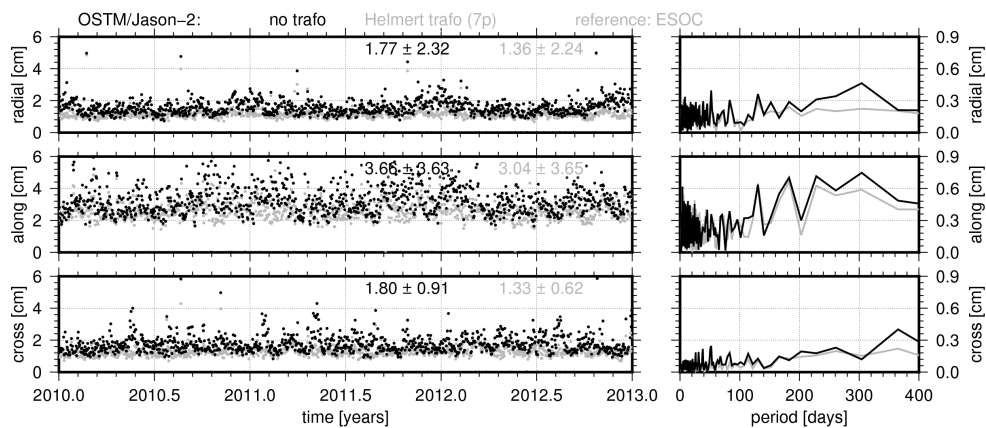


Fig. 4.15: Orbit comparison for OSTM/Jason-2 reduced-dynamic solution against ESOC dynamic orbits based on GPS, SLR, and DORIS

reports. For example, the comparison failed in January 2011 because of the GPS receiver problems mentioned above.

The orbits derived for OSTM/Jason-2 are compared to orbits provided by ESOC (Flohrer et al., 2011). The ESOC OSTM/Jason-2 solution is a combined orbit solution of weighted GPS, SLR, and DORIS observations. Again, the RMS values in radial and cross-track are below or close to 2 cm. In summary, average RMS values of 1.8, 3.7, and 1.8 cm are estimated. When transformations are taken into account, the values decrease to 1.4, 3.0, and 1.3 cm. However, in along-track daily RMS values of up to 5 cm are present. These large variations are most probably related to a mismodeled solar radiation pressure caused by deficiencies of the introduced macro-model. Scaling factors estimated by Flohrer et al. (2011) for the solar radiation pressure were not considered in the orbit determination described here. The impact of adding transformation parameters in the comparison is again rather small. However, the annual signal in cross-track decreases from 4 to 2 mm, when estimating transformation parameters in the orbit comparison. Also a small impact is present for the radial component, where signals between 200 and 360 days decrease. Flohrer et al. (2011) compared their orbit results with JPL and CNES solutions. They derived mean RMS values of 0.9, 2.2, 1.0 and 0.9, 2.4, 1.4 cm in radial, along-track, and cross-track, respectively.

#### 4.3.4 SLR Validation Results

As mentioned in Sect. 4.2.4, SLR provides an independent validation for GPS-derived LEO orbits in the absolute sense. The main challenges concerning SLR tracking of LEOs are, apart from the techniques-specific issues mentioned in Sect. 2.1.2 (like the weather-dependency), the fast velocity and the short passes resulting from the low satellite altitude. Fig. 4.16 shows the geographical distribution of the available SLR tracking data for GRACE-A, GRACE-B, GOCE, and OSTM/Jason-2, respectively. The geographical distribution is considered by counting all SLR observations performed in 2010 in  $1^\circ \times 1^\circ$  bins, which the LEOs cross in  $\approx 20$ s. Three aspects are obvious: (1) the number of observations varies significantly between the LEOs, (2) due to the relatively sparse network the orbit coverage is very low, and (3) the impact of well-performing stations is tremendous (e.g., visible for the station Yarragadee in Western Australia). The amount of processed observations per station is shown in Fig. 4.17 for all four satellites. The station monument numbers belonging to the station names given in Tab. C.1. The considered time span for this figure is 2010.0-2013.0. As visible already in Fig. 4.16, there are tremendous differences in the number of SLR observations between the missions. Considering the 1096 days within the three years, the 60'409 normal points derived at Yarragadee (7090) correspond to about 55 observations per day. The performance of this station is even more impressive, if considering that the number of observations to OSTM/Jason-2 performed at Yarragadee exceeds the number of observations the whole network performed to GOCE significantly. Also the observation capabilities at Zimmerwald, Switzerland (7810) are impressive taking the handicap of often overcast sky into account. Interestingly, there are stations for example Changchun in China (7237), with a significant difference in the number of observations for the two GRACE satellites (6027 vs. 4068 normal points for GRACE-A and GRACE-B, respectively).

The principle idea of an SLR validation was described already in Sect. 4.2.4. A critical issue in the SLR validation process is the specification of reliable outlier criteria. On the one hand, tight thresholds, high elevation cutoffs and a restrictive selection of the stations considered will result in small RMS values based on few observations. On the other hand, a large number of stations and normal points will increase the statistical reliability of the derived RMS, but might lead to higher RMS values. In the literature, a very broad range of SLR outlier definitions are present, starting from considering only three stations and cutoff angles of  $70^\circ$  (e.g. Couhert et al., 2015) to validations based on all SLR tracking stations while applying very loose thresholds (e.g. Sošnica et al., 2015). Within this thesis an elevation cutoff of  $10^\circ$  and a 150 mm threshold for the SLR residual screening was applied. The sigma editing level was set to  $2.5\sigma$  with a maximum overall sigma (i.e., the RMS with respect to the estimated values) of 25 mm. Due to the applied criteria 33.7 % of the GOCE SLR observations were identified as outliers while 25'567 normal points

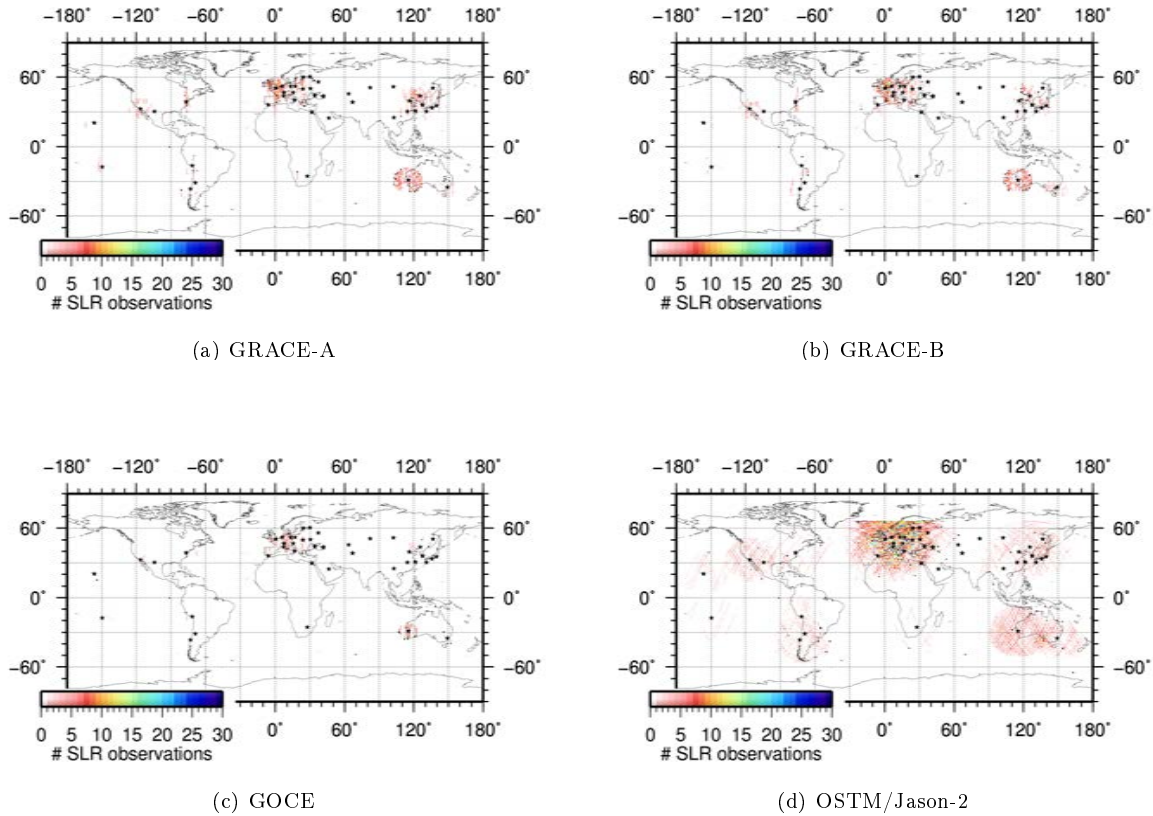


**Fig. 4.16:** Geographical distribution of SLR observations to GRACE, GOCE, and OSTM/Jason-2 during 2010, the number of observations is counted in  $1 \times 1^\circ$  bins, SLR stations are indicated by asterisks

remained. 12.8% and 12.1% of the observations were rejected for GRACE-A and GRACE-B, respectively (95'619 and 95'619 observations remained). For OSTM/Jason-2, 9.4% of the available 432'183 observations were marked and excluded from the validation, whereas 391'504 normal points remained. Tab. 4.4 provides statistical information for the SLR validation. It has to be mentioned that range biases were not estimated nor somehow considered for the LEOs. A small bias below one millimeter remained for the two GRACE satellites and RMS values of 2.0 cm are present. These values agree well with the 2.5 cm presented by Lemoine et al. (2010). For GOCE and OSTM/Jason-2, the derived RMS values are slightly larger than values found in the literature. In both cases this effect is related to the fact that no nadir-dependent range corrections were considered. The GOCE mean offset is reduced when applying additionally a nearest prism approach as demonstrated by Bock et al. (2014).

Fig. 4.18 shows the SLR residuals derived for the satellites GRACE-A, GOCE, and OSTM/Jason-2 in an azimuth-nadir skyplot, i.e., as seen from the satellite. The bin size is  $1^\circ \times 1^\circ$  with averaged values

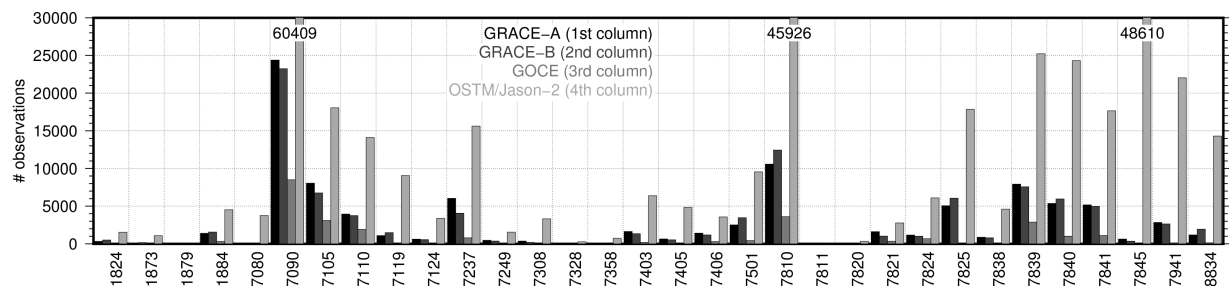


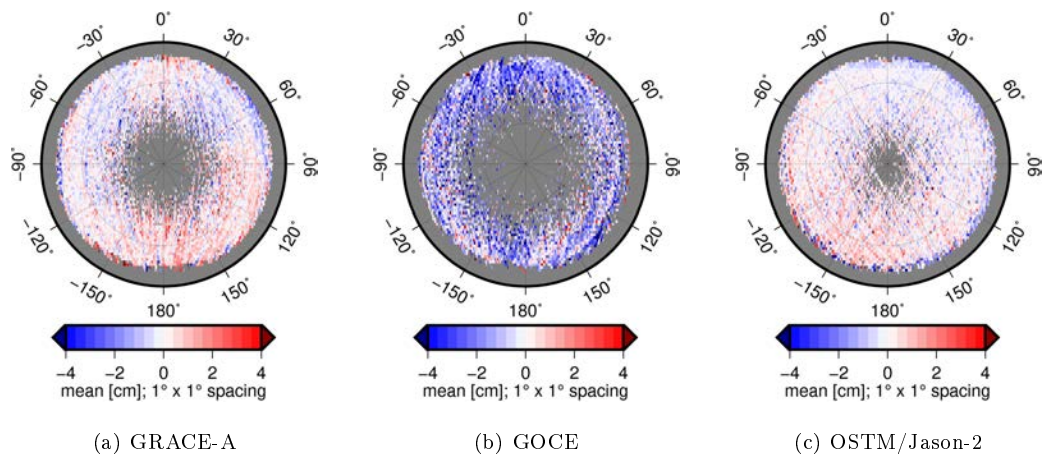
**Fig. 4.17:** Number of SLR observations per station for GRACE, GOCE, and OSTM/Jason-2 (2010.0-2013.0, after outlier detection); station monument numbers are listed in Tab. C.1

**Tab. 4.4:** Mean and RMS of SLR residuals; unit: cm

solution	GRACE-A		GRACE-B		GOCE		OSTM/Jason-2		remark
	mean	RMS	mean	RMS	mean	RMS	mean	RMS	
this study	0.04	1.96	-0.07	1.98	-1.23	2.85	0.06	2.30	
Kang et al. (2006)	1.10 <sup>a</sup>	2.50	1.00 <sup>a</sup>	2.40					nadir-dependent range correction, no tilt nearest prism approximation and 5° tilt
Bock et al. (2014)					0.55	1.82 <sup>b</sup>			
Bock et al. (2014)					0.01	1.44 <sup>b</sup>			
Lemoine et al. (2010)							1.25		GPS reduced-dynamic orbit

<sup>a</sup> estimated range biases instead of mean value

<sup>b</sup> standard deviation instead of RMS, as given in the references

**Fig. 4.18:** GRACE and OSTM/Jason-2 SLR residuals in an azimuth vs. nadir plot

per bin. Apart from the cutoff angle of  $10^\circ$  also observation gaps for large elevations are visible. Not surprisingly, the satellite tracks are visible, especially for GRACE-A and OSTM/Jason-2. The bias in the GOCE residuals (cf. Tab. 4.4) is due to the fact that GOCE azimuth-nadir range corrections have not been considered. According to Bock et al. (2014) these corrections range from  $-15$  to  $-30$  mm. Fig. 4.19 shows the SLR residuals derived for OSTM/Jason-2 depending on the Sun's position with respect to the satellite. The corresponding coordinate system is a  $(\Delta u, \beta_0)$ -system based on the difference  $\Delta u$  in the argument of latitude between Sun and satellite and the elevation  $\beta_0$  of the Sun above the orbit plane, respectively. This plot type is described in detail by Flohrer (2008). The satellite crosses the plot on a horizontal line from left to right during one orbital period. Systematic effects are visible as mainly positive SLR residuals, up to 5 cm, are derived for  $\Delta u$  values close to  $180^\circ$ , which corresponds to shadow crossings for  $|\beta_0| < 40^\circ$ . Mainly negative residuals up to  $-3$  cm are obtained for the opposite orbit region, where OSTM/Jason-2 is close to the Sun's direction as seen from the Earth. As the negative values refer to a closer distance to the Earth, the systematics are most probably related to remaining issues in the solar radiation pressure modeling.

In general, the derived SLR residuals confirm the orbit accuracy level of a few centimeters.

### 4.3.5 Long-term GRACE-A Solution

After analyzing the orbit results for GRACE, GOCE, and OSTM/Jason-2 from 2010 till end of 2012 and discussing the orbit accuracy achieved, also a long-term orbit determination was performed. To do this GRACE-A GPS observations were processed for the time period from 2003 till end of 2012. It has

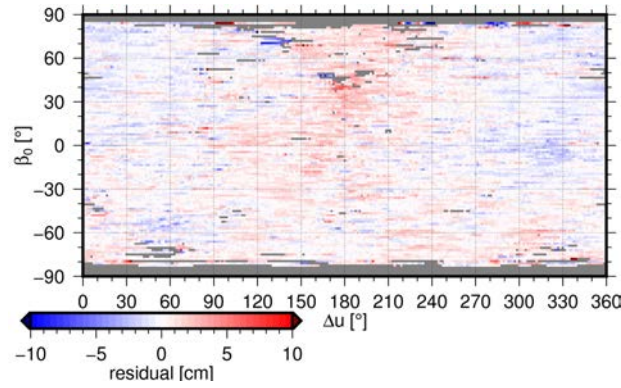


**Fig. 4.19:** OSTM/Jason-2 SLR residuals in an argument of latitude vs  $\beta_0$  angle plot

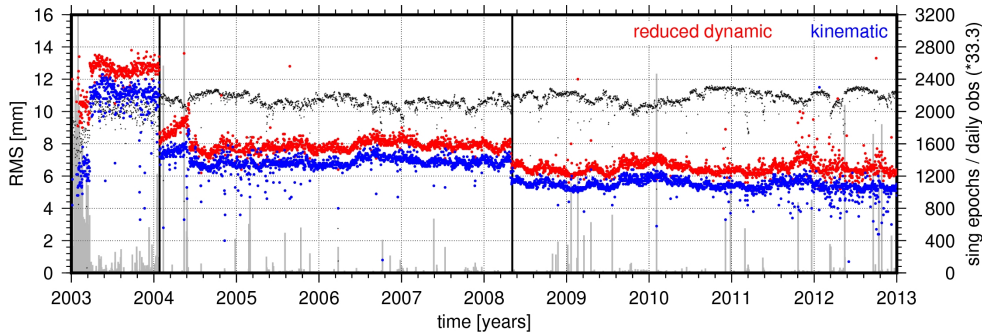


**Fig. 4.20:** Phase residuals of the GRACE-A long-term orbit solution; reduced-dynamic solution (*red*) and kinematic solution (*blue*); number of observations (*black dots*), number of epochs with less than four suitable observations (*gray bars*); the vertical black lines indicate the change from 300 s to 30 s and from 30 s to 5 s GPS clock corrections

to be mentioned that, contrary to the solutions previously discussed, these orbits were determined with pseudo-stochastic orbit parameters estimated every 15 minutes instead of every 6 minutes. Fig. 4.20 shows for each day the number of available observations, the number of epochs with less than four suitable observations, and the RMS of the remaining phase residuals. Since operational GPS products were used, the GPS final products introduced were changed twice within the analyzed 10 years in order to benefit from the improved IGS processing strategies. GPS clock corrections in 30 s instead of 300 s intervals were introduced firstly on January 23, 2004. Secondly, 5 s interval GPS clock corrections became available on May 5, 2008. In all cases CODE products were used for consistency reasons. However, especially for the time before 2004, denser clock corrections are available provided by other IGS analysis centers (e.g., from MIT). The number of GPS observations available per day is stable between 70'000 and 80'000, equivalent to eight to nine GPS satellites tracked per epoch. The daily RMS of the carrier phase residuals is given in Fig. 4.20 for the reduced-dynamic and the kinematic orbit solution. The kinematic orbit solution is

**Tab. 4.5:** Statistics for phase residuals of the GRACE-A long-term orbit solution; mean RMS value and its standard deviation; the GPS satellite clock products are the final CODE clocks introduced to the processing; unit: cm

time span	reduced-dynamic solution	kinematic solution	GPS satellite clock interval
01.01.2003 - 23.01.2004	1.38±1.18	1.01±0.20	CODE 300 sec
01.01.2003 - 22.03.2003	1.12±0.43	0.62±0.07	CODE 300 sec
22.03.2003 - 23.01.2004	1.44±1.27	1.09±0.11	CODE 300 sec
23.01.2004 - 05.05.2008	0.82±0.31	0.69±0.05	CODE 30 sec
05.05.2008 - 31.12.2012	0.71±0.90	0.54±0.05	CODE 5 sec

estimated, as described above, by a zero-difference precise point positioning. An offset of 2-3 mm exists for the derived RMS values with higher values for the reduced-dynamic solution. This difference is clearly related to the larger number of estimated parameters in the case of the kinematic orbit. In the kinematic case, where for each epoch at least four parameters, have to be estimated, the degree of freedom is rather small compared to that of the reduced-dynamic approach. Consequently, the remaining residuals are smaller for the kinematic orbits. A similar effect is present for the first days of 2003 where no kinematic solutions were estimated for more than one quarter of the daily epochs due to very few observations. The resulting kinematic orbit suffers from significant gaps, whereas the derived RMS of the residuals gets, in principle, smaller. Concerning the introduced GNSS satellite clock corrections, a reduction in the RMS time series can be seen for both, reduced-dynamic and kinematic orbit solutions. Especially, the usage of 30 s GPS clock corrections leads to an improvement of 6 and 4 mm for the kinematic and reduced-dynamic solutions, respectively. Tab. 4.5 provides the mean values of the daily RMS values including their standard deviations for the reduced-dynamic and the kinematic orbit solution. The mean values confirm the above mentioned difference of 2-3 mm between the two orbit types. Also the significant impact of the introduced GNSS clock corrections is evident. When looking at the standard deviations a few days with large RMS values of up to 100 mm are found that remain in the reduced-dynamic orbit determination are causing the substantially higher standard deviations. When analyzing both, the number of observations and the RMS curves, several anomalous periods can be identified related to spacecraft issues. In the following, those that are relevant in the subsequent paragraphs will be discussed. Increased RMS values and a decreased number of observations are found between April and May 2004. The effect is most probably related to shadowing effects caused by a piece of insulation next to the GPS antenna, which was discovered in June 2004<sup>9</sup>. Meyer et al. (2015a), who reported a similar increase in their orbit results, recommend to apply a specific PCV for the period from February 29 to June 8, 2004, as they found azimuth/elevation-depend systematics of up to  $\pm 20$  mm in the residuals. Another issue is visible for March 2011, where the number of observations drops down to less than 60'000. Driven by an attitude mis-orientation the GRACE-A GPS receiver was limited to eight channels between March, 8th and March, 18th in order to save battery power<sup>10</sup>. The reason for the reduced number of observations in April and May 2012 is not yet clear. It might be caused by switching off some satellite system components to save power<sup>11</sup>. Starting end of 2011 the reduced-dynamic solution gets weaker as indicated by a higher scatter of the derived RMS values. Most probably this is a result of the lower altitude discussed in the next paragraph.

Variations in GRACE-A orbital elements are discussed within this paragraph. Fig. 4.21 shows the time series and amplitude spectra for the orbital elements semi-major axis  $a$ , numerical eccentricity  $e$ , inclination  $i$ , right ascension of the ascending node  $\Omega$ , and argument of the perigee  $p$  as estimated in the BSW orbit determination process. The semi-major axis was initially at 6870 km, i.e., GRACE-A had an altitude of 492 km. A significant decrease down to 6810 km occurred during the considered 10 years. Interestingly, a deceleration down to 2 km/yr is present for 2006 to 2011 and an acceleration to around 12 km/yr afterwards. The correlation between descent and solar activity is obvious in view of the higher solar activity in 2003/2004 and 2011/2012 (cf. Sect. 2.2.1). The connecting mechanism is that an increasing solar activity leads to an increase in the air density, which causes via air drag the observed altitude decrease. Obviously, the mission provider did not maintain the altitude to keep the initial altitude in order to save fuel. Consequently, the increased RMS values in Fig. 4.20 in 2012 are related to modeling issues regarding the higher air density, aggravated by the lower altitude. Meanwhile the semi-major axis decreased to 6740 km<sup>12</sup>. The numerical eccentricity is rather small and stable at a level of  $0.002 \pm 0.001$  but has a significantly periodic signal at 92 days, which is very close to a 94-day period found for GRACE's argument of perigee (Larson et al., 2007). The inclination shows also a very stable behavior at  $89^\circ$ . The corresponding amplitude spectra show signals at the same periods that those found for the semi-major axis. For example, the

<sup>9</sup> Monthly Report 06/04, available via ISDC

<sup>10</sup> Monthly Report 03/11, available via ISDC

<sup>11</sup> Monthly Report 04/12, available via ISDC

<sup>12</sup> corresponding to  $\approx 20$  km per year; <http://www.csr.utexas.edu/grace/operations/configuration.html>, accessed May 2016

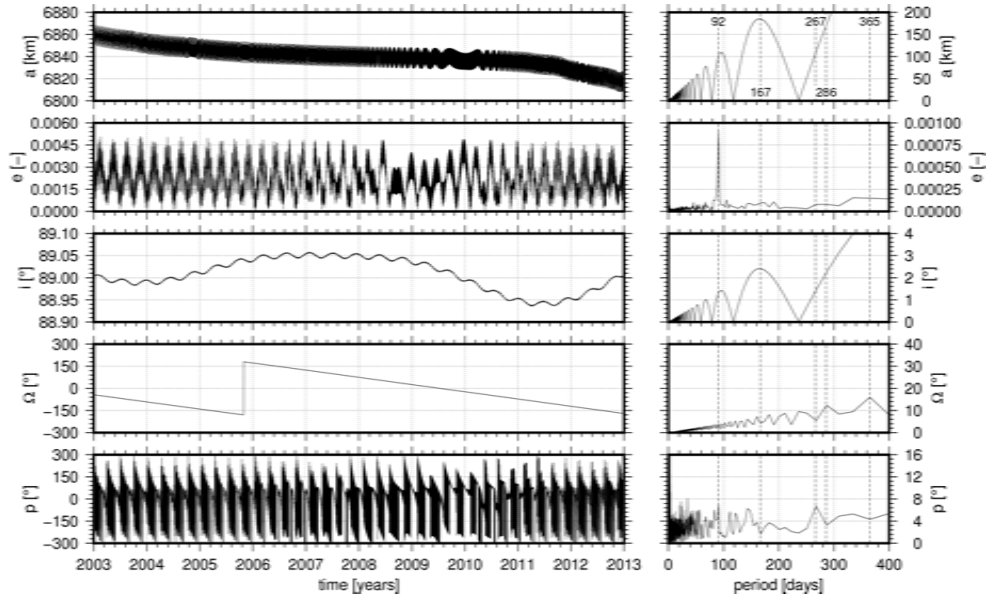


**Fig. 4.21:** GRACE-A orbital elements: semi-major axis  $a$ , numerical eccentricity  $e$ , inclination  $i$ , right ascension of the ascending node  $\Omega$ , and argument of the perigee  $p$ ; time series and amplitude spectra

nearly semi-annual period of  $\approx 167$  days seems to be driven by the semi-diurnal S2 tide (Chen et al., 2009). Due to the nearly polar inclination, the right ascension of the ascending node shows a relatively slow drift of  $\approx 50^\circ/\text{yr}$ . The argument of perigee shows a 94 day period caused by the orbit geometry as mentioned above.

The comparison between kinematic and reduced-dynamic orbit solutions allows the analysis of the overall quality of the orbit models and parameterization introduced, as the kinematic orbit is not affected by them. In Fig. 4.22 the daily RMS of the corresponding orbit differences is plotted for the three orbit components. The orbit comparison was done without estimating any Helmert transformation parameters as both orbits are derived with the same software and the same datum definition and ERPs. The differences show considerable jumps in accordance with the changes in the introduced GPS satellite clock corrections. This behavior is present, especially, in the radial component, where jumps of  $\approx 3$  cm and  $\approx 1$  cm occur at the switching epochs. The large differences visible for the time period before January 23, 2004, are related to a less accurate kinematic orbit determination, when 300 s clock corrections were introduced. A weaker orbit quality is present after summer 2011 due to the higher solar activity around this time period. The differences are larger than 3 cm in all components for the time period before January 23, 2004. Afterwards, a stable level of 3 cm in radial and along-track, and 2 cm in cross-track is achieved. The overall mean RMS is 3.3 cm, 2.7 cm, and 2.3 cm in radial, along-track, and cross-track. Considering the amplitudes, the same periods of 308 and 154 days are present in all three components. These periods coincide with the periods of the  $\beta_0$  angle of GRACE, which amounts to 322 days. As  $\beta_0 = 0$  happens twice a year or every 161 days, the detected periods are most probably related to a mismodeling of the non-gravitational forces. Meyer et al. (2015a), however, saw a correlation between the measurement noise and the  $\beta_0$  angle for a kinematic GRACE orbit determination.

In a second step, an external orbit solution is used to validate the long-term reduced-dynamic solution for GRACE-A (Fig. 4.23). The reference orbits provided by the GRACE mission were considered as described already in Sect. 4.3.3. However, for some days, especially in the early years, the temporal resolution of the reference orbit positions and velocities is only 60 s instead of 10 s. To distinguish the different temporal resolutions, RMS values derived from the 60 s-spaced orbits are marked in gray; they are not considered for the computation of the statistical information given in Fig. 4.23. In summary, the mean values for the daily RMS are 1.3 cm, 2.0 cm, and 1.5 cm in radial, along-track, and cross-track, respectively. However, some time periods showing higher differences. This involves the time before January 23, 2004 and the time

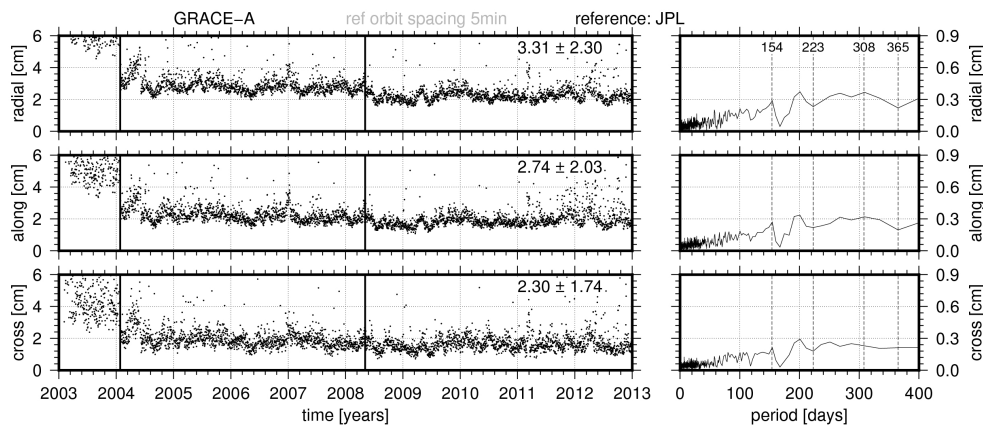


**Fig. 4.22:** Orbit comparison GRACE-A reduced-dynamic solution against kinematic orbit solution; without estimating transformation parameters; time series and amplitude spectra

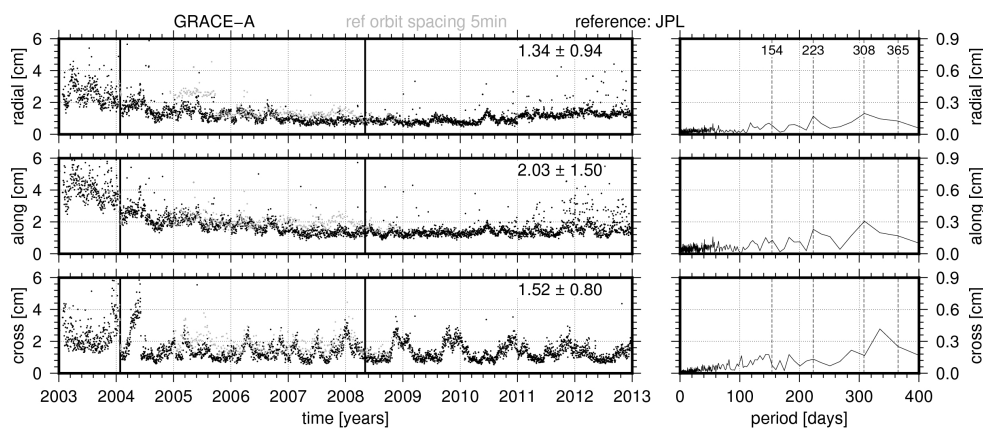


**Fig. 4.23:** Orbit comparison GRACE-A reduced-dynamic solution against JPL GPS-based orbit solution; without estimating transformation parameters; days, where the JPL orbits have a spacing of 60 s are marked in (*gray*); time series and amplitude spectra

after Summer 2011. However, the RMS values are smaller than for the comparison against the kinematic orbit. Larger differences are also present for April and May 2004, especially in cross-track, where the RMS exceeds 4 cm. Concerning the results after November 2011 a re-optimized orbit parameterization was applied for the official GRACE orbits<sup>13</sup>. A periodic behavior is present in the out-of-plane direction for the time after 2005 and especially after 2008. This annual effect is most probably caused by differences in the datum definition. In along-track again periods of 308 and 154 days are detected. Both periodic signals are related to  $\beta_0$  angle mentioned above and discrepancies in the modeling of non-gravitational perturbations.

The analysis of the transformation parameters and their frequency behavior allows further insight into systematics effects between both orbit solutions. Fig. 4.24 shows the derived time series and amplitude spectra for the three translations and the scale parameter. A jump between the orbits derived by introducing 300s and 30s clock corrections is present in all transformation parameter time series. Periodic signals close to an annual period occur in all translations. A small trend of 2 mm per year is visible in the z-translation. Stranger is, however, that several jumps occur in the scale. The first one of 1 ppb is found as expected at the GPS product change in 2004. However, a second one of 1.2 ppb occurs on January 1, 2011. In Fig. 4.12 a radial offset was found between the RMS values for the comparison with and without the estimation of transformation parameters. This offset amounted to 6 mm, which is close to the 8 mm corresponding to 1.2 ppb at a geocentric distance of 6840 km. The reason for this jump is most probably related to the PCV considered in the official GRACE orbit solution. However, it has to be mentioned that, for the period between 2004 and 2011, the scale factor is close to zero. Also somehow strange, the derived

<sup>13</sup> Monthly Report 11/11, available via ISDC

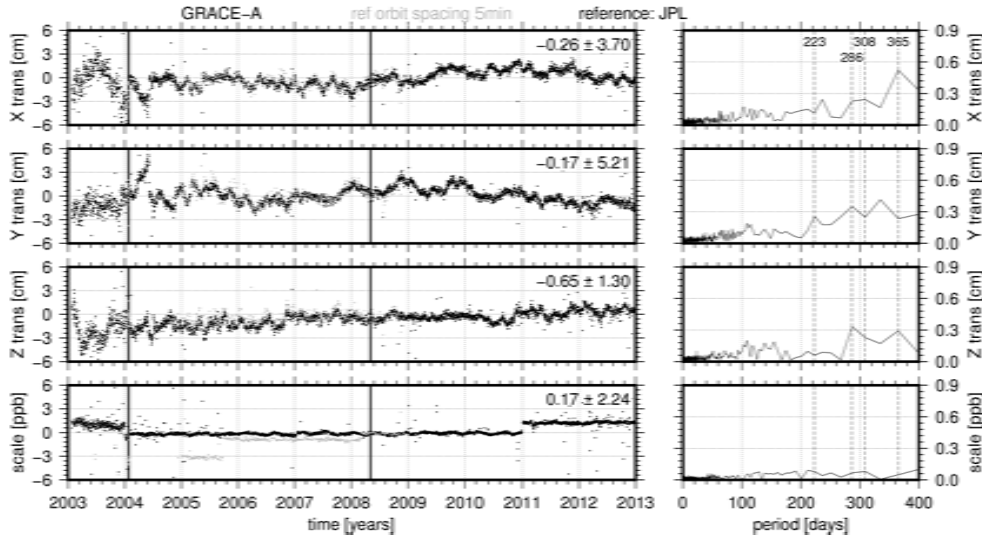


Fig. 4.24: Helmert transformation parameters for GRACE-A reduced-dynamic solution against with respect to the JPL orbit solution; time series and amplitude spectra

scale values show significant differences, when the 60 s spaced reference orbits were used.

#### 4.4 Impact of Non-Gravitational Forces and Pseudo-Stochastic Parameters on the Orbit Determination

Within this section the impact of the non-gravitational forces namely air drag, solar radiation pressure, and Earth radiation pressure on the orbits is discussed by studying the influence of modeling them a priori in the framework of reduced-dynamic LEO orbit determination. As described in Sect. 4.2.2 the significant impact of non-gravitational forces on LEOs can be taken into account by a priori models or by estimating pseudo-stochastic orbit parameters. Therefore, this section aims at answering the following two questions:

- What is the impact of modeling non-gravitational forces a priori on the orbit determination?
- How many pseudo-stochastic orbit parameters are required for a reasonable reduced-dynamic orbit determination, if non-gravitational forces are modeled a priori?

This study involves both GRACE satellites and OSTM/Jason-2. GOCE was omitted within this study as (1) the spacecraft operated mainly in a drag-free mode, where air drag, as the main non-gravitational force, was compensated by the ion propulsion assembly and (2) as no satellite macro-model was available. The orbit determination followed the strategy described above including the estimation of empirical constant and once-per-revolution parameters in radial, along-track, and cross-track. In view of the periodic nature of the non-gravitational forces (see Sect. 4.2.2), a large part of the corresponding periodic accelerations might be absorbed by these empirical parameters. In order to show larger improvements and to highlight the benefits of modeling non-gravitational forces, one might decide to not estimate empirical parameters. However, they are setup in the study presented here. Within this study the following solutions were generated:

- **AIR+SRP+ALB**: air drag, solar radiation pressure, and Earth albedo (based on CERES data) were considered,
- **NON**: non-gravitational forces were not corrected a priori,
- **AIR**: only air drag was considered,
- **SRP**: only solar radiation pressure was considered,
- **ALB**: only Earth albedo (based on CERES data) was considered.

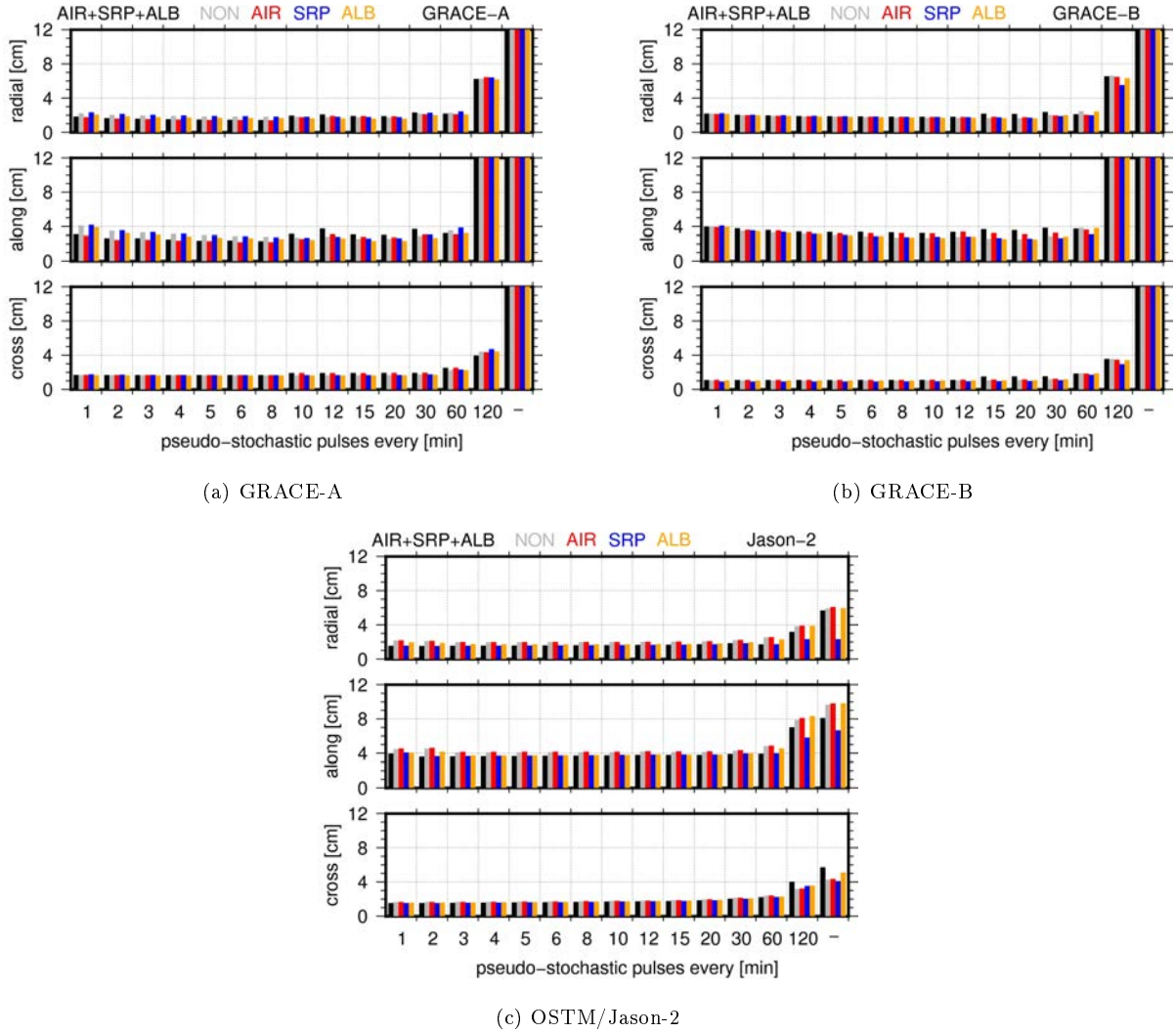
For each solution several sub solutions (**A**, **B**, ..., **O**) with a different number of pseudo-stochastic orbit parameters were generated as listed in Tab. 4.6. The weight of the estimated orbit parameters remains at  $5 \text{ nm/s}^2$ . The time period from August 28 to December 6, 2011, which was a period of higher solar activity, was considered for this study (Fig. 2.2), higher air drag (Fig. 4.8), and also larger orbit differences with respect to the reference orbits (Fig. 4.12-4.15). The selected period is, therefore, more challenging for studying the impact of non-gravitational forces.

Fig. 4.25 shows the average daily RMS of the orbit differences. The orbits described in Tab. 4.2 were used as reference orbits. In the sub-solution **A** (1 minute spacing) an improvement from NON to AIR+SRP+ALB of 4 mm, 10 mm, and 1 mm is visible for GRACE-A in radial, along-track, and cross-track, respectively. These improvements remain also for orbits of up to a parameter spacing of 8 minute (sub-solutions **A-G**). Comparing the three “single-force” solutions (AIR, SRP, ALB) it is obvious that the improvement is dominated by air drag modeling. Interestingly, such improvements are not visible for GRACE-B. As shown already in Sect. 4.3, there are considerable differences in the orbit comparison of GRACE-A and GRACE-B. For orbits with 10 to 30 minute parameter intervals (sub-solutions **H-L**), the solution AIR+SRP+ALB shows larger differences than the solution NON. As this is visible mainly in along-track the differences might be due to deficiencies in the air drag modeling in combination with the estimation of empirical accelerations, while the number of parameters is reduced. The orbits from sub-solutions **N** and **O** (120 minute spacing and no parameters) shows considerably larger average RMS values. Tab. 4.7 shows the mean RMS values for the comparison of the solutions AIR+SRP+ALB and NON (sub-solutions **F**, **N**, and **O** only) against kinematic and reference orbits, respectively. In both comparisons no clear evidence can be found for improvements due to modeling non-gravitational forces. Obviously, empirical once-per-revolution parameters compensate to a large part the non-gravitational accelerations, while the remaining part goes directly into the orbit differences. From Tab. 4.7 it is clear, however, that in the current implementation a dynamic orbit determination is not possible for GRACE, already a less reduced-dynamic approach with only 12 parameter sets results in an orbit accuracy at the decimeter level. From both, GRACE-A and GRACE-B, one can conclude that a spacing between 6 and 10 minute is suitable but values up to 60 minute might also be acceptable. For the OSTM/Jason-2 spacecraft with a higher altitude, similar results are determined for all orbits with stochastic-orbit parameters estimated every 1 up to every 60 min. Driven by the modeling of the solar radiation pressure, an improvement of 5 mm, 7 mm, and 3 mm is observable in radial, along-track, and cross-track, respectively, when comparing AIR+SRP+ALB to NON. For sub-solutions **M**, **N**, and **O**, quite acceptable orbits with differences below 10 cm with respect to the reference solutions are obtained. If only the solar radiation pressure is modeled, the radial component remains almost similar for all sub-solutions and the mean RMS remains below 10 cm and 6 cm for along-track and cross-track, respectively. As visible in sub-solutions **N** and **O**, there are some modeling issues remaining considering air drag and Earth albedo.

In a second step, an SLR validation is performed for each sub-solution and the derived residuals are analyzed. Fig. 4.26 shows the corresponding mean SLR residuals and their standard deviations for the derived SLR residuals. Obviously, for all three satellites, the derived standard deviations are similar within the sub-solutions **A** to **K**. This is also confirmed by a subset of these values provided in Tab. 4.8. As shown there, the standard deviation between the sub-solutions **A**, **F**, and **J** varies by not more than

**Tab. 4.6:** Set up of pseudo-stochastic orbit parameters; the number of parameters (# pulses) contains the number of estimated pseudo-stochastic orbit parameters for a 24 h arc (please note that 3 parameters are estimated per epoch corresponding to the three orbit components)

Sub-solution	A	B	C	D	E	F	G	H	I	J	K	L	M	N	O
Spacing [min]	1	2	3	4	5	6	8	10	12	15	20	30	60	120	-
# Parameters	4320	2160	1440	1080	864	720	540	432	360	288	216	144	72	36	-



**Fig. 4.25:** Impact of orbit modeling on the RMS of the orbit comparison with the reference orbits for GRACE and OSTM/Jason-2 (see. Tab. 4.2); no transformation parameters were estimated

**Tab. 4.7:** Impact of modeling non-gravitational forces on the RMS of the orbit comparison with reference orbits for GRACE and OSTM/Jason-2; averaged daily RMS values and their standard deviations are given; identifiers: (1) AIR+SRP+ALB against kinematic orbit, (2) NON against kinematic orbit, (3) AIR+SRP+ALB against reference orbit, (4) NON against reference orbit

sat	s	solution F (6 min spacing)			solution N (120 min spacing)			solution O (no parameters)		
		orbit comparison: averaged daily RMS and standard deviation [cm]								
		radial	along	cross	radial	along	cross	radial	along	cross
GRCA	1	4.3±5.7	4.0±5.6	3.0±4.1	7.1±6.2	11.1±7.7	4.7± 6.6	36.1±35.7	147.5±59.0	22.3±34.2
	2	3.6±3.4	3.4±3.6	2.4±2.2	7.1±6.9	11.3±8.1	5.2±10.2	36.4±37.9	142.6±61.6	22.1±28.3
GRCB	1	4.3±5.2	4.5±6.7	3.0±4.9	7.2±6.3	11.9±8.9	4.4±6.6	32.9±34.3	146.0±59.0	19.5±26.3
	2	4.3±4.6	4.1±5.9	2.8±3.7	7.0±5.1	11.8±9.2	4.4±4.5	33.5±34.8	144.8±61.2	21.7±31.2
JAS2	1	5.1±4.6	4.3±4.9	4.1±4.6	6.2±9.1	5.8±10.9	5.9±10.6	9.0±34.0	8.6±18.6	8.1±27.0
	2	5.1±3.9	4.1±2.8	4.0±4.2	6.3±7.8	6.4±10.4	5.3± 7.8	8.7±28.0	9.9±23.0	7.0±22.0
GRCA	3	1.5±1.1	2.4±3.7	1.7±0.5	6.2±5.9	13.4±17.5	4.0± 6.4	36.0±36.0	147.9±59.3	22.0±34.3
	4	1.8±2.9	2.9±5.5	1.6±0.5	6.3±7.0	12.7±16.2	4.4± 9.5	35.9±36.4	143.1±61.8	21.6±28.2
GRCB	3	1.9±1.9	3.4±6.5	1.1±0.4	6.6±6.6	13.8±17.8	3.6±5.4	32.8±34.5	146.7±59.2	19.4±26.9
	4	1.8±1.6	2.9±5.5	1.0±0.3	6.6±8.1	13.8±19.6	3.6±4.2	33.3±34.9	145.5±61.4	21.5±31.3
JAS2	3	1.6±0.5	3.7±1.1	1.6±0.4	3.2±10.9	7.0±19.4	4.0±12.8	5.7±33.7	8.1±19.2	5.7±27.0
	4	2.0±2.8	4.1±3.9	1.7±0.7	3.8±10.0	7.9±19.1	3.2± 6.5	5.9±28.1	9.7±22.7	4.3±21.0

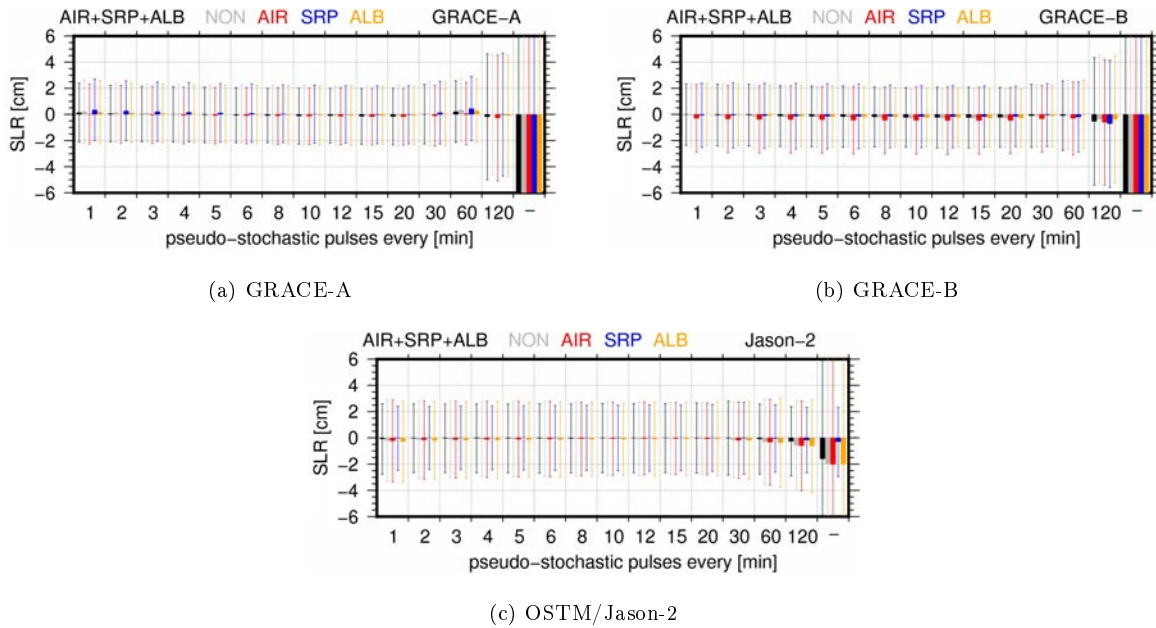


**Fig. 4.26:** Impact of orbit modeling on the SLR validation for GRACE and OSTM/Jason-2

2 mm. Comparing the different solutions (NON, AIR+SRP+ALB, etc.), also no significant differences in the standard deviations are visible, except for OSTM/Jason-2, where again benefits from modeling solely solar radiation pressure are present. The mean values, expressing systematic effects in radial direction, differ without visible systematics between the solutions. No systematic difference can be found between the two GRACE spacecraft. However, higher mean SLR residuals are observable for GRACE-B in solution AIR. This is most probably caused by a spacecraft-specific issue as other effects, like air density model imprecision or an inaccurate macro-model, should affect GRACE-A in the same way. However, due to the outlier detection the number of observations considered is reduced for sub-solution **N** to 95 % and for **O** to only 25 % of the number of normal points considered in sub-solution **A**. In the case of OSTM/Jason-2 the mean SLR residuals are substantially reduced in solution SRP, confirming once again the importance of modeling solar radiation pressure for this satellite. Larger mean values and standard deviations are obtained for all satellites in the sub-solutions **M**, **N**, and **O**. The systematic mean SLR residuals reach values of decimeters for GRACE-A and GRACE-B with standard deviations up to 1 m. For OSTM/Jason-2 systematics of some millimeters and standard deviations of 2-3 cm are still acceptable for sub-solutions **M** and **N**. For a dynamic solution with solar radiation pressure modeling the SLR residuals are biased by only 3 mm and the standard deviation is also below 3 cm. The number of outliers increases only slightly for OSTM/Jason-2, 2.1 % of the SLR data considered in sub-solution **A** are marked in **O**. This result impressively shows, however, the benefits from modeling non-gravitational forces, especially the solar radiation pressure.

## 4.5 Orbit Determination from Single-frequency GPS Observations

### 4.5.1 The Nano-satellite Mission CubETH

The satellite mission CubETH (Fig. 4.27) is a cooperative Swiss CubeSat mission involving ETH Zurich, EPF Lausanne, several universities of applied sciences, and Swiss companies (Ivanov et al., 2014; Willi et al., 2015). The mission aims for technology demonstrations and proof-of-concepts concerning GNSS-based navigation by carrying commercial-of-the-shelf single-frequency GNSS receivers provided by the Swiss

**Tab. 4.8:** Impact of modeling non-gravitational forces on GRACE and OSTM/Jason-2 orbits as seen by SLR

satellite	parameters every [min] solution	A (1 min)	F (6 min)	J (15 min)	M (60 min)	N (120 min)	O (-)
		mean and standard deviation from SLR Validation [mm]					
GRCA	AIR+SRP+ALB	1.4±22.5	-0.6±21.1	-1.5±21.4	2.2±23.5	-1.9±48.1	-112.6±371.7
	NON	2.1±24.3	0.1±22.5	-0.9±22.6	3.4±23.9	-0.3±46.0	-259.4±768.0
	AIR	0.3±22.9	-1.0±21.5	-1.8±21.6	0.7±23.9	-2.8±48.0	-100.7±305.0
	SRP	3.5±23.5	0.9±22.3	-0.3±22.2	4.5±24.5	-0.2±47.0	-265.2±863.1
	ALB	1.8±24.1	-0.1±22.3	-0.8±22.3	2.8±24.4	-1.0±46.6	-328.1±953.4
GRCB	AIR+SRP+ALB	-0.2±23.5	-1.7±23.4	-2.4±23.3	-1.0±26.6	-5.4±48.7	-105.8±475.0
	NON	-0.5±24.2	-2.2±22.9	-2.9±22.6	-0.3±26.5	-3.8±49.2	-188.7±821.4
	AIR	-3.0±25.8	-4.4±25.9	-4.7±25.6	-3.1±27.9	-6.1±48.2	-264.2±1110.3
	SRP	-0.8±24.5	-1.6±24.8	-1.7±23.4	-2.0±26.8	-7.2±48.6	-186.5±842.0
	ALB	0.0±23.7	-1.8±23.3	-2.7±22.5	0.3±26.2	-3.7±48.6	-140.5±699.1
JAS2	AIR+SRP+ALB	-0.9±26.9	-0.4±26.3	-0.1±26.4	-1.0±26.7	-2.7±26.4	-16.1±247.2
	NON	-2.1±31.2	-0.9±28.5	-0.6±27.7	-3.0±32.7	-5.8±34.3	-19.9±208.4
	AIR	-2.4±31.2	-1.0±28.7	-0.5±27.4	-3.3±32.7	-6.1±34.2	-20.3±210.6
	SRP	-0.3±24.4	0.0±24.6	0.0±25.1	-0.5±25.7	-1.8±24.9	-3.1±26.4
	ALB	-2.9±31.0	-1.3±28.5	-0.9±27.9	-3.8±34.0	-6.3±35.4	-20.2±210.7

**Fig. 4.27:** Artists interpretation of CubETH (provided by F. Neyer, ETH Zürich)

manufacturer u-blox<sup>14</sup>. These low-cost receivers are able to track all major GNSS, i.e., GPS, GLONASS, QZSS, Galileo and Beidou, and will be connected pairwise to five patch antennas. In addition, CubETH will carry very small retro-reflectors allowing SLR tracking for orbit validation. CubETH will have a size of 10×10×10 cm and a weight not larger than 1.3 kg, thus, following the CubeSat single-unit guidelines<sup>15</sup>. The launch is planned for 2017 with a mission duration of about 2.5 years considering the aspired orbiting altitude of 450 km. Three major scientific objectives are defined for the CubETH mission, they are: (1) assessment of precise orbit determination strategies, (2) characterization of attitude determination based on short baselines, and (3) comparison of the performance in space between GPS, GLONASS, Galileo and BeiDou. Concerning the last objective, it is very likely that CubETH will bring the first multi-GNSS receiver in space. Apart from these scientific goals, as a joint project of many educational institutions and companies across Switzerland, CubETH will be a milestone for the Swiss space community. As stated in the CubETH science concept, the benefits for Swiss scientific and educational institutions and industrial partners results from the joint development of seminal nano-satellite concepts and miniaturized components<sup>16</sup>. This will be important concerning future formation flying and constellation missions, where miniaturized, inexpensive satellites and sensors are crucial.

<sup>14</sup> NEO-7N (<https://www.u-blox.com/de/product/neo-7-series>, accessed May 2016) and NEO-8N (<https://www.u-blox.com/de/product/neo-m8qm8m-series>, accessed May 2016) receivers will be carried

<sup>15</sup> available at <http://www.cubesat.org/>, accessed June 2016

<sup>16</sup> [www.mpg.igp.ethz.ch/cubeth.html](http://www.mpg.igp.ethz.ch/cubeth.html), accessed July 2016

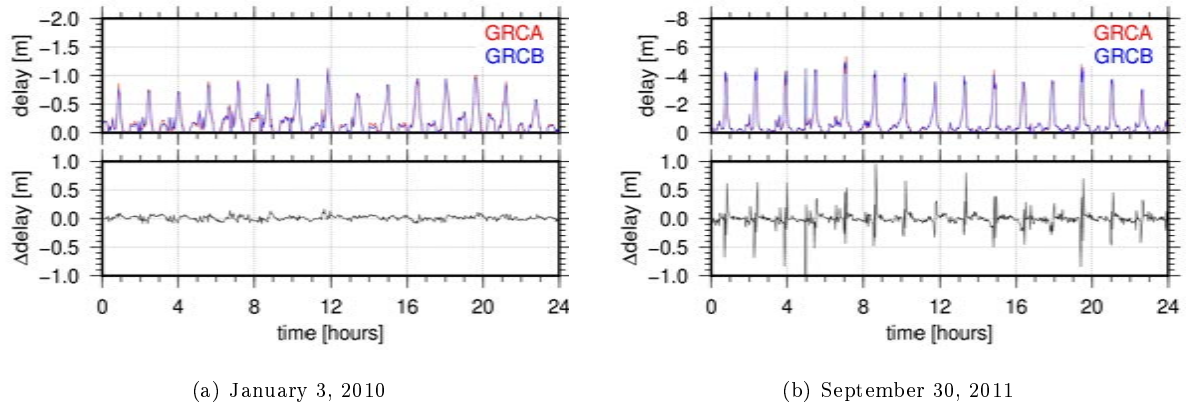


**Fig. 4.28:** Ionospheric zenith delays for GRACE-A and GRACE-B derived from code observations; *below* delay difference GRACE-B - GRACE-A; please note the different scales in sub-figures (a) and (b)

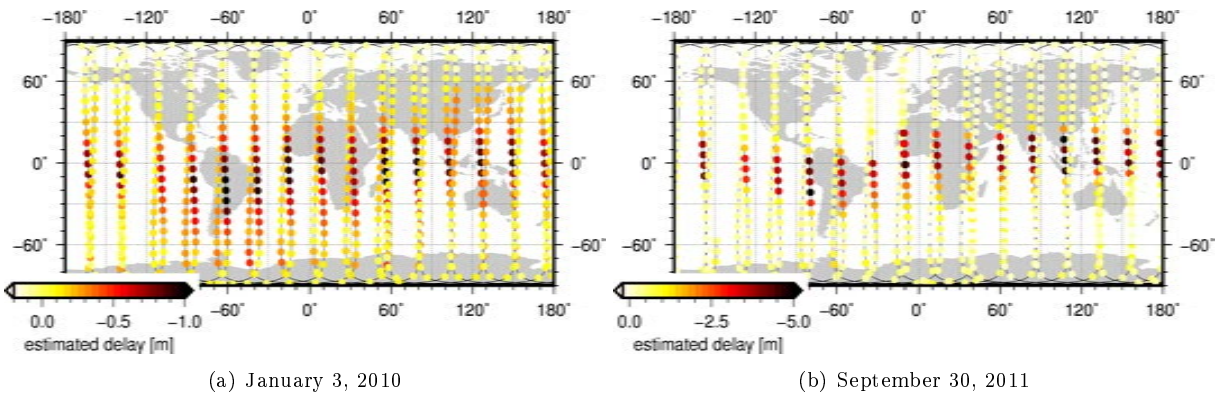


**Fig. 4.29:** Geographical distribution of estimated ionospheric zenith delays for GRACE-A derived from code observations; please note the different scales in figure (a) and (b)

#### 4.5.2 The Impact of the Ionosphere on LEO Orbit Determination

During preparations for the precise orbit determination on-board CubETH, the question arose how the signal delay caused by the ionospheric layers above the spacecraft could be compensated. Based on practical considerations, this can only be done by using the single-layer based Klobuchar model (Klobuchar, 1987). This model was designed to reduce about 50 % of ionospheric range error for ground stations and allows the computation of the slant delay corrections from the vertical delay at the ionospheric piercing point and a mapping function. The vertical delay is computed based on the eight coefficients  $\alpha_n, \beta_n, (n = 0..3)$ , which are broadcast as part of the GPS broadcast message. However, for LEO applications an adapted Klobuchar model has to be used, e.g., by applying a scaling factor based on an additional integration of the Chapman function for the LEO orbit height. To ensure a suitable modification of the Klobuchar model, the ionospheric delays as seen by existing LEOs were estimated within a small study.

The computation was done by forming the geometry-free linear combination with LEO-based GPS code observations, i.e.,  $P_4 = P_1 - P_2$ . The ionospheric zenith delays were computed with a 2 minute spacing for GRACE-A, GRACE-B, and GOCE by considering the zenith angle  $z$  and the ionospheric mapping function to transform the slant delay  $I_s$  into the vertical delay  $I_v$  (Schaer, 1999)

$$I_v = I_s \cdot \cos\left(\frac{R_E}{R_E + H} \cdot \sin z\right). \quad (4.15)$$

The Earth radius is  $R_E$  and  $H$  is the height of the assumed ionospheric single-layer. The elevation cutoff for this analysis was set to  $15^\circ$ , as observations at lower elevation may introduce biases since they might

cross ionospheric bulges. In order to analyze different ionospheric situations, a quiet and an intense stormy day were selected with January 3, 2010 and September 30, 2011. The minimal  $D_{st}$  values for both days were -13 and -137, respectively. Due to the code measurement noise, the accuracy of the derived ionospheric delays might not be better than 20 cm. Corrections for the DCBs were introduced as provided by CODE. The formal errors, however, are around 2 cm. Fig. 4.28 shows the derived ionospheric zenith delays. The largest delays of -1 m and -4 m occur for daylight crossings of the magnetic field's equatorial region. The peaks in-between, reaching 0.5 to 1 m, are related to the second equator crossing within one orbit period. The minima between both peaks are attributed to less strong ionospheric activity in the polar regions. For some of the large maxima during September 30, 2011, not only one single but two peaks are visible (e.g. peaks at 2 h and 19.5 h). This is related to bifurcation describing the splitting of the ionospheric F-layer into maxima located north and south of the magnetic equator. Fig. 4.29 shows the geographical distribution of the derived ionospheric zenith delays along the GRACE-A ground track. Maximal values occur along the magnetic equator especially for the day tracks, when GRACE-A flew in north-south direction. The smallest values can be found close to the poles. For September 30, 2011 (Fig. 4.29 (b)), bifurcation effects can be found for the illuminated equatorial crossings at  $80^\circ$  W,  $105^\circ$  E, and  $155^\circ$  E. A very special comparison can be done between the ionospheric delays derived for GRACE-A and GRACE-B. Theoretically, the differences should be very small as the 2 minute sampling rate for the ionospheric delay is larger than the temporal separation between both satellites, since the  $\approx 200$  km distance corresponds to 29 seconds flight time at 450 km altitude. Therefore, significant differences might only be expected during stormy ionosphere conditions in the equatorial region. Differences below 10 cm confirm this assumption for January 3, 2010. In the case of September 30, 2011, however, peaks of up to 1 m are visible. Considering the fact that the illuminated tracks are north-south oriented and that GRACE-B is leading, positive differences occur north of the magnetic equator and negative ones south of the equator. Obviously, the observed differences are related to the active ionosphere and especially to the bifurcation effects mentioned above.

In order to estimate the resulting effect on a single-frequency orbit determination, GRACE-A  $L_1$  GPS observations were processed for December 25, 2012. A similar study was presented by Bock et al. (2009) who assessed several approaches to correct the ionospheric delay for single-frequency GRACE and MetOp orbit determination. Comparing the usage of (1) GIMs, (2) the GRAPHIC linear combination<sup>17</sup>, and (3) Stochastic Ionosphere Parameters they concluded that either approach (2) or (3) should be applied. For the analyzed period in mid-2007, they showed orbit differences (daily RMS) below 10 cm with respect to a reference  $L_3$  solution. However, it has to be mentioned that they selected a period of weak ionospheric activity and days without eclipses. GRACE-A also experienced no eclipse, for the day analyzed within this study (December 25, 2012) as the  $\beta_0$  angle was around  $-66^\circ$ . Fig. 4.30 shows the orbit comparison between single-frequency kinematic and reduced-dynamic orbits against a ionosphere-free solution as reference. Obviously, the main effect is observed in the radial component, where differences of up to 6 m occur. In the kinematic orbit differences large systematic effects are visible for time periods, when the GRACE-A entered more active ionospheric regions, i.e., the equatorial regions. The positive differences are caused by GPS observations, which passed through ionospheric bulges as the elevation angle was not limited here. In the reduced-dynamic orbit such effects are somehow smoothed. The corresponding variations reach 4 m. In along-track the kinematic orbit shows a better agreement than the reduced-dynamic orbit. A scatter of 5 m is visible in the differences for the reduced-dynamic  $L_1$  orbit comparison. In cross-track, a more or less similar behavior can be seen for kinematic and reduced-dynamic solutions. Bock et al. (2009) shows a similar study for September 30, 2007, and observed a scatter of  $\approx 2$  m and  $\approx 5$  m for radial and along-track differences, respectively. The derived mean radial offset in Fig. 4.30 is 2.01 m, whereas Bock et al. (2009) found an offset of only 0.88 m for the days in 2007, when the ionosphere was less active.

In summary, the ionospheric error will effect CubETH radial orbit component systematically by 1-2 m. As this exceeds the envisaged orbit accuracy, which is at the sub-meter level, the ionospheric delays have to

<sup>17</sup> Group and Phase Ionospheric Calibration

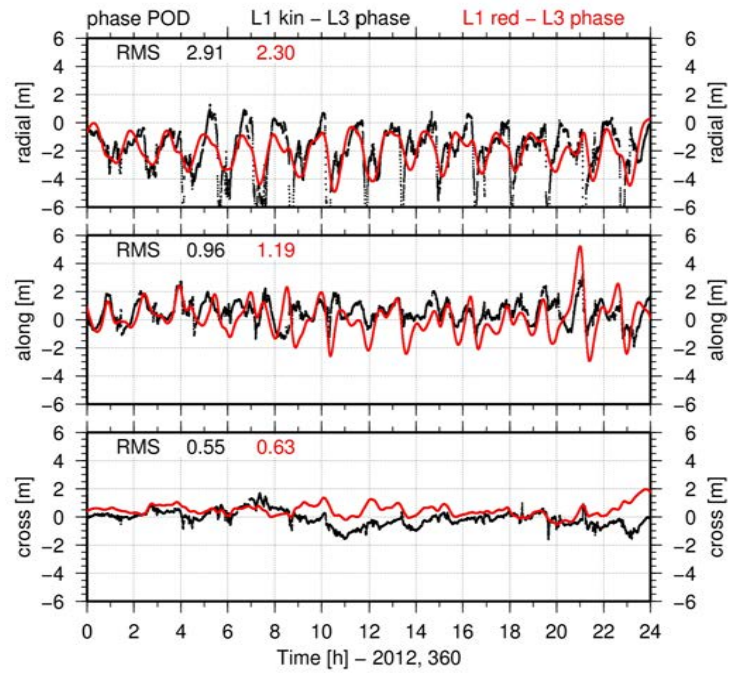


**Fig. 4.30:** Orbit differences of GRACE-A  $L_1$  reduced-dynamic and kinematic solutions with respect to the reference  $L_3$  reduced-dynamic orbit

be reduced by using an appropriate scale factor in the Klobuchar model.



# 5 Investigations on the Combined Processing of Ground- and Space-based GPS Observations

For co-location on-board a LEO the most essential question was mentioned already in the introduction: How could the ground GNSS receivers be tied to the other techniques? An appropriate answer to this question is of immanent importance for a successful co-location in space. In general, the answer is a combined processing of ground- and space-based GNSS observations. In this context, a subsequent question might be formulated: Can geodetic parameters be improved by deriving them not only from ground-based but also from space-based GNSS observations? Within this chapter both questions will be discussed based on the results derived for a combined processing of ground- and space-based GNSS observations at the zero-difference level. As a general remark, it has to be mentioned that LEO orbit determination on the cm accuracy level is a prerequisite for a significant improvement of the geodetic parameters (Hugentobler et al., 2005). The feasibility to achieve this orbit accuracy was shown in the previous chapter. This chapter here is structured in the following way: after discussing possible combination approaches, the processing strategy is explained (Sect. 5.1). Several geodetic parameters are analyzed based on weekly solutions (Sects. 5.3-5.5). In the last section of this chapter (Sect. 5.6) the transition to a long-term solution is done including a discussion on station velocities and geocenter results.

## 5.1 Combined Processing Strategy

The concepts for the combination of ground- and LEO-based GPS observations are described within this section. In a first subsection possible combination strategies are discussed and compared against each other. The processed data and the processing scheme are addressed in the second part of this section.

### 5.1.1 Combination Approaches

In order to improve LEO orbit determination, several authors discussed the differences between so-called single-step and two-step approaches. Both methods are related to the question of how to handle GNSS orbits and geodetic parameters within a LEO orbit determination. The orbit determination discussed in Chap. 4 is the “second step” of the two-step approach as the LEO orbits were estimated based on the final GNSS orbits, clock corrections, and ERPs provided by CODE. Obviously, any error in the introduced orbits, clocks, or ERPs distorts the estimated LEO orbit, as these parameters are fixed to a priori in the orbit determination. In order to avoid related LEO orbit distortions and to be fully consistent a single-step approach can be performed. In this approach global parameters like GNSS orbits, station coordinates, ERPs, clocks, and tropospheric delays are estimated in the same least-squares adjustment as the LEO orbits. Consequently, a higher level of consistency is expected. However, if any systematic effect in station coordinates, Earth orientation, GPS orbits, etc. is not handled correctly within the single-step approach (i.e., the software package used) the accuracy of the LEO orbit is affected. In the early years of space-borne GPS receivers, Rim et al. (1995) found some minor improvements in TOPEX/Poseidon’s radial and along-track components based on a single-step approach. Zhu et al. (2003) recognized also improvements in the GPS orbits and reference frame parameters, when combining GPS observations from CHAMP and the ground network. This was confirmed by Hugentobler et al. (2005), who processed Jason-1 GPS observations together with a 120 station network for six days in 2001. They reported a significant improvement in geocenter coordinates and GPS orbits, but no improvement for the LEO orbit. Zhu et al.

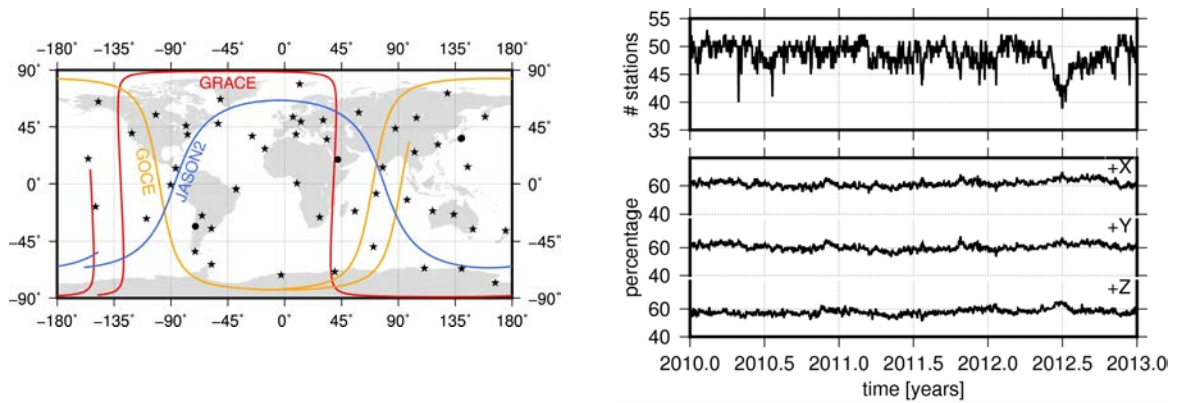
(2004) discussed the single-step, or as they called it, the integrated approach, for CHAMP, GRACE, and a 40 station ground network. Due to limited computational resources only a capability demonstration was performed. They found a considerable improvement of around 40 % for the GPS orbits when adding the three LEOs. Also for the LEO orbits and the geocenter they reported significant improvements. Results derived from an extension of this study to the entire year 2004 were presented by König et al. (2007). By adding CHAMP to the ground network they found a decrease in the average RMS of the CHAMP phase residuals from 9.5 mm to 5.1 mm and a reduction in the bias (2.6 cm instead of -3.7 cm) and the standard deviations (1.0 cm instead of 6.2 cm) of the z-translation of the applied Helmert transformation between estimated and a priori coordinates. Moreover, by adding also GRACE GPS observations a further reduction in the z-translation bias to 0.74 cm was reported.

From the conceptional point of view three methods can be found for adding space-borne GNSS observations to ground network observations:

- **method 1** By integrating the LEO into the double-differenced ground network by forming ground-space baselines.
- **method 2** By adding zero-differenced LEO normal equations to double-differenced ground network normal equations.
- **method 3** By processing zero-difference ground- and space-based observations together.

Obviously, the main differences between these methods are the level of differentiation (cf. Sect. 2.1.1) and the level of combination (cf. Sect. 3.4). As indicated above the computational loading for a ground and LEO combined processing is not negligible. Therefore, a combination at the normal equation level is advantageous as it allows to perform the computationally intensive least-squares adjustment station-wise. Consequently, the stacking requires consistent normal equations, ideally generated with the same software package. However, in any combined processing the GNSS orbits are the crucial element connecting ground and space. As shown in Eqn. 2.1, the GNSS satellite clocks have to be taken into account when relying on zero-differences. Therefore, methods 2 and 3 require the joint estimation of satellite clocks from ground- and space-based observations. Hugentobler et al. (2005) performed and described a combination based on method 1. They formed a set of ground-space baselines in addition to the ground baselines. To avoid redundant baselines, they ensured that only one of the possible ground-space baselines with its double-difference observation was active for a given time epoch. The selection of the ground stations for these baselines was done rather carefully by requiring that considered ground station tracks the same GNSS satellites as the LEO (one exception was allowed). In addition, the time one station could be used was maximized. Jäggi (2007) discussed these ground-space baselines in more detail. However, the definition of these ground-space baselines is a rather challenging task. When processing GNSS observations, the handling of ambiguities has to be considered. Several strategies can be found in the literature mentioned above. For example, Hugentobler et al. (2005) solved ambiguities only for the ground baselines, whereas Zhu et al. (2004) processed a float solution without fixing any ambiguities (while combining zero-differences on the observation level).

The combination presented in this chapter was done in a zero-difference mode using method 3 for two reasons. Firstly, the zero-difference processing ensures the maximal consistency between the ground network and the LEOs. In order to reach the highest consistency, when writing daily normal equations, all observations have to contribute to the estimated parameters, especially to the GNSS satellite orbits and clock corrections, as these are the connection between ground- and space-based observations. Before writing the normal equations epoch-wise clock corrections are usually pre-eliminated epoch-wise due to their huge number. Consequently, all observations have to be processed in a single least-squares adjustment. A station-wise processing and combination on the normal equation level would either reduce the consistency significantly by estimating different clock offsets for the same GNSS satellite or increase the processing load tremendously by keeping the epoch-wise satellite clocks in the normal equation system (around 92'000 satellite clock parameters per day). Secondly, method 3 was selected to save processing time that would



(a) Ground station network and LEO ground tracks (2010 Jan 1st, 0:00-2:00); *circles* indicate stations which were excluded from the NNT+NNR condition

(b) Number of stations in the combined solution and percentage of stations in the +x (90° W to 90° E), +y (0° to 180° E) and +z (0° to 90° N) hemisphere

**Fig. 5.1:** Ground station network and number of stations for the combined processing; the considered stations are listed in Tab. C.1

be required for the rather complex ambiguity resolution between LEOs and ground stations according to method 1. According to Blewitt (2008) the processing time  $O$  grows with the third power of  $n$ , the number of considered stations ( $O_{total} = O(n^3)$ ) for a double-difference processing. For zero-differences, the processing time increases linearly by  $O_{total} = O(n)$ . The major drawback is that the ambiguities cannot be resolved at the zero-difference level within the current BSW implementation. Therefore, only float solutions have been obtained.

### 5.1.2 Database and Processing Scheme

The considered observations and the processing strategy are introduced in this subsection. Firstly, a global GPS ground tracking network with a total of 53 well-distributed IGS stations was selected. This network of mostly stable stations is presented in Fig. 5.1(a). Three stations (Santiago, Koganei, and Tsukuba) were affected significantly by the two large earthquakes, which occurred in the processing time period: the Maule earthquake<sup>1</sup> and the Tohoku earthquake<sup>2</sup>. These three stations and the station Namas (Saudi Arabia, no ITRF2008 coordinates) were excluded from the datum definition. It has to be mentioned that the datum definition was refined for the long-term solution described in Sect. 5.6. Fig. 5.1(a) contains also an example of the ground tracks for the considered LEO missions GRACE, GOCE, and OSTM/Jason-2, which were introduced already in Sect. 4.1. As a poorly distributed tracking network might limit the accuracy of the derived geodetic parameters considerably, Fig. 5.1(b) shows the percentage of stations available in the +x (90° W to 90° E), +y (0° to 180° E) and +z (0° to 90° N) hemispheres. From Fig. 5.1(b) one can conclude that the station distribution is not perfect, but acceptable. Percentages of around 60% are present for the three positive hemispheres. Due to missing observations and station-dependent interruptions, variations of up to 10% (corresponding to five stations) are present. The number of stations fell below 45 for a few days; a minimal value of 39 stations was found for July 1st, 2012. Concerning the network size one has to keep in mind that weekly SLR solutions are usually based on around 20 stations, whereas operational GNSS solutions comprise usually more than 100 stations.

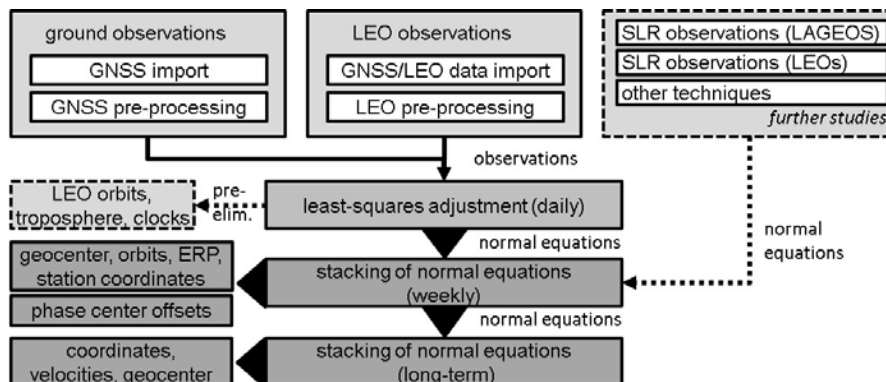
The overall processing strategy is outlined in Fig. 5.2. To derive daily solutions three major steps are required: (1) the pre-processing of the LEO GNSS data including an a priori LEO orbit determination (similar to Chap. 4), (2) the pre-processing of the GNSS ground tracking network, and (3) the combined processing of all observations. As the BSW program ADDNEQ2 is currently not capable of handling different orbit force models simultaneously, it was decided to pre-eliminate the LEO orbits before writing

<sup>1</sup> This earthquake occurred in Chile on February 27, 2010, a magnitude of 8.8  $M_W$  was reached.

<sup>2</sup> This earthquake occurred in Japan on March 11, 2011, a magnitude of 9.0  $M_W$  was reached.

**Tab. 5.1:** Summary of estimation and processing strategy; GPS-related products serve as a priori information

<b>modeling and a priori information</b>	
base observations	zero-difference code and phase observations, data rate: 30 s (ground stations) and 10 s (LEOs), cut-off angle: 3°, elevation-dependent weighting applied for ground stations only ( $\cos^2(z)$ )
GPS-related products	final products from CODE: orbits, 5 s clock corrections, Earth rotation parameters
LEO a priori orbit	six Keplerian elements, nine empirical radiation pressure parameters, piece-wise constant accelerations every six minutes, a priori SRP and Earth albedo modeling for GRACE and OSTM/Jason-2
troposphere modeling	6-hourly ECMWF-based hydrostatic troposphere delays mapped with VMF (Böhm et al., 2006b)
ionosphere modeling	forming the ionosphere-free linear combination, accounting for 2nd- and 3rd-order, and ray bending effects (Fritsche et al., 2005)
antenna phase center	absolute phase center offsets and variations for ground stations, GPS satellites, GOCE (Bock et al., 2011a), and OSTM/Jason-2 (Garcia & Montenbruck, 2007); GPS satellite antenna patterns beyond 14° from Schmid et al. (2016)
gravity potential	EIGEN5C gravity field up to degree and order 120 (Förste et al., 2008)
solid Earth tides	IERS 2010 conventions (Petit & Luzum, 2010)
permanent tide	conventional tide free
ocean tide model	FES2004 (Lyard et al., 2006)
ocean loading	tidal: FES2004 (Lyard et al., 2006), computed with the free ocean tide loading provider <a href="http://holt.oso.chalmers.se/loading/index.html">http://holt.oso.chalmers.se/loading/index.html</a> non-tidal: 6-hourly GRACE AOD1B atmospheric and oceanic de-aliasing product
atmospheric loading	tidal: $S_1$ and $S_2$ corrections from Ray & Ponte (2003) model non-tidal: 6-hourly GRACE AOD1B atmospheric and oceanic de-aliasing product
weighting	ground and LEO observations are equally weighted
clock datum	zero-mean condition applied to satellite clocks and selected station clocks
<b>parameterization</b>	
station coordinates	no-net-translation and no-net-rotation over 49 stations with respect to ITRF2008 (Altamimi et al., 2011)
GPS orbit modeling	six orbital elements, nine empirical radiation pressure parameters (periodic components in D- and Y-direction are constrained with $1 \cdot 10^{-12} \text{ m/s}^2$ ), and three pseudo-stochastic pulses (velocities) per 12 h, a priori CODE radiation pressure model (Springer et al., 1999), arc length 24 h
LEO orbit modeling	six Keplerian elements, nine empirical radiation pressure parameters, velocity changes every six minutes (pre-eliminated before normal equation writing), a priori SRP and Earth albedo modeling for GRACE and OSTM/Jason-2
geocenter	freely estimated
Earth rotation	polar motion coordinates and UT1 for 24 h intervals, piece-wise linear modeling
troposphere	13 zenith delays mapped with wet VMF and two gradients (east-west and north-south) mapped with Chen & Herring (1997) for every station and day
GPS satellite clocks	pre-eliminated every epoch
receiver clocks	pre-eliminated every epoch
GPS phase center offset	satellite-specific offsets per day, removed from the normal equations (except for phase center study)
phase ambiguities	pre-eliminated (as soon as possible) without ambiguity fixing

**Fig. 5.2:** Processing strategy for the ground- and space-based GNSS combination

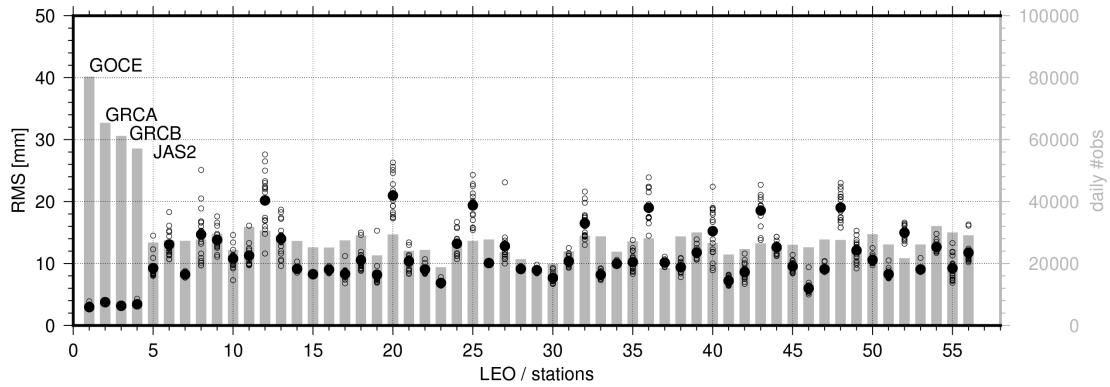


**Fig. 5.3:** Number of daily observations and RMS of carrier phase residuals for all LEOs and stations (computed exemplarily over four weeks in 2010); data rate is 30 s for ground stations and 10 s for LEOs

the normal equations. Consequently, LEO orbits are not part of this study but will be considered and discussed within a follow-on project (in that case the GPS orbits instead of the LEO orbits will be pre-eliminated before writing the normal equations). Tab. 5.1 gives an overview of the a priori models and the parameterization used in the combined processing. The derived normal equations are then accumulated to produce weekly solutions, while keeping the daily satellite arcs. This accumulation is required to reduce the correlations between orbits, ERPs, and the geocenter coordinates (cf. Haines et al., 2015). Consequently, the following parameters are discussed based on the weekly estimation: geocenter coordinates (Sect. 5.2), station coordinates and scale parameters (Sect. 5.4), GPS orbits, and ERPs (Sect. 5.5). In a subsequent stacking process satellite phase centers were estimated; they are discussed in Sect. 5.3. The weekly normal equations were finally stacked subsequently to a long-term solution as shown in Fig. 5.2. The parameterization in this long-term combination step was changed in such a way that geocenter parameters were deleted, whereas station velocities and surface load density coefficients were added to the normal equation system. In the future also SLR observations (as normal equations) might be added to the processing. It has to be mentioned that due to the fact that multi-GNSS receivers on-board LEOs are missing today, this chapter is dedicated to GPS only. Some of the results were already presented to the scientific community, for example, a manuscript discussing the geocenter study based on weekly solutions was published in Journal of Geodesy (Männel & Rothacher, 2017a).

Fig. 5.3 shows the average number of daily observations and the RMS of the carrier phase residuals for the processed stations and LEOs. These exemplary values are given for January 2010. The number of daily observations corresponds to seven to ten GPS satellites per epoch. The derived daily RMS values of the carrier phase residuals vary between 2.7 and 27.6 mm. In average an RMS of  $3.3 \pm 0.3$  mm and  $11.5 \pm 3.7$  mm is obtained for LEOs and ground stations, respectively. The differences in the LEO residuals compared to Fig. 4.10 are caused by the simultaneous estimation of GPS orbits and clocks in this study. The differences between GRACE-A and GRACE-B are related to the slightly better quality of the GRACE-B observations (cf. Sect. 4.3.2).

## 5.2 The Geocenter

As mentioned in Sect. 3.2.1 the origin of the ITRS is conventionally defined to be the center of mass (CM) of the whole Earth's system, including the solid Earth, the oceans, the atmosphere, the hydrosphere, and the cryosphere (Petit & Luzum, 2010). The ITRF as a realization of the ITRS is derived from a globally distributed space geodetic network attached to the surface of the solid Earth. The coordinates of the stations of this network are defined such that the origin of the coordinate system, the center of surface figure (CF), has zero translation (and translation rates) relative to the CM on decadal time scales (Altamimi et al., 2011). Due to mass re-distributions, the CF varies on shorter time scales with predominant annual and semi-annual periods relative to the CM (Dong et al., 2003). This motion is

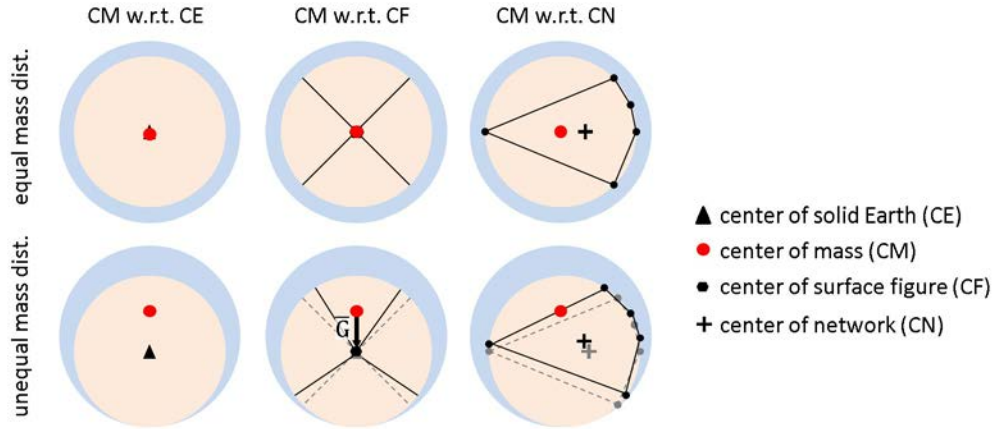


**Fig. 5.4:** Schematic sketch of geocenter motion in various reference frames with the CM as common origin; the first row shows the solid Earth (*orange*) with an equally distributed variable surface load (*blue*), the second row shows an unequally distributed surface load;  $\mathbf{G}$  is defined as CF with respect to CM; the sketches are based on figures presented by Blewitt (2003) and Fritsche (2013)

conventionally called geocenter motion, where the CM is labelled as the geocenter (Petit & Luzum, 2010). The concept of geocenter motion is shown in Fig. 5.4. Assuming an equally distributed temporal variable mass (e.g., ocean, atmosphere) around the solid Earth, the center of solid Earth (CE) and the CM coincides (upper row, left). As CE is not observable with space geodetic techniques (Chen et al., 1999), the CE is approximated by the center of surface figure (CF, upper row, middle), which agree to within 2% of their magnitude (Blewitt, 2003). However, also the CF, realized by a space geodetic network, is only an approximation, as the station network realizes strictly speaking the center of network (CN, right column). CN is assumed to coincide with the CF for well distributed networks (upper row, right). If the temporal variable mass is unequally distributed, the CE differs from the CM (lower row, left). Consequently, also the CF differs from the CM by the vector  $\mathbf{G}$  representing the geocenter motion defined as the position of the CF with respect to the CM (lower row, middle). In some publications the opposite definition is used, derived geocenter values have the opposite sign and the derived phases are shifted by  $180^\circ$ . As a homogeneous station distribution is achieved in this study, it is assumed that CN and CF coincide ( $\text{CN} \equiv \text{CF}$ ). The next section gives an overview of approaches to estimate the geocenter motion from space geodetic techniques. Additionally, the role of the individual space geodetic techniques and the LEOs observations is discussed.

### 5.2.1 Geocenter Estimation Approaches

In recent years a large number of publications presented geocenter results derived by very different approaches. These approaches can be classified into three groups: (1) model-based approaches, (2) degree-1 approaches, and (3) translational approaches. Sometimes, group (1) and (2) methods are summarized as inverse approaches. However, from the geodetic point of view, the direct use of space geodetic observations in the type (2) approach justifies a distinction.

#### Model-base Approaches

As the geocenter motion is driven by mass re-distribution, the inversion of geophysical models should provide geocenter information. Results were presented in the literature based on models for ocean tides, atmospheric and oceanic circulation, land hydrology or the GIA (e.g., Scherneck et al., 2000; Dong et al., 1997; Chen et al., 1999; Crétau et al., 2002; Greff-Lefftz, 2000; Klemann & Martinec, 2011). However, as concluded by Wu et al. (2012), these models might not be sufficiently accurate to estimate the geocenter location at the millimeter level and, therefore, they are not further discussed here.

### Degree-1 Approaches

By assuming a spherical, symmetrical and elastic Earth with radius  $R_E$  and mass  $M_E$ , the main mass re-distributions in the Earth's system occur in a small layer at the Earth's surface ( $\ll R_E$ , cf. Fig. 5.2.1). The surface load density  $\sigma(\varphi, \lambda)$  for a station with latitude  $\varphi$  and longitude  $\lambda$  on this surface can be developed into (cf. Sect. 3.2.3)

$$\sigma(\varphi, \lambda) = \sum_{n=1}^{\infty} \sum_{m=0}^n \sum_{\Phi=C}^S \sigma_{nm}^{\Phi} Y_{nm}^{\Phi}(\varphi, \lambda). \quad (5.1)$$

The spherical harmonic coefficients  $\sigma_{nm}^{\Phi}$  for the surface load density are given for degree  $n$  and order  $m$ . The spherical harmonic base functions  $Y_{nm}^{\Phi}(\varphi, \lambda)$  for each  $\Phi \in \{C, S\}$  are expressed by associated Legendre functions  $P_{nm}$ . As the loading potential causes a deformation  $\Delta s$  of the Earth's surface, the surface load density can be computed from measured surface deformations. Therefore, the estimation of surface load density coefficients is done in a least-squares adjustment with the simultaneous estimation of station coordinates. The system-independent load moment vector  $\mathbf{m}$  is derived from the estimated coefficients by (Blewitt et al., 2001)

$$\mathbf{m} = \begin{pmatrix} m_x \\ m_y \\ m_z \end{pmatrix} = \frac{4\pi R_E^3}{3} \sqrt{3} \begin{pmatrix} \sigma_{11}^C \\ \sigma_{11}^S \\ \sigma_{10}^C \end{pmatrix}. \quad (5.2)$$

The factor  $\sqrt{3}$  accounts for the conversion from non-normalized to normalized surface load coefficients (Blewitt & Clarke, 2003). The geocenter motion is derived from the load moment vector by (Blewitt, 2003)

$$\mathbf{G} = \left( \frac{1}{3} [h'_1 - 2l'_1]_{\text{CE}} - 1 \right) \frac{\mathbf{m}}{M_E}. \quad (5.3)$$

The term  $[h'_1 - 2l'_1]_{\text{CE}}$  describes the frame-dependent isomorphic parameter containing the load Love numbers  $h'_1$  and  $l'_1$  for degree  $n = 1$ . After Blewitt (2003) introduced this degree-1 (or inversion) approach, several improvements were proposed by a number of authors. A main improvement results from the simultaneous estimation of higher-order spherical harmonics in order to overcome aliasing effects (Wu et al., 2003). Depending on the number of processed stations, higher-order coefficients of up to degree and order 6 are considered. A second improvement was initiated by the usage of various constraints. In the so-called constrained inversion approach the heterogeneous network distribution is compensated by introducing constraints based on additional data sets like mass transport information from GRACE or ocean bottom pressure data (Kusche & Schrama, 2005; Wu et al., 2006; Swenson et al., 2008). The unified approach, as another improved version of the degree-1 method, was introduced by Lavallée et al. (2006). They combined the classical translation and the degree-1 approach by estimating translations and deformations simultaneously. Results were also published by Fritsche et al. (2010) and Glaser (2014). The unified approach is applied in Sect. 5.6 based on the combined long-term solution.

### Translational Approaches

The classical translational approaches rely, in general, on satellites orbiting CM and station positions tied to the surface of the solid Earth. Please note that the origin defined by the corresponding station network is CN. In the following it is assumed that the well distributed station network represents the Earth's figure (CN $\equiv$ CF). In principle, all geodetic satellite observations connecting satellites orbiting CM and receivers located on the surface of the solid Earth are related by the very general equation (see also Sect. 3.2.1)

$$D_r^i = |\mathbf{r}^{i,\text{CM}}(t_e) - (\bar{\mathbf{r}}_r^{\text{CN}}(t_r) + \mathbf{G}(t_r))| + \epsilon. \quad (5.4)$$

Here  $D_r^i$  describes the space geodetic observation ( $\epsilon$  contains the biases and measurement noise) the distance between the satellite position  $\mathbf{r}^i$  (relative to CM) and the receiver position  $\bar{\mathbf{r}}_r$  (relative to CN). The vector  $\mathbf{G}$  accounts for the position vector of the network origin (assumed to coincide with the center of surface figure) with respect to CM (CN relative to CM). The time epochs in Eqn. 5.4 are the emission time  $t_e$  and the receiving time  $t_r$  for microwave signals or the reflection time for optical signals ( $t_r \equiv t_e$ ). The term  $\epsilon$  contains several biases, e.g., unaccounted signal delays, sensor offsets, and other technique-specific biases. The network shift approach derives the geocenter from a Helmert transformation between an adjusted network with coordinates based on satellite observations and its corresponding polygonal figure in the reference frame<sup>3</sup>. The relationship between the fiducial-free coordinates  $\mathbf{r}_r^{\text{CM}}$  in the CM frame and the ITRF coordinates  $\bar{\mathbf{r}}_r^{\text{CN}}$  mapped linearly to the solution epoch can be written as (Tregoning & van Dam, 2005; Wu et al., 2012)

$$\mathbf{r}_r^{\text{CM}} = \bar{\mathbf{r}}_r^{\text{CN}} + \epsilon_i^{\text{CN}} + \mathbf{A}_i \mathbf{T}. \quad (5.5)$$

$\mathbf{A}_i$  is the site-specific matrix of partial derivatives, while the vector  $\mathbf{T}$  contains the transformation parameters. The estimated translations represent  $\mathbf{G}$ . The sum of the station displacements  $\epsilon_i^{\text{CN}}$  vanishes by definition (Tregoning & van Dam, 2005). Therefore, ignoring  $\epsilon_i^{\text{CN}}$  has no effect on the estimation, if equal weights are applied and the scale is not estimated simultaneously. Corresponding results were published by Heflin et al. (1992); Bouillé et al. (2000); Crétaux et al. (2002); Moore & Wang (2003); Reischung et al. (2014) and others. In the kinematic approach, a translational offset introduced in the observation equation for each station  $r$  is estimated as  $\mathbf{r}_r(t)^{\text{CN}} - \mathbf{r}_N = \mathbf{T}(t)$  (Wu et al., 2012). The relationship  $\mathbf{r}_r(t)^{\text{CN}} - \mathbf{r}_N$  represents the incremental geocenter motion for the station  $r$ . The unbiased estimate of the negative geocenter motion between CM and CN is derived by (Wu et al., 2012)

$$\hat{\mathbf{T}}(t) = \sum_{i=1}^N \frac{\mathbf{r}_r^{\text{CN}}}{N} - \mathbf{r}_N. \quad (5.6)$$

All stations are equally weighted in Eqn. 5.6. Obviously, individual site displacements contained in the solution will bias the derived geocenter motion. Results from SLR and ground- and LEO-based GPS were shown by Vigue et al. (1992); Eanes et al. (1997); Pavlis (1999); Kang et al. (2009) and others. A fixed reference frame is used in the dynamic approach, where observed satellite orbit perturbations are used to estimate degree-one geopotential Stokes coefficients (Kar, 1997; König et al., 2015). However, this approach is used very rarely due to complications related to the implementation of dynamic parameters (Wu et al., 2012).

The sensitivity of the different space geodetic techniques on the geocenter and their contribution in the estimation is addressed in the following paragraph. Commonly, unambiguous SLR observations to the spherical satellites LAGEOS and ETALON are used to determine the geocenter (e.g., Eanes et al., 1997; Pavlis, 1999; Cheng et al., 2013; Sośnica, 2015). As mentioned in Sect. 3.2.1, SLR is used to align the long-term origin of the ITRF to the CM (Altamimi et al., 2011). The prospects of using the much denser GNSS and DORIS networks to derive the geocenter have been investigated for many years. Corresponding results show large differences of the geocenter z-component compared to SLR, using the translational approach (e.g., Dong et al., 2003; Reischung & Garayt, 2013). In the case of GNSS this weakness is mainly the result of: (1) the reduced sensitivity with respect to the geocenter due to the orbit height, (2) the need to estimate epoch-wise clock offsets or, alternatively, to form double-differences (cf. Meindl et al., 2013), (3) the presence of ambiguities in the raw phase observations, (4) the necessity to estimate tropospheric zenith delays, and (5) difficulties in modeling orbit perturbations caused by solar radiation pressure. Concerning the satellite types, LEOs have been tested for SLR- (and DORIS)-based geocenter estimations for many years, whereas GNSS observations to these satellites have only been considered recently. Kang et al. (2009) presented geocenter results derived from GRACE GPS observations and

<sup>3</sup> Sometimes called fiducial-free transform approach.

a global tracking network. By estimating the LEO orbits, the geocenter and GPS-specific parameters (ambiguities and zenith wet delays) they derived geocenter positions with a remarkable quality. Haines et al. (2015) presented a GPS-only terrestrial reference frame including GPS observations of GRACE-A. They reported a significant improvement for the geocenter z-component based on the addition of the GRACE observations. Based on simulations Kuang et al. (2015) studied accuracy limitations for various tracking configurations including a combined processing of ground- and space-based GPS observations using the kinematic approach. König et al. (2015) presented geocenter results from a combination of LAGEOS and GRACE solutions. However, they concluded that neither the addition of GRACE-based GPS, SLR, nor K-band observations could improve their inverse geocenter solution derived from LAGEOS observations. The status of empirical once-per-revolution parameters compensating unmodelled solar radiation pressure effect in the combination of ground-based GNSS and LAGEOS observations were discussed by Thaller et al. (2014). They concluded that constraining the empirical D and Y radiation pressure parameters to zero, as recommended by Meindl et al. (2013) for GNSS, will prevent LAGEOS from exploiting its potential in the combined solution. Concerning VLBI it was mentioned already in Sect. 3.2.1 that the geocenter is not directly observable due to the relative nature of this technique.

### 5.2.2 Geocenter Results from the Combined GPS Processing

Within this section, the impact on the derived geocenter coordinates is discussed concerning (1) adding LEOs to the ground-only solution, (2) constraining empirical once-per-revolution parameters, and (3) correcting non-tidal loading. The results presented within this subsection were submitted recently for publication (Männel & Rothacher, 2017a).

#### Impact of the Inclusion of LEOs

Fig. 5.5 shows the weekly geocenter time series obtained from the GPS ground network (GR-only solution). While variations in the x- and y-component are below 3 cm, they are up to 10 cm in the z-component. The difference between x- and y-direction and the z-direction is caused by the fact that the geocenter in x- and y-direction is defined by gravity and Earth rotation (the Earth rotation axis is defined to pass through the geocenter), whereas the z-direction is only defined by gravity. However, the variations in the z-component and their scatter (3.2 cm) are more than three times larger than the level reached by comparable results derived by SLR. The main reasons are most probably the sparse 50-station ground network (in terms of GNSS), the unresolved ambiguities, and deficiencies in the empirical solar radiation pressure model. However, when adding the four LEOs to the ground-only solutions (combined solution GR+ALL), variations decrease by a factor of about 2, i.e., to less than 2 cm (some peaks are larger, reaching up to 6 cm in the z-component) and even the scatter of the z-component is reduced to a value that is much closer to SLR geocenter results (but still clearly larger than that of the SLR solutions). The amplitude spectra of all three components show significantly smaller amplitudes at nearly all frequencies for the GR+ALL solution. Especially, the pre-dominant annual signals and the higher-order harmonics thereof are strongly reduced in the combined solution. These signals are most probably related to the draconitic orbit period of GPS (351.4 days, cf. Sect. 4.2.2). However, the processed time span of three years does not allow to separate between annual and GPS draconitic signals. The remaining annual signal is around 3 and 4 mm for the x- and y-component, respectively, and around 6 mm for the z-component. For shorter periods, no significant signal common to all components can be found. Therefore, they might be related to ground network effects and LEO orbit characteristics (cf. Sect. 4.1). The impact of the individual LEOs on the formal errors and the geocenter z-component is discussed in a further paragraph. As indicated in Fig. 5.6 GPS once-per-revolution (OPR) orbit parameters are constrained in D- and Y-direction in both solutions. The impact of applying constraints to the GPS OPR terms is discussed in the next paragraph.

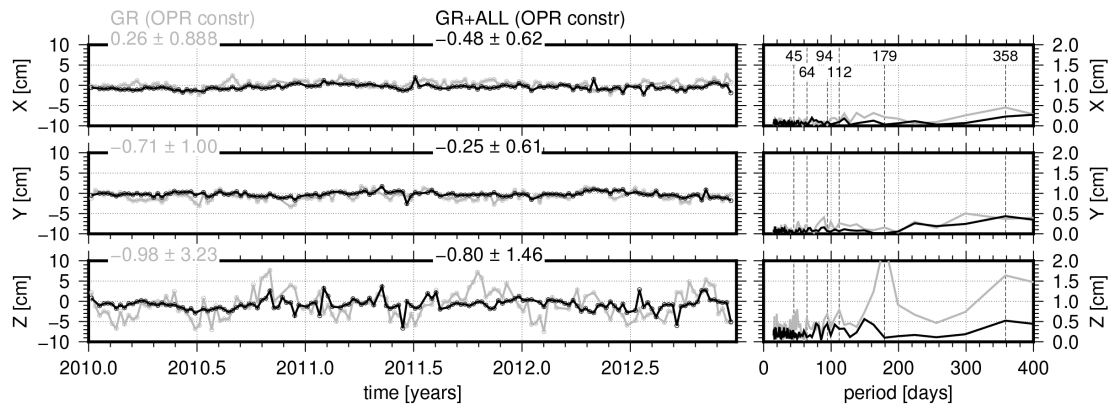


**Fig. 5.5:** Geocenter results from a ground-only (GR, *gray*) and a ground + four LEO combination (GR+ALL, *black*) solution; *left*: time series; *right*: amplitude spectra; the periods of the major peaks are indicated; mean and standard deviation are provided

### Impact of Empirical Radiation Pressure Parameters

The free estimation of GPS OPR parameters parallel to the solar panel rotation axis (Y-direction) in the GNSS orbit determination process was identified by Meindl et al. (2013) as a major reason for the low accuracy of the geocenter z-component by GNSS. However, as mentioned above, Thaller et al. (2014) recommend to estimate GPS OPR parameters freely when combining GNSS and LAGEOS for the geocenter determination. To assess the impact of these GPS OPR parameters two solutions were computed with (1) free GPS OPR parameters and (2) constraining GPS OPR parameters in D and Y direction to zero in the GNSS orbit determination process (as it was done by Thaller et al., 2014)<sup>4</sup>. As the biggest effect is expected in the z-component, the resulting spectra are shown in Fig. 5.6. Looking at the two ground-only solutions the amplitudes of solution (2) are smaller for nearly all periods. As indicated in Fig. 5.5, an annual signal of 18 mm is derived from the ground network in solution (2), while this amplitude increases to 20 mm in solution (1). A similar behavior is present in the semi-annual amplitude (increase from 25 to 29 mm). In the GR+ALL solution the annual amplitude is reduced to 6 mm in solution (2) with respect to the ground-only solution. When estimating GPS OPR freely in the GR+ALL solution, no annual peak is present. In solution (2), the estimated GPS OPR parameters have overall formal errors of  $\approx 0.02 \text{ nm/s}^2$  and repeatabilities (weekly estimates compared to averaged values) of  $\approx 1 \text{ nm/s}^2$ . As mentioned in Sect. 5.2.1, constraining GPS OPR parameters has been found to be crucial for GNSS-based geocenter determination. This is also true for the experiment presented here. The effect reported by Thaller et al. (2014) does not seem to be present in the combination of ground and LEO GPS observations, probably related (1) to the contribution the LEO GPS observations have to the GPS orbits, and (2) to the large number of empirical LEO orbit parameters required to cope with air drag and radiation pressure. However, one has to keep in mind that in the applied zero-difference approach, ambiguities have not been resolved to integers. Therefore, estimated ambiguities might partly absorb systematic geocenter signals. Additionally, an accurate GPS orbit modeling becomes even more critical and the estimation of the full set of GPS OPR parameters might absorb remaining systematic effects. This needs to be tested in the future using the new CODE orbit model presented by Arnold et al. (2015). In the studies presented in the following the GPS OPR parameters in D- and Y-direction have been constrained to zero.

### Impact of Non-tidal Loading Corrections

As indicated in Tab. 5.1, non-tidal loading effects were considered in the processing described above, as the corresponding mass re-distributions affect station coordinates and the geocenter. Studies performed by Sošnica (2015) and Roggenbuck et al. (2015) show a significant impact on the annual geocenter signal. Crétaux et al. (2002) derived on a theoretical basis a reduction by 0.4, 1.3, and 0.7 mm in the SLR-

<sup>4</sup> As described in Sect. 4.2.2 axis D is directed towards the Sun and the Y-axis is parallel to the solar panel rotation axis.

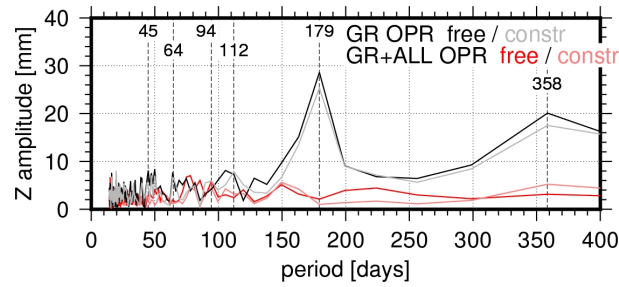


**Fig. 5.6:** Amplitude spectra of geocenter coordinates estimated in a ground-only and a combined processing with constrained and freely estimated empirical OPR parameters; the periods of the major peaks are indicated

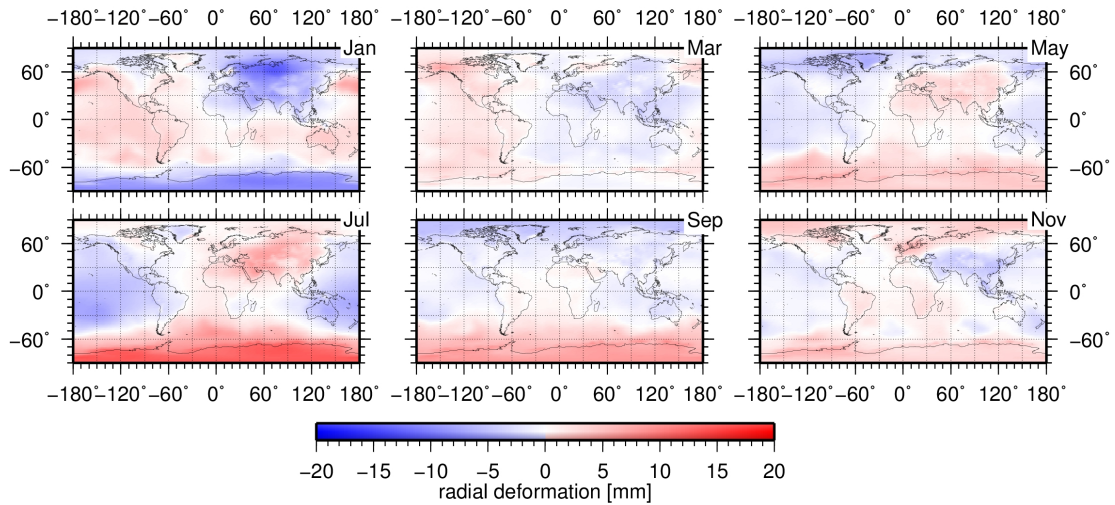


**Fig. 5.7:** Mean vertical Earth crust deformation computed from GRACE AOD products for January, March, May, July, September, and November 2010

based annual  $x$ -,  $y$ -, and  $z$ -geocenter amplitudes. These values were verified by Sošnica (2015), who found reductions of 0.2, 0.4, and 0.8 mm based on LAGEOS observations, thus confirming the size of the impact. To assess the impact of the non-tidal loading corrections, three solutions were computed in this study:

- GR+ALL(AOD): ground and LEO combination including the AOD1B products,
- GR+ALL(TUV): ground and LEO combination including the non-tidal atmospheric corrections provided by the GGOS atmosphere project (TU Vienna)<sup>5</sup>, and
- GR+ALL(none): ground and LEO combination without applying non-tidal loading corrections.

The GRACE atmosphere and ocean de-aliasing products (AOD1B) were applied as they are used in Fritsche et al. (2014). Fig. 5.7 shows the mean vertical crustal deformation derived from AOD products during several months in 2010. The mean radial (i.e., vertical) deformations are in the range of -20 to +20 mm with maximal values in January and July. Analogous values for the non-tidal atmospheric corrections provided by the GGOS atmosphere project are provided in Fig. 5.8. The derived mean vertical deformations are at the same level, also with maximal values for winter and summer times. Comparing both models, slightly larger displacements can be found in the AOD data related to the inclusion of the non-tidal ocean loading. Concerning oceanic and coastal regions it has to be mentioned that the atmospheric non-tidal loading is strongly compensated by the inverse barometer effect. Consequently, inland stations are more affected by the atmosphere than stations close to the ocean. For this reason, Sošnica (2015) stated, based on the

<sup>5</sup> <http://ggosatm.hg.tuwien.ac.at/>, accessed Dec. 2015

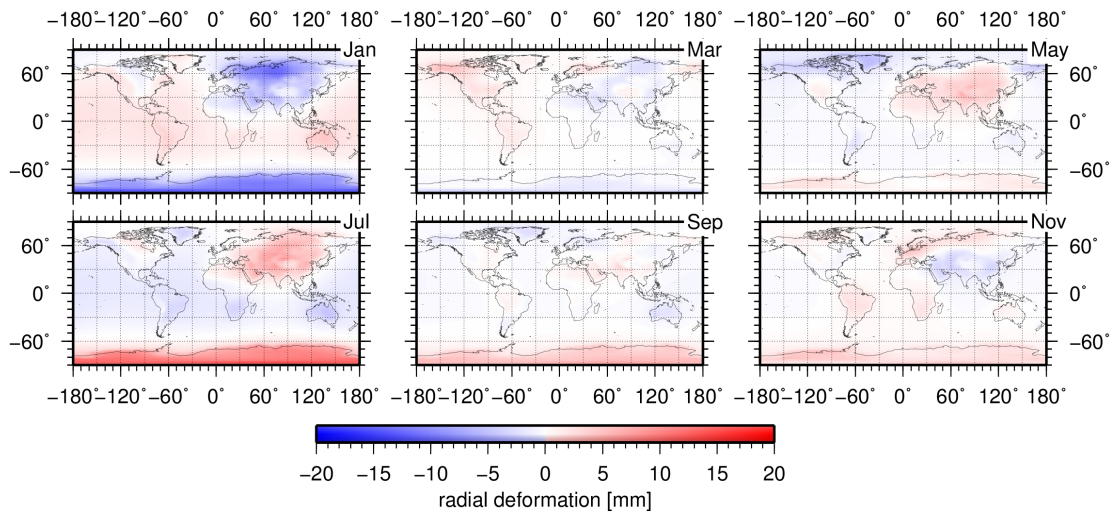


**Fig. 5.8:** Mean vertical Earth crust deformation computed from TU Vienna non-tidal atmospheric loading corrections for January, March, May, July, September, and November 2010

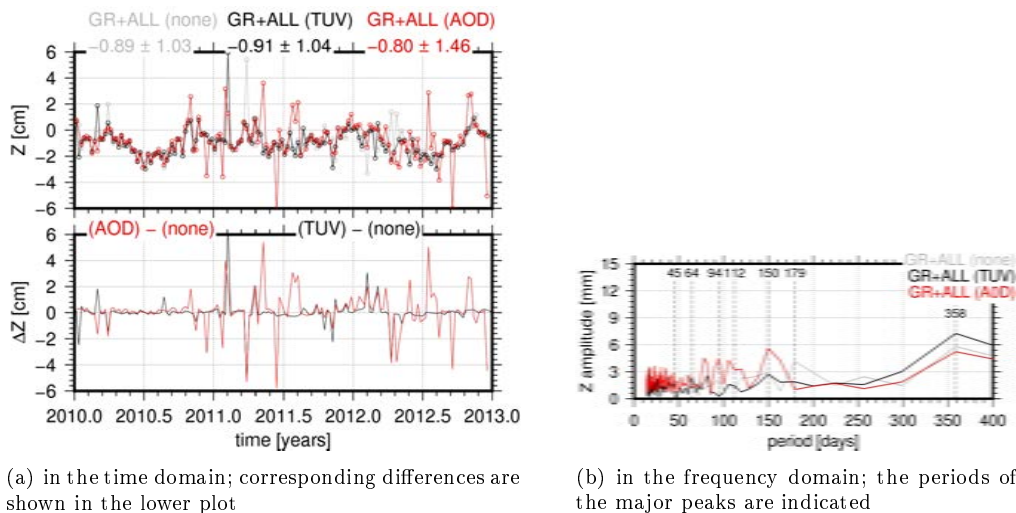


**Fig. 5.9:** Impact of non-tidal loading on the geocenter z-component; *red*: applying AOD1B products; *black*: applying TU Vienna atmospheric non-tidal loading corrections); a solution without non-tidal loading corrections is shown in *gray*

geographical station distribution, that GNSS-derived results are more affected than those derived from SLR and VLBI.

Therefore, the effect of the non-tidal loading on GNSS-derived geocenter coordinates was investigated here based on the analyzed three years. Please note that non-tidal loading effects caused by the continental hydrology were not considered in any of these solutions. The geocenter time series differ by some mm in the horizontal components (not shown here) and by up to some cm in the z-component between the three solutions shown in Fig 5.9(a). Apart from periods with close agreement between the solutions, several weekly estimates show large differences compared to the results in the week before and after. A clear periodic (e.g. annual) behavior is not visible. The difference between results derived with AOD1B and TUV products amounts to up to 5 cm in the z-component, with slightly larger differences in the AOD1B case (due to the considered non-tidal ocean loading). The spectral amplitudes plotted in Fig. 5.9(b) show a different behavior for short and long periods. For periods close to annual, a small difference of 0.6 mm is present between the GR+ALL(AOD) and the solution without correcting for non-tidal loading

(GR+ALL(none)). This value is close to the reduction predicted by Crétaux et al. (2002) (0.7 mm) for SLR based geocenter results and the reduction estimated by Sośnica (2015) (0.8 mm). A bit strange is that the annual signal for GR+ALL(TUV) is 1.5 mm larger than that for the GR+ALL(none) solution. However, the considered three years are a rather short time span to judge on annual signals. For periods shorter than 150 days, the GR+ALL(AOD) solution shows the largest amplitudes, which are caused by several, in the absolute sense, large weekly estimates. In summary, correcting for non-tidal loading is found to be important for this type of geocenter determination.

### Comparing the Impact of Individual LEOs

In view of the geocenter improvements shown in Fig. 5.5 resulting from a combined processing of ground- and LEO-based GPS observations, the question arises, how the individual satellites contribute to this significant improvement. Obviously, the contribution depends on (1) the characteristics of the LEO orbit (e.g., the altitude or the orbital inclination), (2) the amount and the quality of the LEO GPS data, and (3) the quality and availability of additional information (e.g., attitude records). The second and third aspect can be treated together as they determine the quality of the derived LEO orbits. In the following the individual LEO contributions are discussed concerning the formal errors of the derived geocenter components and the behavior of the geocenter z-component.

Kuang et al. (2015) concluded that the formal errors of the geocenter estimates depend on (1) the altitude and the inclination of the LEO orbital plane, (2) the orbit representation, and (3) the node differences, if two LEOs are processed simultaneously. As these findings are based on simulations, the attempt was made within this study to complement them using real GPS observations of the above described LEO missions (except for the LEO orbit representation). This approach is reasonable as the actual observation noise, that is unique for each satellite, is considered. Four conclusions can be obtained from the formal errors of the geocenter coordinates of daily and weekly solutions shown in Fig. 5.10. Firstly, the dramatic decrease from daily to weekly solutions is, apart from the higher number of observations ( $\sqrt{7} = 2.7$ ), caused by a better separation of the correlated dynamic orbit parameters (kept as daily parameters) and the geocenter coordinates (estimated over seven days). This decorrelation effect was discussed in more detail by Haines et al. (2015) who compared correlation factors between the geocenter and other parameters for a 30-h and 9-day solution. In the 30-h solution they found correlation factors of around 0.05 and 0.1 between the geocenter components and the GPS satellite orbital parameters and the clocks, respectively. These, as they stated, high correlations were expected regarding, for example, the difficulties in modeling orbit perturbations (Meindl et al., 2013; Kuang et al., 2015). In the extended solution, which covered 9 days, the correlation factors decrease significantly driven by a decorrelation due to the long orbit arcs of 18 orbit revolutions and the variation of the  $\beta_0$  angle within this time period. Haines et al. (2015) recommend to dissolve the remaining correlations between clocks and geocenter by improving the GPS clock model. Secondly, adding a single LEO decreases the formal errors by about 20%, i. e., eight times more than the theoretical decrease expected due to the increased number of observations. For the x- and the y geocenter coordinate the improvement is almost 50%. Please note that due to the higher data rate, a LEO contributes three times more observations than a ground station. The total number of observations per day increases from  $\approx 1.27 \cdot 10^6$  to  $1.34 \cdot 10^6$  observations for a ground+single LEO combination. Thirdly, when adding more than one LEO, the formal errors decrease again by around 15% per additional LEO. And fourthly, this decrease depends, as expected, on the individual LEO. Unfortunately, it is not possible to assign these differences to the (superimposing) contribution factors mentioned above.

Kuang et al. (2015) also discussed the impact of the angular difference between the LEO orbit's right ascension of the ascending nodes on the geocenter formal errors. Based on simulations they found a decrease of 0.1 mm in the formal error of the geocenter z-component for node differences of around  $180^\circ$ . Fig. 5.11 shows the time series of the right ascension of the ascending node for the four considered spacecrafts. As mentioned already in Sect. 4.3.5, GRACE has a very slowly changing rate for the nodal line of around  $50^\circ/\text{yr}$ . For the sun-synchronous GOCE orbit, the period is forced to be equal to one year, whereas a

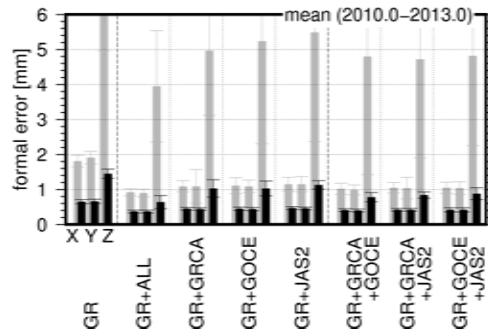


**Fig. 5.10:** Mean formal errors of geocenter estimates from daily (*gray*) and weekly (*black*) solutions

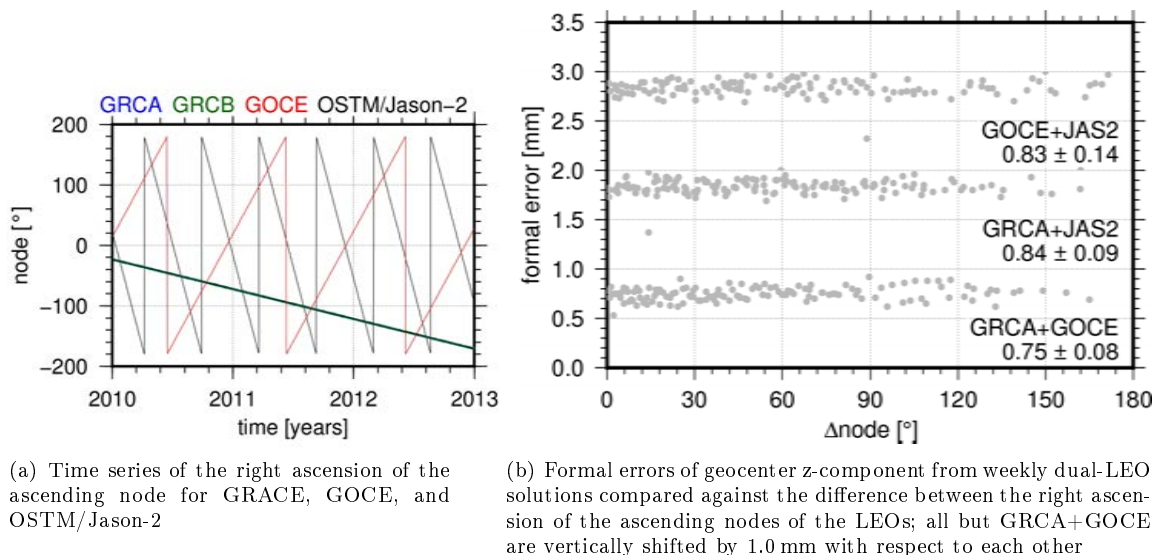
period of  $\approx 175$  days with a drift of  $\approx 2^\circ/\text{day}$  occurs for OSTM/Jason-2. The formal errors of the weekly z-component are plotted in Fig. 5.11 for three different dual-LEO solutions. However, these results do not allow to validate the decrease indicated by Kuang et al. (2015), as the results are probably too noisy and only few values are available for node differences  $>150^\circ$ .

Fig. 5.12 shows the geocenter z-component time series derived from weekly solutions based on three different ground+single-LEO combinations and one ground network+four-LEO combination (GR+ALL). Comparing against the ground-only solution in Fig. 5.5, it is obvious that some suspicious characteristics disappear (e.g., the peak at 2010.4 in GR+GRCA or the peak at 2012.45 in GR+JAS2), whereas others are mitigated but remain visible in all four solutions (e.g. the peak at 2011.35). Please note that due to missing GOCE GPS observations in summer 2010 no GR+GOCE solutions are plotted between 2010.5 and 2010.7. The extent of the damping depends on the characteristics of the LEO orbit. Or, as the ground network distribution plays an important role, the damping depends also on the geometry between LEO trajectory and ground network. Here the LEO-specific repeat orbit period is of importance. This period for OSTM/Jason-2 is  $\approx 10$  days, for GRACE  $\approx 30$  days, and was  $\approx 61$  days for GOCE. Significant differences are visible at almost all periods in the amplitude spectra (Fig. 5.12). The nearly annual and semi-annual amplitudes differ by up to 5 mm between the different single-LEO combinations (13, 11, and 16 mm are present for GR+GRCA, GR+GOCE, and GR+JAS2, respectively). A strong response at annual and semi-annual periods can be found in these single-LEO solutions, whereas both signals are strongly reduced in the GR+ALL solution. However, for this solution a 150-day peak is present, which is not visible in the ground-only results (hidden by the edge of the semi-annual signal) but in the single-LEO combination. In the GR+GRCA+GOCE solution (not shown here) the 179- and the 150-day signal have the same amplitude. In general, long-period signals are damped significantly in the GR+ALL solution. Therefore, it is concluded that using several LEOs will strengthen the geocenter estimation by minimizing the effects of LEO-specific orbit characteristics on the geocenter results. For periods up to 130 days, the differences between the single-LEO solutions are related to the LEO characteristics (e.g., their repeat orbit and draconitic periods). These effects also remain in the GR+ALL solution.

### Comparison to SLR Results

As mentioned above, SLR is probably the technique most used to derive geocenter coordinates. In order to compare the derived results, two SLR solutions were selected. The first one was derived at the Astronomical Institute of the University of Berne (AIUB) based on observations to LAGEOS-1 and LAGEOS-2 (Soćnica et al., 2015). The second one by the author was computed based on LAGEOS-1 and LAGEOS-2 observations using the SLR capabilities of the BSW version used also for the GNSS processing. This solution is in the following referred to as ETHZ.

Within a short excursion, the LAGEOS processing is described here as it was applied for the ETHZ solution. First of all, Fig. 5.13(a,b) show the geographical distribution of LAGEOS observations for 2010. These figures are designed similar to Fig. 4.16. However, a better orbit coverage is visible due to the



**Fig. 5.11:** Formal error of geocenter z-component compared against LEO node differences

higher altitudes. The orbits for the two satellites are characterized by altitudes of 5860 km and 5620 km for LAGEOS-1 and LAGEOS-2, respectively. The inclinations of both orbits are  $109.90^\circ$  and  $98.6^\circ$ . In principle, the solution follows the BSW SLR processing strategy described in detail by Sošnica (2015). As mentioned there, the BSW met the ILRS quality requirements as shown by passing the ILRS benchmark test in 2010. The LAGEOS processing is carried out in a weekly mode based on the GPS week definition. Input data are normal point observations provided by ILRS in the Consolidated Prediction Format. Based on this prediction, a first very loose outlier determination on the 2.5 sigma level with a residual threshold of 1 m and a maximum overall sigma of 100 mm is performed before estimating an a priori orbit. Based on this orbit a more rigorous second outlier detection is performed. Here a residual threshold of 20 mm is applied with a maximum overall sigma of 25 mm. Stations with less than ten observations are excluded from the processing. Subsequently, the final solution is generated. The estimated parameters are six Keplerian elements and five unconstrained empirical accelerations for the LAGEOS orbits, ground station coordinates, geocenter coordinates, and ERPs. Range biases were estimated according to the ILRS recommendations to account for uncalibrated instrumental delays<sup>6</sup>. The empirical accelerations are estimated in along-track as constant and periodical (sine and cosine term), and in cross-track only as periodical accelerations. All parameters were set up as constant (i.e., weekly estimates), except for the ERPs, which were estimated as daily piece-wise linear. The selection of core stations where the NNT and NNR conditions were applied with respect to SLRF2008<sup>7</sup> was done similar to Sošnica (2015). One additional difference to the solution by Sošnica et al. (2015) is that an elevation cut-off of  $10^\circ$  was used instead of  $3^\circ$ . The weekly LAGEOS solutions between 2010 and 2013 were derived from around 2700 observations per week, collected by on average 18 stations.

Fig. 5.14 shows the three time series that are based on weekly solutions: (1) the SLR solutions computed within this thesis (referred to as ETHZ), (2) the SLR solutions computed by AIUB, and (3) the GPS-based GR+ALL geocenter results. The geocenter positions derived in the two SLR solutions agrees well in all components. This was expected as the same software package and a similar processing strategy was used. A good agreement to the GR+ALL solution is present in the x- and y-component, but the x-component of the GR+ALL solution seems to be significantly phase-shifted. For the most interesting z-component, the GR+ALL weekly results are relatively large, compared to both SLR solutions. The corresponding

<sup>6</sup> The station selection was done as recommended in this document: [ilrs.gsfc.nasa.gov/data\\_and\\_products/products/#app1](http://ilrs.gsfc.nasa.gov/data_and_products/products/#app1), accessed June 2016.

<sup>7</sup> Release 2011-09-13, available at [ftp://cddis.gsfc.nasa.gov/pub/slr/products/resource/SLRF2008\\_110913.txt](ftp://cddis.gsfc.nasa.gov/pub/slr/products/resource/SLRF2008_110913.txt), accessed August 2016.

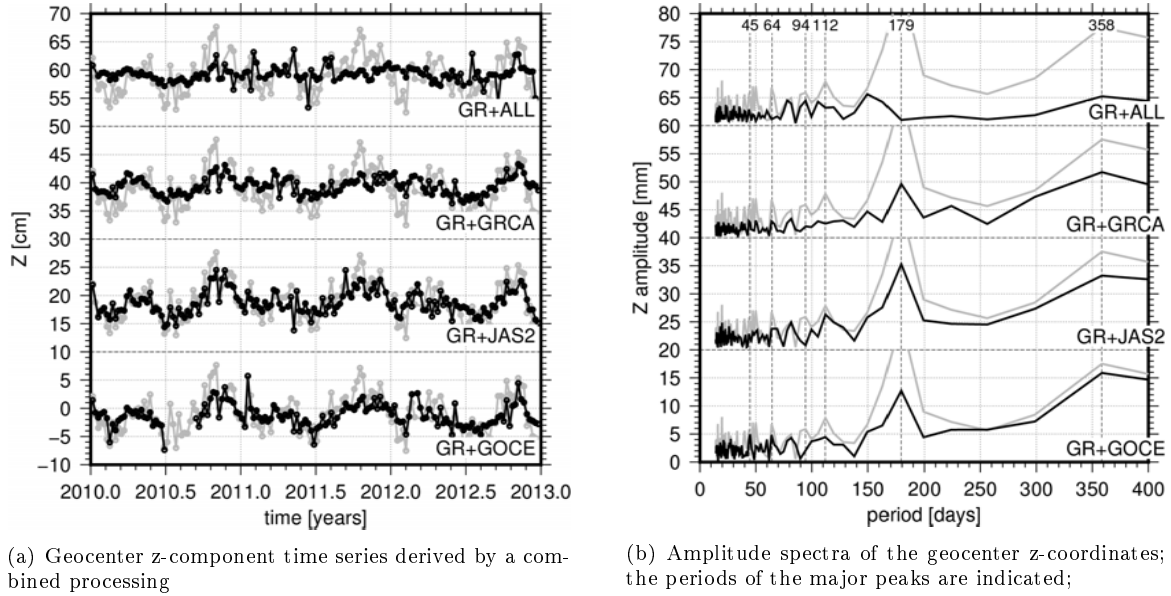


**Fig. 5.12:** Impact of individual LEOs on the geocenter z-component; for comparison the ground-only solution is shown in gray; all but *GR+GOCE* are vertically shifted by 20 cm and 20 mm with respect to each other

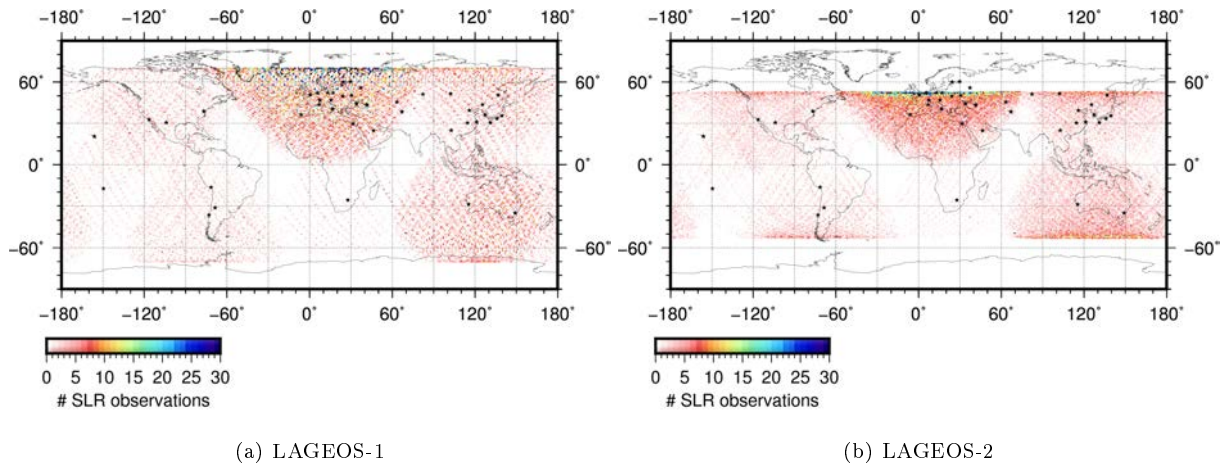


**Fig. 5.13:** Geographical distribution of LAGEOS SLR observations during 2010, the number of observations is counted in  $1 \times 1^\circ$  bins, SLR stations are indicated by asterisks

differences, also shown in Fig. 5.14, are up to  $\pm 4$  cm and show an annual periodic behavior. Concerning the scatter in the time series, the accordance in the x- and y-component is quite good, whereas the scatter of the *GR+ALL* z-component is twice as large as the corresponding values for SLR. However, it should be kept in mind that (in terms of GNSS) a rather small ground network of approx. 50 stations was processed and ambiguities have not been resolved.

To characterize the annual signals in all three directions, amplitudes  $A_i$  and phases  $\phi_i$  were estimated. To determine these, a least-squares fit of a polynomial and trigonometric functions was used similar to that of Kang et al. (2009). The corresponding function reads as

$$C(t) = \sum_{i=1}^n A_i \sin\left(\frac{2\pi}{P_i}(t - t_0) + \phi_i\right) + b_0 + b_1(t - t_0). \quad (5.7)$$

In Eqn. 5.7 the period is indicated by  $P_i$ , the time epoch  $t_0$  is given by January 1st;  $b_0$  and  $b_1$  are bias and trend, respectively. The derived amplitude and phase values for the *GR+ALL* and both SLR time series are summarized in Tab. 5.2 together with a choice of results present in the literature. First of all,

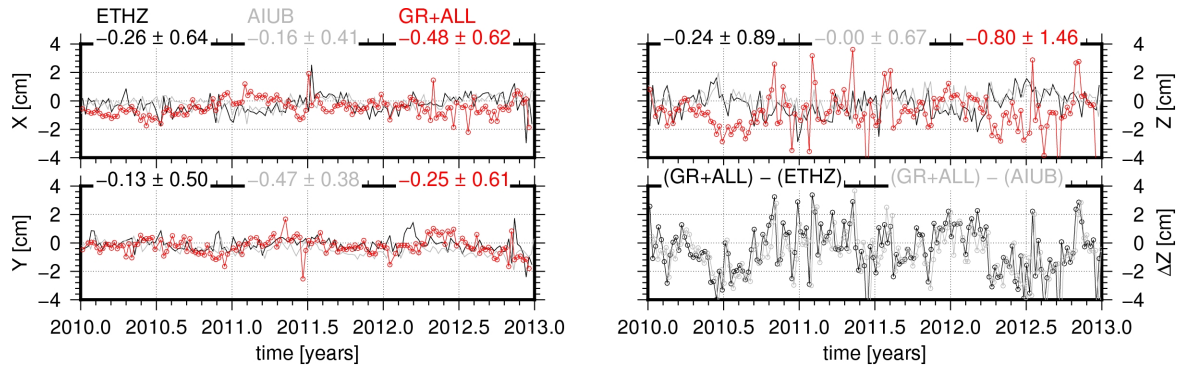


**Fig. 5.14:** Geocenter time series derived by a ground+LEO processing (GR+ALL, red) and SLR observations to LAGEOS in an in-house solution (ETHZ, black) and in the AIUB solution (gray); bottom: corresponding differences ETHZ - GR+ALL (black) and AIUB - GR+ALL (gray), respectively

**Tab. 5.2:** Annual components of geocenter motion; amplitude [mm] and phase [°] of the annual signal (according to Eqn. 5.7)

reference	data <sup>b</sup>	time span	X		Y		Z	
			amp.	phase	amp.	phase	amp.	phase
Blewitt et al. (2001) <sup>a,d</sup>	GPS	1996.0-2001.0	3.4±0.3	184±3	5.0±0.3	285±3	11.3±0.2	214±1
Wu et al. (2006) <sup>a,d</sup>	GPS/OBP	1999.0-2004.2	1.7±0.3	279±11	3.8±0.3	306±4	4.5±0.3	242±4
Rietbroek et al. (2012) <sup>a,d</sup>	GPS/OBP	2003.0-2010.0	2.1	214	2.4	303	3.0	239
Cheng et al. (2013) <sup>a</sup>	SLR	1992.9-2011.0	2.7±0.2	230±2	2.8±0.2	307±2	5.2±0.2	240±3
Dong et al. (2003)	GPS	2000.2-2002.3	4.8±0.4	220±5	3.6±0.4	320±7	9.4±0.5	105±3
Fritsche et al. (2010) <sup>a</sup>	GNSS	1994.0-2008.0	0.1±0.2	231±92	1.8±0.2	293±11	4.0±0.2	248±6
Lavallée et al. (2006) <sup>a</sup>	GPS	1997.2-2004.2	2.1±0.8	228±21	3.2±0.5	287±22	3.9±0.8	193±2
Kang et al. (2009)	GPS/LEO	2003.0-2007.5	3.0±0.2	244±14	2.4±0.2	286±14	4.0±0.2	344±16
König et al. (2015) <sup>a</sup>	SLR/LEO	2006.0-2012.0	1.7±0.6	210±21	2.3±0.8	341±20	2.4±0.8	220±19
Rebischung & Garayt (2013) <sup>a</sup>	GPS	1997.0-2009.0	2.3	272	3.2	315	3.0	104
AIUB (Sošnica et al., 2015) <sup>c</sup>	SLR	2010.0-2013.0	1.6±0.5	238±22	2.1±0.6	337±12	3.1±0.9	235±19
this study (LAGEOS)	SLR	2010.0-2013.0	4.0±0.8	231±13	1.5±0.7	309±29	6.2±0.9	265±13
this study (GR only)	GPS/LEO	2010.0-2013.0	4.5±1.0	103±20	2.6±1.3	297±40	12.6±3.7	112±24
this study (GR+ALL)	GPS/LEO	2010.0-2013.0	3.2±0.8	62±19	4.0±0.6	291±14	5.9±1.7	85±26

<sup>a</sup> phase results are converted to conform definition above

<sup>b</sup> data: the used type of LEO data sets (GPS, SLR, K-band measurements, gravity data) can be found in the corresponding reference

<sup>c</sup> computed from published time series

<sup>d</sup> based on inverse approaches

the annual signal derived from the ETHZ solution agrees well with other values published. However, the phase uncertainties are rather large as in this solution only three years of data were considered. The ground-only GPS solution shows a good agreement in y but large amplitudes and different phases in the x- and z-component. The phase of the z-component is, however, comparable to the values derived by Dong et al. (2003) and Rebischung & Garayt (2013). The GR+ALL solution shows a better agreement in the amplitudes, where especially the z-amplitude is reduced to a more realistic value. In the phase, only the y-component is comparable to the reference values; the values for the x- and z-direction differ significantly from the values estimated by SLR. However, as mentioned before, these disagreements are most probably related to the zero-difference processing including float ambiguities and systematic effects due to solar radiation pressure. In any case, further investigations are needed to solve this issue. Interestingly, Haines et al. (2015) reported also a significant disagreement ( $\approx 100^\circ$ ) between the estimated annual phases in the x- and z-component and their reference solution, which was based on the degree-1 approach (Wu et al., 2013). A topic not discussed here is the effect of the receiver and the satellite clocks, which were estimated epoch-wise. However, if these clocks could be modeled and estimated piece-wise linear in intervals of, e.g., 5 minute it is assumed that the geocenter and other parameters will benefit. For example, with the Galileo

space hydrogen masers and ultra-stable oscillators on-board LEOs this concept will be feasible within the next years.

### 5.3 GPS Satellite Antenna Phase Centers

Contrary to the results discussed in the previous section, in the early GNSS era, Malla & Wu (1989) predicted that daily GPS-only geocenter solutions based on small networks could reach centimeter accuracy. With the advances in GPS processing and the growing space and ground segment, Heflin et al. (2002) presented an independent GPS-based TRF with 1 cm and 1 ppb agreement to the ITRF2000. The long-term stability of this TRF was found to be 6 mm/yr for the origin and 0.6 mm/yr for the scale. However, further studies reported a significantly worse agreement of the scale. As concluded by Zhu et al. (2003), this effect was attributed to phase center biases for the GPS block IIR satellites launched from 1997 onwards to replenish the GPS constellation. According to Sect. 2.1.1, the actual location of the GPS phase center as signal transmission point differs from the antenna reference point and is, moreover, not a unique point but depends on the signal direction. Therefore, individual offsets regarding the spacecraft CoM and individual variations depending on azimuth and nadir direction have to be considered for the GPS satellite antennas. The IGS started in 1996 to consider relative antenna corrections for the receiver antennas. However, at that time the satellite transmitting antennas were considered only by block-specific offsets provided by the GPS operational control segment. Consequently, Ge et al. (2005) found that the GPS derived terrestrial scale changed with a rate of 1 ppb/yr related to insufficiently known offsets for the subsequently launched GPS block IIR satellites. This rate corresponds to 6.4 mm/yr in the station height component. After generating standards for modeling and absolutely calibrating GPS antenna offsets and variations (Schmid et al., 2005, 2007), the IGS starts in 2006 to take absolute PCO/PCVs for the receiver and the satellite antennas into account. Consequently, new GPS-based TRFs with increased accuracy were published, for example, by Rülke (2009). The current IGS standard to determine GPS satellite antenna offsets and variations is based on the processing of a global GNSS network. In order to avoid singularities when estimating GPS satellite phase centers the receiver antenna patterns are fixed. They are determined by absolute antenna calibrations as described in detail by Schmid (2009). The current IGS antenna correction file contains 290 receiver antennas (and 227 transmitter antennas)<sup>8</sup>. Concerning the calibration method 61.4 % of the listed receiver antennas have been determined absolutely by a robot calibration. The major issue in the satellite antenna calibration is the direct correlation between the antenna patterns, the ground station height coordinate, and the terrestrial scale. As a rule of thumb an error in the satellite phase center z-offset  $\Delta z$  will result in a station height error  $\Delta h \approx -0.05\Delta z$  (Schmid, 2009). According to Zhu et al. (2003) the relation between a scale bias  $\Delta_{\text{scale}}$  and an error in the mean z-offset  $\overline{\Delta z}$  (average over all satellite-specific z-offset errors  $\Delta z_i$ ) reads as

$$\Delta_{\text{scale}}[\text{ppb}] = -7.8\overline{\Delta z}[\text{m}] \quad \text{with} \quad \overline{\Delta z} = \sum_{i=1}^n \frac{\Delta z_i}{n} . \quad (5.8)$$

Consequently, the network scale has to be constrained when estimating GNSS antenna phase center patterns from ground observations. Usually this is done by applying a no-net-scale condition to the datum stations. However, when constraining the network scale the scale provided by SLR and VLBI is introduced into the GNSS satellite patterns and by them into any further GNSS-based solution. As mentioned by Haines et al. (2015), the newer GNSS-based TRF realization, derived by using the IGS antenna corrections, are, therefore, not any longer fully independent from other space techniques. Additionally, it has to be mentioned that, due to the constrained network scale, any uncertainty inherent in the applied TRF propagates into the estimated GNSS satellite patterns. Considering Eqn. 5.8, even a small bias in the terrestrial scale will cause a large common error in the estimated z-offset. For example, a rather small systematic station height bias of 1 mm, equivalent to a scale bias of 0.15 ppb, will cause a 2 cm error in

<sup>8</sup> Available at <ftp://igscb.jpl.nasa.gov/pub/station/general/igs08.atx>, accessed May 2016.

the estimated z-offsets. Due to the GPS satellite altitude, ground-based observations and, therefore, also GPS satellite antenna patterns calibrated by ground observations are limited to nadir angles of  $14^\circ$ . LEO missions like OSTM/Jason-2, however, see GPS satellites up to nadir angles of  $17^\circ$  (cf. Sect. 3.5.1). Therefore, a high-quality LEO GPS processing requires extended phase center patterns. Additionally, it has to be mentioned that the newer GPS satellites transmit reasonable signal strength up to a nadir angle of  $23^\circ$  (Schmid, 2009).

### 5.3.1 Impact of LEO GPS Observations on the Determination of GPS Satellite Antenna Patterns

The impact of LEO GPS observations on the estimation of GPS satellite antenna phase centers is discussed within this section. During orbit determination the geocentric receiver position is estimated on the centimeter level and, moreover, this position has a negligible sensitivity to the terrestrial scale (Haines et al., 2015). This so-called gravitational constraint is based on the third Keplerian law, which reads as (with orbital period  $T$  and mean motion  $n$ )

$$\left(\frac{T_1^2}{T_2^2}\right) = \left(\frac{a_1^3}{a_2^3}\right) \quad \Leftrightarrow \quad n^2 a^3 = \text{GM} . \quad (5.9)$$

As the geocentric gravitational constant GM is introduced according to the IERS conventions, Eqn. 5.9 can be re-written as  $n^2 a^3 = \text{const}$ . Consequently, the satellite's semi-major axis  $a$  is constrained as the mean motion  $n$  is defined by the orbit dynamics and measured with a relative accuracy of around  $10^{-10}$ . The corresponding partial derivative of Eqn. 5.9 reads as

$$\frac{\Delta n}{n} = -\frac{3}{2} \frac{\Delta a}{a} . \quad (5.10)$$

This equation shows the relationship between an error  $\Delta n$  in the orbital period and an error  $\Delta a$  in the semi-major axis. Considering the current accuracy of GM which is 0.5 ppb,  $\Delta a$  amounts to 1 mm and 4 mm for 1000 km and 20'000 km altitude, respectively (Haines et al., 2015). However, the measured orbit period could be affected by uncertainties in the Earth rotation. Haines et al. (2015) estimated that a corresponding error in the orbital period of  $10 \mu\text{s}$ , amounts to an error of not more than 4 mm in  $a$ . The error in the semi-major axis can also be transferred into an error  $\Delta s$  in along-track. The corresponding relationship reads as

$$\Delta s = \Delta n T a \quad \Leftrightarrow \quad \frac{\Delta n}{n} = \frac{\Delta s}{2\pi a} . \quad (5.11)$$

Consequently, the relationship between the error in the semi-major axis and an error in along-track for one revolution reads as

$$\Delta s = -3\pi \Delta a . \quad (5.12)$$

Under the assumption that orbit dynamics are appropriated modeled,  $\Delta s$  will be small. Therefore,  $\Delta a$  is well calculated during the orbit determination process. According to Ziebart et al. (2005) and the findings from Sect. 4.4, uncertainties in modeling non-gravitational forces will influence the semi-major axis by not more than 1-2 cm. However, it has to be mentioned that the considerations so far are, in the strict sense, only valid for the dynamic orbit representation as the estimated pseudo-stochastic orbit parameters distort the direct relationship between  $\Delta a$  and  $\Delta s$ . Obviously, the gravitational constraint is applied to the GPS satellites whenever antenna phase patterns and GPS orbits are estimated simultaneous. Contrary to the GPS satellites, the ground stations have no access to the gravitational constraint as they are not in free fall. When using LEO GPS observations to determine GPS antenna phase center pattern, however, the gravitational constraint is applied to the transmitting and to the receiving antennas. Consequently,

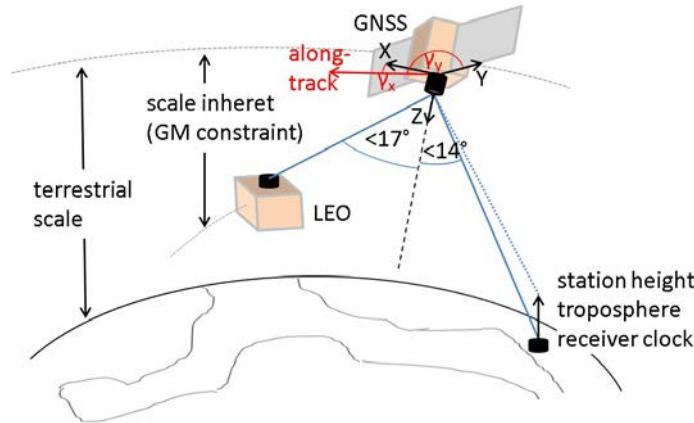


**Fig. 5.15:** Concept of GNSS phase center calibration based on ground receivers and LEOs

the correlation between the GPS antenna phase center patterns and the terrestrial scale will be partially dissolved. Apart from the decorrelation between antenna patterns and scale, estimating GPS satellite phase center patterns from LEO-based observations provides some more benefits as mentioned by Dilbner et al. (2011). First of all, LEO GPS observations are not influenced by the troposphere, whereas for ground stations the high mathematical correlations between station height, tropospheric delay, radial component of the GPS orbits, antenna parameters and receiver clock have to be solved (Rothacher, 2002). Additionally, due to the missing troposphere there is in principle no need to set an elevation cut-off angle. However, Jäggi et al. (2009) recommended to apply a very low cut-off angle to reduce near-field multipath effects. Secondly, the rapidly changed geometry between LEO satellite and GNSS constellation should improve the GPS orbit determination and thus also the estimation of satellite antenna patterns. And thirdly, also related to changing geometry, a GPS receiver on-board a LEO allows to sample GPS signals from all parts of the transmitting antennas within a comparably short time. Fourthly, the increased nadir coverage (in the case of OSTM/Jason-2 up to  $17^\circ$ ) has to be mentioned. Fig. 5.15 shows the concept of estimating satellite antenna patterns from ground- and space-based observations.

In a previous study Haines et al. (2004) estimated GPS satellite antenna PCVs from Jason-1 and GRACE observations in order to improve their Jason-1 orbit determination. Apart from improvements in the derived Jason-1 orbit solution, they found decreased RMS values when applying the derived GPS satellite PCVs. As mentioned already, Haines et al. (2015) provided GPS satellite PCVs and an independent TRF solution derived from TOPEX/Poseidon (1993) and GRACE-B (2002-2012)<sup>9</sup>. Dilbner et al. (2011) determined GPS satellite antenna patterns from a combined processing of GPS observations recorded at the ground, on Jason-1, and on OSTM/Jason-2. They found a good agreement between the derived satellite antenna patterns and the corresponding IGS solutions for nadir angles below  $14^\circ$ . When introducing the derived satellite PCVs, which were estimated up to  $17^\circ$ , the RMS of the phase residuals for the orbit determination dropped from 7.2 mm down to 6.5 mm.

### 5.3.2 Determination of LEO Receiver Antenna Phase Centers

The estimation of GPS antenna phase center patterns requires in any case a priori information concerning the receiver antenna phase centers as otherwise the estimated satellite antenna patterns will absorb the receiver patterns partially. According to Schmid (2009) the relationship between an elevation-dependent receiver pattern  $\phi(z)$  and a nadir-dependent satellite antenna pattern  $\phi'(z')$  is given by

$$\phi'(z') = \phi' \left( \arcsin \left( \frac{R_E}{r_{sat}} \sin(z) \right) \right) = \phi(z). \quad (5.13)$$

<sup>9</sup> As mentioned by them, the patterns are determined using GRACE-B observations, whereas the TRF solutions based on GRACE-A data.

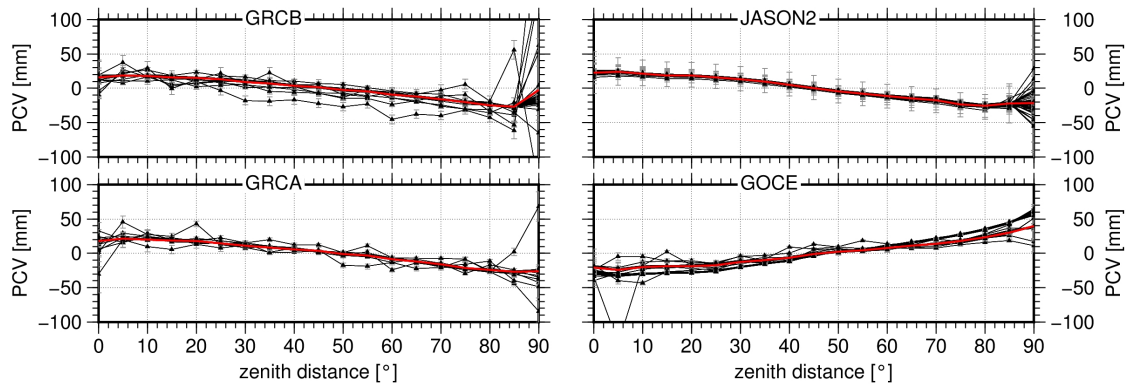


**Fig. 5.16:** Weekly solutions (*black*) of receiver antenna phase centers variation for GRACE, GOCE, and OSTM/Jason-2 (no azimuth-dependent variations were set up); processing period 2010; averaged PCV in *red*

Here,  $R_E$  refers to the Earth radius and  $r_{sat}$  to the geocentric satellite position. Consequently, LEO-specific antenna phase center patterns were estimated in a previous processing step. In order to determine these patterns, LEO orbits and LEO phase center patterns were determined while GPS satellite orbits and clocks were fixed to the CODE products. As LEO receiver antenna phase centers and constant empirical accelerations are highly correlated, the latter were heavily constrained in radial and along-track direction. The LEO phase centers were estimated using a polynomial approach with 19 parameters corresponding to PCVs with a  $5^\circ$  resolution in elevation. No azimuth-dependency was considered for the LEO patterns. Fig. 5.16 shows the derived weekly solutions. The processing was carried out for the year 2010, as in the years 2011 and 2012 slightly reduced orbit accuracies were present, caused by the increased non-gravitational perturbations (cf. Sect. 4.3). The derived weekly patterns show variations of not more than 50 mm depending on the elevation angle. Especially for OSTM/Jason-2 the agreement of the weekly solutions is very good. The corresponding differences reach 20 to 30 mm for the other satellites. The variations in the GRACE and GOCE solutions might be caused by systematics introduced by near-field effects, as the GRACE GPS antennas are lowered with respect to the satellite surface and the GOCE GPS antennas are mounted on the edge of the solar wings (Dilckner et al., 2006). The GPS antennas of OSTM/Jason-2 are mounted on top the satellite bus. The PCV at  $90^\circ$  zenith distance is determined with a larger scatter due to the elevation cut-off at  $3^\circ$ .

Subsequently, the derived LEO receiver patterns are compared and validated against patterns found in the literature. Fig. 5.17(a) shows the phase center pattern for the GOCE GPS helix antenna (GOCE SSTI-A) as derived by Bock et al. (2011a). They estimated the GOCE PCV from ionosphere-free phase residuals derived in a reduced-dynamic orbit determination between April 10 and September 28, 2010. Following the residual approach described by Jäggi et al. (2009) they grouped the residuals in  $1^\circ \times 1^\circ$  bins in azimuth and elevation direction. According to Bock et al. (2011a) the derived variations are mainly between -30 and +30 mm while some extreme values at low elevations reach -55.2 and +127.9 mm. The PCV computed within this analysis shows a different scatter as only an elevation-dependent function was estimated (Fig. 5.17(b)). However, the variations are also between -30 and +30 mm. In order to compare both patterns the following formula was applied (based on Schmid, 2009)

$$\Delta PCV = PCV_2 - PCV_1 + PCO_2 \cos(z) - PCO_1 \cos(z) + \Delta \text{offset} \quad (5.14)$$

to account also for differences in the corresponding PCOs. In Eqn. 5.14, the difference  $\Delta PCV$  between both patterns is estimated considering also an empirically estimated offset difference  $\Delta \text{offset}$ . The corresponding difference between the patterns estimated by Bock et al. (2011a) and that estimated here is shown in Fig. 5.17(c). The differences are between -10 and +10 mm with maximal values for large zenith angles.

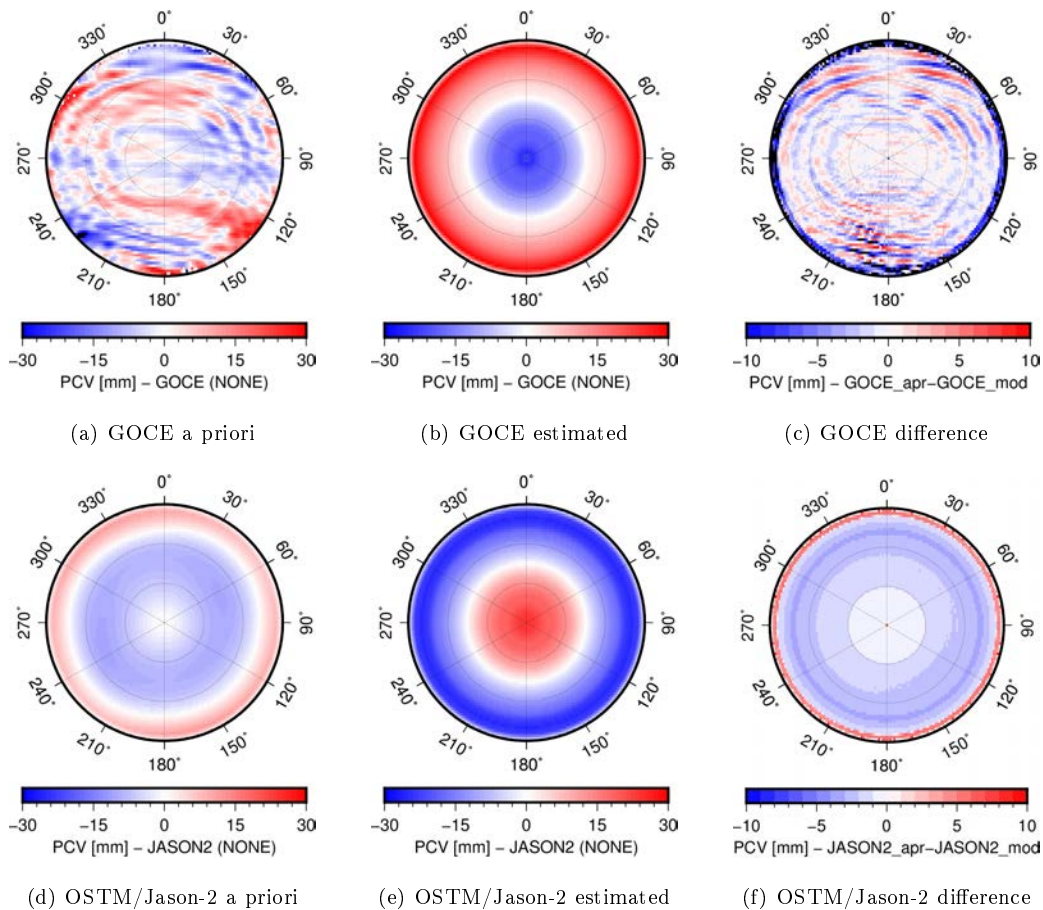


**Fig. 5.17:** Receiver antenna phase centers for GOCE and OSTM/Jason-2; the GOCE a priori pattern refers to Bock et al. (2011a), the OSTM/Jason-2 pattern refers to Montenbruck et al. (2009); Azimuth=0° points in flight direction

The antenna helix structure is visible in the derived differences as it is expected when comparing an elevation-dependent pattern against an azimuth-elevation-dependent one. Fig. 5.17(d-f) are analogous for the phase center pattern of the OSTM/Jason-2 GPS antenna. The reference pattern for the antenna type “S67-1575-14+CRG” (Fig. 5.17(d)) was estimated by Garcia & Montenbruck (2007) during a ground-based field calibration campaign. The calibration procedure is described in detail in Montenbruck et al. (2009). Comparing the reference patterns in Fig. 5.17(a) and 5.17(d) the different antenna designs are clearly visible. For the antenna S67-1575-14+CRG equipped with choke-rings, a very regular pattern with mainly elevation-dependent variations is visible, whereas the GOCE helix antenna shows a highly irregular behavior with larger variations. Driven by the regular shape of the S67-1575-14+CRG antenna the derived differences are below 3 mm in the PCV comparison. Only for large zenith distances, slightly larger differences are present. No comparison was performed for GRACE as corresponding antenna patterns are not freely available. In summary, the derived LEO receiver phase center patterns agree well with the reference patterns found in the literature. Therefore, they are introduced as a priori in the next step, where the GPS satellite antenna offsets are estimated.

### 5.3.3 Determination of GPS Satellite Antenna Phase Center Offsets

The previously estimated LEO receiver antenna patterns are introduced as a priori to estimate GPS satellite antenna offsets. GPS satellite antenna offsets were setup satellite-specific and stacked to weekly solutions<sup>10</sup>. The mean z-offset improvements derived from the GR-only and the GR+ALL solution are

<sup>10</sup> The following results are submitted for publication to the Journal of Geodesy (Männel & Rothacher, 2017b)

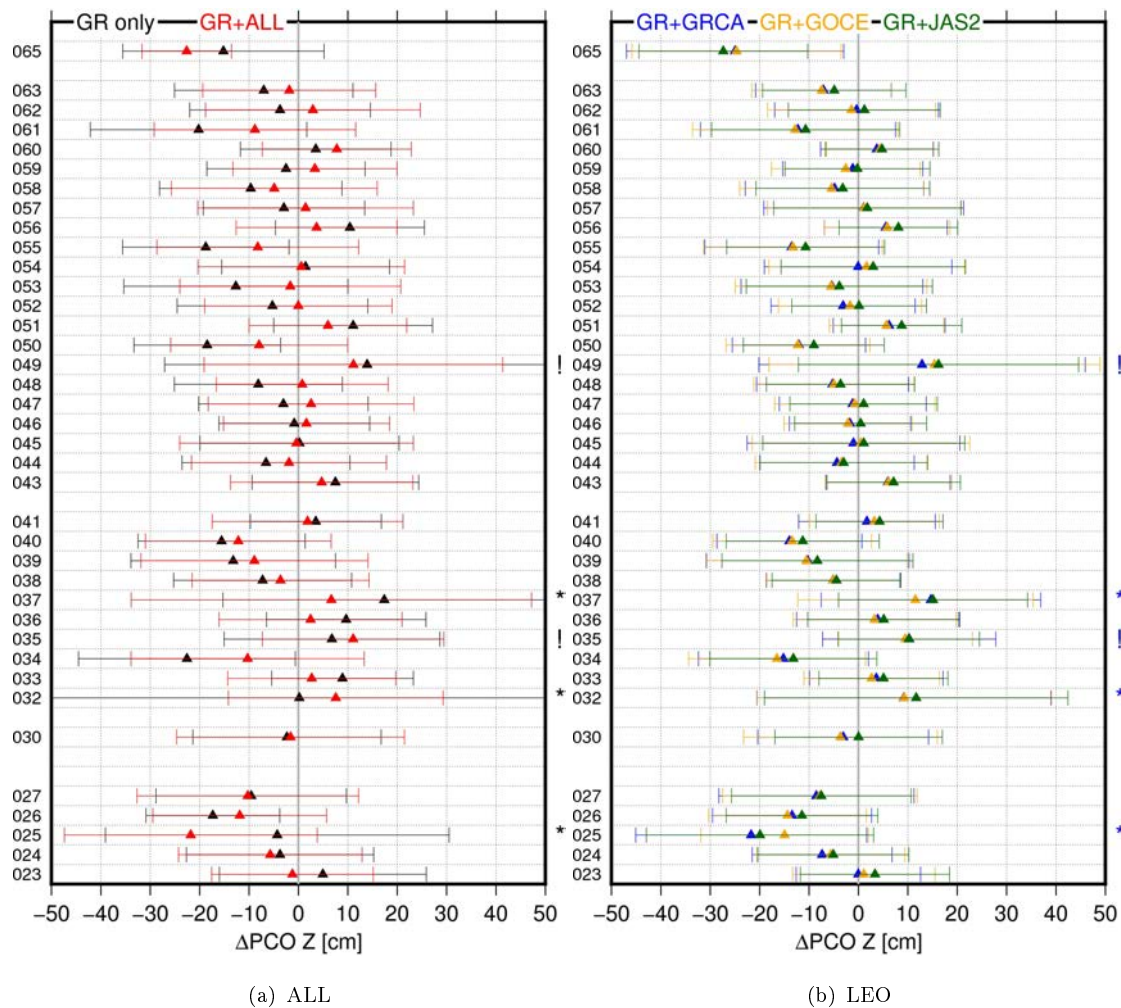


**Fig. 5.18:** Mean corrections for satellite PCO z-component with respect to IGS PCO values (igs08.atx); left side SVN number; (\*) indicates that less than 10 weekly solutions are available; (!) indicates spacecraft related particularities

shown in Fig. 5.18(a) for the GPS satellites with spacecraft vehicle numbers (SVN) 023 to 066. As the official IGS satellite antenna offsets were introduced as a priori values, the term “corrections” is used with respect to these IGS values. Satellites, which participated within less than 10 weekly solutions, are indicated by asterisks. The considered 38 spacecraft belong to five different spacecraft types. Tab. 5.3 provides an overview of all GPS satellite blocks including the corresponding SVNs and some general remarks. In Fig. 5.18(a) some satellites are missing as they were already decommissioned (028 in 1996, 029 in 2007, 031 in 2005) or launched later than end of 2012 (e.g., 064 in 2014). Additionally, two spacecraft suffer from special issues indicated by exclamation marks. Firstly, satellite 035, one of the two GPS spacecraft observable by SLR, was originally decommissioned in 2009 and reactivated in 2011. Secondly, satellite 049, launched in 2009 to demonstrate the new GPS  $L_5$  signal<sup>11</sup>, never entered service officially as the signal quality was too poor. After the decommission in 2011, the spacecraft was subsequently reactivated for testing while switching the PRN several times. The derived mean corrections for the z-offsets differ from the IGS values by up to 20 cm. The standard deviation of the computed mean values is, however, at the level of some decimeters. Averaged over all satellites except 025, 032, 035, 037, 049, the estimated mean offsets differ by  $-1.19 \pm 5.52$  cm from the IGS values as given in igs08.atx<sup>12</sup>. Considering the ground-only solution a difference of  $3.69 \pm 9.46$  cm was found with respect to igs08.atx. Dilskner et al. (2011) derived,

<sup>11</sup> The GPS  $L_5$  signal (frequency 1.176 GHz) is designed for safety-of-life transportation and other high-performance applications. Within the current pre-operational phase  $L_5$  signals are transmitted by 12 GPS spacecraft (June 2016).

<sup>12</sup> [https://igs.cb.jpl.nasa.gov/igs\\_cb/station/general/igs08.atx](https://igs.cb.jpl.nasa.gov/igs_cb/station/general/igs08.atx), accessed June 2016

**Tab. 5.3:** GPS satellite block types

block	SVN	remarks
block I	001-006, 008-011	final decommission in 1995
block II	013-021	final decommission in 2007
block IIA	022-040	transmitting antennas identical to block II, final decommission in 2016
block IIR-A	041, 043-046, 051, 054, 056	R=replenishment
block IIR-B	047, 059-061	transmitting antennas identical to block IIR-M
block IIR-M	048-050, 052-053, 055, 057-058	M=modernized
block IIF	062-073	F=follow-on
block III		first launch scheduled for 3 May 2017
others	007, 012, 042	007 failed to orbit; 012 prototype, never launched; 042 failed to orbit

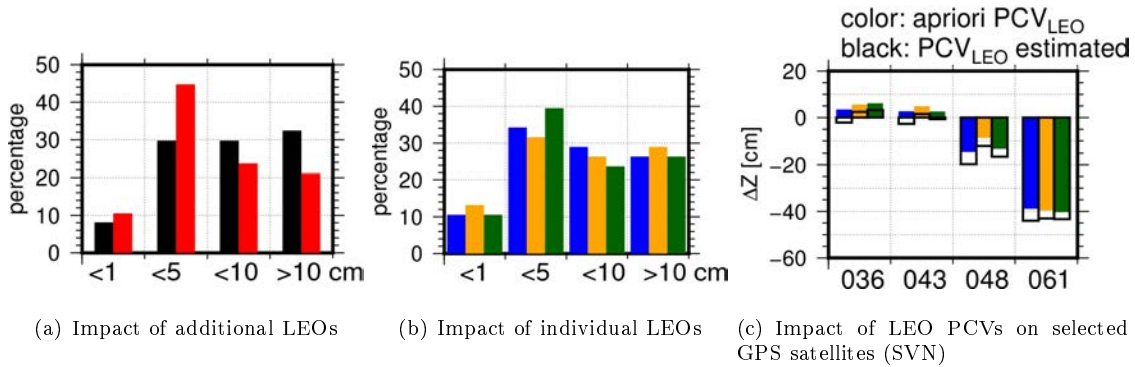


**Fig. 5.19:** Differences of mean corrections for satellite PCO  $z$ -component with respect to IGS PCO values (igs08.atx); the color coding is identical to Fig. 5.18: GR-only (*black*), GR+ALL (*red*), GR+GRACE (*blue*), GR+GOCE (*orange*), GR+OSTM/Jason-2 (*green*)

in a comparable study, a difference with respect to igs08.atx of  $-13.6 \pm 5.2$  cm while considering Jason-1 and OSTM/Jason-2 in addition to a ground network. However, for an unexplained reason they reported a better agreement of  $2.5 \pm 6.4$  cm to igs05.atx.

The distribution of the computed mean corrections is shown in Fig. 5.19(a). Obviously, corrections are smaller in the GR+ALL results than in the ground-only solution. In the GR+ALL solution 85 % of the derived mean corrections are smaller than 10 cm, whereas in the GR-only solution not more than 62 % are below this threshold. Analogous mean corrections are shown in Fig. 5.18(b) for the combination of ground network and individual LEOs. In summary, the results agree very well between the different solutions. Compared to Fig. 5.18(a), the estimated mean corrections are mostly below 10 cm. Fig. 5.19(b) shows the agreement between the single LEO solutions. In summary,  $\approx 70$  % of the mean corrections are below 10 cm for these solutions. The impact of the adjusted LEO antenna patterns is assessed in Fig. 5.19(c), where the mean corrections for solution with estimated LEO PCVs and with the reference LEO PCVs are plotted. Obviously, mean corrections differ by not more than a few centimeters. Even in the case of GRACE-A (where no reference LEO PCV was considered a priori) the differences are only slightly larger than for the other two solutions and do not exceed 4 cm.

Fig. 5.20 shows the estimated mean satellite antenna offset corrections (GR+ALL) in all three directions for solutions with and without applying a no-net-scale condition to the ground stations. The difference between both solutions are found to be rather small. In the  $x$ - and  $y$ - component the difference does not exceed one centimeter and in the  $z$ -direction differences are still below 2 cm. Obviously, the included LEO observations allow to resolve the correlations between satellite antenna PCO and terrestrial scale via the gravitational constraint. A similar conclusion was derived by Dilfner et al. (2011).

Within this paragraph, the impact of the introduced LEO observations on the GPS satellite antenna  $x$ -

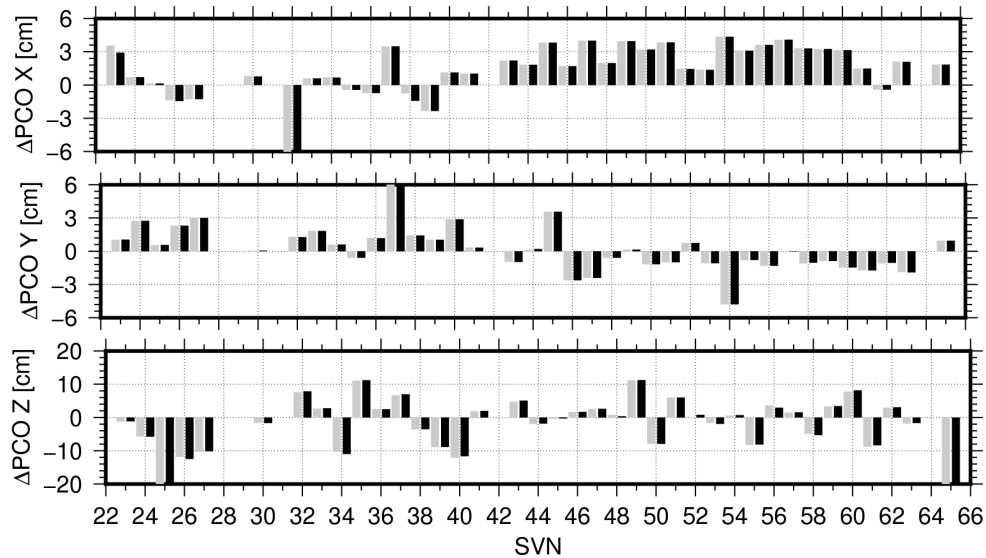


**Fig. 5.20:** Mean satellite antenna PCO corrections in x, y, and z-direction with (*gray*) and without (*black*) the NNS condition; please note the different scales (GR+ALL solution)

and y-offsets is discussed. In general, the horizontal GPS satellite phase center offsets are highly correlated with the GPS satellite orbits. As pointed out by Schmid (2009), it is, for example, impossible to separate a satellite antenna x-offset from an along-track orbit error, if the body-fixed x-axis is orientated parallel or anti-parallel to the flight direction. However, as mentioned in Sect. 4.2.2, GPS satellites are permanently rotating in order to point their transmitting antenna towards the Earth and their solar panels towards the Sun. Consequently, the correlation between orbit and antenna phase center can be resolved by considering a reasonably long time span. As the actual rotation rate depends on the current  $\beta_0$  angle (see Sect. 4.2.2), an additional correlation exists between the antenna phase center and the  $\beta_0$  angle. Schmid et al. (2007) found that the accuracy of the derived GPS satellite phase center increases for smaller  $\beta_0$  angles. The driving mechanism for this behavior is that the GPS satellite rotation rate is faster during periods of low  $\beta_0$  angles (to comply with the attitude rules). Consequently, the separation between x- and y-offset becomes easier during these periods. Fig. 5.21 shows the derived weekly GPS satellite PCOs in x- and y-direction for four satellites belonging to four different block types. For the horizontal PCO components, derived from the ground-only solution, the correlation with the  $\beta_0$  angle is obvious. Especially, SVN 036 (block IIA), exposed to larger  $\beta_0$  angles than the other three satellites, shows large variations for the derived PCOs. Contrary to the findings of Schmid et al. (2007), no significant effect is observable during the eclipse seasons. The reason for this behavior is comparably simple: in the study described here observations to GPS block IIA satellites are not considered during satellite eclipses and within 30 minutes after returning to sunlight. In the GR+ALL solution, the estimated weekly offsets are much smoother, especially in the x-direction. Obviously, the rapidly changing observation geometry between GPS and LEO satellite help to resolve the systematics between  $\beta_0$  angle and horizontal PCOs. In the y-component the improvement is weaker, however, the variations during periods of high  $\beta_0$  angles are slightly smaller for the block IIR and IIF satellites (043, 048, and 062). The difference between SVN 036 and the others is an additional attitude condition applied for the block II/IIA spacecraft which limits the angle between the spacecraft z-axis and the Sun to the range  $0^\circ$  and  $180^\circ$ . For the newer block IIR and IIF type satellites, this angle is allowed to vary between  $0^\circ$  and  $360^\circ$  (Hugentobler et al., 2003). The improvement due to the additional LEOs is very clearly shown in Fig. 5.22. This figure shows the formal errors of the weekly PCO estimation with respect to the satellite-specific weekly mean  $\beta_0$  angle. The estimation based solely on the ground network shows, for large  $\beta_0$  angles, formal errors of 2 and 4 cm in x- and the y-direction, respectively. This dependency on the satellite-specific  $\beta_0$  angle was also reported by Schmid et al. (2007) for GPS offsets and by Steigenberger et al. (2016) for Galileo offsets. Adding the four LEOs the formal errors decrease significantly for larger  $\beta_0$  angles. For small  $\beta_0$  angles ( $|\beta_0| < 20$ ) the formal errors are similar in both

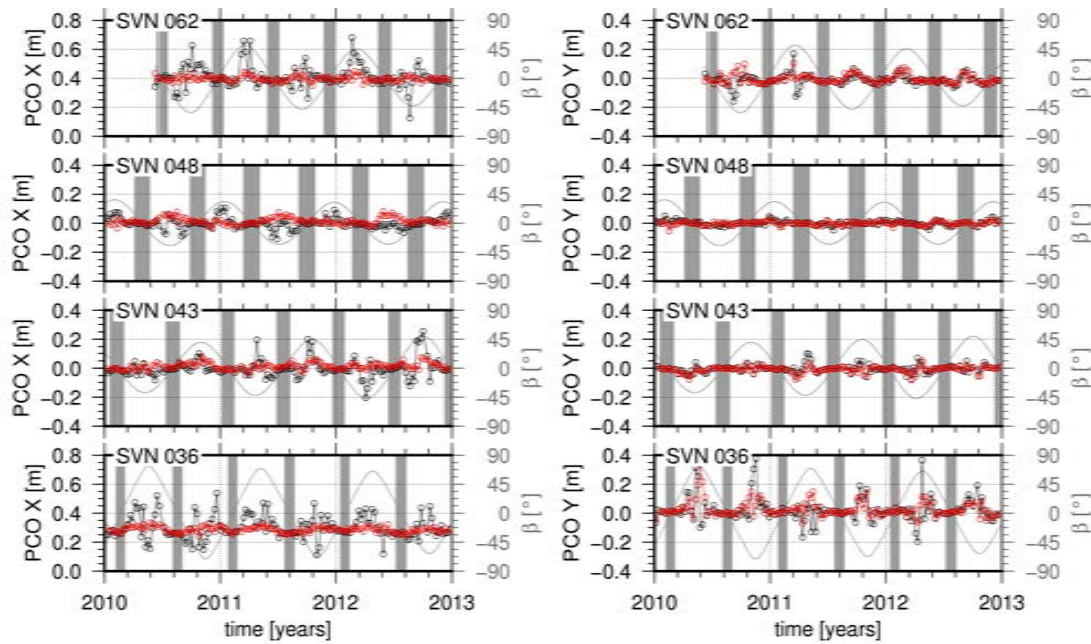


**Fig. 5.21:** Weekly results of GPS satellite antenna phase center offsets in x- and y-direction; GR-only (*black*) and GR+ALL (*red*) solution; satellite-specific  $\beta_0$  angle (*gray*); time periods marked gray are eclipse seasons

solutions, whereas for large  $\beta_0$  angles the formal errors are decreased from about 2 cm to below 0.5 cm compared to the GR-only solution. The correlation factors between formal errors and  $\beta_0$  angle are reduced from around 0.9 to 0.4 for IIA and IIF satellites and from 0.9 to 0.76 for IIR satellites. For the formal errors of the y-component, a dependency on the Sun's elevation above the orbit plane remains. However, the formal errors decrease remarkably. The formal errors are reduced by a factor of 2 for large  $\beta_0$  angles. As indicated in Fig. 5.22, no decrease is found in the correlation factors, which remain at a level of 0.8. The different behavior between the x- and y-component is related to the angles  $\gamma_x$  and  $\gamma_y$ . These angles are opened between along-track direction and the body-fixed x- and y-axis, respectively. As shown by Schmid et al. (2007)  $\gamma_x$  varies constantly without a dependency on  $\beta_0$ , whereas  $\gamma_y$  depends on  $\beta_0$  and remains close to  $0^\circ$  or  $180^\circ$  during periods of large  $\beta_0$  angle. Thus, the spacecraft y-axis is orientated parallel or anti-parallel to the flight direction during this periods. Consequently, it is hard to resolve the correlation between orbit and GPS satellite antenna y-offset.

In summary, GPS satellite antenna offsets were derived based on a combined ground- and space-based GPS processing. The derived z-offsets agree well with the IGS values. Furthermore, it turned out that due to the introduced LEO observations the no-net-scale condition became obsolete and therefore, the derived offsets are not influenced by any scale information. A considerable improvement resulting from introducing LEOs is present for the x- and y-offsets. Especially, the uncertain estimation during periods of large  $\beta_0$  angle was stabilized by the LEOs. For the x-offsets of block IIR-M and IIF, no dependency on the  $\beta_0$  angle exists in the combined solution.

## 5.4 Station Coordinates and Transformation Parameters with Respect to ITRF2008

Within this section ground station coordinates are analyzed based on weekly transformations with respect to ITRF2008. The coordinates were derived in a subsequent processing, while estimating GPS and LEO orbits, station coordinates, ERPs, and tropospheric delays. GPS satellite PCOs and the geocenter were removed from the normal equations and, therefore, fixed to their a priori values. Consequently, the station coordinates were estimated while applying only a NNR condition for the selected core stations. Fig 5.23

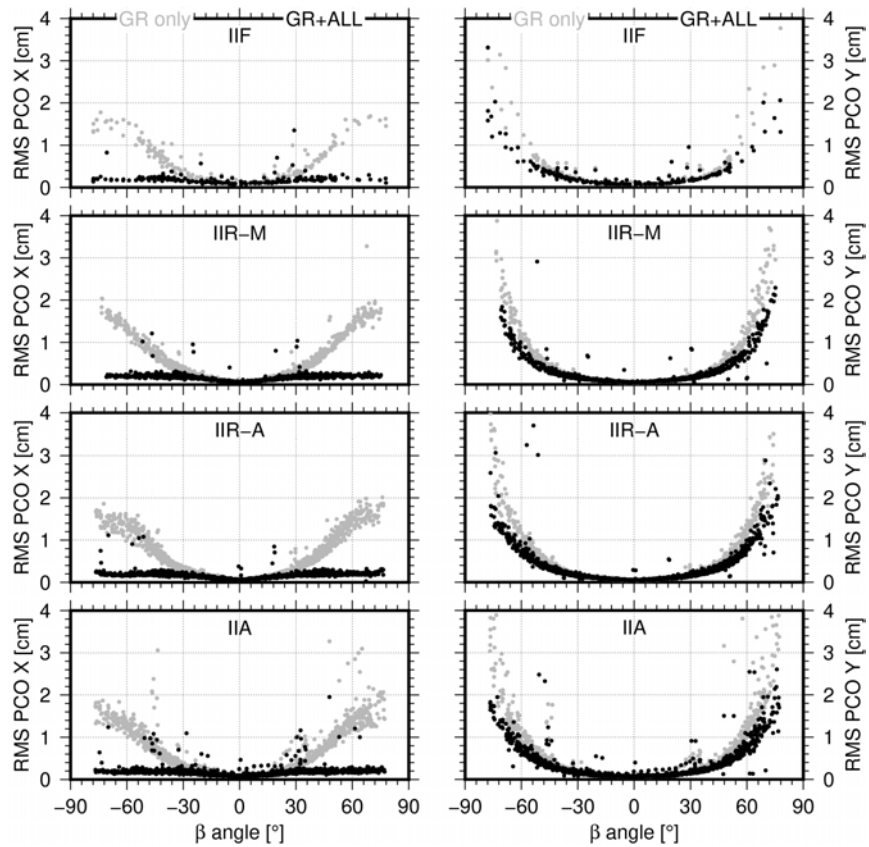


Fig. 5.22: Formal errors of GPS satellite antenna phase center offsets in x- and y-direction with respect to  $\beta_0$  angle; GR-only (gray) and GR+ALL (black) solution

Tab. 5.4: Signals in the weekly transformation parameters to ITRF2008; scale is converted to Earth's surface; phases are shifted by  $180^\circ$  to be consistent with Tab. 5.2

solution	parameter	amplitude [mm]	phase[mm]	bias [mm]	trend [mm/yr]	RMS [mm]
GR-only	translation x	$4.8 \pm 1.1$	$120 \pm 17$	$-1.9 \pm 2.0$	$-2.9 \pm 3.8$	8.5
	translation y	$3.8 \pm 1.4$	$304 \pm 25$	$4.1 \pm 2.3$	$0.5 \pm 4.4$	9.9
	translation z	$15.6 \pm 3.7$	$114 \pm 10$	$27.3 \pm 7.0$	$-33.8 \pm 13.2$	29.55
	scale	$1.1 \pm 0.1$	$246 \pm 11$	$1.8 \pm 0.3$	$-0.1 \pm 0.5$	1.1
GR+ALL	translation x	$3.2 \pm 0.9$	$63 \pm 23$	$5.1 \pm 1.8$	$-3.0 \pm 3.4$	7.4
	translation y	$3.4 \pm 1.0$	$296 \pm 23$	$-1.7 \pm 1.9$	$7.0 \pm 3.7$	7.9
	translation z	$5.4 \pm 1.9$	$79 \pm 31$	$7.4 \pm 3.9$	$2.0 \pm 7.6$	15.7
	scale	$1.0 \pm 0.1$	$246 \pm 10$	$1.6 \pm 0.2$	$0.4 \pm 0.04$	1.0
Haines et al. (2015)	translation x	0.6	$296^a$	3.5	0.2	$3.3^b$
	translation y	3.4	$332^a$	3.0	0.0	$3.5^b$
	translation z	1.3	$297^a$	3.4	0.0	$4.7^b$
	scale	1.0	$53^a$	6.9	0.3	$1.2^b$

<sup>a</sup> phase results are given as provided by Haines et al. (2015) but converted to degrees

<sup>b</sup> indicated as phase residuals

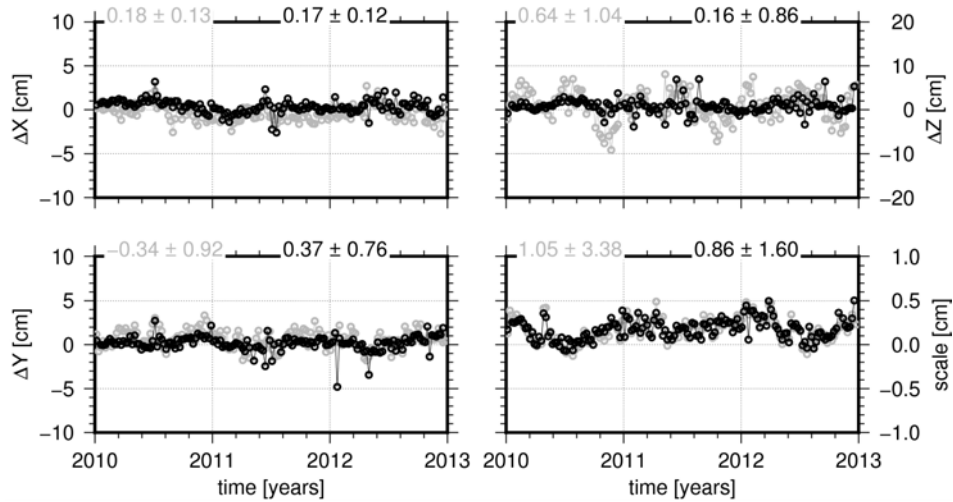


**Fig. 5.23:** Time series of translation and scale with respect to ITRF2008; GR-only (*gray*) and GR+ALL (*black*) solution; please note the different scale for  $\Delta Z$

shows the translation and scale parameters for the GR-only and the GR+ALL solution with respect to the ITRF2008. Obviously, the estimated translation parameters represent the geocenter, but they are derived with equally weighted stations, whereas the estimation in Sect. 5.2 was directly based on the observations. In the x- and y-direction the translations are below 5 cm. Z-translations of up to 10 cm are present with a large improvement due to the included LEOs. Compared to the geocenter results in Fig. 5.5 larger variations are visible in the translation-based estimation plotted here. Nearly similar scale values are derived from the GR-only and the GR+ALL solutions. The derived weekly scale estimates are below 5 mm, which corresponds to a small scale difference of 0.78 ppb with respect to ITRF2008. However, a small offset of 1 mm (0.15 ppb) is present. Compared to the findings of Zhu et al. (2003) and Ge et al. (2005), no abrupt scale inconsistencies can be found. Tab. 5.4 shows amplitude and phase for the annual period as well as bias, trend, and RMS for the estimated translation and scale time series between ITRF2008 and the GR-only and GR+ALL solutions. Between the annual amplitudes for the x- and y-translations derived from GR-only and GR+ALL and the values provided in Tab. 5.2, a good agreement at the millimeter level is found. Especially, the comparison between GR+ALL and the LAGEOS (ETHZ) derived amplitudes agrees well within 1 mm. Also the formal errors are at the same level. Comparing the derived amplitudes against the values published by Haines et al. (2015) also a good agreement is present in the y-translation, whereas the x-amplitude differs by 3 mm (bottom row of Tab. 5.4). As mentioned previously, Haines et al. (2015) combined GPS observations from a ground network and GRACE-A observations for the time period 2003-2013. In order to estimate the LEO impact they weighted the GRACE-A observation five times higher than the ground observations. The phases derived from GR-only and GR+ALL agree analogous to the agreement found for the geocenter time series. The derived bias and trend in the z-direction are very large (27.3 mm and -33.9 mm/yr). With the beneficial impact of the LEOs, a decrease to 7.4 mm and 2.0 mm/yr is present for bias and trend, respectively. The estimated scale parameters show a good agreement to the values provided by Haines et al. (2015). The annual amplitudes and the determined trends agree at the level of 0.1 mm and 0.1 mm/yr (GR+ALL solution). In summary, the additional LEOs improve the z-direction significantly and the x- and y-translations slightly. The impact on scale is nearly negligible.

## 5.5 Earth Rotation Parameter and GPS Satellite Orbits

Within this section the derived ERPs and GPS satellite orbits derived in the GR-only and the GR+ALL solutions are compared to results of a reprocessing campaign performed at CODE<sup>13</sup>. Fig. 5.24 shows the

<sup>13</sup> The processing scheme is available at [ftp://ftp.unibe.ch/aiub/REPRO\\_2013/CODE\\_REPRO\\_2013.ACN](ftp://ftp.unibe.ch/aiub/REPRO_2013/CODE_REPRO_2013.ACN), accessed August 2016

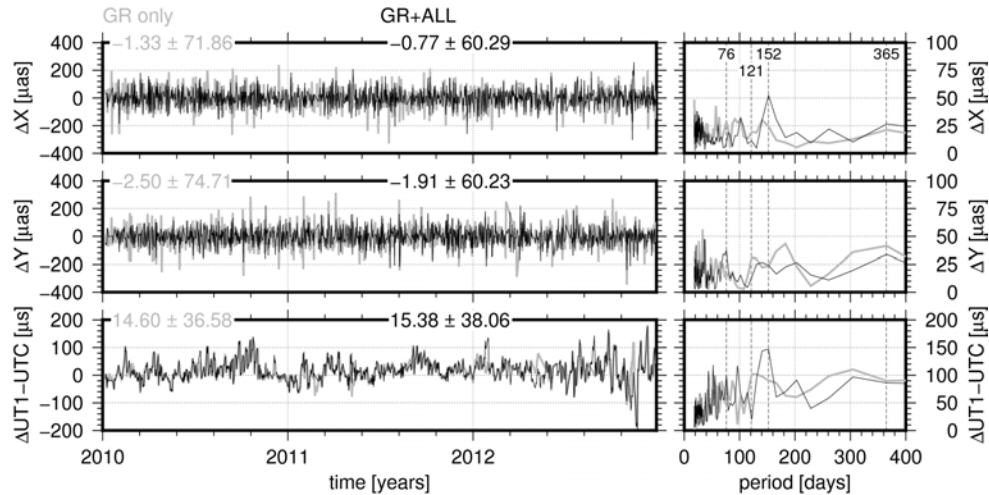


Fig. 5.24: ERP results (improvements); GR+ALL (*black*), GR-only (*gray*)

difference between the estimated Earth Rotation Parameters (x- and y-pole coordinates and UT1-UTC) and the CODE ERP time series. In polar motion a small offset of 1 to 2  $\mu\text{as}$  is present in x- and y-direction. The differences show annual amplitudes of 20 to 40  $\mu\text{as}$ . Signals with short periods are also present, for example the GR+ALL solution shows a large signal in x-direction at a 152-day period (corresponds to the 150-day signal in the geocenter, cf. Fig. 5.5). In UT1-UTC, differences of up to 200  $\mu\text{s}$  are present. However, the GR-only solution shows a slightly better agreement than the GR+ALL estimates for UT1-UTC. In the GR+ALL solution a large signal is found again for the 152-day period.

Based on the weekly solutions daily orbit determination (i.e., orbit improvements) was performed for the GPS satellites. Subsequently, the derived orbital positions were compared against those of the CODE reprocessed orbits, which were also used as a priori orbits in the pre-processing. The average RMS for the comparison of the GR-only orbits amount to 7.5, 37.1, and 6.1 cm for radial, along-track, and cross-track, respectively. GPS orbits derived from the GR+ALL solution show a much better agreement with the CODE orbits. The corresponding RMS values are 1.8, 5.4, and 2.5 cm, for radial, along-track, and cross-track, respectively. The most plausible reason for the relatively low agreement in along-track component can be found in the missing ambiguity fixing within this study. Contrary to the orbit comparisons discussed in Chap. 4 seven Helmert transformation parameters were estimated simultaneously. The estimated transformation parameters are shown in Fig. 5.25. In general, transformation parameters associated to GR+ALL are smaller than those associated to the GR-only solution. In the GR+ALL solutions x- and y-translation and rotation around the x- and the y-axis are very small, they are mostly below 1 cm and 1  $\mu\text{as}$  while a few exceptions are present. Also in scale a significant improvement is present. The translations in z-direction show larger values, however, also here the beneficial influence of the added LEO observations is visible. Even for the rotation around z a benefit is visible. However, both solutions show similar rotation values of up to 1  $\mu\text{as}$ . In end of 2012 the z-rotation increases dramatically to around 6-10  $\mu\text{as}$ . The reason for this behavior is so far unknown.

## 5.6 Transition to a Long-term Solution

After analyzing the weekly solutions, the next step is, naturally, to derive a long-term solution. This requires a stacking of all weekly normal equations. Therefore, parameters which are not of interest in a long-term solution were subsequently pre-eliminated (orbit and troposphere parameters). In addition, the geocenter and phase center offset parameters were removed from the normal equations. To account for station movements, the normal equation system was extended in the way that linear velocities are estimated in addition to constant coordinates (corresponding to the linear station model discussed in Sect. 3.2.1). Consequently, linear velocity rates must not be estimated over instantaneous position or velocity changes.

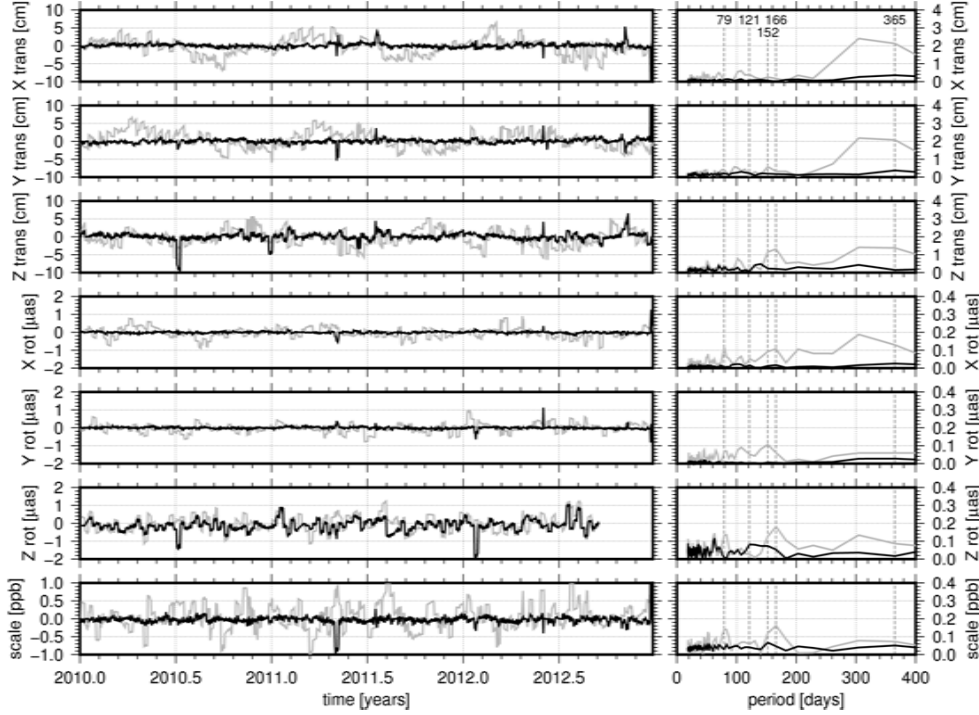


**Fig. 5.25:** GPS orbit comparison (transformation parameters); GR+ALL (*black*), GR-only (*gray*); z-rotation increase to 6-10  $\mu\text{as}$  in end of 2012

Especially, antenna or radome changes and earthquakes cause substantial discontinuities in station motion records. In order to derive a meaningful long-term solution, the weekly coordinate time series were analyzed by means of the BSW program FODITS for corresponding discontinuities. The functionality of FODITS is described in detail by Ostini (2012). In summary, 24 discontinuities and 7 velocity changes are present for the 53 stations over the 3 years processed. They are listed in Tab. 5.5. Eleven of these discontinuities are found for the Japanese stations Kogenai and Tsukuba. Consequently, a new set of station coordinates and velocities is estimated after each discontinuity. Therefore, the stations mentioned in Tab. 5.5 are excluded from the datum definition (i.e., the datum definition is applied to the remaining 34 stations).

The rank deficiency of the stacked normal equations amounts to six as in addition to the orientation, one has to cope also with their temporal variations. Therefore, no-net-rotation conditions were applied to coordinates and velocities of the datum stations. Without estimating the geocenter and antenna patterns, translations are defined by the orbit dynamics and the scale is given by the introduced speed of light (cf. Sect. 3.2.1). To account for un- or incorrectly modeled loading displacements, surface load density coefficients  $\sigma_{nm}^{\Phi}$  were setup as shown in Sect. 5.2.1. The simultaneous estimation of coordinates, velocities, and surface load density coefficients introduces two additional rank deficiencies, as deformations represented by spherical harmonics might be expressed by a systematic pattern of station coordinate variations. Analogously, the temporal variations of these deformations can be expressed by station velocity changes. Rülke (2009) accounted these correlations by introducing two constraints, which force the mean offset and drift of the estimated coefficients to zero. The corresponding equations read as (Rülke, 2009)

$$\sum_{j=1}^k (\sigma_{nm}^{\Phi})_j = 0 \quad \text{and} \quad (5.15)$$

$$\sum_{j=2}^k ((\sigma_{nm}^{\Phi})_{j-1} - (\sigma_{nm}^{\Phi})_j) = 0 \quad \text{with} \quad \Phi = \{S, C\}. \quad (5.16)$$

Obviously, these constraints require a parameterization as a piece-wise linear function. As mentioned in Sect. 5.2.1, to prevent aliasing effects, coefficients up to degree and order six might be estimated. However,

**Tab. 5.5:** Discontinuities for the selected stations; NEW-DISC, NEW-VELO discontinuities and velocity changes detected solely by FODITS; ERQ-DISC discontinuity detected in combination with an earthquake list; STA-DISC discontinuity related to station hardware changes

station	date	type	remark
ALIC 50137M001	2011-02-16 12:00:00	NEW-VELO	
CAS1 66011M001	2012-04-18 12:00:00	NEW-DISC	
COCO 50127M001	2012-04-11 08:23:01	ERQ-DISC	
GUUG 82301M001	2011-05-18 02:25:56	ERQ-DISC	
IRKT 12313M001	2011-05-18 12:00:00	NEW-DISC	
KGNI 21704S005	2011-03-09 02:27:07	ERQ-VELO	Tohoku-earthquake (foreshocks)
KGNI 21704S005	2011-03-16 12:00:00	NEW-DISC	
KGNI 21704S005	2011-04-13 12:00:00	NEW-DISC	
KGNI 21704S005	2011-05-20 00:27:42	ERQ-DISC	
KGNI 21704S005	2011-07-27 12:00:00	NEW-DISC	
KUNM 21609M001	2012-01-25 12:00:00	NEW-DISC	
LPGS 41510M001	2010-02-27 06:20:28	ERQ-DISC	Maule earthquake
LPGS 41510M001	2011-11-09 12:00:00	NEW-VELO	
MANA 41201S001	2011-04-14 20:30:06	ERQ-VELO	
MAS1 31303M002	2012-06-18 14:20:00	STA-DISC	antenna change ASH701945E_M NONE to LEIAR25.R4 NONE
QUIN 40433M004	2011-07-20 12:00:00	NEW-VELO	
REUN 97401M003	2011-07-13 12:00:00	NEW-DISC	
REUN 97401M003	2012-03-28 12:00:00	NEW-DISC	
SANT 41705M003	2010-02-27 06:20:28	ERQ-DISC	Maule earthquake
SANT 41705M003	2011-07-16 00:15:41	ERQ-VELO	
SHAO 21605M002	2011-03-11 05:27:45	ERQ-DISC	Tohoku-earthquake (foreshocks)
SYOG 66006S002	2011-05-18 12:00:00	NEW-DISC	
TIXI 12360M001	2010-10-20 00:00:00	STA-DISC	antenna change: ASH700936D_M SCIS to TPSCR3_GGD NONE
TIXI 12360M001	2010-12-01 00:00:00	STA-DISC	receiver change: ASHTECH Z-XII3 to JPS EGGDT
TSKB 21730S005	2011-03-09 02:27:07	ERQ-VELO	Tohoku-earthquake (foreshocks)
TSKB 21730S005	2011-03-16 12:00:00	NEW-DISC	
TSKB 21730S005	2011-03-23 12:00:00	NEW-DISC	
TSKB 21730S005	2011-05-13 23:21:19	ERQ-DISC	
TSKB 21730S005	2011-07-01 00:00:00	STA-DISC	radome change: DOME to NONE
TSKB 21730S005	2011-08-30 00:00:00	STA-DISC	radome change: NONE to DOME
WTZR 14201M010	2010-06-30 00:00:00	STA-DISC	antenna change: LEIAR25 LEIT to LEIAR25.R3 LEIT

similar to the processing done by Glaser (2014), only coefficients of degree and order one were setup. In contrast to the results presented by Rülke (2009), Fritsche et al. (2010), and Glaser (2014) the coefficients were estimated weekly.

The estimated linear station velocities are plotted in Fig. 5.26. The horizontal motions, shown in the left part of the figure, are clearly driven by plate tectonics. In general, horizontal velocities of 1 to 3 cm/yr are present with larger values for stations located on the Indo-Australian, the Pacific, and the Nazca plate. It was mentioned in Sect. 3.2.1 that linear station velocities have to be estimated over periods of >2.5 years to average seasonal station movements. As new station velocities were estimated after each detected discontinuity some velocities estimated over short time intervals are determined uncertainly. Velocities estimated over periods shorter than 2 years are plotted in gray. The newly defined datum stations mentioned above are identified by the surrounding circles. The corresponding vertical velocities are plotted on the right panel of Fig. 5.26. Motion rates estimated over periods shorter than 2 years are indicated by smaller circles. In general, large uplift rates are present only for stations effected by glacial-isostatic adjustments (Canada, Greenland, Svalbard). As the median of vertical velocities estimated over >2 years is only 0.44 mm/yr, the estimated motions can be considered as meaningful; 61.2% or 24 of the estimated 39 rates are smaller than 2.5 mm/yr. The Japanese stations Kogenai and Tsukuba, strongly affected by the

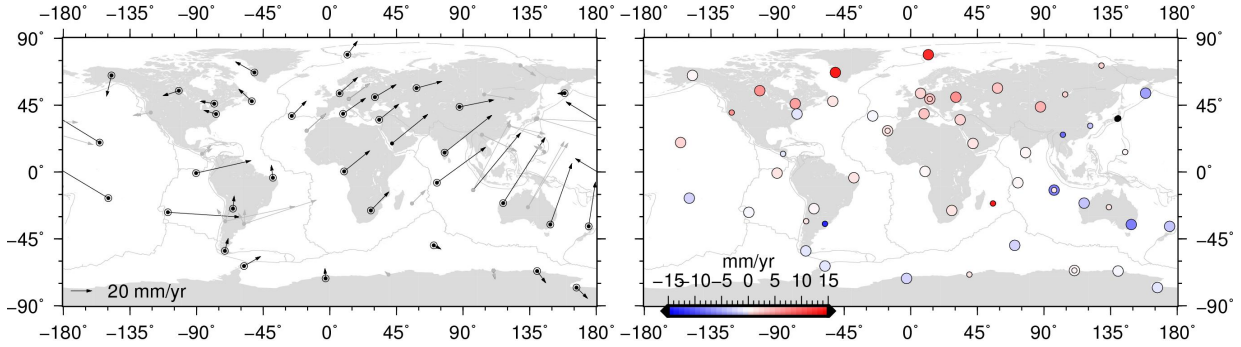


**Fig. 5.26:** Horizontal (*left*) and vertical (*right*) station velocities (2010-2013); station velocities estimated over periods shorter than 2 years are shown in gray (*horizontal*) and by smaller circles (*vertical*); for Kogei-nai und Tsukuba only velocities estimated over 1 year are shown, the vertical velocities are 25.2 and 15.1 mm/yr, respectively

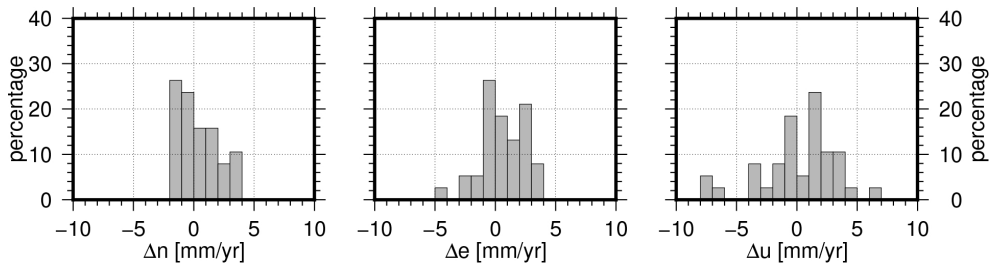


**Fig. 5.27:** Differences between estimated (>2 years) and ITRF2008 velocities; Namas (not in ITRF2008) was excluded; Kangerlussuaq, Greenland showed a vertical rate difference of 11.24 mm/yr due to an increased uplift rate

Tohoku earthquake, show uplift rates of 25.2 and 15.1 mm/yr estimated over periods of 1.2 years. Fig. 5.27 shows the differences between the estimated velocity rates (>2 years) and their ITRF2008 counterparts. The differences are smaller than 5 mm/yr in all components (with 4 exceptions in the height component). One of these exceptions is the rate determined for the station Kangerlussuaq, Greenland. A rate of 13.4 mm/yr was estimated, whereas the rate in ITRF2008 was only 2.2 mm/yr. However, for this station a increase of the non-linear uplift acceleration from 2 to 5 mm/yr<sup>2</sup> between 2010 and 2013 is reported by Wake et al. (2016). The median values of all velocity differences are -0.16, 0.51, and 1.04 mm/yr. Concerning the geographical distribution of velocity differences (not shown here) it was found that vertical motions are overestimated for stations in Europe, Canada, and Greenland and underestimated for some stations in Australia and Antarctica. The horizontal velocity differences show no systematic effects. Compared to the GR-only long-term solution, no substantial differences are present in the velocity field.

The estimated surface load density coefficients can be converted to geocenter coordinates as explained in Sect. 5.2.1. Fig. 5.28 shows the geocenter estimates derived with the unified approach from the GR-only and the GR+ALL data sets. In all components, a good agreement between both solutions is present. The variations do not exceed 2.5 cm, which results in a much narrower spread compared to Fig. 5.5. Small differences between the two solutions are present, for example, in the z-component during the spring season. In total, 67 % of the 155 differences in z-direction are smaller than 5 mm. Concerning the amplitude spectra shown on the right panel of Fig. 5.28, similar signals are present for nearly all periods. The major difference is the 179-day period for the z-component, where the GR+ALL solution shows a significantly reduced signal. A similar reduction was present in the translational results presented in Fig. 5.5. However, only a small impact of the additional LEOs is visible in the geocenter results based on the unified approach. As mentioned in Sect. 5.2.1, this was also noticed by König et al. (2015). The parameterization chosen in this study comprises only coefficients of degree  $n=1$ , estimated piece-wise linear in weekly intervals. Fig. 5.29 shows the impact of selecting other parameterizations on the derived geocenter z-component.

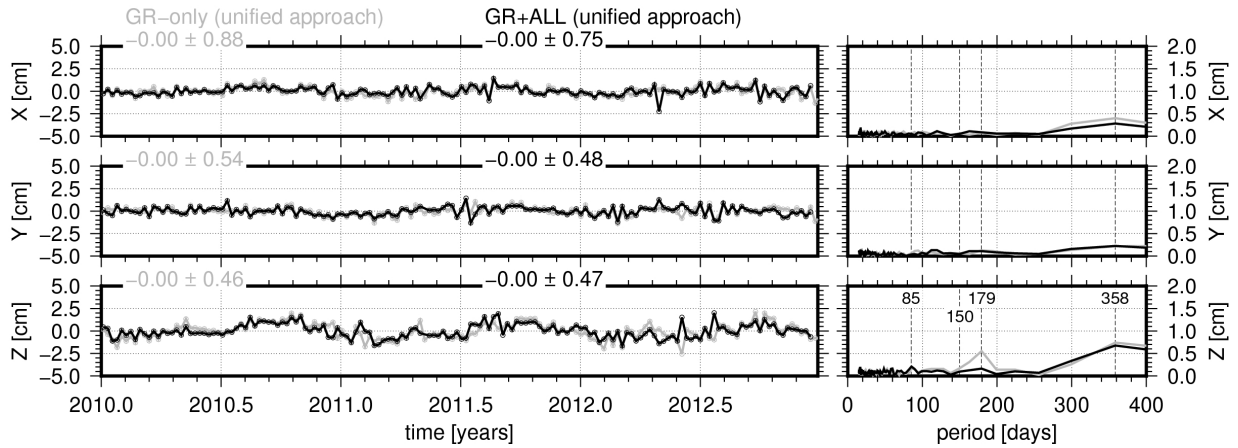


Fig. 5.28: Geocenter results from the GR-only (*gray*) and GR+ALL (*black*) solution based on the unified approach

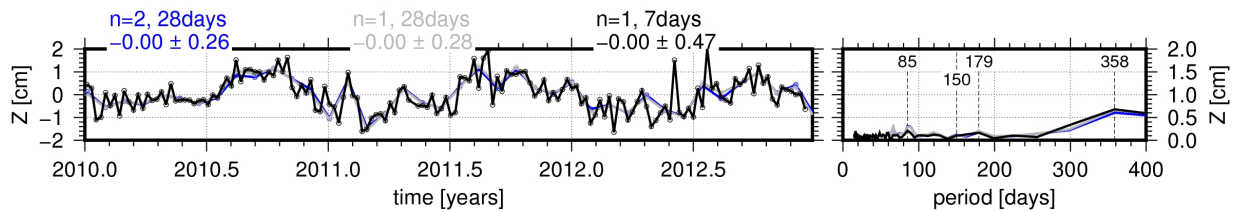
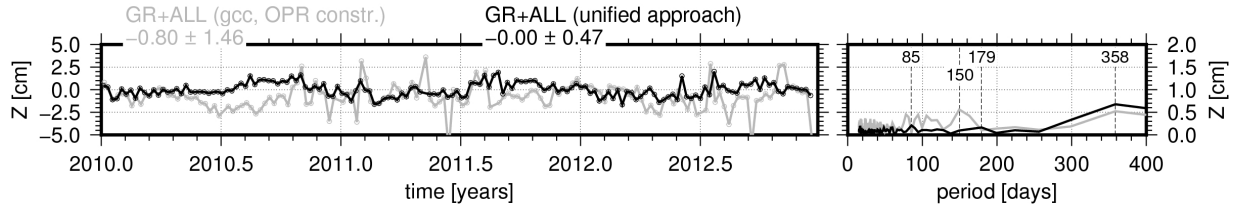
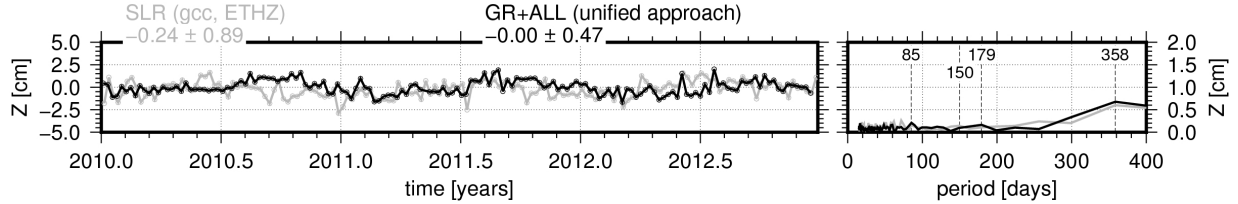


Fig. 5.29: Geocenter results based on different parameterization in the unified approach;  $n=1$  over 28 days (*gray*), up to  $n=2$  over 28 days (*blue*) and  $n=1$  over 7 days (*black*)

Two other setups were tested: (1) keeping  $n=1$  but extending the intervals to 28 days, and (2) estimating also  $n=2$  coefficients over 28 days. Based on the derived results, no significant difference can be found in the geocenter  $z$ -component. Indeed, the results are much smoother, when extending the estimation interval but the derived annual amplitude and phase are similar. The difference between the  $n=1$  and  $n=2$  estimates is in the order of  $-1.5$  to  $+2.5$  mm, while 72.5% of the derived 40 differences are below 1 mm. Glaser (2014) found similar differences in her 28-day geocenter estimates over a much longer time period. In summary, the restriction to  $n=1$  is reasonable within this study.

In the following, the derived geocenter  $z$ -component results are compared against (1) the translational GR+ALL and (2) the LAGEOS results. Fig. 5.30(a) shows the comparison between the geocenter results derived from the GR+ALL data set using the translational and the unified approach. Obviously, the scatter is largely reduced in the unified solution. Comparing both approaches, one has to keep in mind that the unified solution benefits from the long-term consistency introduced by constraining the temporal deviations of the network orientation. Concerning the phase, a substantial shift is present, and reasonable as in the results based on the unified approach the  $z$ -component is negative during the winter season which is related to the snow accumulation in the northern hemisphere (non-tidal continental hydrology was not corrected a priori). In the amplitude spectra the signal at the 150-day period present in the translational results is not present in the unified solution and is, thus, most probably related to artefacts in the weekly solutions. Comparing the unified GR+ALL results against the LAGEOS (ETHZ) solution shows a good agreement. However, the unified solution does not show the same phase as the LAGEOS solution, whereas the annual amplitudes agree well for all periods. Tab. 5.6 shows, similar to Tab 5.2, the annual amplitudes and phases for the geocenter time series derived within this study. The translational results discussed in Sect. 5.2.2 are given for comparison. The amplitudes derived from the three unified solutions based on the GR+ALL data set agree at the 1 mm level. Compared to the GR+ALL translational results, they agree to 1 mm for the  $x$ -component and to 2 mm for the  $y$  and  $z$ -component. The phases agree well between the results based on the unified approach and the LAGEOS solution (and the reference values provided in

(a) Comparison between geocenter results derived by the translational (*gray*) and the unified (*black*) approach for GR+ALL(b) Comparison between LAGEOS (*gray*) and GR+ALL (*black*) results based on the translational and the unified approach**Fig. 5.30:** Comparison of geocenter results: unified and translational approach**Tab. 5.6:** Annual component of geocenter motion; amplitude [mm] and phase [°] of the annual signal (according to Eqn. 5.7);  $n$  degree of estimated surface load density coefficients,  $d$  interval length

data set	approach	X		Y		Z	
		amp.	phase	amp.	phase	amp.	phase
LAGEOS	translational	4.0±0.8	231±13	1.5±0.7	309±29	6.2±0.9	265±13
GR-only	translational	4.5±1.0	103±20	2.6±1.3	297±40	12.6±3.7	112±24
GR+ALL	translational	3.2±0.8	62±19	4.0±0.6	291±14	5.9±1.7	85±26
GR-only	unified ( $n=1, d=7$ )	4.6±0.8	215±8	2.9±0.7	213±12	6.0±1.2	193±8
GR+ALL	unified ( $n=1, d=7$ )	2.9±0.7	217±12	2.3±0.5	265±21	7.4±1.1	187±5
GR+ALL	unified ( $n=1, d=28$ )	2.7±0.7	225±15	2.5±0.6	247±18	8.2±1.7	189±8
GR+ALL	unified ( $n=2, d=28$ )	2.0±0.8	224±20	2.1±0.6	247±20	7.3±1.7	185±9

Tab. 5.2) for the x-component. The differences between the unified solutions is below  $10^\circ$  and the difference to the LAGEOS solution is around  $15^\circ$ , which corresponds to around 2 weeks. In the y-component, the derived phases differ by  $50^\circ$  between the GR-only and the GR+ALL results derived by the unified approach. Compared to the translational solutions the phases are estimated too small; the differences concerning the unified solution is around  $40^\circ$ , which corresponds to slightly more than one month. In the z-component, phases estimated with the unified approach are similar to the translational results (differences are below  $10^\circ$ ). Compared to the LAGEOS solution a phase shift of around  $70^\circ$  is present ( $\approx 2$  months). In summary, the unified approach provide a better agreement with the SLR geocenter estimates, while the benefit due to additional LEOs is small.

# 6 Investigations on VLBI Satellite Tracking

Within this chapter the feasibility and the performance of tracking satellites using radio telescopes is discussed. In the first part satellite tracking concepts are reviewed, especially the recent achievements in tracking GNSS satellites are addressed. So far, GNSS satellites were tracked, with a few exceptions, in a single-frequency mode. Therefore, in the second part, a methodology is presented to derive ionospheric delay corrections from co-located GNSS observations. The third part of this chapter is dedicated to simulation studies for VLBI satellite tracking. This section ends with conclusions and recommendations for further co-location satellite missions. Concerning the terminology in VLBI, one has to distinguish between the observation time, which is the duration of one observation (so-called scan), e.g., 15 seconds or 2 minutes, whereas the tracking time refers to the time span an individual satellite is tracked (i.e., several scans are observed usually within one tracking time).

## 6.1 Tracking Satellites by Radio Telescopes

This section is structured in the following way. Based on general comments concerning VLBI spacecraft tracking, the tracking of Earth-orbiting satellites is highlighted. Sect. 6.1.2 is dedicated to the recent activities in tracking GNSS satellites, whereas Sect. 6.1.2 summarizes considerations and constraints for VLBI tracking of low Earth orbiting (LEO) satellites in circular and high-eccentric orbits.

### 6.1.1 General Remarks on VLBI Spacecraft Tracking

VLBI spacecraft tracking techniques are used since the launch of the first deep space missions in the 1960s and 1970s. Due to its extremely high angular resolution, VLBI is very sensitive to the tangential direction, i.e., the direction perpendicular to the line of sight. Therefore, VLBI observations are considered as a natural complement to range and Doppler measurements for spacecraft tracking (Border, 2009). According to the historical evolution, VLBI as a differential technique helps to solve two demanding problems: (1) the low sensitivity in declination, when the observed spacecraft is near the Earth's equatorial plane and (2) trajectory errors in declination due to unmodeled solar radiation pressure (Plank, 2013). According to Lanyi et al. (2007) four different tracking technologies can be identified nowadays.

- The major technique is the differential one-way Ranging ( $\Delta$ DOR, sometimes called D-VLBI, or  $\Delta$ -VLBI) used in the NASA operated DSN  $\Delta$ DOR, or ESA's  $\Delta$ DOR systems. Here scans of spacecraft and quasar signals are performed in a switching mode with a few minutes scan length. Usually separation angles between spacecraft and quasar of up to  $10^\circ$  are allowed. According to Border (2009) an accuracy of 1 nanoradian ( $\approx 0.2 mas$ ) is obtained routinely.
- The phase referencing method based on the source imaging technique is used by the Very Long Baseline Array (VLBA) and the Planetary Radio Interferometry and Doppler Experiment (PRIDE). The main advantage is the independence from spacecraft-specific tones. However, calibrator sources have to be closer to the target, separation angles should be smaller than  $4^\circ$  and  $2.5^\circ$  for VLBA and PRIDE, respectively. More details can be found in Lanyi et al. (2005) and Duev et al. (2012).
- The Radio Frequency Synthesis, and the Earth Rotation Synthesis are only conceptual techniques (Plank, 2013).

These systems were designed and have been used mostly for lunar and planetary missions as described for example by Border (2009). Observations of Earth-orbiting satellites are considered, so far, only in the

PRIDE phase referencing system operated by the Joint Institute for VLBI in Europe (JIVE). However, finding calibrator sources within the so-called isoplanctic patch is a challenging task<sup>1</sup>. Real satellite tracking observation were conducted by the Chinese VLBI Network, where BeiDou satellites were tracked in an experimental session in 2011 (Huang et al., 2011). Contrary to the GNSS tracking described within Sect. 6.1.2 they observed not the L-band navigation signal but the S-band telemetry link. According to Huang et al. (2011) the achieved low accuracy of 3 ns is caused by narrow bandwidths and limitations due to the beacon design. In 2009 the IVS established a working group on “Space Science Applications” in order to strengthen the link between geodetic and spacecraft tracking VLBI. In the final report also observations to Earth-orbiting satellites were discussed (Nothnagel et al., 2013). In 2015 the IVS established, with the working group on “Satellite Observation with VLBI” a task force dedicated to proceed towards regular Earth-orbiting satellite tracking using radio telescopes<sup>2</sup>.

Compared to the VLBI observation equation described in Sect. 2.1.3 the plane wavefront assumption is replaced by a curved wavefront in spacecraft tracking VLBI<sup>3</sup>. Additionally, the source, i.e., the spacecraft motion with respect to the solar system barycenter, has to be considered. Corresponding delay models were developed by several authors (Klioner, 1991; Fukushima, 1994; Sovers et al., 1998; Moyer, 2003). Especially, Klioner (1991) presented also a dedicated delay model for Earth-orbiting satellites. The main differences between models for inter-planetary, lunar, and Earth-orbiting satellites are the disturbing effects of Sun, Moon, and planets in the light-time equation. In the BSW implementation described previously in Sect. 2.3.2 the formalism of the light-time equation was applied as it is implemented already for differential GNSS code observations<sup>4</sup>. Consequently, the current BSW implementation is in terms of spacecraft tracking applicable to Earth-orbiting satellites only.

A prospective field of study opens by potentially close approaches of VLBI tracked Earth-orbiting satellites and deep-space probes. Somehow, similar to frame ties, these observations will help to constrain the space probe’s position relative to the satellite orbit. Moreover, these observations are an additional data source for the determination of solar system ephemerides. However, required close approaches will occur rarely.

### 6.1.2 Recent Achievements in VLBI tracking of GNSS satellites

Observing GNSS L-band signals by radio telescopes was proposed by Hase (1999) and further discussed among others by the joint “IVS/IGS/ILRS Working Group on GPS Phase Center Mapping” (Corey, 2001), by Rothacher (2003), by Dickey (2010), and by Plank et al. (2014). In principle, two observation strategies are feasible: (1) phase referencing observations between the signals from the GNSS satellite and a calibrator sources as described in Sect. 6.1.1, and (2) stand-alone observations to the GNSS satellite. To distinguish between both strategies the first one is referred to as “D-VLBI” and the second one is named “G-VLBI”. Tab. 6.1 provides an overview of the experimental G-VLBI sessions performed so far. It has to be mentioned that in some sessions quasars were observed at the begin and end of the session for calibration purposes. The first baseline tracking GLONASS  $L_1$  signals was realized in 2010 by the 32 m radio telescope at Medicina and the 25 m telescope at Onsala, which is usually used for astrometry (Tornatore et al., 2011, 2014). According to Haas et al. (2014), a stochastic measurement noise of 4 ps in 15 minutes was achieved. In 2013 a further baseline was observing GLONASS  $L_1$  signals, formed by the 25 m telescope at Onsala and the S-band horn connected to a special L-band receiver on the 20 m radio telescope at Wettzell (Kodet et al., 2014). The RMS-scatter of the derived phase delays was below 10 ps in 2 s (Haas et al., 2014). Due to bandwidth limitations of the feed horns and receivers, the  $L_2$  signal with its lower frequency was not tracked in both experiments. In August 2015, the first baseline on the southern hemisphere was observed between the Australian telescopes in Hobart and Ceduna. In this and some subsequent experiments both

<sup>1</sup> A isoplanctic patch is an angular region of the sky, where the quasar phases can be coherently applied to the target phases (Duvet et al., 2012).

<sup>2</sup> <http://ivscc.gsfc.nasa.gov/about/wg/wg7/index.html>, accessed May, 2016

<sup>3</sup> The plane wavefront assumption is only valid for a source distance of at least 30 light years or  $2.8 \cdot 10^{14}$  km (Sovers et al., 1998).

<sup>4</sup> Due to missing observations, this implementation was not tested with real VLBI satellite tracking data.

**Tab. 6.1:** Overview of performed GNSS satellite tracking sessions (as of June 2016)

date	stations	observed satellites & remarks	reference
16.08.2010	Onsala <sup>a</sup> , Medicina, Jodrell Bank <sup>a</sup>	3 GLONASS satellites observed for each 15 minutes with 45 scans; Jodrell Bank did not observe the first satellite	Tornatore et al. (2014)
2012	Onsala <sup>a</sup> , Medicina, Noto	GLONASS satellites observed	Tornatore (2012)
28.01.2013	Onsala <sup>a</sup> , Wettzell	1 GLONASS satellite in 0.75 h with 9 scans	Haas et al. (2014)
16.01.2014	Onsala <sup>a</sup> , Wettzell	6 GLONASS satellites in 1.5 h	Haas et al. (2015)
21.01.2014	Onsala <sup>a</sup> , Wettzell	5 GLONASS satellites in 2.0 h	Haas et al. (2015)
28.06.2015	Hobart, Ceduna <sup>a</sup>	GPS and GLONASS satellites for 2 h, only conceptual tests	Hellerschmied et al. (2015)
24.08.2015	Hobart, Ceduna <sup>a</sup>	4 GPS satellites in 4 h, 23 scans, $L_1$ and $L_2$ observed	Hellerschmied et al. (2015)
26.08.2015	Hobart, Ceduna <sup>a</sup>	GPS and GLONASS satellites for 4 h	Hellerschmied et al. (2015)
2016	Onsala <sup>a</sup> , Medicina, Sardinia <sup>a</sup>	GPS, GLONASS, Galileo, BeiDou sat.	

<sup>a</sup> solely astronomical used telescope

GNSS frequencies were tracked. Consequently, the ionospheric-free linear combination could be formed, if currently remaining polarization issues could be solved. The experiment on August 24, 2015 lasted for four hours with 23 scans of 5 minutes duration each to in total four satellites. The derived post-fit residual WRMS was found to be 29.6 cm for a single-frequency solution including ionospheric delay corrections from GIMs (Hellerschmied et al., 2015). However, one has to mention that almost all telescopes participating in the experiments listed in Tab. 6.1 are not participating in the IVS nor are they part of the ITRF station network. Therefore, their observation capabilities cannot be fully exploited for co-location in space. In general, from the co-location-in-space point of view, telescopes which participate regularly in geodetic sessions and which are co-located with GNSS and SLR stations are desirable for G-VLBI observations. From the EVN station list<sup>5</sup> one can find only a small number of telescopes, able to track GNSS L-band signals, which meet these requirements.

However, several basic questions remain still open. For example, the optimal size of a satellite tracking network or an optimal tracking time interval are not yet defined. Also more advanced issues need a clear answer like the uncertainty in the GNSS satellite antenna phase centers assumed to be equal for D-VLBI/G-VLBI and GNSS observations. The satellite tracking suffers also from some technical challenges. The main issue is the bandwidth limitation to 3-14 GHz in the new VGOS system (Petrachenko et al., 2012) which excludes the new antennas from tracking GNSS satellites. Also the attenuation of the very strong microwave signals received by the telescopes is a challenging task. In the legacy telescopes so far a step-wise tracking mode was applied, while the transition to a more suitable continuous tracking needs several implementations in the telescope control software (cf. Hellerschmied et al., 2014). Additionally, the existing scheduling software needs to be improved in terms of automatization (see Sect. 6.3.1).

According to the nominal bandwidths none of the telescopes listed in the EVN station list is sensitive to both GNSS frequencies. Also stations, which are able to track both frequencies from the receiving characteristics, might be limited to one frequency due to antenna and receiver control issues (pers. communication R. Haas, June 2016). In principle, this issue could be solved by observing  $L_1$  and  $L_2$  signals subsequently. However, G-VLBI observations suitable for co-location in space will be limited predominantly to one frequency. Consequently, the ionospheric error will be the most important error source in G-VLBI. Therefore, high-quality ionospheric delay corrections will be essential.

With the progress of dedicated co-location satellite missions like GRASP, some questions concerning the purpose of G-VLBI arose. Apart from the unique possibility to get prepared for missions, which will carry dedicated VLBI transmitters like GRASP or E-GRASP/Eratosthenes, one can find three main advantages

<sup>5</sup> The EVN telescope list can be found at [http://www.evbi.org/user\\_guide/EVNstatus.txt](http://www.evbi.org/user_guide/EVNstatus.txt), accessed May 2016

of G-VLBI. Firstly, receivers for all techniques are co-located at a fundamental site, exposed to the same environmental conditions, instead of combining observations tracked in space (GNSS) and on ground (VLBI, SLR) for LEO-type missions (cf. Fig. 1.1(d)). Secondly, tracking the same signal with GNSS and VLBI allows to strengthen the solution by estimating common parameters like station-specific tropospheric delays. And, thirdly, the bigger altitude of GNSS satellites allows the observation of baselines up to the Earth's diameter. Fig. 6.1(a) shows the relation between baseline length, orbital height of the satellite, and the chosen elevation cut-off angle. As in this figure the observation time is not considered, one has to keep in mind that successful G-VLBI observations will require a certain time of visibility, at least a couple of minutes. The requirement of a sufficient observation window will reduce the geometrically-derived maximum baseline length for LEOs and for the perigee passing of satellites in elliptic orbits significantly. In summary, G-VLBI observations will be a good opportunity to reach a suitable co-location in space.

Both conclusions within this section, the limitation on one frequency and the importance of G-VLBI observations, shows the demand for a suitable approach to correct the critical ionospheric delay. A corresponding approach based on co-located GNSS observations is presented in Sect. 6.2.

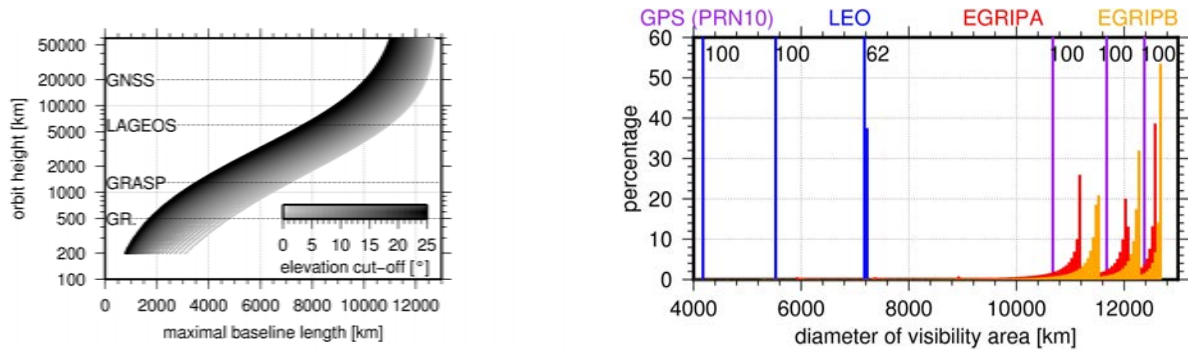
### 6.1.3 Considerations for VLBI tracking of Earth-orbiting satellites

A pioneering experiment for VLBI LEO tracking is described in Espinosa & Haas (2007). Driven by the need for a strong pointing source in the southern hemisphere they considered satellite observations and added a satellite tracking module called SATTRACK in VLBI's telescope control software Field System. Based thereupon they performed single-telescope tracking tests to NASA's Earth Observing System TERRA and AQUA satellites<sup>6</sup>. The tests were performed using the telescopes at Onsala (20 m telescope ONSALA60) and TIGO (Transportable Integrated Geodetic Observatory) located at Concepcion, Chile. The experiment shows good LEO tracking capabilities for both telescopes. However, no baseline was observed and no signal delays were determined.

As mentioned in Sect. 3.5.1, several mission concepts are presently discussed concerning the first satellite dedicated to co-location in space, where the VLBI transmitter is one of the most important instruments. However, due to the satellite altitude, VLBI tracking over long baselines is challenging. The maximal observable baseline length is shown in Fig. 6.1(a) depending on the selected cut-off angle. In summary, it is obvious that the circular low altitude orbits used for Earth observation (mainly below an altitude of 1400 km) are not suitable for the required VLBI tracking. Even at an altitude of 2000 km only a subset of VLBI baselines is observable with reasonable cut-off angles. As an initial step for the VLBI simulation studies described in Sect. 6.3, the distribution of the observable baseline length was determined over one week. The results are shown in Fig. 6.1(b). For a LEO in a circular orbit at an altitude of 2000 km, the baseline lengths vary within a small range of  $\pm 50$  km) and reach values of 4200 km, 5500 km, and 7200 km for cut-off angles of 20°, 10°, and 0°, respectively. These numbers would allow a reasonable VLBI tracking, however, some of the current mission concepts for dedicated co-location satellites have orbits with an altitude significantly lower than 2000 km (e.g., GRASP). Therefore, alternative concepts were considered. For example, the GRASP "VLBI" tracking will be performed mostly by single-station range observations (Plank, 2013). Contrary to that, the European counterpart E-GRASP/Eratosthenes will fly on a more elliptical orbit. These orbits are currently being considered as optimal compromise between launch costs, GNSS, and VLBI observability. Fig. 6.1(b) also shows the baseline length distribution for elliptically-orbiting satellites. Here the baseline length is given epoch-wise for two different orbits considered within E-GRIP's phase 0/A study<sup>7</sup>. As expected, baseline lengths up to the Earth's diameter are observable. However, it is obvious that stations in a global network cannot access the elliptically-orbiting satellite in the same way. This topic and the consequences are discussed in more detail in Sect. 6.3.4.

<sup>6</sup> Both satellites have an orbital height of 700 km, an 98.8° inclined sun-synchronous orbit, and transmit nearly permanently at 8.2155 and 8.1600 GHz, respectively.

<sup>7</sup> The corresponding orbit elements are  $a=24450$  km,  $e=0.636$  and  $a=35000$  km,  $e=0.8$  for EGRIPA and EGRIPB, respectively



(a) Maximal baseline length for different orbital heights and cut-off angles; GR = GRACE

(b) Percentage of observation epochs within baseline length for selected satellites (bin size 50 km); for each satellite cut-off angles of 20°, 10°, and 0° were assumed

**Fig. 6.1:** Considerations for VLBI tracking of Earth-orbiting satellites

A second major topic in VLBI satellite tracking is the received power level, which is usually significantly larger than for quasar observations. Fig. 6.2 shows a rough estimation of the power level received by the telescopes, when observing E-GRIP's microwave link. The corresponding equation for the received power  $P_r$  reads as (Ghasemi et al., 2012)

$$P_r [\text{dBW}] = \underbrace{10 \log (P^i + G_A)}_{\text{EIRP}} + \underbrace{10 \log \left( \frac{4\pi D_A}{\lambda^2} \right)}_{\text{gain of receiving antenna}} - \underbrace{20 \log \left( \frac{4\pi D}{\lambda} \right)}_{\text{free space loss}}. \quad (6.1)$$

Here the telescope has a diameter  $D_A$  and the transmitter gain  $G_A$  (assumed to be 15.9 and 6.1 dBi, respectively). The transmitted power is  $P^i$ , while the distance to the satellite is  $D$  and the wavelength is referred to as  $\lambda$ . EIRP (equivalent isotropically radiated power) describes the amount of power that a theoretical isotropic antenna would emit to produce the peak power density observed in the direction of maximum antenna gain. As basic assumptions a telescope diameter  $D_A = 13$  m and a receiver antenna gain  $G_A = 44$  dBi were introduced. These values were assumed according to the VGOS guidelines (Petrachenko et al., 2012). The transmitted power levels  $P^i$  are 8 W and 2 W, for E-GRIP's K- and X-band link, respectively. The estimation shows that the received power  $P_r$  is higher than -140 dBW even for distances  $D$  of 50'000 km<sup>8</sup>. These values are comparable to the received GNSS signal strength of -114 dBW and -120 dBW mentioned by Tornatore & Haas (2009) for  $L_1$  (C/A-code) and  $L_2$  (P-code), respectively. Therefore, E-GRIP's microwave signals are observable by radio telescopes, but need to be attenuated. A received power of around -150 dBW is assumed regarding the VLBI transmitter considered for E-GRASP/Eratosthenes (at 5° elevation)<sup>9</sup>. Espinosa & Haas (2007) reported received power levels at Onsala of -105 and -75 dBW for the tracking experiment of TERRA and AQUA, respectively.

## 6.2 Ionospheric Delay Corrections for Single-frequency VLBI Satellite Tracking

The L4R method described here allows the estimation of ionospheric corrections based on residuals derived from processing GNSS data in the geometry-free linear combination. The ideas, results and major conclusions were published already by Männel et al. (2014); Männel & Rothacher (2015, 2016).

<sup>8</sup> It was assumed that E-GRIP is located directly above the station.

<sup>9</sup> According to the E-GRASP/Eratosthenes proposal submitted in June 2016.

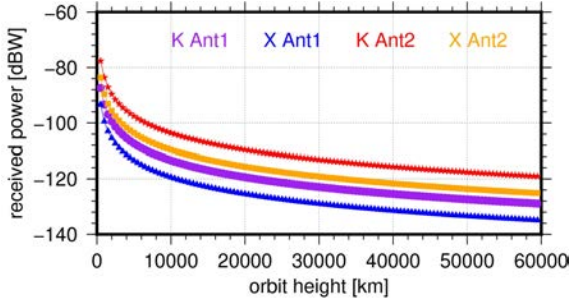


Fig. 6.2: Estimation of the E-GRIP microwave link signal budget for VLBI observation

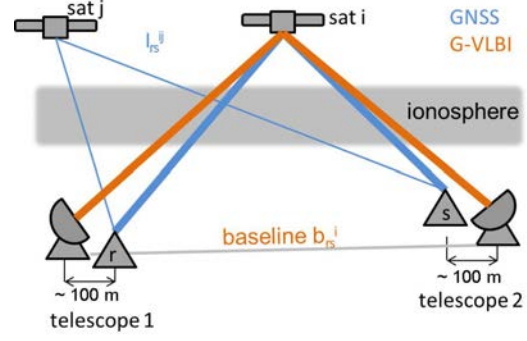


Fig. 6.3: Ionospheric delay corrections for single-frequency G-VLBI observations from co-located GNSS measurements

### 6.2.1 Idea and Formalism

As G-VLBI will observe GNSS L-band signals, the ionospheric delay between a GNSS satellite  $i$  and a radio telescope will almost be identical to the delay between the GNSS satellite  $i$  and a co-located GNSS receiver  $r$ , located not more than a few hundred meters apart. Therefore, an ionospheric delay between satellite  $i$  and GNSS receiver  $r$  determined by dual-frequency GNSS observations can be used to correct the ionospheric delay in the G-VLBI observation (Fig. 6.3). In principle, ionospheric delays can be computed with the geometry-free linear combination  $L_4 = L_1 - L_2$ , where the geometrical range and all frequency-independent biases are removed. Therefore, the ionospheric delay for a special satellite-baseline pair could be estimated using GNSS code observations on the single-difference level as described by Hernández-Pajares et al. (2011). The accuracy of the derived delays will be at several TECU (corresponding to a few meters in  $L_1$ ) due to measurement noise, multipath effects, and uncertainties in the differential code biases. Thus, the approach presented here is based on GNSS carrier phase observations. In order to get rid of phase biases and resolve the carrier phase ambiguities, double differences are formed. For a combined GPS/GLONASS double-difference analysis, the geometry-free linear combination for phase observations  $\Phi_{rs,n}^{ij}$  can be written in metric units as (cf. Eqn. 2.1)

$$L_{rs,4}^{ij} = L_{rs,1}^{ij} - L_{rs,2}^{ij} = \lambda_1^i \Phi_{rs,1}^i - \lambda_2^i \Phi_{rs,2}^i - \lambda_1^j \Phi_{rs,1}^j + \lambda_2^j \Phi_{rs,2}^j + \Delta\lambda_1^{ij} N_{rs,1}^j - \Delta\lambda_2^{ij} N_{rs,2}^j - \lambda_1^i N_{rs,1}^{ij} + \lambda_2^i N_{rs,2}^{ij} - \frac{f_1^2 - f_2^2}{f_1^2 f_2^2} I_{rs}^{ij} + \epsilon_{rs,4}^{ij}. \quad (6.2)$$

Eqn. 6.2 differs from Eqn. 2.1 due to the differentiation applied. The difference between the wavelengths of different satellites is  $\Delta\lambda_n^{ij}$ . These differences are relevant for GLONASS only, where satellites have different carrier frequencies. As a consequence, also the single-differenced ambiguities  $N_{rs,n}^j$  for the reference satellite  $j$  are part of the observation equation. The small biases present in  $L_{rs,4}^{ij}$  due to the frequency difference between the two GLONASS satellites are not significant as  $\Delta\lambda_n^{ij}$  will not exceed 1.5 mm for  $L_1$  and 2.0 mm for  $L_2$ . However, the term  $\Delta\lambda_1^{ij} N_{rs,1}^j$  will cause problems when fixing the ambiguities. After fixing the ambiguities  $N_{rs,n}^{ij}$  for GPS and GLONASS, only the ionospheric delay  $I_{rs}^{ij}$  contained in  $L_4$  remains in the residuals  $\hat{I}_{rs}^{ij}$  computed during a least-squares adjustment. As an alternative to fixing ambiguities, phase observations can be leveled to the corresponding code pseudoranges. However, the disadvantages mentioned earlier - except for the noise level - remain. Therefore, this strategy was not pursued. It should be mentioned, however, that considerable progress was made lately in the determination of the zero-difference code biases in the context of zero-difference ambiguity resolution.

To apply double-difference ionospheric delay corrections to G-VLBI observations, first single-difference residuals have to be derived from the double-difference residuals. Because  $n-1$  linearly independent double-differences have to be transformed into  $n$  baseline single-differences  $\hat{I}_{rs}^i$ , an additional and independent constraint has to be applied. This regularization step can be done by introducing a weighted zero-mean

condition  $\sum_x \omega_{rs}^x \hat{I}_{rs}^x = 0$  with the weights  $\omega_{rs}^x$  (Alber et al., 2000)

$$\begin{bmatrix} 1 & -1 & 0 & 0 & 0 \\ 1 & 0 & -1 & 0 & 0 \\ \vdots & \vdots & \ddots & \ddots & \vdots \\ \vdots & \vdots & \ddots & \ddots & \vdots \\ \omega_{rs}^1 & \omega_{rs}^2 & \dots & \dots & \omega_{rs}^n \end{bmatrix} \cdot \begin{bmatrix} \hat{I}_{rs}^1 \\ \hat{I}_{rs}^2 \\ \vdots \\ \hat{I}_{rs}^n \end{bmatrix} = \begin{bmatrix} \hat{I}_{rs}^{11} \\ \hat{I}_{rs}^{12} \\ \vdots \\ \hat{I}_{rs}^{1n} \\ \sum_{x=i1}^{in} \omega_{rs}^x \hat{I}_{rs}^x \end{bmatrix}. \quad (6.3)$$

Eqn. 6.3 will be computed baseline-wise using the observations to all common satellites as indicated by the indices of  $\hat{I}_{rs}^x$ . The zero-mean condition has to be introduced over a certain time period, here this condition is set up per epoch. A weighting function should not be applied as this will affect the remaining residuals. Once the single-difference residuals have been computed, they represent the difference of the ionospheric delays for a baseline, i.e., they are relative ionospheric delays. The absolute part of the ionospheric delay  $\bar{I}_{rs}$  cannot be computed due to the introduced zero-mean condition and is corrected for by using an ionospheric model, i.e., the GIMs produced by CODE are applied. The corresponding equation for the total ionospheric delay correction  $I_{rs}^i$  can be written as

$$I_{rs}^i = \hat{I}_{rs}^i + \bar{I}_{rs}. \quad (6.4)$$

The model part is defined by

$$\bar{I}_{rs} = \frac{\sum_{x=1}^n I_{rs}^x}{n} = \frac{\sum_{x=1}^n (I_r^x - I_s^x)}{n}. \quad (6.5)$$

where  $n$  is the number of single-differences and  $I^i$  is the satellite-specific ionospheric correction derived from the model. In principle, the described regularization step can be applied for a second time to derive zero-difference delays, i.e., delays for individual satellite-receiver pairs. In analogy to Eqn. 6.3 this step reads as

$$\begin{bmatrix} 1 & -1 & 0 & 0 & 0 \\ 1 & 0 & -1 & 0 & 0 \\ \vdots & \vdots & \ddots & \ddots & \vdots \\ \vdots & \vdots & \ddots & \ddots & \vdots \\ \omega_1^i & \omega_2^i & \dots & \dots & \omega_n^i \end{bmatrix} \cdot \begin{bmatrix} \hat{I}_1^i \\ \hat{I}_2^i \\ \vdots \\ \hat{I}_n^i \end{bmatrix} = \begin{bmatrix} \hat{I}_{12}^i \\ \hat{I}_{13}^i \\ \vdots \\ \hat{I}_{1n}^i \\ \sum_{x=12}^{1n} \omega_x^i \hat{I}_x^i \end{bmatrix}. \quad (6.6)$$

As indicated by the index  $\hat{I}_x^i$ , all observations to one satellite are processed together, therefore, only linearly independent baselines should be introduced in this step. The total ionospheric delay corrections  $I_r^i$  reads as

$$I_r^i = \hat{I}_r^i + \bar{I}_r \quad \text{with} \quad \bar{I}_r = \frac{\sum_{i=1}^n I_r^i}{n}. \quad (6.7)$$

The second step is not required for L4R but might be of interest for studying the ionosphere.

### Implementation and Processing in the Bernese GNSS Software

The performed implementations were described shortly in Sect. 2.3.2. As mentioned there, the implemented Bernese algorithms were adopted from Wang et al. (2014). The processing procedure is shown in Fig. 6.4. Following the GNSS processing part, where ambiguities are resolved, the  $L_4$  residuals are computed and

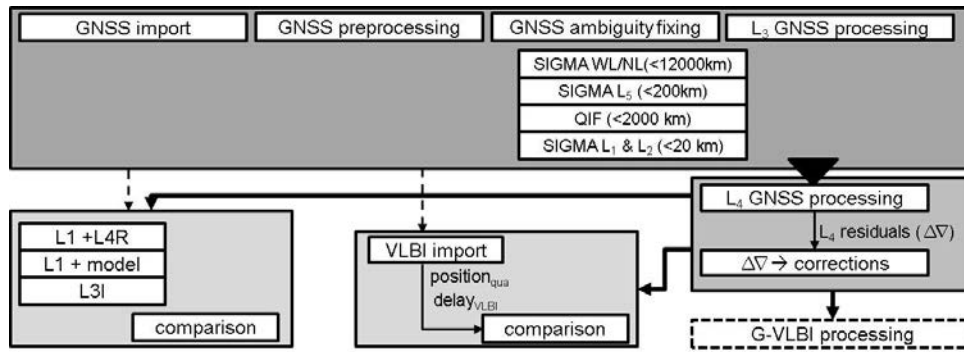


**Fig. 6.4:** Processing procedure, the *upper box* is a common GPS/GLONASS processing, *below, right* the L4R processing, *below, left* validation 1, *below, middle* validation 2 and *bottom, right* the intended correction of G-VLBI observations

the regularization is performed based on Eqn. 6.3 in the program IONEST. The estimated ionospheric corrections are subsequently introduced into the G-VLBI processing. The validation steps in Fig. 6.4 will be described in Sect. 6.2.4 and 6.2.5. The processing of daily sessions is automated using the Bernese Processing Engine.

### Accuracy Estimation and Current Limitations

The achievable accuracy, current limitations, and potential improvements for L4R are discussed in this section. Plank (2013) showed weekly station coordinate repeatabilities of 5-10 mm based on 800-1300 simulated G-VLBI observations per day. Assuming an error of the ionospheric delay correction for an individual observation below 2 TECU (corresponding to 32 cm in  $L_1$  and 20 ps in X-band), these coordinate repeatabilities could be reached. In the following these values will be used during the validation using external solutions. A value of 0.3 TECU (5 cm in  $L_1$ ) will be considered, when analyzing the scatter of the derived ionospheric corrections. Apart from the ionospheric signal the residuals  $L_{rs,4}^{ij}$  will contain errors related to unresolved ambiguities and non-ionospheric, station-specific biases like multipath effects and receiver noise. These non-ionospheric biases are mainly elevation-dependent and can reach cm-level for very short baselines (i.e., shorter than 100 m) as shown by Wang et al. (2014). Considering baseline lengths that are typical for VLBI, these biases are negligible (Crocetto et al., 2008). Remaining unresolved ambiguities in the least-squares adjustment will be estimated as real numbers and will, therefore, influence the corresponding residuals by partly absorbing the ionospheric signal. Using the BSW possibilities a considerable effort was made to fix as many ambiguities as possible. The applied ambiguity resolution strategy is based on that applied by Steigenberger et al. (2006) and described in detail in Männel & Rothacher (2016). The ambiguity resolution procedure worked very well for short and medium-range baselines, for longer baselines and, especially, for GLONASS a considerable number of ambiguities remains unresolved. In the consequence, the ionospheric delay will be partly absorbed by unresolved ambiguities. To reduce this limitation, either (1) a more suitable ambiguity resolution approach, (2) unambiguous observations, or (3) directly a zero-difference strategy can be used. However, option (1) might be very challenging and option (2) was not used, as the potential to reach millimeter accuracy would be lost, when using the unambiguous code observations. A processing of GNSS phase observations at the zero-difference level, as option (3), might benefit from the quality of phase observations and the avoidance of ambiguity-fixing over long baselines as only the satellite-baseline pair of interest has to be considered. However, in the zero-difference processing receiver and transmitter hardware delays cannot be eliminated and have to be estimated (see Sect. 2.1.1). As the zero-difference ambiguity-fixing is currently not implemented in the Bernese GNSS Software, this option would include an implementation effort exceeding the project “Co-location on Ground and in Space”. To evaluate the impact of absorbing ionospheric delays into float ambiguities as a worst case scenario, a float solution was computed and compared to the residuals of a solution including ambiguity fixing. In the float solution, residuals are smaller by up to 20 cm ( $\approx 1$  TECU)

**Tab. 6.2:** Comparison of diverse approaches to derive ionospheric corrections for VLBI processing

		TEC maps	local VTEC	D-VLBI <sup>a</sup>	L4R
<b>corrections</b>	based on GNSS	√ <sup>b</sup>	√		√
	based on VLBI			√	
	based on same source				√
	based on same telescope(s)			√	
	based on same frequency			√	√
	based on same signal path			√ <sup>c</sup>	√ <sup>d</sup>
	based on same epoch		√	√	√
<b>limitations</b>	due to quality of GNSS processing	√	√		√
	due to plasma effects <sup>e</sup>			√	
	due to mapping function	√	√		
	due to temporal smoothing	√			
	due to spatial smoothing	√	√		
	co-located GNSS receiver necessary		√		√
	additional quasar observation necessary			√	
additional processing necessary		√		√	
<b>applications</b>	single-frequency VLBI	√	√		
	G-VLBI	√	√	√	√
	planetary spacecraft	√	√	√	

<sup>a</sup> also known as phase-referencing; only the same-beam method is considered (Kikuchi et al., 2008)

<sup>b</sup> TEC maps based on other techniques (e.g., ionograms) are not considered here

<sup>c</sup> assuming a 1° separation the signal paths are separated by roughly 7 km at a height of 400 km

<sup>d</sup> assuming a local tie of 100 m the signal paths are separated by 98 m at a height of 400 km

<sup>e</sup> interplanetary and interstellar plasma

for baselines of around 1000 km and up to 50 cm ( $\approx 3$  TECU) for baselines longer than 5000 km. A third error source arises by introducing absolute ionospheric delays derived from a (smoothed) model. The CODE GIMs used are developed into spherical harmonics of degree and order 15 valid for two hours. The accuracy of such GIMs is, according to Hernández-Pajares et al. (2011), between a few and 10 TECU in the vertical component depending on solar cycle, station latitude, station local time and geomagnetic activity. Even though the improvement might be rather small, TEC maps with a higher resolution, like the IGS TEC maps with a spatial  $2.5^\circ \times 2.5^\circ$  and a 2 h temporal resolution can be used. Also the use of physical models like the International Reference Ionosphere (Bilitza, 2001) or the Global Assimilative Ionospheric Models (GAIMs)<sup>10</sup> is possible but was not tested here.

### Comparison with other Methods

As mentioned before correcting the ionospheric delay is crucial for single-frequency observations. Consequently, several methods are available to correct for these delays. In this section L4R is compared against the most common methods used in VLBI spacecraft tracking. These methods are

- introduction of TEC maps, respectively GIMs (e.g., Sekido et al., 2003; Gordon, 2010; Tierno Ros et al., 2011)
- estimating the local vertical TEC (VTEC) from GNSS observations (Sardon et al., 1994) and
- using same-beam D-VLBI (e.g., Duev et al., 2012; Kikuchi et al., 2009).

The comparison of these methods will be done with respect to the proximity of the corrections to the observations, the required equipment, and limitations regarding secondary or technique-specific error sources. Additionally, the applicability of the methods and the corresponding corrections will be discussed. This will include not only the range of possible applications, but also the effect on the observation scenario, and the additional processing load. Tab. 6.2 provides the results of this theoretical comparison. From this

<sup>10</sup> <http://iono.jpl.nasa.gov/gaim/intro.html>, accessed August 2015

compilation the following conclusions can be derived. Corrections based on TEC maps are easy to apply but their quality is limited by the TEC map's temporal and spatial resolution (Gordon, 2010; Tierno Ros et al., 2011). In general, a TEC map describes the ionospheric situation over regions with a spatial resolution of a few hundred kilometers averaged over at least one hour. However, it has to be mentioned that TEC maps are also an input for some of the other methods, like L4R or phase-referencing with larger separation angles than allowed for the same-beam approach. As recommended by several authors, local VTEC values can be derived from co-located GNSS observations. The local VTEC represents the local ionospheric situation above the station. However, the vertical delay information has to be mapped to the observed elevations. Applying a mapping function will introduce distortions. Compared to both, the methods D-VLBI and L4R are superior, as their corrections rely on the actual ionospheric situation in the observed direction. Both methods require additional observations, either independent GNSS measurements or subsequent VLBI observations to calibrator sources. However, as the signal paths are not absolutely aligned, the maximal allowed separation angle has to be defined. Obviously, if the threshold for this angle is too large, the ionospheric situation cannot be assumed to be identical. In L4R the separation angle is defined by the distance between radio telescope and GNSS receiver, which is usually below 1 km at geodetic fundamental sites. In D-VLBI the maximal separation angle is defined by a trade-off between baseline length, the number of calibrator sources, and the variability of the ionosphere. Considering the fast moving GNSS satellites and small separation angles, a large set of calibrator sources and fast switching between them are required Plank (2013). In summary, it can be concluded that the L4R method is currently the most promising approach to derive ionospheric corrections for single-frequency tracking of GNSS satellite.

### 6.2.2 Database for the Validation of the L4R Method

The validation of the L4R method described here is based on eleven fundamental sites in Europe and North America (Fig. 6.5), each equipped with a radio telescope contributing to the IVS. This network allows the analysis of G-VLBI baselines with various lengths and orientations. All selected sites are also part of the global IGS tracking network and are equipped with at least one GPS or GPS/GLONASS receiver. Tab. 6.3 gives an overview of the selected sites including the geometrical distances between radio telescope and GNSS receiver as given by the ITRF2008 (Altamimi et al., 2011). GNSS observations at a 30 s rate provided via RINEX files by the IGS and VLBI observations provided by the IVS via NGS card files were processed for 2013. According to the DBC-codes described by the IVS master file format description XA, XB, XE, XH and XK sessions were analyzed<sup>11</sup>. Fig. 6.5 shows the participation of each radio telescope within the analyzed VLBI sessions. Station GGAO7108 at Greenbelt, MD, USA was chosen, but participated only in the skipped intensive sessions. By using the remaining 10 VLBI stations, 45 baselines could be defined with lengths between 200 and 7200 km. During the processing GNSS-related products provided by CODE (final GNSS orbits, 30 s clocks, Earth rotation parameters, and ionospheric maps) and TU Vienna (coefficients for the VMF tropospheric mapping function, Böhm et al., 2006b) were used. Within the analyzed time period only minor gaps occurred, e.g., RINEX files for day of year (DoY) 265 to 294 are missing for station WES2.

### 6.2.3 Analysis of Phase Residuals

The ionospheric delays derived by the L4R approach will be discussed in three main parts in this section. Firstly, double-difference residuals and corresponding CODE GIM values are compared. This allows to characterize the processing results. Secondly, the impact of the introduced zero-mean condition is studied by assessing the splitting of double-difference into single-difference residuals. And thirdly, the station-specific ionospheric behavior will be discussed using zero-difference residuals. All result are provided in the GNSS  $L_1$  frequency.

<sup>11</sup> The IVS master file format description is available via <ftp://cddis.gsfc.nasa.gov/pub/vlbi/ivscontrol/master-format.txt>, accessed August 2016.

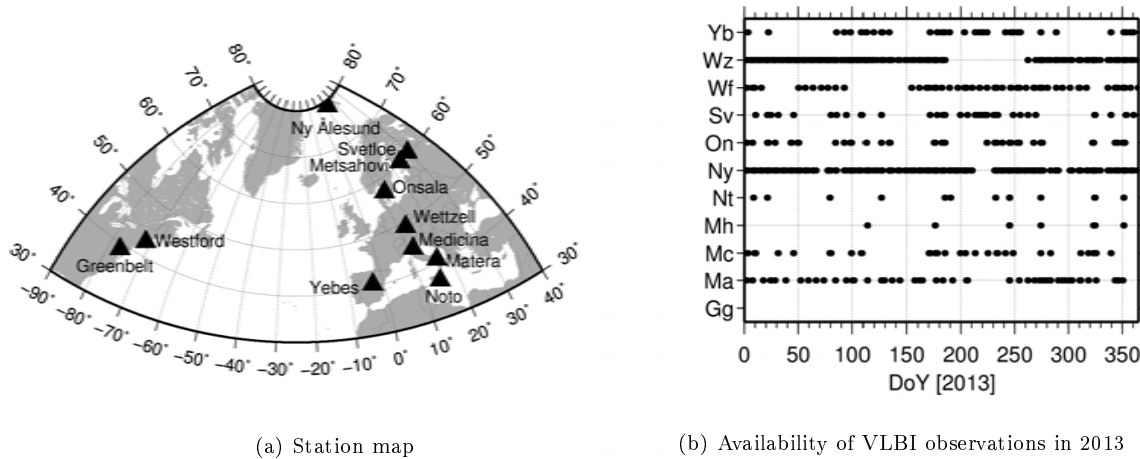


**Fig. 6.5:** Station map and VLBI sessions, station names according to IGS and IVS are given in Tab. 6.3; a detailed station list is given in Tab. C.1

**Tab. 6.3:** Selected radio telescopes and GNSS receivers for each fundamental site; the distance is given between the VLBI telescope and the GNSS receiver; a detailed station list is given in Tab. C.1

site	abbreviation	VLBI telescope	GNSS receiver	GNSS	distance [m]
Greenbelt	Gg	GGAO7108	GODZ	GPS+GLONASS	33.23
Medicina	Ma	MEDICINA	MEDI	GPS	62.77
Matera	Mc	MATERA	MATE	GPS+GLONASS	58.00
Metsahovi	Mh	METSAHOV	METS	GPS	128.88
Noto	Nt	NOTO	NOT1	GPS	71.69
Ny Ålesund	Ny	NYALES20	NYAL	GPS	112.44
Onsala	On	ONSALA60	ONSA	GPS+GLONASS	79.57
Svetloe	Sv	SVETLOE	SVTL	GPS+GLONASS	77.53
Westford	Wf	WESTFORD	WES2	GPS+GLONASS	57.70
Wetzell	Wz	WETTZELL	WTZR	GPS+GLONASS	139.45
Yebes	Yb	YEBES	YEBE	GPS	183.53

### Analysis of Double-difference Residuals

According to Sect. 6.2.1 the double-difference residuals  $\hat{I}_{rs}^{ij}$  are the direct output of the least-squares adjustment of the geometry-free linear combination. As mentioned above, these residuals are affected by float ambiguities. For the following analysis, model-based ionospheric delays, biased by model deficiencies and smoothing effects, are double-differenced to obtain  $\bar{I}_{rs}^{ij}$ . Besides these effects the differences  $\hat{I}_{rs}^{ij} - \bar{I}_{rs}^{ij}$  serve as a first quality indicator. However, as individual differences might be strongly affected by unresolved ambiguities or model smoothing (e.g., during periods of higher ionospheric variability) the analysis is based on mean values and their standard deviations. In order to compare different baseline lengths and orientations the four baselines listed in Tab. 6.4 were selected. Fig. 6.6 shows daily statistics for these baselines. The number of double-differences formed per day shown in the top row is defined by the baseline lengths and the number of observed GNSS satellites. The daily mean values (second row) are expected to be rather small as they represent the difference of four individual delays. Considering the large range of ionospheric conditions and the small number of commonly visible satellites, biases and higher day-to-day variations are expected for the longer baselines. These effects are present in Fig. 6.6, where the baseline length is the dominating impact factor. However, by comparing the shorter east-west baseline MATE-YEBE (length 1667.6 km) against the north-south baseline MATE-ONSA (length 1891.1 km), also the major role of the baseline orientation becomes visible. When considering this effect, the ionospheric variations in latitude and time have to be considered. As the selected baselines are located in the, in general more quite mid- and high-latitude regions (see Sect. 2.2.1) the impact of latitudinal variations

**Tab. 6.4:** Selected GNSS baselines

station 1	station 2	baseline length [km]	orientation	GNSS
ONSA	WTZR	919.7	north-south	GPS+GLONASS
MATE	YEBE	1667.6	east-west	GPS
MATE	ONSA	1891.1	north-south	GPS+GLONASS
GODZ	YEBE	5892.5	east-west	GPS

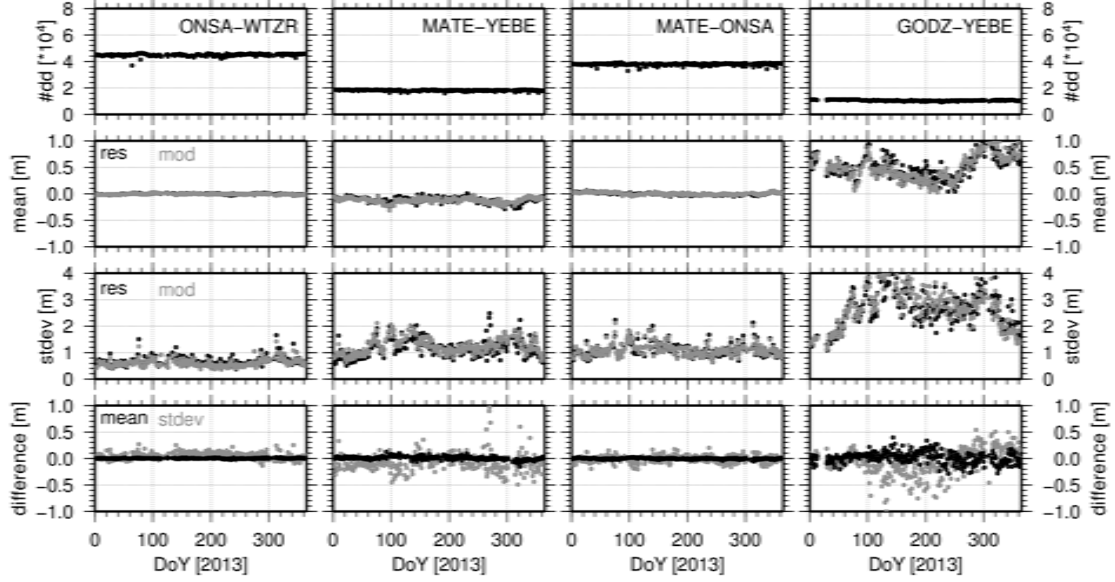


**Fig. 6.6:** Analysis of double-differences; *first row* number of double-differences (dd) per day, *second row* daily mean of  $\hat{I}_{rs}^{ij}$  (black) and  $\bar{I}_{rs}^{ij}$  (gray), *third row* daily standard deviation of  $\hat{I}_{rs}^{ij}$  (black) and  $\bar{I}_{rs}^{ij}$  (gray) and *forth row* mean and standard deviation of differences ( $\hat{I}_{rs}^{ij} - \bar{I}_{rs}^{ij}$ )

might be comparatively small. However, as the underlying ionization processes are mainly based on the interaction between solar radiation and neutral atoms, ionospheric density changes are strongly related to local time. East-west baselines will be highly affected by these variations as the local time will differ by several hours (e.g.,  $\Delta UT_{\text{GODZ-YEBE}} \approx 5 \text{ h}$ ). According to Zolesi & Cander (2013) variations in the total electron content can reach more than 10 TECU per hour. The daily standard deviations are affected in the same way. Comparing the standard deviations in Fig. 6.6 against the TEC values (Fig. 2.2), higher standard deviations coincide with higher TEC values. When analyzing the discrepancies between the mean values as derived from residuals and from the models, a good agreement can be observed, as even for the baseline GODZ-YEBE the differences are below 0.5 m. Interestingly, when considering the standard deviations for the baseline Onsala-Wetzell smaller values for  $\bar{I}_{rs}^{ij}$  are present. They might be caused by a smaller influence of the smoothed model related to the short baseline and the high number of double-differences. As expected, for the other baselines the smoothing causes higher standard deviations for  $\bar{I}_{rs}^{ij}$ .

### Analysis of Single-difference Delay Corrections

The required residual splitting is the main drawback in the current L4R implementation. Therefore, the residual splitting is assessed in two ways. The behavior of the performed zero-mean based splitting will depend on the number of visible satellites. In order to study this impact, epoch-wise standard deviations were computed for the delay corrections  $\hat{I}_{rs}^i$ . The different zenith distances cause the major deviations

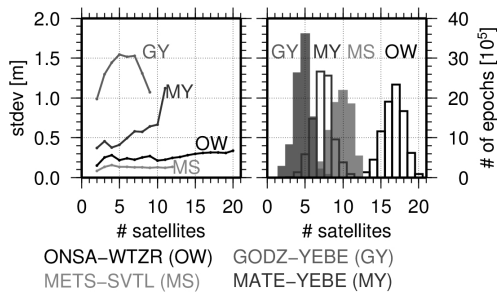


**Fig. 6.7:** Mean value of the epoch-wise standard deviation of the corrections *left* and the number of observed satellites per epoch (*right*)

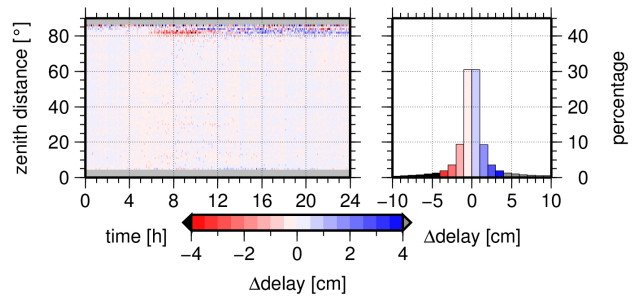


**Fig. 6.8:** Difference between delay corrections of consecutive epochs for baseline ONSA-WTZR (2013); *left* as a function of mean zenith distance and observation epoch and *right* as a histogram.

between individual delays. To convert the original slant delay  $\hat{I}_s$  to a vertical delay  $\hat{I}_v$  the approximation

$$\hat{I}_v = \hat{I}_s \cdot \cos\left(\frac{R_E}{R_E + H} \cdot \sin\left(\frac{z_r + z_s}{2}\right)\right), \quad (6.8)$$

with the Earth's radius  $R_E$ , the ionospheric layer height  $H = 350$  km and the zenith distance  $z$ , was used. To compute vertical delays for the single-differenced corrections, formally the averaged zenith distance in Eqn. 6.8 needs a compensation term (Wang et al., 2014). However, this term will not affect the characterization within this section. The computed standard deviations for all epochs are then compared against the number of visible satellites (Fig. 6.7). In this figure the baseline MATE-ONSA is replaced by the baseline METS-SVTL (GPS-only, baseline length 298 km) to consider also a very short baseline length. In general, and in accordance with Fig. 6.6, the standard deviation increases with the baseline length. The increase with the number of satellites reflects that, especially for longer baselines, the better hemispheric coverage leads to larger differences in the elevation angles and, therefore, in the delay corrections. The amount of epochs with a certain number of satellites heavily depends on the baseline geometry and, as expected, on the available GNSS as shown in the histogram in Fig. 6.7 (*right*). Ideally the differences between slant ionospheric delays of consecutive epochs are given by ionosphere variations and the changed satellite position with respect to the baseline, i.e., in general they will be very small. If the zero-mean condition is applied for each epoch individually, all changes in the visible GNSS satellite constellation will cause additional variations in the derived ionospheric delays. Fig. 6.8 shows the effect on the delays by computing the delay difference between consecutive epochs for the same satellite. Plotting these values as a function of mean zenith distance  $\bar{z}_m$  defined by

$$\bar{z}_m = \frac{1}{2} \left( \frac{z^i(t_1) + z^j(t_1)}{2} + \frac{z^i(t_2) + z^j(t_2)}{2} \right) \quad (6.9)$$

and of the time of the day, in bins of 20 minute and  $2^\circ$ , respectively, differences below 2 cm predominate. As the differences are computed by  $\hat{I}_{rs}^i(t_2) - \hat{I}_{rs}^i(t_1)$ , increasing delays are characterized by positive and decreasing delays by negative values. However, the deviations of single-difference corrections will only represent the differences not the ionospheric delays themselves. Considering all differences, only a minor number exceeds 5 cm. This is visible in the histogram (Fig. 6.8, *right*), where 93.1 % of all computed differences are below this threshold. Therefore, introducing the zero-mean constraints epoch-wise does not seem to degrade the derived ionospheric delays.

However, when focusing on an individual satellite the derived ionospheric delay correction shows several jumps (see Fig. 6.9, *left*). This plot was generated for the Hobart-Ceduna experiment from August 2015. Obviously, these jumps are related to rising and setting GNSS satellites. Conceptually the observed jumps are caused by (1) the introduced zero-mean condition, which is sensitive to the number of GNSS satellites and (2) the applied averaging of the GIM values. To minimize the number of jumps the least-

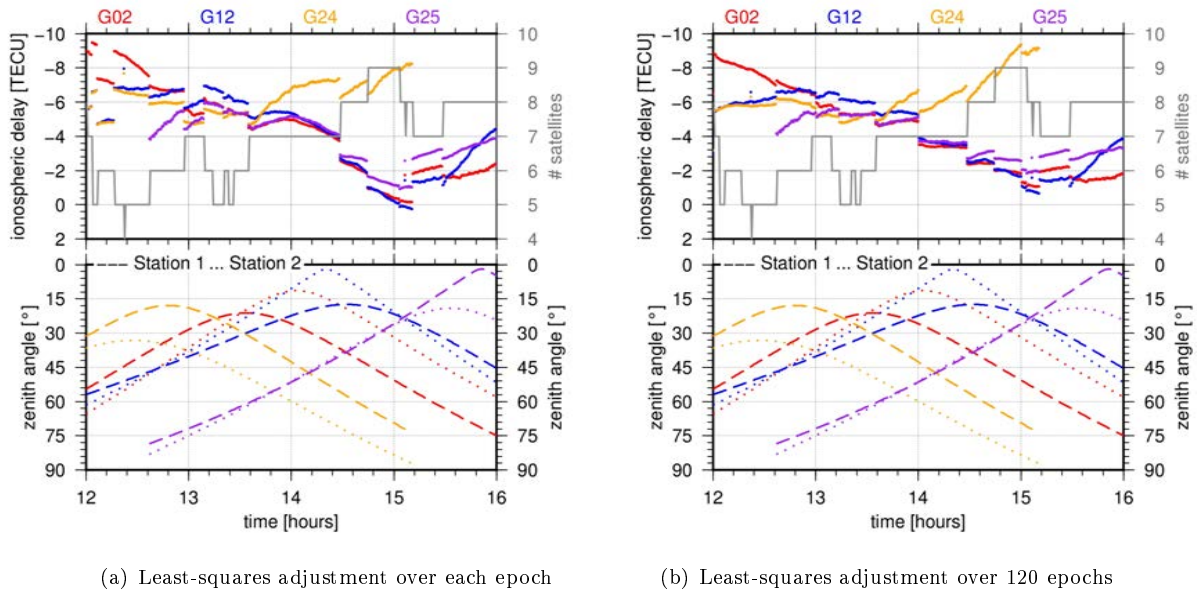


Fig. 6.9: Ionospheric delay corrections computed for the Hobart-Ceduna experiment (August 24, 2015)

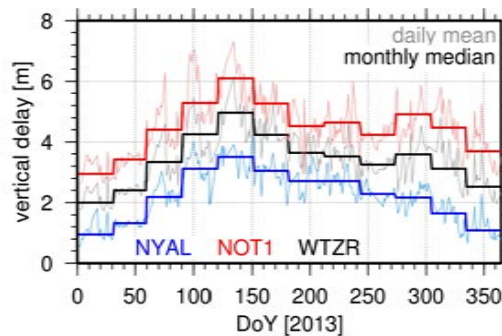


Fig. 6.10: Daily mean vertical delays and their monthly median value for stations NOTO (NOT1,  $36.8^\circ$  N), Wettzell (WTZR,  $49.1^\circ$  N) and Ny Ålesund (NYAL  $73.3^\circ$  N)

squares adjustment was performed over time spans longer than one epoch, without considering temporal correlations. The result shows minimized or even mitigated jumps (see Fig. 6.9, *right*). However, the derived corrections differ by up to one TECU between both strategies.

### Analysis of Zero-difference Residuals

The splitting of the single-difference residuals into zero-differences allows the analysis of station-specific effects. Using the delay differences between consecutive epochs as a quality criterion, the percentage of differences below 5 cm is 79 % for Wettzell. The biggest differences occur at low elevations showing decreasing values during day and increasing values during evening hours. In summary, also the second splitting procedure does not significantly degrade the derived ionospheric delays. Daily mean and monthly median values of the vertical delays for the IGS stations NOT1 (Noto, Italy), WTZR (Wettzell, Germany) and NYAL (Ny Ålesund, Svalbard) are plotted in Fig. 6.10. The main difference is caused by the station latitude: NOT1 and WTZR are located in the mid-latitude region, NYAL already in the high-latitude region. Seasonal effects are visible, one maximum occurs in spring (April, May and June), a second one in autumn (October and November, not present for NYAL). Decreasing day-to-day variations indicated by daily mean values can be found for higher station latitudes. More details concerning the variability of the free electron content and the ionospheric delay can be found, e.g., in Hernández-Pajares et al. (2009).

**Tab. 6.5:** RMS statistics for baseline Matera-Wetzell (mean values and standard deviation [cm])

processed baseline	L4R corrections estimated	GNSS	$V_{L3}$	$V_{L4R}$	$V_M$
MATE-WTZR	MATE-WTZR	GPS+GLONASS	$2.33 \pm 0.50$	$3.77 \pm 0.49$	$42.33 \pm 11.01$
MATE-WTZR	MATE-WTZR	GPS	$2.18 \pm 0.26$	$2.66 \pm 0.24$	$43.56 \pm 12.29$
MAT1-WTZZ	MATE-WTZR	GPS	$2.35 \pm 0.20$	$30.20 \pm 8.12$	$43.63 \pm 13.17$
MATE-WTZR	MAT1-WTZZ	GPS	$2.18 \pm 0.21$	$33.39 \pm 12.82$	$43.56 \pm 12.78$

**Tab. 6.6:** RMS statistics for baseline Greenbelt-Wetzell (mean values and standard deviation [cm])

processed baseline	L4R corrections estimated	GNSS	$V_{L3}$	$V_{L4R}$	$V_M$
GODZ-WTZR	GODZ-WTZR	GPS+GLONASS	$2.52 \pm 0.27$	$7.83 \pm 1.76$	$53.39 \pm 10.36$
GODN-WTZZ	GODN-WTZZ	GPS	$2.46 \pm 0.37$	$7.50 \pm 1.81$	$54.34 \pm 10.82$

## 6.2.4 Validation using GNSS Signals

For a first validation of the L4R corrections GNSS measurements have been used. When processing dual-frequency GNSS data by forming the ionospheric-free linear combination  $L_3$ , 99.9% of the ionospheric delay for GNSS observations is removed (Hernández-Pajares et al., 2011). As mentioned in Sect. 2.2.1, Fritsche et al. (2005) described the correction of remaining higher-order ionospheric effects. The results of an  $L_3$  processing (hereafter referred as  $V_{L3}$ ) are assumed as “truth”. Comparing them to single-frequency results, where the L4R delay corrections are applied ( $V_{L4R}$ ), allows a quality assessment and validation of L4R. In addition, a comparison to solutions, where only corrections derived from the CODE GIMs were applied ( $V_M$ ) is possible. In the following, remaining residuals and station coordinate repeatabilities are studied corresponding to the processing scheme of Fig. 6.5. To minimize the absorption of the ionospheric delay, while analyzing the residuals, all parameters except remaining ambiguities were fixed to their a priori values. In a second step station coordinates were estimated and their repeatabilities were studied.

### Analysis of Residuals

Fig. 6.11 shows daily RMS values of remaining residuals for the 990 km long baseline Matera-Wetzell. The corresponding mean values are listed in Tab. 6.5. The receivers at Matera are denoted by MATE (MT) and MAT1 (0A), those at Wetzell by WTZR (WR) and WTZZ (0M). The RMS of  $V_{L3}$  is around 2 cm for both, a combined GPS/GLONASS and a GPS-only solution. Using the L4R delays to correct a GPS  $L_1$  solution, the RMS increases slightly to 2.5 cm. Caused by a higher number of float ambiguities degrading the L4R corrections, the RMS of the combined GPS+GLONASS solution increases to 4 cm, which is still rather small compared to the  $V_M$  solution. However, the residuals highly benefit from introducing delay corrections derived from the same baseline, as in this case receiver noise, multipath and float ambiguities are identical. As Matera and Wetzell are both equipped with more than one GPS receiver, a co-located baseline can be used to estimate the delay corrections and to assess the impact of different ambiguity, noise and multipath characteristics. The daily RMS values increase to 20-50 cm when applying delay corrections derived for the co-located baseline, although the RMS values are mainly below the  $V_M$  solution. Here the residuals are affected by a number of unresolved phase ambiguities in both baselines. However, this validation step cannot account for radio telescope biases and ambiguity-free delays in the real G-VLBI case. The G-VLBI residuals and results will also be limited by uncorrected biases in the radio telescope.

Analyzing other baselines with comparable lengths, e.g., Onsala-Wetzell and Matera-Onsala, the same level of RMS values can be obtained (Tab. 6.5). Comparing the RMS values for very long baselines, e.g., the baseline between Wetzell and Greenbelt (GODZ, GODN), the  $V_{L3}$  RMS values are around 2.5 cm and increase to 8 cm for  $V_{L4R}$ , while  $V_M$  leads to RMS values  $>50$  cm (see Tab. 6.6). However, residuals express the remaining errors, i.e., the remaining ionospheric delays and the effect of unresolved ambiguities,

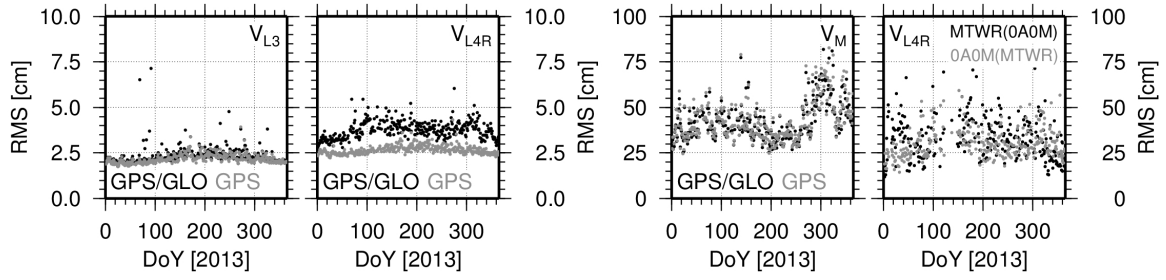


**Fig. 6.11:** Daily RMS of residuals for baseline Matera-Wetzell; *left* residuals of  $V_{L3}$  and residuals of  $V_{L4R}$ ; *right* residuals of  $V_M$  and residuals of  $V_{L4R}$  (corrections derived by co-located baselines); plot 1-3: GPS/GLONASS (*black dots*) and GPS-only (*gray dots*), for plot 4 the colors identify two different baselines

**Tab. 6.7:** Coordinate repeatabilities for Matera-Wetzell in north, east and up direction

baseline	L4R corrections	baseline length [km]	$V_{L3}$ [cm]			$V_{L4R}$ [cm]			$V_M$ [cm]		
			N	E	U	N	E	U	N	E	U
ONSA-WTZR	ONSA-WTZR	920	0.28	0.19	0.51	0.34	0.29	0.65	8.73	3.29	10.91
MATE-WTZR	MATE-WTZR	990	0.23	0.17	0.29	0.32	0.35	0.54	9.39	4.23	15.38
MATE-ONSA	MATE-ONSA	1890	0.30	0.27	0.34	0.44	0.57	0.89	7.62	4.16	15.20
MAT1-WTZZ	MATE-WTZR	990	0.31	0.18	0.28	3.74	2.41	3.83	9.63	4.85	15.96

but not the impact on the targeted parameters. Therefore, a closer look at station coordinates and their repeatabilities is given in the next paragraph.

### Analysis of Station Coordinate Repeatabilities

Station coordinates will be a major result for upcoming G-VLBI analyses. Therefore, the behavior of station coordinate repeatabilities was tested for the baselines Onsala-Wetzell, Onsala-Matera and Matera-Wetzell. The corresponding RMS values in north, east and up direction are listed in Tab. 6.7. The repeatabilities were computed baseline-wise keeping one station fixed. Considering the baseline length (third column of Tab. 6.7) there is a corresponding increase of the coordinate repeatabilities derived by  $V_{L4R}$  compared to  $V_{L3}$ . Nevertheless, the 1 cm coordinate repeatability is achieved for the first three baselines. Having a closer look at the height component of Matera-Wetzell (Fig. 6.12), no significant discrepancies between the results for the baselines MTWR and OA0M are visible for solution types  $V_{L3}$  and  $V_M$ . In  $V_M$ , model deficiencies cause a higher noise level and higher day-to-day variations of the coordinate repeatabilities. They are at the level of a few dm. As the  $V_{L4R}$  coordinates of MTWR agree quite well, the impact of transferring corrections to another baseline is investigated by using the co-located

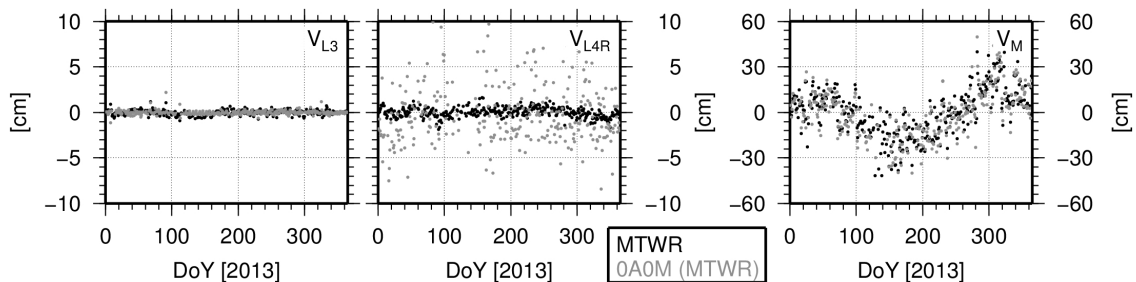


**Fig. 6.12:** Daily height coordinate repeatability for Matera-Wetzell; *left*  $V_{L3}$  and  $V_{L4R}$ ; *right*  $V_M$ ; repeatabilities for MTWR (*black dots*) and OA0M with L4R corrections derived from MTWR (*gray dots*)

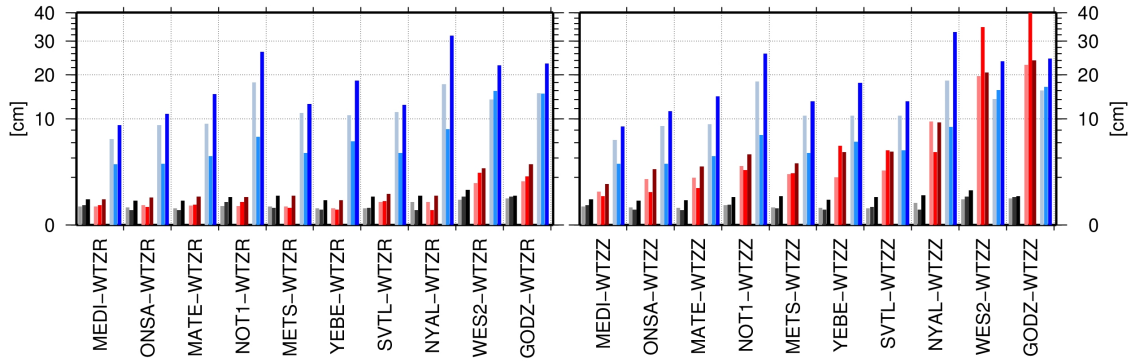


**Fig. 6.13:** Coordinate repeatabilities for  $V_{L3}$  (*black*),  $V_{L4R}$  (*red*), and  $V_M$  (*blue*); *left* same baseline for L4R and processing; *right* co-located baseline for the processing; each triplet shows the north, east, and height component; the baselines are sorted regarding their baseline length

baseline 0A0M. As a consequence, the repeatabilities in  $V_{L4R}$  increase to a level of a few cm and show higher day-to-day variations. This degradation might again be mainly caused by float ambiguities in both baselines. In Fig. 6.13 (*left*) coordinate repeatabilities are shown for all baselines containing Wettzell. In the case of using the same baseline to derive L4R corrections  $V_{L4R}$  is clearly superior to  $V_M$ . Except for the longer baselines between Westford and Wettzell respectively Greenbelt and Wettzell,  $V_{L4R}$  is nearly as good as  $V_{L3}$ . Unfortunately, only a small number of the selected sites are equipped with more than one GNSS receiver delivering to the IGS. Therefore, the co-located baseline comparison was modified in such a way that one station is identical for the estimation of L4R corrections and the  $L_1$  processing. In the following WTZR was replaced by WTZZ in the  $L_1$  processing part. As visible in Fig. 6.13 (*right*) the repeatabilities increase with the baseline length. For very long baselines,  $V_M$  gives the better results. This might be a consequence of the lower percentage of resolved ambiguities in L4R.

### 6.2.5 Validation using VLBI signals

The second validation part aims at getting closer to the G-VLBI situation shown in Fig. 6.3. Therefore, the ionospheric delays derived with the L4R approach are validated against ionospheric delays estimated from dual-frequency VLBI observations to quasars. In order to compare identical ionospheric situations, requirements concerning the spherical distance  $\alpha_j$  between the satellite  $i$  and the quasar  $j$  observed at epochs  $t_j^i$  and  $t_j^q$ , respectively, have to be fulfilled for both stations  $j \in 1, 2$  of the VLBI baseline

$$\alpha_1 < 3^\circ \text{ and } \alpha_2 < 3^\circ \quad (6.10)$$

$$\Delta t_1 < 15' \text{ and } \Delta t_2 < 15' \text{ with } \Delta t_j = t_j^i - t_j^q. \quad (6.11)$$

The spherical distance  $\alpha_j$  for each station is computed by

$$\alpha_j = \cos^{-1} \left( \sin(\epsilon_j^i) \sin(\epsilon_j^q) + \cos(\epsilon_j^i) \cos(\epsilon_j^q) \cos(\Delta a_j) \right) \quad \text{with} \quad \Delta a_j = \frac{a_j^q - a_j^i}{\cos\left(\frac{\epsilon_j^i + \epsilon_j^q}{2}\right)} \quad (6.12)$$

where  $\epsilon_j^i$ ,  $\epsilon_j^q$  denote the elevation angles of the satellite and quasar, respectively, and  $a_j^i$ ,  $a_j^q$  the corresponding azimuth angles. GNSS observations who meet these conditions, will be called associated observations. The ionospheric delays for VLBI are computed by using the X-band and S-band observations provided via the NGS card files. In the following these delays are referred to as NDC (NGS delay correction). In the next section these delays will be discussed in more detail. As the correction values computed by L4R are provided in TECU, also the NDC values are converted to TECU by using Eqn. 2.7. The validation results are finally reconverted into metric units using the VLBI X-band frequency.

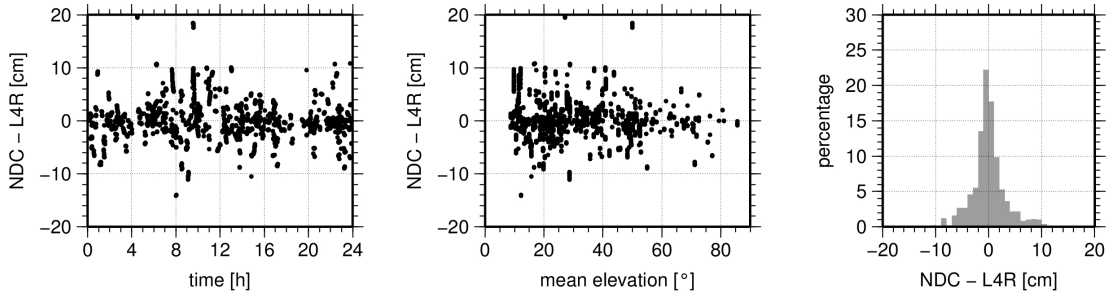


**Fig. 6.14:** Differences NDC-L4R (after subtracting a session-specific mean value) for single-difference L4R corrections with respect to observation time (*left*), mean quasar elevation (*middle*) and as a histogram (*right*)

### Theoretical Considerations

Considering the threshold value for the direction difference, comparable to the separation angle  $\gamma$ , the maximally possible baseline length  $b_{max}$  can be calculated by

$$b_{max} = 2R_E \sin^{-1} \left( a_{GNSS} \frac{\sin \gamma}{R_E} \right). \quad (6.13)$$

Depending on the semi-major axis  $a_{GNSS}$  of the GNSS considered and testing the conditions given in Eqn. 6.10 individually, the maximal baseline length for  $\alpha_j = 3^\circ$  results in 2796 km and 2690 km for GPS and GLONASS, respectively. Hence 28 out of the 45 baselines theoretically available can be used. Assessing the possible total area of the hemisphere covered by these requirements gives the probability of finding associated observations. Using the given threshold values approx. 5% (GPS and GLONASS) of the hemisphere is covered. Therefore, the number of usable quasars will be rather small. Considering the different ionospheric conditions acting on the signals separated by  $\alpha = 3^\circ$ , the horizontal distance between the ray paths can be computed. For zenith distances of  $10^\circ$ , the distance is below 50 km also at a height of 1000 km, for elevations below  $5^\circ$  the separation at an altitude of 1000 km will be larger than 300 km, obviously leading to distinct TEC differences. Concerning the VLBI ionospheric delays two effects are worth to be mentioned. Firstly, the ionospheric signals derived by X/S-band signals of quasars are also affected by the interplanetary and interstellar plasma. Sekido et al. (2003) assumed that the additional delay is below one TECU. Secondly, the VLBI ionospheric delays  $\tau'_{X,ion}$ , that are derived directly from the differences between the X- and S-band observations as defined by (Hobiger, 2006), contain the instrument-specific offsets  $\tau_{1,inst}$  and  $\tau_{2,inst}$

$$\tau'_{X,ion} = \frac{f_S^2}{f_X^2 - f_S^2} (\tau_X - \tau_S) + \tau_{1,inst} - \tau_{2,inst}. \quad (6.14)$$

These instrument-specific offsets are, as mentioned before, typically absorbed by the receiver clock estimation and can be considered as constant during one session (Sekido et al., 2003). This allows to study the difference of the ionospheric delays derived by GNSS and VLBI without knowing  $\tau_{1,inst}$  and  $\tau_{2,inst}$  by either analyzing the differences after subtracting the session-wise mean value or by analyzing the session-wise standard deviation (only if more than ten associated observations are available for one session).

### Validation Results for single-difference L4R Corrections

In a first step, differences NDC-L4R were computed for all associated observations by subtracting the corresponding mean difference. Fig. 6.14 (*right*) shows these reduced differences in a histogram: 91% of the differences are below 5 cm. In Fig. 6.14 (*left* and *center*) the reduced differences are plotted as a function of their observation time and the mean of both quasar elevations. In the first case only small systematic effects are visible. Concerning the elevation, caused by the observation geometry, the number

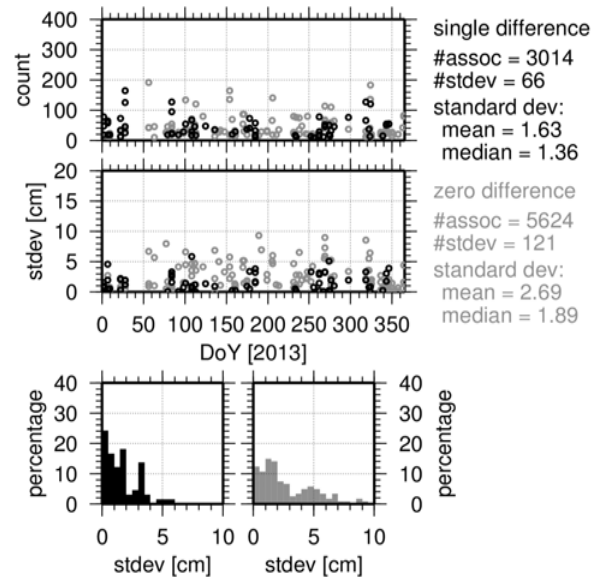


**Fig. 6.15:** Statistics for the validation using VLBI observations: number of associated observations for all baselines and sessions (*top*), corresponding standard deviations (*middle*) and a histogram of the standard deviations (*bottom*); L4R corrections based on single-differences (*black*) and zero-differences (*gray*)

of associated observations is decreasing with increasing elevation angle. Due to the longer signal paths within the ionosphere and larger distances between the signal paths, differences increase for low elevations. Fig. 6.15 shows the number of associated observations for each session and baseline together with the derived standard deviation for the single-difference case (*black dots*). In total 3014 associated observations for 66 baseline-session pairs were analyzed, 96 % of them show a standard deviation smaller than 5 cm. The mean of 1.6 cm and the median of 1.4 cm (corresponding to 2.7 and 2.2 TECU, respectively) are quite small. Because of the baseline geometry and the GNSS satellite trajectories only five out of the 28 possible baselines contribute a significant number of associated observations. In view of the definition of associated observations, it is clear that the standard deviations also contain effects caused by the distribution across the hemisphere and the distribution over time. Also the variable ionospheric behavior within the window in direction and time has an impact on the delay differences. This topic is discussed in the next but one paragraph.

### Validation of Zero-difference Corrections

If the ionospheric corrections are derived for zero differences, two different GNSS satellites or one satellite at different epochs  $t_1^i$ ,  $t_2^i$  might be used for validation, too. Depending on the time difference  $t_1^1 - t_2^1$  and the elevation difference, distinct variations of the ionospheric delays are possible. In order to avoid large degradation in the derived corrections, the time difference  $\Delta t = t_1^1 - t_2^1$  has been limited to 30 seconds. In fact, the number of associated observations increases significantly compared to the single-difference case, if different observation epochs for one GNSS satellite within the time threshold (Eqn. 6.11) are allowed. Fig. 6.15 shows this increase for the zero-difference L4R corrections (*gray dots*). The standard deviations show no significant systematic difference. Also here the majority (around 85 %) of all standard deviations, estimated baseline- and session-wise, are below 5 cm. In the zero-difference validation 14 out of 28 baselines contribute a significant number of associated observations. The increase in the standard deviations compared to the single-difference case are due to the involvement of two different GNSS satellites in combination with a minor degradation of the ionospheric corrections derived from zero-differences due to the second splitting procedure.

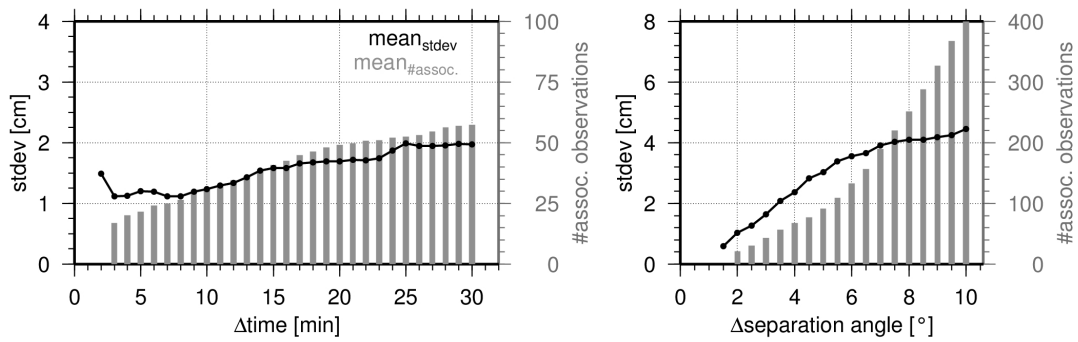


**Fig. 6.16:** Effect of the chosen threshold values for time and separation angle in the VLBI-based validation: the mean value of the corresponding number of associated observations (*gray bars*) and the overall mean value of the standard deviations for all available baselines (*black line*)

### Impact of Threshold Values

In the previous paragraphs the total area of the hemisphere covered by the available set of GNSS satellites was shortly addressed. In fact, for this validation type, the balance between wide open and very restrictive threshold values is crucial. Using very restrictive conditions for associated observations (reducing degrading effects caused by different signal paths), will lead to a small, probably too small data amount. On the other side, using data too far away from the VLBI observation and the original ionospheric situation will also degrade the results. This is shown in Fig. 6.16 for both requirements by fixing the other conditions and using single-difference L4R corrections. Naturally both, the mean number of associated observations per session and the corresponding standard deviations are increasing when threshold values increase. A limitation on the spherical distance between satellite and quasar has a bigger impact than the time offset. Also the number of observations increases quite slowly, when increasing the time window. In summary, the chosen threshold values allow a good balance between the number of associated observations and assuring the same ionospheric conditions as shown by the 40 observations per session and the standard deviations below 2 cm.

### 6.2.6 Applications of L4R apart from G-VLBI

Apart from G-VLBI, the application of the L4R method in tracking other spacecraft or in single-frequency astrometry is conceivable (Männel & Rothacher, 2015). However, a close distance between the VLBI-observed radio source and the GNSS satellite is required. This must be considered during the VLBI scheduling process. Fig. 6.17 shows the probability of finding a GNSS satellite within a certain time window and spherical distance as seen from one ground station (zero-difference mode). Assuming a suitably small separation angle, it will be rather difficult to ensure that for each observed source a GNSS satellite will be within the specified distance. However, in Fig. 6.17, only GPS and GLONASS were considered. With the increasing number of satellites due to the upcoming systems Galileo and BeiDou the scheduling process will become easier.

## 6.3 Simulation Studies for VLBI Satellite Tracking

VLBI satellite tracking is discussed based on simulation studies in this section. Starting with a comprehensive overview of the simulation approach the considered eight satellite and orbit types as well as the station networks are introduced. The performed simulations are divided into GNSS satellite tracking, tracking a circular-orbiting LEO, and tracking an elliptically-orbiting spacecraft. It is important to mention that contrary to the simulations performed e.g., by Plank (2013) no quasar observations were considered within

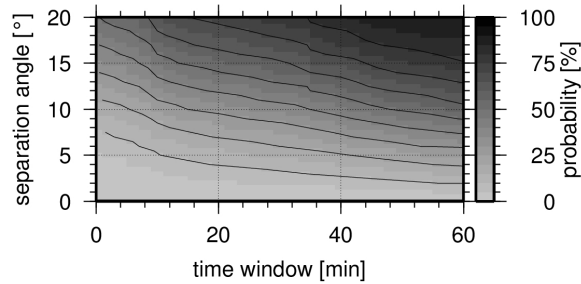


**Fig. 6.17:** Probability of finding a GNSS satellite (GPS or GLONASS) within a certain time window and spherical distance around a fictitious source; black lines indicate 10% probability levels

this study.

### 6.3.1 Simulation Approach

The simulation strategy in the Bernese GNSS Software can be described as a zero-test approach. As preparation for the following studies, the simulation tool GPSSIM was modified in a way to allow the simulation of VLBI satellite tracking data (see Sect. 2.3.2). A reasonable VLBI simulation requires a priori considerations of: (1) the scheduling process, (2) atmospheric and clock delays, and (3) the measurement noise. The applied procedure is a Monte Carlo simulation, where errors are generated based on models and random values. This type of simulation is described for applications in VLBI in detail by Wresnik (2009), Pany et al. (2011), and Plank (2013). Once the observed satellite is defined, i.e., scheduled, the geometrical delay is computed based on spacecraft and station position. Contrary to the usual VLBI simulation procedure, this first step is performed in the BSW at the zero-difference level. Tropospheric zenith wet delays and receiver clock offsets as well as the measurement noise are added at this level, too. In the second step single-differenced baseline observations are formed based on the simulated zero-difference observations. The two major error sources in VLBI satellite tracking are, in general, delays due to the wet part of the troposphere and the receiver clock behavior. The dry part of the troposphere, orbit errors, the ionosphere and other effects are not simulated as they give either much smaller variations or can be mitigated by the observation concept. The simulation and processing chain was performed for seven consecutive days of an arbitrary chosen week in 2015 (January 4th to January 10th). The derived daily normal equations were subsequently stacked to weekly solutions. To achieve statistically reliable information the procedure was repeated 26 times. This repetition number was selected based on the recommendation given by Wresnik (2009). An overview of the selected options for simulation and processing is given in Tab. 6.10.

### Scheduling for VLBI Satellite Tracking

The required scheduling process in VLBI simulations is the major difference compared to GNSS simulations. In general, the scheduling process in VLBI assigns a list of targets to each telescope participating in the scheduled VLBI session. The selection of these sources, the number of telescopes observing the same source, and the duration of each scan is optimized in terms of individual telescope characteristics, i.e., the telescope location, the required cut-off angles, and the slew rate restrictions, and the achievable accuracies (art, 2016). Therefore, the scheduling process is a complex optimization problem, which is solved by dedicated software packages like SKED, SCHED, or VIE\_SCHED. However, scheduling VLBI satellite tracking will be different from that of typical quasar observations. Two scenarios are foreseeable for VLBI satellite tracking:

- In the case of tracking an individual satellite, for example a dedicated co-location satellite, only visibility times and antenna slew rates are required for an efficient scheduling.
- In the case of tracking a satellite constellation (especially GNSS) the observed satellite needs to be

selected for each epoch and each telescope. A wide set of scheduling definitions can be applied for these selections. For example, the telescopes might switch between satellites belonging to different satellite systems or orbit planes. Other criteria are also conceivable like switching according to an ascending PRN list or the maximal elevation angle. Also more general, the tracking time for each satellite has to be considered, as rapid turnarounds sessions or long arc observations are feasible.

However, for the simulations within this work the “scheduling” was done simply by defining a satellite intended to be tracked by all stations. After a certain time interval (i.e., 5 minutes), the next satellite, in terms of the PRN code, is selected. If this satellite is above the selected elevation cut-off angle for an individual station a zero-differenced observation is generated (done in GPSSIM). In a second step the VLBI observations were derived by forming baselines (in VLBI DIF), if simultaneous observations were simulated. Consequently, the implemented strategy is not comparable to the careful scheduling process in the VLBI sense. Station characteristics like the antenna slew rates were not considered. To compensate the unconsidered baseline visibility conditions, it was assumed that the telescopes are available all day.

In recent years several authors discussed VLBI scheduling strategies for satellite observations. Already in 2004 corresponding functionalities were added to the astronomically used scheduling software SCHED (Walker, 2015). Satellite positions are obtained from spice files and propagated by JPL’s Navigation and Ancillary Information Facility software. art (2016) presented a scheduling approach, where the satellite observations are selected by analyzing the Jacobian matrix containing the partial derivatives for clock polynomials, zenith wet delays and ERPs. Satellite positions are introduced as Two Line Elements (TLE) and propagated via a simplified perturbation model. Antenna characteristics and slewing rates are taken into account via the individually computed observation duration. However, their aim was to schedule combined observations to satellites and quasars to establish frame ties. In the mentioned publication they considered only geostationary satellites but no other orbit types. Plank (2013) used a scheduling procedure based on shared visibilities for her simulation studies, while ignoring signal strengths, antenna characteristics, and slewing rates. Hellerschmied et al. (2016) presented a scheduling tool for VLBI satellite observations in the framework of the Vienna VLBI Software (VieVs). Satellite orbits are introduced via TLE elements and propagated based on a simplified perturbation model. Their scheduling considers common visibility, slew rates, cable wrap and axis limits, and the minimal angular distance to the Sun. The optimal satellite tracking duration is so far not automatically calculated. A main benefit of their implementation is that topocentric right ascension and declination positions are provided automatically in the standard VLBI VEX scheduling format. Based on these data the radio telescopes can be repositioned in a stepwise tracking approach to keep the satellite within the antenna beam. Adequate GNSS satellite tracking strategies were discussed by Plank et al. (2015). However, they focused more on combined quasar and satellite observation sessions in order to determine frame ties.

### Atmospheric delay

The variations in the wet delay are simulated as described by the theory of Treuhaft & Lanyi (1987), which is based on the Kolmogorov turbulence theory (Tatarskii, 1971). This approach was proposed for VLBI simulations by Nilsson et al. (2007). Böhm et al. (2006c) provide an appropriate formalism. From the initialization, i.e., a given a priori delay  $l_0^z$  in an arbitrary direction at an arbitrary time epoch, the covariance matrix  $C$  is computed containing the correlations between the observations depending on azimuth, elevation and time. An individual element of the covariance matrix  $C_{ij}$  reads as (Nilsson et al., 2007)

$$C_{ij} = \frac{C_n^2}{2} \int \int \left[ \frac{\|\mathbf{r}_i(z) - \mathbf{r}_0(z') + \mathbf{v}\delta t_{i0}\|^{2/3}}{1 + \frac{\|\mathbf{r}_i(z) - \mathbf{r}_0(z') + \mathbf{v}\delta t_{i0}\|^{2/3}}{L^{2/3}}} + \frac{\|\mathbf{r}_j(z) - \mathbf{r}_0(z') + \mathbf{v}\delta t_{j0}\|^{2/3}}{1 + \frac{\|\mathbf{r}_j(z) - \mathbf{r}_0(z') + \mathbf{v}\delta t_{j0}\|^{2/3}}{L^{2/3}}} - \frac{\|\mathbf{r}_i(z) - \mathbf{r}_j(z') + \mathbf{v}\delta t_{ij}\|^{2/3}}{1 + \frac{\|\mathbf{r}_i(z) - \mathbf{r}_j(z') + \mathbf{v}\delta t_{ij}\|^{2/3}}{L^{2/3}}} - \frac{\|\mathbf{r}_0(z) - \mathbf{r}_0(z')\|^{2/3}}{1 + \frac{\|\mathbf{r}_0(z) - \mathbf{r}_0(z')\|^{2/3}}{L^{2/3}}} \right] dz dz'. \quad (6.15)$$

Here the troposphere is characterized by the structure constant  $C_n$ , the saturation scale height  $L$ , the effective troposphere height  $h$ , and the wind speed  $\mathbf{v}$ . The direction  $\mathbf{r}$  depends on the height  $z$ , whereas the time differences are accounted for by  $\delta t_{12} = t_1 - t_2$ . The zenith wet delays are then simulated by generating a series of random values with covariance matrix  $C$  and adding these to the a priori zenith delay  $l_0^z$ . In Eqn. 6.15  $L$  describes the turbulence saturation scale length. The wind speed  $\mathbf{v}$ , allows in combination with  $\delta t$ , the simulation of temporal variations. This approach assumes a frozen troposphere, where temporal invariable turbulences are moved by the wind across the station network (Wresnik, 2009). Wind speed is usually assumed only in the horizontal direction. The structure constant of the turbulent troposphere  $C_n$  depends in general on the height, however, according to Treuhaft & Lanyi (1987),  $C_n$  can be approximated as constant up to the effective troposphere height  $h$  and zero above. The effective tropospheric height  $h$  is usually set to 2'000 m. Wresnik (2009) shows the significant impact of  $C_n$  and  $h$  on the accuracy of derived station coordinates in the way that a larger  $C_n$  and a larger  $h$  weakens the determination of station positions. He reported that increasing  $C_n$  from  $0.5 \cdot 10^{-7} \text{ m}^{-\frac{1}{3}}$  to  $2.0 \cdot 10^{-7} \text{ m}^{-\frac{1}{3}}$  or  $h$  from 1000 to 3000 m increases the estimated median height RMS by a factor of two. Concerning the wind speed, Wresnik (2009) reported only a minor impact on the station coordinates. However, he mentioned that fast winds have a beneficial impact on the coordinate results in the case of large  $C_n$  and  $h$  values. Once the zenith wet delays have been derived, a mapping function is required to map them to the observed elevation. According to Nilsson et al. (2007) the corresponding mapping function depends on the wet refractivity profile along the slant direction and is, therefore, unknown. However, as the simulated wet delay can be divided into a large constant and a small turbulent delay, the unknown mapping function can be approximated by the one valid for the constant delay (Nilsson et al., 2007). Fig. 6.18(a,b) show the simulated tropospheric zenith delay using three different structure constants and three values for the wind speed in Eastern direction. As expected one can see that the chosen structure constant has a higher impact on the simulated delays than the wind speed has. The considered wind velocities are  $0 \frac{\text{m}}{\text{s}}$ ,  $10 \frac{\text{m}}{\text{s}}$ , and  $20 \frac{\text{m}}{\text{s}}$  in eastern direction. These values correspond to 0, 5, and 8 Beaufort. Interestingly, there is no significant difference visible in the zenith wet delays simulated with wind speeds of  $10 \frac{\text{m}}{\text{s}}$  and  $20 \frac{\text{m}}{\text{s}}$ , respectively.

### Clock delay

Analogous to the wet troposphere delay, Böhm et al. (2006c) also provided an algorithm to simulate the receiver clock behavior. Based on Herring et al. (1990) the characteristics of frequency standards like hydrogen masers can be approximated by a combination of a random walk and an integrated random walk. The stability of a frequency standard is usually described by the Allan Standard Deviation over a specified time  $t$ . According to the VLBI2010 standards  $t$  is usually set to 50 minutes. Wresnik (2009) discussed the effect of different Allan Standard Deviations on the derived station coordinates and found robust results for stability values better than  $1 \cdot 10^{-14}$ . If the frequency standard reaches this accuracy level for a station, the tropospheric delay has a significantly larger impact on the station coordinates than the clock delays. Fig. 6.18(c) shows the simulated clock values using three different values for the Allan Standard Deviation. As visible the simulated clock behavior is nearly linear for Allan Standard Deviations of  $1 \cdot 10^{-15}$  or  $1 \cdot 10^{-16}$  over 50 minutes.

### Measurement noise

Simulated measurement noise is added to each observation to account for the precision of the measured delay. Usually normally distributed, so-called white noise, with a reasonable standard deviation is added to the simulated observation using a random number generator. However, the applied standard deviation is subject to the considered observation scenario, for example, Wresnik (2009) considered 4 ps, whereas Plank et al. (2014) applied a value of 30 ps. For the simulations presented here, one major difference has to be considered. Due to the independent generation of two range observations the noise is added independently to both ranges. The measurement noise of the formed baseline is, therefore,  $\sigma_b = \sqrt{\sigma_1^2 + \sigma_2^2}$ . In the following  $\sigma_b$  is mentioned.

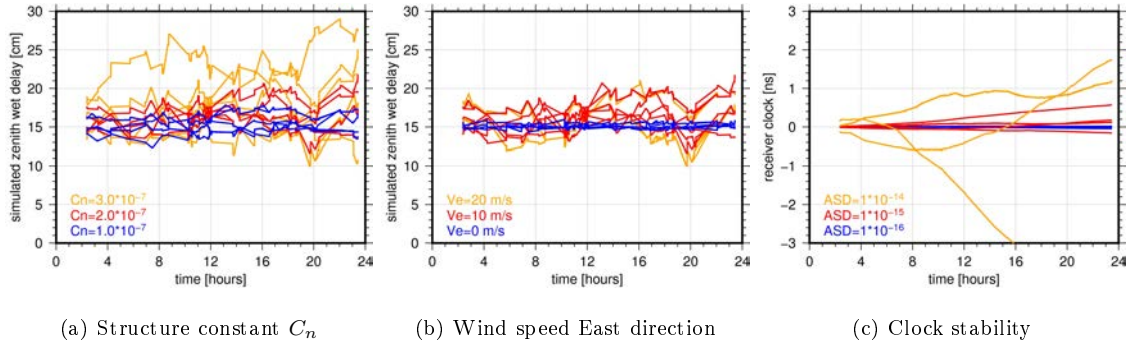


**Fig. 6.18:** Effect of chosen parameters for simulating troposphere and receiver clock; simulated for several days in January 2015 for station Wettzell

**Tab. 6.8:** Stations for the VLBI simulation including their participation in the two networks; antenna slew rates are derived from <ftp://gemini.gsfc.nasa.gov/pub/sked/catalogs/antenna.cat>, accessed June 2016; a detailed station list is given in Tab. C.1

ID	VLBI telescope		participation in network		telescope location	slew rate [ $^{\circ}$ /s]	
	IVS Name	Abb	GLOBAL	EUROPE		azimuth	elevation
7382	BADARY	Bd	✓		Badary, Russia	1.20	0.80
7297	FORTLEZA	Ft	✓		Fortaleza, Brazil	0.60	0.33
7232	HARTRAO	Hh	✓		Hartebeesthoek, South Africa	4.00	2.00
7374	HOBART12	Hb	✓		Hobart, Australia	5.00	1.50
7242	HOBART26	Ho	✓		Hobart, Australia	0.65	0.65
7375	KATH12M	Ke	✓		Katherine, Australia	5.00	1.50
7298	KOKEE	Kk	✓		Kokee, US	1.95	1.95
7243	MATERA	Ma	✓	✓	Matera, Italy	2.00	2.00
7380	METSAHOV	Mh		✓	Metsahovi, Finland	1.00	1.00
7331	NYALES20	Ny	✓	✓	Ny Ålesund, Norway	2.00	2.00
7213	ONSALA60	On	✓	✓	Onsala, Sweden	2.40	1.00
7385	SVETLOE	Sv		✓	Svetloe, Russia	1.00	0.83
7345	TSUKUB32	Ts	✓		Tsukuba, Japan	3.00	3.00
7377	WARK12M	Ww	✓		Warkworth, New Zealand	5.00	1.50
7209	WESTFORD	Wf	✓		Westford, US	3.33	2.00
7224	WETTZELL	Wz	✓	✓	Wettzell, Germany	3.00	1.50
7376	YARRA12M	Yg	✓		Yarragadee, Australia	5.00	1.50
7386	YEBES40M	Yb	✓	✓	Yebes, Spain	1.00	1.00
7381	ZELENCHK	Zc	✓	✓	Zelenchukskaya, Russia	1.20	0.80

## Stations and Satellites

Within this paragraph, the considered radio telescopes and satellites are discussed. In general, two station networks were considered, a global network inspired by the CONT14 network (GLOBAL, 17 stations) and a regional European network (EUROPE, eight stations). Tab. 6.8 shows the selected stations. Their geographical distribution is given in Fig. 6.19(a). The selected global network is not homogeneously distributed as it is the case for the network assumed by Plank (2013). Concerning her definition the global network selected here might be seen as a hybrid between a global and a cluster network of the European and Asian-Australian networks. Tab. 6.8 provides also the antenna slew rates, i.e., the angular speed for antenna re-positioning. Assuming a quasar tracking the required slew rate needed to compensate the Earth rotation is below  $0.004^{\circ}$  per second. As visible in Tab. 6.8 the slew rates in azimuth are between  $0.6^{\circ}/s$  and  $5^{\circ}/s$  and in elevation between  $0.33^{\circ}/s$  and  $3^{\circ}/s$ . This diversity is caused by the antenna size, the antenna main purpose, and antenna age. In general, for the newer telescopes designed in accordance with the VLBI2010 and VGOS guidelines, slew rates of  $6\text{--}12^{\circ}/s$  are achieved. The older legacy telescopes, some built for astronomical purposes, show slower angular velocities. However, in satellite tracking the

**Tab. 6.9:** Orbital elements (semi-major axis  $a$ , numerical eccentricity  $e$ , inclination  $i$ ) of satellites considered in the VLBI simulation

satellite	$a$ [km]	$e$ [-]	$i$ [°]	orbital period [h]	remarks
GPS SVN40	26'500.0	0.0	55.0	11.96	PRN 10, block IIA
GPS constellation	26'500.0	0.0	55.0	11.96	all satellites
EGRIP-A	24'450.0	0.636	63.4	10.57	
EGRIP-B	35'000.0	0.8	63.4	18.10	
E-GRASP	10'481.0	0.32	63.4	6.35	E-GRASP/Eratosthenes, preferred orbit <sup>12</sup>
LEO <sub>63</sub>	8'378.0	0.0	63.4	2.12	critical inclination
LEO <sub>89</sub>	8'378.0	0.0	89.0	2.12	polar orbit
LEO <sub>107</sub>	8'378.0	0.0	107.0	2.12	sun-synchronous

antenna has to follow a fast moving source, therefore, antenna slew rates are the critical limitation for the antenna selection. Due to their large altitude GNSS satellite tracking requires slew rates of not more than  $0.01^\circ/\text{s}$  and  $0.5^\circ/\text{s}$ , in elevation and azimuth, respectively (Plank, 2013). The elevation rate is uncritical also for LEO and elliptical orbits, as for perigee heights above 850 km an angular speed below  $0.5^\circ/\text{s}$  is required. The azimuth direction becomes even more critical, especially, for large elevation angles. In the case of GPS satellite tracking, Plank (2013) mentioned an azimuth rate of  $0.5^\circ/\text{s}$  for observations at an elevation angle of  $89^\circ$ . However, for a LEO at 2000 km altitude an azimuth rate of  $1.0^\circ/\text{s}$  and  $6.0^\circ/\text{s}$  is required for elevation angles of  $75^\circ$  and  $90^\circ$ , respectively. However, to be more accurate, the antenna axis accelerations should be considered instead of the velocities and also the antenna mounting system has to be considered as the azimuth/elevation slew rates have to be transformed, for example, in the case of hour-angle/declination mounts. Moreover, especially for rapid turnarounds, limitations in the slew range due to antenna cables and mechanical reasons have to be considered.

The characteristics of the simulated spacecraft are given in Tab. 6.9. Except for GPS the orbits were generated by integrating the listed Keplerian elements forward over one week. Non-gravitational orbit perturbations were not considered in the orbit integration. In general, two GPS scenarios, three elliptical orbits, and three LEO orbits with different inclinations were analyzed. The first simulation was performed for tracking a single GPS satellite. The background for this scenario is the idea of having a dedicated VLBI transmitter on-board a GNSS satellite. The constellation scenario is related to the G-VLBI satellite tracking described above. The three elliptical orbits are selected based on considerations for the proposed E-GRIP and the E-GRASP/Eratosthenes missions. The two E-GRIP orbits can be called highly elliptical orbits (HEO)<sup>13</sup>. Additionally a fictitious LEO was considered. The selected altitude of 2000 km is rather large for a low Earth orbit. However, a smaller altitude would not be reasonable for a suitable baseline VLBI tracking (cf. Plank, 2013). For this reason, the GRASP VLBI observations will be performed as ranging observations based on modulated X/S-band signals. The ground tracks of a subset of the selected satellites are plotted in Fig. 6.19(b-f). Especially, for EGRIP-B a significant altitude difference between apogee and perigee is present (Fig. 6.9(c)). The LEO orbits are nearly 3-day repeat orbits; the orbit of LEO<sub>107</sub> is shown in Fig. 6.9(f). In the following the different satellites types are discussed concerning their observation number and derived station coordinates.

### Processing Strategy

As mentioned above the simulated observations were processed in a daily mode with a normal equation stacking to derive weekly solutions. Apart from station coordinates, tropospheric delays and receiver clocks were estimated but pre-eliminated in the weekly solution in order to reduce the size of the weekly normal equations, which were stacked to derive station coordinate repeatabilities. Weekly solutions were chosen as they guarantee a suitable amount of observations and, therefore, stable results. Plank (2013) shows

<sup>13</sup> Conventionally, orbits with perigee heights below 1000 and apogee heights above 35'000 km are referred to as highly elliptical.

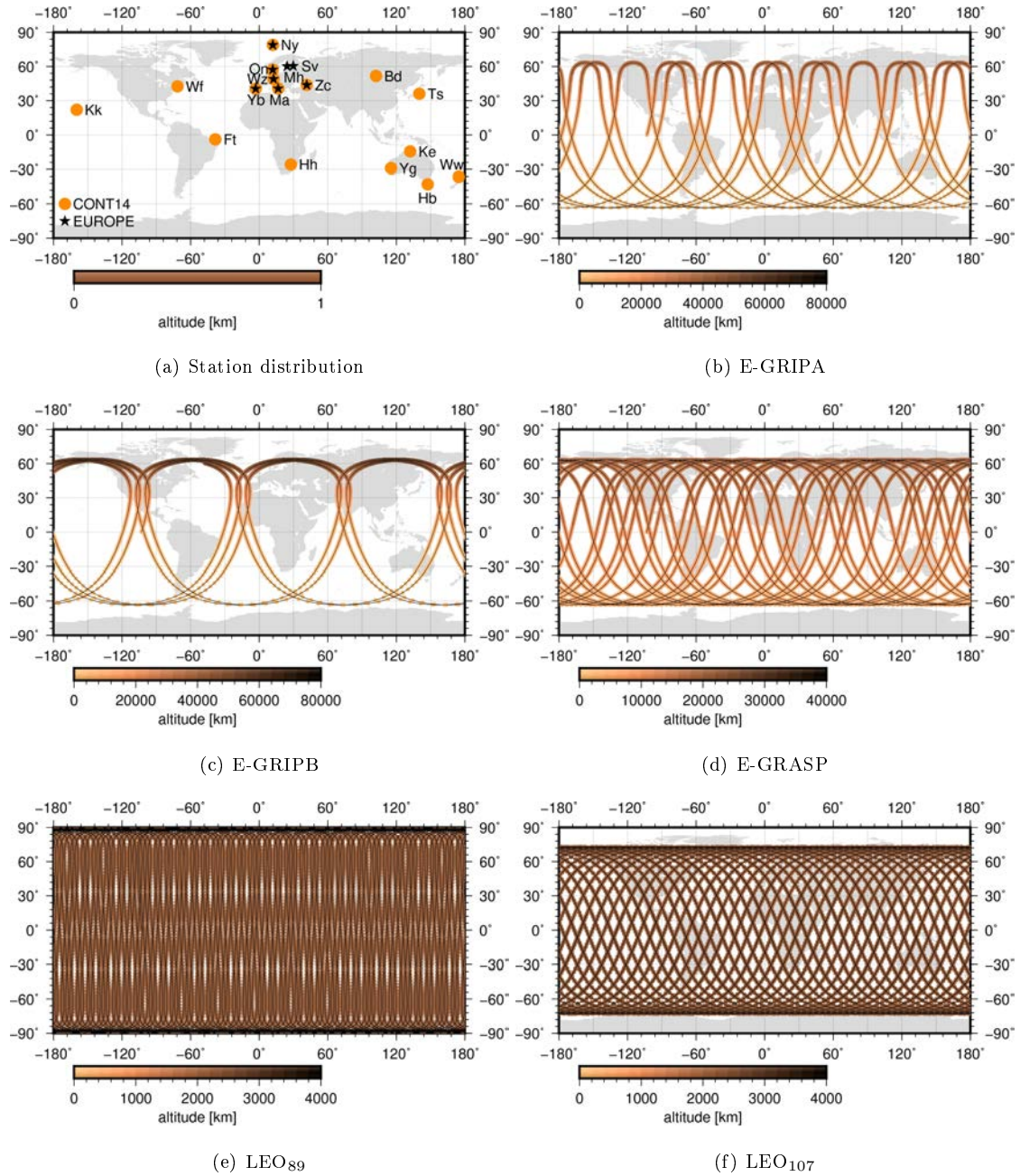


**Fig. 6.19:** Ground tracks of satellites considered in the VLBI simulation; week 1826 January 4th - January 10th 2015; GLOBAL station network; please note the different scales

**Tab. 6.10:** Options in simulations for VLBI satellite tracking and VLBI2010 studies; *st* stations; as Wresnik (2009) used station-specific quantities for the troposphere, minimal and maximal values and the average is given here; please note that Wresnik (2009) provided no information concerning the processing options

	this study	Plank et al. (2014)	Wresnik (2009)
<b>simulation</b>			
simulation purpose	VLBI satellite tracking	VLBI satellite tracking	VLBI2010 simulations
clock Allan deviation	$1 \cdot 10^{-15}$ @ 50 min	$1 \cdot 10^{-14}$ @ 50 min	$1 \cdot 10^{-14}$ @ 50 min
zenith wet delay $l_0^z$	150 mm	150 mm	150 mm
structure constant $C_n$	$1.0 \cdot 10^{-7} \text{ m}^{-\frac{1}{3}}$	$2.0 \cdot 10^{-7} \text{ m}^{-\frac{1}{3}}$	$0.35 - 2.47 \cdot 10^{-7} \text{ m}^{-\frac{1}{3}}$ ( $\overline{C_n} = 1.62 \cdot 10^{-7} \text{ m}^{-\frac{1}{3}}$ )
wind speed $\mathbf{v}$ [m/s]	0 / 8 / 0 (north/east/up)	0 / 8 / 0 (north/east/up)	0.25 - 8.46 / 0.22 - 17.5 / 0 ( $\overline{\mathbf{v}} = 3.4 / 1.4 / 0$ )
tropo height $h$ [m]	2000	2000	1629 - 2414 ( $\overline{h} = 1893$ )
measurement noise	29.70 ps ( $\sqrt{2} \cdot 0.007$ mm)	30 ps	4 ps
considered networks	EUROPE (8 st), GLOBAL (17 st, CONT14)	EUR (7 st), AUS (6 st), ASIA (7 st), GLOBAL (equal distributed 16 and 32 st, partly fictitious)	GLOBAL (equal distributed 16, 24, and 32 st, partly fictitious)
repetitions runs	26	30	25
observation interval [min]	1	1 (GPS: 5)	several intervals tested (0.25 - 6)
elevation cut-off angle [°]	5	10 (GRASP-like sat: 5)	information not provided
<b>processing</b>			
zenith wet delay	piece-wise linear 2 h with 5 cm relative constraints, no gradients	piece-wise linear 0.5 h with 1 cm relative constraints, no gradients	information not provided
clock	piece-wise linear 12 h without relative constraints	piece-wise linear 1 h with 1.3 cm relative constraints, rate and quadratic term estimated	information not provided
EOP	fixed	fixed	information not provided
orbits / Quasars	orbits fixed	orbits fixed	information not provided
station coordinates	NNT, NNR with respect to a priori	NNT, NNR with respect to a priori	information not provided

that the extension from daily to weekly solutions improves the derived coordinates by a factor of two. The zenith wet delays were estimated as piece-wise linear parameters every 2 h with relative constraints of 5 cm to handle periods with less observations. Due to the assumed stable clocks, the receiver clock parameters were setup piece-wise linear every 12 h without relative constraints. The datum definition was realized by NNT and NNR conditions with respect to the a priori coordinates over all stations. EOP and other parameters like satellite orbits were, in general, not estimated.

As results based on simulated observations cannot be compared in a reasonable way without considering the assumed options, Tab. 6.10 provides an overview of the assumption (1) in this study, (2) in Plank et al. (2014), and (3) in Wresnik (2009). Please note that the options used are slightly different in Plank (2013) and Plank et al. (2014). As visible in Tab. 6.10, this study is based on assumptions similar to those of Plank et al. (2014). The largest differences can be found in the tropospheric structure constant and the considered station networks. It has to be mentioned that Wresnik (2009) considered station-specific tropospheric properties. In the study presented in the following a relatively dry troposphere with a structure constant of  $1.0 \cdot 10^{-7} \text{ m}^{-\frac{1}{3}}$  was selected.

### 6.3.2 Simulation Study for GNSS Satellites

The simulation of GNSS satellite tracking can be seen as the most demanding topic, as this type of VLBI satellite observation is feasible today. The number of simulated observations per baseline and day ( $\approx 370$  observations) is, in the regional EUROPE network, similar for all baselines with differences below

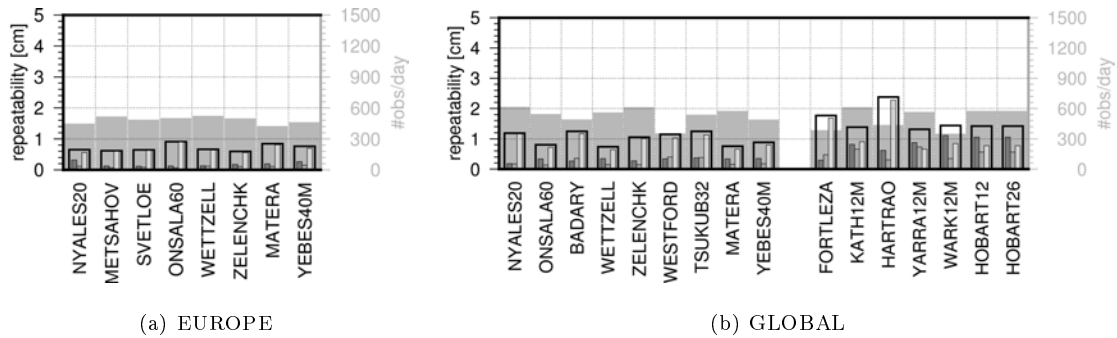


**Fig. 6.20:** Station coordinate repeatabilities derived from tracking a GPS satellite constellation; the columns are ordered in North, East, and Up component, the encasing bar gives the 3D repeatability

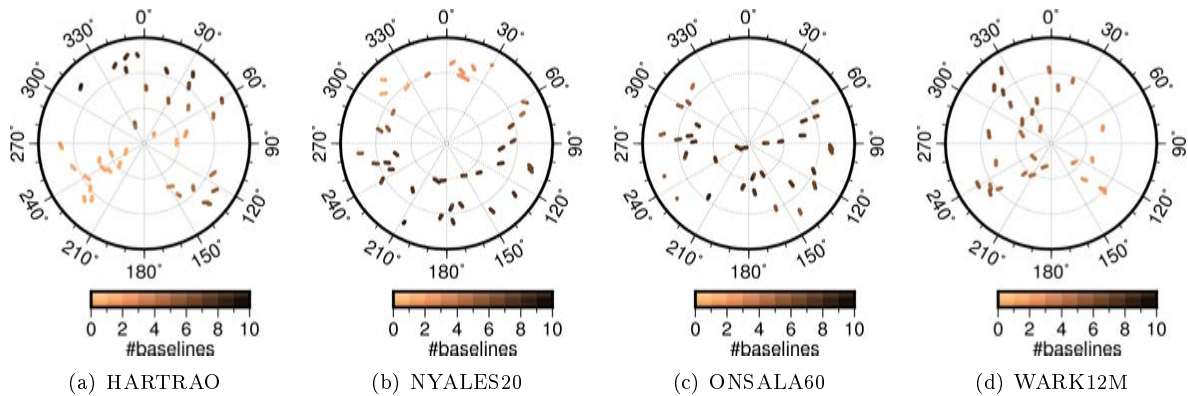


**Fig. 6.21:** VLBI observations of GPS satellites as skyplot for January 4th; the color coding provides the number of baselines formed with the corresponding station

20%. Obviously, the short baseline length, the high satellite altitude, and the high latitude of this regional network are beneficial for the number of observations. Caused by the rough scheduling procedure only  $\approx 480$  observations are simulated per baseline and day for the GPS constellation tracking. However, when using a dedicated scheduling approach, common satellites will be found for each epoch independently of the baseline length and orientation.

Results for tracking a single GPS satellite are not presented here, as the derived station coordinate repeatabilities exceed the 10 cm level. The main reason is the bad observation geometry between the network and the slowly passing satellite. This effect is discussed in the following concerning the tracking of satellites in elliptic orbits. Fig. 6.20(a) shows the coordinate repeatabilities derived from the GPS constellation tracking using the EUROPE network. The weekly 3D position RMS is between 0.6 and 0.9 cm with good determined north and east components (RMS < 0.3 cm and RMS < 0.2 cm, respectively). The stations at the northern and southern network edge show larger uncertainties in the north component, as for these stations north-south orientated baselines are dominating. The east component of all eight stations is determined better than the north component. This effect is also known from differential GNSS processing. The height component is determined slightly worse compared to the horizontal direction, RMS values are between 0.6 and 0.9 cm. Plank et al. (2014) found similar 3D-RMS values of 0.5-1.1 cm in their study including weakly determined height coordinates. The reason for this limited precision might be related to modeling deficiencies. In general, a non-optimal sky coverage causes problems for reducing the correlation between height, tropospheric delay, and receiver clock. This phenomenon is well known from GNSS processing and described, e.g., in Rothacher (2002). The average daily number of observations processed per station is rather similar at a level of 400 to 500.

The derived repeatabilities for the global network are significantly larger as shown in Fig. 6.20(b). The

**Tab. 6.11:** Simulated vs. estimated wet delays  $\Delta_{\text{tr}}$  and receiver clocks  $\Delta_{\text{cl}}$ ; mean and standard deviations; solution 1=GPS constellation, solution 2=E-GRASP/Eratothenes

sol	delay	Matera	Metsahovi	Ny Ålesund	Onsala	Svetloe	Yebes	Zelenchk.	average
1	$\Delta_{\text{cl}}$ [ns]	0.09±0.09	0.07±0.07	0.12±0.11	0.04±0.05	0.11±0.17	0.07±0.06	0.11±0.17	0.09
	$\Delta_{\text{tr}}$ [cm]	0.64±0.83	0.68±0.61	0.64±0.56	0.55±0.54	0.51±0.48	0.71±1.03	0.58±0.45	0.61
2	$\Delta_{\text{cl}}$ [ns]	0.43±0.35	0.22±0.15	0.48±0.25	0.19±0.17	0.27±0.10	0.47±0.31	0.34±0.14	0.34
	$\Delta_{\text{tr}}$ [cm]	1.85±0.78	0.74±0.52	1.45±0.67	1.45±0.67	1.76±0.70	2.84±0.77	3.35±1.68	2.09

weekly 3D position RMS is between 0.7 cm for Matera and Wettzell, thus, comparable to the regional solution, and 2.4 cm for Hartebeesthoek in South Africa. Interestingly, for a subset of stations the uncertainty in the north component exceeds that in the east or even that in the height. Especially the stations in Australia and New Zealand show this effect. The effect is related to the sensitivity of VLBI, which is given exclusively in the plane defined by the two stations and the source, i.e., the spacecraft. Consequently, a somehow systematic distribution of observations causes biases in the determination of horizontal coordinates. Plank (2013) called this the “network effect”. Fig. 6.21 shows skyplots for the GPS satellites observed on January 4th by the stations Hartebeesthoek, Ny Ålesund, Onsala, and Warkworth. The color coding represents the number of baselines formed between the corresponding station and the remaining network. In addition, Fig. 6.25(a) provides an overview of the baselines formed for that day. For the uncertainly determined station Hartebeesthoek, observations are mainly performed together with European stations in the north and with Australian stations in the east. Therefore, the simulated observations are not well distributed across the hemisphere. Additionally, the observations in south-west direction are observed by a single baseline only. The distribution of simulated observations is much more homogeneous for the telescope in Ny Ålesund resulting in a significantly better estimation of north and east coordinates compared to the height. For Onsala, the simulated observations are homogeneously distributed in the southern part of the hemisphere but nearly no satellite was observed in the northern direction (due to the GPS shading area). Consequently, the north coordinate component is estimated with a significantly larger uncertainty. Baselines for the station Warkworth (New Zealand) are simulated only towards east due to the network geometry, therefore, the north component is badly determined (1.6 cm). In general, these effects could be reduced by (1) using a better distributed network and (2) applying a suitable scheduling. The need to use a more sophisticated scheduling approach is also shown by the fact that Kokee at Hawaii had no common visibility with any other station to the selected satellites. The station is, therefore, skipped in the processing. Using a global network of 16 well distributed, but partially fictitious stations, Plank (2013) derived repeatabilities slightly smaller than those in the study presented here (0.5 to 1.2 cm 3D RMS). However, by using a more appropriate scheduling approach (the satellite with the highest elevation angle was scheduled) she simulated around twice the number of observations presented in Fig. 6.20(b).

Fig. 6.22(a-d) shows the simulated zenith wet delays and receiver clock offsets (*gray*) and their estimated counterparts (*black*). The actual, simulated or estimated values are represented by dots and connected by straight lines for reasons of clarity. Especially, for the estimated values this linear connection is reasonable due to the considered piece-wise linear functions. In all four figures an overall good agreement between the simulated and estimated values is visible showing good capabilities to recover the assumed tropospheric delays and receiver clock behavior. The differences presented additionally are computed for the observation epoch by interpolating the estimated piece-wise linear function. The receiver clock shows mainly differences below 0.2 ns between simulated and estimated values, which corresponds to  $\approx 6$  cm. Differences are well below 5 cm for the zenith wet delays. In general, the recovery of receiver clock and wet delays works properly with slightly better results for Onsala. Tab. 6.11 shows the overall differences for all stations within the regional network. The averaged difference is determined for the clock estimation to 0.09 ns, which corresponds to  $\approx 2.7$  cm and for the zenith wet delays to 0.6 cm. For the other satellites, the comparison

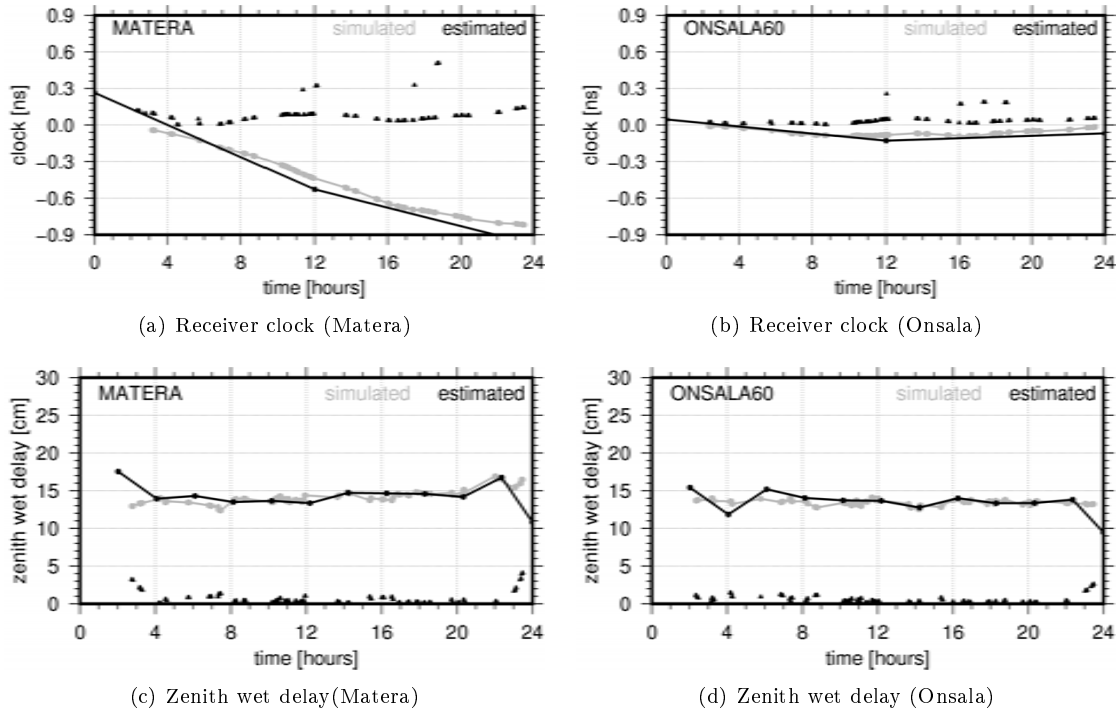


**Fig. 6.22:** Estimated (*black*) and simulated (*gray*) zenith wet delays and receiver clocks; corresponding differences are represented by *triangles*

shows slightly larger differences. Exemplary the corresponding differences for E-GRASP/Eratosthenes are shown in Tab. 6.11. The zenith wet delays show differences of a few centimeters driven strongly by the estimation intervals with less observations or a bad observation geometry, while the receiver clock delays show differences of 0.34 ns ( $\approx 10$  cm). In summary, it can be said that the recovery of zenith wet delays and clock offsets is limited most probably by the unsuitable sky coverage for single-satellite tracking. Plank et al. (2014) showed somehow smaller differences of around 0.5 cm for the tropospheric delays, while estimating the troposphere in 30 min intervals with 1 cm relative constraints. However, they presented no comparison for GPS tracking simulations and the clock delays were not assessed at all.

### 6.3.3 Simulation Study for LEO Satellite

In this subsection VLBI LEO satellite tracking capabilities are discussed. As mentioned in Tab. 6.9, three orbits with different inclinations were selected for comparison reasons. The numbers of daily observations are presented as baseline matrices in Fig. 6.23. These matrices contain the mean number of simulated observations per baseline averaged over the assessed week in January 2015. Significant differences are present according to the different inclinations of  $63.4^\circ$ ,  $89^\circ$ , and  $107^\circ$ , respectively. Obviously, in the regional European network with station latitude between  $40^\circ$  N and  $80^\circ$  N the selected inclination has a significant impact on the common observability. Especially, the Fennoscandian baselines between Onsala, Ny Ålesund, Svetloe, and Metsahovi benefit from a higher inclination. In the case of a polar orbit, around twice the number of observations are derived for these northern baselines compared to the other orbits. Additionally, stations on the southern edge of the tracking network (e.g., Yebes, Matera, Zelenchukskaya) shows also higher observation counts for the polar orbit (Fig. 6.23(c)). In the global station network, a considerable number of baselines cannot observe the LEO as shown in Fig. 6.24. Nearly independent of the selected inclination, not more than 33% of the 153 baselines in total can track the LEOs. For the  $\approx 50$  observing baselines, the data amount varies significantly depending on baseline length and orientation but only slightly regarding the inclination. The highest number of observations is found for the northern stations Onsala and Ny Ålesund and the very short baseline in Hobart. However, for example,

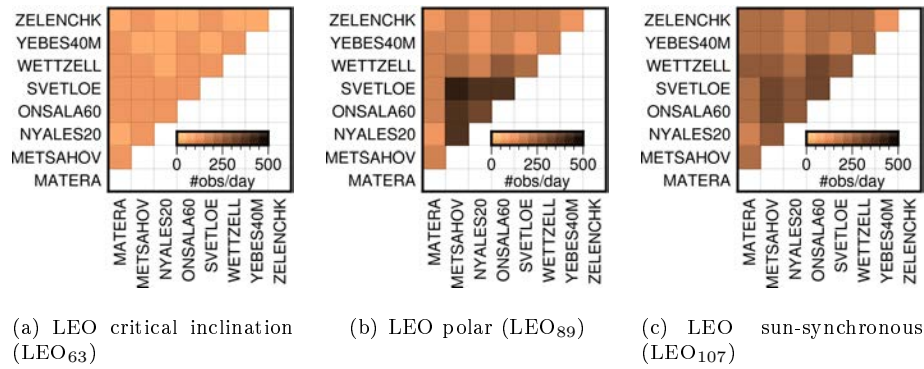


**Fig. 6.23:** Number of simulated VLBI observations to LEO per baseline

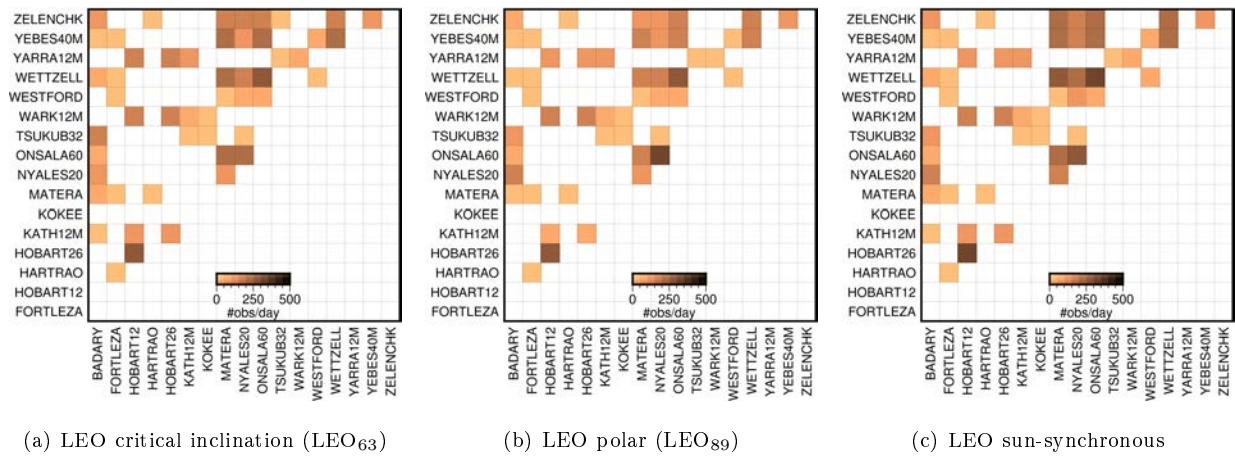
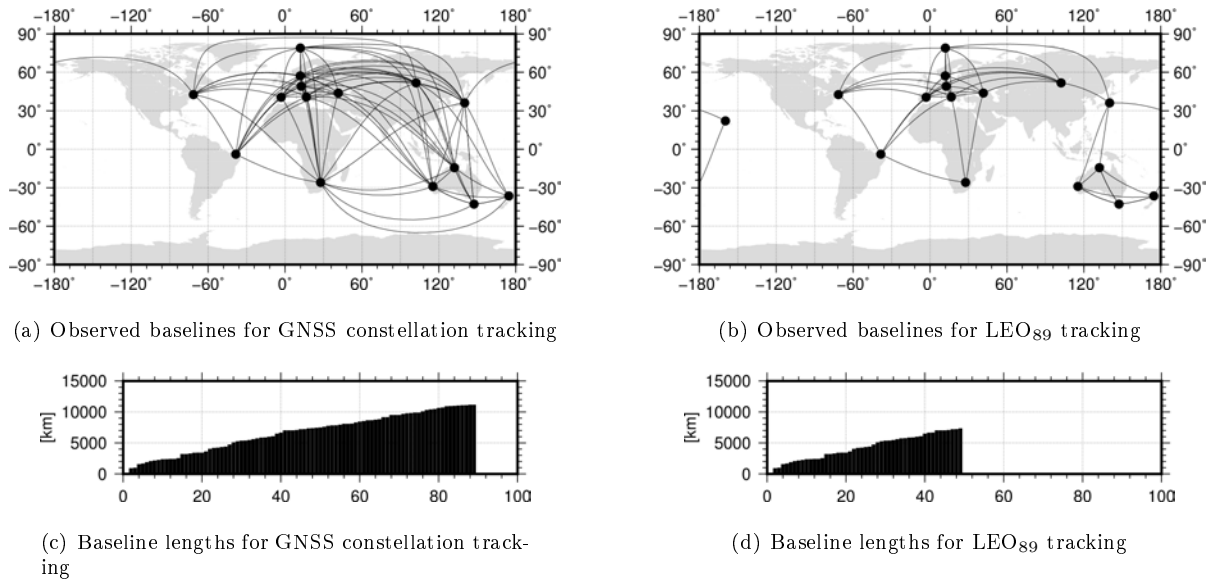


**Fig. 6.24:** Number of simulated VLBI observations to LEO per baseline

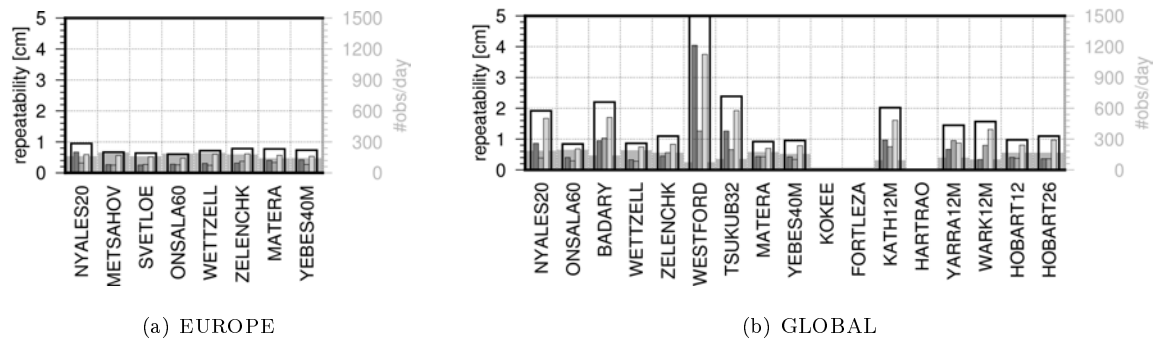
the telescopes in Hobart, Tasmania only have baselines with three other stations (Katherine, Warkworth, and Yarragadee) and Kokee in Hawaii only observed together with two stations (Warkworth and Tsukuba). Therefore, the corresponding station coordinates will be determined rather poorly.

Fig. 6.25(b) shows the baselines formed in the global network, when observing the polar orbiting LEO (LEO<sub>89</sub>). Obviously, a number of stations is connected quite well by several baselines in various directions. Especially, the European stations form a dense network and, to a smaller extend, also the Australian stations do so. However, as seen already in the observation matrix, there are stations connected by only two (Kokee) or three (Hartebeesthoek) baselines. In total 49 baselines are formed in the considered week with a maximal baseline length of 7355 km as shown in Fig. 6.25(d). It has to be mentioned that both figures are similar for LEO<sub>63</sub> and LEO<sub>107</sub>. Concerning their lengths only eight of the formed 49 baselines are within the 2000-3000 km range indicated by Plank (2013) to be ideal for VLBI LEO tracking, i.e., she stated that the majority of baselines in a network should be within this range. In the EUROPE network 12 of 28 baselines were within this range. The difference to the much higher orbiting GPS satellites is obvious in the comparison of Fig. 6.25(a) and 6.25(b). In total 89 baselines up to 11'158 km length observe the GPS constellation. Consequently, stations like Westford or Tsukuba are better connected to the rest of the network.

The LEO orbit with the critical inclination of 63.4° (LEO<sub>63</sub>) is discussed first. The corresponding repeatabilities are presented in Fig. 6.26. In the regional network 3D repeatabilities of 0.6-0.7 cm are determined (Ny Ålesund reaches 0.9 cm). Compared to the regional solution for the GPS constellation tracking horizontal and vertical RMS values are determined here more homogeneously between the stations. The height component, however, is rather well determined with repeatabilities around 0.5 cm. In the global solution somewhat larger 3D repeatabilities are present (Fig. 6.26(b)). Position RMS values between 1 and



**Fig. 6.25:** Observed baselines and distribution of their lengths for GPS constellation and LEO<sub>89</sub> tracking



**Fig. 6.26:** Station coordinate repeatabilities LEO<sub>63</sub>; please note the different scales; the columns are ordered in North, East, and Up component, the enclosing bar gives the 3D repeatability

2 cm are derived for the European and Australian stations. Even for the more isolated stations Badary in Russia and Tsukuba in Japan repeatabilities are close to 2 cm. The slightly higher value for Ny Ålesund is caused by the station's high latitude compared to the satellite inclination of  $63^\circ$ , which causes also the rather high repeatability in the north component. In summary, the derived station coordinate repeatabilities reflect the inhomogeneous station distribution in the global network. Only for Westford very large repeatabilities are present. However, for three stations (Fortaleza, Hartebeesthoek, and Kokee) coordinates were not determined. These stations have significantly less observations as shown previously in Fig. 6.24 and Fig. 6.25(b). As shown in Fig. 6.25(b) these four stations are located at the network edges and thus, they are connected only by long baselines. Therefore, the weak determination of their coordinates is not surprising. Fig. 6.27(a-d) shows the corresponding skyplots for January 4th to emphasize the differences in the derived station repeatabilities. In general, good station coordinates result from several satellite passes, as each pass generating a new geometry. Plank (2013) found a number of three passes as critical for reliable station coordinates. The improvement in the global network with respect to the regional one is related to the improved observation geometry as shown in Fig. 6.27(a,b), exemplarily for Ny Ålesund. Obviously, the additional observations in the northern direction strengthen the derived coordinate results in north and east direction, which do not increase as the height component does. The weaker determination of Westford's station coordinates is related to the unbalanced observation geometry as for this station baselines are observed only in eastern direction. The bad coordinate repeatability for Kokee is driven by the low number of observations and their unfavorable geometry. Kokee is connected to

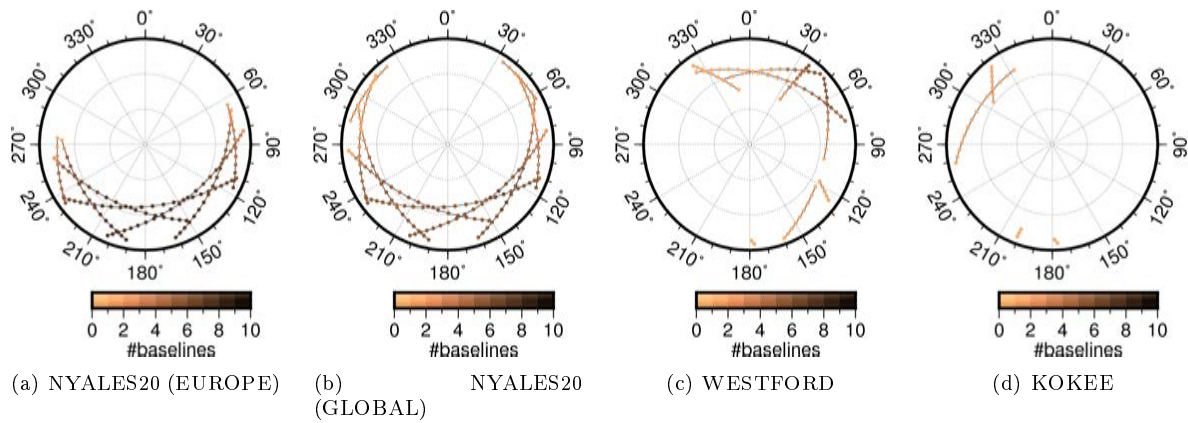


**Fig. 6.27:** VLBI observations of the LEO<sub>63</sub> satellite as skyplot for January 4th; the color coding provides the number of baselines formed with the corresponding station

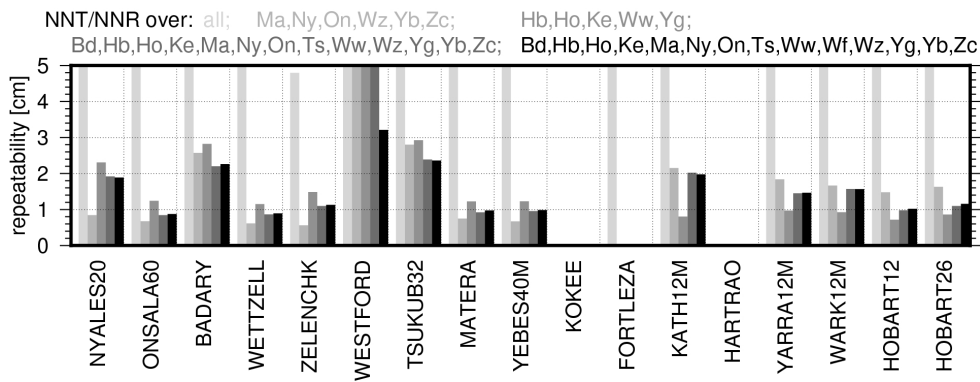


**Fig. 6.28:** Station coordinate repeatabilities for different core station definitions

the network only by the two very long baselines with Warkworth and Tsukuba. Comparing the elevations of these LEO observations to those of the GPS tracking, the sky coverage is very poor here. It has to be mentioned that the results presented in Fig. 6.26(b) are derived by changing the core station definition. According to Tab. 6.10 the NNT and NNR conditions were applied for all stations. However, doing this for the LEO tracking with a few badly determined stations, repeatabilities will explode as errors will be distributed within the network. Therefore, the core station definition was adjusted for the LEO tracking study. Fig. 6.28 shows 3D coordinate repeatabilities derived for the global network and LEO<sub>63</sub> with different core stations. The first column shows the obtained results. If the NNT/NNR conditions are applied to all stations repeatabilities exceed the 10 cm level. If only a regional sub-network is constrained (the European or the Australian stations) results improve with benefits for the corresponding stations. In the end, excluding Fortaleza, Hartebeesthoek, and Kokee from the datum station definition showed the best results. These stations were also excluded from the datum definition for the other two LEOs but not for the satellites in elliptical orbits.

The polar LEO orbit with an inclination of 89° (LEO<sub>89</sub>) is discussed next. 3D repeatabilities of 0.6-0.7 cm are derived for the regional network (Fig. 6.29(a)). The scatter in the global network is similar to that for the previously discussed LEO<sub>63</sub> orbit (Fig. 6.29(b)). Repeatabilities are below or close to 2 cm for all stations except Westford. The more isolated stations Badary and Tsukuba show slightly higher repeatabilities of 2.1 and 2.4 cm, respectively. The derived 3D position RMS is slightly larger compared to LEO<sub>63</sub>, however, the coordinates of Ny Ålesund benefit from the polar orbit, their RMS decreases from 1.8 to 1.2 cm. Fig. 6.30(a-d) show a set of skyplots for Onsala. Due to the dense network in Europe the same passes are observed in the regional and the global network as shown for LEO<sub>63</sub> in Fig. 6.30(a,b). However, the number of observations for a specific epoch decreases in the global solution as Metsahovi

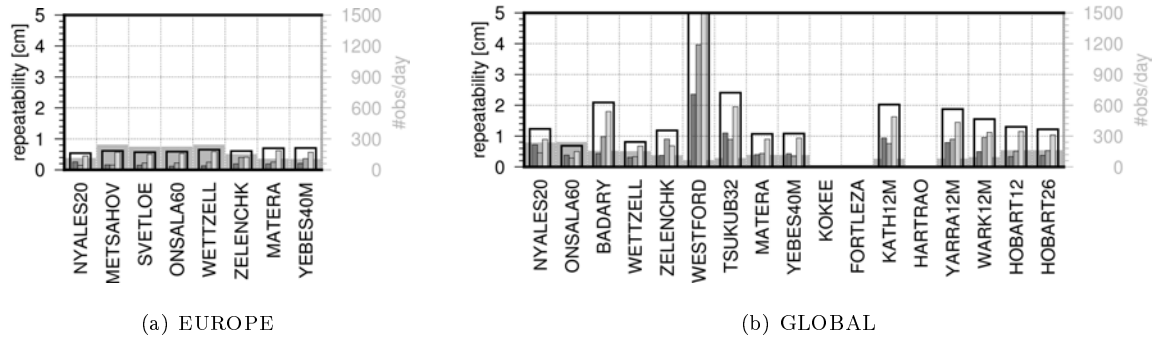


**Fig. 6.29:** Station coordinate repeatabilities  $LEO_{89}$ ; please note the different scales; the columns are ordered in North, East, and Up component, the encasing bar gives the 3D repeatability

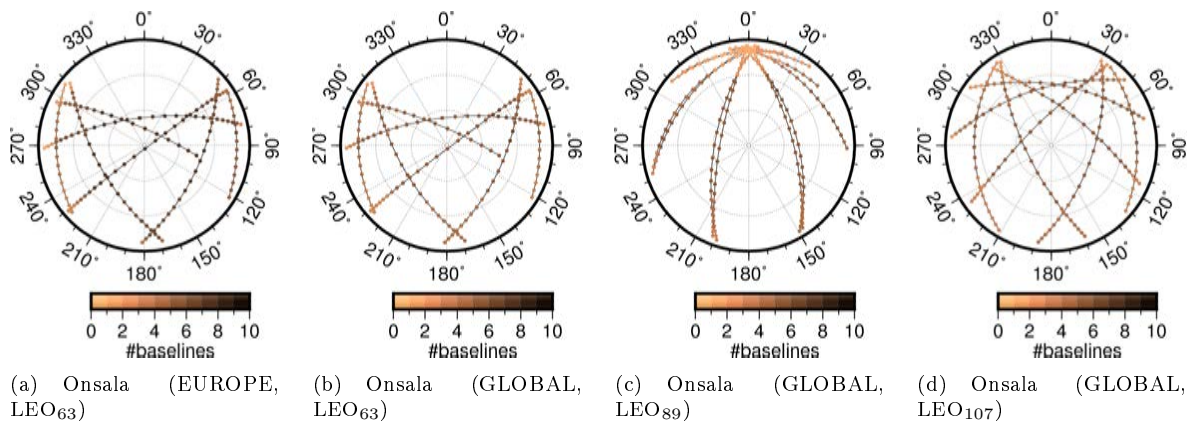


**Fig. 6.30:** Direction to the observed LEO satellites as skyplot for January 4th; the color coding provides the number of baselines formed with the corresponding station

and Svetloe, located close to Onsala, are not part of the global network. The 3D repeatability is only slightly affected and increases from 0.6 to 0.7 cm. Caused by the different inclinations, the skyplots show significant differences in the orientation of the satellite passes when comparing the different LEO solutions (6.30(b-d)).

The third LEO orbit considered in this study has a sun-synchronous orbit with an inclination of  $107^\circ$ . The derived 3D coordinate repeatabilities for the regional network are again between 0.5 and 0.7 cm with a somewhat more weakly determined east component compared to the other two LEO simulations. In average the east repeatability is 0.4 cm, whereas 0.2 and 0.3 cm were derived for  $LEO_{63}$  and  $LEO_{89}$ . In the global network coordinate repeatabilities are similar to the  $LEO_{63}$  solution but with a better determination of Ny Ålesund. Plank (2013) selected a similar LEO orbit with 2000 km altitude and an inclination of  $104.89^\circ$ . For this satellite, she found station coordinate repeatabilities between 1.7 and 10 cm for a homogeneously distributed 16 station network (with partly fictitious stations). However, she reported repeatabilities between 0.9 and 2.0 cm for a cluster network containing 21 stations in Europe, Asia, and Australia. Considering the different station networks the values derived in the study presented within this section are comparable to the results derived by Plank (2013).

### 6.3.4 Simulation Study for Elliptical Orbiters

Regarding the recent E-GRIP and E-GRASP proposals (cf. Sect. 3.5.1), simulation studies for elliptical orbits are also worthwhile. First of all, the observation matrix is considered for the European network (Fig. 6.32). A very homogeneous observation scatter is present, as the satellite's apogee passing is observed within this network. The difference between the baselines is below 20%, which is similar to the

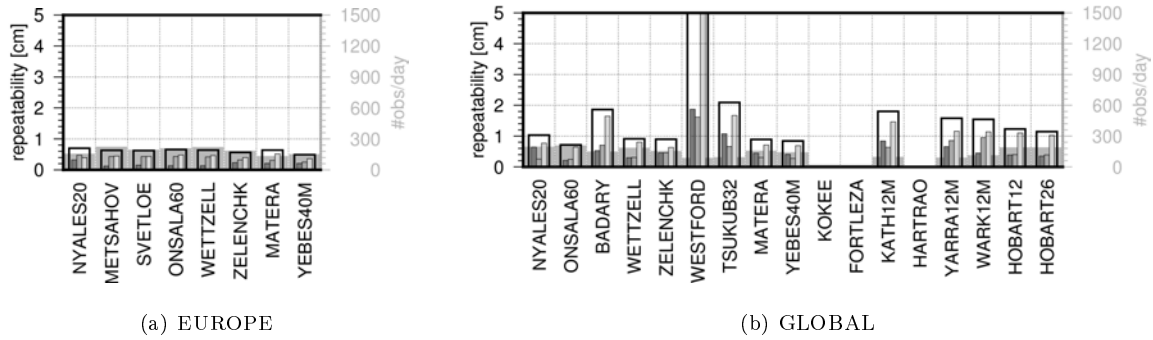


**Fig. 6.31:** Station coordinate repeatabilities LEO<sub>107</sub>; please note the different scales; the columns are ordered in North, East, and Up component, the encasing bar gives the 3D repeatability

single-satellite GPS tracking (cf. Sect 6.3.2). However, the differences between the three orbit types are fundamental with a spread of around 300 observations per baseline and day. The observation matrix for the global solution in Fig. 6.33(a-c) shows a higher percentage (62%) of observing baselines than for the LEO tracking (33%). Higher data amounts are visible for the northern stations which corresponds to the apogee location above the northern hemisphere (cf. Fig. 6.19). Especially, for EGRIP-B, significantly more observations are available for Badary, Matera, Ny Ålesund, Onsala, Tsukuba, and Wettzell. The daily number of observations for the corresponding baselines is two to three times larger than for baselines in the southern hemisphere. Obviously, this imbalance will cause difficulties for the station coordinate estimation.

Fig. 6.34(a-d) shows the baselines formed for the observation of EGRIP-A and E-GRASP in the global network. However, the differences are small; in both cases around 90 baselines up to lengths over 10'000 km are observed (EGRIP-A: 96 baselines, maximal length 11'154 km and E-GRASP 88 baselines, maximal length 10'687 km). From the geometrical point of view, the additional baselines, which were not observable in the LEO tracking, should stabilize the coordinate solutions as they strengthen the connections between the stations. However, as the orbital velocity depends on the altitude, the satellite pass durations show large differences. For the polar LEO<sub>89</sub>, 109 passes of not more than 28 min length are counted in the global network over one day. The number of passes decreases to 42 for E-GRIP-A, while their duration ranges from 2 to 560 min. Consequently, the ability to determine station coordinates is limited for some stations by the slow passing, impeding the separation of height, troposphere, and clock, and for the others by bad visibility conditions.

The first highly elliptically-orbiting satellite discussed here is EGRIP-A. The corresponding orbit has an eccentricity of 0.6. According to Tab. 6.9 the perigee and apogee height is 2528.8 km and 33629.2 km, respectively. Fig. 6.35(a) shows the station coordinate repeatabilities for the regional network stations. The 3D position RMS are between 1.6 and 2.9 cm depending highly on the station latitude. The height

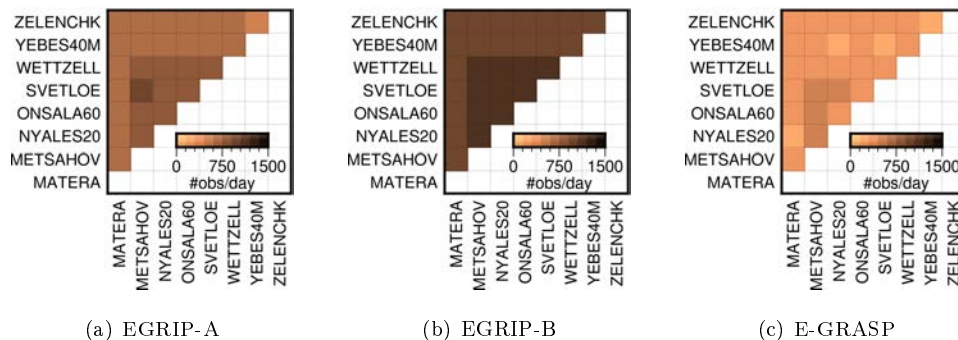


**Fig. 6.32:** Number of simulated VLBI observations to elliptically-orbiting satellite per baseline

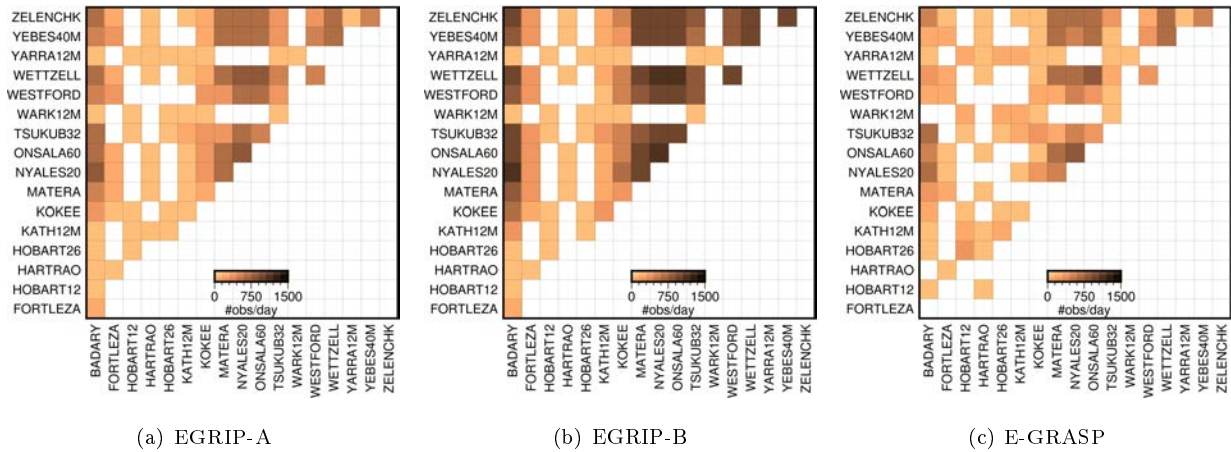


Fig. 6.33: Number of simulated VLBI observations to elliptically-orbiting satellites per baseline

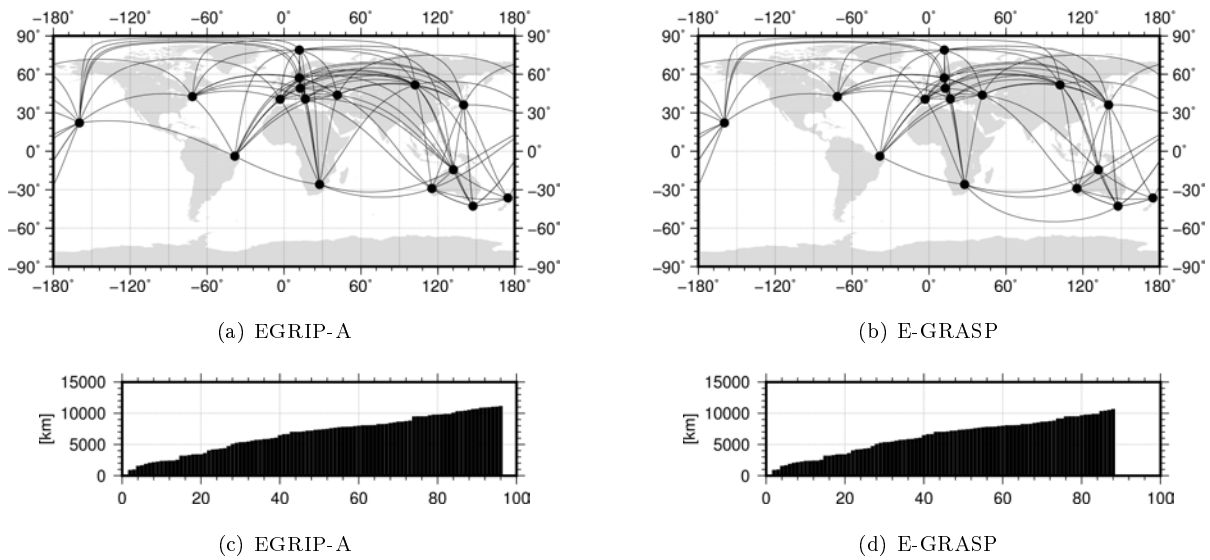
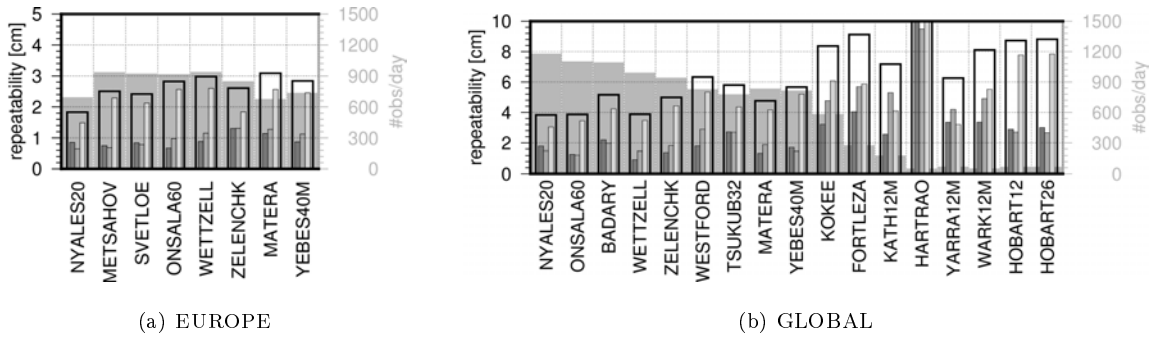


Fig. 6.34: Observed baselines and distribution of their lengths for EGRIP-A and E-GRASP tracking

component is determined more weakly than the other coordinates. The number of observations is, however, large, as the stations are able to observe EGRIP-A for more than twelve hours per day (600-900 observations per day and station). In the global network station coordinates are determined badly, the 3D repeatabilities are at least 4 cm. Driven by the elliptical orbit with the perigee above the southern hemisphere the 3D repeatabilities increase, while the number of observations decrease with decreasing station latitudes. For the stations in the Australian network not more than 60 observations per day could be simulated. The difficulties to derive reliable coordinates are caused by problems in the separation between height, troposphere, and clock delay. Recapitulating the impact of sky coverage and the number of satellite passes, the skyplots shown in Fig. 6.36(a-d) give an impression of the problems related to VLBI tracking of elliptical orbiters. Except for E-GRASP, the pass geometry indicates no suitable sky coverage. Especially, for those stations observing the satellite orbit's apogee, the geometry changes very slowly, thus, troposphere and height cannot be separated well.

The observed problems increase for the even more elliptical orbit of EGRIP-B where altitudes of 56'629.0 km and 629.0 km are present for apogee and perigee, respectively. In the regional network 3D station coordinate repeatabilities are derived between 1.8 and 3.0 cm, while the number of daily observations is incredibly high (900-1200 per baseline). However, the satellite location differs by only  $\approx 0.02^\circ$  between consecutive epochs (compared to  $0.4^\circ$  for GPS and several degrees for LEOs). Therefore, the individual observation do not



**Fig. 6.35:** Station coordinate repeatabilities EGRIP-A; please note the different scales; the columns are ordered in North, East, and Up component, the encasing bar gives the 3D repeatability

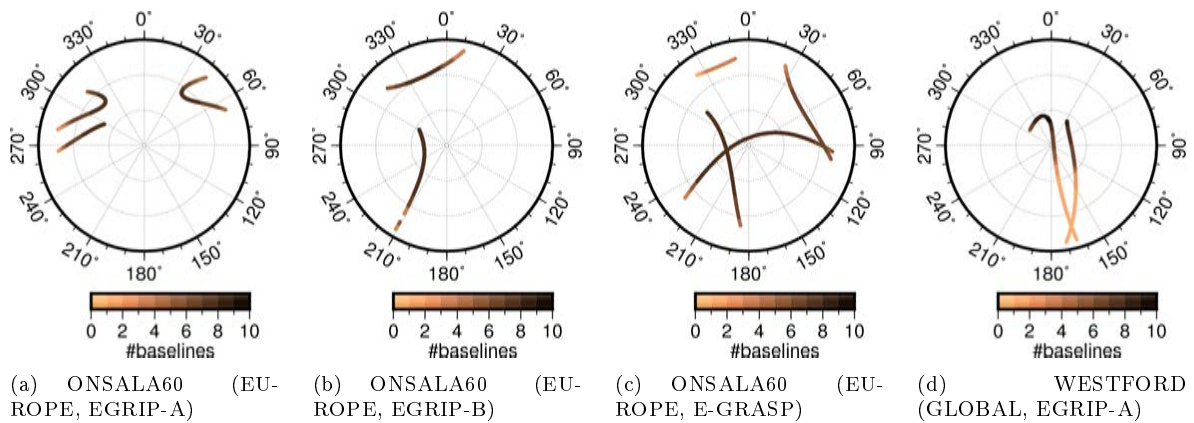


**Fig. 6.36:** Direction to the observed satellites in elliptical orbits as skyplot for January 4th; the color coding provides the number of baselines formed with the corresponding station

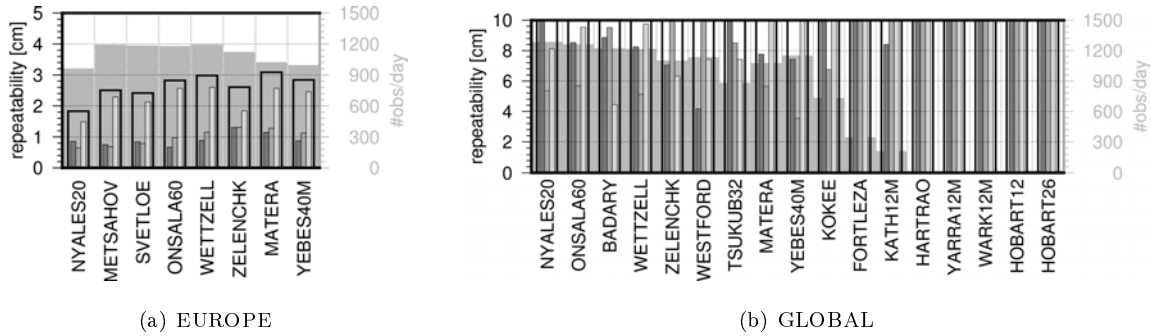


**Fig. 6.37:** Station coordinate repeatabilities EGRIP-B; please note the different scales; the columns are ordered in North, East, and Up component, the encasing bar gives the 3D repeatability

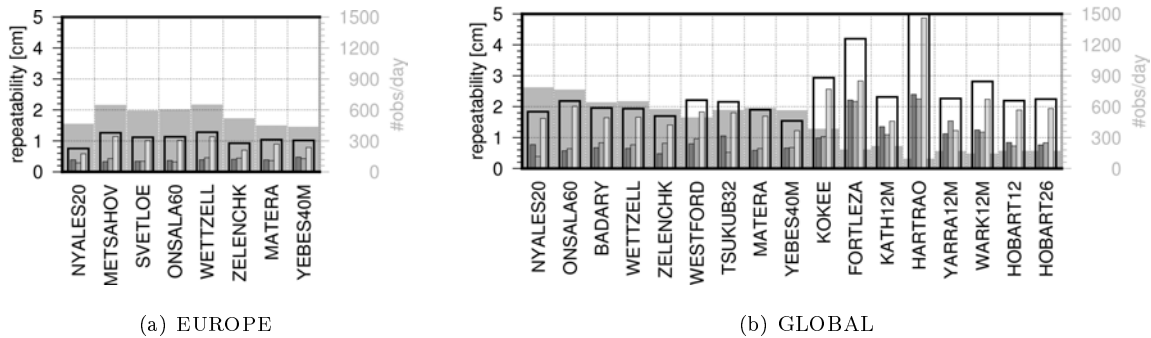


**Fig. 6.38:** Station coordinate repeatabilities E-GRASP; for Hartebeesthoek the 3D value is 5.7 cm; the columns are ordered in North, East, and Up component, the encasing bar gives the 3D repeatability

bring new information and the observation interval could be enlarged to several minutes (as it is discussed in Plank, 2013 for GPS single-satellite tracking). In the global network the situation is different. Whereas the northern stations observe the satellite's slow apogee passes, the southern stations observe the fast perigee passes only in the rare case of having two stations within the decreasing visibility area. Consequently, only 20 observations could be simulated for the stations Hartebeesthoek, Yarragadee, Warkworth, and Hobart during one day. Not surprisingly station coordinate repeatabilities of some decimeters were achieved. For the northern stations, results are also worse due to significant problems in separating height, troposphere and clock. In summary, 3D position RMS values exceed the 10 cm level for all stations.

For the less elliptical orbit of E-GRASP better station coordinate repeatabilities are achieved. As shown in Tab. 6.9, the E-GRASP eccentricity is significantly smaller than that for EGRIP. The perigee and apogee heights for E-GRASP are 755 km and 7465 km, respectively. In the regional network the 3D position RMS is determined to be 0.7 to 1.3 cm with a better repeatability in the horizontal directions. Uncertainties between 0.3 and 0.4 cm are present in both horizontal components. For the global network, 3D repeatabilities of around 2 cm were found with higher values for Kokee, Fortaleza, and Hartebeesthoek. However, compared to the EGRIP orbits at least 100 observations per day are available for all stations. Compared to the E-GRIP simulations and also to the LEO solutions, E-GRASP allows to determine coordinates for all stations.

For E-GRASP the simulation study was extended in such a way that apart from station coordinates, zenith wet delays, and receiver clock offsets also the satellite orbit was determined. Consistent with the artificial generation of the orbits (see Sect. 6.3.1), only the six Keplerian elements were set up. Fig. 6.39 shows the derived RMS of the orbit comparison between the estimated and the a priori orbit. The derived overall orbit differences are 3.48, 5.81, and 0.45 cm in radial, along-track, and cross-track, respectively. The variations between the different simulation runs are, however, small. The corresponding RMS values are 0.62, 2.61, and 0.04 cm in the orbital frame. Therefore, one can conclude that an orbit determination based

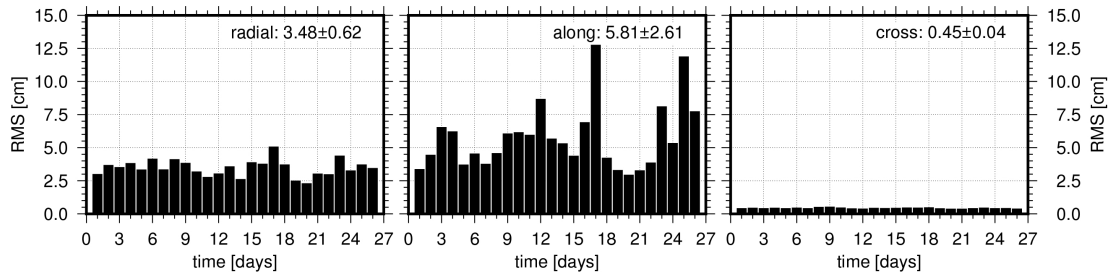


**Fig. 6.39:** E-GRASP orbit determination: differences between simulated and estimated orbit

on VLBI tracking data is achievable at the cm level. Additionally, an E-GRASP orbit determination was performed based on the global network with RMS values derived to 0.33, 1.09, and 0.01 cm in radial, along-track, and cross-track, respectively. Regarding the simulation approach used, it has to be mentioned that a very smooth orbit model was introduced by propagating Keplerian elements over one week considering only gravitational perturbations. Consequently, only Keplerian elements were set up. Obviously, this will not be possible for real tracking data, where the observed spacecraft is subject to non-gravitational forces (cf. Sect. 4.4).

### 6.3.5 Conclusions and Recommendations for Future Co-location Satellite

The study performed here and the work presented previously by Plank (2013) and Plank et al. (2014) show the challenges for station coordinate determination from VLBI satellite tracking. In general, three different spacecraft types are considered nowadays: (near-circular) LEOs, existing GNSS satellites, and elliptically-orbiting satellites. Concerning the observation concept, LEOs are challenging to track as their low altitude allows only short baselines with comparably short and fast passes. This requires high antenna slew rates and an integration of those observations into the regular VLBI sessions. The tracking of GNSS is in this respect easy to handle, as passes are slower and longer baselines are possible. A dedicated scheduling is of utmost importance for a good sky coverage. In agreement with Plank (2013), tracking only a single GNSS satellite (e.g., equipped with an X/S-band noise source) is not sufficient to estimate station coordinates. The considered elliptical orbits allow baselines up to the Earth's diameter with very long and slow passes for some stations and fast passes with small visibility areas for others. For the GNSS tracking (G-VLBI), the most important limitation is the transmitted bandwidth, as GNSS L-band signals are not observable for many telescopes used geodetically. In principle, no limitation is given for the future missions concerning the transmitted signals, therefore, a selection of the VGOS bands between 3 and 14 GHz is recommended. Concerning the coordinate results weekly repeatabilities of  $\approx 1$  cm or better are achievable for LEOs and the GNSS constellation tracking with the assumed tropospheric conditions and clock errors. Tab. 6.12 shows the mean repeatabilities averaged over all network stations. For both networks (EUROPE and GLOBAL), the GPS constellation and the LEO solutions achieve nearly the same precision level, while the coordinate precision is significantly worse in the GLOBAL network (repeatabilities are twice as large as in the EUROPE network). Concerning the different inclinations a high inclination is advantageous, whereas a polar orbit seems not to be the best choice for a global station network. Station coordinates cannot be derived reasonably by solely tracking E-GRIP. Especially, for EGRIP-B ( $e > 0.8$ ) the perigee altitude is very low (629 km) and the number of satellite passes is limited. In agreement with Plank (2013) the number and distribution of satellite passes was found as critical for the separation of troposphere, clock, and station coordinates. The station coordinate repeatabilities derived from E-GRASP are slightly larger than those for LEO and GNSS constellation tracking (1-2 cm coordinate repeatability). Results could be improved by a combined observation strategy, where quasars and the spacecraft are tracked subsequently (Plank et al., 2014, 2015). However, within this work this approach was not studied. Another option might be the introduction of tropospheric delays (and receiver clock offsets) derived by colocated GNSS stations into the VLBI processing.

**Tab. 6.12:** Summary VLBI satellite tracking simulation; mean number of observations is given per day and station; mean values over all EUROPE and GLOBAL stations, respectively

network	satellite	daily observations	$\overline{3D}$ [cm]	$\overline{N}$ [cm]	$\overline{E}$ [cm]	$\overline{U}$ [cm]
EUROPE	GPS PRN10	367.18	20.70±7.47	6.15±3.36	17.62±6.99	7.67±4.45
	GPS constellation	482.29	0.71±0.11	0.18±0.07	0.10±0.03	0.67±0.12
	EGRIP-A	833.61	2.11±0.41	0.69±0.13	0.85±0.22	1.79±0.43
	EGRIP-B	1106.82	2.64±0.40	0.92±0.21	0.99±0.26	2.24±0.40
	E-GRASP	546.29	1.07±0.17	0.39±0.05	0.38±0.06	0.91±0.20
	LEO <sub>63</sub>	170.45	0.73±0.11	0.36±0.14	0.29±0.05	0.56±0.05
	LEO <sub>89</sub>	177.79	0.62±0.06	0.18±0.05	0.25±0.09	0.53±0.07
	LEO <sub>107</sub>	184.93	0.62±0.06	0.19±0.07	0.38±0.08	0.44±0.05
GLOBAL	GPS PRN10	314.07	36.29±21.26	13.81±10.09	28.67±19.69	14.52±7.84
	GPS constellation	518.18	1.26±0.41	0.54±0.33	0.36±0.20	1.01±0.43
	EGRIP-A	584.12	7.05±3.56	2.80±2.08	3.33±2.17	5.35±2.41
	EGRIP-B	689.84	41.67±59.48	17.63±17.35	21.73±30.68	28.42±49.50
	E-GRASP	422.33	2.49±1.06	1.01±0.55	1.00±0.53	2.00±0.85
	LEO <sub>63</sub> <sup>1</sup>	128.37	1.50±0.84	0.61±0.50	0.55±0.31	1.06±0.64
	LEO <sub>89</sub> <sup>1</sup>	120.25	1.83±1.33	0.64±0.40	0.87±0.59	1.43±1.20
	LEO <sub>107</sub> <sup>1</sup>	128.38	1.31±0.89	0.51±0.37	0.52±0.34	1.07±0.76

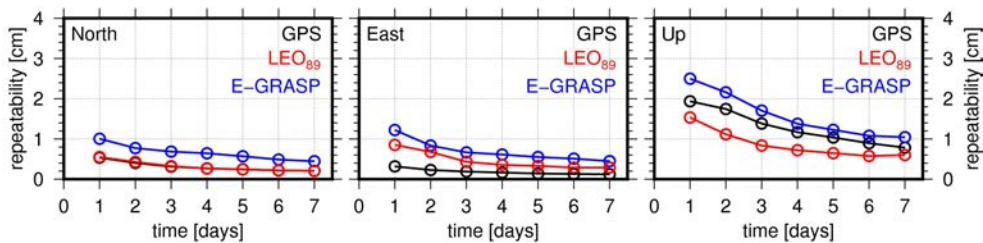


**Fig. 6.40:** Mean station coordinate repeatability derived from processing  $n$  days up to a weekly solution

Concerning the processing time span, Fig. 6.40 shows coordinate repeatability derived for the GPS constellation, E-GRASP, and LEO<sub>89</sub> over  $n$  days ( $n=1..7$ ). Obviously, the coordinate stability improves with increasing observation time. Especially in the height component the generation of weekly solutions is recommended.

## 7 Conclusions and Outlook

Co-location in space as a way to combine space geodetic techniques at the satellite level was discussed and performed in several initial studies over the last decade. Co-location in space provides important prospects regarding the required progress, which is necessary to reach the GGOS goal of realizing a reference frame with an accuracy of 1 mm and a stability of 0.1 mm/yr. First of all, the space ties introduce new geometrical offset vectors between sensors of different space geodetic techniques. In order to perform co-location on the ground, as it is state-of-the-art, huge efforts are required to generate and maintain local ties. Keeping them up-to-date requires resource-intensive terrestrial surveying, repeated regularly for each fundamental site. Besides the outstanding performance achieved at a number of fundamental sites, it is obvious that not all fundamental sites can guarantee this. Combining the techniques on-board a satellite is independent from ground surveys and relies, therefore, only on regularly performed space geodetic observations. Moreover, co-location in space allows not only to connect sensors of different techniques globally but also intra-technique combinations. Co-location in space, thus, allows to assess technique-specific error sources as systematic effects can be assigned either to a certain station or to a certain technique. Last but not least, the additional orbit dynamics introduced by the co-location satellite will improve the estimation of several parameters, like the geocenter or the GNSS satellite antenna phase centers.

However, today's situation does not allow to fully exploit the prospects described above. First of all, no dedicated satellite equipped with sensors of all four space geodetic techniques is available. Several Earth observing satellites are, however, equipped with GNSS, SLR, and DORIS, but they are not designed for co-location in space. Moreover, none of these satellites has a transmitting source observable by VLBI<sup>1</sup>. The only way to include VLBI is to observe GNSS signals by radio telescopes. However, corresponding experiments show that much effort is needed to use these observations for co-location in space. The future is, in contrast, very prospective as dedicated co-location missions are proposed to the space agencies. It can be assumed that within the next decade co-location can be performed on-board one of these spacecraft. Moreover, the recent achievements in VLBI satellite tracking, combining GNSS and SLR in space, and combining ground- and space-based GNSS observations are very promising. In recent years initiatives to further study co-location in space were launched by the international geodetic communities, for example, the GGOS Standing Committee PLATO, which is connected also to IAG's sub-commission on reference frames, was established in 2013.

A fundamental aspect of the work behind this thesis was the implementation of new capabilities into the Bernese GNSS Software, especially those for simulating and processing VLBI data. The established Bernese project version was used and, thus, also proofed by processing VLBI observations from CONT14 and several R1 and R4 sessions. In summary, the derived results are comparable to VLBI solutions derived with dedicated VLBI packages. Therefore, it was decided that the usage of the added VLBI capabilities is reasonable within the project "Co-location on Ground and in Space".

Several core questions concerning co-location in space, aimed to be answered within this thesis, were listed in the introduction. These questions and, therefore, the topics discussed within this thesis were categorized as relating to (1) LEO orbit determination, (2) to the combination of ground- and space GPS observations, and (3) to Earth-orbiting satellite tracking with radio telescopes.

Based on GPS observations, LEO orbit determination at the centimeter level is state-of-the-art. Over the last two decades several authors discussed orbit determination strategies and force models for various

---

<sup>1</sup> For the Chinese mission APOD equipped with a X/S-band transmitter so far no VLBI observations were reported. However, RadioAstron provides a space tie between an SLR retro-reflector and an Earth orbiting VLBI telescope.

satellites. Within this thesis, orbit determination was done and considered as a prerequisite for a suitable co-location in space. Therefore, the aim was to determine the best possible orbits for a selected set of satellites (GRACE, GOCE, OSTM/Jason-2) and to study the impact of modeling non-gravitational perturbations. This study concentrates on the three most important non-gravitational perturbations: solar radiation pressure, Earth albedo, and air drag. These forces are considered, simply spoken, by calculating the impact of each force (derived from dedicated models) on the satellite-specific cross-section exposed to this force. Thus, this procedure is limited by: (1) the accuracy of the underlying model, (2) the accuracy of the satellite's cross-section and its optical properties, and (3) the accuracy of the spacecraft attitude. Taking the non-gravitational forces into account shows a relatively small impact on the GRACE satellites. For a reduced-dynamic orbit determination with pseudo-stochastic orbit parameters estimated every 6-15 min, no clear evidence was found during a period of higher solar activity in 2011. Correcting the solar radiation pressure for OSTM/Jason-2 allows to reduce the number of estimated stochastic orbit parameters considerably (even a spacing of 60 min seems to be feasible). Overall, orbits with cm accuracy were derived for GRACE, GOCE, and OSTM/Jason-2. In the performed validation steps the phase residual RMS values of  $\approx 7$  mm and SLR residual RMS values of  $\approx 2$  cm were achieved. The comparison against external orbit solutions shows RMS values for the orbit differences of 1-3 cm. For a long-term GRACE-A orbit determination (over 10 years), 3D differences with respect to a kinematic and an external solution were found to be 4.8 and 2.9 cm, respectively.

The combination of ground- and space-based GNSS observations is a key element for co-location on-board a LEO, as it allows to include GNSS ground stations into the combination. In fact, the combination of ground and LEO observations is an important and highly-relevant research topic. Basically, the procedure presented in this work is based on a combined processing of zero-difference GPS observations in a common least-squares adjustment, where station coordinates, LEO and GPS orbits, GPS clocks, ERPs, geocenter coordinates, and other parameters are estimated simultaneously. Other approaches, based mainly on the combination of normal equations, were not considered. This study was performed based on 53 well-distributed IGS stations and four LEOs (GRACE, GOCE, OSTM/Jason-2). In a first step, the geocenter estimates were assessed. It was found that OPR parameters in D- and Y-direction have to be constrained for a combined solution including LEO GPS data. The importance of non-tidal corrections was studied by applying GRACE AOD1B de-aliasing products and atmospheric non-tidal loading corrections provided by the GGOS atmosphere project at TU Vienna. Detected differences in the annual amplitude of around 0.6 mm with respect to a solution without non-tidal corrections, emphasized to use the AOD1B products to correct for atmospheric and oceanic non-tidal loading effects. Adding one LEO to the ground-only processing decreases the formal errors by around 20 %, which is eight times more than the improvement expected due to the increased number of observations. Consequently, a huge improvement and considerable potential was found by adding the LEOs to the ground network in a combined processing. However, comparing the derived geocenter time series against SLR and comparing amplitudes and phases of an annual signal against external solutions shows some serious discrepancies. The main issues are the significant phase shifts in the x- and z-component. Especially resolving the carrier phase ambiguities to integer values would improve the derived solutions. Other deficiencies, that are still present, are the comparably small number of processed GNSS ground stations and the parameterization of the solar radiation pressure for the GPS orbit determination. In a second step, GPS satellite phase centers were studied. Improvements due to the additional LEO observations were expected as their orbits are constrained by the gravitational constant and, thus, are not sensitive to the terrestrial scale. Additional benefits result from the fast changing geometry between LEO and GPS satellite, which allows it to scan the antenna pattern rather fast and to reduce correlations between horizontal offsets, orbit, and spacecraft attitude. The weekly derived offsets in z-direction agree well with the IGS offsets with a considerable benefit from the LEO-based observations (averaged improvement decreased from 3.7 to -1.2 cm). Furthermore, it turned out that due to the LEO observations introduced the no-net-scale condition became obsolete and, therefore, the derived offsets are not influenced by any scale information. Considerable improvements were found for the x- and y-offsets.

Especially, the uncertain estimation during periods of large  $\beta_0$  angles was stabilized by the LEOs. A strong reduction of the dependency of the satellite x-offset of block IIR-M and IIF on the  $\beta_0$  angle is present in the combined solution. Concerning the weekly coordinate estimates only small differences are present between a ground-only and the combined solution. The main impact is visible in the z-component, where the annual amplitude is damped in a similar way as in the case of the geocenter study. Also in the derived ERPs only small differences were detected, whereas the GPS orbits benefit from the additional LEO observations, but differ by a few cm from the reference orbits. Transformation parameters estimated in the GPS orbit comparison show smaller translations and smaller scale variations for the combined solutions. The last part of the combination study was the transition to a long-term solution including the estimation of station velocities and surface load density coefficients (the geocenter parameters were removed from the normal equations). In this solution the impact related to the additional introduced LEO observations is much smaller than in the direct geocenter estimation. The derived station velocities differ, however, by only some mm/yr from the ITRF2008 values. Geocenter coordinates derived from estimated surface load density coefficients show a good agreement in the annual amplitudes with the weekly geocenter solutions and to the values found in the literature. Also the phases in x- and z-direction agree much better to the SLR solutions. In summary, a combination of ground- and LEO-based GPS observations works at the zero-difference level quite well. A significant improvement compared to a ground-only solution was found and the potential of a combined solution was shown. Concerning future geocenter studies, (1) the modeling of the LEO orbits has to be studied, (2) the processed time span has to be extended to strengthen the estimated annual signals, and (3) SLR observations have to be incorporated into the combined solutions.

So far it is not possible to include VLBI into co-location in space, as satellites equipped with space geodetic sensors are not observable for VLBI (or no observations were reported so far). However, in recent years progress was achieved by (1) tracking GNSS L-band signals (G-VLBI) and by (2) proposing dedicated co-location satellites equipped with VLBI transmitters to the space agencies. Concerning today's possibilities, G-VLBI observations will be a great opportunity for the integration of VLBI into the co-location of geodetic observation techniques in space. The experiments performed so far are promising but need further investigations in terms of observing dual frequency, correlation, and processing. As nearly all radio telescopes used for geodetic applications, i.e., telescopes appropriate for G-VLBI observations due to the co-location perspective, have difficulties to observe both GNSS frequencies, correcting for the ionospheric delays will be crucial. Using GNSS phase observations derived from co-located GNSS receivers, the L4R method allows to compute delay corrections by considering the actual ionospheric situation. Other approaches to correct the ionospheric delays might result in a lower accuracy or enforce a different observation concept, as it was shown by theoretical comparisons. The validation of the L4R approach presented in this thesis shows good results especially for the baselines between radio telescopes, which observed already GNSS satellites. A 1 cm daily repeatability level for station coordinates could be achieved, when introducing the L4R corrections into a GNSS  $L_1$ -based coordinate estimation. Differences to ionospheric delays derived from VLBI observations show also a good agreement at the level of a few TECU. The method could not be tested against VLBI ionospheric delays for longer baselines, as the quasar and the satellite could not be observed with a reasonable time from both stations. However, for such baselines a precise point processing including ambiguity fixing might be preferable, as the double-difference approach suffers from the small number of common satellites. One way for further improvements will be the introduction of ionospheric models with higher spatial and temporal resolution. The range of L4R applications is, in principle, limited to the tracking of GNSS satellites, as the main advantage is the observation of the same L-band signal. However, in special cases the L4R method might be suitable for single-frequency astrometry. As VLBI satellite tracking is currently in an experimental stage, simulations for tracking satellites with radio telescopes were performed for eight different satellite orbit types. The simulation approach based on a Monte Carlo simulation taking zenith wet delays, receiver clock offsets, and measurement noise into account. Two networks were considered, a regional European and a globally distributed one. In a GNSS constellation tracking, station coordinate repeatabilities on the level of 0.7

and 1.2 cm were found for the regional and the global network, respectively. The recovery of zenith wet delays and receiver clock offsets was achieved at the cm level, thus, confirming the chosen parameterization. LEO tracking was simulated for a fictitious spacecraft orbiting the Earth in an altitude of 2000 km. In order to assess the impact of the inclination, orbits with  $63^\circ$ ,  $89^\circ$ , and  $107^\circ$  inclination were assumed. For the regional network, repeatabilities below 1 cm were found. Some small network effects are visible, for example, Ny Ålesund is determined somehow worse than the other stations for the satellite with an inclination of  $63^\circ$ . In the global network a large set of baselines cannot observe the spacecraft, resulting in inhomogeneous station coordinate repeatabilities. It turned out that the NNT/NNR conditions should be applied carefully only to stations with a substantial observation record. In summary, station coordinates were determined with a precision of around 1 cm for most stations with slightly better results for the spacecraft with  $107^\circ$  inclination. The additionally simulated tracking of elliptically-orbiting satellites (E-GRIP and E-GRASP/Eratosthenes) showed results worse than the results for the LEOs, as the geometry changes either too slowly (causing problems in separating troposphere, clock, and coordinates) or too rapidly (reducing the number of available observations). Stations in the regional network are determined at the 1 cm level in the E-GRASP/Eratosthenes simulation and mostly at the 2 cm level in the global network. In a further processing step also the E-GRASP orbit was estimated from the simulated observations showing RMS values between the simulation runs of a few centimeters with highest values in along-track for the regional network solution (2.61 cm). Thus, not only station coordinates but also orbits could be estimated reasonably based on simulated VLBI satellite tracking. However, the achievable accuracy level has to be proofed by real observations.

A topic (mainly) not covered by this thesis are technique-specific errors. This topic is, however, the main objective within the second phase of the project "Co-location on Ground and in Space". In recent years the geodetic observatory Wettzell became a space geodetic laboratory by comprising nowadays three radio telescopes (TWIN2 will be operational soon), two SLR stations, and several GNSS receivers. Therefore, space geodetic observations will be assessed on short baselines allowing unique insights into the space geodetic techniques as environmental influences are similar within the baselines. The receiver clock offset estimation discussed in Sect. 3.5.4 is a first step in this direction. This experiment allows to study VLBI instrumental biases usually absorbed in the clock in more detail. Further on, SLR differentiation will be studied as indicated in Sect. 3.5.1. A closer insight will be opened by analyzing dual-GNSS stations globally to assess environmental effects also in this technique.

Concerning co-location in space several action items can be defined. The most demanding topic is VLBI satellite tracking. Dedicated studies are required to define observation concepts and to assess remaining biases in the observations and during the correlation process. These investigations should be done in close collaboration between telescope operators, correlation centers, and groups specialized in the processing. A crucial role in this direction is given to the IVS working group on "Satellite Observation with VLBI". A second also demanding topic is the combination of ground- and space-based GNSS observations. Especially, studies on (1) the ambiguity fixing, (2) the impact of the force models used, and (3) on the geodetic parameters are required. Compared to VLBI tracking, these studies can be performed using existing GNSS data sets, but they will allow to prepare for the probably most challenging analysis aspect in co-location on-board a dedicated satellite. Apart from these two topics, further studies on co-location in space on-board existing satellites are helpful to assess additional challenges and to highlight the potential of combining geodetic techniques in space. The real combination, however, will be done on-board of GRASP, E-GRASP/Eratosthenes, or any other dedicated co-location satellite. From today's point of view only these satellites will allow to fully exploit the potential of co-location in space and, therefore, help to achieve the GGOS goals for a terrestrial reference frame suitable for a global society on a changing planet.

# Bibliography

- (2016). In *IAG 150 Years: Proceedings of the IAG Scientific Assembly in Postdam, Germany, 2013*, IAG Symposia (pp. 565–570). Springer International Publishing. doi:10.1007/1345\_2015\_111.
- Abshire, J. & Gardner, C. (1985). Atmospheric Refractivity Corrections in Satellite Laser Ranging. *IEEE T Geosci Remote, GE-23*(4), 414–425. doi:10.1109/TGRS.1985.289431.
- Alber, C., Ware, R., Rocken, C., & Braun, J. (2000). Obtaining single path phase delays from GPS double differences. *Geophys Res Lett*, 27, 2661–2664. doi:10.1029/2000GL011525.
- Altamimi, Z. (2005). ITRF and Co-location Sites. In B. Richter, W. Dick, & W. Schwegmann (Eds.), *Proceedings of the IERS Workshop on Co-location*: Verlag des Bundesamtes für Kartographie und Geodäsie.
- Altamimi, Z., Boucher, C., & Sillard, P. (2002a). New trends for the realization of the International Terrestrial Reference System. *Adv Space Res*, 30(2), 175–184. doi:10.1016/S0273-1177(02)00282-X.
- Altamimi, Z., Collilieux, X., Legrand, J., Garayt, B., & Boucher, C. (2007). ITRF2005: A new release of the International Terrestrial Reference Frame based on time series of station positions and Earth Orientation Parameters. *J Geophys Res*, 112(B9), B09401. doi:10.1029/2007JB004949.
- Altamimi, Z., Collilieux, X., & Métivier, L. (2011). ITRF2008: an improved solution of the international terrestrial reference frame. *J Geod*, 85(8), 457–473. doi:10.1007/s00190-011-0444-4.
- Altamimi, Z., Collilieux, X., & Métivier, L. (2013). ITRF Combination: Theoretical and Practical Considerations and Lessons from ITRF2008. In Z. Altamimi & X. Collilieux (Eds.), *Reference Frames for Applications in Geosciences*, volume 138 of *IAG Symposia* (pp. 7–12). Springer Berlin Heidelberg. doi: 10.1007/978-3-642-32998-2\_2.
- Altamimi, Z., Collilieux, X., Métivier, L., Rebischung, P., & Lercier, D. (2014). ITRF2013: preliminary analysis and early results. In *EGU General Assembly Conference Abstracts*, volume 16 (pp. 2694).
- Altamimi, Z., Rebischung, P., Métivier, L., & Collilieux, X. (2016). ITRF2014: A new release of the International Terrestrial Reference Frame modeling non-linear station motions. *J Geophys Res*, 121(8), 6109–6131. doi:10.1002/2016JB013098.
- Altamimi, Z., Sillard, P., & Boucher, C. (2002b). ITRF2000: A new release of the International Terrestrial Reference Frame for earth science applications. *J Geophys Res*, 107(B10), ETG 2–1–ETG 2–19. 2214.
- Anderson, P. (2000). GEOSAT - a computer program for precise reduction and simulation of satellite tracking data. In *Proc 4th Int. Geodetic Symposium on Satellite Positioning* (pp. 365–376). Austin.
- Angermann, D., Drewes, H., Krügel, M., Meisel, B., Gerstl, M., Kelm, R., Müller, H., Seemüller, W., & Tesmer, V. (2004). ITRS Combination Centre at DGFI - A terrestrial reference frame realization 2003. *Deutsche Geodätische Kommission, Reihe B*, 313.
- Angermann, D., Seitz, M., & Drewes, H. (2013). Global Terrestrial Reference Systems and Their Realizations. In G. Xu (Ed.), *Sciences of Geodesy - II* (pp. 97–132). Springer Berlin Heidelberg. doi:10.1007/978-3-642-28000-9\_3.
- Argus, D. F. & Heflin, M. B. (1995). Plate motion and crustal deformation estimated with geodetic data from the Global Positioning System. *Geophys Res Lett*, 22(15), 1973–1976. doi:10.1029/95GL02006.
- Arnold, D., Meindl, M., Beutler, G., Dach, R., Schaer, S., Lutz, S., Prange, L., Sošnica, K., Mervart, L., & Jäggi, A. (2015). Code's new solar radiation pressure model for gnss orbit determination. *J Geod*, 89(8), 775–791. doi:10.1007/s00190-015-0814-4.
- Auriol, A. & Tourain, C. (2010). DORIS system: The new age. *Adv Space Res*, 46(12), 1484 – 1496. doi:10.1016/j.asr.2010.05.015.
- AVISO (2015). Jason Postlaunch Satellite Characteristics for POD activities. <http://www.avisooceanobs.com/en/calval/orbit/precise-orbit-determination-verification/index.html#c6061>. online; accessed 15-July-2015.
- Bar-Sever, Y. (1996). A new model for GPS yaw attitude. *J Geod*, 70(11), 714–723. doi:10.1007/BF00867149.
- Bar-Sever, Y. E., Haines, B., Wu, S., Lemoine, F., & Willis, P. (2009). Geodetic Reference Antenna in Space (GRASP): A Mission to Enhance the Terrestrial Reference Frame. In *COSPAR colloquium: scientific and fundamental aspects of the Galileo program*. Padua, 2009.
- Bauersima, I. (1983). NAVSTAR Global Positioning System (GPS) II: Mitteilungen der Satelliten-Beobachtungsstation Zimmerwald.
- Beckley, B. D., Lemoine, F. G., Luthcke, S. B., Ray, R. D., & Zelensky, N. P. (2007). A reassessment of global and regional mean sea level trends from TOPEX and Jason-1 altimetry based on revised reference frame and orbits. *Geophys Res Lett*, 34. L14608, doi:10.1029/2007GL030002.

- Bertiger, W., Desai, S., Haines, B., Harvey, N., Moore, A., Owen, S., & Weiss, J. (2010a). Single receiver phase ambiguity resolution with GPS data. *J Geod*, 84(5), 327–337. doi:10.1007/s00190-010-0371-9.
- Bertiger, W. I., Bar-Sever, Y. E., Christensen, E. J., Davis, E. S., Guinn, J. R., Haines, B. J., Ibanez-Meier, R. W., Jee, J. R., Lichten, S. M., Melbourne, W. G., Muellerschoen, R. J., Munson, T. N., Vigue, Y., Wu, S. C., Yunck, T. P., Schutz, B. E., Abusali, P. A., Rim, H. J., Watkins, M. M., & Willis, P. (1994). GPS precise tracking of TOPEX/POSEIDON: Results and implications. *Geophy Res Lett*, 99, 24,449–24,464.
- Bertiger, W. I., Desai, S. D., Dorsey, A., Haines, B. J., Harvey, N., Kuang, D., Sibthorpe, A., & Weiss, J. P. (2010b). Sub-centimeter Precision Orbit Determination with GPS for Ocean Altimetry. *Mar Geod*, 33, 363–378. doi:10.1080/01490419.2010.487800.
- Bettadpur, S. (2012). *Product Specification Document*, 4.6 edition. ftp://podaac.jpl.nasa.gov/allData/grace/docs/ProdSpecDoc\_v4.6.pdf.
- Beutler, G. (2005a). *Methods of Celestial Mechanics I: Physical, Mathematical, and Numerical Principles*, volume 1. Springer-Verlag, Berlin. ISBN 3-540-40749-9.
- Beutler, G. (2005b). *Methods of Celestial Mechanics II: Application to Planetary System, Geodynamics and Satellite Geodesy*, volume 2. Springer-Verlag, Berlin. ISBN 3-540-40750-2.
- Beutler, G., Brockmann, E., Gurtner, W., Hugentobler, U., Mervart, L., Rothacher, M., & Verdun, A. (1994). Extended orbit modeling techniques at the CODE processing center of the international GPS service for geodynamics (IGS): theory and initial results. *Manuscr. Geod.*, 19, 367–386.
- Bevis, M., Alsdorf, D., Kendrick, E., Fortes, L. P., Forsberg, B., Smalley, R., & Becker, J. (2005). Seasonal fluctuations in the mass of the Amazon River system and Earth's elastic response. *Geophys Res Lett*, 32(16), L16308. doi:10.1029/2005GL023491.
- Bilitza, D. (2001). International Reference Ionosphere 2000. *Radio Sci*, 36(2), 261–275. doi:10.1029/2000RS002432.
- Bird, P. (2003). An updated digital model of plate boundaries. *Geochem Geophys Geosyst*, 4(3). doi:10.1029/2001GC000252.
- Blewitt, G. (2003). Self-consistency in reference frames, geocenter definition, and surface loading of the solid Earth. *J Geophys Res*, 108(B2). doi:10.1029/2002JB002082.
- Blewitt, G. (2008). Fixed point theorems of GPS carrier phase ambiguity resolution and their application to massive network processing: Ambizap. *J Geophys Res*, 113(B12), B12410. doi:10.1029/2008JB005736.
- Blewitt, G., Altamimi, Z., Davis, J., Gross, R., C.Kuo, Lemoine, F., Moore, A., Neilan, R., Plag, H. P., Rothacher, M., Shum, C., Sideris, M. G., Schöne, T., Tregoning, P., & Zerbini, S. (2010). Geodetic Observations and Global Reference Frame Contributions of Understanding Sea-level Rise and Variability. In J. A. Church, P. L. Woodworth, T. Aarup, & W. S. Wilson (Eds.), *Understanding Sea-level Rise and Variability*, volume 113: Wileys Blackwells Publishing.
- Blewitt, G. & Clarke, P. (2003). Inversion of Earth's changing shape to weigh sea level in static equilibrium with surface mass redistribution. *J Geophys Res*, 108(B6). doi:10.1029/2002JB002290.
- Blewitt, G., Lavallée, D., Clarke, P., & Nurutdinov, K. (2001). A new global mode of Earth deformation: Seasonal cycle detected. *Science*, 294(5550), 2342–2345. doi:10.1126/science.1065328.
- Bloßfeld, M., Seitz, M., & Angermann, D. (2014). Non-linear station motions in epoch and multi-year reference frames. *J Geod*, 88(1), 45–63. doi:10.1007/s00190-013-0668-6.
- Bock, H. (2003). *Efficient Methods for Determining Precise Orbits of Low Earth Orbiters Using the Global Positioning System*. Geodätisch-geophysikalische Arbeiten in der Schweiz. Schweizerische Geodätische Kommission. ISBN:978-3-908440-08-6.
- Bock, H., Jäggi, A., Beutler, G., & Meyer, U. (2014). GOCE: precise orbit determination for the entire mission. *J Geod*, 88(11), 1047–1060. doi:10.1007/s00190-014-0742-8.
- Bock, H., Jäggi, A., Dach, R., Schaer, S., & Beutler, G. (2009). GPS single-frequency orbit determination for low Earth orbiting satellites. *Adv Space Res*, 43, 783–791. doi:10.1016/j.asr.2008.12.003.
- Bock, H., Jäggi, A., Meyer, U., Dach, R., & Beutler, G. (2011a). Impact of GPS antenna phase center variations on precise orbits of the GOCE satellite. *Adv Space Res*, 47(11), 1885 – 1893. doi:10.1016/j.asr.2011.01.017.
- Bock, H., Meyer, U., Visser, P., van den Ijssel, J., van Helleputte, T., Heinze, M., & Hugentobler, U. (2011b). GPS-derived orbits for the GOCE satellite. *J Geod*, 85, 807–818. doi:10.1007/s00190-011-0484-9.
- Böhm, J., Niell, A., Tregoning, P., & Schuh, H. (2006a). Global Mapping Function (GMF): A new empirical mapping function based on numerical weather model data. *Geophys Res Lett*, 33(7), L07304. doi:10.1029/2005GL025546.
- Böhm, J. & Schuh, H., Eds. (2013). *Atmospheric Effects in Space Geodesy*. Springer Verlag. ISBN:978-3-642-36931-5.
- Böhm, J., Werl, B., & Schuh, H. (2006b). Troposphere mapping functions for GPS and VLBI from European Centre for medium-range weather forecasts operational analysis data. *J Geophys Res*, 111(B2), B02406. doi:10.1029/2005JB003629.
- Böhm, J., Wresnik, J., & Pany, A. (2006c). Simulation of wet zenith delays and clocks. IVS Memorandum 2006-013v03.
- Border, J. S. (2009). Innovations in delta differential one-way range: from Viking to Mars Science Laboratory. *Proc. 21st Int. Sym. Space Flight Dynamics, Toulouse, France*, 28.
- Boucher, C. (2000). Terrestrial coordinate systems and frames. In P. Murdin (Ed.), *Encyclopedia of Astronomy and Astro-*

- physics*, volume 1 (pp. 1906). doi:10.1888/0333750888/1906.
- Boucher, C. & Altamimi, Z. (1985). Towards an Improved Realization of the BIH Terrestrial Frame. In I. I. Mueller (Ed.), *The MERIT/COTES report on earth rotation and reference frame* (pp. 551). OSU/DGS, Columbus.
- Boucher, C. & Altamimi, Z. (1989). *ITRF89 and other realizations of the terrestrial reference system for 1989, IERS tech.* Technical report, note 6, Int. Earth Rotation Serv., Observatoire de Paris.
- Boucher, C. & Altamimi, Z. (1991a). IERS TECHNICAL NOTE 6.
- Boucher, C. & Altamimi, Z. (1991b). ITRF90 and other realizations of the IERS Terrestrial Reference System for 1990. *IERS Technical Note*, 9, 1–143.
- Boucher, C., Altamimi, Z., & Duhem, L. (1992). ITRF91 and its associated velocity field. *IERS Technical Note*, 12, 1–142.
- Boucher, C., Altamimi, Z., & Duhem, L. (1993). ITRF 92 and its associated velocity field. *IERS Technical Note*, 15, 1–164.
- Boucher, C., Altamimi, Z., & Duhem, L. (1994). Results and analysis of the ITRF93. *IERS Technical Note*, 18, 1–313.
- Boucher, C., Altamimi, Z., Feissel, M., & Sillard, P. (1996). Results and analysis of the ITRF94. *IERS technical note*, 20, 1.
- Boucher, C., Altamimi, Z., & Sillard, P. (1999). The International Terrestrial Reference Frame (ITRF97). *IERS Technical Note*, 27, 1–191.
- Bouillé, F., Cazenave, A., Lemoine, J. M., & Crétaux, J. F. (2000). Geocentre motion from the DORIS space system and laser data to the Lageos satellites: comparison with surface loading data. *Geophys J Int*, 143(1), 71–82. doi:10.1046/j.1365-246x.2000.00196.x.
- Bowman, B. R., Tobiska, W. K., Marcos, F. A., Huang, C. Y., Lin, C. S., & Burke, W. J. (2008). A new empirical thermospheric density model JB2008 using new solar and geomagnetic indices. In *AIAA/AAS Astrodynamics Specialist Conference and Exhibit, Honolulu, Hawaii*.
- Brief, K., Kornemann, G., & Wickert, J. (2009). MicroGEM: Microsatellites for GNSS Earth Monitoring, Abschlussbericht Phase 0/A.
- Brockmann, E. (1997). *Combination of solutions for geodetic and geodynamical applications of the Global Positioning System (GPS)*. Geodätisch-geophysikalische Arbeiten in der Schweiz. Schweizerische Geodätische Kommission.
- Buhl, M., Segert, T., Wickert, J., & Rothacher, M. (2012). Machbarkeitsuntersuchung Nano-X, Abschlussbericht Phase 0, GFZ-TN03.
- Burke, B. (1991). Introduction to orbiting VLBI. *Adv Space Res*, 11(2), 349 – 353. doi:10.1016/0273-1177(91)90516-M.
- Cerri, L., Berthias, J. P., Bertiger, W. I., Haines, B. J., Lemoine, F. G., Mercier, F., Reis, J. C., Willis, P., Zelensky, N. P., & Ziebart, M. (2010). Precise Orbit Determination Standards for the Jason Series of Altimeter Missions. *Mar Geod*, 33, 379–418. doi:10.1080/01499419.2010.488966.
- Cerri, L. & Ferrage, P. (2015). *DORIS satellites models implemented in POE processing*. ftp://ftp.ids-doris.org/pub/ids/satellites/DORISatelliteModels.pdf.
- Chen, G. & Herring, T. (1997). Effects of atmospheric azimuthal asymmetry on the analysis of space geodetic data. *J Geophys Res*, 102(B9), 20489–20502. doi:10.1029/97JB01739.
- Chen, J., Wilson, C., Eanes, R., & Nerem, R. (1999). Geophysical interpretation of observed geocenter variations. *Geophys Res Lett*, 104(B2), 2683–2690. doi:10.1029/1998JB900019.
- Chen, J. L., Wilson, C. R., & Seo, K.-W. (2009). S2 tide aliasing in GRACE time-variable gravity solutions. *J Geod*, 83(7), 679–687. doi:10.1007/s00190-008-0282-1.
- Cheng, M., Ries, J., & Tapley, B. (2013). Geocenter variations from analysis of SLR data. In Z. Altamimi & X. Collilieux (Eds.), *Reference Frames for Applications in Geosciences*, volume 138 of *IAG Symposia* (pp. 19–25).: Springer. doi:10.1007/978-3-642-32998-2\_4.
- Choi, K.-R., Ries, J. C., & Tapley, B. D. (2004). Jason-1 Precision Orbit Determination by combining SLR and DORIS with GPS tracking data. *Mar Geod*, 27, 319–331.
- Collilieux, X., Altamimi, Z., Coulot, D., van Dam, T., & Ray, J. (2010). Impact of loading effects on determination of the international terrestrial reference frame. *Adv Space Res*, 45(1), 144 – 154. doi:10.1016/j.asr.2009.08.024.
- Combrinck, L. (2010). Satellite Laser Ranging. In G. Xu (Ed.), *Sciences of Geodesy - I* (pp. 301–338). Springer Berlin Heidelberg. doi:10.1007/978-3-642-11741-1\_9.
- Corey, B. (2001). IVS/IGS/ILRS Working Group on GPS Phase Center Mapping. In N. R. Vandenberg & K. D. Baver (Eds.), *International VLBI Service for Geodesy and Astrometry 2000 Annual Report* (pp. 13). NASA/TP-2001-209979.
- Couhert, A., Cerri, L., Legeais, J.-F., Ablain, M., Zelensky, N. P., Haines, B. J., Lemoine, F. G., Bertiger, W. I., Desai, S. D., & Otten, M. (2015). Towards the 1 mm/y stability of the radial orbit error at regional scales. *Adv Space Res*, 55(1), 2 – 23. 10.1016/j.asr.2014.06.041.
- Coulot, D., Berio, P., Biancale, R., Loyer, S., Soudarin, L., & Gontier, A.-M. (2007). Toward a direct combination of space-geodetic techniques at the measurement level: Methodology and main issues. *Geophys Res Lett*, 112(B5). doi:10.1029/2006JB004336.

- Crétaux, J.-F., Soudarin, L., Davidson, F. J., Gennero, M.-C., Bergé-Nguyen, M., & Cazenave, A. (2002). Seasonal and interannual geocenter motion from SLR and DORIS measurements: Comparison with surface loading data. *Geophys Res Lett*, 107(B12), ETG-16. doi:10.1029/2002JB001820.
- Crocetto, N., Pingue, F., Ponte, S., Pugliano, G., & Sepe, V. (2008). Ionospheric error analysis in GPS measurements. *Ann Geophys*, 51(4), 585–595. doi:10.4401/ag-4456.
- Dach, R., Fridez, P., Hugentobler, U., & Meindl, M. (2007). *Bernese GPS Software 5.0*. Bern.
- Dach, R., Lutz, S., Walser, P., & Fridez, P. (2015). *Bernese GNSS Software Version 5.2*. Bern. doi:10.7892/boris.72297.
- Degnan, J. J. (1993). *Millimeter Accuracy Satellite Laser Ranging: a Review*, (pp. 133–162). American Geophysical Union. doi:10.1029/GD025p0133.
- DeMets, C., Gordon, R. G., Argus, D. F., & Stein, S. (1990). Current plate motions. *Geophys J Int*, 101(2), 425–478. doi:10.1111/j.1365-246X.1990.tb06579.x.
- Desai, S. D. (2002). Observing the pole tide with satellite altimetry. *J Geophys Res*, 107(C11), 7–1–7–13. doi:10.1029/2001JC001224.
- Detmering, D., Schmidt, M., Heinkelmann, R., & Seitz, M. (2011). Combination of different space-geodetic observations for regional ionosphere modeling. *J Geod*, 85(12), 989–998. doi:10.1007/s00190-010-0423-1.
- Dickey, J. M. (2010). How and Why to do VLBI on GPS. *International VLBI Service for Geodesy and Astrometry 2010 General Meeting Proceedings*.
- Dickey, J. O., Bender, P., Faller, J., Newhall, X., Ricklefs, R., Ries, J., Shelus, P., Veillet, C., Whipple, A., Wiant, J., et al. (1994). Lunar laser ranging: A continuing legacy of the Apollo program. *Science*, 265(5171), 482–490. doi:10.1126/science.265.5171.482.
- Dietrich, R., Ivins, E., Casassa, G., Lange, H., Wendt, J., & Fritsche, M. (2010). Rapid crustal uplift in Patagonia due to enhanced ice loss. *Earth Planet Sc Lett*, 289(1), 22 – 29. doi:10.1016/j.epsl.2009.10.021.
- Dietrich, R., Rülke, A., & Scheinert, M. (2005). Present-day vertical crustal deformations in West Greenland from repeated GPS observations. *Geophys J Int*, 163, 865–874. doi:10.1111/j.1365-246X.2005.02766.x.
- Dilckner, F. (2010). GPS IIF-1 satellite antenna phase center and attitude modeling. *Inside GNSS*, 5(6), 59–64.
- Dilckner, F., Otten, M., Springer, T., Flohrer, C., Svehla, D., & Zandbergen, R. (2011). GPS satellite antenna parameters from combined ground-based and space-born data processing. [http://acc.igs.org/antennas/sat-ant-space+grnd\\_egu11.pdf](http://acc.igs.org/antennas/sat-ant-space+grnd_egu11.pdf).
- Dilckner, F., Seeber, G., Schmitz, M., Wübbena, G., Toso, G., & Maeusli, D. (2006). Characterisation of GOCE SSTI antennas. *ZfV*, 131, 61–71.
- Dong, D., Dickey, J., Chao, Y., & Cheng, M. (1997). Geocenter variations caused by atmosphere, ocean and surface ground water. *Geophys Res Lett*, 24(15), 1867–1870. doi:10.1029/97GL01849.
- Dong, D., Yunck, T., & Heflin, M. (2003). Origin of the International Terrestrial Reference Frame. *J Geophys Res*, 108(B4). doi:10.1029/2002JB002035.
- Drewes, H. (2009a). Reference systems, reference frames, and the geodetic datum. In M. Sideris (Ed.), *Observing our Changing Earth*, volume 133 of *IAG Symposia* (pp. 3–9). Springer Berlin Heidelberg. doi:10.1007/978-3-540-85426-5\_1.
- Drewes, H. (2009b). The Actual Plate Kinematic and Crustal Deformation Model APKIM20005 as basis for non-rotating ITRF. In H. Drewes (Ed.), *Geodetic Reference Frames*, IAG Symposia (pp. 95–99).: Wileys Blackwells Publishing.
- Drewes, H., Angermann, D., & Seitz, M. (2013). Alternative Definitions of the Terrestrial Reference System and Its Realization in Reference Frames. In Z. Altamimi & X. Collilieux (Eds.), *Reference Frames for Applications in Geosciences*, volume 138 of *IAG Symposia* (pp. 39–44). Springer Berlin Heidelberg. doi:10.1007/978-3-642-32998-2\_7.
- Duev, D. A., Calvés, G. M., Pogrebenko, S. V., Gurvits, L. I., Cimo, G., & Bahamon, T. B. (2012). Spacecraft VLBI and Doppler tracking: algorithms and implementation. *Astro Astrophys*, 541, A43. doi:10.1051/0004-6361/201218885.
- Dunn, C., Bertiger, W., Bar-Sever, Y., Desai, S., Haines, B., Kuang, D., Franklin, G., Harris, I., Kruizinga, G., Meehan, T., et al. (2003). Instrument of Grace-GPS Augments Gravity Measurements. *GPS World*, 14(2), 16–29.
- Eanes, R., Kar, S., Bettadapur, S., & Watkins, M. (1997). Low-frequency geocenter motion determined from SLR tracking. *Eos Trans. AGU*, 78, 46.
- Eanes, R., Nerem, R., Abusali, P., Bamford, W., Key, K., Ries, J., & Schutz, B. (2000). Glonass orbit determination at the Center for Space Research. In *Proceedings of the International GLONASS Experiment (IGEX-98) Workshop, IGS, Jet Propulsion Laboratory*.
- Espinosa, M. M. & Haas, R. (2007). SATTRACK A satellite tracking module for the VLBI Field System. In *Proc. 18th European VLBI for Geodesy and Astrometry Working Meeting* (pp. 53–58).: Wileys Blackwells Publishing.
- Farrell, W. (1972). Deformation of the Earth by surface loads. *Rev Geophys*, 10(3), 761–797. doi:10.1029/RG010i003p00761.
- Feissel, M. & Mignard, F. (1998). The adoption of ICRS on 1 January 1998: meaning and consequences. *Astro Astrophys*, 331, L33–L36.
- Feltens, J. (1991). *Nicht-gravitative Störeinflüsse bei der Modellierung von GPS-Erdumlaufbahnen*. Dissertation, Bayerische

- Akademie der Wissenschaften. Reihe C 371, Deutsche Geodätische Kommission.
- Fliegel, H. F. & Gallini, T. E. (1996). Solar force modeling of block IIR global positioning system satellites. *J Spacecraft Rockets*, 33(6), 863–866. doi:10.2514/3.26851.
- Fliegel, H. F., Gallini, T. E., & Swift, E. R. (1992). Global Positioning System Radiation Force Model for geodetic applications. *J Geophys Res*, 97(B1), 559–568. doi:10.1029/91JB02564.
- Floberghagen, R., Fehring, M., Lamarre, D., Muzi, D., Frommknecht, B., Steiger, C., Piñeiro, J., & Da Costa, A. (2011). Mission design, operation and exploitation of the gravity field and steady-state ocean circulation explorer mission. *J Geod*, 85(11), 749–758. doi:10.1007/s00190-011-0498-3.
- Flohrer, C. (2008). *Mutual Validation of Satellite-geodetic Techniques and Its Impact on GNSS Orbit Modeling*. Geodätisch-geophysikalische Arbeiten in der Schweiz. Schweizerische Geodätische Kommission. ISBN:978-3-908440-19-2.
- Flohrer, C., Otten, M., Springer, T., & Dow, J. (2011). Generating precise and homogeneous orbits for Jason-1 and Jason-2. *Adv Space Res*, 48, 152–172. doi:10.1016/j.asr.2011.02.017.
- Förste, C., Flechtner, F., Schmidt, R., Stubenvoll, R., Rothacher, M., Kusche, J., Neumayer, H., Biancale, R., Lemoine, J., Barthelmes, F., et al. (2008). EIGEN-GL05C-A new global combined high-resolution GRACE-based gravity field model of the GFZ-GRGS cooperation. In *Geophys Res Abstr*, volume 10 (pp. EGU2008–A).
- Fricke, W. (1982). Determination of the Equinox and Equator of the FK5. *Astronomy and Astrophysics*, 107, L13–L16.
- Fritsche, M. (2013). *Erweiterte Modellbildung zur Bestimmung von Positionszeitreihen global verteilter GPS-Stationen*. Dissertation, Technische Universität Dresden, Dresden.
- Fritsche, M., Dietrich, R., Knöfel, C., Rülke, A., Vey, S., Rothacher, M., & Steigenberger, P. (2005). Impact of higher-order ionospheric terms on GPS estimates. *Geophys Res Lett*, 32. doi: 10.1029/2005GL024342.
- Fritsche, M., Dietrich, R., Rülke, A., Rothacher, M., & Steigenberger, P. (2010). Low-degree earth deformation from reprocessed GPS observations. *GPS solut*, 14(2), 165–175. doi:10.1007/s10291-009-0130-7.
- Fritsche, M., Soñnica, K., Rodríguez-Solano, C. J., Steigenberger, P., Wang, K., Dietrich, R., Dach, R., Hugentobler, U., & Rothacher, M. (2014). Homogeneous reprocessing of GPS, GLONASS and SLR observations. *J Geod*, 88(7), 625–642. doi:10.1007/s00190-014-0710-3.
- Frommknecht, B. (2008). *Integrated sensor analysis of the GRACE mission*. Dissertation, Fakultät für Bauingenieur- und Vermessungswesen, TU München.
- Fukushima, T. (1994). Lunar VLBI observation model. *Astron Astrophys*, 291, 320–323.
- Gambis, D., Biancale, R., Carlucci, T., Lemoine, J., Marty, J., Bourda, G., Charlot, P., Loyer, S., Lalanne, T., Soudarin, L., & Deleflie, F. (2009). Combination of Earth Orientation Parameters and Terrestrial Frame at the Observation Level. In H. Drewes (Ed.), *Geodetic Reference Frames: IAG Symposium Munich, Germany, 9-14 October 2006* (pp. 3–9). Berlin, Heidelberg: Springer. doi:10.1007/978-3-642-00860-3\_1.
- Gambis, D., Richard, J. Y., Biancale, R., & Bizouard, C. (2013). Why Combining at the Observation Level? In Z. Altamimi & X. Collilieux (Eds.), *Reference Frames for Applications in Geosciences* (pp. 111–117). Berlin, Heidelberg: Springer. doi:10.1007/978-3-642-32998-2\_18.
- Garcia, M. & Montenbruck, O. (2007). *TerraSAR-X/TanDEM-X GPS Antenna Phase Center Analysis and Results*. Space Flight Technology, German Space Operations Center, TN 07-03.
- Ge, M., Gendt, G., Dick, G., Zhang, F. P., & Reigber, C. (2005). Impact of GPS satellite antenna offsets on scale changes in global network solutions. *Geophys Res Lett*, 32(6), L06310. doi:10.1029/2004GL022224.
- Ge, M., Gendt, G., Rothacher, M., Shi, C., & Liu, J. (2008). Resolution of GPS carrierphase ambiguities in Precise Point Positioning (PPP) with daily observations. *J Geod*, 82(7), 389–399. doi:10.1007/s00190-007-0187-4.
- Ghasemi, A., Abedi, A., & Ghasemi, F. (2012). *Propagation Engineering in Wireless Communication*. Springer-Verlag New York. doi:10.1007/978-1-4614-1077-5.
- Ghisi, C. E., Steiger, C., Romanazzo, M., & Emanuelli, P. P. (2014). Drag-Free Attitude and Orbit Control System Performance of ESA's GOCE Mission during Low Orbit Operations and De-orbiting. In *SpaceOps Conferences, (AIAA 2014-1906)* Pasadena, CA. doi:10.2514/6.2014-1906.
- Glaser, S. (2014). *Zur Optimierung der Kombinationsstrategie verschiedener Satellitenbeobachtungsverfahren bei der Realisierung eines globalen terrestrischen Referenzsystems*. Dissertation, Technische Universität Dresden, Dresden.
- Glaser, S., Fritsche, M., Soñnica, K., Rodríguez-Solano, C., Wang, K., Dach, R., Hugentobler, U., Rothacher, M., & Dietrich, R. (2015). A consistent combination of GNSS and SLR with minimum constraints. *J Geod*, (pp. 1–16). doi:10.1007/s00190-015-0842-0.
- Goetz, C., Buscaglione, F., & Francis, R. (2007). *CryoSat-2 Precise Orbit Context*. ftp://ftp.ids.doris.org/pub/ids/satellites/CryoSat-2\_Precise\_Orbit\_Context.pdf.
- Gordon, D. (2010). Use of GPS TEC Maps for Calibrating Single Band VLBI Sessions. In D. Behrend & K. Baver (Eds.), *International VLBI Service for Geodesy and Astrometry 2010 General Meeting Proceedings* (pp. 242–246).
- Greff-Lefftz, M. (2000). Secular variation of the geocenter. *Geophys Res Lett*, 105(B11), 25685–25692. doi:10.1029/2000JB900224.

- Haas, R. (1996). *Untersuchungen zu Erddeformationsmodellen für die Auswertung von geodätischen VLBI-Messungen*. Dissertation, Frankfurt am Main. Reihe C 466, Deutsche Geodätische Kommission.
- Haas, R., Hobiger, T., Hellerschmied, A., Neidhardt, A., & Kodet, J. (2015). GLONASS-VLBI: Onsala-Wetzell test observations. In R. Haas & F. Colomer (Eds.), *Proceedings of the 22nd European VLBI Group for Geodesy and Astrometry Working Meeting* (pp. 107–111).
- Haas, R., Neidhardt, A., Kodet, J., Plötz, C., Schreiber, U., Kronschnabl, G., Pogrobenko, S., Duev, D., Casey, S., Martl-Vidal, I., Yang, J., & Plank, L. (2014). The Wetzell-Onsala G130128 Experiment - VLBI observation of a GLONASS satellite. In D. Behrend, K. Baver, & K. Armstrong (Eds.), *IVS 2014 General Meeting Proceedings*: Science Press.
- Haas, R. & Scherneck, H.-G. (1999). The effect of ocean tide loading on the determination of earth rotation parameters. In W. Schlüter & H. Hase (Eds.), *European VLBI for Geodesy and Astrometry* (pp. 178–185).
- Haines, B., Bar-Sever, Y., Bertiger, W., Desai, S., & Willis, P. (2004). One-Centimeter Orbit Determination for Jason-1: New GPS-Based Strategies. *Mar Geod*, 27(1-2), 299–318. doi:10.1080/01490410490465300.
- Haines, B. J., Bar-Sever, Y. E., Bertiger, W. I., Desai, S. D., Harvey, N., Sibois, A. E., & Weiss, J. P. (2015). Realizing a Terrestrial Reference Frame Using the Global Positioning System. *Geophys Res Lett*. doi:10.1002/2015JB012225.
- Hase, H. (1999). Phase center determinations at GPS-satellites with VLBI. In W. Schlüter (Ed.), *Proc. of the 13th Working Meeting on European VLBI for Geodesy and Astrometry*: Wileys Blackwells Publishing.
- Hase, H., Behrend, D., Nothnagel, A., & Schuh, H. (2015). Options for VGOS observation and analysis for 2020. In *EVGA Working Meeting* Ponta Delgada, May 2015.
- Hawarey, M., Hobiger, T., & Schuh, H. (2005). Effects of the 2nd order ionospheric terms on VLBI measurements. *Geophys Res Lett*, 32, L11304. doi: 10.1029/2005GL022729.
- Hedin, A. E. (1987). MSIS-86 thermospheric model. *Geophys Res Lett : Space Physics (1978–2012)*, 92(A5), 4649–4662.
- Heflin, M., Argus, D., Jefferson, D., Webb, F., & Zumberge, J. (2002). Comparison of a GPS-defined global reference frame with ITRF2000. *GPS Solut*, 6(1), 72–75. doi:10.1007/s10291-002-0015-5.
- Heflin, M., Bertiger, W., Blewitt, G., Freedman, A., Hurst, K., Lichten, S., Lindqwister, U., Vigue, Y., Webb, F., Yunck, T., et al. (1992). Global geodesy using GPS without fiducial sites. *Geophys Res Lett*, 19(2), 131–134. doi:10.1029/91GL02933.
- Hellerschmied, A., Böhm, J., Kwak, Y., McCallum, J., & Plank, L. (2016). *VLBI observations of GNSS signals on the baseline Hobart-Ceduna - First results*.
- Hellerschmied, A., Böhm, J., Neidhardt, A., Kodet, J., Haas, R., & Plank, L. (2015). Scheduling VLBI Observations to Satellites with VieVS. doi:10.1007/1345\_2015\_183.
- Hellerschmied, A., Plank, L., Neidhardt, A., Haas, R., Plötz, C., & Kodet, J. (2014). Observing satellites with VLBI radio telescopes - practical realization at Wetzell. In D. Behrend, K. Baver, & K. Armstrong (Eds.), *IVS 2014 General Meeting Proceedings*: Science Press.
- Herman, J., Presti, D., Codazzi, A., & Belle, C. (2004). Attitude Control for GRACE. In *18th International Symposium on Space Flight Dynamics*, volume 548 of *ESA Special Publication* (pp.27).
- Hernández-Pajares, M., Juan, J. M., Sanz, J., Aragón-Ángel, À., García-Rigo, A., Salazar, D., & Escudero, M. (2011). The ionosphere: effects, GPS modeling and the benefits for space geodetic techniques. *J Geod*, 85(12), 887–907. doi:10.1007/s00190-011-0508-5.
- Hernández-Pajares, M., Juan, J. M., Sanz, J., Orús, R., García-Rigo, A., Feltens, J., Komjathy, A., Schaer, S., & Krankowski, A. (2009). The IGS VTEC maps: a reliable source of ionospheric information since 1998. *J Geod*, 83(3-4), 263–275. doi:10.1007/s00190-008-0266-1.
- Herring, T. A., Davis, J. L., & Shapiro, I. I. (1990). Geodesy by radio interferometry: The application of Kalman Filtering to the analysis of very long baseline interferometry data. *J Geophys Res: Solid Earth*, 95(B8), 12561–12581. doi:10.1029/JB095iB08p12561.
- Heuberger, H. (1984). Performance of the GPS package on Landsat-5. In *PLANS '84 - Position Location and Navigation Symposium*.
- Hobiger, T. (2006). *VLBI as a tool to probe the ionosphere*. Dissertation, Institute of Geodesy and Geophysics, TU Vienna.
- Hobiger, T., Gotoh, T., Otsubo, T., Kubooka, T., Sekido, M., Takiguchi, H., & Takeuchi, H. (2010). c5++-Multi-technique analysis software for next generation geodetic instruments. In *IVS 2010 General Meeting Proceedings* (pp. 212–216).
- Hobiger, T. & Haas, R. (2015). CONT14 as a testbed for the combination VLBI and GPS data on the observation level. In *EVGA Working Meeting* Ponta Delgada, May 2015.
- Hobiger, T. & Otsubo, T. (2014). Combination of GPS and VLBI on the observation level during CONT11 common parameters, ties and inter-technique biases. *J Geod*, 88(11), 1017–1028. doi:10.1007/s00190-014-0740-x.
- Hofmann-Wellenhof, B., Lichtenegger, H., & Wasle, E. (2008). *GNSS - Global Navigation Satellite Systems*. Springer. ISBN:9783211730126.
- Huang, Y., Hu, X., Zhang, X., Jiang, D., Guo, R., Wang, H., & Shi, S. (2011). Improvement of orbit determination for geostationary satellites with VLBI tracking. *Chinese Sci Bull*, 56(26), 2765–2772. doi:10.1007/s11434-011-4647-0.

- Hugentobler, U., Ineichen, D., & Beutler, G. (2003). GPS satellites: Radiation pressure, attitude and resonance. *Adv Space Res*, 31(8), 1917 – 1926. doi:10.1016/S0273-1177(03)00174-1.
- Hugentobler, U., Jäggi, A., Schaer, S., & Beutler, G. (2005). Combined processing of GPS data from Ground Station and LEO Receivers in a global solution. In F. Sansó (Ed.), *A Window on the Future of Geodesy* (pp. 169–174). Springer. doi:10.1007/3-540-27432-4\_30.
- IGS (2015). IGS Products. <http://igs.org/products>. online; accessed 16-October-2015.
- ITRF (2016). ITRF2014 Solution. [http://itrf.ign.fr/ITRF\\_solutions/2014/](http://itrf.ign.fr/ITRF_solutions/2014/). online; accessed 22-January-2016.
- Ivanov, A. B., Masson, L. A., Rossi, S., Belloni, F., Wiesendanger, R., Gass, V., Rothacher, M., Hollenstein, C., Männel, B., Fleischmann, P., Mathis, H., Klaper, M., Joss, M., & Styger, E. (2014). CubETH: low cost GNSS space experiment for precise orbit determination. In *Small Satellites Systems and Services Symposium* Porto Petro: CNES & ESA.
- Jäggi, A. (2007). *Pseudo-Stochastic Orbit Modeling of Low Earth Satellites Using the Global Positioning System*. Geodätisch-geophysikalische Arbeiten in der Schweiz. Schweizerische Geodätische Kommission. ISBN:978-3-908440-17-8.
- Jäggi, A., Dach, R., Montenbruck, O., Bock, H., & Beutler, G. (2009). Phase center modeling LEO GPS receiver antennas and its impact on precise orbit determination. *J Geod*, 83(12), 1145–1162. doi:10.1007/s00190-009-0333-2.
- Jäggi, A., Hugentobler, U., & Beutler, G. (2006). Pseudo-stochastic orbit modeling techniques for low-Earth orbiters. *J Geod*, 80(1), 47–60. doi:10.1007/s00190-006-0029-9.
- Jäggi, A., Hugentobler, U., Bock, H., & Beutler, G. (2007). Precise orbit determination for {GRACE} using undifferenced or doubly differenced {GPS} data. *Adv Space Res*, 39(10), 1612 – 1619. doi:10.1016/j.asr.2007.03.012.
- James, T. S. & Ivins, E. R. (1998). Predictions of Antarctic crustal motions driven by present-day ice sheet evolution and by isostatic memory. *J Geophys Res*, 103(B3), 4993–5017. doi:10.1029/98JB03539.
- Jetzer, P., Angéilil, R., Bondarescu, R., Droz, F., Lecomte, S., Männel, B., Meindl, M., Rochat, P., Rothacher, M., Saha, P., Schfer, A., Wang, K., & Wang, Q. (2015). Einstein Gravitational Red-shift Probe, Final Report.
- Kahr, E., O’Keefe, K. P. G., & Skone, S. (2013). Design and Operation of the GPS Receiver Onboard the CanX-2 Nanosatellite. *J Inst Navig*, 60.
- Kang, Z., Tapley, B., Bettadpur, S., Ries, J., Nagel, P., & Pastor, R. (2006). Precise orbit determination for the GRACE mission using only GPS data. *J Geod*, 80(6), 322–331. doi:10.1007/s00190-006-0073-5.
- Kang, Z., Tapley, B., Chen, J., Ries, J., & Bettadpur, S. (2009). Geocenter variations derived from GPS tracking of the GRACE satellites. *J Geod*, 83(10), 895–901. doi:10.1007/s00190-009-0307-4.
- Kar, S. (1997). *Long-period variations in the geocenter observed from laser tracking of multiple Earth satellites*. PhD thesis, Center for Space Research, The University of Texas at Austin. CSR report CSR-97-2.
- Kardashev, N., Khartov, V., Abramov, V., Avdeev, V., Alakoz, A., Aleksandrov, Y., & Ananthakrishnan, S. e. a. (2013). RadioAstron-A telescope with a size of 300 000 km: Main parameters and first observational results. *Astron Rep*, 57(3), 153–194. doi:10.1134/S1063772913030025.
- Kedar, S., Hajj, G. A., Wilson, D. B., & Heflin, M. B. (2003). The effect of the second order GPS ionospheric correction of receiver positions. *Geophys Res Lett*, 30(16), 1829. doi:10.1029/2003GL017639.
- Kikuchi, F., Liu, Q., Hanada, H., Kawano, N., Matsumoto, K., Iwata, T., Goossens, S., Asari, K., Ishihara, Y., Tsuruta, S.-i., et al. (2009). Picosecond accuracy VLBI of the two subsatellites of SELENE (KAGUYA) using multifrequency and same beam methods. *Radio Science*, 44(2). doi: 10.1029/2008RS003997.
- Kikuchi, F., Liu, Q., Matsumoto, K., Hanada, H., & Kawano, N. (2008). Simulation analysis of differential phase delay estimation by same beam vlbi method. *Earth, planets and space*, 60(4), 391–406. doi:10.1186/BF03352804.
- Klemann, V. & Martinec, Z. (2011). Contribution of glacial-isostatic adjustment to the geocenter motion. *Tectonophysics*, 511(3), 99–108. doi:10.1016/j.tecto.2009.08.031.
- Klioner, S. A. (1991). General Relativistic Model of VLBI Observables. In *Proceedings of the AGU Chapman Conference on Geodetic VLBI Monitoring Global Change* (pp. 188–202). NOAA Technical Report NOS 137 NGS 49.
- Klobuchar, J. (1987). Ionospheric Time-Delay Algorithm for Single-Frequency GPS Users. *IEEE T AERO ELEC SYS*, AES-23(3), 325–331. doi:10.1109/TAES.1987.310829.
- Klobuchar, J. (1996). Ionospheric effects on GPS. *Global Positioning System: Theory and applications.*, 1, 485–515.
- Knocke, P., Ries, J., & Tapley, B. (1988). Earth radiation pressure effects on satellites. In *Proceedings of AIAA/AAS Astrodynamics Conference* (pp. 577–587). doi:10.2514/6.1988-4292.
- Koch, K. H. (2004). *Parameterschätzung und Hypothesentests*. Ferd. Dümmlers Verlag, Bonn, 4 edition.
- Kodet, J., Schreiber, U., Panek, P., Prochazka, I., Männel, B., & Schüler, T. (2016). Optical two-way timing system for space geodesy applications. In *2016 European Frequency and Time Forum (EFTF)* (pp. 1–6). doi:10.1109/EFTF.2016.7477788.
- Kodet, J., Schreiber, U., Plötz, Neidhardt, A., Kronschnabl, G., Haas, R., Calvès, G. M., Pogrebenko, S., Rothacher, M., Männel, B., Plank, L., & Hellerschmied, A. (2014). Co-locations of Space Geodetic Techniques on Ground and in Space. In D. Behrend, K. Baver, & K. Armstrong (Eds.), *IVS 2014 General Meeting Proceedings*: Science Press.

- König, D., König, R., & Panafidina, N. (2007). Combination of Ground Observations and LEO Data. In *Observation of the System Earth from Space*. Bavarian Academy of Sciences and Humanities.
- König, R., Dahle, C., Vei, M., & Neumayer, K.-H. (2015). A Geocenter Time Series from a Combination of LAGEOS and GRACE Observations. IAG Symposia (pp. 1–6): Springer Berlin Heidelberg. doi:10.1007/1345\_2015\_24.
- Kouba, J. (2009). *GPS Precise Point Positioning using IGS Orbit Products*.
- Kovalevsky, J., Mueller, I. I., & Kolaczek, B. (1989). Reference frames in astronomy and geophysics. In *Reference frames*, volume 154.
- Kreemer, C., Blewitt, G., Hammond, W. C., & Plag, H.-P. (2006). Global deformation from the great 2004 Sumatra-Andaman Earthquake observed by GPS: Implications for rupture process and global reference frame. *Earth, Planets and Space*, 58(2), 141–148. doi:10.1186/BF03353370.
- Krügel, M. & Angermann, D. (2007). Frontiers in the combination of space geodetic techniques. In *Dynamic Planet* (pp. 158–165): Springer. doi:10.1007/978-3-540-49350-1\_25.
- Krügel, M., Thaller, D., Tesmer, V., Rothacher, M., Angermann, D., & Schmid, R. (2007). Tropospheric parameters: combination studies based on homogeneous VLBI and GPS data. *J Geod*, 81(6-8), 515–527. doi:10.1007/s00190-006-0127-8.
- Kuang, D., Bar-Sever, Y., & Haines, B. (2015). Analysis of orbital configurations for geocenter determination with GPS and low-Earth orbiters. *J Geod*, 89(5), 471–481. doi:10.1007/s00190-015-0792-6.
- Kusche, J. & Schrama, E. (2005). Surface mass redistribution inversion from global GPS deformation and Gravity Recovery and Climate Experiment (GRACE) gravity data. *Geophys Res Lett*, 110(B9). doi:10.1029/2004JB003556.
- Lambeck, K. (1988). *Geophysical Geodesy*. Clarendon Oxford.
- Lambeck, K., Smither, C., & Johnston, P. (1998). Sea-level change, glacial rebound and mantle viscosity for northern Europe. *Geophys J Int*, 134(1), 102–144. doi: 10.1046/j.1365-246x.1998.00541.x.
- Lambin, J., Morrow, R., Fu, L.-L., Willis, J. K., Bonekamp, H., Lillibridge, J., Perbos, J., Zaouche, G., Vaze, P., Bannoura, W., et al. (2010). The OSTM/Jason-2 mission. *Mar Geod*, 33(S1), 4–25. doi:10.1080/01490419.2010.491030.
- Lanyi, G., Bagri, D., & Border, J. (2007). Angular Position Determination of Spacecraft by Radio Interferometry. *Proceedings of the IEEE*, 95(11), 2193–2201. doi:10.1109/JPROC.2007.905183.
- Lanyi, G., Border, J., Benson, J., Dhawan, V., Fomalont, E., Martin-Mur, T., McElrath, T., Romney, J., & Walker, C. (2005). Determination of angular separation between spacecraft and quasars with the very long baseline array. *IPN Progress Report*, (pp. 42–162).
- Larsen, C. F., Motyka, R. J., Freymueller, J. T., Echelmeyer, K. A., & Ivins, E. R. (2004). Rapid uplift of southern Alaska caused by recent ice loss. *Geophys J Int*, 158(3), 1118–1133. doi:10.1111/j.1365-246X.2004.02356.x.
- Larson, K. M., Ashby, N., Hackman, C., & Bertiger, W. (2007). An assessment of relativistic effects for low earth orbiters: the GRACE satellites. *Metrologia*, 44, 484–490. doi:10.1088/0026-1394/44/6/007.
- Laurichesse, D., Mercier, F., Berthias, J.-P., Broca, P., & Cerri, L. (2009). Integer Ambiguity Resolution on Undifferenced GPS Phase Measurements and its Application to PPP and satellite Precise Orbit Determination. *Navigation*, 56(2), 135–149. doi:10.1002/j.2161-4296.2009.tb01750.x.
- Lavallée, D. & Blewitt, G. (2002). Degree-1 Earth deformation from very long baseline interferometry measurements. *Geophys Res Lett*, 29(20), 1–4. doi:10.1029/2002GL015883.
- Lavallée, D. A., Dam, T. V., Blewitt, G., & Clarke, P. J. (2006). Geocenter motions from GPS: A unified observation model. *Geophys Res Lett*, 111(B5), B05405. doi:10.1029/2005JB003784.
- Lee, J., Luo, M., Pullen, S., Park, Y. S., Enge, P., & Brenner, M. (2006). Position-domain geometry screening to maximize LAAS availability in the presence of ionosphere anomalies. *IEEE/ION Position Location, and Navigation Symposium*, (pp. 506–514).
- Leick, A., Rapoport, L., & Tatarnikov, D. (2015). *GPS satellite surveying*. John Wiley & Sons.
- Lemoine, F. G., Zelensky, N. P., Chinn, D. S., Pavlis, D. E., Rowlands, D. D., Beckley, B. D., Luthcke, S. B., Willis, P., Ziebart, M., Sibthorpe, A., Boy, J. P., & Luceri, V. (2010). Towards development of a consistent orbit series for TOPEX, Jason-1 and Jason-2. *Adv Space Res*, 46, 1513–1540. doi:10.1016/j.asr.2010.05.007.
- Letellier, T., Lyard, F., & Lefevre, F. (2004). The new global tidal solution: FES2004. In *Proceeding of the Ocean Surface Topography Science Team Meeting, St. Petersburg, Florida* (pp. 4–6).
- Lieske, J. H., Lederle, T., Fricke, W., & Morando, B. (1977). Expressions for the precession quantities based upon the IAU 1976 system of astronomical constants. *Astron Astrophys*, 58, 1–16.
- Luthcke, S. B., Zelensky, N. P., Rowlands, D. G., Lemoine, F. G., & Williams, T. A. (2003). The 1-Centimeter Orbit: Jason-1 Precision Orbit Determination using GPS, SLR, DORIS and altimeter data. *Mar Geod*, 26(3-4), 399–421. doi:10.1080/714044529.
- Lyard, F., Lefevre, F., Letellier, T., & Francis, O. (2006). Modelling the global ocean tides: modern insights from FES2004. *Ocean Dynamics*, 56(5-6), 394–415. doi:10.1007/s10236-006-0086-x.

- Ma, C., Arias, E., Bianco, G., Boboltz, D., Bolotin, S., Charlot, P., Engelhardt, G., Fey, A., Gaume, R., Gontier, A.-M., et al. (2009). The Second Realization of the International Celestial Reference Frame by Very Long Baseline Interferometry. *IERS Technical Note*, 35, 1.
- Ma, C., Arias, E., Eubanks, T., Fey, A., Gontier, A.-M., Jacobs, C., Sovers, O., Archinal, B., & Charlot, P. (1998). The International Celestial Reference Frame as Realized by Very Long Baseline Interferometry. *ASTRON J*, 116(1), 516.
- Malkin, Z., Schuh, H., Ma, C., & Lambert, S. (2014). Interaction between celestial and terrestrial reference frames and some considerations for the next VLBI-based ICRF. (pp. 66–69).
- Malla, R. P. & Wu, S.-C. (1989). GPS inferred geocentric reference frame for satellite positioning and navigation. *Bulletin Géodésique*, 63(3), 263–279. doi:10.1007/BF02520476.
- Männel, B. & Rothacher, M. (2015). Observing GNSS L-band Signals: Ionospheric Corrections by co-located GNSS Measurements. In R. Haas & F. Colomer (Eds.), *Proceedings of the 22nd European VLBI Group for Geodesy and Astrometry Working Meeting* (pp. 153–157).
- Männel, B. & Rothacher, M. (2016). Ionospheric corrections for single-frequency tracking of GNSS satellites by VLBI based on co-located GNSS. *J Geod*, 90, 189–203. doi:10.1007/s00190-015-0865-6.
- Männel, B. & Rothacher, M. (2017a). Geocenter variations derived from a combined processing of LEO and ground-based GPS observations. *J Geod*, 91(8), 933–944. doi:10.1007/s00190-017-0997-y.
- Männel, B. & Rothacher, M. (2017b). The impact of GPS observations in LEO on the estimation of GPS satellite phase center offsets. *J Geod.* under review.
- Männel, B., Rothacher, M., Jetzer, P., Lecomte, S., & Rochat, P. (2016). E-GRIP: A Highly Elliptical Orbit Satellite Mission for Co-location in Space. In D. Behrend, K. Baver, & K. Armstrong (Eds.), *IVS 2016 General Meeting Proceedings* (pp. 368–372).
- Männel, B., Rothacher, M., Kodet, J., Schreiber, U., & Schmid, R. (2014). GLONASS Satellites Simultaneously Observed by VLBI, GNSS and SLR. In D. Behrend, K. Baver, & K. Armstrong (Eds.), *IVS 2014 General Meeting Proceedings: Science Press*.
- Marini, J. W. & Murray, C. (1973). *Correction of laser range tracking data for atmospheric refraction at elevations above 10 degrees*. Goddard Space Flight Center Greenbelt, MD.
- Meindl, M. (2011). *Combined Analysis of Observations from Different Global Navigation Satellite Systems*. Geodätisch-geophysikalische Arbeiten in der Schweiz. Schweizerische Geodätische Kommission. ISBN:978-3-908440-19-2.
- Meindl, M., Beutler, G., Thaller, D., Dach, R., & Jäggi, A. (2013). Geocenter coordinates estimated from GNSS data as viewed by perturbation theory. *Adv Space Res*, 51, 1047–1064. doi:10.1016/j.asr.2012.10.026.
- Mendes, V. B. & Pavlis, E. C. (2004). High-accuracy zenith delay prediction at optical wavelengths. *Geophysical Research Letters*, 31(14), L14602. doi:10.1029/2004GL020308.
- Mervant, L. (1993). *Ambiguity Resolution Techniques in Geodetic and Geodynamic Applications of the Global Positioning System*. Geodätisch-geophysikalische Arbeiten in der Schweiz. Schweizerische Geodätische Kommission.
- Meyer, U., Jäggi, A., Jean, Y., & Arnold, D. (2015a). Improving the noise model for AIUB monthly gravity field solutions. In *IUGG 2015 Prague, Czech Republic*. [http://www.bernese.unibe.ch/publist/2015/post/UM\\_IUGG15\\_final.pdf](http://www.bernese.unibe.ch/publist/2015/post/UM_IUGG15_final.pdf).
- Meyer, U., Sošnica, K., Maier, A., & Jäggi, A. (2015b). Combined GRACE / SLR monthly gravity field solutions. In *EGU 2015 Vienna, Austria*. [http://www.bernese.unibe.ch/publist/2015/post/UM\\_EGU2015\\_GRACE\\_SLR.pdf](http://www.bernese.unibe.ch/publist/2015/post/UM_EGU2015_GRACE_SLR.pdf).
- Milani, A., Nobill, A., & Farinella, P. (1987). *Non-gravitational perturbations and satellite geodesy*. Adam Hilger Ltd., Accord, MA.
- Mitrovica, J. X., Davis, J. L., & Shapiro, I. I. (1994). A spectral formalism for computing three-dimensional deformations due to surface loads: 1. Theory. *J Geophys Res*, 99(B4), 7057–7073. doi:10.1029/93JB03128.
- Montenbruck, O. (2003). Kinematic GPS positioning of LEO satellites using ionosphere-free single frequency measurements. *AEROSP SCI TECHNOL*, 7, 396–405. doi:10.1016/S1270-9638(03)00034-8.
- Montenbruck, O., Garcia-Fernandez, M., Yoon, Y., Schön, S., & Jäggi, A. (2009). Antenna phase center calibration for precise positioning of LEO satellites. *GPS solut*, 13, 23–34. doi:10.1007/s10291-008-0094-z.
- Montenbruck, O. & Gill, E. (2000). *Satellite Orbits: Models, Methods and Applications*. Springer-Verlag Berlin Heidelberg. doi:10.1007/978-3-642-58351-3.
- Montenbruck, O., Markgraf, M., Garcia-Fernandez, M., & Helm, A. (2008). GPS for Microsatellites—Status and Perspectives. In *Small Satellites for Earth Observation* (pp. 165–174). Springer. doi:10.1007/978-1-4020-6943-7\_15.
- Montenbruck, O., Schmid, R., Mercier, F., Steigenberger, P., Noll, C., Fatkulin, R., Kogure, S., & Ganeshan, A. (2015). GNSS Satellite Geometry and Attitude Models. *Adv Space Res*. 10.1016/j.asr.2015.06.019.
- Moore, P. & Wang, J. (2003). Geocentre variation from laser tracking of Lageos1/2 and loading data. *Adv Space Res*, 31(8), 1927 – 1933. doi:10.1016/S0273-1177(03)00170-4.
- Morel, L. & Willis, P. (2005). Terrestrial reference frame effects on global sea level rise determination from TOPEX/Poseidon altimetric data. *Adv Space Res*, 36(3), 358 – 368. doi:10.1016/j.asr.2005.05.113.

- Moyer, T. D. (2003). *Formulation for Observed and Computed Values of Deep Space Network Data Types for Navigation*. John Wiley & Sons, Inc. doi:10.1002/0471728470.
- Munk, W. H. & MacDonald, G. J. (1960). The Rotation of the Earth: A Geophysical Discussion.
- Neubert, R. (2001). *The Center of Mass Correction (CoM) for Laser Ranging Data of the CHAMP Reflector*. [http://ilrs.gsfc.nasa.gov/docs/CH\\_GRACE\\_COM\\_c.pdf](http://ilrs.gsfc.nasa.gov/docs/CH_GRACE_COM_c.pdf).
- Niell, A. (2000). Improved atmospheric mapping functions for VLBI and GPS. *Earth, Planets and Space*, 52(10), 699–702. doi:10.1186/BF03352267.
- Niell, A. E. (1996). Global mapping functions for the atmosphere delay at radio wavelengths. *J Geophys Res*, 101(B2), 3227–3246. doi:10.1029/95JB03048.
- Niemeier, W. (2008). *Ausgleichsrechnung: statistische Auswertemethoden*. Walter de Gruyter, 2 edition.
- Nilsson, T., Haas, R., & Elgered, G. (2007). Simulations of atmospheric path delays using turbulence models. *Proceedings of the 18th European VLBI for geodesy and astrometry working meeting*, 79, 175–180.
- Nothnagel, A. (2009). Conventions on thermal expansion modelling of radio telescopes for geodetic and astrometric VLBI. *J Geod*, 83, 787–792. doi:10.1007/s00190-008-0284-z.
- Nothnagel, A., Angermann, D., Bröger, K., Dietrich, R., Drewes, H., Görres, B., Hugentobler, U., Ihde, J., Müller, J., Oberst, J., Pätzold, M., Richter, B., Rothacher, M., Schreiber, U., Schuh, H., & Soffel, M. (2010). *Space-Time Reference Systems for Monitoring Global Change and for Navigation. Mitteilungen des Bundesamtes für Kartographie und Geodäsie*, volume 44. Verlag des Bundesamtes für Kartographie und Geodäsie, 2 edition. doi:10.1007/s00190-008-0284-z.
- Nothnagel, A., Charlot, P., Dehant, V., Fienga, A., Hase, H., Plank, L., & Schuh, H. (2013). Short Report of the IVS Working Group 5 (WG5) on Space Science Applications - An IVS Perspective. <http://ivsc.gsfc.nasa.gov/about/wg/wg5/index.html>.
- Ostini, L. (2012). *Analysis and Quality Assessment of GNSS-Derived Paramter Time Series*. Dissertation, Philosophisch-naturwissenschaftlichen Fakultät of the University of Bern.
- Otten, M., Flohrer, C., Springer, T., & Enderle, W. (2012). Multi-technique combination at observation level with NAPEOS: combining GPS, GLONASS and LEO satellites. In *EGU General Assembly Conference Abstracts*, volume 14 (pp. 7925).
- Otten, M., Flohrer, C., Springer, T., & Enderle, W. (2014). Identifying technique systematics by multi-technique combination at observation level. In *EGU General Assembly Conference Abstracts*, volume 16 (pp. 13970).
- Pánek, P., Kodet, J., & Procházka, I. (2013). Accuracy of two-way time transfer via a single coaxial cable. *Metrologia*, 50(1), 60. doi:10.1088/0026-139450160.
- Pany, A., Böhm, J., MacMillan, D., Schuh, H., Nilsson, T., & Wresnik, J. (2011). Monte Carlo simulations of the impact of troposphere, clock and measurement errors on the repeatability of VLBI positions. *J Geod*, 85(1), 39–50. doi:10.1007/s00190-010-0415-1.
- Pavlis, E. (1999). Fortnightly Resolution Geocenter Series: A Combined Analysis of Lageos 1 and 2 SLR Data. *IERS Technical Note*, 25, 75–84.
- Pavlis, E. C. (1985). On the geodetic applications of simultaneous range differences to LAGEOS. *J Geophys Res*, 90(B11), 9431–9438. doi:10.1029/JB090iB11p09431.
- Peltier, W. (1974). The impulse response of a Maxwell Earth. *Rev. Geophys. Space Phys*, 12(4), 649–669.
- Peltier, W. (2004). GLOBAL GLACIAL ISOSTASY AND THE SURFACE OF THE ICE-AGE EARTH: The ICE-5G (VM2) Model and GRACE. *Annu Rev Earth Pl Sc*, 32(1), 111–149. doi:10.1146/annurev.earth.32.082503.144359.
- Peltier, W. R. (1994). Ice age paleotopography. *Science*, (pp. 195–201).
- Petit, G. & Luzum, B. (2010). *IERS Conventions (2010). IERS Technical Note 36*. Frankfurt am Main: Verlag des Bundesamts für Kartographie und Geodäsie. ISBN 3-89888-989-6.
- Petit, G. & Luzum, B. (2013). The 2010 reference edition of the iers conventions. In Z. Altamimi & X. Collilieux (Eds.), *Reference Frames for Applications in Geosciences*, volume 138 of *IAG Symposia* (pp. 57–61).: Springer. doi:10.1007/978-3-642-32998-2\_10.
- Petrachenko, W., Niell, A., Corey, B., Behrend, D., Schuh, H., & Wresnik, J. (2012). VLBI2010: Next Generation VLBI System for Geodesy and Astrometry. In S. Kenyon, M. C. Pacino, & U. Marti (Eds.), *Geodesy for Planet Earth*, volume 136 of *IAG Symposia* (pp. 999–1005). Springer Berlin Heidelberg. doi:10.1007/978-3-642-20338-1\_125.
- Plag, H.-P. & Pearlman, M. (2009). *Global Geodetic Observing System, Meeting the Requirements of a Global Society on a Changing Planet in 2020*. Springer-Verlag Berlin Heidelberg, 2 edition. doi: 10.1007/978-3-642-02687-4.
- Plank, L. (2013). *VLBI satellite tracking for the realization of frame ties*. Dissertation, TU Vienna.
- Plank, L., Böhm, J., & Schuh, H. (2014). Precise station positions from VLBI observations to satellites: a simulation study. *J Geod*, 88(7), 659–673. doi:10.1007/s00190-014-0712-1.
- Plank, L., Böhm, J., & Schuh, H. (2015). Simulated VLBI Satellite Tracking of the GNSS Constellation: Observing Strategies. In *IAG Symposia* (pp. 1–6).: Springer Berlin Heidelberg. doi:10.1007/1345\_2015\_87.

- Prölls, G. (2008). Ionospheric storms at mid-latitude: A short review. *Midlatitude Ionospheric Dynamics and Disturbances*, 181, 9–24. doi: 10.1029/181GM03.
- Ray, J. & Altamimi, Z. (2005). Evaluation of co-location ties relating the VLBI and GPS reference frames. *J Geod*, 79(4), 189–195. doi:10.1007/s00190-005-0456-z0.
- Ray, J., Altamimi, Z., van Dam, T., & Herring, T. (2007). Principles for conventional contributions to modeled station displacements. In *IERS Workshop on Conventions, BIPM, Sèvres, France–20-21 September*.
- Ray, R. & Ponte, R. (2003). Barometric tides from ecmwf operational analyses. *Ann Geophys*, 21(8), 1897–1910.
- Rebischung, P., Altamimi, Z., & Springer, T. (2014). A collinearity diagnosis of the GNSS geocenter determination. *J Geod*, 88(1), 65–85. 10.1007/s00190-013-0669-5.
- Rebischung, P. & Garayt, B. (2013). Recent results from the igs terrestrial frame combinations. In Z. Altamimi & X. Collilieux (Eds.), *Reference Frames for Applications in Geosciences*, volume 138 of *IAG Symposia* (pp. 69–74).: Springer. doi:10.1007/978-3-642-32998-2\_12.
- Richard, J.-Y., Biancale, R., Bizouard, C., Deleflie, F., Gambis, G., König, R., Loyer, S., Sciarretta, C., Seitz, M., Spicakova, H., Springer, T., & Thaller, D. (2012). IERS Working group on Combination of Space Geodetic Techniques at the Observation Level. In *EGU General Assembly Conference Abstracts*, volume 14 (pp. 1439).
- Richter, B. (1995). Die Parametrisierung der Erdorientierung. *ZfV*, 120(3), 109–114.
- Rietbroek, R., Fritsche, M., Brunnabend, S.-E., Daras, I., Kusche, J., Schröter, J., Flechtner, F., & Dietrich, R. (2012). Global surface mass from a new combination of GRACE, modelled OBP and reprocessed GPS data. *J Geodyn*, 59-60, 64 – 71. doi:10.1016/j.jog.2011.02.003.
- Rim, H., Schutz, B., Abusali, P., & Tapley, B. (1995). Effect of GPS Orbit Accuracy on GPS-determined Topex/Poseidon Orbit. In *Proceedings of the 8th International Technical Meeting of the Satellite Division of The Institute of Navigation* (pp. 613–617). Palm Springs, CA: (ION GPS 1995).
- Rodell, M., Houser, P., Jambor, U. e. a., Gottschalck, J., Mitchell, K., Meng, C., Arsenault, K., Cosgrove, B., Radakovich, J., Bosilovich, M., et al. (2004). The global land data assimilation system. *B Am Meteorol Soc*, 85(3), 381–394. doi:10.1175/BAMS-85-3-381.
- Rodriguez-Solano, C., Hugentobler, U., Steigenberger, P., & Allende-Alba, G. (2013). Improving the orbits of GPS block IIA satellites during eclipse seasons. *Adv Space Res*, 52(8), 1511 – 1529. doi:10.1016/j.asr.2013.07.013.
- Rodríguez-Solano, C. J. (2014). *Impact of non-conservative force modeling on GNSS satellite orbits and global solutions*. Dissertation, Technische Universität München, München.
- Roggenbuck, O., Thaller, D., Engelhardt, G., Franke, S., Dach, R., & Steigenberger, P. (2015). *Loading-Induced Deformation Due to Atmosphere, Ocean and Hydrology: Model Comparisons and the Impact on Global SLR, VLBI and GNSS Solutions*, (pp. 1–7). Springer Berlin Heidelberg: Berlin, Heidelberg. doi:10.1007/1345\_2015\_214.
- Rothacher, M. (2002). *Estimation of Station Heights with GPS*, (pp. 81–90). Springer Berlin Heidelberg: Berlin, Heidelberg. doi:10.1007/978-3-662-04683-8\_17.
- Rothacher, M. (2003). Towards a rigorous combination of space geodetic techniques. In *Proc IERS Workshop on combination research and global geophysical fluids, IERS Technical Note*, volume 30 (pp. 7–18).
- Rothacher, M. (2011). Mission requirements: NanoGEM. In *MRD-Meeting*.
- Rothacher, M., Tapley, B. D., Reigber, C., König, R., Falck, C., Grunwaldt, L., Köhler, W., Massmann, F.-H., & Michalak, G. (2007). The Tracking, Occultation and Ranging (TOR) Instrument onboard TerraSAR-X and on TanDEM-X. *IEEE*.
- Rülke, A. (2009). *Zur Realisierung eines terrestrischen Referenzsystems in globalen und regionalen GPS-Netzen*. Dissertation, Technische Universität Dresden.
- Sardon, E., Rius, A., & Zarraoa, N. (1994). Ionospheric calibration of single frequency VLBI and GPS observations using dual GPS data. *Bull Geod*, 68(4), 230–235. doi:10.1007/BF00808103.
- Sarti, P., Abbondanza, C., & Altamimi, Z. (2013). Local ties and co-location sites: some considerations after the release of itrf2008. In Z. Altamimi & X. Collilieux (Eds.), *Reference Frames for Applications in Geosciences*, volume 138 of *IAG Symposia* (pp. 75–80).: Springer. doi:10.1007/978-3-642-32998-2\_13.
- Sarti, P., Abbondanza, C., Petrov, L., & Negusini, M. (2010). Height bias and scale effect induced by antenna gravitational deformations in geodetic VLBI data analysis. *J Geod*, 85(1), 1–8. doi:10.1007/s00190-010-0410-6.
- Sauber, J., Plafker, G., Molnia, B. F., & Bryant, M. A. (2000). Crustal deformation associated with glacial fluctuations in the eastern Chugach Mountains, Alaska. *J Geophys Res*, 105(B4), 8055–8077. doi:10.1029/1999JB900433.
- Savcenko, R. & Bosch, W. (2012). *EOT11a-empirical ocean tide model from multi-mission satellite altimetry*.
- Schaer, S. (1999). *Mapping and predicting the Earth's ionosphere using the Global Positioning System*. Geodätisch-geophysikalische Arbeiten in der Schweiz. Schweizerische Geodätische Kommission. ISBN:978-3-908440-01-7.
- Scherneck, H., Johansson, J., & Webb, F. (2000). Ocean loading tides in GPS and rapid variations of the frame origin. In K.-P. Schwarz (Ed.), *Geodesy Beyond 2000*, volume 121 of *IAG Symposia* (pp. 32–40). Springer Berlin Heidelberg. doi:10.1007/978-3-642-59742-8\_6.

- Scherneck, H.-G., Johansson, J. M., Koivula, H., van Dam, T., & Davis, J. L. (2003). Vertical crustal motion observed in the BIFROST project. *J Geodyn*, 35(4), 425 – 441. doi:10.1016/S0264-3707(03)00005-X.
- Schmid, R. (2009). *Zur Kombination von GPS und VLBI*. Dissertation, Technische Universität München.
- Schmid, R. (2014). IGS Antenna Working Group. In R. Dach & Y. Jean (Eds.), *International GNSS Service Technical Report 2013* (pp. 133–136).: IGS Central Bureau.
- Schmid, R., Dach, R., Collilieux, X., Jäggi, A., Schmitz, M., & Dilssner, F. (2016). Absolute IGS antenna phase center model igs08.atx: status and potential improvements. *J Geod*, 90(4), 343–364. doi:10.1007/s00190-015-0876-3.
- Schmid, R. & Rothacher, M. (2003). Estimation of elevation-dependent satellite antenna phase center variations of GPS satellites. *J Geod*, 77(7-8), 440–446. doi:10.1007/s00190-003-0339-0.
- Schmid, R., Rothacher, M., Thaller, D., & Steigenberger, P. (2005). Absolute phase center corrections of satellite and receiver antennas. Impact of global GPS solutions and estimation of azimuthal phase center variations of the satellite antenna. *GPS Solut*, 9(4), 283–293. doi:10.1007/s10291-005-0134-x.
- Schmid, R., Steigenberger, P., Gendt, G., Ge, M., & Rothacher, M. (2007). Generation of a consistent absolute phase center correction model of GPS receiver and satellite antennas. *J Geod*, 81(12), 781–798. doi:10.1007/s00190-007-0148-y.
- Schuh, H. (1987). *Die Radiointerferometrie auf langen Basen zur Bestimmung von Punktverschiebungen und Erdrotationssparametern*. Dissertation, University of Bonn. Reihe C 328, Deutsche Geodätische Kommission.
- Schuh, H. & Behrend, D. (2012). VLBI: A fascinating technique for geodesy and astrometry. *J Geodyn*, 61, 68 – 80. doi:10.1016/j.jog.2012.07.007.
- Schuh, H., Boehm, J., Engelhardt, G., MacMillan, D., Lanotte, R., Tomasi, P., Negusini, M., Vereshchagina, I., Gubanov, V., & Haas, R. (2005). Determination of tropospheric parameters within the new IVS Pilot Project. In F. Sansò (Ed.), *A Window on the Future of Geodesy: Proceedings of the International Association of Geodesy IAG General Assembly Sapporo, Japan* (pp. 125–130). Berlin, Heidelberg: Springer. doi:10.1007/3-540-27432-4\_22.
- Schuh, H. & Böhm, J. (2013). Very Long Baseline Interferometry for Geodesy and Astrometry. In G. Xu (Ed.), *Sciences of Geodesy - II* (pp. 339–376). Springer Berlin Heidelberg. doi:10.1007/978-3-642-28000-9\_7.
- Schuh, H., König, R., Ampatzidis, D., Glaser, S., Flechtner, F., Heinkelmann, R., & Nilsson, T. (2015). *GGOS-SIM: Simulation of the Reference Frame for the Global Geodetic Observing System*, (pp. 1–6). Springer: Berlin, Heidelberg. doi:10.1007/1345\_2015\_217.
- Sechi, G., Buonocore, M., Cometto, F., Saponara, M., Tramutola, A., Vinai, B., Andre, G., & Fehring, M. (2011). In-Flight Results from the Drag-Free and Attitude Control of GOCE Satellite. In *Preprints of the 18th IFAC World Congress, Milano*.
- Seeber, G. (2003). *Satellite Geodesy*. Walter de Gruyter, 2 edition.
- Seitz, M. (2009). *Kombination geodätischer Raumberechnungsverfahren zur Realisierung einer terrestrischen Referenzsystems*. Dissertation, München. Reihe C 630, Deutsche Geodätische Kommission.
- Seitz, M. (2015). Comparison of different combination strategies applied for the computation of terrestrial reference frames and geodetic parameter series. In *The 1st International Workshop on the Quality of Geodetic Observation and Monitoring Systems (QuGOMS'11)* (pp. 57–64).: Springer.
- Seitz, M., Angermann, D., Bloßfeld, M., Drewes, H., & Gerstl, M. (2012). The 2008 DGF1 realization of the ITRS: DTRF2008. *J Geod*, 86(12), 1097–1123. doi:10.1007/s00190-012-0567-2.
- Sekido, M. & Fukushima, T. (2006). A VLBI delay model for radio sources at a finite distance. *J Geod*, 80(3), 137–149.
- Sekido, M., Kondo, T., & Kawai, E. (2003). Evaluation of GPS-based ionospheric TEC map by comparing with VLBI data. *Radio Sci*, 38, 1069. doi:10.1029/2000RS002620.
- Sillard, P., Altamimi, Z., & Boucher, C. (1998). The ITRF96 realization and its associated velocity field. *Geophys Res Lett*, 25(17), 3223–3226. doi:10.1029/98GL52489.
- Soja, B., Nilsson, T., Karbon, M., Lu, C., Li, X., Balidakis, K., Anderson, J., Glaser, S., Liu, L., Mora-Diaz, J., Xu, M., Heinkelmann, R., & Schuh, H. (2015). Comparison of tropospheric delays from GPS and Kalman filtered VLBI data. In R. Haas & F. Colomer (Eds.), *Proceedings of the 22nd European VLBI Group for Geodesy and Astrometry Working Meeting* (pp. 240–244).
- Sokolova, J. & Malkin, Z. (2007). On comparison and combination of catalogues of radio source positions. *Astron Astrophys*, 474(2), 665–670. doi:10.1051/0004-6361:20077450.
- Sośnica, K. (2015). *Determination of Precise Satellite Orbits and Geodetic Parameters using Satellite Laser Ranging*. Geodätisch-geophysikalische Arbeiten in der Schweiz. Schweizerische Geodätische Kommission. ISBN:978-3-908440-38-3.
- Sośnica, K., Jäggi, A., Meyer, U., Thaller, D., Beutler, G., Arnold, D., & Dach, R. (2015). Time variable Earth's gravity field from SLR satellites. *J Geod*, (pp. 1–16). doi:10.1007/s00190-015-0825-1.
- Sovers, O. J., Fanselow, J. L., & Jacobs, C. S. (1998). Astrometry and geodesy with radio interferometry: experiments, models, results. *Rev Mod Phys*, 70, 1393–1454. doi:10.1103/RevModPhys.70.1393.
- Springer, T., Beutler, G., & Rothacher, M. (1999). A new solar radiation pressure model for GPS satellites. *GPS solutions*,

- 2(3), 50–62. doi:10.1007/PL00012757.
- Springer, T. A. (2002). *Modeling and validating orbits and clocks using the global positioning system*. Geodätisch-geophysikalische Arbeiten in der Schweiz. Schweizerische Geodätische Kommission. ISBN:978-3-908440-02-4.
- Steigenberger, P. (2009). *Reprocessing of a Global GPS Network*. Dissertation, Technische Universität München.
- Steigenberger, P., Fritsche, M., Dach, R., Schmid, R., Montenbruck, O., Uhlemann, M., & Prange, L. (2016). Estimation of satellite antenna phase center offsets for Galileo. *J Geod*, 90(8), 773–785. doi:10.1007/s00190-016-0909-6.
- Steigenberger, P., Hugentobler, U., Loyer, S., Perosanz, F., Prange, L., Dach, R., Uhlemann, M., Gendt, G., & Montenbruck, O. (2015). Galileo orbit and clock quality of the {IGS} multi-gnss experiment. *Adv Space Res*, 55(1), 269 – 281. doi:10.1016/j.asr.2014.06.030.
- Steigenberger, P., Rothacher, M., Dietrich, R., Fritsche, M., Rülke, A., & Vey, S. (2006). Reprocessing of a Global GPS Network. *J Geophys Res*, 111(B5), B05402.
- Steigenberger, P., Tesmer, V., Krügel, M., Thaller, D., Schmid, R., Vey, S., & Rothacher, M. (2007). Comparisons of homogeneously reprocessed GPS and VLBI long time-series of troposphere zenith delays and gradients. *J Geod*, 81(6-8), 503–514. doi:10.1007/s00190-006-0124-y.
- Svehla, D., Haagmans, R., Floberghagen, R., Cacciapuoti, L., Sierk, B., Kirchner, G., Rodriguez, J., Wilkinson, M., Appleby, G., Ziebart, M., et al. (2016). Geometrical SLR approach for reference frame determination - the first SLR double-difference baseline. In C. Rizos & P. Willis (Eds.), *IAG Scientific Assembly – IAG 150 Years*, IAG Symposia (pp. 1–6).
- Svehla, D. & Rothacher, M. (2003). Kinematic and Reduced-Dynamic Precise Orbit Determination of Low Earth Orbiters. *Adv Geoscience*, 1, 47–56.
- Swenson, S., Chambers, D., & Wahr, J. (2008). Estimating geocenter variations from a combination of GRACE and ocean model output. *J Geophys Res*, 113(B8). doi:10.1029/2007JB005338.
- Tapley, B. D., Bettadpur, S., Ries, J. C., Thompson, P. F., & Watkins, M. M. (2004). GRACE measurements of mass variability in the Earth system. *Science*, 305(5683), 503–505.
- Tatarskii, V. I. (1971). The effects of the turbulent atmosphere on wave propagation. In *Jerusalem: Israel Program for Scientific Translations, 1971*.
- Teke, K., Böhm, J., Nilsson, T., Schuh, H., Steigenberger, P., Dach, R., Heinkelmann, R., Willis, P., Haas, R., García-Espada, S., Hobiger, T., Ichikawa, R., & Shimizu, S. (2011). Multi-technique comparison of troposphere zenith delays and gradients during CONT08. *J Geod*, 85(7), 395–413. doi:10.1007/s00190-010-0434-y.
- Teke, K., Nilsson, T., Böhm, J., Hobiger, T., Steigenberger, P., García-Espada, S., Haas, R., & Willis, P. (2013). Troposphere delays from space geodetic techniques, water vapor radiometers, and numerical weather models over a series of continuous VLBI campaigns. *J Geod*, 87(10), 981–1001. doi:10.1007/s00190-013-0662-z.
- Tesmer, V., Steigenberger, P., Rothacher, M., Böhm, J., & Meisel, B. (2009). Annual deformation signals from homogeneously reprocessed VLBI and GPS height time series. *J Geod*, 83(10), 973–988. doi:10.1007/s00190-009-0316-3.
- Thaller, D. (2008). *Inter-technique combination based on homogeneous normal equation systems including station coordinates, Earth orientation and troposphere parameters*. Dissertation, Technische Universität München, München. Scientific Technical Report 20, GeoForschungsZentrum, Potsdam.
- Thaller, D., Dach, R., Seitz, M., Beutler, G., Mareyen, M., & Richter, B. (2011). Combination of GNSS and SLR observations using satellite co-locations. *J Geod*, 85(5), 257–272.
- Thaller, D., Krügel, M., Rothacher, M., Tesmer, V., Schmid, R., & Angermann, D. (2006). Combined Earth orientation parameters based on homogeneous and continuous VLBI and GPS data. *J Geod*, 81(6), 529–541. doi:10.1007/s00190-006-0115-z.
- Thaller, D., Sošnica, K., Dach, R., Jäggi, A., Beutler, G., Mareyen, M., & Richter, B. (2014). Geocenter coordinates from GNSS and combined GNSS-SLR solutions using satellite co-locations. In *Earth on the edge: science for a sustainable planet* (pp. 129–134). Springer. doi:10.1007/978-3-642-37222-3\_16.
- Tierno Ros, C., Böhm, J., & Schuh, H. (2011). Use of GNSS-derived TEC maps for VLBI observations. In *Proceedings of the 20th Meeting of the European VLBI Group for Geodesy and Astrometry*.
- Torge, W. & Müller, J. (2012). *Geodesy*. Walter de Gruyter.
- Tornatore, V. (2012). *PMD IVS Analysis Center*, (pp. 302–304).
- Tornatore, V. & Haas, R. (2009). Considerations on the observation of GNSS-signals with the VLBI2010 system. In *Proceedings of the 19th European VLBI for Geodesy and Astrometry Working Meeting*.
- Tornatore, V., Haas, R., Deev, D., Pegrebenko, S., Casey, S., & Calvés, G. M. (2014). Direct VLBI Observations of GLobal Navigation Satellite System Signals. In C. Rizos & P. Willis (Eds.), *Earth on the Edge: Science of a Sustainable Planet*. doi:10.1007/978-3-642-37222-3\_32.
- Tornatore, V., Haas, R., Deev, D., Pegrebenko, S., Casey, S., Calvés, G. M., & Keimpema, A. (2011). Single baseline GLONASS observations with VLBI: data processing and first results. In *Proceedings of the 20th Meeting of the European VLBI Group for Geodesy and Astrometry*.

- Tregoning, P. & van Dam, T. (2005). Effects of atmospheric pressure loading and seven-parameter transformations on estimates of geocenter motion and station heights from space geodetic observations. *J Geophys Res*, 110(B3), n/a–n/a. doi:10.1029/2004JB003334.
- Treuhaft, R. N. & Lanyi, G. E. (1987). The effect of the dynamic wet troposphere on radio interferometric measurements. *Radio Science*, 22(2), 251–265. doi:10.1029/RS022i002p00251.
- Urschl, C., Beutler, G., Gurtner, W., Hugentobler, U., & Schaer, S. (2007). Contribution of SLR tracking data to GNSS orbit determination. *Adv Space Res*, 39, 1515–1523. doi:10.1016/j.asr.2007.01.038.
- Urschl, C., Gurtner, W., Hugentobler, U., Schaer, S., & Beutler, G. (2005). Validation of GNSS orbits using SLR observation. *Adv Space Res*, 36, 412–417. doi:10.1016/j.asr.2005.03.021.
- van Dam, T., Wahr, J., Milly, P., Shmakin, A., Blewitt, G., Lavallée, D., Larson, K., et al. (2001). Crustal displacements due to continental water loading. *Geophys Res Lett*, 28(4), 651–654. doi:10.1029/2000GL012120.
- Vigue, Y., Lichten, S. M., Blewitt, G., Heflin, M. B., & Malla, R. P. (1992). Precise determination of Earth's center of mass using measurements from the global positioning system. *Geophys Res Lett*, 19(14), 1487–1490. doi:10.1029/92GL01575.
- Volland, H. (1997). Atmospheric Tides. In H. Wilhelm, W. Zürn, & H.-G. Wenzel (Eds.), *Tidal Phenomena*, volume 66 of *Lecture Notes in Earth Sciences* (pp. 221–246). Springer Berlin Heidelberg. doi:10.1007/BFb0011464.
- Wahr, J. M. (1981). Body tides on an elliptical, rotating, elastic and oceanless Earth. *Geophys J Int*, 64(3), 677–703. doi:10.1111/j.1365-246X.1981.tb02690.x.
- Wake, L. M., Lecavalier, B. S., & Bevis, M. (2016). Glacial Isostatic Adjustment (GIA) in Greenland: a Review. *Current Climate Change Reports*, 2(3), 101–111. doi:10.1007/s40641-016-0040-z.
- Walker, C. (2015). *The SCHED User Manual, Version 11.4*. <http://www.aoc.nrao.edu/~cwalker/sched/sched.html>.
- Wang, K., Meindl, M., Geiger, A., Rothacher, M., Scaramuzza, M., Troller, M., & Truffer, P. (2014). Assessment of Single-difference Ionospheric Residuals in a Regional Network for GBAS. In *Proceedings of the 27th International Technical Meeting of The Satellite Division of the Institute of Navigation (ION GNSS+ 2014)* (pp. 2384–2393). Tampa, 2014.
- Wegener, A. (1912). Die Entstehung der Kontinente. *Geologische Rundschau*, 3(4), 276–292.
- Wegener, A. (1929). *Die Entstehung der Ozeane und Kontinente*, volume 4. Friedrich Vieweg & Sohn Aktien-Gesellschaft, Braunschweig.
- Wickert, J., Rothacher, M., Brieß, K., Wahnschaffe, G., & Pilz, N. (2011). NanoGEM: Phase A.
- Wijaya, D., Böhm, J., Karbon, M., Krásná, H., & Schuh, H. (2013). Atmospheric Pressure Loading. In J. Böhm & H. Schuh (Eds.), *Atmospheric Effects in Space Geodesy* (pp. 137–157). Springer Berlin Heidelberg. doi:10.1007/978-3-642-36932-2\_4.
- Wijaya, D. D. & Brunner, F. K. (2011). Atmospheric range correction for two-frequency SLR measurements. *J Geod*, 85(9), 623–635. doi:10.1007/s00190-011-0469-8.
- Willi, D., Hollenstein, C., Rothacher, M., & Männel, B. (2015). The Cube Satellite Mission CubETH. In *Swiss national report on the geodetic activities in the years 2011-2015: presented to the XXVI General Assembly of the International Union for Geodesy and Geophysics in Prague, Czech Republic, June/July 2015* (pp. 37–39). Zürich: Schweizerische Geodätische Kommission.
- Willis, P., Fagard, H., Ferrage, P., Lemoine, F. G., Noll, C. E., Noomen, R., Otten, M., Ries, J. C., Rothacher, M., Soudarin, L., et al. (2010). The international DORIS service (IDS): toward maturity. *Adv Space Res*, 45(12), 1408–1420. doi:10.1016/j.asr.2009.11.018.
- Winternitz, L. B., Bamford, W. A., Price, S. R., Carpenter, J. R., Long, A. C., & Farahmand, M. (2016). In *39th AAS GN&C Conference* Breckenridge, USA. submitted to J Inst Navig.
- Wresnik, J. (2009). *Simulationen für die neue Generation von VLBI-Systemen*. PhD thesis, TU Vienna.
- Wresnik, J., Haas, R., Böhm, J., & Schuh, H. (2007). Modeling thermal deformation of VLBI antennas with a new temperature model. *J Geod*, 81, 423–431. doi:10.1007/s00190-006-0120-2.
- Wu, S.-C., Yunck, T. P., & Thornton, C. L. (1991). Reduced-dynamic technique for precise orbit determination of low Earth satellites. *J Guid Control Dynam*, 14(1), 24–30. doi:DOI: 10.2514/3.20600.
- Wu, X., Abbondanza, C., Altamimi, Z., Chin, T. M., Collilieux, X., Gross, R., Heflin, M., Jiang, Y., & Parker, J. (2013). Geocenter Motion and Degree-1 Surface Mass Variations - Reconciling Annual Results from Direct SLR Determination and Inverse Estimation. In *2013 GRACE Science Team Meeting*. Austin, Texas. available at <http://www.csr.utexas.edu/grace/GSTM/2013/proceedings.html>.
- Wu, X., Heflin, M. B., Ivins, E. R., Argus, D. F., & Webb, F. H. (2003). Large-scale global surface mass variations inferred from gps measurements of load-induced deformation. *Geophys Res Lett*, 30(14), 1742. doi:10.1029/2003GL017546.
- Wu, X., Heflin, M. B., Ivins, E. R., & Fukumori, I. (2006). Seasonal and interannual global surface mass variations from multisatellite geodetic data. *J Geophys Res*, 111(B9). doi:10.1029/2005JB004100.
- Wu, X., Ray, J., & van Dam, T. (2012). Geocenter motion and its geodetic and geophysical implications. *J Geodyn*, 58, 44–61. doi:10.1016/j.jog.2012.01.007.
- Wübbena, G., Schmitz, M., Mader, G., & Czopek, F. (2007). GPS Block II/IIA satellite antenna testing using the automated

- absolute field calibration with robot. In *ION GNSS*, volume 2007 (pp.42).
- Xu, G. (2003). *GPS. Theory, Algorithms and Applications*. Springer Science & Business Media. ISBN:9783540678120.
- Xu, G. (2010). *Science of Geodesy - I*. Springer-Verlag Berlin Heidelberg, 1 edition. doi:10.1007/978-3-642-11741-1.
- Yaya, P. (2002). *Apport des combinaisons de techniques astrométriques et géodésiques à l'estimation des paramètres d'orientation de la terre*. Dissertation, Observatoire de Paris.
- Yoon, Y. T., Eineder, M., Yague-Martinez, N., & Montenbruck, O. (2009). TerraSAR-X Precise Trajectory Estimation and Quality Assessment. *IEEE Transactions on geoscience and remote sensing*, 47. doi:10.1007/s10291-008-0094-z.
- Yunck, T., Wu, S.-C., Wu, J.-T., & Thornton, C. (1990). Precise tracking of remote sensing satellites with the Global Positioning System. *IEEE Geosci Remote S*, 28(1), 108–116. doi:10.1109/36.45753.
- Zhu, S., Reigber, C., & König, R. (2004). Integrated adjustment of CHAMP, GRACE, and GPS data. *J Geod*, 78(1), 103–108. doi:10.1007/s00190-004-0379-0.
- Zhu, S. Y., Reigber, C., & Kang, Z. (1997). Apropos laser tracking to GPS satellites. *J Geod*, 71(7), 423–431. doi:10.1007/s001900050110.
- Zhu, Y. S., Massmann, F.-H., Yu, Y., & Reigber, C. (2003). Satellite antenna phase center offsets and scale errors in GPS solutions. *J Geod*, 76(11), 668–672. doi:10.1007/s00190-002-0294-1.
- Ziebart, M., Adhya, S., Sibthorpe, A., Edwards, S., & Cross, P. (2005). Combined radiation pressure and thermal modelling of complex satellites: Algorithms and on-orbits tests. *Adv Space Res*, 36, 424–430. doi:10.1016/j.asr.2005.01.014.
- Ziebart, M. & Dare, P. (2001). Analytical solar radiation pressure modelling for GLONASS using a pixel array. *J Geod*, 75(11), 587–599. doi:10.1007/s001900000136.
- Zolesi, B. & Cander, L. R. (2013). *Ionospheric Prediction and Forecasting*. Springer Geophysics. Springer.



# Appendix

## A List of Co-location Satellites

The following tables provide the main characteristics for available co-locations satellites in the LEO and GNSS satellite domain. Tab. A.1 gives an overview of active and inactive satellites allowing co-location in space. Tab. A.2 lists the offset vectors between their sensor systems (so-called space ties).

### References

AIUB	<a href="ftp://ftp.unibe.ch/aiub/REPRO_2013/BSWUSER52/GEN/SAT_NONE.I08">ftp://ftp.unibe.ch/aiub/REPRO_2013/BSWUSER52/GEN/SAT_NONE.I08</a> , accessed 15-July-2015
AVISO JASON	<a href="http://www.aviso.oceanobs.com/en/calval/orbit/precise-orbit-determination-verification/index.html#c6061">http://www.aviso.oceanobs.com/en/calval/orbit/precise-orbit-determination-verification/index.html#c6061</a> , accessed 15-July-2015
CRS ICESAT	<a href="http://www.csr.utexas.edu/glas/podinfo/">http://www.csr.utexas.edu/glas/podinfo/</a> , accessed 15-July-2015
ILRS APOD	<a href="http://ilrs.gsfc.nasa.gov/missions/satellite_missions/current_missions/pn1a_general.html">http://ilrs.gsfc.nasa.gov/missions/satellite_missions/current_missions/pn1a_general.html</a> , accessed 05-August-2016
ILRS COMPASS	<a href="http://ilrs.gsfc.nasa.gov/missions/satellite_missions/current_missions/cmgl_com.html">http://ilrs.gsfc.nasa.gov/missions/satellite_missions/current_missions/cmgl_com.html</a> , accessed 15-July-2015
ILRS ENVISAT	<a href="http://ilrs.gsfc.nasa.gov/missions/satellite_missions/current_missions/env1_com.html">http://ilrs.gsfc.nasa.gov/missions/satellite_missions/current_missions/env1_com.html</a> , accessed 15-July-2015
ILRS GALILEO	<a href="http://ilrs.gsfc.nasa.gov/missions/satellite_missions/current_missions/ga04_com.html">http://ilrs.gsfc.nasa.gov/missions/satellite_missions/current_missions/ga04_com.html</a> , accessed 15-July-2015
ILRS GLONASS	<a href="http://ilrs.gsfc.nasa.gov/missions/satellite_missions/current_missions/g123_com.html">http://ilrs.gsfc.nasa.gov/missions/satellite_missions/current_missions/g123_com.html</a> , accessed 15-July-2015
ILRS GPS	<a href="http://ilrs.gsfc.nasa.gov/missions/satellite_missions/past_missions/gp35_com.html">http://ilrs.gsfc.nasa.gov/missions/satellite_missions/past_missions/gp35_com.html</a> , accessed 15-July-2015
ILRS GRACE	<a href="http://ilrs.gsfc.nasa.gov/missions/satellite_missions/current_missions/graa_com.html">http://ilrs.gsfc.nasa.gov/missions/satellite_missions/current_missions/graa_com.html</a> , accessed 15-July-2015
ILRS JASON1	<a href="http://ilrs.gsfc.nasa.gov/missions/satellite_missions/past_missions/jas1_com.html">http://ilrs.gsfc.nasa.gov/missions/satellite_missions/past_missions/jas1_com.html</a> , accessed 15-July-2015
ILRS JASON2	<a href="http://ilrs.gsfc.nasa.gov/missions/satellite_missions/current_missions/jas2_com.html">http://ilrs.gsfc.nasa.gov/missions/satellite_missions/current_missions/jas2_com.html</a> , accessed 15-July-2015
ILRS QZSS	<a href="http://ilrs.gsfc.nasa.gov/missions/satellite_missions/current_missions/qzs1_com.html">http://ilrs.gsfc.nasa.gov/missions/satellite_missions/current_missions/qzs1_com.html</a> , accessed 15-July-2015
ILRS SARAL	<a href="http://ilrs.gsfc.nasa.gov/missions/satellite_missions/current_missions/sara_com.html">http://ilrs.gsfc.nasa.gov/missions/satellite_missions/current_missions/sara_com.html</a> , accessed 15-July-2015
ILRS SWARM	<a href="http://ilrs.gsfc.nasa.gov/missions/satellite_missions/current_missions/swma_com.html">http://ilrs.gsfc.nasa.gov/missions/satellite_missions/current_missions/swma_com.html</a> , accessed 15-July-2015
ILRS TERRASAR	<a href="http://ilrs.gsfc.nasa.gov/missions/satellite_missions/current_missions/tsar_com.html">http://ilrs.gsfc.nasa.gov/missions/satellite_missions/current_missions/tsar_com.html</a> , accessed 15-July-2015
ILRS TP	<a href="http://ilrs.gsfc.nasa.gov/missions/satellite_missions/past_missions/topx_com.html">http://ilrs.gsfc.nasa.gov/missions/satellite_missions/past_missions/topx_com.html</a> , accessed 15-July-2015
MGEX COMPASS	<a href="http://igs.org/mgex/status-BDS">http://igs.org/mgex/status-BDS</a> , accessed 15-July-2015
MGEX GALILEO	<a href="http://igs.org/mgex/status-GAL">http://igs.org/mgex/status-GAL</a> , accessed 15-July-2015
MGEX GPS	<a href="http://igs.org/mgex/status-GPS">http://igs.org/mgex/status-GPS</a> , accessed 30-October-2015
MGEX IRNSS	<a href="http://igs.org/mgex/status-IRNSS">http://igs.org/mgex/status-IRNSS</a> , accessed 15-July-2015
MGEX QZSS	<a href="http://igs.org/mgex/status-QZSS">http://igs.org/mgex/status-QZSS</a> , accessed 15-July-2015

**Tab. A.1:** List of satellite missions suitable for co-location in space; mass = launch mass; \* satellite constellation; dates = first/last satellite; \* APOD has a X/S-band transmitter for VLBI

mission name	sat	COSPAR	operation		spacecraft		orbit elements			techniques			main purpose
			BoL	EOl	mass [kg]	shape	axis [km]	inc. [°]	ecc. [-]	GNSS	SLR	DORIS	
TOPEX/Poseidon		1992-052A	10.08.1992	18.01.2006	2388	box-wing	7714.4	66.04	0.000095	✓	✓	✓	altimetry
Jason-1		2001-055A	07.12.2001	03.07.2013	489	box-wing	7714.4	66.04	0.000095	✓	✓	✓	altimetry
OSTM Jason-2		2008-032A	20.06.2008		505	box-wing	7714.4	66.04	0.000095	✓	✓	✓	altimetry
Jason-3		2016-002A	17.01.2016		553	box-wing	7714.4	66.04	0.000095	✓	✓	✓	altimetry
Envisat		2002-009A	01.03.2002	08.04.2012	8211	box-wing	7138.0	98.60		✓	✓	✓	Earth observ.
CryoSat-2		2010-013A	08.04.2010		720	box-wing	7089.0	92.00		✓	✓	✓	altimetry
HY-2A		2011-043A	15.08.2011		1500	box-wing	7349.1	99.30		✓	✓	✓	altimetry
SARAL		2013-009A	25.02.2013		407	box-wing	7161.0	98.54		✓	✓	✓	altimetry
APOD		2015-049E	19.09.2015		15	box	6828.0	97.40		✓	✓	✓	co-location
CHAMP		2000-039A	15.07.2000	19.09.2010	522	box	6823.3	87.18	0.00017	✓	✓	✓	gravity field
GRACE-A		2002-012A	17.03.2002		487	box	6877.0	89.00	0.0018	✓	✓	✓	gravity field
GRACE-B		2002-012B	17.03.2002		487	box	6877.0	89.00	0.0018	✓	✓	✓	gravity field
GOCE		2009-013A	17.03.2009	10.11.2013	1077	box	6625.0	96.7	0.0045	✓	✓	✓	gravity field
SWARM	A	2013-067B	22.11.2013		468	box	6901.0	88.00		✓	✓	✓	Earth's magnetic field
	B	2013-067A	22.11.2013		468	box	6831.0	87.40		✓	✓	✓	
	C	2013-067C	22.11.2013		468	box	6831.0	87.40		✓	✓	✓	
ICESAT		2003-002A	13.01.2003	30.08.2010	970	box-wing	6961.0	94.00			✓	✓	altimetry
PROBA-2		2009-059B	16.03.2010		130	box-wing	7135.0	98.44		✓	✓	✓	altimetry
TerraSAR-X		2007-026A	15.06.2007		1230	box	6885.0	97.40	0.00014	✓	✓	✓	remote sensing
TanDEM-X		2010-030A	21.06.2010		1230	box	6885.0	97.40	0.00014	✓	✓	✓	remote sensing
Sentinel	3A	2016-011A	16.02.2016		1250	box-wing	7193	98.6		✓	✓	✓	remote sensing
GPS	35	1993-054A	30.08.1993		1816	box-wing	26566.0	55.00	0.000	✓	✓	✓	navigation
	36	1994-016A	10.03.1994		1816	box-wing	26401.0	55.00	0.006	✓	✓	✓	navigation
GLONASS*			12.10.1982		1418	box-wing	25511.0	64.80	0.006	✓	✓	✓	navigation

continued on next page

Tab. A.1 – continued from previous page

mission name	mission		COSPAR	mission		spacecraft		orbit elements			techniques			main purpose
	Sat	BoL		EoL	mass [kg]	shape	axis [km]	Inc. [°]	ecc. [-]	GNSS	SLR	DORIS		
	M	10.12.2003		1570	box-wing	25511.0	64.80	0.006	✓			navigation		
	K	26.02.2011		745	box-wing	25511.0	64.80	0.006	✓	✓		navigation		
COMPASS*	M	13.04.2007		2200	box-wing	27871.0	55.00	0.00068	✓	✓		navigation		
	I	17.01.2010		2200	box-wing	42161.2	55.60	0.00018	✓	✓		navigation		
	G	10.04.2011		2200	box-wing	42163.9	1.53	0.0023	✓	✓		navigation		
GALILEO*	IOV	21.10.2011			box-wing	29591.0	56.00	0.0001	✓	✓		navigation		
	FOC	27.03.2015			box-wing	29591.0	56.00	0.0001	✓	✓		navigation		
IRNSS*		01.07.2013		1330	box-wing	42157.0	29.00	0.002	✓	✓		navigation		
QZSS*		11.09.2010		4100	box-wing	42164.0	45.00	0.099	✓	✓		navigation		

**Tab. A.2:** List of available space ties; CoG = center of gravitation; CM = center of mass

mission	sensor	offset vector			sensor boresight vector			sensor azimuth vector				
		x [m]	y [m]	z [m]	x	y	z	x	y	z		
TOPEX/ Poseidon	CoM	0.1530	-0.416	0.0490							ILRS TP	initial
	GNSS	1.9485	-0.0405	-4.6316	0.0000	0.0000	-1.0000	1.0000	0.0000	0.0000	AIUB	w.r.t. CoM
	DORIS	0.0920	1.092	1.1820							Cerri & Ferrage (2015)	w.r.t. S/C origin; 2 GHz
	SLR	0.0920	1.092	1.0140							Cerri & Ferrage (2015)	w.r.t. S/C origin; 0.4 GHz
		1.2390	0.000	0.8760							ILRS TP	w.r.t. S/C origin
S/C frame X=in/opposite along-track, Y=solar panel rotation axis, Z=towards Earth (Cerri & Ferrage, 2015)												
JASON-1	CoM	0.9550	0.0000	0.0000							Cerri & Ferrage (2015)	initial, w.r.t. S/C origin
		0.9420	0.0000	0.0000							Luthcke et al. (2003)	w.r.t. CoG
	DORIS	1.1710	-0.5980	1.0270							Cerri & Ferrage (2015)	w.r.t. S/C origin; 2 GHz
		1.1710	-0.5980	0.8590							Cerri & Ferrage (2015)	w.r.t. S/C origin; 0.4 GHz
		1.7110	-0.5980	1.2070							Choi et al. (2004)	w.r.t. S/C origin
		1.1710	-0.5980	1.2070							Luthcke et al. (2003)	w.r.t. S/C origin
	GNSS	1.4285	0.2164	-0.4721	0.4980	0.0440	-0.8661	0.8672	-0.0250	0.4974	AIUB	w.r.t. CoM
		2.3890	-0.2180	-0.5040							Choi et al. (2004)	w.r.t. S/C origin
		2.3890	-0.2180	-0.5040							Luthcke et al. (2003)	w.r.t. S/C origin
		2.4080	0.2197	-0.5372							AVISO JASON	L1, w.r.t. S/C origin
	2.4201	0.2207	-0.5583							AVISO JASON	L2, w.r.t. S/C origin	
	2.4080	-0.2197	-0.5371							AVISO JASON	L1, w.r.t. S/C origin	
	2.4202	-0.2208	-0.5585							AVISO JASON	L2, w.r.t. S/C origin	
SLR	0.2290	0.5980	0.6828	0.0000	0.0000	1.0000	1.0000	0.0000	0.0000	AIUB	w.r.t. CoM	
	1.7110	0.5980	0.6830							Choi et al. (2004)	w.r.t. S/C origin	
	1.1580	0.5980	0.6828							Luthcke et al. (2003)	w.r.t. S/C origin	
	0.2160	0.5980	0.6830							ILRS JASON1	w.r.t. CoM	
	1.1710	0.5980	0.6820							AVISO JASON	w.r.t. S/C origin	
SLR offset optical center -49 mm ILRS JASON1												
S/C frame origin=launcher interface ring, X=in/opposite along-track, Y=solar panel rotation axis, Z=towards Earth (Cerri & Ferrage, 2015)												
OSTM/ Jason-2	CoM	0.9780	0.0001	0.0011							Cerri & Ferrage (2015)	w.r.t. S/C origin
		0.9350	0.0000	0.0000							AVISO JASON	w.r.t. S/C origin, BoL

continued on next page

Tab. A.2 – continued from previous page

mission	sensor Type	offset vector			sensor boresight vector			sensor azimuth vector			source	remark
		x [m]	y [m]	z [m]	x	y	z	x	y	z		
Envisat	GNSS	0.9420	0.0000	0.0000	0.2589	0.0	-0.9658	-0.9658	0.0	0.2589	AVISO JASON	w.r.t. S/C origin
		1.4049	-0.2170	-0.5923	0.2589	0.0	-0.9658	-0.9658	0.0	0.2589	Bertiger et al. (2010b)	w.r.t. S/C origin
		1.4241	-0.2171	-0.5942	0.2590	0.0000	-0.9660	-0.9660	0.0000	0.2590	AIUB	w.r.t. CoM
		2.4080	0.2197	-0.5372	0.2590	0.0000	-0.9660	-0.9660	0.0000	0.2590	AVISO JASON	L1, w.r.t. S/C origin
	2.4201	0.2207	-0.5583	0.2590	0.0000	-0.9660	-0.9660	0.0000	0.2590	AVISO JASON	L2, w.r.t. S/C origin	
	2.4080	-0.2197	-0.5371	0.2590	0.0000	-0.9660	-0.9660	0.0000	0.2590	AVISO JASON	L1, w.r.t. S/C origin	
	2.4202	-0.2208	-0.5585	0.2590	0.0000	-0.9660	-0.9660	0.0000	0.2590	AVISO JASON	L2, w.r.t. S/C origin	
	0.2132	0.5979	0.6829	0.0000	0.0000	0.0000	1.0000	1.0000	0.0000	0.0000	AIUB	w.r.t. CoM
	0.2170	0.5980	0.6830	0.0000	0.0000	0.0000	1.0000	1.0000	0.0000	0.0000	ILRS JASON2	w.r.t. CoM
	1.1710	0.5980	0.6820	0.0000	0.0000	0.0000	1.0000	1.0000	0.0000	0.0000	AVISO JASON	w.r.t. S/C origin
1.1940	-0.5980	1.0220	0.0000	0.0000	0.0000	1.0000	1.0000	0.0000	0.0000	Cerri & Ferrage (2015)	w.r.t. S/C origin; 2 GHz	
1.1940	-0.5980	0.8580	0.0000	0.0000	0.0000	1.0000	1.0000	0.0000	0.0000	Cerri & Ferrage (2015)	w.r.t. S/C origin; 0.4 GHz	
GPS antenna Sensor Systems S67-1575-14 + choke ring (Flohrer et al., 2011), SLR offset optical center -49 mm ILRS JASON2												
S/C frame origin=launcher interface ring, X=in/opposite along-track, Y=solar panel rotation axis, Z=towards Earth												
Envisat	CoM	-4.3650	-0.0020	-0.0390							(Cerri & Ferrage, 2015)	initial, w.r.t. S/C origin
	SLR	-4.9200	1.3500	-1.1800							ILRS ENVISAT	initial, w.r.t. S/C origin
	DORIS	-7.0520	-1.0850	-1.7250							Cerri & Ferrage (2015)	w.r.t. S/C origin; 2 GHz
		-7.0520	-1.0850	-1.5600							Cerri & Ferrage (2015)	w.r.t. S/C origin; 0.4 GHz
S/C frame X=cross-track, Y=opposite along-track, Z=pointing away from Earth												
Cryosat-2	CoM	1.6312	0.0112	0.0137							Cerri & Ferrage (2015)	w.r.t. S/C origin
		1.6570	0.0130	0.0150							Goetz et al. (2007)	w.r.t. S/C origin
	DORIS	1.8480	-0.2000	-0.7510	0.1045	0.000	-0.9945	-0.9945	0.000	-0.9945	Cerri & Ferrage (2015)	w.r.t. S/C origin; 2 GHz
		1.8480	-0.2000	-0.5980	0.1045	0.000	-0.9945	-0.9945	0.000	-0.9945	Cerri & Ferrage (2015)	w.r.t. S/C origin; 0.4 GHz
		1.8514	-0.2000	-0.7583	0.1045	0.000	-0.9945	-0.9945	0.000	-0.9945	Goetz et al. (2007)	w.r.t. S/C origin; 2 GHz
SLR		1.8345	-0.2000	-0.5972							Goetz et al. (2007)	w.r.t. S/C origin; 0.4 GHz
		1.8085	-0.9350	-0.4500							Goetz et al. (2007)	w.r.t. S/C origin
S/C frame origin=center of satellite mounting plate, X=cross-track, Y=opposite along-track, Z=pointing away from Earth												
HY-2A	CoM	1.2464	0.0000	0.0008	-	-	-	-	-	-	Cerri & Ferrage (2015)	w.r.t. S/C origin
	DORIS	0.8500	-0.7500	1.3060	-	-	-	-	-	-	Cerri & Ferrage (2015)	w.r.t. S/C origin; 2 GHz

continued on next page

Tab. A.2 – continued from previous page

mission	sensor Type	offset vector			sensor boresight vector			sensor azimuth vector			source	remark
		x [m]	y [m]	z [m]	x	y	z	x	y	z		
		0.8500	-0.7500	1.1440							Cerri & Ferrage (2015)	w.r.t. S/C origin; 0.4 GHz
S/C frame X=velocity, Y=opposite cross-track, Z=opposite radial												
SARAL	CoM	-0.0113	-0.0067	-0.6583	-	-	-	-	-	-	Cerri & Ferrage (2015)	w.r.t. S/C origin
	SLR	0.4850	0.0070	-0.2820							ILRS SARAL	w.r.t. S/C origin
	DORIS	0.8050	-0.3040	-1.1290							Cerri & Ferrage (2015)	w.r.t. S/C origin; 2 GHz
		0.6470	-0.3040	-1.1290							Cerri & Ferrage (2015)	w.r.t. S/C origin; 0.4 GHz
S/C frame X=nadir pointing, Y=orthogonal right-handed basis, Z=opposite cross-track; SLR offset optical center -43.4 mm ILRS SARAL												
APOD	CoM	0.1941	0.0	0.0								w.r.t. S/C origin
	GNSS											
	SLR VLBI	0.0470	-0.1470	0.2034							ILRS APOD	w.r.t. S/C origin
GHAMP	CoM	-0.0113	-0.0067	-0.6583							Cerri & Ferrage (2015)	w.r.t. S/C origin
	GNSS	-1.4880	0.0000	-0.3928	0.0000	0.0000	-1.0000	1.0000	0.0000	0.0000	AIUB	w.r.t. CoM
		-1.4880	0.0000	-0.3928							Jäggi (2007)	w.r.t. S/C origin
	OCC1	0.0000	0.0000	0.0000	0.0000	0.0000	1.0000	1.0000	0.0000	0.0000	AIUB	w.r.t. CoM
	OCC2	0.0000	0.0000	0.0000	0.0000	0.0000	1.0000	1.0000	0.0000	0.0000	AIUB	w.r.t. CoM
	SLR	0.0000	0.0000	0.2500	0.0000	0.0000	1.0000	1.0000	0.0000	0.0000	AIUB	w.r.t. CoM
	0.0000	0.0000	0.2500							Jäggi (2007)	w.r.t. S/C origin	
GRACE-A	GNSS	-0.0004	-0.0004	-0.4516	0.0000	0.0000	-1.0000	0.0000	-1.0000	0.0000	AIUB	w.r.t. CoM
		0.0000	0.0000	-0.4440							Montenbruck et al. (2009)	w.r.t. CoG
		-0.0004	-0.0004	-0.4514							Jäggi (2007)	w.r.t. S/C origin
	SLR	-0.6000	-0.3275	0.2178	0.0000	0.0000	1.0000	1.0000	0.0000	0.0000	AIUB	w.r.t. CoM
		-0.6000	-0.3275	0.2178	0.0000	0.0000	1.0000	1.0000	0.0000	0.0000	ILRS GRACE	w.r.t. CoM
		0.6000	-0.3275	0.2178	0.0000	0.0000	1.0000	1.0000	0.0000	0.0000	Montenbruck et al. (2009)	w.r.t. CoG
	-0.6000	-0.3275	0.2178							Jäggi (2007)	w.r.t. S/C origin	
S/C frame origin = CoG, X=along velocity, Y=orthogonal right-handed basis, Z=towards nadir (ILRS)												
GRACE-B	GNSS	0.0006	-0.0008	-0.4519	0.0000	0.0000	-1.0000	0.0000	-1.0000	0.0000	AIUB	w.r.t. CoM
		0.0000	0.0000	-0.4440							Montenbruck et al. (2009)	w.r.t. CoG

continued on next page



Tab. A.2 – continued from previous page

mission	sensor Type	offset vector			sensor boresight vector			sensor azimuth vector			source	remark
		x [m]	y [m]	z [m]	x	y	z	x	y	z		
GPS35	GNSS	0.2790	0.0000	2.6220	0.0000	0.0000	1.0000	0.0000	0.0000	0.0000	AIUB	w.r.t. CoM
	SLR	0.8626	-0.5245	0.6695							Flohrer (2008)	w.r.t S/C origin
		0.8626	-0.5245	0.6695							ILRS GPS	w.r.t S/C origin
GPS36	GNSS	0.2790	0.0000	2.8786	0.0000	0.0000	1.0000	0.0000	0.0000	0.0000	AIUB	w.r.t. CoM
	SLR	0.8626	-0.5245	0.6717							Flohrer (2008)	w.r.t S/C origin
		0.8626	-0.5245	0.6717							ILRS GPS	w.r.t S/C origin
GLONASS	GNSS	-1.8401	0.0000	0.0000							Montenbruck et al. (2015)	w.r.t CoM
	SLR	0.0000	0.0000	1.5416							Flohrer (2008)	w.r.t S/C origin
		0.0000	0.0000	1.5826							ILRS GLONASS	w.r.t. CoM
		-1.5547	0.0000	0.0000							Montenbruck et al. (2015)	w.r.t. CoM
		0.0000	0.0000	1.5545	0.0000	0.0000	1.0000	0.0000	0.0000	0.0000	AIUB	w.r.t. CoM
		-2.2981	0.5450	0.0000							Montenbruck et al. (2015)	w.r.t CoM; $L_1, L_2$
GLONASS M	GNSS	-2.0670	1.1000	0.0000							Montenbruck et al. (2015)	w.r.t CoM; $L_3$
	SLR	0.1370	0.0030	1.8740							Flohrer (2008)	w.r.t S/C origin
		0.1370	-0.0030	1.9016							ILRS GLONASS	w.r.t. CoM
		-1.8737	0.1370	0.0030							Montenbruck et al. (2015)	w.r.t. CoM
		0.1370	-0.0030	1.8735	0.0000	0.0000	1.0000	0.0000	0.0000	0.0000	AIUB	w.r.t. CoM
		-1.7601	0.0000	0.0000							Montenbruck et al. (2015)	w.r.t CoM, $L_1; L_2$
GLONASS K1	GNSS	-1.7980	0.6200	-0.5700							Montenbruck et al. (2015)	w.r.t CoM, $L_3; 701$
		-1.4260	0.0000	0.0000							Montenbruck et al. (2015)	w.r.t CoM, $L_3; 702$
	SLR	0.0000	0.0000	1.4654							ILRS GLONASS	w.r.t. CoM
		-1.4730	0.0000	0.0000							Montenbruck et al. (2015)	w.r.t. CoM
COMPASS MEO	CoM	0.0000	0.0000	1.4700	0.0000	0.0000	1.0000	0.0000	0.0000	0.0000	AIUB	w.r.t. CoM
		1.0820	-0.0004	-0.0005							ILRS COMPASS	w.r.t. S/C origin
		0.6499	-0.5625	1.1123							MGEX COMPASS	w.r.t. S/C origin
	GNSS	0.6000	0.0000	1.1000							MGEX COMPASS	w.r.t. CoM, conventional
	SLR	0.6499	-0.5625	1.1123							ILRS COMPASS	w.r.t. S/C origin
		1.0820	-0.0004	-0.0005							MGEX COMPASS	w.r.t. S/C origin

continued on next page

Tab. A.2 – continued from previous page

mission	sensor Type	offset vector			sensor boresight vector			sensor azimuth vector			source	remark
		x [m]	y [m]	z [m]	x	y	z	x	y	z		
		-0.4321	-0.5621	1.1128							Montenbruck et al. (2015)	w.r.t. CoM
S/C frame X=orthogonal right-handed basis, Y=parallel to solar panel axis, Z=boresight vector (IGS)												
COMPASS GEO	CoM	1.1525	0.0002	0.0000							ILRS COMPASS	w.r.t. S/C origin
		0.6088	-0.5702	1.0930							MGEX COMPASS	w.r.t. S/C origin
	GNSS	0.6000	0.0000	1.1000							MGEX COMPASS	w.r.t. CoM, conventional
	SLR	0.6088	-0.5702	1.0930							ILRS COMPASS	w.r.t. S/C origin
		1.1520	0.0002	0.0000							MGEX COMPASS	w.r.t. S/C origin
		-0.5437	-0.5704	1.1093							Montenbruck et al. (2015)	w.r.t. CoM
S/C frame X=orthogonal right-handed basis, Y=parallel to solar panel axis, Z=boresight vector (IGS)												
COMPASS IGSO	CoM	1.0756	0.0000	-0.0004							ILRS COMPASS	w.r.t. S/C origin
		0.6730	-0.5730	1.0930							MGEX COMPASS	w.r.t. S/C origin
	GNSS	0.6000	0.0000	1.1000							MGEX COMPASS	w.r.t. CoM, conventional
	SLR	0.6730	-0.5730	1.0930							ILRS COMPASS	w.r.t. S/C origin
		1.0756	0.0000	-0.0004							MGEX COMPASS	w.r.t. S/C origin
		-0.4026	-0.5730	1.0934							Montenbruck et al. (2015)	w.r.t. CoM
S/C frame X=orthogonal right-handed basis, Y=parallel to solar panel axis, Z=boresight vector (IGS)												
GIOVE-A	CoM	-0.0040	0.0010	0.7960							MGEX GALILEO	w.r.t. S/C origin
	GNSS	-0.0000	0.0000	1.6900							MGEX GALILEO	w.r.t. S/C origin, $E_1$
	SLR	-0.8320	-0.6540	1.4760							MGEX GALILEO	w.r.t. S/C origin
		-0.8280	-0.6550	0.6800							Montenbruck et al. (2015)	w.r.t. CoM
GIOVE-B	CoM	-0.0032	0.0034	0.9375							MGEX GALILEO	w.r.t. S/C origin
	GNSS	-0.0000	0.0000	2.2892							MGEX GALILEO	w.r.t. S/C origin, $E_1$
	SLR	-0.8075	0.2975	2.2676							MGEX GALILEO	w.r.t. S/C origin
		-0.8043	-0.2941	1.3301							Montenbruck et al. (2015)	w.r.t. CoM
Galileo IOV	CoM	1.2106	0.6289	0.5534							ILRS GALILEO	w.r.t. S/C origin
		1.2059	0.6629	0.5534							MGEX GALILEO	w.r.t. S/C origin
	GNSS	0.2000	0.0000	0.6000							MGEX GALILEO	w.r.t. CoM, conventional
	SLR	2.2980	0.5950	1.1740							ILRS GALILEO	w.r.t. S/C origin
		1.0921	-0.0339	0.6206							MGEX GALILEO	w.r.t. CoM

continued on next page

Tab. A.2 – continued from previous page

mission	sensor Type	offset vector			sensor boresight vector			sensor azimuth vector			source	remark
		x [m]	y [m]	z [m]	x	y	z	x	y	z		
S/C frame $X=$ orthogonal right-handed basis, $Y=$ parallel to solar panel axis, $Z=$ boresight vector (IGS)												
Galileo FOC	CoM	0.3317	-0.0014	0.5619							ILRS GALILEO	w.r.t. S/C origin
	GNSS	-0.1500	0.0000	1.0000							ILRS GALILEO	w.r.t. S/C origin
	SLR	-0.7030	-0.0275	1.1205							ILRS GALILEO	w.r.t. S/C origin
IRNSS		-1.0347	-0.0140	0.5586							Montenbruck et al. (2015)	w.r.t. CoM; FOC-1
	CoM	0.9360	0.0020	-0.0036							MGEX IRNSS	w.r.t. S/C origin
	GNSS	1.2808	-0.0114	-0.0001							Montenbruck et al. (2015)	w.r.t. CoM
QZSS QZS-1	SLR	1.3720	0.5260	1.1165							MGEX IRNSS	w.r.t. S/C origin
		1.1200	0.4360	-0.5280							Montenbruck et al. (2015)	w.r.t. S/C origin
	CoM	-0.0010	0.0016	1.8184							ILRS QZSS	w.r.t. S/C origin
QZSS-1		-0.0009	0.0029	1.8192							MGEX QZSS	w.r.t. S/C origin, BoL
		-0.0009	0.0031	1.8512							MGEX QZSS	w.r.t. S/C origin, EoL
	GNSS	1.1509	0.6971	3.0151							MGEX QZSS	w.r.t. CoM; L-Ant; $L_1$
		0.0009	-0.0029	3.1979							MGEX QZSS	w.r.t. CoM; LS-Ant; $L_1$
	SLR	-1.1500	-0.5500	4.5053							ILRS QZSS	w.r.t. S/C origin
		-1.1491	-0.5529	2.6854						Montenbruck et al. (2015)	w.r.t. CoM	

## B Satellite Macro-models

Tab. B.1 provides macro-models for the different GPS block types and for OSTM/Jason-2 and GRACE.

**Tab. B.1:** Satellite-specific macro-model for GPS satellites, OSTM/Jasoin-2, and GRACE; Geometry: A=1 flat, A=2 cylindrical; B=0 non rotating, B=1 rotating; Size; Optical: reflection coefficient  $\delta$ ; diffusion coefficient  $\rho$ ; absorption coefficient  $\alpha$ ; *nr* value is not relevant as surface is not exposed to corresponding forces

Type		Geometry			front (+ side)						Geometry			rear (- side)					
		A	B	[m <sup>2</sup> ]	Visible light			Infrared			A	B	[m <sup>2</sup> ]	Visible light			Infrared		
					$\delta$	$\rho$	$\alpha$	$\delta$	$\rho$	$\alpha$				$\delta$	$\rho$	$\alpha$	$\delta$	$\rho$	$\alpha$
GPS I <sup>ab</sup>	X	1	0	2.05	0.13	0.43	0.43	<i>nr</i>	<i>nr</i>	<i>nr</i>	1	0	2.05	0.13	0.43	0.43	<i>nr</i>	<i>nr</i>	<i>nr</i>
	Y	1	0	2.27	0.15	0.46	0.39	<i>nr</i>	<i>nr</i>	<i>nr</i>	1	0	2.27	0.15	0.46	0.39	<i>nr</i>	<i>nr</i>	<i>nr</i>
	Z	1	0	1.51	0.22	0.64	0.14	0.1	0.1	0.8	1	0	1.51	0.09	0.37	0.54	<i>nr</i>	<i>nr</i>	<i>nr</i>
	S	1	1	6.05	0.04	0.24	0.72	0.1	0.1	0.8	1	1	6.05	<i>nr</i>	<i>nr</i>	<i>nr</i>	0.1	0.1	0.8
GPS II /IIA <sup>abcd</sup>	X	1	0	2.72	0.40	0.10	0.50	<i>nr</i>	<i>nr</i>	<i>nr</i>	1	0	2.72	0.40	0.10	0.50	<i>nr</i>	<i>nr</i>	<i>nr</i>
	Y	1	0	3.38	0.39	0.10	0.51	<i>nr</i>	<i>nr</i>	<i>nr</i>	1	0	3.38	0.39	0.10	0.51	<i>nr</i>	<i>nr</i>	<i>nr</i>
	Z	1	0	2.88	0.45	0.11	0.44	0.1	0.1	0.8	1	0	2.88	0.03	0.08	0.58	<i>nr</i>	<i>nr</i>	<i>nr</i>
	S	1	1	11.8	0.06	0.20	0.74	0.1	0.1	0.8	1	1	11.8	<i>nr</i>	<i>nr</i>	<i>nr</i>	0.1	0.1	0.8
GPS IIR <sup>e</sup>	X	1	0	4.11	0.06	0.00	0.94	<i>nr</i>	<i>nr</i>	<i>nr</i>	1	0	4.11	0.06	0.00	0.94	<i>nr</i>	<i>nr</i>	<i>nr</i>
	Y	1	0	4.46	0.06	0.00	0.94	<i>nr</i>	<i>nr</i>	<i>nr</i>	1	0	4.46	0.06	0.00	0.94	<i>nr</i>	<i>nr</i>	<i>nr</i>
	Z	1	0	4.25	0.06	0.00	0.94	0.1	0.1	0.8	1	0	4.25	0.06	0.00	0.94	<i>nr</i>	<i>nr</i>	<i>nr</i>
	S	1	1	13.9	0.04	0.25	0.71	0.1	0.1	0.8	1	1	13.9	<i>nr</i>	<i>nr</i>	<i>nr</i>	0.1	0.1	0.8
GPS IIF <sup>f</sup>	X	1	0	5.72	0.45	0.11	0.44	<i>nr</i>	<i>nr</i>	<i>nr</i>	1	0	5.72	0.45	0.11	0.44	<i>nr</i>	<i>nr</i>	<i>nr</i>
	Y	1	0	7.01	0.45	0.11	0.44	<i>nr</i>	<i>nr</i>	<i>nr</i>	1	0	7.01	0.45	0.11	0.44	<i>nr</i>	<i>nr</i>	<i>nr</i>
	Z	1	0	5.40	0.45	0.11	0.44	0.1	0.1	0.8	1	0	5.40	0.00	0.00	1.00	<i>nr</i>	<i>nr</i>	<i>nr</i>
	S	1	1	22.3	0.04	0.19	0.77	0.1	0.1	0.8	1	1	22.3	<i>nr</i>	<i>nr</i>	<i>nr</i>	0.1	0.1	0.8
OSTM/ Jason-2 <sup>g</sup>	X	1	0	1.65	0.44	0.21	0.00	0.43	0.18	0.03	1	0	1.65	0.43	0.22	0.01	0.41	0.19	0.01
	Y	1	0	3.00	0.36	0.38	0.27	0.33	0.34	0.25	1	0	3.00	0.32	0.40	0.31	0.27	0.37	0.30
	Z	1	0	3.10	0.24	0.40	0.33	0.24	0.38	0.31	1	0	3.10	0.32	0.37	0.27	0.30	0.34	0.24
	S	1	1	9.80	0.34	0.01	0.65	0.10	0.10	0.80	1	1	9.80	0.00	0.30	0.70	0.04	0.04	0.93
OSTM/ Jason-2 <sup>h</sup>	X	1	0	1.65	0.09	0.28	0.21	0.43	0.18	0.03	1	0	1.65	0.43	0.21	0.01	0.41	0.19	0.01
	Y	1	0	3.00	1.19	0.01	0.01	0.33	0.34	0.25	1	0	3.00	1.20	0.00	0.00	0.27	0.37	0.30
	Z	1	0	3.10	0.24	0.40	0.33	0.24	0.38	0.31	1	0	3.10	0.32	0.37	.27	0.30	0.34	0.24
	S	1	1	9.80	0.34	0.01	0.65	0.10	0.10	0.80	1	1	9.80	0.00	0.30	0.70	0.04	0.04	0.93
GRACE <sup>i</sup>	1	1	0	0.96	0.40	0.26	0.34	0.23	0.15	0.62	1	0	0.96	0.40	0.26	0.34	0.23	0.15	0.62
	2	1	0	3.16	0.05	0.30	0.65	0.03	0.16	0.81	1	0	3.16	0.05	0.30	0.65	0.03	0.16	0.81
	3	1	0	0.23	0.40	0.26	0.34	0.23	0.15	0.62	1	0	0.23	0.40	0.26	0.34	0.23	0.15	0.62
	4	1	0	6.07	0.68	0.20	0.12	0.19	0.06	0.75	1	0	2.17	0.05	0.30	0.65	0.03	0.16	0.81

<sup>a</sup> Fliegel et al. (1992), surfaces are X = normal to sun illuminated surface, Y = solar panel rot axis, Z = to the Earth, S = solar panel

<sup>b</sup> Feltens (1991)

<sup>c</sup> Wübbena et al. (2007)

<sup>d</sup> Bar-Sever et al. (2009)

<sup>e</sup> Fliegel & Gallini (1996), surface definition see <sup>a</sup>

<sup>f</sup> Ziebart & Dare (2001), surface definition see <sup>a</sup>

<sup>g</sup> AVISO (2015), surfaces are X = away from the sun, Y = solar panel rot axis, Z = to the Earth, S = solar panel

<sup>h</sup> Cerri & Ferrage (2015), surfaces are X = away from the sun, Y = solar panel rot axis, Z = to the Earth, S = solar panel

<sup>i</sup> Bettadpur (2012); surfaces are 1=front/rear, 2=outer starboard/part, 3= inner starboard/port, 4=nadir/zenith

## C Station list

**Tab. C.1:** List of stations used within the project, co-located instruments are listed as well; list is not exhaustive; <sup>1</sup> IGS station used in the ground-LEO combination (Chap. 5), <sup>2</sup> core station in the weekly combination, <sup>3</sup> core station in long-term solution; <sup>4</sup> datum station in VLBI CONT14 processing (Sect. 2.3.3); rem. = removed IDS stations

IERS DOMES	Location	IGS Site	ILRS Site	IVS Site	IDS Site
10002	Grasse, France	GRAS GRAC	GRSM (7845)		GR4B
10302	Tromso, Norway	TROM			rem.
10317	Ny Ålesund, Svalbard	NYAL <sup>1,2,3</sup>		NYALES20 (7331, Ny) <sup>4</sup>	SPJB
10402	Onsala, Sweden	ONSA		ONSALA85 (7212, O8) ONSALA60 (7213, On) <sup>4</sup>	
10503	Metsahovi, Finland	METS	METL (7806)	METSAHOV (7385, Mh)	MEUB
11001	Graz, Austria	GRAZ	GRZL (7839)		
12205	Borowiec, Poland	BOR1	BORL (7811)		
12302	Riga, Latvia	RIGA	RIGL (1884)		
12313	Irkutsk, Russia	IRKT <sup>1,2</sup>	IRKL (1891)		
12362	Arti, Russia	ARTU <sup>1,2,3</sup>			
12337			SIML (1873)		
12338	Badary, Russia	BADG	BADL (1890)	BADARY (7382, Bd) <sup>4</sup>	BADB
12350	Svetloe, Russia	SVTL	SVEL (1888)	SVETLOE (7380, Sv)	
12351	Zelenchukyska, Russia	ZECK	ZELL (1889)	ZELENCHK (7381, Zc) <sup>4</sup>	
12355	Petropavlovsk, Russia	PETS <sup>1,2,3</sup>			
12356	Golosiiv, Ukraine	GLSV <sup>1,2,3</sup>	GLSL (1824)		
12360	Tixi, Russia	TIXI <sup>1,2</sup>			
12372	Altay, Russia		ALTL (1879)		
12711	Medicina, Italy	MEDI		MEDICINA (7230, Mc)	
12717	Noto, Italy	NOTO NOT1		NOTO (7547, Nt)	
12734	Matera, Italy	MATE MAT1	MATM (7941)	MATERA (7243, Ma) <sup>4</sup>	
12725	Cagliari, Italy	CAGZ <sup>1,2,3</sup>	CAGL (7548)		
13212	Herstmonceux, United Kingdom	HERS	HERL (7840)		
13402	San Fernando, Spain	SFER	SFEL (7824)		
13420	Yebes, Spain	YEBE YEB1		YEBES (7333, Yb) YEBES40M (7386, Ys) <sup>4</sup>	
13506	Westerbork, Netherlands	WSRT <sup>1,2,3</sup>			
14001	Zimmerwald, Switzerland	ZIMM ZIM2 ZIMJ	ZIML (7810)		
14106	Potsdam, Germany	POT3	POT3 (7841)		
14201	Wettzell, Germany	WTZR <sup>1,2</sup> WTZS WTZA WTZZ	WETL (8834) SOSW (7825)	WETTZELL (7224, Wz) <sup>4</sup> WETTZ13N (7387, Wn) WETTZ13S (7388, Ws)	
14302	Nicosia, Cyprus	NICO <sup>1,2,3</sup>			
20103	Namas, Saudi Arabia	NAMA <sup>1</sup>			
21601	Beijing, China	BJFS	BEIL (7249)		
21605	Shanghai, China	SHAO <sup>1,2</sup>	SHA2 (7821)	SESHAN25 (7727, Sh)	
21609	Kunming, China	KUNM <sup>1,2</sup>	KUNL (7820)	KUNMING (7367, Km)	

continued on next page

Tab. C.1 – continued from previous page

IERS DOMES	Location	IGS Site	ILRS Site	IVS Site	IDS Site
21611	Changchun, China	CHAN	CHAL (7237)		
21612	Urumqi, China	URUM <sup>1,2,3</sup>	URUL (7355)	URUMQI (7330)	
21704	Koganei, Japan	KGNI <sup>1</sup>	KOGC (7308) KOGL (7328)	KOGANEI (7327, Kg)	
21726	Simosato, Japan	SMST	SISL (7838)		
21730	Tsukuba, Japan	TSUK TSKB <sup>1</sup> TKBA		TSUKUB32 (7345, Ts)	
21749	Tanegashima, Japan	GMSD	GMSL (7358)		
22306	Bangalore, India	IISC <sup>1,2,3</sup>			
30802	Diego Garcia, United Kingdom	DGAR <sup>1,2,3</sup>			
30302	Hartebeesthoek, South Africa	HARB HRAO <sup>1,2,3</sup>	HARL (7501)	HARTRAO (7232, Hh) HART15M (7378, Ht) <sup>4</sup>	HBMB
31303	Maspalomas, Spain	MAS1 <sup>1,2</sup>			
31906	Ponta Delgada, Portugal	PDEL <sup>1,2,3</sup>			PDOC
32809	Libreville, Gabon	NKLG <sup>1,2,3</sup>			LICB
40101	St John's, Canada	STJO <sup>1,2,3</sup>			STKB
40104	Algonquin, Canada	ALGO <sup>1,2,3</sup>		ALGOPARK (7282, Ap)	
40135	Flin Flon, Canada	FLIN <sup>1,2,3</sup>			
40408	Fairbanks, USA	FAIR <sup>1,2,3</sup>		GILCREEK (7225, Gc)	rem.
40424	Kauai, USA	KOKB KOKV		KOKEE (7298, Kk) <sup>4</sup>	KOLB
40433	Quincy, USA	QUIN <sup>1,2</sup>			
40440	Westford, USA	WES1 WES2		WESTFORD (7209, Wf) <sup>4</sup>	
40442	McDonald Observatory, USA	MDO1	MDOL (7080)	FD-VLBA (7613, Fd)	
40445	Haleakala, Hawaii	MAUI	HA4T (7119)		
40451	Greenbelt, USA	GODE <sup>1,2,3</sup> GODZ GODN GODS	GODL (7105)	GGAO12M (7622, Gs) GGAO7108 (7108, Gg)	GRFB
40477	Mauna Kea, USA	MKEA <sup>1,2,3</sup>		MK-VLBA (7617, Mk)	
40497	Monument Peak, USA	MONP	MONL (7110)		
41201	Managua, Nicaragua	MANA <sup>1,2</sup>			MNAC
41508	San Juan, Argentina		SJUL (7406)		
41510	La Plata, Argentina	LPGS <sup>1,2</sup>			
41514	Salta, Argentina	UNSA <sup>1,2,3</sup>			
41602	Forteleza, Brazil	BRFT <sup>1,2,3</sup>		FORTLEZA (7297, Ft)	
41703	Easter Island, Chile	ISPA <sup>1,2,3</sup>			rem.
41705	Santiago, Chile	SANT <sup>1</sup>		SANTIA12 (1404, St)	rem.
41716	Punta Arenas, Chile	PARC <sup>1,2,3</sup>			
42005	Santa Cruz, Bolivia	GLPS <sup>1,2,3</sup>			SCRB
42202	Arequipa, Peru	AREG	AREL (7403)		ARFB
43005	Kangerlussuaq, Greenland	KELY <sup>1,2,3</sup>			
50103	Tidbinbilla, Australia	TID2 TIDB <sup>1,2,3</sup>		TIDBIN64 (1543, Ti)	ORRA
50107	Yarragadee, Australia	YAR2 YAR3 YARR	YARL (7090)	YARRA12M (7376, Yg)	YASB

continued on next page

Tab. C.1 – continued from previous page

IERS DOMES	Location	IGS Site	ILRS Site	IVS Site	IDS Site
50116	Hobart, Australia	HOB1 HOB2		HOBART26 (7242, Ho) <sup>4</sup> HOBART12 (7374, Hb)	
50119	Mt Stromlo, Australia	STR1	STL3 (7825)		MSPB
50127	Coco Islands, Australia	COCO <sup>1,2</sup>			
50137	Alice Springs, Australia	ALIC <sup>1,2</sup>			
50139	Karratha, Australia	KARR <sup>1,2,3</sup>			
50209	Auckland, New Zealand	AUCK <sup>1,2,3</sup>			
50243	Warkworth, New Zealand	WARK		WARK12M (7377, Ww)	
59968	Katherine, Australia	KAT1 KAT2		KATH12M (7375, Ke)	
66001	Mc Murdo, Antarctica	MCM <sup>1,2,3</sup>			
66006	Syowa, Antarctica	SYOG <sup>1,2</sup>			SYQB
66008	O'higgins, Antarctica	OH1 <sup>1,2,3</sup>		OHIGGINS (7245, Oh)	
66009	Sanea, Antarctica	VESL <sup>1,2,3</sup>			
66011	Casey, Antarctica	CAS1 <sup>1,2</sup>			
82301	Dededo, Guam	GUUG <sup>1,2</sup>			rem.
91201	Port-aux-Francais, Kerguelen	KERG <sup>1,2,3</sup>			KEVC
91501	Dumont d'Urville, Antarctica	DUM1 <sup>1,2,3</sup>			ADEA
92201	Tahiti, French Polynesia	TH1 <sup>1,2,3</sup> TAH1	THTL (7124)		PAUB
97401	La Reunion, France	REUN <sup>1,2</sup>			REUB